TECHNISCHE
UNIVERSITÄT
DARMSTADT

PHASE STRUCTURE AND EQUATION OF STATE OF DENSE STRONG-INTERACTION MATTER

Vom Fachbereich Physik
der Technischen Universität Darmstadt

zur Erlangung des Grades
Doctor rerum naturalium
(Dr. rer. nat.)

genehmigte Dissertation von
M.Sc. Marc Leonhardt
geb. in Offenbach a. M.

Referent: Prof. Dr. Jens Braun
Korreferent: Prof. Ph.D. Achim Schwenk

Tag der Einreichung: 16.07.2019
Tag der Prüfung: 14.10.2019

Darmstadt 2019
D17

Phase Structure and Equation of State of Dense Strong-Interaction Matter
Phasenstruktur und Zustandsgleichung von dichter, stark wechselwirkender Materie

Genehmigte Dissertation von M.Sc. Marc Leonhardt, geb. in Offenbach a. M.

Referent: Prof. Dr. Jens Braun
Korreferent: Prof. Ph.D. Achim Schwenk

Tag der Einreichung: 16.07.2019
Tag der Prüfung: 14.10.2019

Darmstadt 2019 - D17

Bitte zitieren Sie dieses Dokument als:
URN: urn:nbn:de:tuda-tuprints-92559
URL: https://tuprints.ulb.tu-darmstadt.de/id/eprint/9255

ABSTRACT

The understanding of matter at extreme temperatures or densities is of great importance since it is essential to various fundamental phenomena and processes, such as the evolution of the early universe or the description of astrophysical objects. Under such conditions, the governing interaction is the strong force between the elementary constituents of matter, i.e., quarks and gluons, which is described by quantum chromodynamics (QCD).

In this work, we study the phase structure of dense strong-interaction matter with two massless quark flavors at finite temperature and the equation of state in the zero-temperature limit employing functional renormalization group techniques. Four-quark self-interactions, which play an essential role in the description of the strongly correlated low-energy dynamics, are fully incorporated in the sense of *Fierz*-complete interactions only constrained by symmetries.

In order to analyze the importance of *Fierz* completeness and how incomplete approximations affect the predictive power, we study different versions of the *Nambu–Jona-Lasinio* model. The predictions from such low-energy effective models for dense QCD matter are of great interest as this regime is at least difficult to access with fully first-principles approaches such as lattice Monte Carlo techniques. We analyze the fixed-point and phase structure at finite temperature and quark chemical potential based on the RG flow of the four-quark interactions at leading order of the derivative expansion. By studying the relative strengths of the various four-quark couplings, we obtain insights into condensate formation in phases governed by spontaneous symmetry breaking. We find that *Fierz* completeness is particularly important at large quark chemical potentials and leads to a shift of the phase boundary to higher temperatures.

The incorporation of dynamical gauge fields allows us to adopt an approach directly based on quark-gluon dynamics. Without any fine-tuning, we observe a natural emergence of dominances among the four-quark couplings indicating spontaneous chiral symmetry breaking at small chemical potentials and a color superconducting phase at high chemical potentials. These dominances are found to be very robust against details of the approximations in the gauge sector, indicating that the dynamics within the quark sector are crucial in this respect.

Toward lower energy scales, we recast the RG flow in the form of a quark-meson-diquark-model truncation in order to access the regime governed by spontaneously broken symmetries. This allows us to derive for the first time constraints on the equation of state of cold isospin-symmetric QCD matter at high densities in a *Fierz*-complete setting directly anchored in the fundamental gauge theory. Our results are found to be remarkably consistent with chiral effective field theory approaches applicable at smaller densities and with perturbative QCD approaches at very high densities. At supranuclear densities, we observe that condensation effects are essential and give rise to a maximum in the speed of sound which exceeds the asymptotic non-interacting limit, with potential implications for astrophysical applications.

ZUSAMMENFASSUNG

Das Verständnis von Materie bei extremen Temperaturen oder Dichten ist von großer Bedeutung für fundamentale Vorgänge und Prozesse, zum Beispiel die Entwicklung unseres frühen Universums oder die Beschreibung von astrophysikalischen Objekten. Bei solchen Bedingungen ist die starke Wechselwirkung die vorherrschende Kraft zwischen den elementaren Bestandteilen der Materie, den Quarks und Gluonen, beschrieben durch die Quantenchromodynamik (QCD).

In dieser Arbeit untersuchen wir sowohl die Phasenstruktur von dichter, stark-wechselwirkender Materie mit zwei masselosen Quarktypen bei endlicher Temperatur als auch deren Zustandsgleichung im Grenzfall verschwindender Temperatur mit Hilfe der funktionalen Renormierungsgruppe. Vier-Quark-Wechselwirkungen, welche eine wichtige Rolle in der Beschreibung der stark korrelierten Niederenergiedynamik spielen, sind vollständig eingebunden im Sinne von *Fierz*-vollständigen Wechselwirkungen, welche lediglich durch Symmetrieüberlegungen eingegrenzt sind.

Um die Bedeutung von *Fierz*-Vollständigkeit sowie die Auswirkungen von *Fierz*-unvollständigen Näherungen auf die Vorhersagekraft von theoretischen Studien zu untersuchen, betrachten wir verschiedene Varianten des *Nambu–Jona-Lasinio*-Modells. Die Vorhersagen von solchen Niederenergiemodellen für dichte QCD-Materie sind von großem Interesse, da ab-initio Zugänge, wie zum Beispiel Gitter-Monte-Carlo-Simulationen, in diesem Bereich allenfalls nur sehr schwer anwendbar sind. Wir analysieren die Fixpunkt- und Phasenstruktur bei endlicher Temperatur und endlichem quarkchemischen Potential auf Grundlage des Renormierungsgruppenflusses der Vier-Quark-Wechselwirkungen in führender Ordnung der Ableitungsentwicklung. Durch die Analyse der relativen Kopplungsstärken gewinnen wir Einblicke in die Kondensatbildung innerhalb der symmetriegebrochenen Phase. Wir zeigen auf, dass *Fierz*-Vollständigkeit besonders wichtig bei hohem quarkchemischen Potential ist und zu einer Verschiebung der Phasengrenze hin zu höheren Temperaturen führt.

Die Einbindung von dynamischen Eichfeldern verschafft uns einen direkt auf der Quark-Gluon-Dynamik basierenden Zugang. Wir beobachten eine natürliche Entstehung von Dominanzen bestimmter Vier-Quark-Wechselwirkungskanälen, welche die spontane Brechung der chiralen Symmetrie bei niedrigen quarkchemischen Potentialen sowie eine farbsupraleitende Phase bei hohem quarkchemischen Potential anzeigt, und dies gänzlich ohne dass Parameter gezielt eingestellt würden. Diese Dominanzen stellen sich als sehr robust gegenüber Details in den betrachteten Eichsektor-Näherungen heraus, was auf die Bedeutung der Dynamik innerhalb des Quarksektors in dieser Hinsicht hinweist.

Zu niedrigeren Energien hin beschreiben wir den Renormierungsgruppenfluss in Form einer Quark-Meson-Diquark-Modell-Trunkierung, um Zugriff auf die symmetriegebrochene Phase zu erhalten. Dies erlaubt uns erstmalig, die Zustandsgleichung von isospinsymmetrischer, kalter

QCD-Materie bei hohen Dichten mit Hilfe eines *Fierz*-vollständigen Zugangs einzuschränken, welcher direkt in der fundamentalen Eichtheorie verankert ist. Unsere Ergebnisse sind bemerkenswert konsistent sowohl mit Berechnungen basierend auf chiraler effektiven Feldtheorie bei kleinen Dichten als auch mit störungstheoretischen Rechnungen bei sehr hohen Dichten. Wir stellen fest, dass bei supranuklearen Dichten Kondensationseffekte essentiell sind und zu einem Maximum in der Schallgeschwindigkeit führen, welches den asymptotischen Wert des nicht-wechselwirkenden Grenzfalls übersteigt, mit potentieller Bedeutung für astrophysikalische Anwendungen.

CONTENTS

1

INTRODUCTION

1.1 Challenges in strong-interaction matter physics

The subatomic realm of the visible matter in our universe is very successfully described by the *Standard Model of particle physics*. The Standard Model is a quantum field theory of elementary particles as the building blocks of the matter surrounding us and describes three of the four fundamental forces, i.e., the electromagnetic interaction, the weak interaction and the strong interaction. The interactions are constructed as gauge field theories which give rise to gauge bosons as the mediators of these interactions. The fundamental particles are thus categorized either as matter particles, i.e., the quarks and the leptons, or as force carriers.[1] From a modern perspective, the Standard Model might be considered as an effective field theory for a more fundamental theory which becomes manifest at higher energies [5]. Indeed, the Standard Model is incomplete and leaves certain aspects unanswered. Most prominently, it does not include gravity nor does it explain the existence, let alone the nature, of dark matter and dark energy [6]. Nevertheless, it describes the fundamental structure of visible matter with an unmatched comprehensiveness and can be considered to be the most successful theory ever devised, with an astonishing agreement between theoretical calculations and experimental high-precision measurements. All the particles predicted by the Standard Model have been confirmed, with the discovery of the *Higgs* boson at CERN's Large Hadron Collider marking the most recent success [7, 8].

The part of the Standard Model describing the quarks and their interaction via the strong force is called *quantum chromodynamics* (QCD). The quarks are the fundamental constituents of the hadrons which are subdivided into baryons and mesons. While baryons are composed of three quarks, the mesons consist of quark-antiquark pairs. Typical examples for baryons are the protons and the neutrons. The nuclear force binding them together into nuclei is a residual force of the strong interaction between the quarks. This example already illustrates

---

[1] The *Higgs* particle defies this classification. This scalar boson is associated with the *Higgs* mechanism which is responsible for generating the masses of the gauge bosons of the weak interaction as well as the current quark masses [1–4].

that quarks and their strong interaction give rise to various manifestations. Therefore, the terms *QCD matter* or *strong-interaction matter* are used to broadly refer to matter governed by QCD in its various forms.

The concept of quarks as the elementary constituents of hadrons was originally proposed by *Gell-Mann* [9] and *Zweig* [10, 11] independently to explain and organize the “hadron zoo” emerging from the discovery of a plethora of new particles considered “elementary” in the 1950s and 1960s. In his *Nobel* prize acceptance speech, *Willis Lamb* is famously quoted as saying: “I have heard it said that ‘the finder of a new elementary particle used to be rewarded by a *Nobel* prize, but such a discovery now ought to be punished by a $10,000 fine’ ” [12]. With the quark model, the observed spectrum of the hadrons and their quantum numbers could be successfully explained. The “Eightfold Way”, devised earlier by *Gell-Mann* [13] and *Ne’eman* [14] in order to classify and to structure the hadrons, follows naturally from the quark model. Although initially faced with skepticism as attempts to directly observe quarks individually have not been successful, strong indications in favor of the quark model, i.e., hadrons possessing an internal structure of point charges, were provided by deep inelastic scattering experiments [15–19]. It was eventually established by the discovery of the J/ψ meson [20, 21], as in line with the quark model this discovery could be readily explained by proclaiming the existence of a heavier quark. The existence of such a heavier quark was in fact already proposed earlier by *Bjorken* and *Glashow* [22, 23].

Quarks are fermionic spin-1/2 particles of fractional charge. They come in so-called *flavors* named *up*, *down*, *strange*, *charm*, *bottom* and *top*. In much the same way as the discovery of the J/ψ meson entailed the charm quark, later discoveries [24–26] led to the introduction of the third generation of quarks consisting of the bottom and the top quark. In addition to flavor and the electromagnetic charge, quarks carry a *color* charge which takes on the values *red*, *green* or *blue*. The additional color quantum number was originally introduced by *Greenberg* [27] in order to resolve the apparent violation of the *Pauli* exclusion principle by the observation of the fermionic Δ^{++} particle and its construction within the framework of the quark model: This particle consists of three up quarks and the totally antisymmetric color wavefunction must ensure the overall antisymmetry of these three quarks, which are apart from that all in the same state.

The color charge of the quarks in QCD plays a very similar role as the electromagnetic charge in *quantum electrodynamics* (QED). Particles carrying an electromagnetic charge are subject to the electromagnetic interaction via the exchange of photons as the force carriers. The interaction is described as an *Abelian* gauge theory based on a $U_{\mathrm{EM}}(1)$ symmetry with the photons as the gauge field excitations. Analogously in QCD, the color-charged quarks are subject to the strong interaction. The interaction is constructed as a *non-Abelian* gauge theory [28, 29] based on the $SU(N_{\mathrm{c}})$ color symmetry, where $N_{\mathrm{c}} = 3$ is the number of colors. The field excitations of the gauge field are now the *gluons*, i.e., the quarks interact via the exchange of gluons as the force carriers of the strong interaction. First experimental indications for the existence of gluons were provided by so-called three-jet events [30–34].

Due to the non-*Abelian* nature of the gauge theory, the gluons are color-charged themselves. This crucial difference to QED, where the photons do not carry an electromagnetic charge, has important implications. As opposed to the screening effect of the electromagnetic interaction, the self-interaction of gluons leads to an “anti-screening” effect, i.e., the interaction becomes *weaker* and the associated coupling of the interaction decreases at higher momentum transfers or, correspondingly, at shorter distances. This phenomenon is known as *asymptotic freedom* [35, 36] which is a distinct property of non-*Abelian* gauge theories [37]. Indeed, this property is crucial since asymptotically free theories are in agreement with observations from deep inelastic scattering experiments: Hadrons probed at high energies behave as a collection of practically free pointlike scattering centers [17–19]. The interaction strength decreasing with increasing energy implies the existence of a regime at sufficiently high energies which is accessible by perturbative methods. Such approaches actually lead to a very precise and successful quantitative description of deep inelastic scattering experiments. Nowadays, the property of asymptotic freedom is well established by high-precision laboratory experiments [38, 39].

In the reverse direction, however, asymptotic freedom implies an increasing interaction strength for lower energies and gives rise to non-perturbative phenomena: In the low-energy regime, quarks and gluons are subject to *confinement*, i.e., colored objects are trapped inside color-singlet bound states, or, in other words, *the only energy eigenstates of finite energy are color neutral* [5]. This property explains why the search for isolated color sources such as free quarks did not succeed, quarks and gluons remain hidden inside color-neutral baryons and mesons. Still, the nature of confinement remains not fully understood despite intensive research [40]. Confinement is believed to be associated with a non-trivial vacuum structure [41], but a rigorous analytical derivation has yet to be found. There exists evidence for confinement from both experiments as well as from theoretical studies based on *lattice QCD* [42–44]. Indeed, computations based on the latter approach provide us with a simple picture of confinement by means of the free energy between static, “infinitely heavy” quarks as color sources. The free energy increases linearly with the distance of the two color sources, with the proportionality factor given by a so-called “string tension”. In case of infinitely heavy quarks, i.e., pure gluodynamics, the energy keeps rising and the complete separation of the color sources would require an infinite amount of energy. For finite quark masses, the energy stored in the system becomes sufficiently large at a certain distance such that the creation of a new quark-antiquark pair is energetically favored. This newly created pair then forms again color-singlet states with the original pair which entails that the free energy flattens out. This process is referred to as “string breaking” and is associated with the fragmentation processes in high-energy collision experiments [40].

Another crucial non-perturbative phenomenon of QCD is *spontaneous chiral symmetry breaking* [45, 46]. Chirality refers to the projection of quark fields onto their left- and right-handed chiral components. This rather abstract concept becomes more comprehensible for ultra-relativistic or massless particles: For these particles chirality is the same as helicity and describes the projection of the particle’s spin onto the direction of its momentum. The up and the down quark can indeed be considered as approximately massless. In this light-quark sector, the right-handed components then decouple completely from the left-handed components giving rise to the so-called *chiral symmetry* of QCD. Based on *Coleman*’s theorem [47], the chiral symmetry would imply the existence of degenerate states of opposite parity in the hadron spectrum. The actual observation of large mass differences between such chiral partners, however, suggests that the ground state is not invariant under chiral transformations. Indeed, non-perturbative dynamics lead to the formation of the *chiral condensate* in the QCD vacuum which breaks the chiral symmetry and leaves only the isospin symmetry intact. The formation of the chiral condensate is associated with the dynamic generation of the *constituent* quark masses, as distinguished from the *current* quark masses which are in case of the up and the down quark assumed to be zero in the so-called *chiral limit*. The constituent quark mass makes up the vast portion of, e.g., the proton's or the neutron's total mass. This mechanism of dynamical mass generation associated with a non-trivial chirally invariant QCD vacuum is thus responsible for almost the entire mass of the visible matter in our universe.

Spontaneous chiral symmetry breaking as a mechanism to dynamically generate mass also explains the unusually small masses of the pions in the light hadron spectrum. According to *Goldstone*'s theorem [48, 49], the spontaneous breakdown of a continuous global symmetry gives rise to the appearance of massless *Nambu-Goldstone* bosons. Applied to chiral symmetry breaking in the light-quark sector, these *Nambu-Goldstone* bosons correspond to the three pions. However, as the current masses of the up and the down quark are in fact small but non-zero, the chiral symmetry becomes only an approximate symmetry. As a consequence, the masses of the pions as *pseudo Nambu-Goldstone* bosons become non-zero as well, yet remain unusually small compared to the masses of the other hadrons. Thus, spontaneous chiral symmetry breaking constitutes an elegant mechanism to explain the hadronic mass spectrum.

1.1.1 Phases of strong-interaction matter

The QCD vacuum alone is already highly non-trivial, with intriguing mechanisms at play. It appears all the more interesting to ask what happens to QCD matter when it is heated to extreme temperatures or compressed to extreme densities. The understanding of strong-interaction matter in such extreme conditions is of great interest and has been the focus of intensive research efforts for several decades now, see, e.g., the reviews [41, 50, 51]. In order to illustrate its importance, one can consider how our understanding of hot QCD matter impacts for instance cosmology. The evolution of the universe during the first microseconds after the *Big Bang* is characterized by very dilute strong-interaction matter cooling down from extreme temperatures. The rate of the universe's expansion is strongly affected by the pressure conditions of this thermodynamic system and the knowledge about the precise form of this process is thus essential to aspects such as the gravitational wave background [52], baryogenesis [53], primordial nucleosynthesis [54] or even dark matter [55].

The thermodynamics of QCD describes the bulk properties of strong-interaction matter in equilibrium. As the total number of particles in a relativistic quantum field theory is not fixed, the system is described in terms of a grand canonical ensemble. QCD matter in extreme conditions gives rise to a wealth of interesting phenomena and lead to the prediction of various different phases. Our knowledge about these different phenomena is summarized in the *QCD phase diagram*, most commonly depicted in the plane spanned by the intensive parameters temperature T and baryon chemical potential μ_{B} (or equivalently quark chemical potential $\mu = \mu_{\mathrm{B}}/3$). The various phases are characterized by different symmetry properties and are

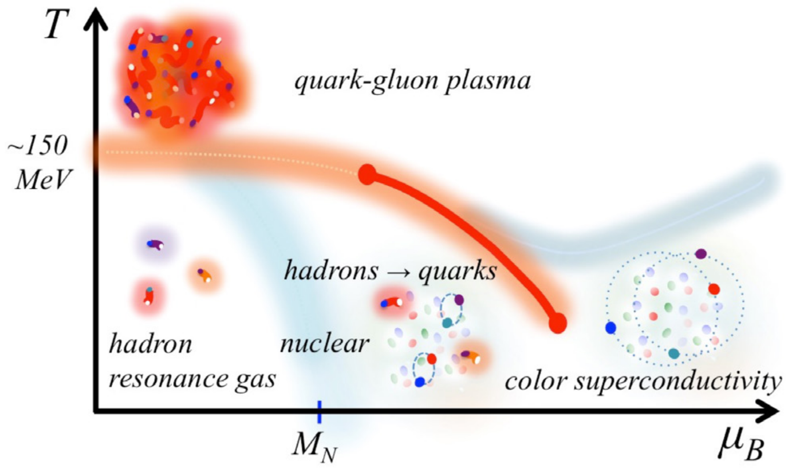

FIGURE 1.1: Sketch of the conjectured phase diagram of strong-interaction matter, taken from Ref. [56]. See main text for details.

governed by different degrees of freedom. However, the phase diagram is as rich as it is difficult to explore, and only little is firmly established.

Fig. 1.1 shows a sketch of the conjectured phase diagram. At low temperature and small baryon chemical potential, strong-interaction matter is characterized by a dilute hadron gas. The quarks are confined in baryons and mesons, and the constituent mass is generated by spontaneous chiral symmetry breaking. Asymptotic freedom suggests that these non-perturbative aspects change for increasing temperature, as they are after all associated with the increasing interaction strength toward the low-energy regime. With rising temperature, the typical scale of momentum transfer increases as well and the strong interaction becomes weaker. Indeed, at sufficiently high temperatures a transition to the *quark-gluon plasma* (QGP) is observed, a phase characterized by quarks and gluons as the essential degrees of freedom: The strong-interaction matter becomes deconfined, i.e., the quarks are not trapped anymore within bound states forming color singlets, and the chiral condensate "melts away". The restored chiral symmetry implies that only the current quark mass remains.

The region along the temperature axis of the QCD phase diagram can be explored in heavy-ion collision experiments at facilities such as the Relativistic Heavy-Ion Collider (RHIC) at the Brookhaven National Laboratory (BNL) or the Large Hadron Collider (LHC) at CERN. The LHC is at present the most powerful collider and is designed to reach center-of-mass energies of up to 14 TeV in proton-proton collision experiments [57]. These experiments are able to generate conditions as they are expected to have been present in our universe microseconds after the Big Bang and allow the probing of the QGP [58–60]. The QGP can be described as a nearly perfect liquid of quarks and gluons which, however, remains strongly coupled [61].

Much of our present-day knowledge about hot QCD matter at vanishing baryon chemical potential is obtained from lattice QCD studies, see, e.g., the reviews [62, 63]. These studies show that the transition from hadronic matter to the QGP is an analytic crossover, with rapid but smooth changes in the order parameters for chiral symmetry breaking and deconfinement [64–67]. This property of the transition is also indicated by observations in heavy-ion collision experiments [41, 62]. The crossover temperature assigned to these transitions is found to be approximately 155 MeV [65–72],[2] although the nature of a crossover defies a unique definition of a critical temperature and the exact value thus depends on the chosen definition. As indicated above, the transition to deconfined matter is observed to be accompanied by the restoration of the chiral symmetry. However, an analytic derivation of this close relation is yet to be accomplished and is complicated again, if possible at all, by the fact of the transition being a crossover. At even higher temperatures, lattice QCD computations of the pure gluon plasma could establish the link to perturbative calculations [73].

The QCD phase diagram at larger baryon chemical potentials is more difficult to access and presently more speculative. Collider experiments probe the regime at rather small chemical potentials, while novel experiments specifically designed to explore strong-interaction matter at larger densities are only future endeavors planned for example at the Facility for Antiproton and Ion Research (FAIR) at GSI or at the Nuclotron-based Ion Collider Facility (NICA) at JINR. In this density regime, lattice QCD studies suffer severely from the *sign problem* [74] and despite various approaches to circumvent this problem, see, e.g., Refs. [62, 75, 76], these studies are currently still limited to small chemical potentials. In this context, a longstanding question concerns the existence of the *QCD critical endpoint* (CEP) [77]. Phenomenological model studies suggest that the transition from the hadronic phase to the QGP becomes a first-order transition at lower temperatures and sufficiently high baryon chemical potentials. With the crossover at vanishing chemical potential, this would imply the existence of a CEP where the first-order transition turns into a second-order transition before the transition eventually becomes a crossover at even smaller baryon chemical potentials. The existence of the CEP is of great interest as it would be a distinct prediction of QCD and would leave clear signatures in collision experiments as associated with critical fluctuations [78–80]. With lattice QCD studies supporting the existence as well as providing rather opposing indications, the existence of the CEP, let alone its exact location, remains at present debatable [63, 81–88].

The QCD phase diagram along the axis of the baryon chemical potential at smaller temperatures potentially gives rise to a rich phase structure. At lower chemical potentials, up to approximately twice the nuclear saturation (number) density $n_0 \approx 0.16/\mathrm{fm}^3$ (or equivalently the nuclear saturation mass density $\rho_0 \approx 2.7 \times 10^{14}\,\mathrm{g/cm}^3$), strong-interaction matter in the hadronic phase can be very successfully described by chiral effective field theory [89–93]. For increasing baryon chemical potential, one first encounters the nuclear liquid-gas phase transition [51, 94] at densities around the nuclear saturation density. This first-order phase transition can be studied in low-energy heavy-ion collision experiments and terminates also in a CEP at temperatures of approximately 15-20 MeV [51]. However, the exploration of the QCD phase diagram beyond these densities is very challenging and our knowledge about this region is rather conjectural. Only at asymptotically high densities, where the typical scale of the momentum transfer is set by a large *Fermi* momentum, the strong interaction is sufficiently weak due to asymptotic freedom that weak-coupling methods are applicable [95–108]. These calculations show that for sufficiently low temperatures QCD matter gives rise to *color superconductivity* [96, 97, 106, 107, 109, 110]. In analogue to the *Bardeen-Cooper-*

---

[2] In SI units, this temperature corresponds to 1.8×10^{12} K. For comparison, the temperature in the core of our Sun is approximately 1.5×10^7 K. Note that we employ so-called natural units, i.e., we set $\hbar = c = k_\mathrm{B} = 1$, throughout this work.

Schrieffer (BCS) theory of superconductivity in condensed matter physics [111, 112], the *Fermi* sphere of the quarks becomes unstable with respect to the formation of *Cooper* pairs [113], where the necessary attractive interaction is provided by one-gluon exchange [109]. Toward smaller densities, various pairing patterns might emerge in the color-superconducting ground state. We refer to, e.g., the reviews [107, 114–116] for a more detailed description. As weak-coupling methods cannot be applied anymore to QCD matter in this regime, the exploration of the phase diagram at intermediate densities mainly relies on effective low-energy models such as *Nambu–Jona-Lasinio* (NJL) models and their relatives [45, 46, 106, 107, 115–140]. Such model studies point to the existence of pairing gap sizes of up to $\sim 100\,\mathrm{MeV}$ [50, 109, 110, 141], suggesting correspondingly large transition temperatures to the phase of the QGP. We note that in the case of three flavors there are indications for a first-order phase transition of color-superconducting QCD matter to the QGP at higher temperatures as well as for a first-order phase transition to the hadronic phase toward smaller densities [115]. However, different scenarios such as the quark-hadron continuity are conceivable as well [56, 142, 143]. In fact, the phase diagram at intermediate densities might give rise to various more exotic phases such as chiral-density waves or crystalline color superconductivity. We refer to, e.g., the review [51] for a more comprehensive discussion.

The discussion of the QCD phase diagram illustrates that only little is firmly established and the manifestation of strong-interaction matter in a significant portion of the phase diagram is merely conjectured. In fact, only the part along the temperature axis in the limit of vanishing baryon chemical potential, the hadronic phase at smaller temperature and chemical potential including the liquid-gas phase transition, as well as QCD matter at asymptotically large densities in the zero-temperature limit are on solid grounds. However, in particular the regime of intermediate densities at vanishing to small temperatures is of exceptional interest since this regime is relevant for astrophysical applications. For instance, precise knowledge about strong-interaction matter at densities beyond the nuclear saturation density is essential for our understanding of the dynamics of *neutron stars*.[3]

1.1.2 Neutron stars and the equation of state

Neutron stars are the densest objects in our universe, surpassed only by black holes. The typical radius is $\sim 10\,\mathrm{km}$, while the typical mass is of the order of our Sun's mass, i.e., $M \sim 1.4 M_{\odot}$, with the solar mass $M_{\odot} = 1.9891 \times 10^{33}\,\mathrm{g}$ [144]. The estimated total number of neutron stars in our galaxy ranges from 100 million to one billion. They are the final product of the evolution of massive stars with masses heavier than about eight solar masses [145]. Lighter stars result in the formation of white dwarfs, while with increasing mass above approximately $12\,M_{\odot}$ the formation of black holes becomes increasingly likely. Neutron stars are the remnants of *core-collapse supernova* (type II) explosions [146]: At the end of a massive star's life, the "nuclear fuel" is used up and the burning cannot sustain the gravitational pressure anymore, leading to a gravitational collapse of the core. The supernova explosion expels the outer layers into space and leaves behind a proto-neutron star. The proto-neutron star is initially hot,

---

[3] We use the traditional term "neutron star" instead of the more general term "compact star".

with temperatures up to $\sim 10\,\mathrm{MeV}$. Within the first seconds of its generation, the star cools down by *neutrino emission* [147], and *electron-capture* processes (inverse beta decay) due to the high degeneracy of electrons lower the proton-neutron ratio. Eventually, *beta equilibrium* is reached, i.e., the beta decay of neutrons is balanced by the rate of electron captures on protons, and the star is composed of mostly neutron-rich nuclear matter with only a small fraction of protons and electrons [144]. After a timescale of $\sim 100\,\mathrm{s}$, the neutron star is cooled to temperatures much smaller than $1\,\mathrm{MeV}$ [56, 148]. As the associated *Fermi* temperature of the degenerate matter is much higher, temperature effects are not relevant for the description of neutron stars [141].

The neutron star is bound by gravitation, while the neutron degeneracy pressure as well as repulsive forces from nuclear interactions, i.e., strong interactions, stabilize the star and prevent it from contracting further. The internal structure of the neutron star can be described in terms of layers. The outermost layer consists of nuclei forming a lattice [145], thus giving rise to a solid crust with a thickness of $\sim 0.5\,\mathrm{km}$ [56]. The nuclei are surrounded by a degenerate electron gas and become increasingly more neutron-rich deeper into the crust because of the increasing density. A liquid of free neutrons starts to form in the inner part of the crust. Eventually, the lattice composed of nuclei vanishes and the nuclei disintegrate into homogeneous neutron-rich matter, marking the beginning of the outer core consisting of superfluid neutrons and of a small fraction of superconductive protons [145]. The central densities in the inner region of the core are conjectured to be from several up to ten times the nuclear saturation density. Such high densities might give rise to strong-interaction matter in various forms [144, 149]. In particular, the core might consist of deconfined quark matter, in which case the neutron star is then referred to as a *hybrid star*.

As our discussion illustrates, neutron stars basically “live” along the density axis of the QCD phase diagram, i.e., the conditions of strong-interaction matter in neutron stars is represented by this region. The description and modeling of neutron stars thus crucially depends on the *equation of state* (EOS) of dense strong-interaction matter, whose theoretical understanding has been one of the main frontiers in nuclear physics in recent decades. The EOS in the zero-temperature limit typically describes the pressure as a function of the energy density.[4] From a given EOS, we can directly infer macroscopic properties of the neutron star. With the help of the *Tolman–Oppenheimer–Volkov* (TOV) equation [150, 151], which is a general relativistic equation describing a spherically symmetric, isotropic body in hydrostatic balance, the EOS is mapped onto the mass-radius (M-R) relation of non-rotating neutron stars.[5] In this way, the EOS as resulting from fundamental microscopic interactions is directly connected to the M-R relation as a macroscopic observable. In fact, the EOS is essential for the description of various astrophysical processes such as merger dynamics in binary systems, the formation of black holes or processes related to nucleosynthesis [152–154]. Temperature corrections to the EOS become relevant in order to describe, e.g., core-collapse supernovae and the associated neutrino signal, the remnant shortly after supernova explosions or the late stages and the aftermath of inspiral processes in binary systems of two neutron stars [155, 156].

---

[4] The EOS can also be given as the pressure as a function of the chemical potential or baryon density.

[5] This equation does not take into account the influence of the usually strong magnetic fields of neutron stars which we have left out in our discussion here [144].

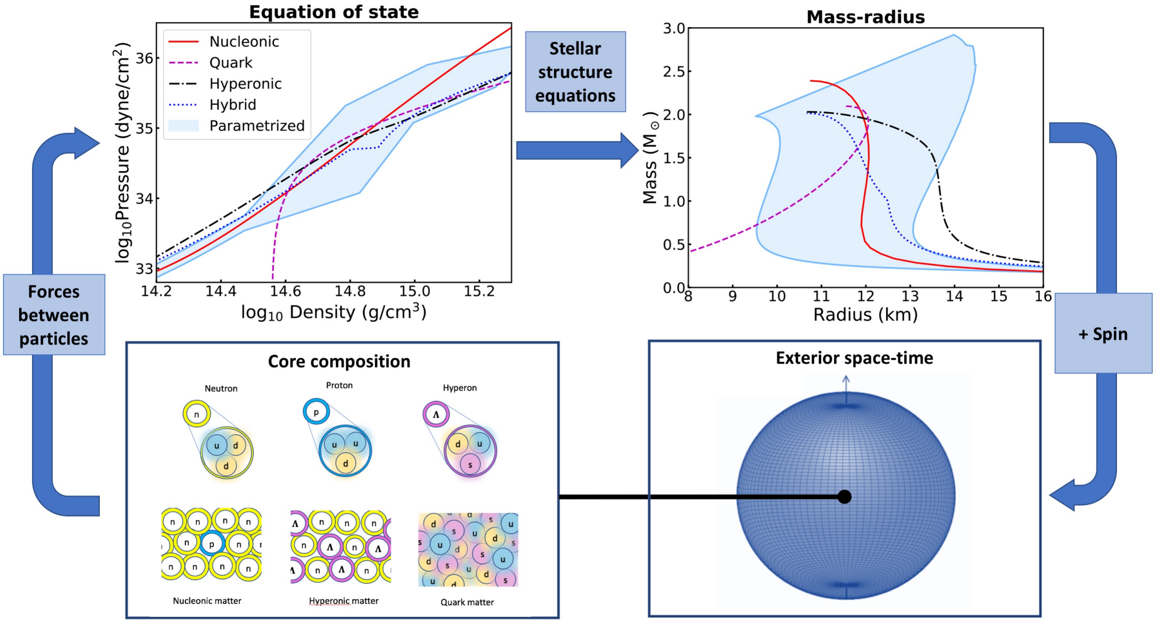

FIGURE 1.2: Illustration of the close interrelation of strong-interaction matter physics and astrophysical observations, taken from Ref. [157]. The state of strong-interaction matter in the interior of neutron stars and the forces between the particles determine the EOS, which in turn is connected to the M-R relation via stellar structure equations such as the TOV equation. Here, further aspects are addressed which we have not included in our discussion, such as strange quarks and associated hyperonic matter, or the role of the spin and the exterior space-time of neutron stars in astrophysical observations. We refer to Ref. [157] for more details on these aspects.

The connection between strong-interaction matter physics and astrophysics holds promise to be very fruitful in both directions as astrophysical observations in turn help to constrain the EOS, see Fig. 1.2 for an illustration of this close relation. Neutron stars are unique environments, with strong-interaction matter under conditions which cannot be achieved in laboratory experiments on Earth. Thus, astrophysical measurements complement our knowledge obtained from heavy-ion collision experiments [158] and can provide model-independent constraints on the EOS.

A first non-trivial constraint was given by the observations of very massive neutron stars with masses of $\sim 2M_\odot$ in recent years [159–161], where the millisecond pulsar J0740+6620 is possibly the most massive neutron star yet observed with the mass of $2.17^{+0.11}_{-0.10}\,M_\odot$ [162]. The existence of such heavy neutron stars poses specific requirements on the “stiffness” of the EOS, i.e., how quickly the pressure increases with the energy density, such that these high masses are supported [163, 164]. Further constraints would be obtained by simultaneous measurements of the mass and the radius as implied by the direct correspondence of the M-R relation to the EOS, see, e.g., Refs. [165–168, 168]. Unfortunately, however, the measurement of radii is very difficult such that novel observational approaches must be pursued. For example, the recently launched Neutron Star Interior Composition Explorer (NICER) on the International Space Station is very promising in achieving more accurate radius measurements using x-ray timing [148, 157, 169–171]. Lastly, the recent first direct observations of gravitational waves by the (Advanced) Laser Interferometer Gravitational-Wave Observatory (LIGO), later joined by the (Advanced) Virgo interferometer, of binary black hole coalescences [172–176] and also of a binary neutron star inspiral [177, 178] herald the onset of a new era of observational astronomy. As gravitational wave signals are sensitive to the EOS of dense strong-interaction matter at zero as well as at finite temperature, these signals constitute a new source of constraints on the EOS from astrophysical observations [153, 154, 179–182]. However, all such measurements can only provide indirect insight into the microscopic nature of matter at high densities. Determining the composition of dense matter requires microscopic calculations, which eventually need to be benchmarked against the observational constraints.

1.2 Focus of this thesis

The discussion of the EOS as one of the essential ingredients in the description of crucial astrophysical processes emphasizes the importance of our understanding of strong-interaction matter at intermediate and high densities. However, this part of the phase diagram in particular is notoriously difficult to access. The composition and properties of matter at supranuclear densities is still a mystery and poses *one of the great unsolved problems in modern science* [148]. Various theoretical approaches are either restricted to small densities, e.g., lattice QCD computations suffer from the sign problem at non-zero chemical potential, or to asymptotically large densities where asymptotic freedom allows the application of weak-coupling approaches. Thus far, much of our knowledge about strong-interaction matter at intermediate densities resorts to low-energy effective models mimicking certain aspects of the underlying fundamental theory, i.e., QCD. However, these model studies remain unsatisfactory in the light of generic shortcomings, such as being associated with the inability to unambiguously determine the model parameters, or the intrinsic limited range of validity in terms of external parameters, such as temperature or baryon chemical potential, owing to the omission of fundamental degrees of freedom.

A very promising approach to meet the challenges of exploring QCD at finite densities is given by functional methods such as the *functional renormalization group* (FRG) [183] or *Dyson-Schwinger equations* [184, 185]. These continuum methods are conceptually based on non-perturbative loop equations and are suited for studies at finite chemical potential [124, 186–188]. In this thesis, we shall employ the FRG as our key method for the analysis of hot and dense strong-interaction matter. The FRG is a powerful and versatile non-perturbative approach to studying quantum field theories and is capable of describing the physics over a wide range of scales. This method can be described as an efficient realization of *Wilson*'s idea not to incorporate all corrections arising from quantum or thermal fluctuations at once, but successively in going from large momentum scales to small momentum scales [189–191]. This allows us to systematically examine the effect of fluctuations associated with a specific momentum scale and gives rise to the *renormalization group* (RG) *flow* from the classical theory in the ultraviolet (UV) to the full quantum theory in the infrared (IR) once all fluctuations are integrated out. The FRG can be viewed as a “theoretical microscope” where the “resolution” is gradually changed from the microscopic to the macroscopic perspective. This process of “zooming out” allows us to study the changes in the theory caused by fluctuation effects in a systematic manner, such as with respect to the realization of symmetries, the assumed ground state or the strength of interactions. The FRG is able to reveal and account for emerging relevant degrees of freedom, which is essential as QCD matter turns strongly interacting when the long-range limit is approached and the formation of condensates as bound states might occur. In particular, the FRG allows the description of strong-interaction matter in a "top-down" approach from first principles, i.e., the only input is given by the fundamental parameters of QCD fixed at a large momentum scale in the perturbative regime. Recent studies aimed at quantitative precision made crucial progress toward quantitative first-principles studies of the QCD phase diagram with the FRG [192–197].

In this work, we study the phase structure of two-flavor QCD in the chiral limit, i.e., we assume vanishing current quark masses, at finite temperature and finite quark chemical potential. A central aspect in our analysis concerns *four-quark self-interactions* which play an important role in the description of strongly correlated low-energy dynamics of QCD. They are not fundamental in the sense that they do not appear in the classical QCD *Lagrangian* which couples matter only via the quark-gluon vertex. However, as soon as quantum corrections are integrated out, four-quark self-interactions are dynamically generated by two-gluon exchange. These interactions are the first emerging interactions toward an effective low-energy description of the matter sector and already encode information on the realized ground state of the theory, i.e., on the formation of condensates such as the chiral condensate related to spontaneous chiral symmetry breaking or diquark condensates associated with color superconducting QCD matter. In approaching the long-range limit, it is thus essential to fully capture the dynamics within this sector of four-quark interactions. Yet, various different four-quark interactions are generated as they are only constrained by the symmetries of the underlying theory. For our analysis of the phase structure, we incorporate *all* four-quark interactions in the pointlike limit by making use of a *Fierz*-complete basis. This basis is only constrained by the symmetries as well. In particular, we take into account the explicit breaking of the *Poincaré* invariance, induced by the presence of a heat bath as well as the finite quark chemical potential, which implies an even larger variety of possible interaction channels. Every compatible four-quark interaction potentially generated is then reducible by means of so-called *Fierz* transformations.

By studying a simplified system where the gluonic degrees of freedom are considered integrated out, amounting to a *Fierz*-complete NJL-type model, we analyze in detail the significance of four-fermion interactions and *Fierz* completeness for the quark dynamics. This consideration aims in particular at a better understanding of how *Fierz*-incomplete approximations of QCD low-energy models affect the predictions for the phase structure at finite temperature and density. Moreover, we examine symmetry breaking mechanisms and the dynamics related to changes in the dominant degrees of freedom at high densities. The latter play an important role in the context of strong-interaction matter in a color superconducting state. We temporarily simplify the system even further to a *Fierz*-complete NJL-type model with only a single fermion species. This reduction in the number of fermion species defines a very accessible model and allows us to study the crucial dynamics in a comprehensible manner while still sharing important aspects with the low-energy dynamics in QCD.

The understanding of the quark dynamics as obtained from the *Fierz*-complete NJL-type model studies lays the groundwork to our analysis of the phase structure including dynamic gauge fields. As the four-quark interactions are dynamically generated in the RG flow, the only free parameter is given by the strong coupling. This coupling can be fixed in the perturbative regime to the values extracted from experiment. The approach to study the finite-temperature phase boundary based on dynamic gauge fields in combination with a *Fierz*-complete basis of four-quark self-interactions allows us to capture the onset of the formation of various condensates, i.e., it realizes a very advantageous sensitivity to the different symmetry-breaking scenarios.

The information carried by the RG flow of the various four-quark couplings reveals the degrees of freedom which become dominant in the low-energy regime. This information thus allows us to define a customized low-energy ansatz which ensures the incorporation of the relevant dynamics of the low-energy regime by including auxiliary mesonic fields to account for the formation of the associated condensates. Based on this customized ansatz, the RG flow can be continued to access the low-energy regime governed by spontaneous symmetry breaking. For the computation of these dynamics, it is crucial that any cutoff effects or regularization scheme dependences are removed. The FRG constitutes the ideal tool to analyze such aspects and to ensure *renormalization group consistency.* Following this approach, we eventually obtain access to thermodynamic quantities. In particular, we shall analyze the zero-temperature EOS of isospin-symmetric QCD matter at intermediate densities which contributes to our understanding of dense strong-interaction matter.

1.2.1 Outline

This thesis is organized as follows: We begin in Chapter 2 with a recapitulation of aspects of QCD which are key to our discussions in this work. First, we give a brief summary of the theoretical formulation of QCD in Section 2.1, where we also introduce the finite-temperature formalism including chemical potential, i.e., the thermodynamics of QCD, and discuss the essential symmetries of QCD. Cold strong-interaction matter at high densities gives rise to the phenomenon of color superconductivity. We explain important aspects of this phenomenon in Section 2.2. In Section 2.3, we give a brief overview of selected alternative methods to study strong-interaction matter, each coming with its individual benefits but also shortcomings. These methods were already mentioned in the introduction and here we provide some more information.

The FRG as the "workhorse" of this thesis is introduced in Chapter 3. In Section 3.1, after explaining the main ideas underlying the FRG, we derive the exact RG equation which is our central tool to compute RG flows. The application of the FRG to a theory at hand requires the specification of a regularization scheme in terms of a regularization function. Basic aspects of these functions are discussed in Section 3.2, where we also demonstrate the construction of the regulator we shall mainly employ. In the regularization and renormalization procedure as generally required by the computation of quantum corrections in field theories, it is important to avoid or at least reduce cutoff effects and regularization scheme dependences. The FRG constitutes an ideal method to systematically analyze such aspects. In Section 3.3, we introduce the concept of renormalization group consistency and discuss in general terms how cutoff artifacts can be suppressed with the help of the FRG. This becomes particularly important in studies with finite external control parameters such as temperature or quark chemical potential.

Chapter 4 is devoted to our *Fierz*-complete NJL-type model studies. We begin Section 4.1 by explaining the significance of four-quark interactions in QCD and subsequently discuss general aspects of NJL-type models in Section 4.1.1. After introducing the generic ansatz for the effective average action underlying our NJL-type model studies in Section 4.1.2, we outline how the phase structure can be accessed by analyzing the RG flow of four-fermion couplings in the pointlike limit. In Section 4.2, we present our *Fierz*-complete NJL-type model with a single fermion species. The reduction to a single species simplifies the analysis and demonstrates in a very accessible manner the importance of *Fierz* completeness in the study of the phase structure at finite temperature and finite quark chemical potential. In Section 4.3, we then study a *Fierz*-complete NJL-type model with quarks coming in two flavors and N_{c} colors. We analyze the phase structure and show again how *Fierz* incompleteness may affect the predictive power of such model studies. Moreover, we discuss a mechanism based on the fixed-point structure which is related to the emergence of color superconductivity at high densities in the zero-temperature limit.

In Chapter 5, we proceed to incorporate gluodynamics by extending our *Fierz*-complete ansatz to include dynamical gauge fields. After a discussion of the details of this ansatz in Section 5.1 and of the general structure of the RG flow equations in Section 5.2, we analyze the phase diagram and symmetry breaking patterns in Section 5.3. We also address in-medium effects on the gauge anomalous dimension and the influence of an explicit breaking of the axial $U_{\mathrm{A}}(1)$ symmetry.

Chapter 6 is devoted to the EOS of isospin-symmetric strong-interaction matter at intermediate densities. In Section 6.1, based on the information contained in the RG flow of the four-quark couplings at high energies, we identify the relevant low-energy effective degrees of freedom and define a new ansatz in form of a quark-meson-diquark-model truncation to access the low-energy regime. In particular, we discuss the implementation of a “pre-initial” flow to ensure RG consistency and provide several example computations in order to illustrate the effect of this criterion in Section 6.1.2. In Section 6.2, we present our results on the EOS in terms of the pressure as a function of the baryon density.

We give a final conclusion and an outlook in Chapter 7. Notational and technical details can be found in the Appendix.

The compilation of this dissertation was done solely by the author. The results were obtained with my collaborators and are largely published or available as preprint, see the following listing:

[198] *Fierz-complete NJL model study: Fixed points and phase structure at finite temperature and density*
Jens Braun, Marc Leonhardt, Martin Pospiech
Published in Phys. Rev. D **96**, 076003 (2017)
E-print: arXiv:1705.00074 [hep-ph]

[199] *Fierz-complete NJL model study. II. Toward the fixed-point and phase structure of hot and dense two-flavor QCD*
Jens Braun, Marc Leonhardt, Martin Pospiech
Published in Phys. Rev. D **97**, 076010 (2018)
E-print: arXiv:1801.08338 [hep-ph]

[200] *Renormalization group consistency and low-energy effective theories*
Jens Braun, Marc Leonhardt, Jan M. Pawlowski
Published in SciPost Phys. 6, 056 (2019)
E-print: arXiv:1806.04432 [hep-ph]

[201] *Symmetric nuclear matter from the strong interaction*
Marc Leonhardt, Martin Pospiech, Benedikt Schallmo, Jens Braun, Christian Drischler, Kai Hebeler, Achim Schwenk
E-print: arXiv:1907.05814 [nucl-th]

Texts and figures taken from these articles are not marked explicitly, but mainly incorporated as follows: Chapter 4 as well as Sections 2.1.2 and 3.2 are based on the publications [198, 199]. Also parts of Appendix B.3 and the Appendices E and F originate from these publications. Sections 3.3 and 6.1.2 as well as parts of Section 6.1.1 and the Appendix D were published in [200]. Parts of Section 6.2 originate from [201].

2

FUNDAMENTALS

2.1 Quantum chromodynamics

Quantum chromodynamics (QCD) is the quantum field theory of the strong interaction, one of the fundamental forces in the standard model of particle physics. A distinctive phenomenon of the strong interaction is the so-called asymptotic freedom, i.e., the interaction strength becomes smaller for higher momentum transfers. To accommodate this feature, QCD is a non-*Abelian* gauge theory [37] with an underlying $SU(N_\mathrm{c})$ color gauge group. The fundamental degrees of freedom are quarks, i.e., spin-1/2 fermions which come in $N_\mathrm{c} = 3$ colors (fundamental representation) and $N_\mathrm{f} = 6$ flavors (up, down, strange, charm, bottom, top), see Table 2.1 for further properties. The gauge bosons or the so-called gluons as the quanta of the gauge field are the force carriers of the strong interaction and mediate the interaction between the quarks. Due to the non-*Abelian* nature of the gauge group, the gauge bosons can also interact among themselves. In the following, we give a brief summary of the theoretical formulation of QCD. For a more detailed discussion, we refer to, e.g., Refs. [202–205].

The classical *Lagrangian* of QCD in *Euclidean* space-time[1] is given by

$$\mathcal{L}^0_{\mathrm{QCD}} = \bar{\psi}\left(\mathrm{i}\not{D} + \mathrm{i}m\right)\psi + \frac{1}{4}F^a_{\mu\nu}F_{a,\mu\nu}\,. \tag{2.1}$$

The quark fields are represented by *Dirac* spinors ψ and carry *Dirac*, color, and flavor indices. They are assumed to be contracted pairwise, e.g. $(\bar{\psi}\mathcal{O}\psi) \equiv \bar{\psi}_\chi\mathcal{O}_{\chi\xi}\psi_\xi$, where ξ and χ represent collective indices for the *Dirac*, flavor and color indices and $\mathcal{O}$ represents an arbitrary operator.[2] The diagonal mass matrix m might carry a flavor index as well to account for quark flavors

---

[1] This work is formulated in imaginary-time formalism with *Euclidean* space-time unless stated otherwise. For more information on the transition from *Minkowski* to *Euclidean* space-time see Appendix A.2.

[2] In the representation of operators suitable insertions of $\mathbb{1}$-operators in *Dirac*, color, and flavor space are tacitly assumed.

Quark	up	down	strange	charm	bottom	top
Charge	$+2/3$	$-1/3$	$-1/3$	$+2/3$	$-1/3$	$+2/3$
Mass	2.2 MeV	4.7 MeV	95 MeV	1275 MeV	4.18 GeV	173 GeV

TABLE 2.1: Electric charges of the quarks in units of the elementary charge and approximate values of the (current) quark masses in the $\overline{\text{MS}}$ scheme taken from Ref. [39]. The baryon number of all quarks is 1/3.

of different masses. The *Lagrangian* is invariant under color $SU(N_\text{c})$ gauge transformations where the quark fields transform as

$$U(x) = \exp\left(\mathrm{i}\theta^a(x)T^a\right), \tag{2.2}$$

$$\psi(x) \mapsto U(x)\psi(x), \qquad \bar{\psi}(x) \mapsto \bar{\psi}(x)U^\dagger(x), \tag{2.3}$$

with the real parameters $\theta^a(x)$ specifying the element of the group. Due to the dependence of these parameters on the space-time coordinates x, the transformation becomes a local one. As the transformation acts in the color subspace only, every quark flavor is affected in the same manner. The matrices T^a denote the $N_\text{c}^2 - 1$ generators of the *Lie* group $SU(N_\text{c})$ in the fundamental representation and are given by the Gell-Mann matrices $T^a = \lambda^a/2$ $(a = 1, 2, \ldots, 8)$ in the case of $N_\text{c} = 3$ colors. They fulfill the commutator relation

$$[T^a, T^b] = \mathrm{i}f^{abc}T^c, \tag{2.4}$$

where f^{abc} denotes the structure constants of the *Lie* group. With the latter relation (2.4) the generators form the corresponding *Lie* algebra. For the *Lagrangian* to be invariant under *local* $SU(N_\text{c})$ transformations, the usual derivative in the kinetic term of the quark fields $\bar{\psi}(\mathrm{i}\not{\partial} + \mathrm{i}m)\psi$ must be replaced by the covariant derivative

$$\partial_\mu \longrightarrow D_\mu = \partial_\mu - \mathrm{i}\bar{g}_\text{s}A_\mu, \tag{2.5}$$

introducing the gauge field $A_\mu \equiv A_\mu^a T^a$ with the adjoint color index $a = 1, \ldots, N_\text{c}^2 - 1$. The gauge fields transform under local gauge transformations as

$$A_\mu(x) \mapsto U(x)\left(A_\mu(x) + \frac{\mathrm{i}}{\bar{g}_s}\partial_\mu\right)U^\dagger(x) \tag{2.6}$$

and counteract in this way the change of the kinetic term of the quark fields, caused by the derivative acting on the space-time dependence of the parameters $\theta^a(x)$. Thus, the principle of local gauge invariance leads to an interaction term of the form $\bar{g}_\text{s}\bar{\psi}\not{A}\psi$. In a quantized theory this term gives rise to a quark-gluon vertex with the coupling strength $\bar{g}_\text{s}$, i.e., the coupling of the strong interaction. As the gauge field affects only the color indices, the coupling strength $\bar{g}_\text{s}$ is the same for each quark flavor. Lastly, the dynamics of the gauge fields are described by the gauge invariant term $\frac{1}{4}F_{\mu\nu}^a F_{a,\mu\nu}$ with the field strength tensor given by

$$F_{\mu\nu}^a = \partial_\mu A_\nu^a - \partial_\nu A_\mu^a + \bar{g}_\text{s}f^{abc}A_\mu^b A_\nu^c, \tag{2.7}$$

which can be considered as the generalization of the field tensor in quantum electrodynamics (QED) to the present case of a non-*Abelian* gauge theory. More specifically, the terms proportional to the structure constants f^{abc} originate from the non-*Abelian* nature of the gauge group. As a consequence, the kinetic term of the gluons entails expressions that are cubic and quartic in the gauge field variables and hence gives rise to three-gluon and four-gluon vertices at the classical level. In fact, exactly these self-interactions are responsible for an "antiscreening" effect and lead to asymptotic freedom as opposed to the ordinary screening effect in *Abelian* gauge theories such as QED. An additional mass term for the gluons such as $\frac{1}{2}m^2A^2$ cannot be included as this term would violate local gauge invariance. Thus, the principle of local gauge invariance necessarily leads to massless gauge bosons.[3]

Functional quantization

So far, the QCD *Lagrangian* has been discussed from a point of view of a classical theory. In order to calculate observables as, e.g., cross sections, the theory must be quantized. This can be done by employing functional quantization. In the functional-integral formalism, the time-ordered vacuum expectation value of an operator $O(\phi)$ is formulated in terms of a path integral:

$$\langle O(\phi)\rangle := \langle\Omega|\mathcal{T}O(\phi)|\Omega\rangle = \frac{\int\mathcal{D}\phi\;\; O[\phi]\;\; \mathrm{e}^{-S[\phi]}}{\int\mathcal{D}\phi\,\mathrm{e}^{-S[\phi]}}\,, \tag{2.8}$$

where $\mathcal{T}$ denotes time-ordering and $|\Omega\rangle$ is the ground state of an interacting field theory, in contrast to the ground state $|0\rangle$ of a free theory. For the sake of a concise notation, we have introduced the generalized field variable

$$\phi^{\mathrm{T}}(x) = \Big(\varphi(x),\, \psi^{\mathrm{T}}(x),\, \bar{\psi}(x),\, \ldots\Big)\,, \tag{2.9}$$

which summarizes the various fields of the theory under consideration and might include, e.g., gauge fields as well. For further details on the notation, see Appendix A.3. In the functional-integral formalism fermionic fields $\psi(x)$ are represented by anticommuting *Grassmann* variables. This is due to the fact that fermionic fields obey canonical anticommutation relations in the operator formalism in order to be consistent with the spin-statistics theorem. Bosonic fields $\varphi(x)$ are quantized in terms of canonical commutation relations and thus are represented by ordinary commuting variables. The operator $O(\phi)$ on the left-hand side of Eq. (2.8) translates into a functional $O[\phi]$ of the fields on the right-hand side. In the definition of the action $S[\phi] = \int_x \mathcal{L}$ in terms of the *Lagrangian* $\mathcal{L}$ (see again Appendix A.3 for our notational convention for integrals) the integral is extended over the entire space-time volume. For the

---

[3] Other contributions, i.e., other gauge invariant combinations of the quark and gluon fields can be excluded as they would either lead to non-renormalizable interactions in four space-time dimensions or they would violate one or several of the discrete symmetries parity $\mathcal{P}$, charge conjugation $\mathcal{C}$ and time reversal $\mathcal{T}$. For example, the so-called θ term violates the discrete symmetries P and CP and would lead to a non-vanishing electric dipole moment of the neutron. Experimental results suggests that this term is very small and thus can be neglected in our considerations [206, 207].

choice $O(\phi) = \phi_i(x_1)\phi_j(x_2)\cdots\phi_k(x_n)$, where the index specifies the field component of the generalized field variable, we obtain the n-point correlation functions or n-point *Green*'s functions. The correlation functions contain all information on a given physical process: Every operator that might appear on the left-hand side of Eq. (2.8) can be expressed in terms of the field variables [208, 209] and thus the corresponding expectation value can be decomposed into n-point correlation functions. In order to calculate scattering amplitudes and cross sections, the S-matrix elements are related to the *Fourier* transformed n-point *Green*'s functions by the LSZ reduction formula [210]. In general, all n-point correlation functions can be computed from the generating functional $Z[J]$,

$$Z[J] := \int \mathcal{D}\phi \;\, \mathrm{e}^{-S[\phi]+\int_x J^{\mathrm{T}}\phi}\,, \tag{2.10}$$

by taking the functional derivative with respect to the corresponding generalized external source J given by

$$J^{\mathrm{T}}(x) = \Big(j(x),\, \bar{\eta}(x),\, -\eta^{\mathrm{T}}(x),\, \ldots\Big)\,. \tag{2.11}$$

This makes the generating functional $Z[J]$ and related generating functionals the central quantities of interest in solving a quantum field theory [124, 211]. From Eq. (2.10) we obtain the generating functional for connected n-point correlation functions by the relation $W[J] := \log Z[J]$ which in the context of statistical field theory relates the *Helmholtz* free energy to the partition function Z. In analogy to the *Gibbs* free energy, the generating functional of one-particle irreducible (1PI) n-point correlation functions, the so-called effective action Γ, is related to the generating functional $Z[J]$ by means of a Legendre transform, i.e.,

$$\Gamma[\Phi] := \sup_J \left(\int_x J^{\mathrm{T}}\Phi - \log Z[J]\right)\,, \tag{2.12}$$

where for any given argument the source J is specified by demanding the expression to assume its supremum. As a result, the functional is convex by construction. The newly introduced so-called classical field Φ is the “thermodynamic” variable conjugate to the source J [202] and describes the expectation value $\Phi = \langle\Omega|\phi|\Omega\rangle_J$ of the generalized field variable ϕ in the presence of the source J. The effective action Γ can be considered as the quantum analogue to the classical action S and governs the dynamics on the macroscopic scale by taking into account all quantum and thermal fluctuations. An advantage of the effective action is that it provides a geometrical picture of the assumed stable ground state in consideration of all quantum corrections: Assuming a homogeneous solution, i.e., the classical field $\Phi(x) = \Phi$ is independent of the position-space variable x, the effective action as an extensive quantity can be written as $\Gamma[\Phi] = \mathcal{V}U(\Phi)$, with the space-time volume $\mathcal{V}$ and the effective potential $U(\Phi)$. The stable quantum states of a theory are then given by the global minima of the effective potential where the value of the minimum itself is related to the free energy density of the state [202], cf. the discussion in Section 2.1.1.

Faddeev-Popov method

The quantization of gauge theories contains further subtleties which must be taken care of. The simple approach to directly apply Eq. (2.8) or Eq. (2.10) to the classical QCD *Lagrangian* (2.1) would not lead to meaningful results but to ill-defined divergent quantities: The functional integral over the gauge fields is highly redundant since the domain of integration repeatedly involves field configurations which are related to each other by gauge transformations (2.6), the so-called gauge orbits. Such field configurations are physically equivalent and give superfluous contributions to the integral. Therefore, the integration has to be constrained to a domain of actually physically different field configurations by implementing a gauge-fixing condition. This can be achieved by making use of the *Faddeev-Popov* method [212], which we briefly sketch following the lines of [202, 204, 211]. A gauge-fixing term $\mathsf{F}^a[A_\mu] = 0$ can be introduced to the generating functional $Z[J]$ by inserting the identity[4]

$$1 = \int \mathcal{D}\mathsf{F}^a \, \delta[\mathsf{F}^a] = \int \mathcal{D}\theta \, \delta(\mathsf{F}^a[A'_\mu]) \, \det\left(\frac{\delta \mathsf{F}^a[A'_\mu]}{\delta\theta^b}\right) . \tag{2.13}$$

The field A'_μ denotes the transformed gauge field A_μ according to Eq. (2.6) and thus depends on the parameters $\theta^a(x)$. The functional determinant that appears in Eq. (2.13) is independent of the parameter functions $\theta^a(x)$ and thus gauge invariant as long as the gauge-fixing conditions are linear in the gauge fields. Specifying the gauge-fixing condition to be the generalized *Lorenz* gauge $\mathsf{F}^a[A_\mu] = \partial^\mu A^a_\mu(x) - C^a(x)$ with C^a being an arbitrary function, the identity (2.13) also holds for a *Gaußian* weighted functional integral over C^a up to an irrelevant normalization constant. This allows us to rewrite the functional delta distribution $\delta(F^a)$ in terms of the exponential expression $\exp\Big(-\int_x (\partial^\mu A^a_\mu(x))^2/(2\xi)\Big)$ so that it can be later included as an additional term to the action. The gauge parameter ξ originates from the *Gaußian* weight. Inserting the identity to the generating functional and exploiting the gauge invariance of the measure $\mathcal{D}A$ and the action $S[A]$ (for the sake of brevity we include in our considerations here the gauge sector only), we can reorder the arrangement of the integrals to find

$$Z[0] = \text{const.} \times \left(\int \mathcal{D}\theta\right) \int \mathcal{D}A \;\; \mathrm{e}^{-S[A] - \int_x (\partial^\mu A^a_\mu(x))^2/(2\xi)} \;\; \det\left(\frac{\delta \mathsf{F}^a[A'_\mu]}{\delta\theta^b}\right) . \tag{2.14}$$

The integral over the parameter functions θ^a can be factored out and leads to a mere constant factor that is not relevant in the computation of physical quantities. This is exactly the superfluous contribution due to physically equivalent gauge field configurations, i.e., the functional integral over the gauge orbits. Since it is our aim to exclude such superfluous contributions, we drop this constant in the following and we are left with the integral over the physical degrees of freedom only. In order to also bring the expression of the determinant to

---

[4] Here, it is assumed that the *Faddeev-Popov* determinant is positive definite and that there is only one gauge copy per gauge orbit that satisfies the gauge-fixing condition. However, typical choices of gauge-fixing conditions violate both assumptions, leading to the so-called Gribov problem [213]. Furthermore, the *Faddeev-Popov* method assumes that the operators as they appear in the definition (2.8) are gauge invariant.

the exponent, the determinant can be reformulated as a path integral over newly introduced anticommuting scalar fields, leading to

$$\det\left(\frac{\delta\mathsf{F}^a[A'_\mu]}{\delta\theta^b}\right) = \text{const.} \times \int \mathcal{D}\bar{c}\mathcal{D}c \, \exp\left[-\int_x \bar{c}^a(x)\Big(\delta^{ab}\partial^2 + \bar{g}_s f^{acb}\partial^\mu A^c_\mu\Big)c^b(x)\right], \tag{2.15}$$

where the ghost fields have been defined to absorb a factor $1/\bar{g}_\mathrm{s}$. As anticommuting scalar fields violate the spin-statistics theorem [202], the quanta of these fields cannot be real physical particles. As a consequence, these so-called *Faddeev-Popov* ghosts cannot appear as external fields in *Feynman* diagrams but only as internal lines in loop diagrams. Eventually, assembling all parts including the matter fields, the generating functional reads

$$Z[\eta,\bar{\eta},j,\zeta,\bar{\zeta}] = \int \mathcal{D}\psi\mathcal{D}\bar{\psi}\mathcal{D}A\mathcal{D}c\mathcal{D}\bar{c}\,\mathrm{e}^{-\int_x \mathcal{L}_{FP}+\int_x(\bar{\psi}\eta+\bar{\eta}\psi+jA+\bar{c}\zeta+\bar{\zeta}c)}\,, \tag{2.16}$$

with the *Faddeev-Popov* (FP) *Lagrangian*

$$\mathcal{L}^{\mathrm{FP}}_{\mathrm{QCD}} := \bar{\psi}\left(\mathrm{i}\not{D} + \mathrm{i}m\right)\psi + \frac{1}{4}(F^a_{\mu\nu})^2 + \mathcal{L}_{\mathrm{GF}} + \mathcal{L}_{\mathrm{FPG}}\,, \tag{2.17}$$

where $\mathcal{L}_{\mathrm{GF}} := 1/(2\xi)(\partial^\mu A^a_\mu)^2$ denotes the gauge-fixing term and $\mathcal{L}_{\mathrm{FPG}} := \bar{c}^a(-\partial^2\delta^{ab} + \bar{g}_s f^{acb}\partial^\mu A^c_\mu)c^b$ the *Faddeev-Popov* ghost term. The latter term implies a propagator for the ghosts and gives rise to interactions between gauge and ghost fields. Typical choices for the gauge parameter ξ include the *Feynman-'t Hooft* gauge $\xi = 1$ and the *Landau* gauge $\xi = 0$.

Now, with the *Faddeev-Popov Lagrangian* (2.17) at hand, we can for instance compute the leading term of the *Callan-Symanzik* β function of the strong coupling in perturbation theory, provided the coupling is sufficiently small to allow a weak-coupling expansion. We briefly discuss the result and its implications following Refs. [202, 204]. The β function describes the rate at which the renormalized coupling changes under variation of the renormalization scale. This behavior is of great interest as it determines the strength of the interaction and hence, e.g., the applicability of perturbative approaches. It can be shown that the leading term of the β function is invariant under gauge transformations [203]. This term can be derived, e.g., from the leading-order loop corrections to the quark-gluon vertex by studying the divergences of the vertex and the field strength renormalizations or from the one-loop corrections in perturbation theory in the background-field formalism. The gauge invariance in the perturbative regime implies that calculations of the leading contribution to the β function using the three- or four-gluon vertex must give the same result.[5] The leading term of the β function in a $SU(N_\mathrm{c})$ gauge theory with N_f quark flavors is given by, e.g., Ref. [202],

$$\beta(g_\mathrm{s}) = -\frac{g_\mathrm{s}^3}{(4\pi)^2}\left(\frac{11}{3}N_\mathrm{c} - \frac{2}{3}N_\mathrm{f}\right)\,, \tag{2.18}$$

---

[5] The leading term of the perturbative β function of the strong coupling is universal and independent of the regularization scheme, whereas the two-loop coefficient is only universal if mass-independent regularization schemes are employed [211]. In the non-perturbative regime, however, the coupling constants as defined from the different vertices show different renormalizations.

where we have assumed massless quarks in the fundamental representation and g_s denotes the renormalized strong coupling. The second term in Eq. (2.18) can be attributed to the fermionic fields. Neglecting the first term, the overall sign of the β function turns positive and describes a scenario similar to that in QED, i.e., the effective electric charge decreases for larger distances. The virtual creation of electron-positron pairs leads to a polarization of the vacuum and screens the electric charge. In contrast to that, the gauge bosons in a non-*Abelian* gauge theory have the opposite effect. The gluons give rise to the first term in Eq. (2.18) which is opposite in sign as compared to the quark contribution. As long as the number of quark flavors is small enough (smaller than 17 flavors for $N_\mathrm{c} = 3$ as implied by Eq. (2.18)) the overall sign of the β function is negative. The dominating "antiscreening" effect of the gluons leads to a coupling constant that becomes weaker at higher momentum transfers. This behavior is called asymptotic freedom and is a distinctive property of non-*Abelian* gauge theories [37]. The renormalized coupling constant g_s is defined to satisfy the equation

$$\frac{\mathrm{d}}{\mathrm{d}\log(Q/M)} g_\mathrm{s} = \beta(g_\mathrm{s}), \tag{2.19}$$

with the boundary condition $g_\mathrm{s}(M) = g_\mathrm{s}$ at the renormalization scale M. The arbitrary renormalization scale M can be eliminated by introducing the QCD scale Λ_QCD which describes the position of the *Landau* pole. The QCD scale is experimentally determined to be approximately $\Lambda_\mathrm{QCD} \sim 200\,\mathrm{MeV}$ [202].[6] The solution to the renormalization group equation (2.19) in terms of $\alpha_\mathrm{s} = g_\mathrm{s}^2/(4\pi)$ is given by

$$\alpha_\mathrm{s}(Q) = \frac{2\pi}{\left(\frac{11}{3}N_\mathrm{c} - \frac{2}{3}N_\mathrm{f}\right)\log(Q/\Lambda_\mathrm{QCD})}, \tag{2.20}$$

showing the decrease in the interaction strength for increasing momentum transfer Q. In experimental precision tests the strong coupling is extracted at different momentum scales from various physical processes, e.g., from hadronic τ decays or from deep inelastic lepton-nucleon scattering [39]. In order to compare the results, the coupling constant is conventionally evolved to a common renormalization scale by employing the modified minimal subtraction ($\overline{\mathrm{MS}}$) scheme [214]. The renormalization scale is typically given by the Z-boson mass of the weak interaction, i.e., $Q = M_Z = 91.19\,\mathrm{GeV}$. The current average value is $\alpha_\mathrm{s}(M_Z) = 0.1181 \pm 0.0011$ [39]. In Fig. 2.1 current experimental results on the measurement of the strong coupling constant α_s are summarized.

2.1.1 Thermodynamics of QCD

The thermodynamics of QCD aims at describing the equilibrium bulk properties of dense strong-interaction matter at finite temperature T. Owing to its relativistic nature and the associated

---

[6] The exact value depends on details of the calculation which conventionally employs the modified minimal subtraction scheme [214]. The essential aspect is that the QCD scale, describing the scale at which the coupling becomes "strong", is of the order of several hundred MeV [5].

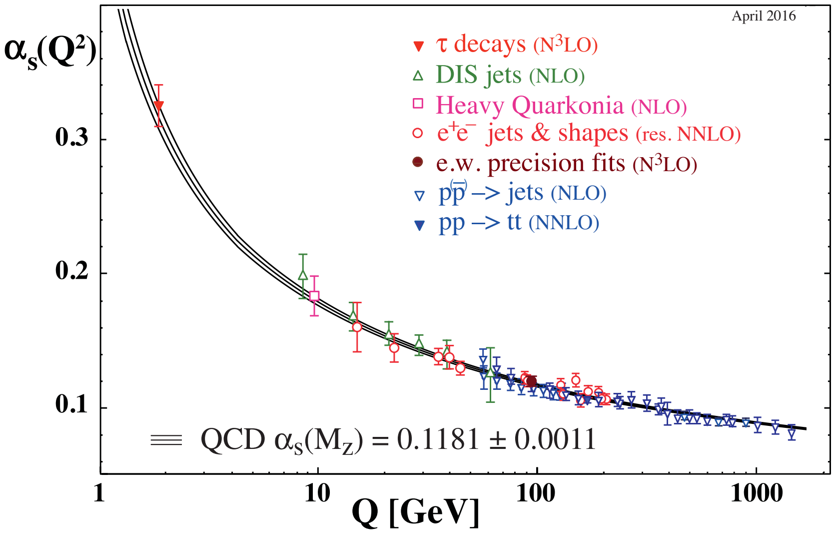

FIGURE 2.1: Summary of measurements of the strong coupling constant α_s as a function of the momentum transfer Q, taken from Ref. [39].

non-conservation of the particle number,[7] the appropriate thermodynamic description is given by the grand canonical ensemble. The ensemble average of any observable represented by an operator $\hat{O}$ can be computed by employing the statistical density matrix $\hat{\rho}$ according to

$$\langle \hat{O} \rangle = \frac{\operatorname{tr} \hat{O}\hat{\rho}}{\operatorname{tr} \hat{\rho}} , \qquad \text{with} \quad \hat{\rho} = \mathrm{e}^{-(\hat{H} - \mu_i \hat{N}_i)/T} , \tag{2.21}$$

where μ_i's are the chemical potentials associated with the conserved charge operators $\hat{N}_i$. In this context, the grand canonical partition function

$$Z := \operatorname{tr} \hat{\rho} = \operatorname{tr} \mathrm{e}^{-(\hat{H} - \mu_i \hat{N}_i)/T} , \tag{2.22}$$

is the central quantity of interest. All thermodynamic properties can be derived from this function, e.g., the free energy density $f = \mathcal{F}/V$, the pressure p, the entropy density $s = S/V$ or the densities of the conserved charges $n_i = N_i/V$:

$$f = -\frac{T}{V} \log Z , \quad p = \frac{\partial (T \log Z)}{\partial V} , \quad s = \frac{1}{V} \frac{\partial (T \log Z)}{\partial T} , \quad n_i = \frac{1}{V} \frac{\partial (T \log Z)}{\partial \mu_i} , \tag{2.23}$$

where V denotes the spatial volume. Against the background of the thermodynamic limit, we consider here the corresponding densities, i.e., the intensive analogs of the thermodynamic quantities. With these quantities the energy density is determined by $\epsilon = -p + Ts + \mu_i n_i$.

The partition function (2.22) of quantum statistical mechanics in a three dimensional space can be recast as a path integral in a $(3+1)$-dimensional *Euclidean* quantum field theory by *Wick* rotating to the imaginary time $t = -\mathrm{i}\tau$ [215]. For a bosonic quantum field φ and the

---

[7] Due to creation and annihilation processes, only the net number of quarks minus antiquarks is conserved and not the number of particles and antiparticles separately.

associated conjugate momentum $\pi = \partial\mathcal{L}_\mathrm{M}/\partial(\partial_t\varphi)$ in terms of the *Lagrangian* in *Minkowski* space-time, the path integral representation reads[8]

$$Z \;=\; \int\limits_{\varphi(0,\vec{x})=\varphi(\beta,\vec{x})} \mathcal{D}\pi\,\mathcal{D}\varphi\,\exp\left\{-\int_0^\beta \mathrm{d}\tau \int \mathrm{d}^3x\,\left(\mathcal{H}(\pi,\varphi) - \mathrm{i}\pi(\partial_0\varphi) - \mu_i\mathcal{N}_i(\pi,\varphi)\right)\right\}\,, \tag{2.24}$$

with the inverse temperature $\beta = 1/T$, the charge density $\mathcal{N}(\pi,\varphi)$ and the *Hamiltonian* density $\mathcal{H}(\pi,\varphi)$. The latter is related to the *Lagrangian* $\mathcal{L}_\mathrm{M}$ through the usual Legendre transformation $\mathcal{H} = \mathrm{i}\pi(\partial_0\varphi) - \mathcal{L}_\mathrm{M}$. For a detailed derivation of the functional integral representation we refer to, e.g., Refs. [208, 216]. The integral over φ is constrained by the periodic boundary condition $\varphi(0,\vec{x}) = \varphi(\beta,\vec{x})$ on account of the initial trace operation, whereas the integration over the conjugate momentum π is unconstrained. Typically, the conjugate momentum appears at most quadratically in the exponent and the functional integral can be evaluated as a generalized *Gaußian* integral. In this way, the exponent can be rewritten in terms of the *Euclidean Lagrangian* density and the partition function assumes again the form of the generating functional (2.10), apart from the periodic boundary condition and terms associated with the chemical potentials in the presence of conserved quantities. This illustrates the very close relation between quantum statistical mechanics and quantum field theory [124]. The generating functional $Z[J]$ in Eq. (2.10) can be considered as the partition function with an added source term in the limit of zero temperature and vanishing chemical potentials. The path integral representation of the partition function (2.24) can easily be extended to various fields and conserved charges. The conjugate momentum of a *Dirac* field is given by $\mathrm{i}\psi^\dagger$ which is treated as independent field variable. In contrast to the case of a bosonic field, the separate evaluation of the functional integral over the conjugate variable $\mathrm{i}\psi^\dagger$ is not considered and the functional integral already assumes its final form in terms of its field content. Thus, the exponent can readily be reformulated in terms of the *Euclidean Lagrangian* with the replacement

$$\mathcal{L} \longrightarrow \mathcal{L} - \mu_i\mathcal{N}_i\,, \tag{2.25}$$

in case of chemical potentials associated with conserved quantities. This leads again to a path integral representation in form of the generating functional (2.10), cf. also the matter part of Eq. (2.16). Due to the *Grassmann* nature of fermionic fields, the integral is constrained by antiperiodic boundary conditions $\psi(0,\vec{x}) = -\psi(\beta,\vec{x})$. The compactification of the time integration at finite temperature leads to a discretization in momentum space and gives rise to the *Matsubara* frequencies $\omega_n := 2\pi nT$ and $\nu_n := (2n+1)\pi T$, with $n \in \mathbb{Z}$, in the case of bosonic and fermionic fields, respectively. However, these are the only modifications arising due to a finite temperature. For this reason, we do not explicitly distinguish in the following between the case of vanishing temperature and the case of finite temperature. For most of the time we can use the same notation for both cases, see Appendix A.3 for details. In this context, the quantity $Z[J]$ denotes the generating functional generalized to the case of finite temperature, i.e., the time direction is compactified. Alternatively, the other way around, the

---

[8] The imaginary unit i in the term $\mathrm{i}\pi(\partial_0\varphi) \equiv \mathrm{i}\pi(\partial_\tau\varphi)$ in Eq. (2.24) appears due to the imaginary-time formalism.

partition function is extended by an external source J, providing a generating functional for finite temperature expectation values.

2.1.2 Symmetries of QCD

In the vacuum limit, i.e., in the limit of zero temperature and vanishing chemical potentials, the QCD *Lagrangian* is manifest *Lorentz* invariant and is assumed to be invariant under the discrete symmetries parity $\mathcal{P} : (t, \vec{x}) \mapsto (t, -\vec{x})$, time reversal $\mathcal{T} : (t, \vec{x}) \mapsto (-t, \vec{x})$, and charge conjugation $\mathcal{C}$, i.e., the replacement of particles with the corresponding antiparticles and vice versa. The generation of interactions between the quarks via the gauge principle introduces the invariance under local $SU(N_\mathrm{c})$ transformations. We now turn to the important global symmetries of QCD related to the quark fields and briefly discuss the main aspects following Refs. [202–204, 207, 215]. The discussion is restricted to $N_\mathrm{f} = 2$ quark flavors as this is the considered number of quark flavors throughout this work. Furthermore, we work in the chiral limit, i.e., the current quark masses are set to zero. This assumption is justified since the masses of the two lightest quark flavors, i.e., $m_u \approx 2\,\mathrm{MeV}$ and $m_d \approx 5\,\mathrm{MeV}$ (cf. Table 2.1) is negligibly small as compared to typical scales of the theory such as the QCD scale $\Lambda_\mathrm{QCD} \approx 200\,\mathrm{MeV}$ [202] or the mass of the sigma meson $m_\sigma \approx 500\,\mathrm{MeV}$ [39] as the lightest meson not being a *Goldstone* boson. To reveal the global symmetries it is helpful to introduce the projection operators

$$P_\mathrm{R} = \frac{1}{2}(1 + \gamma_5)\,, \quad P_\mathrm{L} = \frac{1}{2}(1 - \gamma_5)\,, \tag{2.26}$$

with $\gamma_5 = \gamma_1\gamma_2\gamma_3\gamma_0$. The projectors are idempotent, i.e., $P^2_{\mathrm{L/R}} = P_{\mathrm{L/R}}$, and fulfill the completeness relation $P_\mathrm{R} + P_\mathrm{L} = 1$ as well as the orthogonality relations $P_\mathrm{R}P_\mathrm{L} = P_\mathrm{L}P_\mathrm{R} = 0$. With the help of these operators we project the *Dirac* field onto its chiral components, i.e., onto the left-hand and right-handed components

$$\psi_\mathrm{L} = P_\mathrm{L}\psi\,, \quad \psi_\mathrm{R} = P_\mathrm{R}\psi\,, \tag{2.27}$$

respectively. Rewritten in terms of these chiral components, the *Lagrangian* decouples into parts that connect left-handed components only with left-handed ones and vice versa, as we find

$$\bar{\psi}\mathrm{i}\not{D}\psi \quad \longrightarrow \quad \bar{\psi}_\mathrm{R}\mathrm{i}\not{D}\psi_\mathrm{R} + \bar{\psi}_\mathrm{L}\mathrm{i}\not{D}\psi_\mathrm{L}\,. \tag{2.28}$$

This formulation shows that the QCD *Lagrangian* has a classical global $U_\mathrm{L}(2) \otimes U_\mathrm{R}(2)$ symmetry which can be decomposed into $SU_\mathrm{L}(2) \otimes SU_\mathrm{R}(2) \otimes U_\mathrm{V}(1) \otimes U_\mathrm{A}(1)$. The so-called chiral symmetry $SU_\mathrm{L}(2) \otimes SU_\mathrm{R}(2)$ describes the invariance under separate $SU(2)$ transformations of the left-handed or the right-handed components. In summary, the chiral components transform as

$$SU_\mathrm{L}(2): \qquad \psi_\mathrm{L} \mapsto \mathrm{e}^{\mathrm{i}\theta^i_\mathrm{L} T^i_{(f)}}\psi_\mathrm{L}\,, \qquad \psi_\mathrm{R} \mapsto \psi_\mathrm{R}\,, \qquad \bar{\psi}_\mathrm{L} \mapsto \bar{\psi}_\mathrm{L}\mathrm{e}^{-\mathrm{i}\theta^i_\mathrm{L} T^i_{(f)}}\,, \qquad \bar{\psi}_\mathrm{R} \mapsto \bar{\psi}_\mathrm{R}\,,$$

$$\begin{aligned}
SU_\mathrm{R}(2): \quad & \psi_\mathrm{L} \mapsto \psi_\mathrm{L}\,, & \psi_\mathrm{R} &\mapsto \mathrm{e}^{\mathrm{i}\theta^i_\mathrm{R} T^i_{(f)}} \psi_\mathrm{R}\,, & \bar\psi_\mathrm{L} &\mapsto \bar\psi_\mathrm{L}\,, & \bar\psi_\mathrm{R} &\mapsto \bar\psi_\mathrm{R} \mathrm{e}^{-\mathrm{i}\theta^i_\mathrm{R} T^i_{(f)}}\,,\\
U_\mathrm{V}(1): \quad & \psi_\mathrm{L} \mapsto \mathrm{e}^{\mathrm{i}\theta_\mathrm{V}}\psi_\mathrm{L}\,, & \psi_\mathrm{R} &\mapsto \mathrm{e}^{\mathrm{i}\theta_\mathrm{V}} \psi_\mathrm{R}\,, & \bar\psi_\mathrm{L} &\mapsto \bar\psi_\mathrm{L}\mathrm{e}^{-\mathrm{i}\theta_\mathrm{V}}\,, & \bar\psi_\mathrm{R} &\mapsto \bar\psi_\mathrm{R} \mathrm{e}^{-\mathrm{i}\theta_\mathrm{V}}\,,\\
U_\mathrm{A}(1): \quad & \psi_\mathrm{L} \mapsto \mathrm{e}^{-\mathrm{i}\theta_\mathrm{A}}\psi_\mathrm{L}\,, & \psi_\mathrm{R} &\mapsto \mathrm{e}^{\mathrm{i}\theta_\mathrm{A}} \psi_\mathrm{R}\,, & \bar\psi_\mathrm{L} &\mapsto \bar\psi_\mathrm{L}\mathrm{e}^{\mathrm{i}\theta_\mathrm{A}}\,, & \bar\psi_\mathrm{R} &\mapsto \bar\psi_\mathrm{R} \mathrm{e}^{-\mathrm{i}\theta_\mathrm{A}}\,, \qquad (2.29)
\end{aligned}$$

where in the fundamental representation the generators $T^i_{(f)} = \tau^i/2$ of the $SU_f(2)$ flavor group are given by the *Pauli* matrices τ^i. On a classical level, continuous symmetries of a field theory can be related to corresponding conserved currents by *Noether*'s theorem [217, 218]. In a simple version, cf. Ref. [215], the theorem states that the invariance of the *Lagrangian* $\mathcal{L}$ under an infinitesimal change $\delta\phi_i$ of the field multiplet ϕ_i implies the conservation of a current j^μ given by

$$j^\mu = \frac{\partial \mathcal{L}}{\partial\left(\partial_\mu \phi_i\right)}\delta\phi_i\,, \tag{2.30}$$

i.e., $\partial_\mu j^\mu = 0$. For a *Lie* group with generators T^a and an invariance under the infinitesimal transformation $\phi_i \mapsto \phi_i - \mathrm{i}\epsilon^a T^a_{ij}\phi_j \equiv \phi_i + \epsilon^a \delta\phi^a_i$ with parameters ϵ^a, we find a conserved current j^a_μ for each generator. The corresponding conserved charges are obtained by taking the space integral of the zero component of the conserved currents as the associated charge densities, i.e., $Q^a = \int \mathrm{d}^3x\, j^a_0$. We note that in a quantized theory the charge operators of a conserved *Noether* current are the generators of the related symmetry, i.e., the field operator ϕ_i transforms according to

$$\phi_i \mapsto \phi_i' = \mathrm{e}^{\mathrm{i}\epsilon^a Q^a}\phi_i \mathrm{e}^{-\mathrm{i}\epsilon^a Q^a} \approx \phi_i + \mathrm{i}\epsilon^a\left[Q^a, \phi_i\right] = \phi_i - \mathrm{i}\epsilon^a T^a_{ij}\phi_j, \tag{2.31}$$

where the matrices T^a form a representation of the generators Q^a.

Noether's theorem applied to the $U_\mathrm{V}(1)$ symmetry in Eq. (2.29) leads to baryon number conservation. The conserved charge is given by

$$Q_V = \int \mathrm{d}^3x\,\left(\bar\psi_\mathrm{L}\gamma_0\psi_\mathrm{L} + \bar\psi_\mathrm{R}\gamma_0\psi_\mathrm{R}\right) = \int \mathrm{d}^3x\,\psi^\dagger(x)\psi(x)\,, \tag{2.32}$$

with the quark number density $\mathcal{N}_q(x) = \psi^\dagger(x)\psi(x)$. In fact, the QCD *Lagrangian* is invariant under separate $\mathrm{U}_V(1)$ phase transformations of the single quark flavors and the currents $\bar\psi_u\gamma^\mu\psi_u$, $\bar\psi_d\gamma^\mu\psi_d, \ldots$ of the individual quark flavors are also conserved. The quark number Eq. (2.32) describes the sum of these individually conserved charges. In order to study strong-interacting matter at finite density, the conserved quark number density $\mathcal{N}_q(x)$ can be incorporated into the path integral representation of the partition function according to Eq. (2.24) and gives rise to the additional contribution $\bar\psi(-\mathrm{i}\mu\gamma_0)\psi$ to the kinetic part of the quark fields $\hat{T}_{\bar\psi\psi}$ which then reads[9]

$$\hat{T}_{\bar\psi\psi} := \bar\psi\left(\mathrm{i}\partial\!\!\!/ - \mathrm{i}\mu\gamma_0\right)\psi\,. \tag{2.33}$$

---

[9] The imaginary unit i originates from the replacement $\bar\psi \to \mathrm{i}\bar\psi$ according to our chosen conventions for the imaginary-time formalism with *Euclidean* space-time, see Appendix A.2.

The quark chemical potential μ is a *Lagrange* multiplier and introduces, somewhat loosely speaking, an imbalance between quarks and antiquarks.

At low energy the chiral symmetry $SU_{\mathrm{L}}(2) \otimes SU_{\mathrm{R}}(2)$ is not manifest, i.e., hidden in nature. Only the subgroup of the isospin rotations $SU_{\mathrm{V}}(2)$ that describes the simultaneous transformation of left- and right-handed quark fields with $\theta_{\mathrm{L}} = \theta_{\mathrm{R}}$ is a realized symmetry in the chiral limit[10] and gives rise to isospin conservation. Indeed, the ground state can be shown to be necessarily invariant under $SU_{\mathrm{V}}(2) \otimes U_{\mathrm{V}}(1)$ in the chiral limit [219].

The invariance under the orthogonal axial transformations generated by the linear combination

$$Q^i_{\mathrm{A}} = Q^i_{\mathrm{R}} - Q^i_{\mathrm{L}} = \frac{1}{2} \int \mathrm{d}^3x \, \bar{\psi} \gamma_0 \gamma_5 \tau^i \psi \tag{2.34}$$

of the right- and left-handed charge operators of the chiral symmetry Q^i_{R} and Q^i_{L}, respectively, would imply degenerate states of opposite parity in the hadron spectrum. However, this so-called parity doubling is not observed, e.g. a low-energy baryon octet of negative parity corresponding to the existing octet of positive parity is missing in the particle spectrum. The symmetry of the ground state is strongly connected to the symmetry of the spectrum by *Coleman*'s theorem [47]. Therefore, the symmetry pattern of the hadron spectrum shows strong evidence that the ground state is not invariant under axial transformations.

Based on an analogy with superconductivity [45, 46], this led to the hypothesis that the invariance of the QCD action under chiral transformations is an accurate symmetry which is spontaneously broken down to $SU_{\mathrm{L}}(2) \otimes SU_{\mathrm{R}}(2) \to SU_{\mathrm{V}}(2)$ by the ground state, i.e., the generators $Q^i_{\mathrm{A}}|0\rangle \neq 0$ do not annihilate the vacuum. This non-perturbative phenomenon of the theory of the strong interaction is called chiral symmetry breaking (χSB). According to *Goldstone*'s theorem [48, 49], the spontaneous breaking of a continuous global symmetry gives rise to the appearance of massless *Nambu-Goldstone* bosons in the channels of each broken symmetry, i.e., the number of massless bosons equals the number of generators of transformations that do not leave the ground state invariant. The properties of the *Nambu-Goldstone* bosons are closely related to the associated "broken" generators, cf. Appendix C for more details. The hadron spectrum contains indeed particles of unusually low masses, i.e., in the case of 2-flavor QCD the pion triplet, which are considered to be pseudo *Nambu-Goldstone* bosons. The reason for the addition *pseudo* is the small but non-zero masses of the pions as the QCD *Lagrangian* is only approximately invariant under chiral transformations due to the small but finite current quark masses at the physical point.

The pions have negative parity which matches the transformation behavior of the generators Q_{A} of the axial transformations. Indeed, the QCD vacuum can be expected to be not invariant under axial transformations. The strong attractive interactions give rise to the appearance of condensates of quark-antiquark pairs as the energy cost to produce a pair of at least approximately massless quarks is small. Such pairs, due to the requirement of vanishing momentum and angular momentum, possess a net chiral charge [202]. The spontaneous

---

[10] Regarding the two lightest flavors up and down, this symmetry is approximately realized for physical current quark masses as well, since both masses are almost equal and negligibly small compared to, e.g., the QCD scale Λ_{QCD}.

breakdown of the chiral symmetry is therefore associated with the formation of a corresponding chiral condensate $\langle\bar{\psi}\psi\rangle$ which is according to

$$\langle 0|[\mathrm{i}Q_A^i, \bar{\psi}\mathrm{i}\gamma_5\tau^i\psi]|0\rangle = \langle 0|\bar{\psi}\psi|0\rangle = \langle 0|\bar{\psi}_\mathrm{L}\psi_\mathrm{R} + \bar{\psi}_\mathrm{R}\psi_\mathrm{L}|0\rangle, \quad i \in \{1,2,3\}\,, \tag{2.35}$$

a sufficient criterion for χSB. The formation of the chiral condensate renders the quarks massive and provides in this way a mechanism for the dynamical generation of the constituent quark masses.

The restoration of chiral symmetry does not necessarily imply the axial $U_\mathrm{A}(1)$ symmetry to be restored. In fact, this symmetry is not realized in nature but is broken by quantum corrections. Global symmetries of a classical action that are not realized in a quantum theory are referred to as anomalous symmetries [220–222].[11] The so-called axial or chiral anomaly is caused by topologically non-trivial gauge configurations [223, 224] that lead to a divergence of the classical *Noether* current $j_A^\mu = \bar{\psi}\gamma^\mu\gamma_5\psi$ in the form of

$$\partial_\mu j_A^\mu \sim g_\mathrm{s}^2 N_\mathrm{f}\epsilon^{\mu\nu\rho\sigma}F_{\mu\nu}^a F_{a,\rho\sigma}\,, \quad \text{with } \epsilon^{0123} = 1\,, \tag{2.36}$$

c.f. Refs. [202, 203]. For the phenomenologically more relevant three-flavor case, the explicit breaking of the $U_\mathrm{A}(1)$ symmetry has been put forward even earlier to explain the η-η' mixing in the mesonic particle spectrum [225, 226], resulting in the mass splitting of the respective particles. The absence of the $U_\mathrm{A}(1)$ symmetry may be deduced from other observations as well, e.g. from the missing parity doubling of hadronic states [227] again, at least at low energies.[12]

Silver-Blaze property

In order to study strong-interaction matter at finite density, the kinetic term of the quark fields is modified to include the quark chemical potential, see Eq. (2.33). It appears that any finite chemical potential changes the eigenspectrum of the propagator and consequently the partition function Z and derived thermodynamic quantities such as the free energy or the quark number density as well. At *zero* temperature, however, the so-called *Silver-Blaze* property, or “problem”, refers to the fact that the partition function of, e.g., a fermionic system does not exhibit a dependence on the chemical potential, i.e., it remains as that of the vacuum, provided that the chemical potential is less than some critical value [228], see also, e.g., Refs. [229–231]. The critical value is determined by the (pole) mass of the lightest particle carrying a finite charge associated with the chemical potential, i.e., in case of the quark chemical potential a finite baryon number, see below. The *Silver-Blaze* property of the partition function or free energy carries over to the correlation functions, see, e.g., Ref. [229]. Phenomenologically speaking, this property simply states that the fermion density (corresponding to the difference in the numbers of fermions and antifermions) remains zero at *zero* temperature as long as the chemical potential is less than the (pole) mass of the lightest charged particle. For the sake of simplicity, let us consider in the following a theory where

---

[11] In the path integral formalism the anomalous breaking of a classical symmetry can be traced back to an integral measure that is not invariant.

[12] The spontaneous breaking of chiral symmetry dynamically generates the constituent quark mass which breaks the $U_\mathrm{A}(1)$ symmetry anyway.

only the fermions carry a charge. Mathematically speaking, the *Silver-Blaze* property is then a consequence of the fact that the theory is invariant under the following transformation:[13]

$$\bar{\psi} \mapsto \bar{\psi}\,\mathrm{e}^{-\mathrm{i}\alpha\tau}\,,\quad \psi \mapsto \mathrm{e}^{\mathrm{i}\alpha\tau}\psi\,,\quad \mu \mapsto \mu + \mathrm{i}\alpha\,, \tag{2.37}$$

where α parametrizes the transformation and τ is the imaginary time. Setting $\alpha = q_0$, Eq. (2.37) immediately implies the following invariance of the partition function Z:

$$Z\Big|_{\mu\to\mu+\mathrm{i}q_0} = Z\,. \tag{2.38}$$

Thus, the partition function is invariant under a shift of the chemical potential μ along the imaginary axis. Assuming that Z is analytic, it follows that Z does not depend on μ at all. In particular, we deduce from an analytic continuation of Eq. (2.38) from q_0 to $\mathrm{i}q_0$ that Z does not depend on the actual value of the real-valued chemical potential μ.

For the effective action Γ, it follows in the same way from Eq. (2.37) that

$$\Gamma[\bar{\psi}\mathrm{e}^{-\mathrm{i}q_0\tau}, \mathrm{e}^{\mathrm{i}q_0\tau}\psi]\Big|_{\mu\to\mu+\mathrm{i}q_0} = \Gamma[\bar{\psi},\psi]\,, \tag{2.39}$$

and similarly for higher n-point functions, since the latter are obtained from Γ by taking functional derivatives with respect to the fields and setting them to zero subsequently.

On the level of correlation functions, we recall that, for example, the two-point function has a pole at $p_0^2 = -m_\mathrm{f}^2$ at $\vec{p} = 0$, where m_f is the (pole) mass of the fermion. Thus, an analytic continuation of the two-point function in the complex p_0-plane is restricted to the domain $|p_0| \leq m_\mathrm{f}$, as the pole mass is the singularity closest to the origin of the complex p_0-plane. From Eq. (2.39), on the other hand, we find the following relation for the two-point function:

$$\Gamma^{(1,1)}(p_0 - q_0, \vec{p}; p_0' - q_0, \vec{p}\,')\big|_{\mu\to\mu+\mathrm{i}q_0} = \Gamma^{(1,1)}(p_0, \vec{p}; p_0', \vec{p}\,')\,, \tag{2.40}$$

where the four-momenta $(p_0^{(\prime)}, \vec{p}^{\,(\prime)})$ are associated with the ingoing and outgoing fermion lines, respectively. Note that $\Gamma^{(1,1)}$ is diagonal in momentum space, i.e.,

$$\Gamma^{(1,1)}(p_0, \vec{p}; p_0', \vec{p}\,') = \tilde{\Gamma}^{(1,1)}(p_0, \vec{p})(2\pi)\delta(p_0 - p_0')(2\pi)^3\delta^{(3)}(\vec{p} - \vec{p}\,')\,. \tag{2.41}$$

For $q_0 = \mathrm{i}\mu$, Eq. (2.40) implies

$$\left(\lim_{\mu\to 0}\Gamma^{(1,1)}(p_0, \vec{p}; p_0', \vec{p}\,')\right)\Bigg|_{p_0^{(\prime)}\to p_0^{(\prime)} - \mathrm{i}\mu} = \Gamma^{(1,1)}(p_0, \vec{p}; p_0', \vec{p}\,') \tag{2.42}$$

for $\mu < m_\mathrm{f}$. The latter constraint follows from the definition of the pole mass: $\Gamma^{(1,1)} = 0$ for $(p_0 - \mathrm{i}\mu)^2 = -m_\mathrm{f}^2$, i.e., $p_0 = \mathrm{i}(\mu \pm m_\mathrm{f})$, and $\vec{p} = 0$. Note that m_f refers to the pole mass at $\mu = 0$. This line of argument can be generalized straightforwardly to higher n-point functions.

---

[13] Here, we effectively treat the chemical potential as an external constant background field.

Overall, it follows that, at *zero* temperature and $\mu < m_{\mathrm{f}}$, the free energy of the system does not exhibit a dependence on μ, as stated above [228]. The μ-dependence of the correlation functions is trivially obtained by replacing the zeroth components of the four-momenta in the vacuum correlation functions with suitably μ-shifted zeroth components, see, e.g., Eq. (2.42). This then implies that these functions also do not exhibit a dependence on μ due to the analytic properties of these functions for $\mu < m_{\mathrm{f}}$. In any case, these statements cannot be generalized to the finite-temperature case as the zeroth component of the *Euclidean* four-momentum becomes discrete due to the compactification of the *Euclidean* time direction and the analytic continuation entering the above line of arguments cannot be defined uniquely.

2.2 ASPECTS OF COLOR SUPERCONDUCTIVITY

As dense strong-interaction matter at small temperatures gives rise to the phenomenon of color superconductivity, we briefly recapitulate in the following some basic aspects of superconductivity in general and in the context of cold, dense quark matter. This summary is mainly based on the reviews [107, 108, 115, 116, 232].

The instability with respect to the formation of *Cooper* pairs [113] in the *Bardeen-Cooper-Schrieffer* (BCS) theory of superconductivity [111, 112] is a very generic phenomenon: At sufficiently small temperature the *Fermi* sphere of *any* fermionic system becomes unstable as soon as an arbitrarily weak attractive interaction is turned on. For a fermion at the *Fermi* surface it is then energetically favorable to slightly rise above the sphere to form a bound state together with a fermion of opposite momentum and spin.[14] The system stabilizes in the state in which the energy gain of the bound state formation is balanced by the kinetic energy cost to assume a momentum larger than the initial *Fermi* momentum. The *Cooper* pairs are bosonic fermion-fermion pairs and macroscopically occupy the same quantum state of lowest energy which leads to the formation of a condensate. The dispersion relation of a one-particle excitation becomes gapped by the condensate and assumes the characteristic form [115]

$$\omega_{\pm} = \sqrt{(E_{\vec{p}} \pm \mu)^2 + |\Delta|^2}\,, \tag{2.43}$$

with $E_{\vec{p}} := \sqrt{\vec{p}^{\,2} + m^2}$ for a fermion with mass m and the size of the gap energy denoted by $|\Delta|$. The charges carried by the condensate are related to the symmetries which become spontaneously broken by its formation. As implied by the initial symmetries of the theory, these charges are still conserved. Yet, the system in the condensed phase is described in terms of quasiparticles that are superpositions of particle and "particle-hole" excitations and thus are no eigenstates of the charge operator anymore. The condensate can be thought of as a reservoir the quasiparticles can deposit charges to and extract charges from. The gapped energy spectrum finally gives rise to the macroscopic properties of superfluidity or superconductivity, i.e., a superflow transports the charge of the associated broken symmetry.

---

[14] This introductory discussion does not take into account further degrees of freedom such as flavor or color, or the possibility of pairs with non-zero spin.

Quark matter at asymptotically high densities precisely constitutes such a system that is susceptible to the formation of *Cooper* pairs. The scale of the momentum transfer is assumed to be set by the *Fermi* momentum or quark chemical potential, i.e., $Q/\Lambda_{\mathrm{QCD}} \sim \mu/\Lambda_{\mathrm{QCD}} \gg 1$.[15] On account of asymptotic freedom [35], the coupling of the strong interaction becomes small, i.e., $g_{\mathrm{s}}(Q) \ll 1$, and the strong-interaction matter allows a first-principles approach based on weak-coupling methods [95–108]. At such high densities the interaction of quarks is dominated by one-gluon exchange [109]. The scattering amplitude is proportional to the following color tensor:

$$\sum_{a=1}^{N_c^2-1} T^a_{ij} T^a_{kl} = -\frac{N_c+1}{4N_c}\left(\delta_{ij}\delta_{kl} - \delta_{il}\delta_{kj}\right) + \frac{N_c-1}{4N_c}\left(\delta_{ij}\delta_{kl} + \delta_{il}\delta_{kj}\right). \tag{2.44}$$

This tensor can be decomposed into an attractive antitriplet[16] channel and a repulsive sextet channel [116, 232]. With the antitriplet channel the strong interaction immediately provides an attractive interaction and thus gives rise to the *Cooper* instability of the *Fermi* sphere. As the *Cooper* pairs of two quarks would carry a finite color charge, this phenomenon is referred to as color superconductivity [96, 97, 106, 107, 109, 110].

Indeed, phases of color-superconducting quark matter were already conceived in early studies [95–97]. The potential significance of such phases, however, was realized only later on as studies found that the energy gap induced by the condensate might be as large as $\sim 100\,\mathrm{MeV}$ at densities relevant for astrophysical objects [109, 110, 141]. The baryon number densities reached in the interior of neutron stars are in the range $n_{\mathrm{B}} \gtrsim (2-10)n_0$,[17] which corresponds in our case to a quark chemical potential of approximately $\mu \gtrsim (300-700)\,\mathrm{MeV}$, and in principle allow for quark matter in a superconducting phase [56, 232]. However, such intermediate densities are very difficult to access since quark matter is still strongly coupled and is therefore not accessible within perturbative or weak-coupling approaches. The phases of hadronic matter and the possibility of color superconducting quark matter at intermediate densities occurring in neutron stars are of great phenomenological importance, yet are still far from being fully understood. The transition to a superconducting phase is linked to a reduction in energy depending on the size of the energy gap $|\Delta|$ and the *Fermi* momentum p_{F}^2. The latter is associated with the phase space that is available to the formation of *Cooper* pairs [56]. The energy reduction affects besides other thermodynamic properties, e.g. the specific heat, particularly the equation of state and consequently the mass-radius relation via the *Tolman-Oppenheimer-Volkov* (TOV) equation [150, 151]. Color superconductivity should also influence transport properties in terms of conductivities and viscosities and might affect experimental observables such as the cooling rate or the slowing down of the rotation [116]. Depending on the specific pairing pattern, the presence of an energy gap can also modify the neutrino

---

[15] The *Fermi* momentum of a relativistic fermion of mass m is given by $p_{\mathrm{F}} = \sqrt{\mu^2 - m^2}\Theta(\mu^2 - m^2)$. For fermions in the ultra-relativistic limit $m \to 0$ or at very high densities, i.e., $\mu/m \gg 1$, the *Fermi* momentum is approximately $p_{\mathrm{F}} \simeq \mu$.

[16] The channel is antisymmetric under the exchange of either the indices j, l of the incoming quarks or the indices i, k of the outgoing quarks.

[17] The nuclear saturation density is in terms of a number density $n_0 \approx 0.16/\mathrm{fm}^3$ or in terms of a mass density $\rho_0 \approx 2.7 \times 10^{14}\,\mathrm{g/cm}^3$.

emissivity [233] and the interplay with magnetic fields on the account of the electromagnetic Meissner effect [2, 234, 235].

First-principles calculations at asymptotically high densities [98–105] find that the energy gap on the *Fermi* surface of color-superconducting quark matter at zero temperature behaves as a function of the interaction strength g_s according to

$$|\Delta| \propto \frac{\mu}{g_\mathrm{s}^5 N_\mathrm{f}^{5/2}} \exp\left(-\frac{3\pi^2}{\sqrt{2} g_\mathrm{s}}\right) . \tag{2.45}$$

Although this result is obtained in the weak-coupling limit,[18] it is of non-perturbative nature as it effectively includes the resummation of infinitely many diagrams. Compared to the solution in standard BCS theory, the gap in Eq. (2.45) is parametrically enhanced, i.e., $|\Delta| \propto \exp(-\mathrm{const.}/g_\mathrm{s}^2)$ versus $|\Delta| \propto \exp(-\mathrm{const.}/g_\mathrm{s})$ [108]. The reason for this is the structure of the gluon propagator in a dense medium. In essence, the electric gluon exchange is screened by the *Debye* mass whereas the chromomagnetic part gives rise to an unscreened long-range interaction which leads to large forward scattering, see, e.g., Refs. [51, 107] for reviews. The relation (2.45) shows that for even arbitrarily small coupling g_s there is an energy gap of small but finite size. This behavior is qualitatively distinguished from, e.g., spontaneous chiral symmetry breaking. For the chiral condensate to form, the coupling of the interaction has to be greater than a certain critical value that depends on the scale under consideration.

For increasing temperature, more and more *Cooper* pairs are broken up again by thermal fluctuations. The condensate becomes smaller and finally melts away at a critical temperature. As in standard mean-field BCS theory, the critical temperature can be related to the size of the energy gap at zero temperature according to [102–105, 236–238]

$$T_\mathrm{cr} = \chi \frac{\mathrm{e}^\gamma}{\pi} |\Delta| , \tag{2.46}$$

with the *Euler-Mascheroni* constant $\gamma \approx 0.5772$. For the proportionality constant, we have $\chi = 1$ in standard BCS theory, but it depends otherwise on the specific pairing pattern. In any case, however, it is of the order of one and consequently the critical temperature and the energy gap at zero temperature are of the same order of magnitude [107].

As quarks are spin one-half particles that carry not only electric charge but also the quantum numbers flavor and color, the pairing patterns in color superconductivity are more diverse as compared to *Cooper* pairs with electrons. Depending on the specific pattern, the condensed phase of color-superconducting quark matter can simultaneously be a baryonic superfluid and/or an electromagnetic superconductor.[19] In the following, we characterize the pairing pattern in the case of two flavors that is considered to be the most dominant condensate generated by one-gluon exchange [109] and topologically non-trivial gauge configurations [109, 110, 239]: At the *Fermi* surface two quarks form a *diquark* pair in the scalar $J^P = 0^+$ state.[20] On the account of the *Pauli* principle, the diquark state must be antisymmetric with respect

---

[18] The expression (2.45) is obtained from solving the mean-field gap equation in the weak-coupling limit, assuming that the interaction is only non-vanishing for fermions close to the *Fermi* surface, see, e.g., Ref. [108].

[19] In a super*fluid* the associated symmetry that becomes spontaneously broken is *global* while in a super*conductor* the symmetry is *local*.

[20] A similar pseudoscalar state is disfavored by instanton effects [116].

to the exchange of the two quarks. The coupling of the spins is necessarily antisymmetric to obtain a scalar spin-0 state. As introduced above, see Eq. (2.44), the coupling in color space is also antisymmetric in the attractive channel of one-gluon exchange. As a consequence, the coupling in flavor space must be antisymmetric as well to fulfill the *Pauli* principle. As a result, the structure of the diquark condensate is given by

$$\Delta^l \sim \langle \mathrm{i}\bar{\psi}^C \gamma_5 \epsilon_{(f)} \varepsilon^l_{(c)} \psi \rangle \,, \tag{2.47}$$

with the totally antisymmetric tensors $\epsilon_{(f)} \equiv \epsilon^{\alpha\beta}_{(f)}$ and $\varepsilon^l_{(c)} \equiv \varepsilon^{lmn}_{(c)}$ in flavor and color space, respectively. Moreover, we have introduced charge conjugated fields $\psi^C = \mathcal{C}\bar{\psi}^T$ and $\bar{\psi}^C = \psi^T \mathcal{C}$ with $\mathcal{C} = \mathrm{i}\gamma_2\gamma_0$ being related to the charge conjugation operator. The phase represented by this condensate (2.47) is referred to as a two-flavor color superconductor (2SC). The flavor antisymmetric structure of this color-superconducting condensate corresponds to a singlet representation of the global chiral group which implies that the formation of such a condensate does not violate the chiral symmetry of the theory [116]. This can be seen by rewriting the antisymmetric tensor in flavor space in terms of the *Pauli* matrix $\epsilon^{\alpha\beta}_{(f)} = \mathrm{i}(\tau_2)^{\alpha\beta}$ and noting that $(T^i_{(f)})^{\mathrm{T}}\tau_2 + \tau_2 T^i_{(f)} = 0$, where $T^i_{(f)} = \tau^i/2$ denotes the generators of the $SU_f(2)$ flavor group. We emphasize that this is different in QED-like theories where the formation of a *Poincaré*-invariant superconducting ground state also requires the chiral symmetry to be broken, see Section 4.2. In addition to that, let us note that the condensate (2.47) breaks the axial $U_{\mathrm{A}}(1)$ symmetry.

To discuss the symmetry properties of the diquark condensate Δ^l in color space, it is again helpful to rewrite the antisymmetric tensor $\varepsilon^l_{(c)}$ in terms of the antisymmetric generators T^A, with $A \in \{2, 5, 7\}$, of the $SU(3)$ color group. The condensate behaves as an antitriplet under color transformations and can always be rotated into the T^2-direction. The diquark condensate is then invariant under the first three generators $T^{(1-3)}$ of the $SU(3)$ color group while the remaining generators become broken. Owing to the *Anderson-Higgs* mechanism [2, 235], five of the eight gluons become massive and acquire an additional longitudinal degree of freedom.[21] While the gapped gluons decouple [240], the other three gluons remain gapless and give rise to a residual $SU(2)$ color symmetry. Calculations of the so-called *Meissner* mass of the gapped gluons in quark matter can be found in, e.g., Refs. [241–244].

As the diquark condensate also carries a net baryon and electromagnetic charge, it appears that the global $U_{\mathrm{V}}(1)$ symmetry and the electromagnetic (EM) local $U_{\mathrm{EM}}(1)$ symmetry are spontaneously broken as well. However, corresponding intact symmetries can be identified by "rotating" the respective generators to mix with the $SU(3)$ color group. With the generator of the $U_{\mathrm{V}}(1)$ group in the form $B = \frac{1}{3}\mathrm{diag}_{(c)}(1, 1, 1)$ we can construct the "rotated" generator $\tilde{B} = B - \frac{2}{\sqrt{3}}T^8 = \mathrm{diag}_{(c)}(0, 0, 1)$. We denote the symmetry group that belongs to this generator $\tilde{B}$ by $\tilde{U}_{\mathrm{V}}(1)$ which gives rise to a corresponding conserved rotated baryon number. Similarly, we obtain a rotated electromagnetic charge by constructing the generator $\tilde{Q} = Q - \frac{1}{\sqrt{3}}T^8$ of an associated $\tilde{U}_{\mathrm{EM}}(1)$ symmetry group, with $Q = \mathrm{diag}_{(f)}(2/3, -1/3)$ being the generator of the local $U_{\mathrm{EM}}(1)$ group. There is consequently no electromagnetic *Meissner* effect and the rotated photon remains massless. To summarize, the 2SC phase represented by the diquark

---

[21] Loosely speaking, the *Goldstone* modes are "eaten up" by the gauge bosons which in turn become massive [202].

condensate (2.47) is a color superconductor but neither an electromagnetic superconductor nor a baryonic superfluid.

Lastly, a brief comment on the diquark condensate breaking gauge symmetries is in order. In fact, the spontaneous breaking of a local symmetry is not truly possible [245] and is only a consequence of gauge fixing. The occurrence of spontaneous breaking after gauge fixing is nevertheless of physical significance and leads to correct predictions [106, 107]. The diquark condensate (2.47) itself is a gauge dependent object, whereas the corresponding energy gap in the excitation spectrum of the quasiparticles can be shown to be gauge invariant, see, e.g., Refs. [246–248].

For further discussion of color superconductivity and especially for a discussion of the case of more than two flavors, we refer to the reviews [107, 114–116], see also Ref. [239].

2.3 BRIEF OVERVIEW OF METHODS

Strong-interaction matter appears in many facets and gives rise to various intriguing phenomena. Owing to its strongly-coupled nature, however, the theory of the strong interaction is very difficult to access, with the result that QCD is equally rich of different theoretical approaches. Before we introduce the functional renormalization group in the next chapter which we shall employ to study strong-interaction matter, we give in the following a brief overview of selected alternative methods. Each method has its own benefits and shortcomings and might be only applicable within certain regimes. This overview is mainly based on reviews and introductory texts, see Refs. [51, 74, 207, 209, 232, 249–251]

2.3.1 Lattice QCD

Lattice QCD is a non-perturbative first-principles approach that attempts to directly compute the partition function numerically. The functional integral is discretized on a *Euclidean* space-time lattice and solved by employing Monte Carlo techniques based on importance sampling. For the original formulation and early contributions to this method see Refs. [252, 253], and for broader introductions and introductory reviews we refer to Refs. [74, 209, 249, 254].

The method is in principle exact but owing to computational limits requires extrapolation techniques to obtain the physical limit in terms of the continuum limit of vanishing lattice spacing $a \mapsto 0$ and the thermodynamic limit $\mathcal{V} \mapsto \infty$, where $\mathcal{V}$ denotes the space-time volume. Consequently, results from lattice QCD always receive a statistical error due to importance sampling as well as systematic errors such as from the extrapolation procedure to the physical limit. Lattice QCD studies have been very successful, e.g., in the determination of hadron masses [255], in the study of the finite-temperature QCD crossover transition [64] or in the computation of the equation of state at vanishing or small quark chemical potential [66, 67, 70, 87], see also Refs. [62, 63] for reviews on finite-temperature computations and the introductory reviews [249, 256].

At finite quark chemical potential, however, lattice QCD is plagued by the infamous "sign-problem": The fermion determinant becomes complex which consequently spoils the interpretation as probability weight and prohibits the direct application of importance sampling [74]. As a result, the computational cost grows exponentially with increasing space-time lattice volume. To circumvent the sign-problem various approaches have been pursued [51, 62, 76], e.g., the reweighting method [257], Taylor expansion techniques [72, 82, 258], simulations at imaginary chemical potential with subsequent analytical continuation to real values [259–262], the canonical ensemble method [263–265], the density of states approach [266, 267] or the complex *Langevin* method [268–272]. However, despite of these various approaches to circumvent the difficulty of the sign-problem, reliable results are only achieved in the regime with $\mu/T \lesssim 1$, see, e.g., Refs. [62, 63, 74, 269] for reviews on lattice QCD simulations at finite quark chemical potential.

2.3.2 Chiral effective field theory

Chiral effective field theory (chiral EFT) is a modern and very successful approach to describe nuclear forces at low energies based on the symmetries of QCD which allows a systematic improvement and access to uncertainty estimations, see, e.g., Refs. [89, 90, 250, 251] for reviews and Refs. [273–275] for the seminal works by *Steven Weinberg*.

Nuclear interactions can be considered as residual forces of the underlying fundamental strong interaction in much the same way as *Van-der-Waals* interactions between molecules are residual forces of the electromagnetic interaction between the atoms as constituents. In the low-momentum regime of nuclear physics, however, quarks and gluons as fundamental degrees of freedom are not resolved and the strongly-coupled nature at such scales restrains a direct derivation of nuclear interactions from QCD. Based on the so-called *separation of scales*, chiral EFT takes into account only the degrees of freedom that are relevant at the typical momentum scales under consideration, i.e., nucleons and pions as exchange particles, and constructs the most general *Lagrangian* compatible with the symmetry constraints imposed by QCD as underlying fundamental theory. The description is valid up to a *breakdown scale* $\Lambda_\mathrm{b} \sim 500\,\mathrm{MeV}$ beyond which the inclusion of higher momentum excitations apart from the pions would be required.[22] The various terms contributing to the *Lagrangian* are classified according to a *power-counting* scheme in terms of the expansion parameter $Q/\Lambda_\mathrm{b} \sim m_\pi/\Lambda_\mathrm{b} \approx 1/3$, where the typical momentum scale Q is given by the pion mass m_π. The power-counting scheme establishes a hierarchy of importance with only a finite number of terms at each order. As nucleons are finite-sized objects composed of fundamental constituents, multi-body interactions appear at higher orders as well. The free parameters of the expansion are the so-called *low-energy constants* (LECs) and incorporate the higher-momentum degrees of freedom that are not resolved by the EFT. In principle, such LECs can be calculated from, e.g., lattice QCD. In practice, however, they are determined by fits to experimental data. Once the set of LECs at a certain order are determined by specific experimental data, the nuclear interactions can then be employed to calculate the target nuclear observables.

Chiral EFT interactions have successfully been employed in structure and reaction studies of light and medium-mass nuclei as well as in calculations of nucleonic matter, see, e.g.,

---

[22] The exact value depends on details of the calculation such as the employed regularization scheme.

Refs. [91, 276–283] and Refs. [284, 285] for reviews. For recent results on the computation of nucleonic matter, we refer to Refs. [93, 286–288]. Current efforts include chiral interactions even up to fifth order [288], yet the application to symmetric matter at densities beyond twice the nuclear saturation density ρ_0 or to neutron-rich matter at $\rho \sim (1-2)\rho_0$ remains up to the present day highly non-trivial.

2.3.3 Perturbative QCD

Strong-interaction matter becomes weakly coupled at asymptotically high energy scales on the account of asymptotic freedom which eventually enables perturbative computations in terms of an expansion in the strong coupling constant. Although seemingly straightforward, a naive application of perturbation theory at finite temperature or chemical potential is not sufficient and more involved techniques are required in order to consistently treat the theory perturbatively as well as to improve convergence properties. The so-called dimensional reduction [289–292] at high temperatures and the presence of massless modes in the form of gauge fields lead to different infrared properties of QCD. The proper treatment of the dynamics of such soft modes can be achieved by resummation techniques as the “hard thermal loop” (HTL) resummation scheme [293–295] and accordingly the “hard dense loop” HDL resummation scheme at zero temperature and finite density [296–298].

In perturbative computations in the high-temperature regime the pressure has been worked out through order $\mathcal{O}(g_\mathrm{s}^6 \log g_\mathrm{s})$ [299, 300] and the results on the equation of state at zero density are in good agreement with lattice results down to a temperature of approximately two to three times the deconfinement temperature [301]. At lower temperatures, however, the strong coupling becomes large and the perturbation series inevitably breaks down.

In the regime of high densities and zero temperature the perturbative expansion has been fully determined at next-to-next-to-leading order (N^{2}LO) [302], i.e., $\mathcal{O}(g_\mathrm{s}^4)$, extending the computations of the earlier works [303–305]. Current efforts focus on the perturbative computation of the equation of state at N^{3}LO. The results on the leading-logarithm contribution proportional to $\mathcal{O}(g_\mathrm{s}^6 \log^2 g_\mathrm{s})$ were just recently published [306]. An extension of the results to non-zero temperatures has been worked out at order $\mathcal{O}(g_\mathrm{s}^5)$, see Ref. [307], while the weak-coupling expansion in the deconfined regime at higher temperatures and quark chemical potentials has been determined at order $\mathcal{O}(g_\mathrm{s}^4)$ [308]. Yet again, at lower temperatures and densities, the perturbative series eventually breaks down as the matter becomes strongly coupled. Furthermore, the effect of pairing and condensates in cold strong-interaction matter are not incorporated which become significant at least below $\mu \lesssim 1\,\mathrm{GeV}$ as we discuss in Sections 5.3 and 6.1. Consequently, the results on the equation of state in the zero-temperature limit as obtained from perturbative QCD computations are only reliable at very high densities, i.e., approximately $n_\mathrm{B} \gtrsim 70 n_0$ or $\mu \gtrsim 1\,\mathrm{GeV}$ [148, 309, 310], and are at least not directly applicable to the regime of intermediate densities that are expected to be prevalent in the interior of neutron stars.

For more information and introductory reviews on the perturbative approach to QCD, we refer to, e.g., Refs. [208, 216, 311–313].

2.3.4 Low-energy models

As the individual limitations of each approach discussed above illustrate, strong-interaction matter in the regime of intermediate densities is very difficult to access. This is why low-energy models of QCD are still crucial to our understanding of dense matter, despite the tremendous progress that has been made in the development of fully first-principles approaches to the theory of the strong interaction in recent years. Low-energy effective theories have provided valuable insights into a plethora of phenomena, ranging from bound-state formation and symmetry breaking patterns to phase transitions in QCD. In such models, the low-energy dynamics are described in terms of effective degrees of freedom that are expected to be relevant at the scale under consideration. The high-energy degrees of freedom, i.e., essentially gluodynamics, are considered to be integrated out and the full QCD interactions are replaced with effective interactions. The construction of low-energy models is generally guided by the symmetries of QCD. Prominent examples are NJL-type models and their relatives such as quark-meson (QM)-type models [45, 46, 117–138] and quark-meson-diquark models [106, 107, 115, 116, 139, 140]. Baryonic degrees of freedom are included in nucleon-meson models, see, e.g., Refs. [314–317]. The aforementioned models may even be augmented with statistical confinement in terms of a *Polyakov* loop background and a corresponding *Polyakov* loop potential [318–332]. In fact, all of these different models can be considered as different representations of the low-energy sector of QCD that emerge after the dynamical decoupling of the gluonic degrees of freedom at cutoff scales $\sim 0.4 \ldots 1\,\mathrm{GeV}$. However, despite the great success of such models, studies suffer from their generic features as well as from underlying approximations, also bearing on the phenomenological interpretation of the results: First, the range of validity of such models is typically limited by a physical UV cutoff. The non-renormalizability of models, see, e.g., Refs. [333, 334] for the NJL model in four space-time dimensions, even entails that the UV cutoff scale becomes a parameter itself and the regularization scheme belongs to the definition of the model. The parameters of a low-energy effective model are usually fixed such that the correct values of a given set of low-energy observables is reproduced at, e.g., vanishing temperature and quark chemical potential. Unfortunately, there may exist different parameter sets which reproduce the correct values of a given set of low-energy observables equally well. In fact, these model parameters may depend on the external control parameters, such as the temperature and the quark chemical potential [335]. Lastly, applied approximations that are often unavoidable take into account only specific sets of interactions. Other possibly important interaction channels are ignored which might amount to neglecting associated effective degrees of freedom, thus limiting the predictive power. The potential existence of mathematical equivalent formulations might even lead to ambiguities as, e.g., in mean-field studies of QCD low-energy models related to the possibility to perform so-called *Fierz* transformations of four-fermi interactions [336].

In summary, also in case of low-energy effective models the range of applicability is limited and generic features necessarily leave model studies in some respects unsatisfactory.

3

THE FUNCTIONAL RENORMALIZATION GROUP

The functional renormalization group (FRG) provides a powerful and versatile non-perturbative approach to study quantum field theories and constitutes the key method in our analysis of strong-interaction matter. Here, we briefly illustrate the main ideas underlying the FRG and subsequently demonstrate the derivation of the flow equation, the so-called *Wetterich* equation [183]. The application of the FRG to a theory at hand requires the specification of a regularization scheme in terms of a regularization function. In Section 3.2, we discuss some general aspects of such functions and outline the construction of the regulator we mainly employ in this work. Lastly, in Section 3.3, we introduce the concept of renormalization group consistency. This concept becomes particularly important in studies concerned with external control parameters such as temperature or the quark chemical potential. This chapter is mainly based on Refs. [124, 202, 211, 333, 337].

The principal aim of functional methods is the computation of generating functionals of correlation functions. A generating functional, such as Eq. (2.10) introduced in Section 2.1, contains the entire information on a physical system. Computing the generating functional amounts to solving the theory. The crucial advantage of functional methods is that they enable non-perturbative approaches: The computation is not restricted to the perturbative regime since they allow truncation schemes that do not rely on a small expansion parameter, cf. also studies employing *Dyson-Schwinger* equations, e.g., Refs. [338–343] or nPI methods, e.g., Refs. [337, 344, 345]. All such functional methods share the common aspect to be conceptually based on non-perturbative loop equations. A great asset is their analytic accessibility which can for instance facilitate unveiling underlying physical mechanisms.

The FRG combines this functional approach to quantum field theories with the concept of the *Wilsonian* renormalization group (RG) [189–191]. In general, the RG is concerned with the manifestation of physical systems at different scales and describes the changes in going from a microscopic to a macroscopic perspective. In the context of functional approaches, the FRG describes the change of correlation functions in the transition to macroscopic scales. The changes arise from quantum or thermal fluctuations and lead to corrections to the "effective" description of the field theory. Instead of incorporating all fluctuations at once, only the incremental change under a scale variation is considered, as caused by the associated fluctuations at this scale. If such an RG step is taken to be infinitesimally small, the series of such steps results in a continuous change of the correlation functions described in terms of an RG flow equation. As the fluctuations are successively integrated out, this equation determines the flow from the microscopic theory to the macroscopic description. In this way, the FRG is capable to describe the physics over a wide range of scales and allows the study of the influence of fluctuations at different scales in a controlled manner, enabling us for instance to reveal the emerging relevant degrees of freedom. In fact, the transition from microscopic to macroscopic scales might drastically alter the characteristics of the system under consideration, as prominently illustrated by the various arising phenomena in QCD as the long-range limit is approached: The system turns from weakly coupled at high energy scales to strongly coupled at lower scales, making non-perturbative methods such as functional approaches indispensable. Along this transition, other aspects, e.g., the realized ground state of the field theory, the associated realization of symmetries or the relevant degrees of freedom, might change as well [211].

The FRG enables to capture the various emerging phenomena in approaching macroscopic scales. In particular, the FRG allows us to describe strong-interaction matter in a "top-down" approach from first principles, i.e., the only input is given by the fundamental parameters of QCD: the current quark masses and the value of the strong coupling set at a large, perturbative momentum scale, see, e.g., Refs. [192, 194–197]. In principle, such an FRG approach does not rely on additional model parameters that would require further experimental values of, e.g., low-energy observables. Recent studies of first-principles approaches to QCD with the FRG have aimed at quantitative precision [192, 194–197], based on self-consistent approximations which allow systematic uncertainty estimates. In Ref. [195], the quark, gluon and meson 1PI correlation functions were studied in unquenched *Landau*-gauge QCD with two flavors in the vacuum, and the results, e.g., for the gluon propagator and the quark mass function, were found to be in very good agreement with lattice QCD studies. At finite temperature, 1PI correlation functions of *Landau*-gauge *Yang-Mills* theory were also found to compare very well to results as obtained from lattice QCD studies as well as from hard thermal loop perturbation theory [196]. These works constitute essential advances toward predictive first-principles investigations of the QCD phase diagram with the FRG. Against this background, the FRG appears as a promising tool to describe strong-interaction matter at intermediate densities from first principles and to study this region of the phase diagram which is in general at least difficult to access, cf. our discussion of alternative approaches in Section 2.3.

Before we proceed to derive the *Wetterich* equation, i.e., the flow equation of the FRG, we briefly discuss the *Wilsonian* approach to renormalization [189–191] as this approach provides a comprehensible and clear description of the RG in the context of functional methods. Following the lines of Ref. [202], we consider a theory defined at the microscopic scale, i.e., at some large momentum cutoff Λ, by the classical action $S[\phi] = \int_x \mathcal{L}(\phi)$. The UV-regularized generating functional Z of the correlation functions is then given by

$$Z[J] = \int_\Lambda \mathcal{D}\phi \;\, \mathrm{e}^{-\int_x \mathcal{L}(\phi) + \int J^{\mathrm{T}} \phi} \,, \tag{3.1}$$

with the field variable ϕ and the source J as introduced in Section 2.1. The subscript Λ of the functional integral in Eq. (3.1) indicates a sharp momentum cutoff. In momentum space, only the Fourier components $\phi(p)$ with $|p| \leq \Lambda$ are taken into account, whereas $\phi(p) = 0$ for $|p| > \Lambda$. Instead of integrating out all fluctuations at once, *Wilson*'s idea describes the approach to isolate the contributions corresponding to large momenta and to perform the integration over these degrees of freedom separately [189–191]. This integration over a single momentum shell defines an RG step. In gradually going from high to low momenta, this procedure then allows the incorporation and analysis of the effects of short distance fluctuations in a systematic fashion while approaching the macroscopic long-range physics.

The integral over such a single high-momentum shell can be obtained by splitting the field $\phi \to \phi + \tilde{\phi}$ into a contribution $\tilde{\phi}(p)$ that is only non-vanishing for $b\Lambda \leq |p| < \Lambda$ (with $0 < b < 1$) and the remaining degrees of freedom $\phi(p)$ which are only non-vanishing for $0 \leq |p| < b\Lambda$. The integration over $\tilde{\phi}$ then yields

$$\int_\Lambda \mathcal{D}\phi \;\mathrm{e}^{-\int_x \mathcal{L}(\phi)} \to \int \mathcal{D}\phi \int \mathcal{D}\tilde{\phi} \;\mathrm{e}^{-\int_x \mathcal{L}(\phi+\tilde{\phi})} = \int_{b\Lambda} \mathcal{D}\phi \;\mathrm{e}^{-\int_{x'} \mathcal{L}'_{\mathrm{eff}}(\phi)} \equiv \int_\Lambda \mathcal{D}\phi \;\mathrm{e}^{-\int_x \mathcal{L}_{\mathrm{eff}}(\phi)}$$

$$\Rightarrow Z[J] = \int_\Lambda \mathcal{D}\phi \;\mathrm{e}^{-\int_x \mathcal{L}_{\mathrm{eff}}(\phi) + \int_x J^{\mathrm{T}}\phi}\,, \tag{3.2}$$

where we have first changed the notation to $x \to x'$ and $p \to p'$ and then rescaled the distances and momenta according to $p = p'/b$ and $x = x'b$ in order to enable a direct comparability of the generating functional Z before and after the integration over the momentum shell. We observe that after the integration the generating functional can be written again in its original form, only the *Lagrangian* has been changed to an effective *Lagrangian* $\mathcal{L}_{\mathrm{eff}}$ since the integration leads to correction terms. These correction terms incorporate the effects of the high-momentum degrees of freedom which have been removed by integrating over the momentum shell. In other words, the interactions that have been mediated by these degrees of freedom are taken account of by modifying the original *Lagrangian*. Such modifications might change already existing couplings but in general also lead to new types of terms involving the fields $\phi(p)$ and derivatives thereof [202].

The procedure of momentum-shell integration and subsequent rescaling leads to the transformation of the *Lagrangian* $\mathcal{L}$ to an effective *Lagrangian* $\mathcal{L}_{\mathrm{eff}}$. The physical content has not changed in this procedure and calculations, e.g., of correlation functions at a scale much smaller than the UV cutoff Λ, employing the formulation in terms of the effective *Lagrangian* $\mathcal{L}_{\mathrm{eff}}$ are equivalent and will yield the same results as before. However, while the calculation of loop diagrams using the original formulation (3.1) amounts to integrating out fluctuations at all scales at once, the effective *Lagrangian* $\mathcal{L}_{\mathrm{eff}}$ has already absorbed the effects of the high-momentum degrees of freedom. The repeated momentum-shell integration gradually incorporates the fluctuations in a systematic manner from large to small momenta, until the effective *Lagrangian* provides a suitable description of the physics at macroscopic length scales. If the width of the single momentum shell is taken to be infinitesimally thin, i.e., the parameter b close to 1, the transformation of the *Lagrangian* becomes continuous and successive integrations of momentum shells can be described as a flow in the space of all possible *Lagrangians*, with the set of these continuous transformations referred to as the renormalization group [202]. On the level of a coupling associated with a certain term of the *Lagrangian*, the rate of change in the course of such RG steps is then given by a corresponding so-called β function. Thus, these β functions describe the transition from the microscopic scale to the macroscopic scale by describing the rate of change of the couplings due to the incorporation of higher momentum fluctuations.

3.1 DERIVATION OF THE EXACT RG EQUATION

The *Wilsonian* concept discussed above illustrates the RG in the context of functional methods in a very comprehensive manner. However, it does not provide a practical approach in actual computations. We now turn to the derivation of the *Wetterich* equation which introduces a method that transforms *Wilson*'s idea to successively integrate out momentum shells into an efficient tool to compute the flow equations of a given theory. Here, we follow the lines of Ref. [211].

The central quantity of interest is the effective action

$$\Gamma[\Phi] := \sup_J \left(\int_x J^{\mathrm{T}} \Phi - \log Z[J] \right) , \tag{3.3}$$

introduced in Section 2.1, which can be considered as the quantum analog to the classical action S and determines the dynamics of the classical field $\Phi = \langle \Omega | \phi | \Omega \rangle_J$ through the quantum equation of motion [211] given by

$$\Gamma[\Phi] \frac{\overleftarrow{\delta}}{\delta \Phi(x)} = J^{\mathrm{T}}(x) \, . \tag{3.4}$$

To realize the *Wilsonian* approach of integrating out momentum shells applied to the effective action, we introduce the so-called effective average action Γ_k which interpolates between the bare classical action S at some UV cutoff Λ, i.e., at the microscopic scale for $k \to \Lambda$, and the full quantum effective action Γ for $k \to 0$:

$$\lim_{k \to \Lambda} \Gamma_k \simeq S \, , \qquad \lim_{k \to 0} \Gamma_k = \Gamma \, . \tag{3.5}$$

The RG scale k parametrizes the *Wilsonian* RG transformations and indicates that all fluctuations with momenta $k \lesssim |p| \leq \Lambda$ have been integrated out, corresponding to fluctuations on a length scale smaller than $\sim 1/k$. Thus, the interpolating action Γ_k is also known as the so-called coarse-grained effective action [333]. In order to construct such an interpolating action Γ_k, a regulator term ΔS_k is implemented into the generating functional of the *Green*'s functions according to

$$Z_k[J] := \int_\Lambda \mathcal{D}\phi \ \mathrm{e}^{-S[\phi] - \Delta S_k[\phi] + \int J^{\mathrm{T}} \phi} \, , \tag{3.6}$$

with the regulator term defined by

$$\Delta S_k[\phi] = \frac{1}{2}\int_p \phi^{\mathrm{T}}(-p) R_k(p)\phi(p)\,. \tag{3.7}$$

The regulator insertion is defined in terms of the regulator function R_k which is matrix-valued in field space and assumes the form

$$R_k(p) = \begin{pmatrix} R_\varphi(p) & 0 & 0 \\ 0 & 0 & -R_\psi^{\mathrm{T}}(-p) \\ 0 & R_\psi(p) & 0 \end{pmatrix}, \tag{3.8}$$

denoted here in the subspace of the scalar field φ and the *Dirac* spinor ψ.[1] The dependence of the regulator insertion on the RG scale k renders the functional and consequently all couplings k-dependent as well.

The interpolating action Γ_k is now obtained by a *Legendre* transform which receives a modification due to the regulator insertion and reads

$$\Gamma_k[\Phi] = \sup_J \left(\int J^{\mathrm{T}}\Phi - \log Z_k[J] \right) - \Delta S_k[\Phi]\,, \tag{3.9}$$

where the classical field Φ is again defined as the vacuum expectation value of the fields according to

$$\Phi(x) = \langle \phi(x) \rangle_{k,J} = \frac{\overrightarrow{\delta}}{\delta J^{\mathrm{T}}(x)} \log Z_k[J]\,. \tag{3.10}$$

The convexity of the interpolating action is potentially spoiled by the regulator term at finite scales k but is restored again in the limit $k \to 0$ as the effective action Γ is approached. It should be noted that the source $J = J[\Phi, k)$ in Eq. (3.9) becomes scale-dependent as well since it is determined by requiring the supremum. The regulator insertion modifies the quantum equation of motion (3.4) as well which is now given by

$$\Gamma_k[\Phi]\frac{\overleftarrow{\delta}}{\delta\Phi(x)} = J^{\mathrm{T}}(x) - \int_y \Phi^{\mathrm{T}}(y) R_k(y,x). \tag{3.11}$$

For the desired behavior of the effective average action in the limits (3.5), the regulator function must fulfill certain basic constraints [183]. First, the regulator must vanish for the RG scale k approaching zero, i.e.,

$$\lim_{k^2/p^2 \to 0} R_k(p) = 0\,, \tag{3.12}$$

---

[1] The transposed term comes with an extra minus sign due to the *Grassmann* nature of the fermionic field variable, while its dependence on $-p$ is entailed by the definition of the generalized field variable in momentum space, see Appendix A.3.

which ensures that in the limit $k \to 0$ the scale-dependent generating functionals reduce to the ordinary generating functionals, especially the interpolating effective action Γ_k to the full quantum effective action Γ. The second condition is given by

$$\lim_{k \to \Lambda \to \infty} R_k(p) \quad \longrightarrow \quad \infty \,. \tag{3.13}$$

It implies that the effective average action approaches the bare classical action S at the UV cutoff $k = \Lambda$. This can be seen from rewriting the definition of the effective average action Eq. (3.9) in the form

$$\begin{aligned} e^{-\Gamma_k[\Phi]} &= \int_\Lambda \mathcal{D}\phi \;\; \mathrm{e}^{-S[\phi]-\Delta S_k[\phi]+\int J^{\mathrm{T}}(\phi-\Phi)+\Delta S_k[\Phi]} \\ &= \int_\Lambda \mathcal{D}\phi \;\; \mathrm{e}^{-S[\phi+\Phi]+\int(\Gamma_k[\Phi]\overleftarrow{\delta}/\delta\Phi)\phi-\Delta S_k[\phi]} \,, \end{aligned} \tag{3.14}$$

where in the step from the first to the second line the integration variable has been shifted according to $\phi \to \phi + \Phi$ and we have used relation (3.11). As a consequence of the condition (3.13), the exponential of the regulator term behaves like a functional delta distribution in the limit $k \to \Lambda \to \infty$, i.e.,

$$\lim_{k \to \Lambda \to \infty} \exp(-\Delta S_k[\phi]) \quad \sim \quad \delta[\phi] \,, \tag{3.15}$$

and the functional integral can be evaluated by setting $\phi = 0$. This finally leads to the relation $\Gamma_{k\to\Lambda}[\Phi] = S[\Phi] + \text{const.}$ which provides the initial condition for the effective average action Γ_k in regard to the RG flow. Lastly, the regulator should be non-vanishing for the momentum p approaching zero, i.e.,

$$\lim_{p^2/k^2 \to 0} R_k(p) > 0 \,. \tag{3.16}$$

As the regulator term is quadratic in the fields and thus can be considered as a mass term, this constraint effectively introduces an IR regularization.

Having imposed these constraints, the interpolating action Γ_k fulfills the desired limits (3.5) for the RG scale k approaching zero or the UV cutoff Λ. In order to determine the evolution of the interpolating action between these limits, we now turn to the derivation of the flow equation for the effective average action. We first calculate the derivative of the scale-dependent generating functional $W_k = \log Z_k$ of the connected *Green*'s functions with respect to the parameter k while keeping the source J fixed:[2]

$$\begin{aligned} \partial_t W_k[J] =& \frac{1}{Z_k[J]} \int_\Lambda \mathcal{D}\phi \left\{ -\frac{1}{2} \int_p \phi^{\mathrm{T}}(-p) \partial_t R_k(p) \phi(p) \right\} \mathrm{e}^{-S[\phi]-\Delta S_k[\phi]+\int J^{\mathrm{T}}\phi} \\ =& -\frac{1}{2} \int_p \partial_t R_k^{ab}(p) \langle \phi_a(-p)\phi_b(p) \rangle_{c,k,J} - \frac{1}{2} \int_p \langle \phi^{\mathrm{T}}(-p) \rangle_{k,J} \partial_t R_k(p) \langle \phi(p) \rangle_{k,J} \end{aligned}$$

---

[2] In the context considered here, the source J is only the argument of the functional, thus being independent of the scale.

$$= -\frac{1}{2}\mathrm{STr}\left\{\partial_t R_k G_{c,k}(p)\right\} - \partial_t \Delta S_k[\Phi]\,. \tag{3.17}$$

Here, we have introduced the RG time $t = \ln(k/\Lambda)$ with the associated total derivative $\partial_t = k(\partial/\partial k)$ and we have employed the connected two-point *Green*'s function

$$\begin{aligned}\frac{\overrightarrow{\delta}}{\delta J^{\mathrm{T}}(-p)}\frac{\overrightarrow{\delta}}{\delta J(p)}W_k[J] &= \langle\phi(p)\phi^{\mathrm{T}}(-p)\rangle_{c,k,J} =: G_{c,k}(p)\\ &= \langle\phi(p)\phi^{\mathrm{T}}(-p)\rangle_{k,J} - \langle\phi(p)\rangle_{k,J}\langle\phi^{\mathrm{T}}(-p)\rangle_{k,J}\,,\end{aligned} \tag{3.18}$$

which is matrix-valued in field space. The supertrace STr denotes a summation over indices, fields as well as the integration over momenta. Moreover, it accounts for the additional minus sign in the subspace of fermionic fields that is generated by swapping the fields $\phi_a\phi_b \to \phi_b\phi_a$ from the second to the last line in Eq. (3.17) due to the *Grassmann* property. From differentiating the modified quantum equation of motion (3.11) once more with respect to the classical field Φ we obtain the relation

$$\frac{\overrightarrow{\delta}}{\delta\Phi^{\mathrm{T}}(x)}J^{\mathrm{T}}(y) = \frac{\overrightarrow{\delta}}{\delta\Phi^{\mathrm{T}}(x)}\Gamma_k[\Phi]\frac{\overleftarrow{\delta}}{\delta\Phi(y)} + R_k(x,y)\,, \tag{3.19}$$

and from differentiating the classical field Φ with respect to the source J, see Eq. (3.10), we obtain the corresponding conjugate relation

$$\frac{\overrightarrow{\delta}}{\delta J^{\mathrm{T}}(x)}\Phi^{\mathrm{T}}(y) = \frac{\overrightarrow{\delta}}{\delta J^{\mathrm{T}}(x)}\frac{\overrightarrow{\delta}}{\delta J(y)}W_k[J] = G_{c,k}(x,y)\,. \tag{3.20}$$

Combining the latter two relations leads to the identity

$$\begin{aligned}\mathbb{1}_{\text{Field Space}}\delta^{(D)}(x-y) &= \frac{\overrightarrow{\delta}}{\delta J^{\mathrm{T}}(x)}J^{\mathrm{T}}(y) = \int_z \frac{\overrightarrow{\delta}}{\delta J^{\mathrm{T}}(x)}\Phi^{\mathrm{T}}(z)\frac{\overrightarrow{\delta}}{\delta\Phi^{\mathrm{T}}(z)}J^{\mathrm{T}}(y)\\ &= \int_z G_{c,k}(x,z)\left(\Gamma_k^{(1,1)} + R_k\right)(z,y)\,,\end{aligned} \tag{3.21}$$

i.e., the operator $(\Gamma_k^{(1,1)} + R_k)$ is the inverse of the connected propagator $G_{c,k}$, where we have introduced the notation

$$\Gamma_k^{(n,m)}[\Phi] = \underbrace{\frac{\overrightarrow{\delta}}{\delta\Phi^{\mathrm{T}}}\cdots\frac{\overrightarrow{\delta}}{\delta\Phi^{\mathrm{T}}}}_{n-\text{times}}\Gamma_k[\Phi]\underbrace{\frac{\overleftarrow{\delta}}{\delta\Phi}\cdots\frac{\overleftarrow{\delta}}{\delta\Phi}}_{m-\text{times}}\,. \tag{3.22}$$

We finally obtain the *Wetterich* equation by differentiating the defining relation of the effective average action Eq. (3.9) with respect to the RG time t. Using the relations (3.17) and (3.21) as well as taking into account the scale-dependence of the source J entailed by the supremum prescription, we find

$$\begin{aligned}\underline{\underline{\partial_t\Gamma_k[\Phi]}} &= \int (\partial_t J^{\mathrm{T}})\Phi - \partial_t\Delta S_k[\Phi] - \partial_t W_k[J]\big|_{J\ \text{fixed}} - \int (\partial_t J^{\mathrm{T}})\frac{\overrightarrow{\delta}}{\delta J^{\mathrm{T}}} W_k[J] \\ &= \underline{\underline{\frac{1}{2}\mathrm{STr}\left\{\left[\Gamma_k^{(1,1)}[\Phi]+R_k\right]^{-1}\cdot(\partial_t R_k)\right\}}} \;=\; \frac{1}{2}\end{aligned}$$

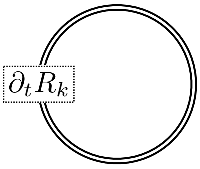

$$. \qquad (3.23)$$

The *Wetterich* equation is an exact RG equation as it depends on the full propagator $(\Gamma_k^{(1,1)} + R_k)^{-1} = G_{c,k}$. The diagrammatic depiction shown in Eq. (3.23) emphasizes the one-loop structure, where the double line represents the full propagator and the box the regulator insertion $(\partial_t R_k)$. The equation's non-perturbative nature allows the study of strongly correlated systems and is not restricted to weakly coupled regimes associated with the vicinity of a *Gaußian* fixed-point. In fact, perturbation theory is contained in the *Wetterich* equation. For instance, perturbation theory at one loop can readily be recovered by replacing $\Gamma_k^{(1,1)}$ by the second functional derivative of the classical action $S^{(1,1)}$ on the right hand side of Eq. (3.23). The regulator term and its derivative are then the only remaining scale-dependent objects on the right hand side. As a consequence, the integration over the RG scale k can easily be calculated, leading to

$$\Gamma_k = \Gamma_\Lambda + \frac{1}{2}\mathrm{STr}\log\Big(S^{(1,1)} + R_k\Big) - \frac{1}{2}\mathrm{STr}\log\Big(S^{(1,1)} + R_\Lambda\Big)\,, \qquad (3.24)$$

where the boundary condition is given by the classical action $\Gamma_\Lambda = S$ and the last term is a counterterm that makes the expression finite. In the limit $k \to 0$ we obtain the effective action in one-loop approximation:

$$\Gamma\big|_{\text{one-loop}} = \Gamma_\Lambda + \frac{1}{2}\mathrm{STr}\log\Big(S^{(1,1)}\Big) - \frac{1}{2}\mathrm{STr}\log\Big(S^{(1,1)} + R_\Lambda\Big)\,, \qquad (3.25)$$

Reinserting this results into the right-hand side of the *Wetterich* equation yields higher loop-order corrections to the effective action.

The FRG approach turns the calculation of the effective action from a functional integral structure into a functional differential equation, thereby improving the analytical accessibility as well as the stability in numerical computations [211, 337]. The equation describes the differential change of the interpolating action Γ_k due to corrections from fluctuations at the momentum scale $p \sim k$. The evolution of the interpolating action can be thought of as a flow in the so-called theory space, i.e., the space of all action functionals compatible with the symmetries of a given theory, from the classical action S in the limit $k \to \Lambda$ to the full quantum effective action Γ in the limit $k \to 0$. The specific trajectory in theory space between these endpoints depends in general on the choice of the regulator function R_k due to the dependence of non-universal quantities on the renormalization scheme [211]. As long as the regulator insertion shares the symmetries of the classical action S, however, so-called modified

Ward identities imply that the effective average action Γ_k is invariant as well[3] and the RG flow is constrained to this hypersurface of invariant functionals. The study of such RG flows then allows to examine the manifestation of a physical system across scales in a systematic manner and, e.g., in terms of a fixed-point analysis, can provide valuable insights into aspects such as universality, critical exponents or renormalizability [333].

In most cases, the *Wetterich* equation cannot be solved exactly and approximation schemes must be employed. A considerable advantage of the FRG is the flexibility in regard to the application of such schemes [337]. In a vertex expansion the generating functional is expanded in terms of the vertices $\Gamma_k^{(m,n)}$. The flow equation for each vertex can be derived from Eq. (3.23) by taking the appropriate functional derivatives and describe the RG flow from the bare vertex $S^{(m,n)}$ to the dressed vertex $\Gamma^{(m,n)}$. The equation for a vertex of order $(m+n)$ generally depends on the vertices of order $(m+n+1)$ and $(m+n+2)$ due to the $\Gamma_k^{(1,1)}$-term in the denominator of the *Wetterich* equation. A vertex expansion thus leads to a so-called infinite tower of coupled functional differential equations. In order to obtain some finite set of equations, the vertex expansion must be truncated at a certain order. However, this implies that the system is not closed anymore. Similarly, a so-called operator expansion can be applied in form of a derivative expansion, which can be considered as an expansion in the anomalous dimension, and an expansion in powers of the fields. Again, the number of operators must usually be truncated to obtain a manageable system. The choice of operators in the ansatz for the interpolating action Γ_k is guided by the symmetries of the theory that apply to the RG flow according to the above mentioned modified *Ward* identities. All operators that are not explicitly forbidden by these symmetries are allowed. The necessity to apply truncations might affect some of the statements made above which assume an exact solution of the flow, e.g., a truncation might cause a residual dependence of the interpolating action Γ_k on the regulator and thus on the cutoff Λ even in the limit $k \to 0$. The quality or reliability of the chosen truncation can be tested by studying the sensitivity of the results either under a variation of the included operators in the truncation, i.e., usually an extension of the truncation, or under a variation of the chosen regulator function. For a more detailed discussion of the functional RG and the *Wetterich* equation we refer the reader to, e.g., Refs. [124, 211, 337].

3.2 REGULATOR FUNCTIONS

The explicit calculation of RG flow equations requires the specification of the regulator function R_k which encodes the regularization scheme. In the following, we discuss some general aspects of regularization schemes and introduce the regulator functions we employ in this work. For a detailed discussion of regularization schemes in RG studies see, e.g., Ref. [337].

The regulator function is to a large extent at one's own disposal and is only required to fulfill the basic constraints introduced above [183], see Eqs.(3.12), (3.13) and (3.16). In Fig. 3.1 a sketch of the qualitative behavior of a typical regulator function R_k and its derivative $\partial_t R_k$ with respect to the scale k is shown (inspired by Ref. [211]). The regulator function R_k appears in the denominator of the *Wetterich* equation and leads to an IR regularization since

---

[3] We assume here that the measure of the functional integral is invariant, too.

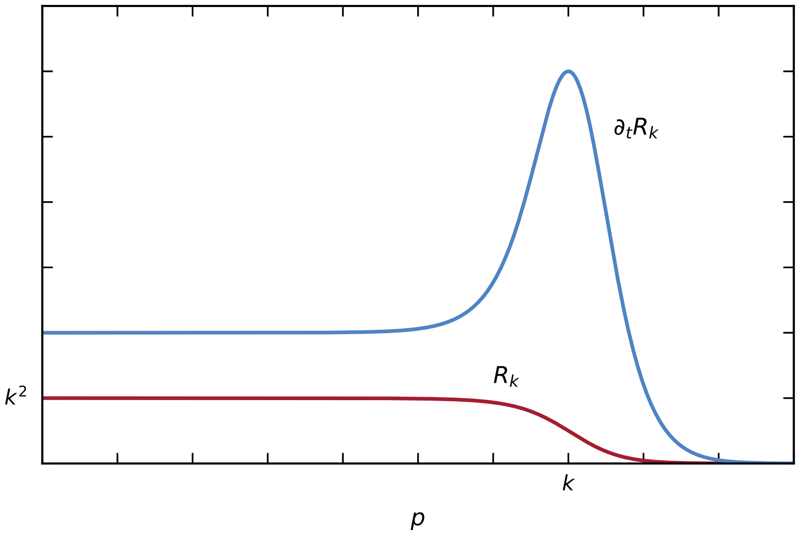

Figure 3.1: Sketch of the regulator function R_k and its derivative $\partial_t R_k$ with respect to the RG scale k as functions of the momentum p, inspired by Ref. [211].

it behaves as a mass-like term for $p^2/k^2 \to 0$. The derivative $\partial_t R_k$ in the numerator assumes the form of a peaked function centered at the scale $p^2 \sim k^2$. As a consequence, the derivative term $\partial_t R_k$ singles out the contributions of fluctuations with momenta within the vicinity of $p^2 \sim k^2$ which realizes the *Wilsonian* idea of integrating out single momentum shells. The freedom in the choice of the regulator can be taken advantage of, e.g., by optimizing the RG flow in terms of stability of the flow and faster convergence, i.e., the results of the truncated flow are already closest to the full theory and, at best, the essential information is already contained in the leading order terms [337, 346–348]. In general, it is favorable to choose a regulator that preserves the symmetries of the theory as the intact symmetries constrain the interpolating action and serve as guidance in finding a suitable ansatz. In contrast to that, a symmetry breaking regulator insertion would lead to additional terms in the associated modified *Ward* identities. To obtain an invariant effective action in the limit $k \to 0$, it would be then necessary to add appropriate counterterms to the initial action Γ_Λ which exactly balance the symmetry breaking contributions of the regulator in the course of the flow such that the symmetry is restored in the limit $k \to 0$.[4] The regulator is usually defined in terms of a dimensionless so-called regulator shape function r which determines the asymptotic behavior in the IR and UV. In a covariant formulation, for instance, a regulator for bosonic fields and a chirally symmetric regulator for fermionic fields are given by

$$R_k^{\varphi} \sim p^2 r_{\varphi}(p^2/k^2)\,, \qquad R_k^{\psi} \sim \not{p}\, r_{\psi}(p^2/k^2)\,, \tag{3.26}$$

---

[4] In gauge theories, the regulator necessarily breaks gauge invariance as the regulator insertion behaves for small momenta like a mass term in the regularized propagator of the gauge fields, see Eq. (3.16). In gauge-fixed calculations, however, the regulator is in fact just another source of gauge symmetry breaking. In order to obtain gauge-invariant results, the RG flow must be solved together with the *Ward* identities which are known in this context as modified *Ward-Takahashi* identities [349–354]. Other approaches include the construction of gauge-invariant regularization schemes, see, e.g., Ref. [355–358] or the application of the so-called background-field formalism [359, 360].

respectively. Typical choices for the regulator shape function are the *Litim* or linear regulator [346–348] given by

$$r_\varphi = \left(\frac{k^2}{p^2} - 1\right)\theta(k^2 - p^2)\,, \qquad r_\psi = \left(\sqrt{\frac{k^2}{p^2}} - 1\right)\theta(k^2 - p^2)\,, \tag{3.27}$$

the sharp-cutoff regulator

$$r_\varphi = \lim_{\kappa\to\infty}\left(\frac{k^2}{p^2}\right)^{\kappa}\,, \qquad r_\psi = \lim_{\kappa\to\infty}\sqrt{1 + \left(\frac{k^2}{p^2}\right)^{\kappa}} - 1\,, \tag{3.28}$$

or the exponential regulator [122, 123] given by

$$r_\varphi = \frac{1}{\mathrm{e}^{p^2/k^2} - 1}\,, \qquad r_\psi = \frac{1}{\sqrt{1 - \mathrm{e}^{-p^2/k^2}}} - 1\,, \tag{3.29}$$

for bosonic and fermionic fields, respectively. The prefactor of the regulator shape function is related to the classical dispersion relation of the field. Alternatively, so-called RG- or spectrally adjusted regulators, see, e.g., Refs. [337, 361–364], make instead use of the momentum- and scale-dependent part of the full-inverse two-point function, i.e., $R_k = \Gamma_k^{(1,1)} r$.[5] It should be added that fast decays of $r(x)$ improve the convergence of the employed approximation scheme, for details see Refs. [337, 365]. The derivative expansion, a common approximation scheme that is also used in the present work, is based on the expansion in powers of momenta. The applicability of this scheme to any order requires shape functions that decay faster than any polynomial in x. Consequently, exponential or even compact support regulators are best suited for common systematic approximation schemes, ranging from the derivative expansion to vertex expansions as used in QCD.

In the continuum formulation of QCD, the theory is *Poincaré*-invariant in the vacuum limit. As we intend to study strong-interaction matter at finite temperature and density, however, the presence of a heat bath or a finite quark chemical potential breaks the *Lorentz* invariance down to $SO(3)$ rotations among spatial coordinates. This remaining symmetry lets so-called three-dimensional/spatial regularization schemes appear to be a suitable choice which are indeed often used in, e.g., model studies. Such schemes act only on the spatial momenta and leave the temporal direction unaffected [366–369]. We obtain corresponding spatial regularization schemes from Eq. (3.26) by the replacement $p \to \vec{p}$, e.g., for the *Litim* regulator we have

$$R_k^\varphi \sim \vec{p}^{\,2} r_\varphi(\vec{p}^{\,2}/k^2)\,, \qquad R_k^\psi \sim \vec{\not{p}}\, r_\psi(\vec{p}^{\,2}/k^2)\,, \tag{3.30}$$

with

$$r_\varphi = \left(\frac{k^2}{\vec{p}^{\,2}} - 1\right)\theta(k^2 - \vec{p}^{\,2})\,, \qquad r_\psi = \left(\sqrt{\frac{k^2}{\vec{p}^{\,2}}} - 1\right)\theta(k^2 - \vec{p}^{\,2})\,. \tag{3.31}$$

---

[5] Note that in the latter relation the regulator shape function r is matrix-valued in field space.

In the calculation of loop diagrams, spatial regularization schemes often allow an analytic evaluation of the *Matsubara* summations which makes such schemes attractive. However, this class of regulator functions introduces an artificial explicit breaking of *Poincaré* invariance in the RG flow which is present even in the limit $T \to 0$ and $\mu \to 0$, i.e., in the *Poincaré*-invariant vacuum limit, see, e.g., Refs. [370–373]. This leads to a contamination of the results in this limit and is particularly severe since this limit is in general also used to fix the parameters in model studies. At finite temperature or quark chemical potential a spatial regulator poses an additional source of explicit breaking of *Poincaré* invariance which potentially leads to a distortion of the RG flow. This aspect is of great relevance. For instance, such an additional breaking of the *Poincaré* symmetry might affect the dynamics of condensate formation and possibly spoils the phenomenological interpretation of results, see our discussion in Section 4.2, particularly Section 4.2.4, for an explicit analysis in the context of the NJL model. In principle, one may solve this problem by taking care of the symmetry violating terms with the aid of corresponding *Ward* identities by adding appropriate counterterms such that the theory remains *Poincaré*-invariant in the limit $T \to 0$ and $\mu \to 0$, see Ref. [370].

With respect to RG studies, we add that, apart from the fact that spatial regularization schemes explicitly break *Poincaré* invariance, they lack locality in the temporal direction, i.e., all time-like momenta are taken into account at any RG scale k whereas spatial momenta are restricted to small momentum shells around the scale $k \simeq |\vec{p}\,|$. Loosely speaking, fluctuation effects are therefore washed out by the use of this class of regularization schemes and the construction of meaningful expansion schemes of the effective action is complicated due to this lack of locality.

In this work, we therefore employ a four-dimensional regularization scheme instead which is parametrized in form of an exponential shape function. In the limit $T \to 0$ and $\mu \to 0$, our regularization scheme becomes covariant which is of great importance. Furthermore, the regulator should take into account the presence of a *Fermi* surface as we intend to study systems at finite quark chemical potential. For this reason, we construct in the following a four-dimensional *Fermi*-surface-adapted regulator specifically tailored to the fermionic propagator structure given by Eq. (2.33). For the construction of this regulator, we start with an analysis of the spectrum of the kinetic term which is in momentum space given by

$$\hat{T}_{\bar{\psi}\psi} = -(\not{p} + \mathrm{i}\gamma_0\mu)\,. \tag{3.32}$$

This operator has four eigenvalues which are partially degenerate. In fact, there are only two distinct pairs of eigenvalues:

$$\epsilon_{1,2} = \pm\sqrt{(p_0 + \mathrm{i}\mu)^2 + \vec{p}^{\,2}}\,. \tag{3.33}$$

For $p_0 = 0$, we note that the eigenvalues assume the following form:

$$\epsilon_{1,2}\big|_{p_0=0} = \pm\sqrt{\vec{p}^{\,2} - \mu^2}\,. \tag{3.34}$$

Thus, for $p_0 = 0$, the eigenvalues tend to zero for momenta close to the *Fermi* momentum μ. Moreover, we note that the eigenvalues are in general complex-valued quantities at finite μ.

We now construct a regulator function which also takes into account the presence of a potential zero mode at the *Fermi* surface, i.e., $p_0 = 0$, see Eq. (3.34). To this end, we first note that the fermion propagator appearing in the loop integrals can be written in terms of the eigenvalues $\epsilon_{1,2}$:

$$\frac{1}{\not{p} + \mathrm{i}\gamma_0\mu} = \frac{\not{p} + \mathrm{i}\gamma_0\mu}{\epsilon_{1,2}^2} = \frac{(\not{p} + \mathrm{i}\gamma_0\mu)((p_0 - \mathrm{i}\mu)^2 + \vec{p}^{\,2})}{\omega_+^2\omega_-^2}\,, \tag{3.35}$$

where

$$\omega_\pm^2 \equiv \omega_\pm^2(p_0,\vec{p}\,) = p_0^2 + (|\vec{p}\,| \pm \mu)^2\,. \tag{3.36}$$

Here, $\omega_\pm$ is related to the quasiparticle dispersion relation associated with ungapped massless fermions: For example, $\omega_-(0,\vec{p}\,)$ may be viewed as the energy required to create a particle with momentum $\vec{p}$ above the *Fermi* surface. Correspondingly, $\omega_+(0,\vec{p}\,)$ is associated with the energy to create an antiparticle. Note that, for $\mu = 0$, $\omega_\pm^2$ reduces to

$$\omega_\pm^2\big|_{\mu=0} = p_0^2 + \vec{p}^{\,2}\,. \tag{3.37}$$

For $p_0 \to 0$, we have

$$\frac{1}{\epsilon_{1,2}^2}\bigg|_{p_0\to 0} \sim \frac{1}{\vec{p}^{\,2} - \mu^2}\,. \tag{3.38}$$

For our computations based on the *Wetterich* equation, we now construct a regularized kinetic term:

$$\hat{T}^{\text{reg.}}_{\bar{\psi}\psi} = \hat{T}_{\bar{\psi}\psi} + R_k^\psi = -(\not{p} + \mathrm{i}\gamma_0\mu)(1 + r_\psi)\,, \tag{3.39}$$

with the regulator function

$$R_k^\psi = -(\not{p} + \mathrm{i}\gamma_0\mu)r_\psi\,. \tag{3.40}$$

As already mentioned, the regulator function is to a large extent at our disposal and only required to fulfill a few constraints [183], see also below. Assuming that r_ψ is a real-valued dimensionless function depending on p_0, $\vec{p}$, μ, and the RG scale k, the regularized eigenvalues are given by

$$\epsilon_{1,2}^{\text{reg.}} = \pm\sqrt{(p_0 + \mathrm{i}\mu)^2 + \vec{p}^{\,2}}\,(1 + r_\psi)\,. \tag{3.41}$$

To regularize the finite-μ zero modes appearing at any finite k, see Eq. (3.34), we require that

$$r_\psi\big|_{p_0=0\,,|\vec{p}\,|\approx\mu} \sim \frac{k}{\sqrt{|\vec{p}^{\,2} - \mu^2|}}\,. \tag{3.42}$$

Moreover, we require that

$$r_\psi\big|_{\mu=0,\{p_\nu\to 0\}} \sim \frac{k}{\sqrt{p_0^2+\vec{p}^{\,2}}}\,, \tag{3.43}$$

which ensures that the regulator function reduces to the conventionally employed covariant chirally symmetric regulator functions in the limit $\mu \to 0$. A specific choice for the shape function, which fulfills these conditions and has been employed in this work, is given by

$$r_\psi = \frac{1}{\sqrt{1-\mathrm{e}^{-\bar{\omega}_+\bar{\omega}_-}}} - 1\,, \tag{3.44}$$

where $\bar{\omega}_\pm = \omega_\pm/k$. Note that this regularization scheme reduces to the four-dimensional exponential scheme (3.29) in the vacuum limit. We add that other shape functions, such as *Litim*-type regulator functions introduced in Eq. (3.27), can in principle be adapted accordingly by replacing p^2 with $\omega_+\omega_-$. In any case, with a regulator function fulfilling the constraints (3.42) and (3.43), the eigenvalues of the kinetic term are finite at any finite value of k.

Phenomenologically speaking, the so-defined class of shape functions also ensures that the momentum modes are integrated out around the *Fermi* surface, similarly to regulator functions employed in RG studies of ultracold *Fermi* gases [374] with spin- and mass-imbalance [375, 376]. This implies that modes with momenta $|\vec{p}| \simeq \mu$ (at $p_0 = 0$) are only taken into account in the limit $k \to 0$ where the regulator vanishes, $R_k^\psi \to 0$. Thus, our regulator function screens modes with momenta close to the *Fermi* surface μ but leaves modes with (spatial) momenta farther away from the *Fermi* surface unchanged. This behavior is illustrated in Fig. 3.2. The left panel shows the regulator shape function r_ψ as a function of the spatial momentum normalized to the quark chemical potential, i.e., $|\vec{p}|/\mu$, for $p_0 = 0$ and for various different values of k/μ. In the right panel, the corresponding regularized eigenvalues $|\epsilon_{1,2}^{\text{reg.}}|/k$ are shown with the screened zero mode at the *Fermi* surface at $|\vec{p}| \simeq \mu$. We note that this class of shape functions also fulfills the standard requirements [183]:

(i) It remains finite in the limit of vanishing four-momenta.

(ii) It diverges suitably for $k \to \infty$ to ensure that the quantum effective action approaches the classical action.

(iii) It vanishes in the limit $k \to 0$.

In addition, our *Fermi*-surface-adapted class of regulator functions fulfills a set of “weak” or “convenience” requirements:

(iv) It does not violate the chiral symmetry of the kinetic term in the fermionic action.

(v) It does not introduce an artificial breaking of *Poincaré* invariance and, in particular, it preserves *Poincaré* invariance in the limit $T \to 0$ and $\mu \to 0$.

(vi) It respects the invariance of relativistic theories under the transformation $\mu \to -\mu$.

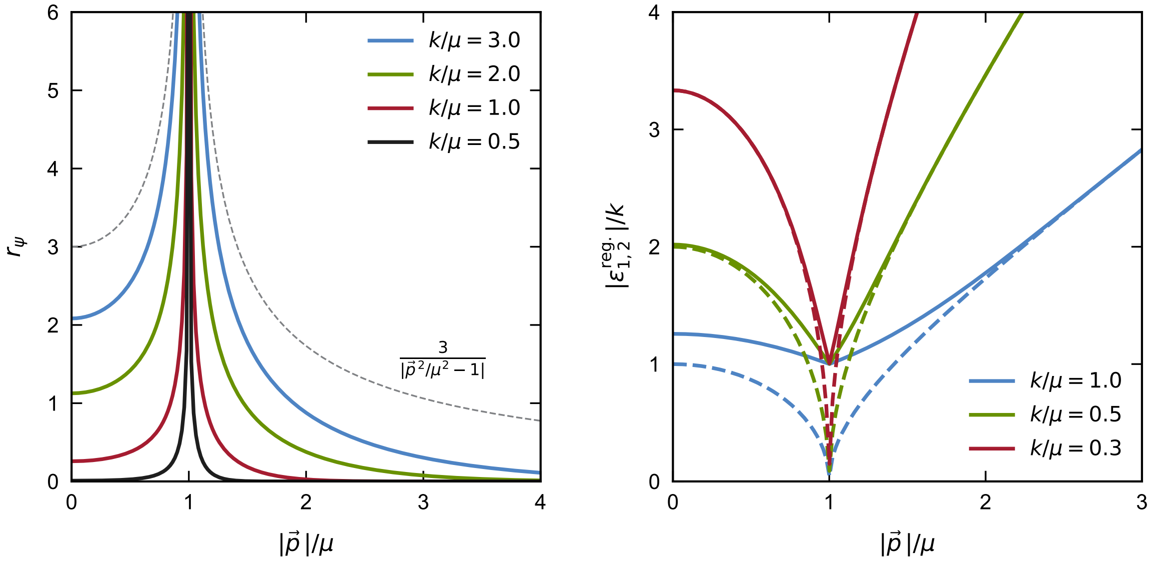

FIGURE 3.2: Left panel: The *Fermi*-surface-adapted regulator shape function r_ψ, see Eq. (3.44), as a function of the spatial momentum normalized to the quark chemical potential, i.e., $|\vec{p}\,|/\mu$, at $p_0 = 0$ for $k/\mu = 0.5$, 1, 2, 3, illustrating the integration over momentum modes around the *Fermi* surface at $|\vec{p}\,| \simeq \mu$. The gray dashed line depicts as an example the required limit (3.42) for $k/\mu = 3.0$. Right panel: The regularized eigenvalues $|\epsilon^{\text{reg.}}_{1,2}|/k$ normalized to the RG scale k as a function of $|\vec{p}\,|/\mu$ at $p_0 = 0$ for $k/\mu = 0.3$, 0.5, 1. By comparison, the eigenvalues without regularization, depicted by the dashed lines of corresponding color, become zero at the *Fermi* surface.

(vii) It ensures that the regularization of the loop diagrams is local in terms of temporal and spatial momenta at any finite value of the RG scale k.

The requirement (vii) essentially corresponds to the fact that the regulator function defines the details of the *Wilsonian* momentum-shell integrations.

At finite chemical potential, regularization schemes face an additional complication in that the regulator should in principle also preserve the symmetry transformation (2.37) associated with the *Silver-Blaze* property introduced in Section 2.1.2, see Refs. [230, 231]. In cases where the full momentum dependence of the correlation functions is resolved, the only source of an explicit breaking of the *Silver-Blaze* property is the regularization scheme. With respect to the regularization scheme in RG studies, in addition to the requirements (i)-(vii) listed above, the eigenvalues of the (matrix-valued) regulator function R_k^ψ are required to be only functions of the spatial momenta $\vec{p}$ and the complex variable $z = p_0 - \mathrm{i}\mu$, $R_k^\psi = R_k^\psi(z, \vec{p}\,)$ [230] in order to preserve the *Silver-Blaze* property, i.e., the corresponding invariance of the theory under the transformation (2.37).

Assuming that the invariance of the theory under the transformation (2.37) is an exact statement, i.e., neither the regularization scheme violates this invariance nor the expansion/approximation scheme in some other way, the *Silver-Blaze* property also leaves its imprint on the RG flow. For the sake of simplicity, we consider in the following a purely fermionic theory, with the fermions carrying a charge. The regulator induces a gap $\sim k$ for the two-point function and renders the correlation functions k-dependent. Provided that $\mu < m_{\text{gap}}(k)$, the μ-dependence of the correlation functions at $T = 0$ is now trivially obtained from the vacuum correlation functions by replacing the zero-components $q_0^{(i)}$ of their momentum space arguments with $(q_0^{(i)} - \mathrm{i}\mu)$. Here, m_{gap} denotes the k-dependent gap determined by the distance of the singularity closest to the origin in the complex $q_0^{(i)}$-plane at $T = 0$. For massless fermions, we have $m_{\text{gap}} \sim k$, whereas in case of fermions with (pole) mass m_{f} we have $m_{\text{gap}} \to m_{\text{f}}$ for $k \to 0$ and $m_{\text{gap}} \sim k$ for $k \gg m_{\text{f}}$. It follows that the RG flows of correlation functions for a given $\mu < m_{\text{gap}}(k)$ at $T = 0$ are identical to their vacuum flows.

Spatial regularization schemes (such as the class of regulator functions defined in Refs. [366–369]) do not depend on $z = p_0 - \mathrm{i}\mu$ at all and thus trivially fulfill the requirement to preserve the *Silver-Blaze* property. However, our preferred class of four-dimensional/covariant *Fermi*-surface-adapted regulator functions fulfilling the requirements (i)-(vii) listed above explicitly breaks the symmetry associated with the transformation (2.37) as it depends on $\omega_+\omega_- = |(p_0 - \mathrm{i}\mu)^2 + \vec{p}^{\,2}|$. In Section 4.2.4, with a concrete theory at hand, we shall therefore examine the strength of the violation of the *Silver-Blaze* property in comparison to the application of spatial regularization schemes in order to assess the potential influence on the results.

3.3 Renormalization group consistency

In the following, we introduce the concept of RG consistency, where we begin with a discussion from a general perspective. In particular, we discuss the role of external control parameters, e.g., temperature or quark chemical potential, and address the UV extension of low-energy effective models (LEMs).[6] Violations of RG consistency are associated with cutoff artifacts as well as regularization-scheme dependences and may significantly spoil predictions for physical observables. The analysis of such effects is crucial for a meaningful application of LEMs and a test of the individual range of applicability in terms of the external control parameters. Following the general discussion, we then employ the FRG perspective to discuss how cutoff artifacts can be consistently removed within a given LEM. The FRG provides an ideal tool to resolve such issues systematically, as it allows us to study the dependence of the couplings on the UV cutoff scale.

The computation of quantum corrections in field theories, as typically associated with the computation of loop diagrams, requires in general a regularization and renormalization procedure. The regularization procedure allows us to compute the loop diagrams in a well-defined fashion, e.g., by introducing a momentum cutoff Λ for the momentum integrals. In the subsequent renormalization the cutoff dependence is absorbed by counterterms which are added to the underlying bare action Γ_Λ in the form of Λ-dependent couplings. The bare action Γ_Λ then consists of all UV relevant terms allowed by the symmetry of the classical

---

[6] Here, we do not distinguish between the terms low-energy effective *model* and *theory* and use them interchangeably, since, in fact, a model might be considered as a consistent quantum field theory by itself, see, e.g., Refs. [203, 377].

theory or classical action S. The explicit cutoff dependence of the bare action Γ_Λ ensures the cutoff independence of the full quantum effective action Γ, i.e.,

$$\Lambda \frac{\mathrm{d}\Gamma}{\mathrm{d}\Lambda} = 0\,. \tag{3.45}$$

This is the requirement of a consistent regularization and renormalization of a given theory, and is called *RG consistency*. It simply states that the quantum effective action Γ should not depend on the cutoff scale Λ, even in the presence of external parameters. These considerations are very general and are not bound to specific class of models.[7] In fact, they apply equally well to any computation of the quantum effective action, including perturbative approaches as well as non-perturbative functional methods such as the FRG, Dyson-Schwinger equations and nPI methods.

Potential cutoff effects and regularization scheme dependences are amplified in studies of the effect of external parameters on the dynamics of the system. In such studies, we have in principle to ensure that the scale Λ is much greater than the scale set by the external parameter under consideration. Otherwise, peculiarities of the employed regularization scheme are resolved when the external parameter is varied. This scale is said to be asymptotically large when

$$\frac{s_i}{\Lambda} \ll 1 \quad \text{with} \quad s = \{m_{\text{phys}}, m_{\text{ext}}\}\,, \tag{3.46}$$

where the set s stands for all mass scales in the theory, including dimensionful couplings. In particular, this set consists of the intrinsic fundamental parameters m_{phys} of the theory, for example masses of particles, as well as the external scales m_{ext} such as the temperature T or the quark chemical potential μ.

Provided that Eq. (3.46) holds, the bare action Γ_Λ only encodes the microphysics of the system at hand, and changes of the intrinsic parameters are simply triggered by changing the respective bare parameters in the action. In particular, Eq. (3.46) entails that a change of the external parameters of the theory does not change the regularization and renormalization of the theory encoded in the Λ-dependence of Γ_Λ. For $m_{\text{ext},i}/\Lambda \to 0$, the corresponding property then reads

$$\frac{\mathrm{d}}{\mathrm{d}m_{\text{ext},i}} \left[\Lambda \frac{\mathrm{d}\Gamma_\Lambda}{\mathrm{d}\Lambda}\right] = 0\,, \tag{3.47}$$

which highlights the similarity of this condition to the RG-consistency condition given in Eq. (3.45). In turn, if Eq. (3.46) does not hold, Γ_Λ has to vary with a change of m_{ext} to ensure that the RG-consistency condition (3.45) holds, i.e., we have

$$\frac{\mathrm{d}}{\mathrm{d}m_{\text{ext},i}} \left[\Lambda \frac{\mathrm{d}\Gamma_\Lambda}{\mathrm{d}\Lambda}\right] \neq 0\,. \tag{3.48}$$

Note that, if Eq. (3.47) is violated, at least part of the physics related to the fluctuation physics of the respective external parameters is already carried by the bare action Γ_Λ. It

---

[7] The cutoff scale Λ should not assigned any phenomenological meaning as it is a regularization-scheme dependent quantity. It should only be viewed as the scale where the couplings/parameters of a given model are fixed.

has to be computed separately, which necessitates an explicit expression for the right-hand side of Eq. (3.48). This computation is then crucial to properly capture the fluctuations in the presence of external parameters. A procedure to obtain the initial bare action Γ_Λ for an asymptotically free theory in a well-defined way is presented in Appendix D. Otherwise, violations of RG consistency may indeed significantly spoil predictions for physical observables, see Section 6.1.2 for the discussion of explicit examples.

For a plethora of physically interesting theories, the cutoff Λ may be limited by a validity bound. A strict bound is present, if the effective theory under consideration cannot be extended beyond a certain UV scale. For example, a Landau pole at the scale Λ_{UV} is such a strict bound. Then, we have to choose $\Lambda \leq \Lambda_{\text{UV}}$. This situation applies to most effective theories for the low-energy regime of QCD, such as NJL-type models and quark-meson-type models (QM) with or without *Polyakov*-loop extensions [45, 46, 106, 107, 115–126, 128–140, 314–326, 329–332, 378, 379], and it also applies to, e.g., quantum electrodynamics and a variety of condensed-matter models.

A further, qualitatively different, validity bound of LEMs is related to the fact, that they typically lack some of the microscopic degrees of freedom which are relevant at momentum scales $\Lambda > \Lambda_{\text{phys}}$. Then, Eq. (3.46) may hold for a given LEM but, beyond the scale Λ_{phys}, the LEM lacks the dynamics associated with the fundamental microscopic degrees of freedom. Consequently, such an LEM cannot describe the physics at hand beyond Λ_{phys}. For example, in conventional QCD low-energy effective theories, the gluon dynamics is missing. These LEMs describe QCD solely in terms of hadronic degrees of freedom which can only hold true for low momentum scales. Of course, by definition, a determination of the scale Λ_{phys} is involved as it requires an actual study of the fundamental dynamics at all momentum scales. Within the FRG approach to fundamental QCD [186, 192, 193, 195, 211, 380, 381], however, it has been shown in various studies that the gluonic sector of QCD at low baryon density decouples from the matter sector at scales $\Lambda_{\text{phys}} \sim 0.4 \ldots 1\,\text{GeV}$, see, e.g., Refs. [187, 326, 330, 335, 382, 383]. In this context, it should be noted that the scales Λ, Λ_{UV}, and Λ_{phys} depend on the chosen regularization scheme, and are only related to physical momentum scales by the renormalization procedure.

In conclusion, we typically have to deal with the existence of an actual finite UV extent of low-energy models given in form of a maximal UV cutoff scale Λ_{UV} due to an instability of the theory, or a phenomenologically existing UV extent Λ_{phys} above which a given LEM does no longer provide a valid description of a more fundamental theory. A priori, a safe choice is then

$$\Lambda \leq \Lambda_{\text{max}}\,, \tag{3.49}$$

where $\Lambda_{\text{max}} = \min\left(\Lambda_{\text{phys}}, \Lambda_{\text{UV}}\right)$. For such a choice, Λ may not be sufficiently large compared to the external parameters m_{ext} of interest and we are left with the situation as described by Eq. (3.48). Moreover, the intrinsic scales may not even be small compared to Λ.[8] Then, the initial effective action is a complicated object itself and its determination highly non-trivial.

---

[8] In the following we focus on the external parameters for clarity. However, the discussion can be straightforwardly generalized to the case of intrinsic scales.

In LEMs of QCD, for example, this issue may potentially be surmounted by computing Γ_Λ with the aid of RG studies of the fundamental theory, cf. our study presented in Chapter 6 and see also, e.g., Refs. [330, 335, 366, 383]. However, if a sufficiently accurate determination of Γ_Λ from a more fundamental theory is not available, we still have to ensure that cutoff artifacts associated with a specific choice for the scale Λ are suppressed or even removed in our model study. Otherwise, over a wide range of the external parameters, such a model study may only resolve peculiarities of the underlying regularization scheme. In this case, we have to make use of "pre-initial" flows which provide a systematic determination of the effects of the violations described in Eq. (3.48) by an RG-consistent UV completion of the LEM under consideration.

To this end, we make use of the FRG perspective to describe the scale-dependence of the effective action by a flow equation in the generic form

$$k\partial_k \Gamma_k[\Phi] = \mathcal{F}_k[\Phi]\,, \tag{3.50}$$

where $\mathcal{F}_k[\Phi]$ could, e.g., represent the non-perturbative one-loop structure in the *Wetterich* equation (3.23). The effective action Γ is obtained by integrating this equation from the initial UV scale $k = \Lambda$ to $k = 0$. The formal solution for finite k is readily given by

$$\Gamma_k[\Phi] = \Gamma_\Lambda[\Phi] + \int_\Lambda^k \frac{\mathrm{d}k'}{k'} \mathcal{F}_{k'}[\Phi]\,. \tag{3.51a}$$

Note that here the scale Λ is not necessarily the largest scale possible in the theory under consideration, i.e., Λ_{UV}. It is only some scale at which we fix the couplings of the theory. The RG-consistency condition (3.45) follows immediately for any $k \neq \Lambda$ from Eq. (3.51a) by taking the Λ-derivative:[9]

$$\Lambda\partial_\Lambda \Gamma_k[\Phi] = \Lambda\partial_\Lambda \Gamma_\Lambda[\Phi] - \mathcal{F}_\Lambda[\Phi] = 0\,. \tag{3.51b}$$

The latter relation implies that in the FRG approach RG consistency and hence cutoff independence of a theory, fundamental or effective, is trivially fulfilled provided that the bare effective action at the initial scale $k = \Lambda$ obeys the flow equation if the initial scale is varied.

In order to illustrate the pre-initial flow in the presence of external parameters, let us assume that we know the effective action at some scale. In case of QCD models, for example, the effective action is often chosen to assume a simple quadratic form at some scale. In the following, this scale is denoted as Λ_0. The UV completion Γ_Λ of the LEM is then obtained by following the RG flow from $k = \Lambda_0 < \Lambda$ to $k = \Lambda \leq \Lambda_{\mathrm{UV}}$, such that we have $\Lambda\partial_\Lambda\Gamma \to 0$ for $m_{\mathrm{ext},i}/\Lambda \ll 1$, i.e., RG consistency is ensured in the presence of finite external parameters. The effective action Γ_Λ can be determined from Eq. (3.51) as

$$\Gamma_\Lambda[\Phi; m_{\mathrm{ext}}^{(0)}] = \Gamma_{\Lambda_0}[\Phi; m_{\mathrm{ext}}^{(0)}] - \int_\Lambda^{\Lambda_0} \frac{\mathrm{d}k'}{k'} \mathcal{F}_{k'}[\Phi; m_{\mathrm{ext}}^{(0)}]\,, \tag{3.52}$$

---

[9] Note that, within the standard convention of the FRG approach, the partial derivative with respect to Λ corresponds to the total derivative in Eq. (3.45).

with Λ chosen such that $m_{\mathrm{ext},i}/\Lambda \ll 1$ for all parameters of interest. Here, $\mathcal{F}_{k'}$ depends on Φ and $m_{\mathrm{ext}}^{(0)}$, the latter denoting a given set of "benchmark values" for the external parameters at which Γ_{Λ_0} has been fixed with the aid of some set of physical low-energy observables. Typical benchmark values are the vacuum values of the external parameters. For QCD, this is vanishing temperature and vanishing quark chemical potential.

If not indicated otherwise, we shall assume from now on that Γ_Λ has been fixed in the limit of vanishing external parameters. From our choice (3.52), we then deduce that the effective action Γ_k remains unchanged in this limit:

$$\begin{aligned} \Gamma_k[\Phi; m_{\mathrm{ext}}^{(0)}] &= \Gamma_{\Lambda_0}[\Phi; m_{\mathrm{ext}}^{(0)}] + \int_{\Lambda_0}^{k} \frac{\mathrm{d}k'}{k'} \mathcal{F}_{k'}[\Phi; m_{\mathrm{ext}}^{(0)}] \\ &= \Gamma_{\Lambda}[\Phi; m_{\mathrm{ext}}^{(0)}] + \int_{\Lambda}^{k} \frac{\mathrm{d}k'}{k'} \mathcal{F}_{k'}[\Phi; m_{\mathrm{ext}}^{(0)}] \,, \end{aligned} \tag{3.53}$$

where $k < \Lambda_0$. However, note that the Φ-dependence of Γ_Λ and Γ_{Λ_0} is in general different. At the same time, the choice (3.52) allows us to ensure $\Lambda\partial_\Lambda\Gamma \to 0$ for $m_{\mathrm{ext},i}/\Lambda \to 0$, see also below. Indeed, the condition $m_{\mathrm{ext},i}/\Lambda \to 0$ ensures that Eq. (3.47) is fulfilled for Γ_Λ. Eq. (3.52) also offers a practical way to compute the dependence of Γ_{Λ_0} on the external parameters. In other words, the chosen UV completion in form of $\mathcal{F}_{k>\Lambda_0}$ has to ensure the overall consistency of the LEM, and, in particular, the thermodynamical consistency. Of course, this procedure is very general and also applies to the case of asymptotically free theories as well as to asymptotically safe theories where Λ_{UV} is infinite.

For the construction of Γ_Λ in case of LEMs with $\Lambda_{\mathrm{phys}} < \Lambda_{\mathrm{UV}}$, it may even be required to choose $\Lambda > \Lambda_{\mathrm{phys}}$. At first glance, this appears to be in contradiction to the very definition of the scale Λ_{phys}. Strictly speaking, this is correct and an extension of LEMs beyond Λ_{phys} does not carry the physical fluctuation dynamics of the underlying fundamental theory for scales $\Lambda > \Lambda_{\mathrm{phys}}$. Nevertheless, we may have to choose $\Lambda > \Lambda_{\mathrm{phys}}$ in order to suppress cutoff artifacts, i.e., the failure of Eq. (3.47).

For the generic flow equation (3.50), the change of the initial condition with respect to $m_{\mathrm{ext},i}$ reads

$$\Lambda \frac{\partial^2 \Gamma_\Lambda[\Phi, m_{\mathrm{ext}}]}{\partial m_{\mathrm{ext},i}\, \partial\Lambda} = \frac{\partial \mathcal{F}_\Lambda[\Phi, m_{\mathrm{ext}}]}{\partial m_{\mathrm{ext},i}} \,. \tag{3.54}$$

Integrating (3.54) from $m_{\mathrm{ext},i}^{(0)}$ to $m_{\mathrm{ext},i}$ leads to an even more convenient form,

$$\Lambda\partial_\Lambda\Gamma_\Lambda[\Phi; m_{\mathrm{ext}}] - \Lambda\partial_\Lambda\Gamma_\Lambda[\Phi; m_{\mathrm{ext}}^{(0)}] = \mathcal{F}_\Lambda[\Phi; m_{\mathrm{ext}}] - \mathcal{F}_\Lambda[\Phi; m_{\mathrm{ext}}^{(0)}] \,. \tag{3.55}$$

If Eq. (3.47) holds, then the initial effective action is not changed apart from its explicit dependence on m_{ext}. The same holds for the flow equation itself. Accordingly, if Eqs. (3.54) and (3.55) are non-vanishing for a fixed initial effective action Γ_Λ, then the (pre-)initial flow – and hence the initial effective action – has to change for the RG-consistency condition (3.45) to hold: With the representation of Γ as the integrated flow, see Eqs. (3.51) and (3.55), we are immediately led to the RG-consistency condition (3.45). In turn, assuming Eq. (3.47), and using the representation (3.51) of Γ as the integrated flow, we arrive at the important constraint

$$\Lambda\partial_\Lambda\Gamma[\Phi;m_{\text{ext}}] = -\Big(\mathcal{F}_\Lambda[\Phi;m_{\text{ext}}] - \mathcal{F}_\Lambda[\Phi;m_{\text{ext}}^{(0)}]\Big) \overset{!}{=} 0\,. \tag{3.56}$$

Here, the first term on the right-hand side arises from the Λ-derivative of the integrated flow (3.51), whereas the second term originates from the Λ-derivative of the initial effective action which is kept at its benchmark values for the external parameters. Note that Eq. (3.56) has been used in Ref. [371] for defining the "thermal range" $\Lambda_T[r] \equiv \Lambda[r;T]$ being the minimal cutoff value for which Eq. (3.56) holds to a given accuracy. Similarly, it is possible to extract a corresponding "density range" $\Lambda[r;\mu]$ in studies at finite quark chemical potential. Of course, the actual values of these quantities depend on the regularization scheme specified by the regulator shape function r.

More generally speaking, the external parameters set the minimal value $\Lambda[r;m_{\text{ext}},m_{\text{ext}}^{(0)}]$ of the cutoff for which Eq. (3.56) holds to a given accuracy. For the standard benchmark defined by choosing the vacuum values for the external parameters as benchmark values, the third variable can be dropped. For a given LEM with a maximal physical UV range Λ_{phys}, this entails that only results with m_{ext} in the set $\mathcal{M}_{\text{ext}}$,

$$\mathcal{M}_{\text{ext}}(m_{\text{ext}}^{(0)}) = \Big\{m_{\text{ext}}\,|\,\Lambda[r;m_{\text{ext}},m_{\text{ext}}^{(0)}] \leq \Lambda_{\text{phys}}[r]\Big\}\,, \tag{3.57}$$

are fully trustworthy. We emphasize that all the above cutoff scales naturally depend on the regularization scheme as defined by the choice for the regulator function r. In turn, the set $\mathcal{M}_{\text{ext}}$ should not depend on r, but may be r-dependent in given low-level approximations.

Provided that Λ_{phys} is known for an LEM at hand, the set $\mathcal{M}_{\text{ext}}$ defines the physics range of this LEM. Interestingly, this discussion makes also clear that the physics range for the external parameters depends on the chosen benchmark value for the external parameters. Of course, the latter cannot be chosen freely, as the parameters in the initial effective action $\Gamma_\Lambda[\Phi;m_{\text{ext}}^{(0)}]$ are fixed with the aid of observables at $m_{\text{ext}}^{(0)}$. Only $m_{\text{ext}}^{(0)}$, for which these observables are known, can be used as a benchmark. Still, this suggests to use available first-principles result from lattice or functional studies at finite temperature and chemical potential with $m_{\text{ext}}^{(0)} \neq 0$ as a benchmark instead of the vacuum values. In case of QCD, this in principle allows for more reliable LEM computations of, e.g., finite-density effects, and is pursued within "QCD-assisted" LEMs.

Irrespective of the existence of possible fundamental UV completions or of the knowledge of Λ_{phys} and the corresponding physics range of the LEM under consideration, it is still crucial to use the strategy associated with Eq. (3.52) to remove or at least suppress cutoff artifacts in the results for physical observables within a given LEM study.

In summary, the RG-consistency condition (3.45) of a given theory is in general a non-trivial constraint on the initial effective action at finite external parameters if Eq. (3.48) applies to this theory. In the present FRG framework, this is practically accessible via Eqs. (3.54) and (3.55). Moreover, the formal discussion in the present section leaves us with a practical toolbox for amending computations of observables in the presence of finite external parameters. In any case, we note that the initial effective action is non-trivial if Eq. (3.46) does not hold.

4

A FIERZ-COMPLETE STUDY OF THE NJL MODEL

4.1 Four-fermion interactions in QCD

Four-fermion interactions play an important role in the description of strongly correlated low-energy dynamics of QCD. They are the first key building block toward an effective low-energy description of the matter sector and, as we discuss below in Section 4.1.3, already contain information on ground-state properties related to the formation of condensates. Such interactions are not fundamental in the sense that they do not appear in the classical QCD *Lagrangian* (2.1) but are dynamically generated by two-gluon exchange as soon as quantum corrections are incorporated, see our discussion in Chapter 5 and Refs. [192, 195, 384] for further RG studies of QCD on this aspect. The fluctuations generally induce all types of four-fermion interaction channels that are compatible with the symmetries of the underlying theory, i.e., QCD. Among themselves, the various couplings of these channels are interrelated in a complex manner and can induce each other as well. Four-quark interactions can be recast into effective bosonic degrees of freedom that connect to a low-energy description of the dynamics. The dominance of a specific four-quark interaction relative to the other interaction channels points to the importance of the associated effective degree of freedom. A priori, the relevant low-energy effective degrees of freedom are not known and must be determined by the dynamics of the system on its own terms, provided it has the required freedom to do so. These aspects make clear that only the consideration of four-fermion interactions in their entirety is able to fully capture the dynamics toward the low-energy regime, whereas the consideration of incomplete subsets potentially results in loss of information. In this chapter, we therefore study the impact of so-called *Fierz-complete* four-fermion interaction channels in the pointlike limit which are only constrained by the symmetries of the theory, i.e., any pointlike four-fermion interaction compatible with the underlying symmetries is incorporated. To focus on and emphasize the significance of four-fermion interactions and *Fierz* completeness for the dynamics of the quark sector, we consider in the following the gluonic degrees of freedom to be integrated out and study a purely fermionic NJL-type model. In particular, we aim at a better understanding of how *Fierz*-incomplete approximations of QCD low-energy models affect the predictions for the phase structure at finite temperature and density. This understanding of the quark dynamics is considered to be essential and sets the stage for our study including dynamic gauge fields presented in Chapter 5.

After a discussion of general aspects of NJL-type models, we introduce in the next section our ansatz for the effective average action that we employ in our study on *Fierz*-complete NJL models. Subsequently, in Section 4.1.3, we discuss the connection between the RG flow of four-fermion couplings on the one hand and spontaneous symmetry breaking and the formation of condensates on the other. To illustrate the mechanisms at work, we consider a generic one-channel approximation which allows to a large extent an analytical treatment. In Section 4.2, we begin with a discussion of a *Fierz*-complete NJL model with the number of fermion species temporarily reduced to a single one. This corresponds to a simplification as the number of fermion species is drastically reduced compared to, e.g., QCD with two flavors and three colors. Still, this simplified model already shares many aspects with QCD in the low-energy limit and allows us to analyze in a more accessible fashion how neglected four-fermion interaction channels and the associated issue of *Fierz* incompleteness affect the predictions for the phase structure at finite temperature and density. In particular, we take into account the explicit symmetry breaking arising from the presence of a heat bath and the chemical potential in our study anchored at the leading order of the derivative expansion of the effective action. We demonstrate that *Fierz* completeness as associated with the inclusion of more “exotic” four-fermion channels does not only play a prominent role at large chemical potential but also affect the dynamics at small chemical potential. The latter is illustrated by a significant dependence of the curvature of the finite-temperature phase boundary at small chemical potential on the number of four-fermion channels included in the calculations. In Section 4.3, we extend our analysis to an NJL model with massless quark flavors coming in N_{c} colors and two flavors to gain a better understanding of how our previous results on the effect of *Fierz*-incomplete approximations on the phase boundary at finite temperature and density translates to QCD low-energy models. Within our *Fierz*-complete framework including 10 four-quark channels, we observe that channels associated with an explicit breaking of *Poincaré* invariance tend to increase significantly the critical temperature at large chemical potential. In accordance with many conventional model studies (see, e.g., Refs. [107, 115, 120, 385] for reviews), diquarks are nevertheless found to be the most dominant degrees of freedom in this regime.

4.1.1 NJL-type models

The NJL model and its relatives, such as the quark-meson (QM) model, play a very prominent role in theoretical physics. Originally, the NJL model has been introduced as an effective theory to describe spontaneous symmetry breaking in particle physics based on an analogy with superconducting materials [45, 46]. Since then, it has frequently been employed to study the phase structure of QCD, see, e.g., Refs. [115, 119–121, 386] for reviews. In particular at low temperature and large quark chemical potential, NJL-type models have become an important tool to analyze the low-energy dynamics of QCD as this regime is at least difficult to access with lattice Monte Carlo techniques. The models give us an insight into the rich symmetry breaking patterns that may potentially be at work in the high-density regime.

NJL/QM-type models indeed provide us with an effective description of the low-energy dynamics underlying the QCD phase diagram. The great relevance of NJL-type model studies for our understanding of dense strong-interaction matter is undisputed. However, despite the great success of the studies of these models, the phenomenological analysis and corresponding predictions of the results suffer from generic features of these models as well as from approximations underlying these studies. For example, NJL-type models in four space-time dimensions are defined with an UV cutoff Λ as they are perturbatively non-renormalizable. In fact, non-perturbative studies even indicate that they are also not non-perturbatively renormalizable (see, e.g., Refs. [333, 334]), in contrast to three-dimensional versions of this class of models [387]. Therefore, in case of four space-time dimensions, the UV cutoff scale becomes a parameter of the model and, as an immediate consequence, the regularization scheme belongs to the definition of the model. In particular, this implies that a given value of the UV cutoff scale has always to be viewed against the background of the chosen regularization scheme. From an RG standpoint, this scale should anyhow *not* be considered as an actual UV extent of the model but rather as the scale where the couplings of the model are fixed, cf. our discussion of RG consistency in Section 3.3. In addition, we note that the use of so-called three-dimensional/spatial regularization schemes for studies of hot and dense matter may not be unproblematic. This issue originates from the fact that this class of schemes explicitly breaks *Poincaré* invariance, even at zero temperature where the model parameters are usually fixed. This may then eventually lead to spuriously emerging symmetry breaking patterns as we shall discuss in Section 4.2.4.

The classical action underlying NJL-type model studies is typically given by a kinetic term for the quarks and a set of four-quark interactions which are usually selected by a phenomenological reasoning. The most basic version, which is a frequently employed approximation for studies of the QCD phase structure at finite temperature and density, only includes the scalar-pseudoscalar four-quark interaction channel and reads

$$S[\bar{\psi},\psi] = \int_0^\beta \mathrm{d}\tau \int \mathrm{d}^3x \, \left\{ \bar{\psi}\left(\mathrm{i}\partial\!\!\!/ - \mathrm{i}\mu\gamma_0\right)\psi + \frac{1}{2}\bar{\lambda}_{(\sigma\text{-}\pi)}\left[(\bar{\psi}\psi)^2 - (\bar{\psi}\gamma_5\tau_i\psi)^2\right]\right\} . \tag{4.1}$$

Here, $\beta = 1/T$ is the inverse temperature, μ is the quark chemical potential, and $\bar{\lambda}_{(\sigma\text{-}\pi)}$ is the coupling associated with the scalar-pseudoscalar channel. The τ_i's represent the *Pauli* matrices and couple the spinors in flavor space. The scalar-pseudoscalar four-quark interaction is usually considered most relevant for studies of chiral symmetry breaking because of its direct relation to the chiral order parameter: By means of a *Hubbard-Stratonovich* transformation, auxiliary fields can be introduced and the four-quark interaction channel is converted into a (screening) mass term for the auxiliary fields and a *Yukawa* interaction channel between the latter and the quarks. Conventionally, the auxiliary fields are chosen to carry the quantum numbers of the σ meson and the pions in case of the scalar-pseudoscalar four-quark interaction channel. The interactions between the quarks are then said to be mediated by an exchange of the aforementioned mesons. This choice for the auxiliary fields eventually allows a straightforward projection on the chiral order parameter.

Several aspects immediately point to insufficiencies of an NJL model that takes into account only the scalar-pseudoscalar interaction channel. Embedded in full QCD, as mentioned at the beginning of this chapter, the four-quark interactions may be viewed as dynamically generated by quark-gluon interactions at high energy scales. However, two-gluon exchange diagrams do not only generate the scalar-pseudoscalar four-quark self-interaction channel, but all four-quark self-interaction channels compatible with the fundamental symmetries of QCD. From the standpoint of an RG evolution of QCD from high to low energies, the gluon-induced four-quark interactions may then become strong enough to trigger spontaneous symmetry breaking at some intermediate energy scale, depending on, e.g., the temperature and the quark chemical potential. This scale may be associated with the UV cutoff scale of NJL-type models. In this spirit, we may therefore consider the general form of NJL-type models to be rooted in QCD. In practice, however, the four-quark couplings in NJL-type models are usually not fixed in this way. They are considered as fundamental parameters and are fixed by tuning them such that the correct values of a given set of low-energy observables is reproduced at, e.g., vanishing temperature and quark chemical potential. Unfortunately, the values of the chosen set of low-energy observables may in general be reproduced by various different set of parameters. Moreover, the parameters may depend on external control parameters such as the temperature and the quark chemical potential [335].

In any case, even in studies of the NJL/QM model defined with only a scalar-pseudoscalar interaction channel, by computing quantum corrections to the classical action (4.1) we immediately observe that four-quark self-interactions other than the scalar-pseudoscalar channel are generated, see, e.g., Ref. [333] for a review. Although these interactions do not appear in the original definition of the action (4.1), as for example a vector-channel interaction $\sim (\bar{\psi}\gamma_\mu\psi)^2$, they are necessarily induced by fluctuations but have often been ignored in the literature. Once other four-fermion channels are generated, it is reasonable to expect that these channels also alter dynamically the strength of the original scalar-pseudoscalar interaction. In particular at finite temperature and density, the number of possibly induced interaction channels is even increased because of the reduced symmetry of the theory. From a phenomenological point of view, the four-quark interaction channels may be recast into effective bosonic degrees of freedom. In particular at large chemical potential, the effective degrees of freedom associated with the scalar-pseudoscalar channel, namely the σ meson and the pions, are no longer expected to dominate the low-energy physics. Here, other degrees of freedom, such as diquarks, play a dominant role, see our discussion in Section 4.3 and, e.g., Refs. [97, 107, 115, 385] for reviews.

Apart from this phenomenologically guided point of view, the inclusion of more than one four-quark channel is of field-theoretical relevance as a given pointlike four-quark interaction channel is reducible by means of so-called *Fierz* transformations. These transformations refer to a rearrangement of the fermionic fields in a product of two *Dirac* bilinears and lead to linear relations among the four-quark interactions channels, the so-called *Fierz* identities, typically in the form of[1]

$$\left(\bar{\psi}\mathcal{O}_i\psi\right)^2 \equiv \left(\bar{\psi}^{(1)}\mathcal{O}_i\psi^{(2)}\right)\left(\bar{\psi}^{(3)}\mathcal{O}_i\psi^{(4)}\right) = \sum_j \chi_{ij}\left(\bar{\psi}^{(1)}\mathcal{O}_j\psi^{(4)}\right)\left(\bar{\psi}^{(3)}\mathcal{O}_j\psi^{(2)}\right), \tag{4.2}$$

with coefficients χ_{ij}, cf. Appendix B.3. Here, we have labeled the fermionic fields to distinguish the field variables explicitly, emphasizing the exchanged positions of $\psi^{(2)}$ and $\psi^{(4)}$. The four-fermion structures $(\bar{\psi}\mathcal{O}_i\psi)^2$ represent the interaction channels that are invariant under the symmetries of the theory, with the $\mathcal{O}_i$'s denoting the operators in *Dirac*, flavor and color space. For a more detailed discussion of *Fierz* transformations and identities, we refer to Appendix B.3. As QCD low-energy model studies in general do not take into account a *Fierz*-complete basis of four-quark interactions, they are incomplete with respect to these transformations. This naturally causes ambiguities in studies where the considered set of four-quark interaction channels is incomplete and also implies the necessity to use very general ansätze for the quark propagator as employed in, e.g., *Dyson-Schwinger*-type studies [388]. In mean-field studies of QCD low-energy models, the ambiguities related to the possibility to perform *Fierz* transformations might even lead to the dependence of the results on an unphysical parameter which reflects the choice on the mean field and limits the predictive power of the mean-field approximation [336].

4.1.2 Ansatz for the effective average action

Our discussion of conventional NJL-type model studies in the previous section clearly illustrates the problematic nature of considerations that take into account only selected few, typically phenomenologically motivated four-quark interaction channels while deliberately disregarding others. For our present study of the quantum effective action at leading order (LO) of the derivative expansion, we therefore consider the most general ansatz for the effective average action compatible with the symmetries of the theory. In particular, we take into account the explicit symmetry breaking arising from the presence of a heat bath and the chemical potential. An ansatz including every four-quark interaction channel invariant under the symmetries would be overdetermined as the *Fierz* relations imply that some channels are redundant and consequently the associated couplings not independent. By exploiting *Fierz* identities we can reduce the overdetermined set of four-fermion interactions to a minimal *Fierz*-complete set. The generic ansatz for our studies at finite temperature $T = 1/\beta$ and quark chemical potential μ is then given by

$$\Gamma_{\mathrm{LO}}[\bar{\psi},\psi] = \int_0^\beta \mathrm{d}\tau \int \mathrm{d}^3x \left\{\bar{\psi}\left(Z_\psi^{\parallel}\mathrm{i}\gamma_0\partial_0 + Z_\psi^{\perp}\mathrm{i}\gamma_i\partial_i - Z_\mu \mathrm{i}\mu\gamma_0\right)\psi + \frac{1}{2}\sum_{j\in\mathcal{B}} Z_j\bar{\lambda}_j\,\mathcal{L}_j\right\}, \tag{4.3}$$

---

[1] Invariant four-fermion interaction channels might already be given as sums of such elementary structures $(\bar{\psi}\mathcal{O}_i\psi)^2$, cf., e.g., the scalar-pseudoscalar interaction channel $\left[(\bar{\psi}\psi)^2 - (\bar{\psi}\gamma_5\tau_i\psi)^2\right]$. Conversely, in case of fewer symmetries, four-quark self-interactions in the pointlike limit can in principle be of the less restrictive form $(\bar{\psi}\mathcal{O}_i\psi)(\bar{\psi}\mathcal{O}_j\psi)$ as well.

where the elements $\mathcal{L}_j$ form a *Fierz*-complete basis $\mathcal{B}$ of pointlike four-quark interactions accompanied by the associated bare couplings $\bar{\lambda}_j$ and the corresponding vertex renormalizations Z_j.[2] The explicit expressions of the elements $\mathcal{L}_j$ are given in Sections 4.2.1 and 4.3.1 for the specific NJL-type model at hand. Any other pointlike four-quark interaction compatible with the symmetries of our model is then reducible by means of *Fierz* transformations.[3] Fermion self-interactions of higher order (e.g. eight-fermion interactions) may also be induced due to quantum fluctuations at leading order of the derivative expansion but do not contribute to the RG flow of the four-fermion couplings at this order and are therefore not included in our ansatz (4.3), see Ref. [333] for a detailed discussion.

The renormalization factors associated with the kinetic term are given by $Z_\psi^{\parallel}$ and $Z_\psi^{\perp}$, respectively. In general, the chemical potential is also accompanied by a renormalization factor Z_μ.[4] At $T = 0$, however, we have $Z_\mu^{-1} = Z_\psi^{\parallel} = Z_\psi^{\perp}$ for $\mu_{\mathrm{r}} = Z_\mu \mu < m_{\mathrm{f}}$ as a direct consequence of the *Silver-Blaze* property of general quantum field theories discussed in Section 2.1.2. Here, $m_{\mathrm{f}} \equiv \bar{m}_{\mathrm{f}}/Z_\psi^{\perp}$ is the potentially dynamically generated renormalized (pole) mass of the fermions, with $\bar{m}_{\mathrm{f}}$ being the bare fermion mass. In the following, we set $Z_\psi^{\parallel} = Z_\psi^{\perp} \equiv 1$ as the RG flow of these quantities vanishes identically at this order of the derivative expansion anyhow, i.e., $\partial_t Z_\psi^{\parallel} = \partial_t Z_\psi^{\perp} = 0$, see Ref. [333].

With the ansatz (4.3), we can proceed to study the RG flow of the four-fermion couplings appearing in the effective action which already allows us to gain a valuable insight into the phase structure of our model.

4.1.3 Access to the phase structure

Before we actually analyze the fixed-point structure of our model and its phase structure at finite temperature and chemical potential, we briefly discuss how a study of the quantum effective action (4.3) at leading order of the derivative expansion can give us access to the phase structure of our model. A detailed discussion can be found in, e.g., Ref. [333].

The leading order of the derivative expansion implies that we treat the four-fermion interactions in the pointlike limit, i.e., in the limit of vanishing external momenta according to

$$\bar{\lambda}_j(\bar{\psi}\mathcal{O}_j\psi)^2 = \lim_{\{p_k \to 0\}} \bar{\psi}_a(p_1)\bar{\psi}_b(p_2)\Gamma^{(4)}_{j,abcd}(p_1,p_2,p_3,p_4)\psi_c(p_3)\psi_d(p_4)\,,$$

where a, b, c, d are understood as generalized indices accounting for all applicable subspaces such as *Dirac*, flavor and color space and $\mathcal{O}_j$ denotes the operator related to the corresponding

---

[2] The leading order of the derivative expansion implies that the four-quark self-interactions are treated in the pointlike limit.

[3] The couplings λ_j appearing in the effective action (4.3) should not be confused with the couplings $\bar{\lambda}_j$ appearing in the classical action S, see, e.g., Eq. (4.1). The couplings appearing in the effective action include quantum corrections whereas, from an RG standpoint, the couplings appearing in the classical action only determine the values of the RG flows of the four-quark couplings at the initial scale Λ.

[4] In case of scale-dependent renormalization factors $Z_\psi^{\parallel}$, $Z_\psi^{\perp}$, and Z_μ, the following replacements in the definition of the regulator function R_k^ψ (excluding the shape function r_ψ), see Section 3.2, may be required: $p_0 \to Z_\psi^{\parallel} p_0$, $p_i \to Z_\psi^{\perp} p_i$, and $\mu \to Z_\mu \mu$.

four-fermion interaction channel $\mathcal{L}_j$ of the *Fierz*-complete basis $\mathcal{B}$ in Eq. (4.3) with the associated bare coupling $\bar{\lambda}_j$.

Apparently, the leading order of the derivative expansion does not give us access to the mass spectrum of our model which is encoded in the momentum structure of the correlation functions, i.e., the momentum structure of the general four-fermion vertex in the present case. In particular, the dynamics of regimes governed by the spontaneous formation of condensates is not accessible at this order. The formation of such condensates associated with spontaneous symmetry breaking is in fact indicated by singularities in the four-fermion correlation functions. Nevertheless, the effective action (4.3) at leading order in the derivative expansion still allows us to study regimes which are not governed by condensate formation, e.g. the dynamics at high temperature where the symmetries are expected to remain intact. By lowering the temperature at a given value of the chemical potential, we can then determine a critical temperature T_{cr} below which the pointlike approximation breaks down and a condensate related to a spontaneous breaking of one of the symmetries of our model is expected to be generated dynamically.

The breakdown of the pointlike approximation can be indeed used to detect the onset of spontaneous symmetry breaking. This can be most easily seen by considering a *Hubbard-Stratonovich* transformation [389, 390] to obtain a partially bosonized formulation of our ansatz (4.3). With the aid of this transformation, we can reformulate our purely fermionic action in terms of quark fields and auxiliary bosonic fields which are composites of two fermion fields such as a pion-like field or a diquark-like field. On the level of the path integral, the four-fermion interactions of a given theory are then replaced by terms bilinear in the so introduced auxiliary fields and corresponding *Yukawa*-type interaction terms between the auxiliary fields and the fermions, see also Section 4.1.3. Formally, we have

$$\bar{\lambda}_j(\bar{\psi}\mathcal{O}_j\psi)^2 \mapsto \sum_a \frac{1}{\bar{\lambda}_j}\phi_a^{(j)}\phi_a^{(j)} + \sum_{a,b,c} \bar{\psi}_b \bar{h}_j \tilde{\mathcal{O}}_j^{abc}\phi_a^{(j)}\psi_c \,. \tag{4.4}$$

Here, the couplings $\bar{h}_j$ denote the various *Yukawa* couplings. The structure of the quantity $\tilde{\mathcal{O}}_j^{abc}$ with respect to internal indices may be non-trivial and depends on the tensor structure of the corresponding four-fermion interaction channel $\mathcal{O}_j$. The same holds for the exact transformation properties of the possibly multi-component auxiliary field $\phi_a^{(j)}$.

Once a *Hubbard-Stratonovich* transformation has been performed, the *Ginzburg-Landau*-type effective potential for the bosonic fields $\phi_a^{(j)}$ can be computed conveniently, allowing for a straightforward analysis of the ground-state properties of the theory under consideration. For example, a non-trivial minimum of this potential indicates the spontaneous breakdown of the symmetries associated with those fields which acquire a finite vacuum expectation value.

From Eq. (4.4), we also deduce that the four-fermion couplings are inverse proportional to the mass-like parameters $\bar{m}_j^2 \sim 1/\bar{\lambda}_j$ associated with terms bilinear in the bosonic fields. Recall now that the transition from the symmetric regime to a regime with spontaneous symmetry breaking is indicated by a qualitative change of the shape of the *Ginzburg-Landau*-type effective potential as some fields acquire a finite vacuum expectation value. In fact, in case of a second-order transition, at least one of the curvatures $\bar{m}_j^2$ of the effective potential at the origin changes its sign at the transition point. This is not necessarily the case for a first-order transition. Still, taking into account *all* quantum fluctuations, the *Ginzburg-Landau*-type effective potential becomes convex in any case, implying that the curvature tends to zero in the long-range limit at both a first-order as well as a second-order phase transition point. As the pointlike four-quark couplings are inverse proportional to the curvatures $\bar{m}_j^2$, we conclude that a diverging four-quark coupling in the purely fermionic formulation indicates the onset of spontaneous symmetry breaking.

With respect to the RG analysis underlying this work, these considerations imply that the observation of a divergence of a four-quark coupling at an RG scale k_{cr} can be used as an indicator for the onset of spontaneous symmetry breaking. We shall use this criterion to estimate the phase structure of our NJL-type models in this chapter and also in our study including dynamic gauge fields in Chapter 5. For a given chemical potential, the above-mentioned critical temperature T_{cr} is then given by the temperature at which the divergence occurs at $k_{\mathrm{cr}} \to 0$. Such an analysis has indeed been successfully applied to compute the phase structure of various systems including gauge theories with many flavors (see, e.g., Ref. [391–394]), see Ref. [333] for a review. However, it should also be noted that this type of analysis is limited.[5] For example, it does not allow us to resolve the order of a phase transition. In fact, the divergence of a four-quark coupling at k_{cr} is not a sufficient criterion for spontaneous symmetry breaking as quantum fluctuations may restore the symmetries of the theory in the deep IR limit, see, e.g., Ref. [333] for a detailed discussion. If the true phase transition is of first order, this criterion at leading order of the derivative expansion may even only point to the onset of a region of metastability and not to the actual phase transition line. From a QCD standpoint, this implies that the liquid-gas phase transition, which is expected to be of first order, cannot be reliably assessed in the setup underlying our present work but requires to extend the truncation of the effective action. Moreover, the phenomenological meaning of a critical temperature obtained from such an analysis is potentially ambiguous. Different symmetry breaking patterns associated with the various four-quark channels exist in our model. Therefore, it is at least difficult to relate the breakdown of the pointlike approximation to the spontaneous breakdown of a specific symmetry, even more so since a divergence in a specific four-quark channel entails corresponding divergences in all other channels. However, a "dominantly diverging" four-quark channel can in general be identified, i.e., the modulus of the coupling of this channel is greater than the ones of the other four-quark couplings. Of course, this does not necessarily imply that a condensate associated with this channel is generated. It should only be viewed as an indicator for the symmetry breaking scenario at work. In Sections 4.2 and 4.3, we present an analysis of the "hierarchy" of the various four-quark interactions in terms of their strength and show that our "criterion of dominance" is at least in accordance with the simplest phenomenological expectation of the symmetry breaking patterns at work at small and large chemical potential [115], see also Ref. [395] for a similar approach in the context of condensed matter physics. For example, (color) superconducting ground states can in principle be detected within our present setup if the transition is of second order. Indeed, we shall show in Section 4.2 that the scaling behavior of physical observables associated with a superconducting ground state can be recovered correctly from our analysis of the RG flow of four-fermion couplings. Furthermore, we have

---

[5] For a detailed discussion of such an analysis and its limitations, we also refer to Ref. [333].

checked that our results from such an analysis are not altered when we rescale the channels $\mathcal{L}_j$ in our ansatz (4.3) with factors of $\mathcal{O}(1)$. Thus, despite the discussed restrictions of our present analysis, it already provides a valuable insight into the dynamics underlying spontaneous symmetry breaking of a given fermionic theory.

Instead of using the purely fermionic formulation of our model, one may be tempted to consider the partially bosonized formulation of our model right away in order to compute the *Ginzburg-Landau*-type effective potential for the various auxiliary fields, as indicated above. However, in contrast to the purely fermionic formulation, in which *Fierz* completeness at, e.g., leading order of the derivative expansion can be straightforwardly fully preserved by using a suitable basis of four-fermion interaction channels, conventional approximations entering studies of the partially bosonized formulation may easily induce a so-called *Fierz* ambiguity. Most prominently, mean-field approximations are known to show a basic ambiguity related to the possibility to perform *Fierz* transformations [336]. Therefore, results from this approximation potentially depend on an unphysical parameter which is associated with the choice of the mean field and limits the predictive power of this approximation. However, it has been shown [336] that the use of so-called dynamical hadronization techniques [192, 193, 195, 337, 380, 396–399] allow to resolve this issue, see also Ref. [211] for an introduction to dynamical hadronization in RG flows. As this is beyond the scope of the present work, we focus exclusively on the purely fermionic formulation of our model.

In order to elaborate our discussion of the mechanisms at work related to the spontaneous breakdown of symmetries within our model and especially of the connection to the RG flow of the four-fermion couplings $\bar{\lambda}_j$ and its fixed points, we shall next examine a scalar-pseudoscalar one-channel approximation, once in a mean-field computation employing the *Hubbard-Stratonovich* transformation and once in a purely fermionic description. The one-channel approximation allows to a large extent an analytical treatment and thus illustrates the mechanisms in an accessible manner.

Mean-field and one-channel approximation in the vacuum limit

We first discuss the one-channel approximation in the vacuum limit, i.e., at zero temperature and zero quark chemical potential, taking into account only the scalar-pseudoscalar interaction channel. In order to derive the mean-field gap equation for the chiral order-parameter field, we employ the *Hubbard-Stratonovich* transformation by inserting the relation

$$\int \mathcal{D}\phi \; \mathrm{e}^{-\int_x \frac{1}{2}\bar{m}^2_{(\sigma\text{-}\pi)}\phi^2} = \mathcal{N}\,, \tag{4.5}$$

where $\mathcal{N}$ is a normalization constant, into the partition function $Z[J]$, see Eq. (2.10), with the classical action (4.1) in the vacuum limit. This insertion introduces the auxiliary fields $\phi^{\mathrm{T}} = (\sigma, \vec{\pi}^{\,\mathrm{T}})$ but does not change the physical content as it only amounts to a redefinition of the normalization in the computation of correlation functions from this generating functional. By shifting the bosonic fields according to

$$\sigma \mapsto \sigma + \frac{\mathrm{i}\bar{h}_{(\sigma\text{-}\pi)}}{\bar{m}^2_{(\sigma\text{-}\pi)}}(\bar{\psi}\psi)\,, \qquad \pi_i \mapsto \pi_i + \frac{\mathrm{i}\bar{h}_{(\sigma\text{-}\pi)}}{\bar{m}^2_{(\sigma\text{-}\pi)}}(\bar{\psi}\mathrm{i}\gamma_5\tau_i\psi)\,, \tag{4.6}$$

and identifying $\bar{\lambda}_{(\sigma\text{-}\pi)} = \bar{h}^2_{(\sigma\text{-}\pi)}/\bar{m}^2_{(\sigma\text{-}\pi)}$, the four-fermion interaction is replaced by a *Yukawa*-type interaction and we obtain the partially bosonized version of the action given by

$$S[\bar{\psi},\psi,\phi] = \int_x \left\{ \bar{\psi}\mathrm{i}\partial\!\!\!/\psi + \frac{1}{2}\bar{m}^2_{(\sigma\text{-}\pi)}\phi^2 + \mathrm{i}\bar{h}_{(\sigma\text{-}\pi)}\bar{\psi}\left(\sigma + \mathrm{i}\gamma_5\tau_i\pi_i\right)\psi \right\} . \tag{4.7}$$

The auxiliary fields can be considered as the composites $\sigma \sim (\bar{\psi}\psi)$ and $\pi_i \sim (\bar{\psi}\gamma_5\tau_i\psi)$, see also, e.g., Ref. [333]. As the fermionic fields appear only bilinearly, the quark degrees of freedom can be readily integrated out, which leads to a functional determinant of the operator $(\mathrm{i}\partial\!\!\!/ + \mathrm{i}\bar{h}_{(\sigma\text{-}\pi)}[\sigma + \mathrm{i}\gamma_5\tau_i\pi_i])$, and we arrive at a partition function in terms of a path integral over the auxiliary fields ϕ. In the mean-field approximation, the bosonic fluctuations are omitted as well as the running of the *Yukawa* coupling.[6] Therefore, we can simply redefine the auxiliary fields to absorb the factor $\bar{h}_{(\sigma\text{-}\pi)}$, i.e., $\bar{h}_{(\sigma\text{-}\pi)}\phi \mapsto \phi$, as it is only a constant and does not change from its initial UV value. The curvature of the order-parameter potential, i.e., the coefficient of the term bilinear in the auxiliary fields, is then directly given by the inverse of the initial four-fermion coupling $\bar{\lambda}^{(\mathrm{UV})}_{(\sigma\text{-}\pi)}$ at the UV scale Λ.[7] From an evaluation in the mean-field approximation, we then obtain the following implicit equation for the constituent quark mass $\bar{m}_{\mathrm{q}}^2 = \langle\sigma\rangle^2$ at $T = \mu = 0$:

$$\lambda^*_{(\sigma\text{-}\pi)}\mathcal{J}(0) = \lambda^{(\mathrm{UV})}_{(\sigma\text{-}\pi)}\mathcal{J}(\bar{m}_{\mathrm{q}}^2) , \tag{4.8}$$

where $\lambda^{\mathrm{UV}}_{(\sigma\text{-}\pi)} = \Lambda^2\bar{\lambda}^{(\mathrm{UV})}_{(\sigma\text{-}\pi)}$ and $\lambda^*_{(\sigma\text{-}\pi)} \equiv \lambda^*_{(\sigma\text{-}\pi)}[r_\psi]$ is a dimensionless functional of the regularization scheme since $\mathcal{J}$ is not only a function of $\bar{m}_{\mathrm{q}}$ but also a functional of the regulator shape function r_ψ specifying the regularization scheme:

$$\mathcal{J}(\bar{m}_{\mathrm{q}}^2) = 8N_{\mathrm{c}}\int\frac{\mathrm{d}^4p}{(2\pi)^4}\left(\frac{1}{p^2+\bar{m}_{\mathrm{q}}^2} - \frac{1}{p^2(1+r_\psi(\frac{p^2}{\Lambda^2}))^2+\bar{m}_{\mathrm{q}}^2}\right) , \tag{4.9}$$

see also, e.g., Refs. [200, 333] for details. Diagrammatically, this integral is associated with a purely fermionic loop integral evaluated at vanishing external momenta. The parameter Λ may be considered as a UV cutoff scale for the loop-momentum integral. However, from our RG standpoint, it should be rather associated with the initial RG scale at which we fix the initial conditions of the four-quark couplings in our RG study below.

For a given regularization scheme, the functional $\lambda^*_{(\sigma\text{-}\pi)}$ determines the critical value of the four-quark coupling above which the ground state is governed by a finite vacuum expectation value $\langle\sigma\rangle \neq 0$. We find

$$\lambda^*_{(\sigma\text{-}\pi)} = \frac{\Lambda^2}{\mathcal{J}(0)} . \tag{4.10}$$

Thus, we have $\bar{m}_{\mathrm{q}} > 0$ for $\lambda^{(\mathrm{UV})}_{(\sigma\text{-}\pi)} > \lambda^*_{(\sigma\text{-}\pi)}$ and $\bar{m}_{\mathrm{q}} = 0$ otherwise. For example, we obtain $\lambda^*_{(\sigma\text{-}\pi)} = 2\pi^2/N_{\mathrm{c}}$ for the four-dimensional sharp cutoff often employed in mean-field

---

[6] The running of the *Yukawa* coupling in the limit of neglected bosonic fluctuations would only be given through the running of the mesonic wavefunction renormalizations that receive corrections from purely fermionic loops.

[7] From now on, we identify $\bar{\lambda}^{(\mathrm{UV})}_{(\sigma\text{-}\pi)}$ with the value of the coupling $\bar{\lambda}_{(\sigma\text{-}\pi)}$ appearing in the classical action since the latter determines the value of this coupling at the UV scale Λ in our RG study below.

calculations and $\lambda^{*}_{(\sigma\text{-}\pi)} = 4\pi^2/N_{\mathrm{c}}$ for the *Litim* regulator. In the following, however, we shall employ the same scheme as in our studies of the RG flow of four-quark couplings to ensure comparability, i.e., the four-dimensional *Fermi*-surface-adapted regulator which turns into the well-known four-dimensional exponential scheme at vanishing quark chemical potential, see Section 3.2 for details of the regulator shape functions. For this scheme, we find $\lambda^{*}_{(\sigma\text{-}\pi)} = 2\pi^2/N_{\mathrm{c}}$. In any case, we deduce from Eq. (4.8) that the actual value of $\lambda^{*}_{(\sigma\text{-}\pi)}$ is of no importance. For a given regularization scheme together with a specific choice for the UV scale Λ, the quark mass $\bar{m}_{\mathrm{q}}$ only depends on the "strength" $\Delta\lambda_{(\sigma\text{-}\pi)}$ of the scalar-pseudoscalar coupling relative to its critical value for chiral symmetry breaking:

$$\Delta\lambda_{(\sigma\text{-}\pi)} = \frac{\lambda^{(\mathrm{UV})}_{(\sigma\text{-}\pi)} - \lambda^{*}_{(\sigma\text{-}\pi)}}{\lambda^{(\mathrm{UV})}_{(\sigma\text{-}\pi)}}\,. \tag{4.11}$$

The implicit equation (4.8) for the constituent quark mass in terms of $\Delta\lambda_{(\sigma\text{-}\pi)}$ is given by

$$\Delta\lambda_{(\sigma\text{-}\pi)} = 1 - \mathcal{J}(\bar{m}_{\mathrm{q}}^2)/\mathcal{J}(0)\,. \tag{4.12}$$

From this discussion it follows immediately that a specific choice for $\Delta\lambda_{(\sigma\text{-}\pi)}$ also determines the sign of the curvature $\bar{m}^2_{(\sigma\text{-}\pi)}$ of the order-parameter potential U at the origin. Indeed, we have

$$\bar{m}^2_{(\sigma\text{-}\pi)} := 2\frac{\partial U}{\partial \sigma^2}\bigg|_{\sigma=0} = -\Lambda^2 \frac{\Delta\lambda_{(\sigma\text{-}\pi)}}{\lambda^{*}_{(\sigma\text{-}\pi)}}\,, \tag{4.13}$$

implying that, at the "critical point" $\Delta\lambda_{(\sigma\text{-}\pi)} = 0$, the curvature $\bar{m}^2_{(\sigma\text{-}\pi)}$ of the order-parameter potential changes its sign. As the renormalized scalar-pseudoscalar coupling $\bar{\lambda}_{(\sigma\text{-}\pi)}$ is inverse proportional to the curvature $\bar{m}^2$, see our discussion of the *Hubbard-Stratonovich* transformation at the beginning of this section (in particular the relation below Eq. (4.6)), the scalar-pseudoscalar four-quark coupling diverges at the "critical point" $\Delta\lambda_{(\sigma\text{-}\pi)} = 0$, i.e.,

$$\Lambda^2 \bar{\lambda}_{(\sigma\text{-}\pi)} = \frac{\Lambda^2}{\bar{m}^2_{(\sigma\text{-}\pi)}} = -\frac{\lambda^{*}_{(\sigma\text{-}\pi)}}{\Delta\lambda_{(\sigma\text{-}\pi)}}\,. \tag{4.14}$$

As discussed on more general grounds at the beginning of this Section 4.1.3, these observations regarding the critical behavior and the formation of a non-trivial ground state can be carried over to studies of the RG flow of four-quark interactions, even beyond the mean-field limit. We refer the reader to Ref. [333] for a corresponding detailed discussion. In the following, we discuss generic characteristics of the RG flow of the four-quark interaction in a one-channel approximation to illustrate the mechanisms at work that generally come into play in our RG flow analysis to access the phase structure. We employ the ansatz (4.3) for the interpolating effective action with only the scalar-pseudoscalar interaction channel and compute the corresponding flow equation with the help of the *Wetterich* equation. The derivation of the flow equation essentially amounts to the computation of a purely fermionic loop regularized by the four-dimensional exponential scheme, see again Ref. [333] for an introduction to the computation of RG flows of fermion self-interactions. The flow equation for the dimensionless scale-dependent renormalized scalar-pseudoscalar coupling $\lambda_{(\sigma\text{-}\pi)} = Z_{(\sigma\text{-}\pi)} k^2 \bar{\lambda}_{(\sigma\text{-}\pi)}/(Z_\psi^\perp)^2$ at $T = \mu = 0$ assumes the generic form[8]

$$\partial_t \lambda_{(\sigma\text{-}\pi)} = 2\lambda_{(\sigma\text{-}\pi)} - \frac{2}{\lambda^*_{(\sigma\text{-}\pi)}} \lambda^2_{(\sigma\text{-}\pi)} \,. \tag{4.15}$$

The flow equation (4.15) has two fixed points: a *Gaußian* fixed point and a non-*Gaußian* fixed point $\lambda^*_{(\sigma\text{-}\pi)}$. In the large-$N_\mathrm{c}$ limit, the value of the latter is nothing but the critical value (4.10) for chiral symmetry breaking in the mean-field approximation as shown in Ref. [333], see also our discussion in Section 4.3.2. In general, note that the flow equation (4.15) is ambiguous in the sense that the prefactor of the term quadratic in the four-quark coupling is not unique on the account of the *Fierz* ambiguity and the dependence on the regularization scheme. Again, however, the actual value of the non-*Gaußian* fixed point is of no importance concerning the question of the formation of a non-trivial ground state. Only the value of the scalar-pseudoscalar coupling at the initial RG scale Λ relative to the value of the non-*Gaußian* fixed point matters, i.e., the "strength" $\Delta\lambda_{(\sigma\text{-}\pi)}$ defined in Eq. (4.11). The solution for $\lambda_{(\sigma\text{-}\pi)}$ in terms of $\Delta\lambda_{(\sigma\text{-}\pi)}$ is given by

$$\lambda_{(\sigma\text{-}\pi)}(k) = \lambda^{(\mathrm{UV})}_{(\sigma\text{-}\pi)} \frac{1 - \Delta\lambda_{(\sigma\text{-}\pi)}}{1 - \Delta\lambda_{(\sigma\text{-}\pi)} \left(\frac{\Lambda}{k}\right)^{\Theta}} \,, \tag{4.16}$$

where $\lambda^{(\mathrm{UV})}_{(\sigma\text{-}\pi)}$ is the initial condition for the coupling $\lambda_{(\sigma\text{-}\pi)}$ at the UV scale Λ and Θ denotes the critical exponent which governs the scaling behavior of physical observables close to the "quantum critical point" λ^*_σ:

$$\Theta := -\frac{\partial \beta_\sigma}{\partial \lambda_\sigma}\bigg|_{\lambda^*_\sigma} = 2 \,. \tag{4.17}$$

As $\Theta > 0$, the fixed point $\lambda^*_{(\sigma\text{-}\pi)}$ is IR repulsive. Indeed, we readily observe from the solution (4.16) that $\lambda_{(\sigma\text{-}\pi)}$ is repelled by the fixed point. Moreover, $\lambda_{(\sigma\text{-}\pi)}$ diverges at a finite RG scale k_cr, if $\lambda^{(\mathrm{UV})}_{(\sigma\text{-}\pi)}$ is chosen to be greater than the fixed-point value $\lambda^*_{(\sigma\text{-}\pi)}$, i.e., $\Delta\lambda_{(\sigma\text{-}\pi)} > 0$. Note that in this case $\Delta\lambda_{(\sigma\text{-}\pi)} \in [0;1[$. Thus, by varying the initial condition $\lambda^{(\mathrm{UV})}_{(\sigma\text{-}\pi)}$, we can induce a "quantum phase transition", i.e., a phase transition in the vacuum limit, from a symmetric phase to a phase governed by spontaneous symmetry breaking while the non-*Gaußian* fixed point separates these two regimes.

To be more precise, we find that in case of $\lambda^{(\mathrm{UV})}_{(\sigma\text{-}\pi)} > \lambda^*_{(\sigma\text{-}\pi)}$ the scalar-pseudoscalar coupling diverges at the scale k_cr given by

$$k_\mathrm{cr} = \Lambda \left(\Delta\lambda_{(\sigma\text{-}\pi)}\right)^{\frac{1}{\Theta}} \theta(\Delta\lambda_{(\sigma\text{-}\pi)}) \,, \tag{4.18}$$

indicating the onset of chiral symmetry breaking, i.e., the curvature of the order-parameter at the origin changes its sign at this so-called chiral symmetry breaking scale k_cr. This

---

[8] Recall that the RG flow of the wavefunction renormalizations vanishes identically at this order of the derivative expansion and we set $Z_\psi^\perp = 1$.

scale sets the scale for the (chiral) low-energy observables $\mathcal{Q}$ with mass dimension $d_{\mathcal{Q}}$ in our model, $\mathcal{Q} \sim k_{\mathrm{cr}}^{d_{\mathcal{Q}}}$, such as the constituent quark mass $\bar{m}_{\mathrm{q}} \sim k_{\mathrm{cr}}$.

One-channel approximation at finite temperature and quark chemical potential

Let us finally illustrate our general approach to compute the phase structure in the plane spanned by the temperature and the quark chemical potential in the one-channel approximation. This approximation has also been discussed in Refs. [333, 400]. The RG flow equation for $\lambda_{(\sigma\text{-}\pi)}$ then assumes the generic form:

$$\partial_t \lambda_{(\sigma\text{-}\pi)} = 2\lambda_{(\sigma\text{-}\pi)} - \frac{2}{\lambda^*_{(\sigma\text{-}\pi)}} \lambda^2_{(\sigma\text{-}\pi)}\, \mathcal{L}(\tau, \tilde{\mu}_\tau)\,, \tag{4.19}$$

where $\tau = T/k$ is the dimensionless temperature, $\tilde{\mu}_\tau = \mu/(2\pi T) = \mu/(2\pi k\tau)$ and the auxiliary function $\mathcal{L}$ is a sum of so-called threshold functions which essentially represent 1PI diagrams describing the decoupling of massive modes and modes in a thermal and/or dense medium. At this point, we do not specify this function any further and refer to Sections 4.2 and 4.3 where the explicit expressions of this function is given in the specific cases. We only note that the auxiliary function $\mathcal{L}$ is normalized to one in the vacuum limit, i.e., $\mathcal{L}(0,0) = 1$. Thus, we recover the flow equation (4.15) in the limit $T \to 0$ and $\mu \to 0$. Here and in the following, we do not take into account the renormalization of the chemical potential and set $Z_\mu = 1$.

The modification of the flow equation by the auxiliary function $\mathcal{L}$ causes the non-*Gaußian pseudo* fixed point $\lambda^{(*)}_{(\sigma\text{-}\pi)}(\tau, \tilde{\mu}_\tau) := \lambda^*_{(\sigma\text{-}\pi)}/\mathcal{L}(\tau, \tilde{\mu}_\tau)$ to become scale-dependent. The effect of the temperature is to push the pseudo fixed point to higher values and in this way tends to restore the symmetry of the system. For a more detailed analysis, especially in regard to the effect of the quark chemical potential, we refer again to the subsequent sections, particularly Section 4.2.3.

The flow equation (4.19) can be solved analytically, we find

$$\lambda_{(\sigma\text{-}\pi)}(T, \mu, k) = \lambda^{(\mathrm{UV})}_{(\sigma\text{-}\pi)} \frac{1 - \Delta\lambda_{(\sigma\text{-}\pi)}}{\left(1 - \Delta\lambda_{(\sigma\text{-}\pi)} + 2\mathcal{I}(T, \mu, k)\right)\left(\frac{\Lambda}{k}\right)^{\Theta}}\,, \tag{4.20}$$

where

$$\mathcal{I}(T, \mu, k) = \frac{1}{\Lambda^2} \int_\Lambda^k \mathrm{d}k' k' \mathcal{L}(\tau', \tilde{\mu}_{\tau'})\,, \tag{4.21}$$

and we have again defined $\Delta\lambda_{(\sigma\text{-}\pi)}$ in terms of the non-*Gaußian* fixed point $\lambda^*_{(\sigma\text{-}\pi)}$ of the scalar-pseudoscalar coupling in the vacuum limit, see Eq. (4.11). Note that Eq. (4.21) reduces to $\mathcal{I}(0, 0, k) = ((k/\Lambda)^\Theta - 1)/2$ at zero temperature and chemical potential and we recover the solution (4.16). The solution can then be employed to compute the critical temperature $T_{\mathrm{cr}} = T_{\mathrm{cr}}(\mu)$ as a function of the quark chemical potential μ. The latter is defined as the temperature at which the scalar-pseudoscalar four-quark coupling diverges at $k \to 0$:

$$\lim_{k\to 0} \frac{1}{\lambda_{(\sigma\text{-}\pi)}(T_{\mathrm{cr}}, \mu, k)} = 0\,, \tag{4.22}$$

i.e., it is defined as the highest temperature for which the four-quark coupling still diverges. For our studies with more than one channel, this definition can be generalized straightforwardly. The critical temperature is then defined to be the highest temperature at which the four-quark couplings still diverge. Note that a divergence in one channel at a scale $k_{\mathrm{cr}}(T,\mu)$ entails corresponding divergences in all the other channels at the same scale. However, the associated four-quark couplings in general have a different strength relative to each other, see our discussions in Sections 4.2 and 4.3.

With this definition, we obtain the following implicit equation for the critical temperature T_{cr}:

$$0 = 1 - \Delta\lambda_{(\sigma\text{-}\pi)} + 2\,\mathcal{I}(T_{\mathrm{cr}},\mu,0)\,. \tag{4.23}$$

Using Eq. (4.18), we can rewrite this equation in terms of the critical scale k_0 at $T=\mu=0$, $k_0 = k_{\mathrm{cr}}(T=0,\mu=0)$:

$$k_0 = \Lambda\left(1 + 2\,\mathcal{I}(T_{\mathrm{cr}},\mu,0)\right)^{\frac{1}{\Theta}}\ . \tag{4.24}$$

Apparently, the critical temperature T_{cr} depends on our choice for the UV scale Λ as well for k_0 which sets the scale for the low-energy observables such as the constituent quark mass in the vacuum limit. Recall that the scale k_0 in turn is directly related to the initial condition $\lambda^{(\mathrm{UV})}_{(\sigma\text{-}\pi)}$ for the scalar-pseudoscalar four-quark coupling relative to its fixed-point value. From our discussion of the one-channel approximation in the vacuum limit it follows immediately that a finite critical temperature is only found if $\lambda^{(\mathrm{UV})}_{(\sigma\text{-}\pi)} > \lambda^{*}_{(\sigma\text{-}\pi)}$, i.e., $\Delta\lambda_{(\sigma\text{-}\pi)} > 0$.

Let us close this discussion by noting that at first glance it seems that Eq. (4.18) defining k_0, and thereby the critical temperature, implies that the low-energy dynamics is independent of the combinatoric prefactor of the term quadratic in the four-quark coupling in Eq. (4.15). However, this turns out to be too naive. A study of the partially bosonized formulation of our model reveals that quantum corrections to the *Yukawa* coupling yield $1/N_{\mathrm{c}}$-corrections to the critical scale [333, 397]. It should then also be noted that order-parameter fluctuations, which are nothing but $1/N_{\mathrm{c}}$-corrections, tend to restore the chiral symmetry in the infrared limit, thereby lowering the value of the critical temperature compared to its value in the large-N_{c} approximation (see, e.g., Ref. [370]).

Having introduced these basic underlying mechanisms and relations, let us now proceed to our discussion of *Fierz*-complete NJL models where we start with the NJL model with a single fermion species in the next section.

4.2 THE NJL MODEL WITH A SINGLE FERMION SPECIES

We begin with a study of a *Fierz*-complete NJL model with only a single fermion species, i.e., one flavor and one color degree of freedom, $N_{\mathrm{c}} = N_{\mathrm{f}} = 1$. The reduction in the number of fermion species as compared to, e.g., QCD with two flavors and three colors defines a more accessible model and simplifies the analysis while nonetheless sharing important aspects with the low-energy dynamics in QCD. The structures of the corresponding symmetry groups are simplified and the reduced degrees of freedom entail a smaller total number of four-quark interactions that need to be considered. In our *Fierz*-complete basis of four-fermion interactions we explicitly take into account the reduced symmetry owing to the explicit breaking of *Poincaré* invariance at finite temperature and chemical potential. We find that the inclusion of more unconventional interaction channels does affect the phase boundary not only at large but also at small quark chemical potential. The latter is reflected in the curvature of the finite-temperature phase boundary. Moreover, we present a reformulation of the four-fermion interactions in terms of difermion-type degrees of freedom. This can be considered as groundwork for the introduction of diquarks in Section 4.3, which are expected to become important in QCD at larger chemical potentials, but also serves to study the effect of different parametrizations of the *Fierz*-complete basis.

In Section 4.2.1, we start with a discussion of symmetry aspects relevant for our analysis and of the details of our employed model. The RG fixed-point structure of the model at zero temperature and density at leading order of the derivative expansion of the effective action is then discussed in Section 4.2.2. In Section 4.2.3, we finally discuss the phase structure of our model at finite temperature and chemical potential and analyze how it is affected when *Fierz*-incomplete approximations are considered. In particular, we analyze the curvature of the phase boundary at small chemical potential, the critical value of the chemical potential above which no spontaneous symmetry breaking occurs, and the possible interpretation of the underlying dynamics in terms of effective difermion-type degrees of freedom. After the discussion of some technical aspects related to the *Silver-Blaze* property of our approach and to the employed regularization scheme contrasted with more conventionally applied three-dimensional regularization schemes in Section 4.2.4, we close this section on the NJL model with a single fermion species with a brief conclusion in Section 4.2.5.

4.2.1 Definition of the model

To begin with, we discuss the symmetries of the classical action S with a scalar-pseudoscalar four-fermion interaction term conventionally employed in studies of the chiral low-energy dynamics of QCD. In the case of a single fermion species, i.e., $N_{\mathrm{f}} = N_{\mathrm{c}} = 1$, the action is given by

$$S[\bar{\psi}, \psi] = \int_0^{\beta} \mathrm{d}\tau \int \mathrm{d}^3 x \left\{ \bar{\psi}(\mathrm{i}\partial\!\!\!/ - \mathrm{i}\mu\gamma_0)\psi + \frac{1}{2}\bar{\lambda}_{\sigma} \left[(\bar{\psi}\psi)^2 - (\bar{\psi}\gamma_5\psi)^2 \right] \right\}, \tag{4.25}$$

with the inverse temperature $\beta = 1/T$ and the chemical potential μ. This action is invariant under simple phase transformations,

$$U_{\mathrm{V}}(1): \bar{\psi} \mapsto \bar{\psi}\mathrm{e}^{-\mathrm{i}\alpha}, \;\; \psi \mapsto \mathrm{e}^{\mathrm{i}\alpha}\psi\,. \tag{4.26}$$

As we do not allow for an explicit fermion mass term, the action is also invariant under chiral $U_{\mathrm{A}}(1)$ transformations, i.e., axial phase transformations:

$$U_{\mathrm{A}}(1): \bar{\psi} \mapsto \bar{\psi}\mathrm{e}^{\mathrm{i}\gamma_5\alpha}, \;\; \psi \mapsto \mathrm{e}^{\mathrm{i}\gamma_5\alpha}\psi\,, \tag{4.27}$$

where α is the “rotation” angle in both cases. As discussed in Section 2.1.2, the chiral symmetry is broken spontaneously if a finite ground-state expectation value $\langle\bar{\psi}\psi\rangle$ is generated by quantum fluctuations. The $U_{\mathrm{V}}(1)$ symmetry is broken spontaneously if, e.g., a difermion condensate $\langle\psi^T\mathcal{C}\gamma_5\psi\rangle$ is formed, where $\mathcal{C} = \mathrm{i}\gamma_2\gamma_0$ is the charge conjugation operator, cf. Section 2.2.

Because of the presence of a heat bath and a chemical potential, *Poincaré* invariance is explicitly broken and the *Euclidean* time direction is distinguished. Note also that a finite chemical potential explicitly breaks the charge conjugation symmetry $\mathcal{C}$. However, the rotational invariance among the spatial components as well as the invariance with respect to parity transformations $\mathcal{P}$ and time reversal transformations $\mathcal{T}$ remain intact, see Section 2.1.2 for a brief description of the above mentioned discrete symmetries.

As discussed in Section 4.1, the computation of quantum corrections immediately induce four-fermion interaction channels other than the scalar-pseudoscalar interaction channel such as a vector-channel interaction $\sim (\bar{\psi}\gamma_\mu\psi)^2$, even though they do not appear in the classical action S in Eq. (4.25). Once other four-fermion channels are generated, it is reasonable to expect that these channels also alter dynamically the strength of the original scalar-pseudoscalar interaction. In particular at finite temperature and density, the number of possibly induced interaction channels is even increased because of the reduced symmetry of the theory. For our present study of the quantum effective action at leading order (LO) of the derivative expansion, we therefore consider the most general ansatz for the effective average action compatible with the symmetries of the theory:

$$\begin{aligned}\Gamma_{\mathrm{LO}}[\bar{\psi},\psi] = \int_0^\beta \mathrm{d}\tau \int \mathrm{d}^3x \,\Big\{ &\bar{\psi}(Z_\psi^{\parallel}\mathrm{i}\gamma_0\partial_0 + Z_\psi^{\perp}\mathrm{i}\gamma_i\partial_i - Z_\mu \mathrm{i}\mu\gamma_0)\psi \\ &+ \frac{1}{2}Z_\sigma\bar{\lambda}_\sigma(\mathrm{S}-\mathrm{P}) - \frac{1}{2}Z_{\mathrm{V}}^{\parallel}\bar{\lambda}_{\mathrm{V}}^{\parallel}\left(\mathrm{V}_{\parallel}\right) - \frac{1}{2}Z_{\mathrm{V}}^{\perp}\bar{\lambda}_{\mathrm{V}}^{\perp}\left(\mathrm{V}_{\perp}\right) \\ &- \frac{1}{2}Z_{\mathrm{A}}^{\parallel}\bar{\lambda}_{\mathrm{A}}^{\parallel}\left(\mathrm{A}_{\parallel}\right) - \frac{1}{2}Z_{\mathrm{A}}^{\perp}\bar{\lambda}_{\mathrm{A}}^{\perp}\left(\mathrm{A}_{\perp}\right) - \frac{1}{2}Z_{\mathrm{T}}^{\parallel}\bar{\lambda}_{\mathrm{T}}^{\parallel}\left(\mathrm{T}_{\parallel}\right)\Big\}\,, \end{aligned} \tag{4.28}$$

where $\bar{\lambda}_\sigma$, $\bar{\lambda}_{\mathrm{V}}^{\parallel}$, $\bar{\lambda}_{\mathrm{V}}^{\perp}$, $\bar{\lambda}_{\mathrm{A}}^{\parallel}$, $\bar{\lambda}_{\mathrm{A}}^{\perp}$, and $\bar{\lambda}_{\mathrm{T}}^{\parallel}$ denote the bare four-fermion couplings which are accompanied by their vertex renormalizations Z_σ, $Z_{\mathrm{V}}^{\parallel}$, $Z_{\mathrm{V}}^{\perp}$, $Z_{\mathrm{A}}^{\parallel}$, $Z_{\mathrm{A}}^{\perp}$, and $Z_{\mathrm{T}}^{\parallel}$, respectively. The various four-fermion interaction channels are defined as follows:

$$(\mathrm{S}-\mathrm{P}) \equiv (\bar{\psi}\psi)^2 - (\bar{\psi}\gamma_5\psi)^2\,, \tag{4.29}$$

$$\left(\mathrm{V}_{\parallel}\right) \equiv (\bar{\psi}\gamma_0\psi)^2\,, \qquad (\mathrm{V}_{\perp}) \equiv (\bar{\psi}\gamma_i\psi)^2\,, \tag{4.30}$$

$$\left(\mathrm{A}_{\parallel}\right) \equiv (\bar{\psi}\gamma_0\gamma_5\psi)^2\,, \qquad (\mathrm{A}_{\perp}) \equiv (\bar{\psi}\gamma_i\gamma_5\psi)^2\,, \tag{4.31}$$

$$\left(\mathrm{T}_{\parallel}\right) \equiv (\bar{\psi}\sigma_{0i}\psi)^2 - (\bar{\psi}\sigma_{0i}\gamma_5\psi)^2\,, \tag{4.32}$$

where $\sigma_{\mu\nu} = \frac{\mathrm{i}}{2}[\gamma_\mu, \gamma_\nu]$ and summations over $i = 1, 2, 3$ are tacitly assumed. On account of the *Silver-Blaze* property, the renormalization factors associated with the kinetic term are related to each other at zero temperature according to $Z_\mu^{-1} = Z_\psi^{\parallel} = Z_\psi^{\perp}$ as long as the renormalized quark chemical potential is smaller than a potentially generated renormalized (pole) mass of the fermions, see our discussion in Section 4.1.2.

The ansatz (4.28) is overdetermined. By exploiting the *Fierz* identities detailed in Appendix B.3.1, we can reduce the overdetermined set of four-fermion interactions in Eq. (4.28) to a minimal *Fierz*-complete set:

$$\Gamma_{\mathrm{LO}}[\bar{\psi}, \psi] = \int_0^\beta \mathrm{d}\tau \int \mathrm{d}^3x \, \Big\{ \bar{\psi}(Z_\psi^{\parallel}\mathrm{i}\gamma_0\partial_0 + Z_\psi^{\perp}\mathrm{i}\gamma_i\partial_i - Z_\mu \mathrm{i}\mu\gamma_0)\psi \\ + \frac{1}{2}Z_\sigma\bar{\lambda}_\sigma(\mathrm{S}-\mathrm{P}) - \frac{1}{2}Z_{\mathrm{V}}^{\parallel}\bar{\lambda}_{\mathrm{V}}^{\parallel}\left(\mathrm{V}_{\parallel}\right) - \frac{1}{2}Z_{\mathrm{V}}^{\perp}\bar{\lambda}_{\mathrm{V}}^{\perp}(\mathrm{V}_{\perp}) \Big\}\,. \tag{4.33}$$

Any other pointlike four-fermion interaction invariant under the symmetries of our model is indeed reducible by means of *Fierz* transformations. Recall that fermion self-interactions of higher order (e.g. eight fermion interactions) may also be induced due to quantum fluctuations at leading order of the derivative expansion[9] but do not contribute to the RG flow of the four-fermion couplings at this order and are therefore not included in our ansatz (4.33), see Ref. [333] for a detailed discussion.

In the following, we shall study the RG flow of the four-fermion couplings appearing in the effective action (4.33). The flow equations derived from the *Wetterich* equation for the dimensionless renormalized four-fermion couplings defined as $\lambda_i = Z_i k^2 \bar{\lambda}_i/(Z_\psi^{\perp})^2$ with $\bar{\lambda} = \{\bar{\lambda}_\sigma, \bar{\lambda}_{\mathrm{V}}^{\parallel}, \bar{\lambda}_{\mathrm{V}}^{\perp}\}$ and $Z = \{Z_\sigma, Z_{\mathrm{V}}^{\parallel}, Z_{\mathrm{V}}^{\perp}\}$, are listed in Appendix F.1. Note again that the wavefunction renormalizations remain unchanged in the RG flow at this order of the derivative expansion, i.e., $\partial_t Z_\psi^{\parallel} = \partial_t Z_\psi^{\perp} = 0$, and we set them to $Z_\psi^{\parallel} = Z_\psi^{\perp} = 1$ at the initial RG scale.

We find that the RG flow is essentially governed by two classes of 1PI diagrams, see Fig. 4.1, which are distinguished by the sign structure of how the fermionic propagators depend on the quark chemical potential. The different characteristics especially in regard to the qualitative behavior as a function of the quark chemical potential are elucidated in Section 4.2.3. Moreover, each of the two classes contains diagrams which are associated with contributions longitudinal and transversal to the heat bath. These diagrams can be recast into threshold functions which are defined in Appendix E. For the regularization of the loop integrals we employ the four-dimensional *Fermi*-surface-adapted scheme in form of an exponential regulator shape function introduced in Section 3.2. Recall that this scheme becomes manifest covariant in the vacuum limit which is of great importance. In contrast to that, as discussed in Section 3.2, spatial regularization schemes introduce an explicit breaking

---

[9] Note again that the leading order of the derivative expansion corresponds to treating the fermion self-interactions in the pointlike limit, see also our discussion below.

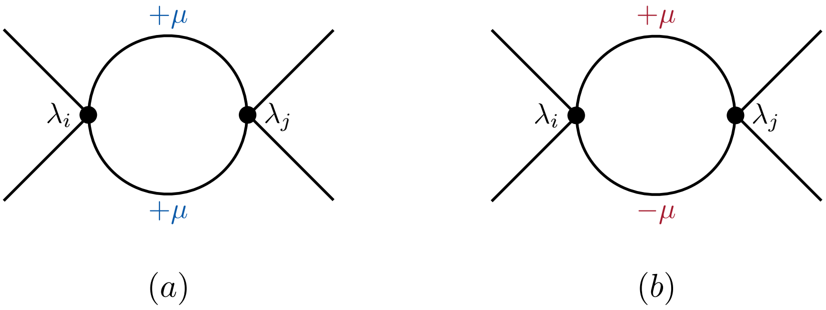

FIGURE 4.1: The two classes of 1PI diagrams contributing to the RG flow of the four-quark couplings.

of the *Poincaré* invariance even in limit of vanishing temperature and chemical potential. In the concrete case of the present NJL model, we have observed that the predictions for the phase structure are significantly spoilt when a spatial regularization scheme is used without properly taking care of the associated symmetry-violating terms in the limit $T \to 0$ and $\mu \to 0$, see Section 4.2.4 for details. Therefore, we have chosen a scheme which respects *Poincaré* invariance in this limit.

Scale fixing

Before we go on to extract information on the phase structure from the RG flow of the four-fermion couplings, we discuss in the following the scale fixing procedure of our model. The free parameters that are to be fixed are in principle the values of all the four-fermion couplings at the initial UV scale Λ. In the following, however, we shall use $\lambda_{\mathrm{V}}^{\parallel} = \lambda_{\mathrm{V}}^{\perp} = 0$ as initial conditions for the couplings associated with the vector channel interaction, independent of our choice for the temperature and the chemical potential. Thus, these couplings are solely induced by quantum fluctuations and do not represent free parameters in our study. In other words, the initial value of the scalar-pseudoscalar interaction channel is the only free parameter in our analysis below. Note that this general setup for the initial conditions of the four-fermion couplings mimics the situation in many QCD low-energy model studies. However, since we do not have access to low-energy observables at this order of the derivative expansion, we shall fix the initial condition of the scalar-pseudoscalar coupling such that a given value of the critical temperature at vanishing chemical potential is reproduced. This determines the scale in our studies of the phase structure below.[10]

To illustrate the scale-fixing procedure, we consider the approximation with only a scalar-pseudoscalar interaction channel again. We derive the RG flow equation for the scalar-pseudoscalar coupling λ_σ from the full set of flow equations by setting $\lambda_{\mathrm{V}}^{\parallel} = \lambda_{\mathrm{V}}^{\perp} = 0$ and also dropping the flow equations associated with these two couplings, see Appendix F.1 for details.

---

[10] Fixing the critical temperature T_{cr} to some value at $\mu = 0$ is equivalent to fixing the zero-temperature fermion mass in the IR limit since $T_{\mathrm{cr}}(\mu = 0)$ is directly related to the zero-temperature fermion mass at $\mu = 0$, at least in a one-channel approximation.

Moreover, we do not take into account the renormalization of the chemical potential and set $Z_\mu = 1$. The RG flow equation for λ_σ then reads

$$\beta_{\lambda_\sigma} = 2\lambda_\sigma - 8v_4\,\lambda_\sigma^2\,\mathcal{L}(\tau,\tilde{\mu}_\tau)\,, \tag{4.34}$$

where $v_4 = 1/(32\pi^2)$ and

$$\begin{aligned}\mathcal{L}(\tau,\tilde{\mu}_\tau) = 6\left(l_{\perp+}^{(\mathrm{F}),(4)}(\tau,0,-\mathrm{i}\tilde{\mu}_\tau) + l_{\|+}^{(\mathrm{F}),(4)}(\tau,0,-\mathrm{i}\tilde{\mu}_\tau)\right)\\ -2\left(l_{\perp\pm}^{(\mathrm{F}),(4)}(\tau,0,-\mathrm{i}\tilde{\mu}_\tau) + l_{\|\pm}^{(\mathrm{F}),(4)}(\tau,0,-\mathrm{i}\tilde{\mu}_\tau)\right)\,,\end{aligned} \tag{4.35}$$

cf. Eqs. (4.19) and (4.15) with $\lambda_\sigma^* = 8\pi^2$, where Eq. (4.15) is obtained in the limit of zero temperature and chemical potential with $\mathcal{L}(0,0) = 1$.[11] Here, we have again the dimensionless temperature $\tau = T/k$ and $\tilde{\mu}_\tau = \mu/(2\pi T) = \mu/(2\pi k\tau)$. The definitions of the threshold functions $l_{\|/\perp+/\pm}^{(\mathrm{F}),(4)}$ can be found in Appendix E.

As discussed in Section 4.1.3, we can derive an implicit equation for the critical temperature T_{cr} from a formal solution to the RG flow equation, see Eq. (4.23). The critical temperature depends on the initial condition $\lambda_\sigma^{(\mathrm{UV})}$ of the scalar-pseudoscalar coupling relative to its fixed-point value through $\Delta\lambda_\sigma$. To make a phenomenological connection to QCD, we shall choose a value for the critical temperature at $\mu = 0$ in units of the UV cutoff Λ which is close to the chiral critical temperature at $\mu = 0$ found in conventional QCD low-energy model studies [115, 119–121]. To be more specific, we shall fix the scale at zero chemical potential by tuning the initial condition of the scalar-pseudoscalar coupling such that $T_0/\Lambda \equiv T_{\mathrm{cr}}(\mu = 0)/\Lambda = 0.15$ and set $\Lambda = 1\,\mathrm{GeV}$ in the numerical evaluation:

$$0 = 1 - \Delta\lambda_\sigma + 2\,\mathcal{I}(T_0{=}0.15\Lambda,0,0)\,. \tag{4.36}$$

This initial condition for the four-fermion coupling is then kept fixed to the same value for all temperatures and chemical potentials and we shall measure all physical observables in units of T_0.

To ensure comparability of our studies with different numbers of interaction channels, we employ the same scale-fixing procedure in all cases. As illustrated for the one-channel approximation, we only choose a finite value for the initial condition of the scalar-pseudoscalar coupling and fix it at zero chemical potential such that the critical temperature is given by $T_0/\Lambda \equiv T_{\mathrm{cr}}(\mu = 0)/\Lambda = 0.15$ in this limit. The other channels are only generated dynamically. The critical temperature for a given chemical potential is still defined to be the temperature at which the four-fermion couplings diverge at $k \to 0$. Note that the structure of the underlying set of flow equations is such that a divergence in one channel implies a divergence in all interaction channels. However, the various couplings may have a different strength relative to each other, see also Fig. 4.2 and our discussion in the next section.

---

[11] In this section, the scalar-pseudoscalar coupling λ_σ of the model with one fermion species corresponds to the scalar-pseudoscalar coupling $\lambda_{(\sigma\text{-}\pi)}$ of the model with $N_{\mathrm{f}} = 2$ and $N_{\mathrm{c}} = 3$.

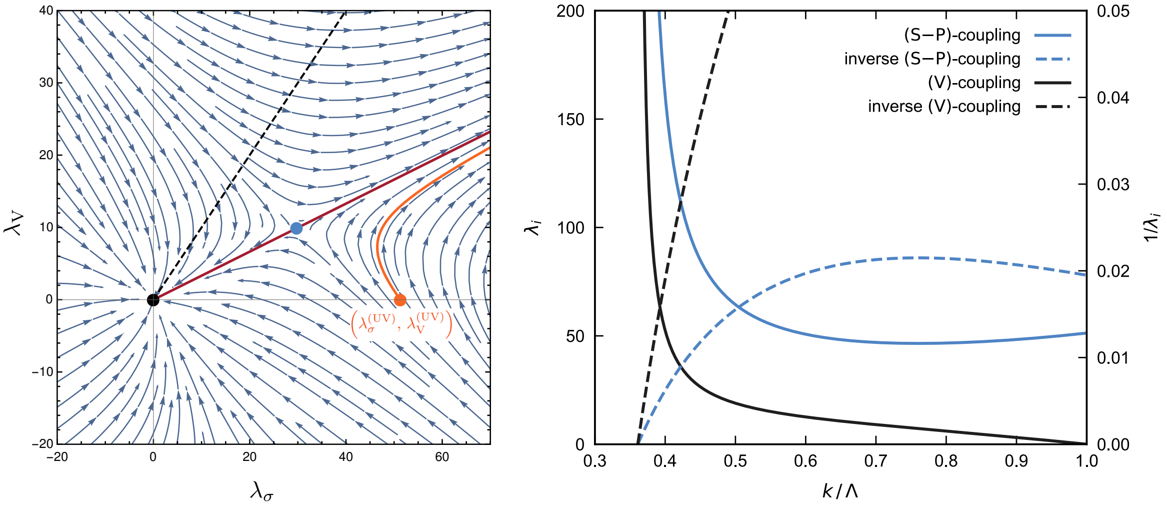

FIGURE 4.2: Left panel: RG flow at zero temperature and chemical potential in the plane spanned by the scalar-pseudoscalar coupling λ_σ and the vector-channel coupling λ_{V}. The black dot depicts the *Gaußian* fixed point whereas the blue dot depicts one of the two non-*Gaußian* fixed points. The orange line represents an example of an RG trajectory. This particular trajectory describing four-fermion couplings diverging at a finite scale k_{cr} approaches a separatrix (red line) for $k \to k_{\mathrm{cr}}$. The dominance of the scalar-pseudoscalar interaction channel is illustrated by the position of this separatrix relative to the bisectrix (dashed back line). Right panel: RG scale dependence of the four-fermion couplings λ_σ and λ_{V} corresponding to the RG trajectory depicted by the orange line in the left panel. The inverse of these two four-fermion couplings associated with the mass-like parameters $m_i^2 \sim 1/\lambda_i$ of terms bilinear in the auxiliary fields in a *Ginzburg-Landau*-type effective potential is shown by the dashed lines.

4.2.2 Vacuum fixed-point structure and spontaneous symmetry breaking

With these prerequisites, let us now turn to the discussion of the RG flow of our *Fierz*-complete model, beginning with an analysis of the fixed-point structure in the limit $T \to 0$ and $\mu \to 0$. In this *Poincaré*-invariant limit, the couplings $\lambda_{\mathrm{V}}^{\parallel}$ and $\lambda_{\mathrm{V}}^{\perp}$ can be identified, $\lambda_{\mathrm{V}}^{\parallel} = \lambda_{\mathrm{V}}^{\perp} = \lambda_{\mathrm{V}}$, provided the two couplings assume the same value at the initial RG scale $k = \Lambda$. The β functions then simplify to[12]

$$\partial_t \lambda_\sigma = \beta_{\lambda_\sigma} = 2\lambda_\sigma - 8v_4 \left(\lambda_\sigma^2 + 4\lambda_\sigma\lambda_{\mathrm{V}} + 3\lambda_{\mathrm{V}}^2\right) , \tag{4.37}$$

$$\partial_t \lambda_{\mathrm{V}} = \beta_{\lambda_{\mathrm{V}}} = 2\lambda_{\mathrm{V}} - 4v_4 \left(\lambda_\sigma + \lambda_{\mathrm{V}}\right)^2 . \tag{4.38}$$

Up to regularization-scheme dependent factors, this set of equations agrees with the one found in previous vacuum studies of this model [333, 336]. The RG flow equations (4.37) and (4.38) have three different fixed points $(\lambda_\sigma^*, \lambda_{\mathrm{V}}^*)$.[13] The *Gaußian* fixed point at $(0,0)$ is IR attractive whereas the two non-*Gaußian* fixed points at $(3\pi^2, \pi^2)$ and at $(-32\pi^2, 16\pi^2)$ have both one IR attractive and one IR repulsive direction, see also Fig. 4.2.

For an analysis of the fixed-point structure of our model, the exact value of the initial condition of the scalar-pseudoscalar coupling is not required. Aiming at qualitative aspects

---

[12] Note that, for a spatial regularization scheme, we find $\lambda_{\mathrm{V}}^{\parallel} \neq \lambda_{\mathrm{V}}^{\perp}$ even for $T = \mu = 0$ since such a scheme explicitly breaks *Poincaré* invariance.

[13] This can be seen by shifting $\lambda_\sigma \to \lambda_\sigma - \lambda_{\mathrm{V}}$ in Eq. (4.38), see Ref. [333].

and taking advantage of the clarity of the present two-coupling system, we shall in fact temporarily relax the scale fixing conditions introduced in Section 4.2.1 and allow for a finite vector-channel coupling at the initial UV scale Λ as well. Such a consideration sheds some light on the underlying dynamics and reveals interesting relations. Similarly to our discussion of the one-channel approximation, the qualitative features of the ground state of our model are already determined by the choice for the initial values of the various couplings relative to the fixed points. Provided that the initial value of the scalar-pseudoscalar coupling is chosen suitably, i.e., it is chosen greater than a critical value $\lambda_\sigma^{(\mathrm{cr})}$ depending on the initial value of the vector-channel coupling,[14] we observe that the four-fermion couplings start to increase rapidly and even diverge at a finite scale k_{cr}, indicating the onset of spontaneous symmetry breaking.

In the left panel of Fig. 4.2, an example for an RG trajectory (orange line) at zero temperature and chemical potential is shown in the space spanned by the remaining two couplings λ_σ and λ_{V}. In this case, the initial condition has been chosen such that the four-fermion couplings diverge at a finite scale k_{cr}. For $k \to k_{\mathrm{cr}}$, the trajectory approaches a separatrix (red line in Fig. 4.2) defining an invariant subspace [401] and indicates a dominance of the scalar-pseudoscalar channel, i.e., $\lambda_\sigma/\lambda_{\mathrm{V}} \approx 3$, see also right panel of Fig. 4.2 where the RG scale dependence of the two couplings corresponding to this RG trajectory is shown. This observation appears to be in accordance with the naive expectation that the ground state of our model is governed by spontaneous chiral symmetry breaking as associated with a dominance of the scalar-pseudoscalar interaction channel.

The dominance of the scalar-pseudoscalar channel is also observed when finite initial values of the vector-channel coupling λ_{V} are chosen, provided that we use a sufficiently large initial value of the scalar-pseudoscalar coupling, see left panel of Fig. 4.2. However, we would like to emphasize again that this dominance should only be considered as an indicator that the ground state in the vacuum limit is governed by chiral symmetry breaking. In particular, our analysis cannot rule out, e.g., a possible formation of a vector condensate. For the moment, we shall also leave aside the issue that the *Fierz*-complete set of four-fermion interaction channels underlying this analysis can be transformed into an equivalent *Fierz*-complete set of channels with different transformation properties regarding the fundamental symmetries of our model. This further complicates the phenomenological interpretation, see our discussion of the finite-temperature phase diagram in Section 4.2.3.

Let us close our discussion of the dynamics of our model in the vacuum limit by commenting on the scaling behavior of the critical scale k_{cr}. In the one-channel approximation, we have found that the scaling of k_{cr} is of the power-law type with respect to the distance of the initial value $\lambda_\sigma^{(\mathrm{UV})}$ from the fixed-point value λ_σ^*, see Eq. (4.18). In our *Fierz*-complete setup, this is not necessarily the case. In fact, even if we set the initial value $\lambda_\sigma^{(\mathrm{UV})}$ of the scalar-pseudoscalar coupling to zero, the system can still be driven to criticality. This can be achieved by a sufficiently large value of the initial condition of the vector-channel coupling, see left panel

---

[14] This holds true in case of all three couplings λ_σ, $\lambda_{\mathrm{V}}^{\parallel}$ and $\lambda_{\mathrm{V}}^{\perp}$ as well. Note that the function $\lambda_\sigma^{(\mathrm{cr})} = \lambda_\sigma^{(\mathrm{cr})}(\lambda_{\mathrm{V}}^{\parallel}, \lambda_{\mathrm{V}}^{\perp})$ then defines a two-dimensional manifold, a separatrix in the space spanned by the couplings, while it defines a one-dimensional manifold in case of the two couplings λ_σ and λ_{V}. In our one-channel approximation, loosely speaking, this separatrix is a point which can be identified with the non-*Gaußian* fixed point of the associated coupling.

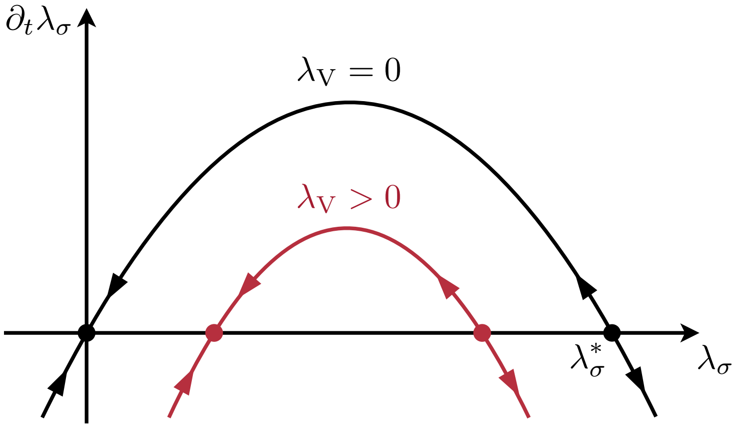

FIGURE 4.3: Sketch of the β_{λ_σ} function of the scalar-pseudoscalar four-fermion coupling for $\lambda_V = 0$ (black line) and $\lambda_V > 0$ (red line). The arrows indicate the direction of the RG flow toward the infrared.

of Fig. 4.2. To be more specific, a variation of the vector-channel coupling λ_V in the flow equation (4.37) of the scalar-pseudoscalar coupling allows to shift the fixed points of the latter. In particular, a finite value of λ_V turns the *Gaußian* fixed point into an interacting fixed point, see Fig. 4.3. We also deduce from Eq. (4.37) and Fig. 4.3 that a critical value $\lambda_V^{(cr)}$ for the vector-channel coupling exists at which the two fixed points of the λ_σ coupling merge. For $\lambda_V > \lambda_V^{(cr)} > 0$, the fixed points of the λ_σ coupling then annihilate each other and the RG flow is no longer governed by any (finite) real-valued fixed point, resulting in a diverging λ_σ coupling. Assuming that the running of the vector-channel coupling is sufficiently slow, it has been shown [333] that the dependence of k_{cr} on the initial value of the vector coupling obeys a *Berezinskii-Kosterlitz-Thouless* (BKT) scaling law [402–404],

$$k_{\rm cr} \sim \Lambda\theta(\lambda_V^{(UV)} - \lambda_V^{(cr)}) \exp\left(-\frac{c_{\rm BKT}}{\sqrt{\lambda_V^{(UV)} - \lambda_V^{(cr)}}}\right), \tag{4.39}$$

rather than a power law. Here, $c_{\rm BKT}$ is a positive constant. This so-called essential scaling plays a crucial role in gauge theories with many flavors where it is known as *Miransky* scaling and the role of our vector coupling is played by the gauge coupling [405–407]. Corrections to this type of scaling behavior arising because of the finite running of the gauge coupling have found to be of the power-law type [408] which would translate into corresponding corrections associated with the running of the vector coupling in our present study. We emphasize that the dynamics of our present model close to the critical scale is still dominated by the scalar-pseudoscalar interaction channel in this case, even though the latter has been set to zero initially, as can be seen in the flow diagram in the left panel of Fig. 4.2.

A detailed study of the scaling behavior and the associated universality class associated with the quantum phase transitions potentially occurring in our model in the vacuum limit is beyond the scope of the present work. From now on, we shall rather set the vector coupling to zero at the initial scale and let it only be generated dynamically, i.e., we only tune the scalar-

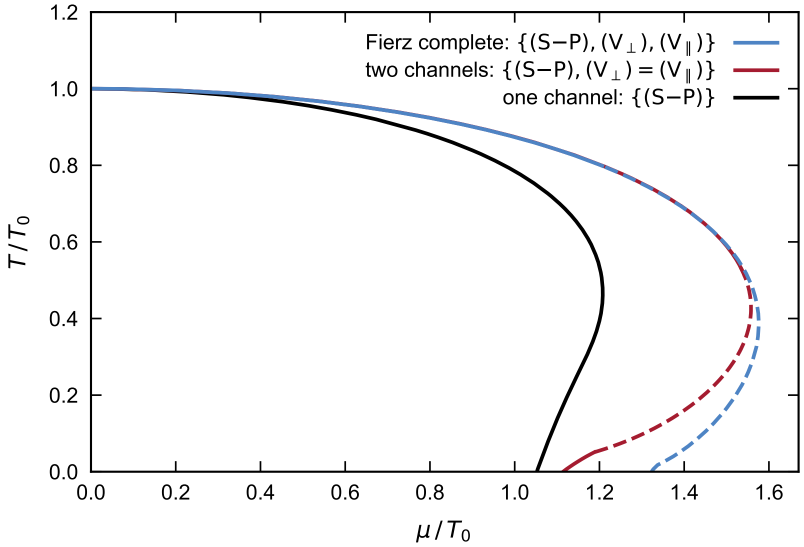

FIGURE 4.4: Phase boundary associated with the spontaneous breakdown of at least one of the fundamental symmetries of our model as obtained from a one-channel, two-channel, and *Fierz*-complete study of the ansatz (4.33), see main text for details.

pseudoscalar coupling to fix the scale in our calculations as initially discussed in Section 4.2.1. Still, it is worth mentioning that the mechanism, namely the annihilation of fixed points, resulting in the exponential scaling behavior of k_{cr} is quite generic. In fact, it also underlies the exponential behavior associated with the scaling of, e.g., a gap as a function of the chemical potential in case of the formation of a BCS superfluid in relativistic fermion models. We shall discuss the potential occurrence of this type of scaling in more detail in the subsequent section.

4.2.3 Phase structure

In the following, we consider the one-channel approximation discussed above, a two-channel approximation, and the *Fierz*-complete system. The RG flow equations for the *Fierz*-complete set of couplings can be found in Appendix F.1. Our two-channel approximation is obtained from this *Fierz*-complete system by setting $\lambda_{\mathrm{V}}^{\parallel} = \lambda_{\mathrm{V}}^{\perp}$ and dropping the flow equation of the $\lambda_{\mathrm{V}}^{\parallel}$-coupling. Note that this two-channel approximation is still *Fierz*-complete at zero temperature and chemical potential.

In Fig. 4.4, we show our results for the (T, μ) phase boundary associated with the spontaneous breakdown of at least one of the fundamental symmetries of our model. We observe right away that the curvature κ of the finite-temperature phase boundary,

$$\kappa = -T_0 \frac{\mathrm{d}T_{\mathrm{cr}}(\mu)}{\mathrm{d}\mu^2}\bigg|_{\mu=0}\,, \tag{4.40}$$

channels	curvature κ
(S − P)	0.157
(S − P), $(V_\perp) = (V_\parallel)$	0.108
Fierz-complete	0.109

Table 4.1: Curvature κ of the finite-temperature phase boundary at $\mu = 0$ as obtained from a study of a one-channel approximation, a two-channel approximation, and the *Fierz*-complete set of four-fermion channels. Note that the quoted two-channel approximation is *Fierz*-complete at $T = \mu = 0$.

is significantly smaller in the *Fierz*-complete study than in the one-channel approximation.[15] To be specific, the curvature κ in the one-channel approximation is found to be about 44% greater than in the *Fierz*-complete study. Interestingly, the curvature from our two-channel approximation, which is still *Fierz*-complete at $T = \mu = 0$, agrees almost identically with the curvature from the *Fierz*-complete study, see also Table 4.1.

From a comparison of the results from the one- and two-channel approximation as well as the *Fierz*-complete study, we also deduce that the phase boundary is pushed to larger values of the chemical potential when the number of interaction channels is increased. In particular, we observe that the critical value μ_{cr} above which the four-fermion couplings remain finite is pushed to larger values. In fact, μ_{cr} as obtained from the *Fierz*-complete calculation is found to be 16% greater than in the two-channel approximation and 20% greater than in the one-channel approximation. Note that μ_{cr} is an estimate for the value of the chemical potential above which no spontaneous symmetry breaking of any kind occurs.

In addition to these quantitative changes of the phase structure, we observe that the dynamics along the phase boundary changes on a qualitative level. In the one-channel approximation, the dynamics is completely dominated by the scalar-pseudoscalar channel by construction. In the two-channel approximation, we then observe a competition between the scalar-pseudoscalar channel and the vector channel. Indeed, we find that the vector channel dominates close to the phase boundary for temperatures $0.1 \lesssim T/T_0 \lesssim 0.5$, as indicated by the red dashed line in Fig. 4.4. In case of the *Fierz*-complete study, we even observe that the scalar-pseudoscalar channel is only dominant close to the phase boundary for $T/T_0 \gtrsim 0.8$. For $T/T_0 \lesssim 0.8$, we find a dominance of the $(V_\parallel)$-channel, apart from a small regime $0.02 \lesssim T/T_0 \lesssim 0.09$ in which the $(V_\perp)$-channel dominates, see also Fig. 4.5 for an illustration of how the dominance pattern of the channels along the phase boundary changes. The dominance of the $(V_\parallel)$-channel may not come unexpected as it is related to the density, $n \sim \langle \bar{\psi} \mathrm{i} \gamma_0 \psi \rangle$, which is controlled by the chemical potential.

We emphasize again that the dominance of a particular interaction channel only states that the modulus of the associated coupling is greater than the ones of the other four-fermion couplings. It does not necessarily imply that a condensate associated with the most dominant interaction channel is formed. It may therefore only be viewed as an indication for the formation of such a condensate. Moreover, it may very well be that condensates of different types coexist.

---

[15] In order to estimate the curvature, we have fitted our numerical results for $T_{\text{cr}}(\mu)/T_0$ for $0 \leq \mu/T_0 \leq 2/3$ to the ansatz $T_{\text{cr}}(\mu)/T_0 = 1 - \kappa \left(\frac{\mu}{T_0}\right)^2 + \kappa' \left(\frac{\mu}{T_0}\right)^4 + \mathcal{O}(\mu^6)$.

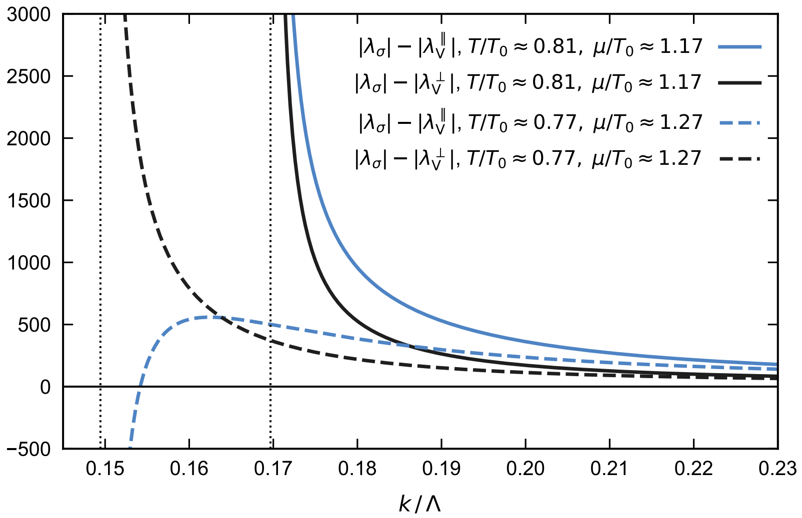

FIGURE 4.5: RG scale dependence of $|\lambda_\sigma| - |\lambda_V^{\parallel}|$ and $|\lambda_\sigma| - |\lambda_V^{\perp}|$ for two sets of values (T, μ) corresponding to two points on the phase boundary associated with the *Fierz*-complete study shown in Fig. 4.4. The two points are located closely to the point where the dominance pattern of the four-fermion channels changes. From the depicted RG scale dependence of the couplings, we indeed deduce that, at the latter point, the $(V_{\parallel})$-channel starts to dominate over the (S − P)-channel while the $(V_{\perp})$-channel remains to be subdominant. The thin dotted vertical lines indicate the position of the critical scale k_{cr} for the chosen values for the temperature and chemical potential.

For example, note that the dominance of the scalar-pseudoscalar channel close to the phase boundary may be associated with the formation of a finite chiral condensate, $\varphi \sim \langle\bar{\psi}\psi\rangle$, which signals the spontaneous breakdown of the chiral $U_{\text{A}}(1)$ symmetry of our model. On the other hand, loosely speaking, a dominance of the $(V_{\parallel})$-channel may be viewed as an indicator for a "spontaneous breakdown" of *Lorentz* invariance in addition to the inevitable explicit breaking of this invariance introduced by the chemical potential and the temperature. A vector-type condensate $\langle\bar{\psi}\gamma_i\psi\rangle$ associated with a dominance of the $(V_{\perp})$-channel would furthermore indicate a breakdown of the invariance among the spatial coordinates. Note that the condensates $\langle\bar{\psi}\mathrm{i}\gamma_0\psi\rangle$ and $\langle\bar{\psi}\gamma_i\psi\rangle$ break neither the $U_{\text{V}}(1)$ symmetry nor the chiral $U_{\text{A}}(1)$ symmetry of our model.

The explicit symmetry breaking caused by a finite chemical potential also becomes apparent if we introduce an effective density field n by means of a *Hubbard-Stratonovich* transformation. The resulting effective action then depends on the density n in form of an explicit field.[16] In such a functional, the chemical potential μ appears as a term linear in the density field. The ground state can then be found by solving the quantum equation of motion in the presence of a finite source being nothing but the chemical potential, $(\delta\Gamma/\delta n)|_\mu = 0$. A divergence of the four-fermion coupling associated with the $(V_{\parallel})$-channel is then related to the coefficient of the n^2-term becoming zero or even negative. If the appearance of the divergence in the $(V_{\parallel})$-channel is indeed related to a "spontaneous breakdown" of *Lorentz* invariance, then corresponding pseudo-*Goldstone* bosons reminiscent in some aspects of a (massive) photon field in temporal gauge may appear in the spectrum in this regime of the

---

[16] Strictly speaking, the field n is proportional to the density and shares the quantum numbers of the associated field operator.

phase diagram.[17] Symmetry breaking scenarios of this kind have indeed been discussed in the literature [409–413]. However, their analysis is beyond the scope of the present work. In any case, such a phenomenological interpretation has to be taken with some care as we shall see next.

Difermion parametrization

Our choice for the *Fierz*-complete ansatz (4.33) is not unique. In order to gain a deeper understanding of the dynamics of our model and how *Fierz*-incomplete approximations may affect the predictive power of model calculations in general, we consider a second *Fierz*-complete parametrization of the four-fermion interaction channels. To this end, we introduce explicit difermion channels in our ansatz for the effective action:

$$\Gamma_{\mathrm{LO}}^{(\mathrm{D})} = \int_0^\beta d\tau \int d^3x \Big\{ \bar{\psi}(Z_\psi^{\parallel}\mathrm{i}\gamma_0\partial_0 + Z_\psi^{\perp}\mathrm{i}\gamma_i\partial_i - Z_\mu \mathrm{i}\mu\gamma_0)\psi + \frac{1}{2}\bar{\lambda}_{\mathrm{D},\sigma}\,(\mathrm{S}-\mathrm{P}) - \frac{1}{2}\bar{\lambda}_{\mathrm{DSP}}\,(\mathrm{S}\mathcal{C}-\mathrm{P}\mathcal{C}) - \frac{1}{2}\bar{\lambda}_{\mathrm{D0}}\left(\mathrm{A}_{\parallel}\mathcal{C}\right) \Big\}\,, \tag{4.41}$$

where

$$\begin{aligned} (\mathrm{S}\mathcal{C}-\mathrm{P}\mathcal{C}) &\equiv (\bar{\psi}\psi^C)(\bar{\psi}^C\psi) - (\bar{\psi}\gamma_5\psi^C)(\bar{\psi}^C\gamma_5\psi)\,, \\ \left(\mathrm{A}_{\parallel}\mathcal{C}\right) &\equiv (\bar{\psi}\gamma_0\gamma_5\psi^C)(\bar{\psi}^C\gamma_0\gamma_5\psi)\,, \end{aligned} \tag{4.42}$$

see Section 2.2 for the definition of the charge conjugated fields $\bar{\psi}^C$ and ψ^C. By means of *Fierz* transformations (see Appendix B.3.1), we can rewrite this ansatz in terms of our original set of interaction channels introduced in Eq. (4.33):

$$\begin{aligned} \Gamma_{\mathrm{LO}}^{(\mathrm{D})} = \int_0^\beta d\tau \int d^3x \Big\{ &\bar{\psi}(Z_\psi^{\parallel}\mathrm{i}\gamma_0\partial_0 + Z_\psi^{\perp}\mathrm{i}\gamma_i\partial_i - Z_\mu \mathrm{i}\mu\gamma_0)\psi \\ &+ \frac{1}{2}(\bar{\lambda}_{\mathrm{D},\sigma} + \bar{\lambda}_{\mathrm{DSP}} + \frac{1}{2}\bar{\lambda}_{\mathrm{D0}})\,(\mathrm{S}-\mathrm{P}) \\ &- \frac{1}{2}(-\bar{\lambda}_{\mathrm{DSP}} - \frac{3}{2}\bar{\lambda}_{\mathrm{D0}})\left(V_{\parallel}\right) - \frac{1}{2}(-\bar{\lambda}_{\mathrm{DSP}} + \frac{1}{2}\bar{\lambda}_{\mathrm{D0}})\,(V_{\perp}) \Big\}\,. \end{aligned} \tag{4.43}$$

This allows us to identify the following relations between the various couplings:

$$\begin{gathered} \bar{\lambda}_\sigma = \bar{\lambda}_{\mathrm{D},\sigma} + \bar{\lambda}_{\mathrm{DSP}} + \frac{1}{2}\bar{\lambda}_{\mathrm{D0}}\,, \\ \bar{\lambda}_{\mathrm{V}}^{\parallel} = -\bar{\lambda}_{\mathrm{DSP}} - \frac{3}{2}\bar{\lambda}_{\mathrm{D0}}\,, \qquad \bar{\lambda}_{\mathrm{V}}^{\perp} = -\bar{\lambda}_{\mathrm{DSP}} + \frac{1}{2}\bar{\lambda}_{\mathrm{D0}}\,. \end{gathered} \tag{4.44}$$

---

[17] Note that our fermionic theory of a single fermion species may also be viewed as an effective low-energy model for *massless* electrons. In QED with *massless* electrons (i.e., $U_{\mathrm{A}}(1)$-symmetric QED), such photon-like pseudo-*Goldstone* bosons potentially appearing at high densities could mix with the real photons.

By inverting these relations we eventually obtain the β functions of the couplings in our "difermion parametrization" of the effective action:

$$\begin{aligned} \partial_t \lambda_{\mathrm{D},\sigma} &= \beta_{\lambda_\sigma} + \frac{1}{2}\beta_{\lambda_{\mathrm{V}}^{\parallel}} + \frac{1}{2}\beta_{\lambda_{\mathrm{V}}^{\perp}}\,, \\ \partial_t \lambda_{\mathrm{DSP}} = -\frac{1}{4}\beta_{\lambda_{\mathrm{V}}^{\parallel}} - \frac{3}{4}\beta_{\lambda_{\mathrm{V}}^{\perp}}\,, &\qquad \partial_t \lambda_{\mathrm{D0}} = -\frac{1}{2}\beta_{\lambda_{\mathrm{V}}^{\parallel}} + \frac{1}{2}\beta_{\lambda_{\mathrm{V}}^{\perp}}\,. \end{aligned} \tag{4.45}$$

The β functions on the right-hand side depend on the couplings $\{\bar{\lambda}_\sigma, \bar{\lambda}_{\mathrm{V}}^{\parallel}, \bar{\lambda}_{\mathrm{V}}^{\perp}\}$ and can be expressed in terms of the couplings $\{\bar{\lambda}_{\mathrm{D},\sigma}, \bar{\lambda}_{\mathrm{DSP}}, \bar{\lambda}_{\mathrm{D0}}\}$ using Eqs. (4.44). Note that, at $T = \mu = 0$, the flow of the λ_{DSP} coupling is up to a global minus sign identical to the flow of the vector coupling λ_{V} in the effective action (4.33).

The $(\mathrm{S}-\mathrm{P})$-channel in our ansatz (4.41) is again the conventional scalar-pseudoscalar channel. A dominance of this channel indicates the onset of spontaneous chiral $U_{\mathrm{A}}(1)$ symmetry breaking in our model. A dominance of the difermion channel $(\mathrm{S}\mathcal{C}-\mathrm{P}\mathcal{C})$ is associated with the spontaneous breakdown of both the chiral $U_{\mathrm{A}}(1)$ symmetry and the $U_{\mathrm{V}}(1)$ symmetry of our model. Thus, a dominance of the $(\mathrm{S}\mathcal{C}-\mathrm{P}\mathcal{C})$-channel also suggests chiral symmetry breaking as measured by the conventional $(\mathrm{S}-\mathrm{P})$-channel and, loosely speaking, the information encoded in both channels is therefore not disjunct. In contrast to our previous ansatz (4.33), however, the parametrization of the four-fermion couplings in the ansatz (4.41) allows us to probe more directly a possible spontaneous breakdown of the $U_{\mathrm{V}}(1)$ symmetry. Phenomenologically, the latter may naively be associated with the formation of a BCS-type superfluid ground state. In particular, a dominance of this channel may indicate the formation of a finite difermion condensate $\langle\bar{\psi}^C\gamma_5\psi\rangle$ in the scalar $J^P = 0^+$ channel, cf. our discussion in Section 2.2.[18] We emphasize that these considerations do not imply that the ansatz (4.41) is more general by any means. In fact, as we have shown, both ansätze are equivalent as they are related by *Fierz* transformations. Therefore, these considerations only make obvious that the potential formation of a $U_{\mathrm{V}}(1)$-breaking ground state may just not be directly visible in a study with the ansatz (4.33) but may nevertheless be realized by specific simultaneous formations of the condensates $\langle\bar{\psi}\psi\rangle$, $\langle\bar{\psi}\gamma_0\psi\rangle$ and $\langle\bar{\psi}\gamma_i\psi\rangle$, according to Eqs. (B.26)-(B.28).[19] We add that a dominance of the $(\mathrm{A}_{\parallel}\mathcal{C})$-channel may indicate the formation of a condensate $\langle\bar{\psi}^C\gamma_0\gamma_5\psi\rangle$ with positive parity which breaks the $U_{\mathrm{V}}(1)$ symmetry of our model but leaves the chiral $U_{\mathrm{A}}(1)$ symmetry intact. However, this channel also breaks explicitly *Poincaré* invariance.

From our comparison of the ansätze (4.33) and (4.41), we immediately conclude that a phenomenological interpretation of the symmetry breaking patterns of our model requires

---

[18] Note that it is not possible in our present model to construct a *Poincaré*-invariant $J^P = 0^+$ condensation channel (from a corresponding four-fermion interaction channel) which only breaks $U_{\mathrm{V}}(1)$ symmetry but leaves the chiral $U_{\mathrm{A}}(1)$ symmetry intact. In QCD, the formation of the associated diquark condensate can be realized at the price of a broken $SU(3)$ color symmetry, even if the chiral symmetry remains unbroken. In QED, on the other hand, the required breaking of the $U_{\mathrm{A}}(1)$ symmetry is realized by a finite explicit electron mass.

[19] Within a truncated bosonized formulation (e.g. mean-field approximation), the specific choice for the parametrization of the four-fermion interaction channels is of great importance as it determines the choice for the associated bosonic fields (e.g. mean fields). The latter effectively determine a specific parametrization of the momentum dependence of the four-fermion channels. Therefore, the parametrization of the action in terms of four-fermion channels is of relevance from a phenomenological point of view. To be specific, even if two actions are equivalent on the level of *Fierz* transformations, the results from the mean-field studies associated with the two actions will in general be different.

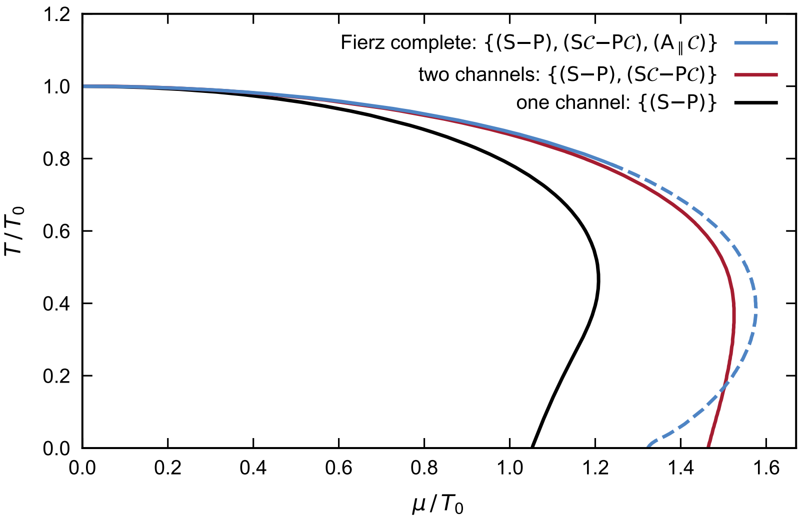

Figure 4.6: Phase boundary associated with the spontaneous breakdown of at least one of the fundamental symmetries of our model as obtained from a one-channel, two-channel, and *Fierz*-complete study of the ansatz (4.41), see main text for details.

great care. This is even more the case when a *Fierz*-incomplete set of four-fermion interactions is considered which has been extracted from a specific *Fierz*-complete parametrization of the interaction channels.

In Fig. 4.6, we show our results for the (T, μ) phase boundary associated with the spontaneous breakdown of at least one of the fundamental symmetries of our model which are now encoded in the four-fermion interaction channels as parametrized in our ansatz (4.41) for the effective action. The one-channel approximation is the same as in the case of our ansatz (4.33) for the effective action and the results for the phase boundary (solid black line) are only shown to guide the eye. Moreover, the location of the phase boundary from the *Fierz*-complete study of the effective action (4.41) agrees identically with the *Fierz*-complete study of the effective action (4.41), as it should be. In the present case, we observe again a dominance of the $(\mathrm{S}-\mathrm{P})$-channel close to the phase boundary for temperatures $1 \geq T/T_0 \gtrsim 0.8$ (solid blue line in Fig. 4.6). In the light of our results from the parametrization (4.33) of the effective action, where the $(\mathrm{S}-\mathrm{P})$-channel has also been found to be dominant close to the phase boundary for $1 \geq T/T_0 \gtrsim 0.8$, we may now cautiously conclude from the combination of the results from the two ansätze that at least the phase boundary in the temperature regime $1 \geq T/T_0 \gtrsim 0.8$ is associated with spontaneous chiral symmetry breaking as the latter is indicated by a dominance of either the $(\mathrm{S}-\mathrm{P})$-channel or the $(\mathrm{S}\mathcal{C}-\mathrm{P}\mathcal{C})$-channel.

In line with our study based on the parametrization (4.33) of the effective action, we now also observe a dominance of a channel associated with broken *Poincaré* invariance at $0 \leq T/T_0 \lesssim 0.8$ in the *Fierz*-complete study (dashed blue line in Fig. 4.6), namely a dominance of the $(\mathrm{A}_{\parallel}\mathcal{C})$-channel. In case of the two-channel approximation, which has been obtained by setting $\bar{\lambda}_{\mathrm{D}0} = 0$ and dropping the corresponding flow equation, we only observe a dominance of the $(\mathrm{S}-\mathrm{P})$-channel (solid red line) close to the phase boundary for all temperatures $1 \geq T/T_0 \geq 0$.

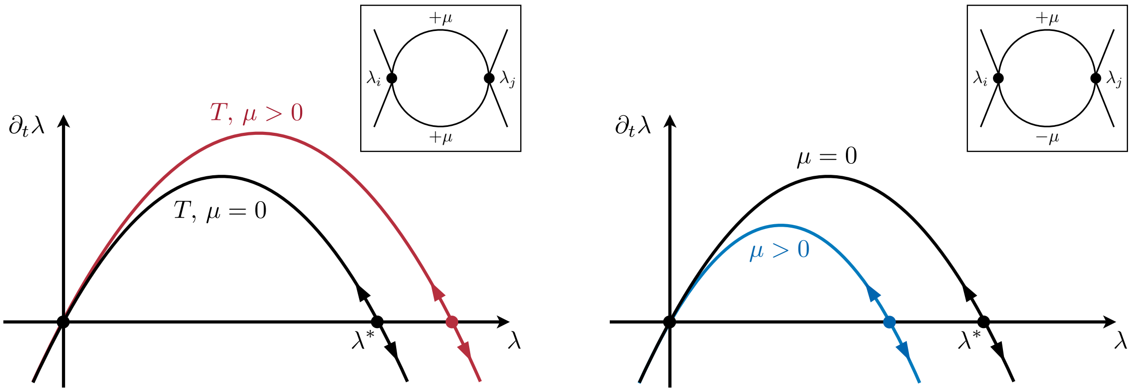

FIGURE 4.7: Left panel: Sketch of the β function of a four-fermion coupling which is only driven by a diagram of the type as shown in the inset. For increasing T/k and μ/k, the non-*Gaußian* fixed point is shifted to larger values. Right panel: Sketch of the β function of a four-fermion coupling at $T=0$ which is only driven by a diagram of the type as shown in the inset. For increasing μ/k, the non-*Gaußian* fixed point is shifted to smaller values and eventually merges with the *Gaußian* fixed point.

From a comparison of the results from the one- and two-channel approximation, we also deduce that the phase boundary is again pushed to larger values of the chemical potential. However, we now observe that the phase boundary is pushed back to smaller values of the chemical potential again at low temperature when we go from the two-channel approximation to the *Fierz*-complete ansatz. This underscores again that a phenomenological interpretation of the phase structure and symmetry breaking patterns in *Fierz*-incomplete studies have to be taken with some care.

Whereas the phenomenological interpretation of the dominance of the various interaction channels in different parametrizations of the effective action may be difficult, a qualitative insight into the symmetry breaking mechanisms can be obtained from an analysis of the fixed-point structure of the four-fermion couplings. To this end, we may consider the temperature and the chemical potential as external couplings, governed by a trivial dimensional RG running $\partial_t(T/k) = -(T/k)$ and $\partial_t(\mu/k) = -(\mu/k)$.

The two classes of diagrams that essentially contribute to the RG flow of the four-fermion couplings at finite chemical potential are shown in Fig. 4.1, see also the insets of Fig. 4.7 and Appendix F.1 for explicit expressions of the flow equations. In a partially bosonized formulation of our model, the interaction between the fermions is mediated by the exchange of bosons carrying fermion number $F=0$ and zero chemical potential (corresponding to states with zero baryon number in QCD, such as pions) in the diagram in the inset of the left panel of Fig. 4.7. On the other hand, the fermion interaction is mediated by a bosonic difermion state carrying fermion number $|F|=2$ and an effective chemical potential $\mu_{\mathrm{D}} = F\mu$ in the diagram in the inset of the right panel of Fig. 4.7.

Let us now assume that the RG flow of a given four-fermion coupling λ is only governed by diagrams of the type shown in the inset of the left panel of Fig. 4.7. The RG flow equation is then given by

$$\partial_t\lambda = 2\lambda - c_+ l_+^{(\mathrm{F})}\lambda^2\,, \tag{4.46}$$

where, without loss of generality, we assume c_+ is a positive numerical constant. This flow equation has a *Gaußian* fixed point and a non-*Gaußian* fixed point λ^*. Strictly speaking, the latter becomes a pseudo fixed point in the presence of an external parameter, such as a finite temperature and/or finite chemical potential. The threshold function $l_+^{(\mathrm{F})}$ depends on the dimensionless temperature T/k as well as the dimensionless chemical potential μ/k and essentially represents the loop diagram in the inset of the left panel of Fig. 4.7. For an explicit representation of such a threshold function, we refer the reader to Appendix E. Note that these threshold functions come in two different variations, e.g. $l_{\parallel,+}^{(\mathrm{F})}$ and $l_{\perp,+}^{(\mathrm{F})}$, which can be traced back to the tensor structure becoming more involved due to the explicit breaking of *Poincaré* invariance. Although we have taken this into account in our numerical studies, we leave this subtlety aside in our more qualitative discussion at this point.

For increasing dimensionless temperature T/k at fixed dimensionless chemical potential μ/k, we have

$$l_+^{(\mathrm{F})} \to 0 \quad \text{for} \quad \frac{T}{k} \gg 1\,, \tag{4.47}$$

due to the thermal screening of the fermionic modes. Moreover, we also have $l_+^{(\mathrm{F})} \to 0$ for sufficiently large values of μ/k for a given fixed dimensionless temperature T/k. This implies that the fermions become effectively weakly interacting in the dense limit. Overall, we have $\lambda^* \to \infty$ for the non-*Gaußian* fixed point for $T/k \to \infty$ and/or $\mu/k \to \infty$, see left panel of Fig. 4.7. Let us now assume that we have fixed the initial condition $\lambda^{(\mathrm{UV})}$ of the four-fermion coupling such that $\lambda^{(\mathrm{UV})} > \lambda^*$ at $T = 0$ and $\mu = 0$ and keep it fixed to the same value for all values of T and μ. As discussed in detail above, the four-fermion coupling at $T = 0$ and $\mu = 0$ then increases rapidly toward the IR, indicating the onset of spontaneous symmetry breaking. However, since the value of the non-*Gaußian* fixed point increases with increasing T/k and/or increasing μ/k, the rapid increase of the four-fermion coupling toward the IR is effectively slowed down and may even change its direction in the space defined by the coupling λ, the dimensionless temperature T/k and the dimensionless chemical potential μ/k. This behavior of the (pseudo) non-*Gaußian* fixed point suggests that, for a fixed initial value $\lambda^{(\mathrm{UV})} > \lambda^*$, a critical temperature T_{cr} as well as a critical chemical potential μ_{cr} exist above which the four-fermion coupling does not diverge anymore but approaches zero in the IR and therefore the symmetry associated with the coupling λ is restored. At least at high temperature, such a behavior is indeed expected since the fermions become effectively "stiff" degrees of freedom due to their thermal *Matsubara* mass $\sim T$. This is the type of symmetry restoration mechanism which dominantly determines the phase structure of our model at finite temperature and chemical potential, as indicated in Figs. 4.4 and 4.6 by the finite extent of the regime associated with spontaneous symmetry breaking in both T- and μ-direction. We may even cautiously deduce from this observation that the dynamics close to and below the phase boundary at low temperature is governed by the formation of a condensate with fermion number $F = 0$ as the general structure of the phase diagram appears to be dominated by diagrams of the type shown in the inset of the left panel of Fig. 4.7.

A dominance of the RG flow by diagrams of the type shown in the inset of the right panel of Fig. 4.7 would suggest the formation of a condensate with fermion number $|F| = 2$, i.e., a difermion-type condensate. In this case, we would indeed expect a different phase structure, at least at (very) low temperature and large chemical potential. To illustrate this, let us now assume that the RG flow of a given four-fermion coupling λ is only governed by diagrams of the form shown in the inset of the right panel of Fig. 4.7:

$$\partial_t \lambda = 2\lambda - c_{\pm} l_{\pm}^{(\mathrm{F})} \lambda^2 \,, \tag{4.48}$$

where, again without loss of generality, we assume $c_{\pm}$ is a positive numerical constant. This flow equation has a *Gaußian* fixed point and a non-*Gaußian* fixed point λ^*. The threshold function $l_{\pm}^{(\mathrm{F})}$ depends again on the (dimensionless) temperature T/k and the dimensionless chemical potential μ/k and represents the associated loop integral. Explicit representations of this type of threshold function can be found in Appendix E. For increasing T/k at fixed μ/k, we find again

$$l_{\pm}^{(\mathrm{F})} \to 0 \quad \text{for} \quad \frac{T}{k} \gg 1 \,, \tag{4.49}$$

due to the thermal screening of the fermionic modes. However, we have

$$l_{\pm}^{(\mathrm{F})} \sim \left(\frac{\mu}{k}\right)^2 \quad \text{for} \quad \frac{\mu}{k} \gg 1 \tag{4.50}$$

at $T = 0$. For finite fixed T/k, we then observe that $l_{\pm}^{(\mathrm{F})}$ increases as a function of μ/k until it reaches a maximum and then tends to zero for $\mu/k \to \infty$. The position of the maximum is shifted to smaller values of μ/k for increasing T/k.

Let us now focus on the strict zero-temperature limit. In this case, the value of the non-*Gaußian* fixed point is decreased for increasing μ/k and eventually merges with the *Gaußian* fixed point. This implies immediately that the four-fermion coupling always increases rapidly toward the IR for $\mu > 0$, indicating the onset of spontaneous symmetry breaking, provided that the initial condition $\lambda^{(\mathrm{UV})}$ has been chosen positive, $\lambda^{(\mathrm{UV})} > 0$.[20] Thus, the actual choice for $\lambda^{(\mathrm{UV})}$ relative to the value of the non-*Gaußian* fixed point plays a less prominent role in this case, at least on a qualitative level. In other words, any infinitesimally small positive coupling triggers the formation of a condensate with fermion number $|F| = 2$. This is nothing but the *Cooper* instability in the presence of an arbitrarily weak attraction [113] which destabilizes the *Fermi* sphere and results in the formation of a *Cooper* pair condensate [111, 112], inducing a gap in the excitation spectrum (see our discussion in Section 2.2). For $\lambda^{(\mathrm{UV})} = 0$, the four-fermion coupling remains at the *Gaußian* fixed point. For $\lambda^{(\mathrm{UV})} < 0$, the theory approaches the *Gaußian* fixed point in the IR limit. Thus, there is no spontaneous symmetry breaking for $\lambda^{(\mathrm{UV})} \leq 0$.

The fact that the two fixed points merge for $\mu/k \to \infty$ at $T = 0$ leaves its imprint in the μ-dependence of the critical scale k_{cr} at which the four-fermion coupling diverges. In fact,

---

[20] For $c_{\pm} < 0$, $\lambda^{(\mathrm{UV})}$ has to be chosen negative in order to trigger spontaneous symmetry breaking in the long-range limit.

from the flow equation (4.48), we recover the typical BCS-type exponential scaling behavior of the critical scale:

$$k_{\mathrm{cr}} = \Lambda' \theta(\bar{\lambda}^{(\Lambda')}) \exp\left(-\frac{c_{\mathrm{BCS}}}{\mu^2 \bar{\lambda}^{(\Lambda')}} \right) . \tag{4.51}$$

Here, we have assumed that the RG flow equation (4.48) has been initialized in the IR regime at $k = \Lambda' < \Lambda$ with an initial value $\bar{\lambda}^{(\Lambda')} > 0$, such that $l_{\pm}^{(\mathrm{F})}$ can be approximated by $l_{\pm}^{(\mathrm{F})} = c_{\infty}(\mu/k)^2$ with $c_{\infty} > 0$. Moreover, we have introduced the numerical constant $c_{\mathrm{BCS}} = 1/(c_{\infty} c_{\pm}) > 0$. The value $\bar{\lambda}^{(\Lambda')}$ of the four-fermion coupling can be directly related to the UV coupling $\lambda^{(\mathrm{UV})}$. Recall that the dependence of k_{cr} on the chemical potential is then handed down to physical observables in the IR limit, leading to the typical exponential scaling behavior [97].

The observed exponential-type scaling behavior of the scale k_{cr} appears to be generic in cases where two fixed points merge, see, e.g., our discussion of essential scaling (BKT-type scaling) in Section 4.2.2 which plays a crucial role in gauge theories with many flavors [405–408].

At finite temperature and chemical potential, the shift of the non-*Gaußian* fixed point toward the *Gaußian* fixed point is slowed down and eventually inverted such that the value of the non-*Gaußian* fixed point eventually increases with increasing T/k. This suggests again that a critical temperature exists above which the symmetry associated with the coupling λ is restored.

If the ground state of our model at large chemical potential was governed by the *Cooper* instability as associated with the exponential scaling behavior (4.51) of the scale k_{cr}, then the phase boundary would extend to arbitrarily large values of the chemical potential, at least in the strict zero-temperature limit. However, this is not observed in the numerical solution of the full set of RG flow equations, see Figs. 4.4 and 4.6. Of course, this does not imply that difermion-type phases are not favored at all in this model (e.g., a phase with a chirally invariant $U_{\mathrm{V}}(1)$-breaking $\langle \bar{\psi}^C \gamma_0 \gamma_5 \psi \rangle$-condensate) since the phase structure also depends on our choice for the initial conditions of the four-fermion couplings. The formation of such phases may therefore be realized by a suitable tuning of the initial conditions. Still, the vacuum phase structure of our model suggests that the general features of the phase diagrams presented in Figs. 4.4 and 4.6 persist over a significant range of initial values for the couplings λ_σ and λ_{V}, see Fig. 4.2.

4.2.4 Excursion: Silver-Blaze property and spatial regulators

In our approach, we avoid the introduction of an additional source of explicit breaking of *Poincaré* invariance by employing a covariant *Fermi*-surface-adapted regularization scheme as opposed to a spatial, i.e., three-dimensional, regulator, see our discussion in Section 3.2. However, this comes at the price that the invariance under the transformation (2.37) associated with the *Silver-Blaze* property becomes explicitly broken by the regularization scheme. In this excursion, we discuss the implications of these aspects in more detail and from two different angles: First, we discuss our truncation in view of the *Silver-Blaze* property, in particular in the context of the derivative expansion, and analyze the strength of the explicit breaking of the *Silver-Blaze* property in our present study. Second, we illustrate the consequences of the use of a spatial regularization scheme by comparing the results on the finite-temperature phase boundary as obtained from a computation employing a spatial regulator with those as obtained from a computation with our covariant *Fermi*-surface-adapted regularization scheme.

Silver-Blaze property of the truncation

The *Silver-Blaze* property introduced in Section 2.1.2 imposes as an intrinsic physical property certain constraints on the behavior of the physical system at hand as a function of the chemical potential at zero temperature. An immediate consequence is, e.g., that the renormalization factors associated with the kinetic term of our model (4.3) are related to each other in a strict manner as long as the renormalized quark chemical potential is smaller than the potentially generated (renormalized) mass gap. The *Silver-Blaze* property is a consequence of the invariance of fermionic theories under the transformation defined in Eq. (2.37) in Section 2.1.2. This symmetry implies additional requirements for the computational approach such as the regularization and the approximation scheme. In Section 3.2, we have already discussed that a regulator function must only be a function of the spatial momentum $\vec{p}$ and the complex variable $z = p_0 - \mathrm{i}\mu$ in order to preserve this symmetry. The covariant *Fermi*-surface-adapted regulator, however, depends on $\omega_+\omega_- = |(p_0 - \mathrm{i}\mu)^2 + \vec{p}^{\,2}|$ and consequently breaks the symmetry associated with the transformation (2.37).

With respect to, e.g., the derivative expansion of the effective action, an expansion of the correlation functions about the point $(p_0 - \mathrm{i}\mu, \vec{p}) = (0, 0)$ rather than $(p_0, \vec{p}) = (0, 0)$ is required to preserve exactly the *Silver-Blaze* property [231]. This follows immediately from the fact that the correlation functions do not have an explicit μ-dependence but depend only on the chemical potential via a μ-shift of the zeroth component of the four momenta, see, e.g., Eq. (2.42). If the derivative expansion is nevertheless anchored at the point $(p_0, \vec{p}) = (0, 0)$, an explicit breaking of the invariance under the transformation (2.37) is introduced which, however, has been found to be mild in RG studies of QCD low-energy models with conventional spatial regulator functions [128, 139, 230, 231, 329, 414]. Even so, note that this choice of the expansion point in combination with the use of conventional spatial regulator functions without an adaption due to the presence of a *Fermi* surface, see, e.g., Refs. [366–369] for a definition of this class of regularization schemes, may be problematic in other respects. This class of regulators lacks locality in the direction of the zeroth component of the four-momentum, i.e., the corresponding regulator functions are “flat” in this direction and therefore all time-like momentum modes effectively contribute to the RG flow at any value of k. In fact, in our present analysis, we even observe that the choice of the expansion point $(p_0, \vec{p}) = (0, 0)$ leads to ill-defined RG flows because of the analytic properties of the threshold functions $l_{\parallel\pm}^{(\mathrm{F})}$ and $l_{\perp\pm}^{(\mathrm{F})}$ at $T = 0$ and $\mu > 0$, see Appendix E.2 and the right panel of Fig. 4.7 for the *Feynman* diagram associated with these functions. The use of a suitably chosen expansion point, i.e., a point respecting the *Silver-Blaze* property, cures this problem. But then again, such a choice may not be unproblematic as well since crucial aspects, e.g., the characteristic BCS-type exponential scaling behavior discussed in Section 4.2.3, are potentially missed:

Although a suitably chosen expansion point respecting the *Silver-Blaze* property might cure such pathologies in case of spatial regulator functions, we should keep in mind a subtlety coming along with the choice of a particular expansion point. Usually, we are interested in choosing a point for the expansion which is suitable to study a particular physical effect. This point may indeed be in conflict with the above considerations regarding the *Silver-Blaze* property. To be specific, we may only be interested in an evaluation of the fully momentum-dependent correlation functions for a specific configuration of the external momenta. For an estimate of the phase structure of a given theory, for example, the limit of vanishing external momenta may be considered for the two-point function in order to project on screening masses. This evaluation point may then serve as the anchor point for a derivative expansion but violates the *Silver-Blaze* property as discussed above. On the other hand, the choice of an expansion point respecting the *Silver-Blaze* property may require to include high orders in the derivative expansion in order to be able to reach reliably the actual point of physical interest which, as an expansion point, may violate the *Silver-Blaze* property. This is indeed the situation in many studies and it is also the case in our present work as we are interested in the evaluation of the four-fermion correlation functions in a specific limit in order to estimate the phase structure. To be concise, we have chosen the limit of vanishing external momenta as the expansion point. If we had chosen an expansion point respecting the *Silver-Blaze* property, then we would have *not* been able to reach reliably our actual point of interest at leading order of the derivative expansion. A consideration of an expansion about such a *Silver-Blaze* compatible expansion point and a detailed discussion of the aforementioned issue are deferred to future work.

Our discussion with respect to the regularization scheme and the derivative expansion calls for an analysis of the strength of the explicit breaking of the *Silver-Blaze* property in our present study. To this end, we consider the RG flow of the scalar-pseudoscalar coupling λ_σ in a simple one-channel approximation and compute the dependence of the scale $k_{\rm cr}$ on the chemical potential μ using the covariant regulator function defined by Eqs. (3.40) and (3.44) and the spatial regularization scheme defined by Eqs. (3.30) and (3.31) in Section 3.2. Recall that the scale $k_{\rm cr}$ is defined as the scale at which the four-fermion coupling λ_σ diverges. The scale dependence of the λ_σ-coupling is governed by the following flow equation:

$$\partial_t \lambda_\sigma = 2\lambda_\sigma - 48 v_4 \left(l_{\parallel +}^{(\mathrm{F})}(\tau, 0, -\mathrm{i}\tilde{\mu}_\tau) + l_{\perp +}^{(\mathrm{F})}(\tau, 0, -\mathrm{i}\tilde{\mu}_\tau) \right) \lambda_\sigma^2 \,, \tag{4.52}$$

where again $\tau = T/k$ and $\tilde{\mu}_\tau = \mu/(2\pi T)$. The definition of the threshold functions $l_{\parallel +}^{(\mathrm{F})}$ and $l_{\perp +}^{(\mathrm{F})}$ for the two regularization schemes can be found in Appendix E. Compared to the flow equation (4.34), we do not include the threshold functions $l_{\parallel \pm}^{(\mathrm{F})}$ and $l_{\perp \pm}^{(\mathrm{F})}$ associated with the loop diagram depicted in the inset of the right panel of Fig. 4.7 in this analysis since, for the spatial regularization scheme, these threshold functions lead to “spurious” divergences in the integration of the RG flow equations at $T = 0$ due to a non-removable second-order pole at $k = \mu$. We refer to Appendix E.2 for explicit representations of these functions. This behavior is associated with the presence of a zero mode in the two-point function at $k = \mu$, see Eq. (3.34) in Section 3.2. Note that, for any even infinitesimally small finite temperature, these functions are well-behaved, i.e., no “spurious” divergences in the integration of the

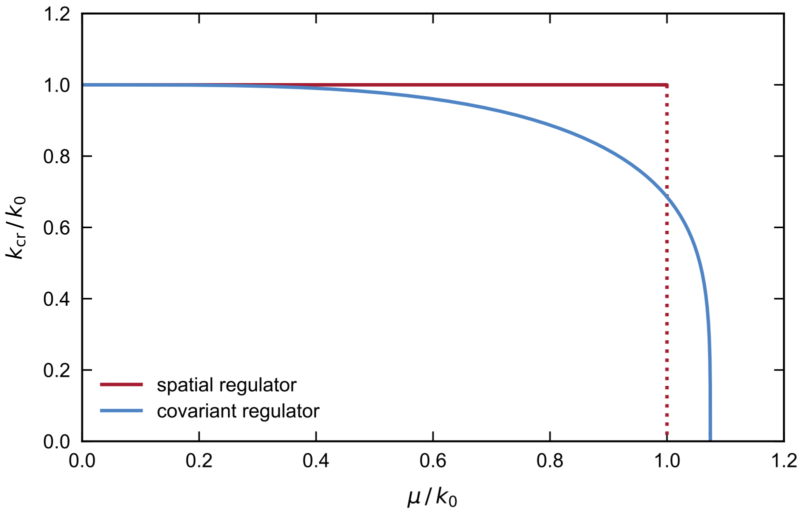

FIGURE 4.8: Critical scale k_{cr}/k_0 with $k_0 = k_{\mathrm{cr}}(\mu = 0) \approx 0.35\Lambda$ as a function of μ/k_0 at zero temperature for two different regularization schemes, see main text for details.

RG flow equations appear. Still, the contributions from these threshold functions become arbitrarily large at $\mu > 0$ for decreasing temperature and therefore dominate artificially the RG flow of the couplings at finite chemical potential and low temperature. Note that this is not the case for our covariant regulator function, which is well-defined for $T = 0$ and $T > 0$, as it is constructed such that the zero mode at $k = \mu$ is regularized.

Since $k_{\mathrm{cr}}(\mu)$ sets the scale for all low-energy observables including the fermion mass $m_{\mathrm{f}} \sim k_{\mathrm{cr}}$ (see our discussion in Section 4.1.3), $k_{\mathrm{cr}}(\mu)$ should be independent of μ for $\mu < m_{\mathrm{f}}$ at *zero* temperature because of the *Silver-Blaze* property. Unfortunately, we do not have direct access to the fermion mass m_{f} in our present study. However, at least at zero temperature and chemical potential, the RG flow equation (4.52) for the λ_σ in the one-channel approximation can be mapped onto a corresponding mean-field equation for the fermion mass, see, e.g., Ref. [333]. This provides us at least with an estimate for the vacuum fermion mass m_{f} in our studies. Specifically, we find $m_{\mathrm{f}}/k_0 \approx 0.53$ for the covariant regulator function and $m_{\mathrm{f}}/k_0 \approx 0.44$ for the spatial regulator. Note that k_0 has been fixed to the same value in both calculations. In Fig. 4.8, we show k_{cr} as a function of μ at zero temperature for the covariant regulator function defined by Eqs. (3.40) and (3.44) and the spatial regularization scheme defined by Eqs. (3.30) and (3.31) in Section 3.2. In order to ensure comparability, we have fixed the initial condition of the flow equation (4.52) such that the symmetry breaking scale $k_0 = k_{\mathrm{cr}}(\mu = 0)$ assumes the same value in both cases. In accordance with our discussion, we observe that k_{cr} does not depend on μ for $\mu < k_0$ in case of the spatial regulator, where k_0 plays the role of the zero-temperature fermion mass. Thus, this class of spatial regularization schemes in general respects the symmetry (2.37) at zero temperature, as already mentioned above. For our covariant regulator function, we observe that k_{cr} exhibits a weak dependence on μ for $\mu \lesssim m_{\mathrm{f}}$. This dependence becomes stronger for increasing μ. For $\mu/k_0 \to 1$, k_{cr} then does not terminate but tends to zero continuously at $\mu/k_0 \approx 1.1$. In any case, we find in both cases that the critical scale k_{cr} is only finite for chemical potentials below some critical value $\mu_{\mathrm{cr}}/k_0 \sim \mathcal{O}(1)$.

We emphasize that the artificial regulator-induced dependence on the chemical potential illustrated in Fig. 4.8 is an immediate consequence of the fact that our covariant regulator function violates the *Silver-Blaze* property. This violation becomes evident by the fact that the four-fermion couplings depend on the chemical potential μ at $T = 0$ for any value of k. For $k \gg \mu$, for example, we indeed deduce from Eq. (4.52) that

$$\lambda_\sigma \simeq \lambda_\sigma^* \left(1 + c_0 \left(\frac{\mu}{k}\right)^2 \ln\left(\frac{k}{\Lambda}\right) - \left(\frac{\Lambda}{k}\right)^2 \left(\left(\frac{\lambda_\sigma^*}{\lambda_\sigma^{(\mathrm{UV})}}\right) - 1\right) + \dots\right), \tag{4.53}$$

where $c_0 < 0$ is a numerical constant.

Covariant regulators versus spatial regulators

Our four-dimensional *Fermi*-surface-adapted regulator function defined by Eq. (3.44) violates the *Silver-Blaze* property. Nevertheless, we have restricted ourselves to the use of this regulator in the present study since spatial regularization schemes violate the requirements (v) and (vii) listed in Section 3.2, i.e., they introduce an explicit breaking of *Poincaré* invariance and they lack locality in the direction of time-like momenta. Our four-dimensional *Fermi*-surface-adapted regulator fulfills both requirements.

In our *Fierz*-complete studies, we have indeed found that the artificial breaking of *Poincaré* invariance and the lack of locality affects the dynamics of the system already at zero chemical potential. Even more, also at $T = \mu = 0$, the $\lambda_{\mathrm{V}}^{\parallel}$- and $\lambda_{\mathrm{V}}^{\perp}$-coupling differ due to the explicit breaking of *Poincaré* invariance. This eventually results in a dominance of the $\lambda_{\mathrm{V}}^{\parallel}$-channel at finite temperature and zero chemical potential, see Fig. 4.9. In our study with the covariant regulator function, on the other hand, we find a clear dominance of the $(\mathrm{S}-\mathrm{P})$-channel along the temperature axis at $\mu = 0$. This aspect is of relevance as such spatial regularization schemes may spoil the phenomenological interpretation of the results. In fact, at low temperature and large chemical potential, a study with the spatial regulator function even suggests that the dynamics of the system is strongly dominated by the $(V_\perp)$-channel such that the ground state appears to be governed by spontaneous symmetry breaking for all values of the chemical potential considered in this study $(\mu/T_0 \lesssim 2)$, see Fig. 4.9. Using a different basis of four-fermion channels, e.g. including difermion-type channels, one may even be tempted to associate the appearance of spontaneous symmetry breaking at (arbitrarily) large chemical potential with the formation of a difermion condensate in our model as it is the case in QCD, see our discussion of color superconductivity in Section 2.2. In our present model, however, the appearance of a regime governed by spontaneous symmetry breaking at large chemical potential is only observed when the spatial regulator function is used but not when our covariant *Fermi*-surface adapted regulator is applied. In fact, we consider the very appearance of spontaneous symmetry breaking at large chemical potential in our present model as an artifact of the use of the spatial regulator function, at least at the order of the derivative expansion considered in this work. Recall that the threshold functions $l_{\parallel\pm}^{(\mathrm{F})}$ and $l_{\perp\pm}^{(\mathrm{F})}$ associated with the involved loop integrals are not well behaved at $T = 0$ and $\mu > 0$ in case of the spatial regulator, i.e., these threshold functions lead to "spurious" divergences in the integration of the RG flow equations, see our discussion below Eq. (4.52). The definitions of the threshold

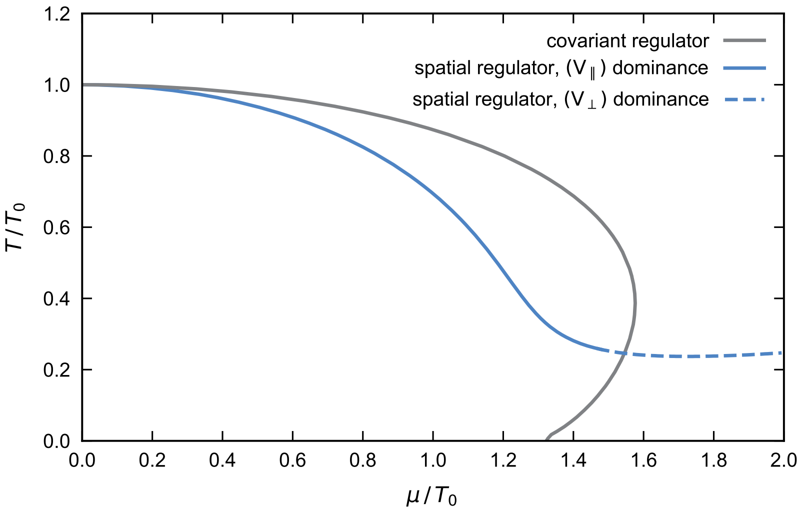

FIGURE 4.9: Phase boundary associated with the spontaneous breakdown of at least one of the fundamental symmetries of our model as obtained from the *Fierz*-complete ansatz (4.33) using two different regulator functions, see main text for a discussion of the origin of the differences between the two phase boundaries. The gray line corresponds to the blue line in Fig. 4.4 and is only included to guide the eye.

functions in case of the spatial regulator are given in Section E.2. From a phenomenological point of view, we note that, in contrast to QCD, the formation of a *Poincaré*-invariant difermion condensate associated with $U_{\mathrm{V}}(1)$ symmetry breaking also entails chiral symmetry breaking in our present model, see Section 4.2.3.

The relevance of covariant regularization schemes has also been discussed in the context of real-time RG studies [372, 378, 415]. Along the lines of the construction of corresponding regulator functions [372], it should in principle be possible to construct a four-dimensional regulator which fully respects the symmetry (2.37) at zero temperature by introducing a suitable deformation of the contour of the associated integration in the complex p_0 plane. However, this is beyond the scope of the present work and deferred to future work. Finally, we add that the complications associated with the regularization of a theory in the presence of a finite chemical potential as well as the issues arising because of the use of spatial regularization schemes are not bound to our FRG approach but are in principle present in any approach.

4.2.5 Conclusions

In this section we have analyzed the phase structure of a one-flavor NJL model at finite temperature and chemical potential. With the aid of RG flow equations, we aimed at an understanding of how *Fierz*-incomplete approximations affect the predictive power of general NJL-type models, which are also frequently employed to study the phase structure of QCD. To this end, we have considered the RG flow of four-fermion couplings at leading order of the derivative expansion. This approximation already includes corrections beyond the mean-field approximation which is inevitable to preserve the invariance of the results under *Fierz* transformations.

We have found that *Fierz* incompleteness affects strongly key quantities, such as the curvature of the phase boundary at small chemical potential. Indeed, the curvature obtained in a calculation including only the conventional scalar-pseudoscalar channel has been found to be about 44% greater than in the *Fierz*-complete study. With respect to the critical value μ_{cr} of the chemical potential above which no spontaneous symmetry breaking occurs, we have found that μ_{cr} in the *Fierz*-complete study is about 20% greater than in the conventional one-channel approximation. Moreover, we have observed that the position of the phase boundary depends strongly on the number of four-fermion channels included in *Fierz*-incomplete studies. In general, *Fierz*-incomplete calculations may either overestimate or underestimate the size of the regime governed by spontaneous symmetry breaking in the (T, μ) plane. The actual approach to the result from the *Fierz*-complete study depends strongly on the type of the channels included in such studies. In fact, our analysis suggests that the use of *Fierz*-incomplete approximations may even lead to the prediction of spurious phases, in particular at large chemical potential.

With respect to a determination of the properties of the actual ground state in the phase governed by spontaneous symmetry breaking, our present study based on the analysis of RG flow equations at leading order of the derivative expansion is limited. In order to gain at least some insight into this question, we have analyzed which four-fermion channel dominates the dynamics of the system close to the phase boundary. A dominance of a given channel may then indicate the formation of a corresponding condensate. As we have discussed, however, this criterion has to be taken with some care, in particular when only one specific parametrization of the four-fermion channels is considered. This also holds for *Fierz*-complete studies. In this study, we have used two different *Fierz*-complete parametrizations and found that, over a wide range of the chemical potential, the dynamics close to the phase boundary is dominated by the conventional scalar-pseudoscalar channel associated with chiral symmetry breaking. At large chemical potential, the dynamics close to the phase boundary then appears in both cases to be dominated by channels which break explicitly *Poincaré* invariance.

As a second criterion for the determination of at least some properties of the ground state of the regime governed by spontaneous symmetry breaking, we have analyzed on general grounds the scaling behavior of the loop diagrams contributing to the RG flow of the four-fermion couplings. The scaling of these diagrams as a function of the dimensionless temperature and chemical potential determines the fixed-point structure of the theory at finite temperature and chemical potential. Our fixed-point analysis suggests that the dynamics close to and below the phase boundary is governed by the formation of a condensate with fermion number $F = 0$. In contrast to QCD (see, e.g., Refs. [97, 107, 115, 385] for reviews), the formation of difermion-type condensates with fermion number $|F| = 2$ does not appear to be favored, at least at large chemical potential for the initial conditions of the RG flow equations employed in this study.

Of course, at the present order of the derivative expansion, the employed criteria can only serve as indicators for the actual properties of the ground state in regimes governed by spontaneous symmetry breaking. In order to determine the ground-state properties of a system unambiguously, a calculation of the full order-parameter potential is eventually required. Still, we expect that the findings of this analysis may already turn out to be useful to guide future NJL-type model studies.

4.3 En route to QCD: The NJL model with two flavors and N_c colors

By considering an NJL model with a single fermion species in Section 4.2, we have demonstrated that *Fierz* completeness as associated with the inclusion of more "exotic" four-fermion channels crucially affects the dynamics of the model, not only at large but already at small values of the quark chemical potential as measured by the curvature of the finite-temperature phase boundary. In this section, we now extend our analysis to an NJL model with *massless* quarks coming in N_c colors and two flavors to gain a better understanding of how *Fierz*-incomplete approximations of QCD low-energy models affect the predictions for the phase structure at finite temperature and density. Again, we explicitly take into account the breaking of *Poincaré* invariance by the presence of the heat bath and the chemical potential. Within our *Fierz*-complete framework including 10 four-quark channels, we demonstrate that channels associated with an explicit breaking of *Poincaré* invariance tend to increase significantly the critical temperature at large chemical potential. In accordance with many conventional model studies (see, e.g., Refs. [107, 115, 120, 385] for reviews), diquarks are nevertheless found to be the most dominant degrees of freedom in this regime. Moreover, we introduce sum rules for the various four-quark couplings that allow us to monitor the strength of the breaking of the axial $U_A(1)$ symmetry close to and above the phase boundary. The study of the RG flow of the four-quark couplings shows that the dynamics in the ten-dimensional *Fierz*-complete space of four-quark couplings can only be reduced to a one-dimensional space associated with the scalar-pseudoscalar coupling in the strict large-N_c limit. Still, the interacting fixed point associated with this one-dimensional subspace appears to govern the dynamics at small quark chemical potential even beyond the large-N_c limit. At large chemical potential, we shall see that corrections beyond the large-N_c limit become important and the dynamics is dominated by diquarks, favoring the formation of a chirally symmetric diquark condensate.

In Section 4.3.1 we begin with a discussion of the symmetries and the *Fierz*-complete basis of four-quark interaction channels of our model. Whereas the number of colors N_c is a free parameter in this more general discussion, we emphasize that we exclusively consider $N_c = 3$ in the subsequent numerical computations. The description of the scale fixing procedure is also included in Section 4.3.1. The RG fixed-point and phase structure of our *Fierz*-complete NJL-type model at finite temperature and density at leading order of the derivative expansion of the effective action is analyzed in Sections 4.3.2 - 4.3.5. After a brief consideration of the relation of the mean-field approximation and an RG study of four-quark interactions in a one-channel approximation, we discuss the symmetry breaking patterns based on our "criterion of dominance", i.e., the analysis of the "hierarchy" of the various four-quark interactions in terms of their strength, in Section 4.3.2. The effect of $U_A(1)$ breaking and its fate at high temperature is analyzed in Section 4.3.3. In order to gain a better understanding of the mechanisms underlying symmetry breaking at finite temperature and density in our *Fierz*-complete study involving 10 four-quark interaction channels, we then discuss the RG flow of the *Fierz*-complete system in the large-N_c limit in Section 4.3.4. In Section 4.3.5, we finally analyze the dynamics of the *Fierz*-complete system with the aid of a two-channel approximation which is composed of the scalar-pseudoscalar channel and a diquark channel associated with the condensate (2.47) introduced in Section 2.2. This study is motivated by our analysis of the "hierarchy" in the *Fierz*-complete system. There, we also comment on the effect of *Fierz*-incomplete approximations on the curvature of the finite-temperature phase boundary at small chemical potential. We close this section with a concluding summary in Section 4.3.6.

4.3.1 Definition of the model

Before we introduce the *Fierz*-complete set of four-quark interactions defining our model, we first review the relevant symmetries that constrain these interaction channels. In Section 4.1.1, we discussed aspects of conventional NJL-type models often employed in studies of the low-energy dynamics of QCD and introduced the classical action

$$S[\bar{\psi},\psi]=\int_0^\beta \mathrm{d}\tau \int \mathrm{d}^3x\ \left\{\bar{\psi}\left(\mathrm{i}\partial\!\!\!/ - \mathrm{i}\mu\gamma_0\right)\psi+\frac{1}{2}\bar{\lambda}_{(\sigma\text{-}\pi)}\left[\left(\bar{\psi}\psi\right)^2-\left(\bar{\psi}\gamma_5\tau_i\psi\right)^2\right]\right\}. \tag{4.54}$$

Let us begin our symmetry analysis by noting that the action (4.54) is invariant under (global) $SU(N_\mathrm{c})$ color rotations of the quark fields. As we do not allow for an explicit quark mass term, we also have an invariance under (independent) global flavor rotations of the left- and right-handed quark fields, $\psi_{\mathrm{L,R}}=\frac{1}{2}(1\pm\gamma_5)\psi$, i.e., the action is invariant under $SU_\mathrm{L}(2)\otimes SU_\mathrm{R}(2)$ transformations. The spontaneous breakdown of this chiral symmetry is associated with the formation of a corresponding chiral condensate $\langle\bar{\psi}\psi\rangle$ rendering the quarks massive, see our discussion in Section 2.1.2.

The action (4.54) is also invariant under simple global phase transformations,

$$U_\mathrm{V}(1):\bar{\psi}\mapsto\bar{\psi}\mathrm{e}^{-\mathrm{i}\alpha},\ \ \psi\mapsto\mathrm{e}^{\mathrm{i}\alpha}\psi\,, \tag{4.55}$$

but is *not* invariant under axial phase transformations:

$$U_\mathrm{A}(1):\bar{\psi}\mapsto\bar{\psi}\mathrm{e}^{\mathrm{i}\gamma_5\alpha},\ \ \psi\mapsto\mathrm{e}^{\mathrm{i}\gamma_5\alpha}\psi\,. \tag{4.56}$$

Note that, in contrast to the case of a single fermion species, i.e., the case of one color and one flavor, a broken $U_\mathrm{A}(1)$ symmetry does not necessarily entail the existence of a finite expectation value $\langle\bar{\psi}\psi\rangle$ as associated with spontaneous chiral symmetry breaking. However, the spontaneous breakdown of the chiral symmetry also entails the breakdown of the $U_\mathrm{A}(1)$ symmetry [203]. In fact, the $U_\mathrm{A}(1)$ symmetry is not realized in nature but anomalously broken by topologically non-trivial gauge configurations [223, 224], even if the chiral $SU_\mathrm{L}(2)\otimes SU_\mathrm{R}(2)$ is restored, see Section 2.1.2.

In any case, in the action (4.54), we can artificially restore the $U_\mathrm{A}(1)$ symmetry by adding an additional four-quark channel,

$$\sim \det\nolimits_\mathrm{f}\left(\bar{\psi}(1+\gamma_5)\psi\right)+\det\nolimits_\mathrm{f}\left(\bar{\psi}(1-\gamma_5)\psi\right)\,, \tag{4.57}$$

provided that the coupling associated with this channel is adjusted suitably relative to the coupling $\bar{\lambda}_{(\sigma\text{-}\pi)}$ of the scalar-pseudoscalar channel, see also Ref. [119].[21] Indeed, the topologically non-trivial gauge configurations violating the $U_{\mathrm{A}}(1)$ symmetry can be recast into a four-quark interaction channel of the form (4.57) in the case of two-flavor QCD [224, 239, 416–418]. We shall come back to the issue of $U_{\mathrm{A}}(1)$ symmetry breaking below.

Apart from the chiral symmetry and the $U_{\mathrm{A}}(1)$ symmetry, the $U_{\mathrm{V}}(1)$ symmetry associated with baryon number conservation may also be spontaneously broken. In contrast to chiral symmetry breaking, this is indicated by the formation of, e.g., the diquark condensate

$$\Delta^l \sim \langle \mathrm{i}\bar{\psi}^C \gamma_5 \epsilon_{(f)} \varepsilon^l_{(c)} \psi \rangle\,, \tag{4.58}$$

carrying a net baryon and net color charge. This condensate was introduced and discussed in more detail in Section 2.2. Here, we briefly recapitulate the main characteristics: The diquark condensate Δ^l is a state with $J^P = 0^+$ and has been found to be most dominantly generated by one-gluon exchange [109] and topologically non-trivial gauge configurations [109, 110]. The flavor antisymmetric structure of this color-superconducting condensate corresponds to a singlet representation of the global chiral group which implies that the formation of such a condensate does not violate the chiral symmetry of the theory [116]. Note that this is different in QED-like theories where the formation of a *Poincaré*-invariant superconducting ground state also requires the chiral symmetry to be broken, see, e.g., our study of the NJL model with a single fermion species in Section 4.2. Instead, the formation of the color-superconducting condensate Δ^l in QCD comes at the price of a broken $SU(N_{\mathrm{c}})$ color symmetry.

In addition to the breaking of the aforementioned symmetries, we have to deal again with the explicit breaking of *Poincaré* invariance because of the presence of a heat bath and a finite quark chemical potential. With respect to the fundamental discrete symmetries associated with charge conjugation, time reversal, and parity, we add that invariance under parity transformations and time reversal transformations remain intact in the presence of a finite quark chemical potential as the latter only breaks explicitly the charge conjugation symmetry.

Based on our symmetry considerations above, let us now specify the *Fierz*-complete basis $\mathcal{B}$ of four-quark interaction channels $\mathcal{L}_j$ which we use to parametrize our ansatz (4.3) for the effective average action at leading order of the derivative expansion, see Section 4.1.2. Recall that we assume here that the $U_{\mathrm{A}}(1)$ symmetry is broken explicitly, see below for a detailed discussion of this issue. We then find that this basis is composed of 10 four-quark channels. We choose six of them to be invariant under $SU(N_{\mathrm{c}}) \otimes SU_{\mathrm{L}}(2) \otimes SU_{\mathrm{R}}(2) \otimes U_{\mathrm{V}}(1) \otimes U_{\mathrm{A}}(1)$ transformations:

$$\mathcal{L}_{(V+A)_\parallel} = \left(\bar{\psi}\gamma_0\psi\right)^2 + \left(\bar{\psi}\mathrm{i}\gamma_0\gamma_5\psi\right)^2\,, \tag{4.59}$$

$$\mathcal{L}_{(V+A)_\perp} = \left(\bar{\psi}\gamma_i\psi\right)^2 + \left(\bar{\psi}\mathrm{i}\gamma_i\gamma_5\psi\right)^2\,, \tag{4.60}$$

$$\mathcal{L}_{(V-A)_\parallel} = \left(\bar{\psi}\gamma_0\psi\right)^2 - \left(\bar{\psi}\mathrm{i}\gamma_0\gamma_5\psi\right)^2\,, \tag{4.61}$$

$$\mathcal{L}_{(V-A)_\perp} = \left(\bar{\psi}\gamma_i\psi\right)^2 - \left(\bar{\psi}\mathrm{i}\gamma_i\gamma_5\psi\right)^2\,, \tag{4.62}$$

---

[21] Note that the determinant in Eq. (4.57) is taken in flavor space.

$$\mathcal{L}_{(V+A)^{\mathrm{adj}}_{\parallel}} = \left(\bar{\psi}\gamma_0 T^a\psi\right)^2 + \left(\bar{\psi}\mathrm{i}\gamma_0\gamma_5 T^a\psi\right)^2 , \tag{4.63}$$

$$\mathcal{L}_{(V-A)^{\mathrm{adj}}_{\perp}} = \left(\bar{\psi}\gamma_i T^a\psi\right)^2 - \left(\bar{\psi}\mathrm{i}\gamma_i\gamma_5 T^a\psi\right)^2 . \tag{4.64}$$

The remaining four channels are then chosen to be invariant under $SU(N_{\mathrm{c}}) \otimes SU_{\mathrm{L}}(2) \otimes SU_{\mathrm{R}}(2) \otimes U_{\mathrm{V}}(1)$ transformations but break the $U_{\mathrm{A}}(1)$ symmetry explicitly:

$$\mathcal{L}_{(\sigma\text{-}\pi)} = \left(\bar{\psi}\psi\right)^2 - \left(\bar{\psi}\gamma_5\tau_i\psi\right)^2 , \tag{4.65}$$

$$\mathcal{L}_{(S+P)_-} = \left(\bar{\psi}\psi\right)^2 - \left(\bar{\psi}\gamma_5\tau_i\psi\right)^2 + \left(\bar{\psi}\gamma_5\psi\right)^2 - \left(\bar{\psi}\tau_i\psi\right)^2 , \tag{4.66}$$

$$\mathcal{L}_{\mathrm{csc}} = 4\left(\mathrm{i}\bar{\psi}\gamma_5\tau_2\, T^A\psi^C\right)\left(\mathrm{i}\bar{\psi}^C\gamma_5\tau_2\, T^A\psi\right) , \tag{4.67}$$

$$\mathcal{L}_{(S+P)^{\mathrm{adj}}_{-}} = \left(\bar{\psi}T^a\psi\right)^2 - \left(\bar{\psi}\gamma_5\tau_i T^a\psi\right)^2 + \left(\bar{\psi}\gamma_5 T^a\psi\right)^2 - \left(\bar{\psi}\tau_i T^a\psi\right)^2 , \tag{4.68}$$

where the T^a's denote again the generators of $SU(N_{\mathrm{c}})$. Note that this basis is not unique. In principle, we can combine elements of the basis to perform a basis transformation. Our present choice is motivated by the four-quark channels conventionally employed in QCD low-energy models. Apparently, the scalar-pseudoscalar channel appearing in Eq. (4.54) is given by the channel $\mathcal{L}_{(\sigma\text{-}\pi)}$. A channel of the form of Eq. (4.57) is associated with the presence of topologically non-trivial gauge configurations and is given by the channel $\mathcal{L}_{(S+P)_-}$ up to a numerical factor. There is also a channel associated with the formation of a diquark condensate of the type (4.58) in our basis. In fact, taking into account that such a condensate leaves the chiral symmetry intact, the corresponding four-quark channel $\mathcal{L}_{\mathrm{csc}}$ can be constructed from the tensor structure of the condensate (4.58) by rewriting the antisymmetric tensors $\epsilon_{(f)}$ and $\varepsilon^{l}_{(c)}$ in terms of the antisymmetric generators in flavor and color space, respectively, see our discussion in Section 2.2. Accordingly, our conventions in Eq. (4.67) are such that we only sum over the antisymmetric (A) generators of the $SU(N_{\mathrm{c}})$ color group. The normalization of this channel is chosen as in the standard literature (see, e.g., Ref. [115]). Note that the channel $\mathcal{L}_{\mathrm{csc}}$ is invariant under $SU(N_{\mathrm{c}}) \otimes SU_{\mathrm{L}}(2) \otimes SU_{\mathrm{R}}(2) \otimes U_{\mathrm{V}}(1)$ transformations. The formation of a diquark condensate then goes along with the breakdown of the $U_{\mathrm{V}}(1)$ symmetry as well as the $SU(N_{\mathrm{c}})$ color symmetry, for details we refer again to our discussion in Section 2.2. Finally, we add that the channel (4.68) may be viewed as a counterpart of the channel $\mathcal{L}_{(S+P)_-}$ with a non-trivial color structure.

It is worth pointing out that our *Fierz*-complete set of pointlike four-quark interactions allows us to monitor $U_{\mathrm{A}}(1)$ symmetry breaking. Indeed, by requiring that the effective action Γ is invariant under $U_{\mathrm{A}}(1)$ transformations, we find the following two sum rules for the four pointlike couplings violating the $U_{\mathrm{A}}(1)$ symmetry:

$$\mathcal{S}^{(1)}_{U_{\mathrm{A}}(1)} = \bar{\lambda}_{\mathrm{csc}} + \bar{\lambda}_{(S+P)^{\mathrm{adj}}_{-}} = 0 , \tag{4.69}$$

$$\mathcal{S}^{(2)}_{U_{\mathrm{A}}(1)} = \bar{\lambda}_{(S+P)_-} - \frac{N_{\mathrm{c}}-1}{2N_{\mathrm{c}}}\,\bar{\lambda}_{\mathrm{csc}} + \frac{1}{2}\bar{\lambda}_{(\sigma\text{-}\pi)} = 0 , \tag{4.70}$$

see Appendix B.3.2 for a derivation. These two sum rules are only fulfilled simultaneously if the $U_\mathrm{A}(1)$ symmetry of the theory is intact. For example, choosing only the scalar-pseudoscalar coupling $\bar{\lambda}_{(\sigma\text{-}\pi)}$ to be finite in the classical action (4.54), we find that the $U_\mathrm{A}(1)$ symmetry is violated. This symmetry is only found to be approximately restored on the quantum level at high temperatures, see our discussion in Section 4.3.3.

From the sum rules (4.69) and (4.70), we deduce that the four-dimensional space spanned by the $U_\mathrm{A}(1)$-violating channels contains a $U_\mathrm{A}(1)$-symmetric subspace. In particular, the two sum rules imply that a *Fierz*-complete basis of pointlike four-quark interactions in case of a theory invariant under $SU(N_\mathrm{c}) \otimes SU_\mathrm{L}(2) \otimes SU_\mathrm{R}(2) \otimes U_\mathrm{V}(1) \otimes U_\mathrm{A}(1)$ transformations is composed of eight channels.[22]

The RG flow equations for the *Fierz*-complete basis of four-quark interaction channels defined by Eqs. (4.59)-(4.68) are listed in Appendix F.2. The RG flow is again governed by the two classes of 1PI diagrams shown in Fig. 4.1, where each class contains diagrams which are associated with contributions longitudinal and transversal to the heat bath. The corresponding threshold functions can be found in Appendix E.1.

Scale fixing procedure

Let us now discuss the scale-fixing procedure underlying the calculations in our study of the model (4.3) with the basis (4.59)-(4.68). The values of the 10 four-quark couplings at the initial RG scale $k = \Lambda$ can be considered as free parameters of our model. To pin them down, let us consider RG studies of QCD where the strengths of pointlike gluon-induced four-quark interactions have been analyzed in detail in the vacuum limit within a *Fierz*-complete setting [192, 195, 384]. There, it was found that the scalar-pseudoscalar channel $\mathcal{L}_{(\sigma\text{-}\pi)}$ is generated predominantly at high momentum scales $p \sim k$. Moreover, it was found that this channel remains to be the most dominant one over a wide range of scales down to $k \sim 1\,\mathrm{GeV}$, i.e., the modulus of any other four-quark coupling remains smaller than the one of the scalar-pseudoscalar coupling. With respect to our present study, it is also reasonable to expect that effects associated with an explicit breaking of *Poincaré* and $\mathcal{C}$ invariance are subleading as long as $T/k \ll 1$ and $\mu/k \ll 1$. In the light of these facts, we only choose the scalar-pseudoscalar coupling $\bar{\lambda}_{(\sigma\text{-}\pi)}$ to be finite at the initial RG scale Λ and set all other four-quark couplings to zero, similarly to our approach in Section 4.2. Thus, at the initial scale, we are left with the action S given in Eq. (4.54), $\Gamma_{k=\Lambda} = S$. This implies that we assume the $U_\mathrm{A}(1)$ symmetry to be broken explicitly at the initial RG scale.[23] Clearly, these considerations do not represent a rigorous determination of the initial conditions of our NJL-type model from QCD but rather serve as a motivation for our scale-fixing procedure in the present study. The determination of the initial conditions from QCD would require the dynamical inclusion of gauge degrees of freedom which we discuss in Chapter 5, see also the RG studies [192, 193, 384, 391–394] on this subject.

---

[22] Albeit possible, we do not use a basis of four-quark channels composed of an eight-dimensional subspace invariant under $SU(N_\mathrm{c}) \otimes SU_\mathrm{L}(2) \otimes SU_\mathrm{R}(2) \otimes U_\mathrm{V}(1) \otimes U_\mathrm{A}(1)$ transformations and a remaining two-dimensional subspace only invariant under $SU(N_\mathrm{c}) \otimes SU_\mathrm{L}(2) \otimes SU_\mathrm{R}(2) \otimes U_\mathrm{V}(1)$ transformations in order to make better contact to conventional QCD model studies.

[23] In Section 4.3.3, we discuss the effect of $U_\mathrm{A}(1)$ symmetry breaking in more detail with the aid of the sum rules (4.69) and (4.70).

The initial condition of the remaining coupling, the scalar-pseudoscalar coupling $\bar{\lambda}_{(\sigma\text{-}\pi)}$, can be fixed in different ways. For example, see Section 4.2, we may tune it in the vacuum limit such that the resulting symmetry breaking scale k_{cr} leads to a given value for the critical temperature at vanishing chemical potential. In the following, however, we employ a different procedure which exploits the mean-field gap equation (4.12) for the chiral order-parameter field in a scalar-pseudoscalar one-channel approximation as discussed in Section 4.1.3. From this equation (4.12) we inferred that for a given UV scale Λ the quark mass $\bar{m}_{\mathrm{q}}$ only depends on the "strength" $\Delta\lambda_{(\sigma\text{-}\pi)}$ of the scalar-pseudoscalar coupling relative to its critical value for chiral symmetry breaking, see Eq. (4.11). In the following, we shall fix the scale in our studies by setting $\bar{m}_{\mathrm{q}} \approx 0.300\,\mathrm{GeV}$ for the constituent quark mass in order to relate our model study to QCD. In terms of the scalar-pseudoscalar coupling, this choice corresponds to $\Delta\lambda_{(\sigma\text{-}\pi)} \approx 0.234$ for $\Lambda/\bar{m}_{\mathrm{q}} \approx 10/3$.

Let us now exploit the relation between the order-parameter potential and the RG flow of four-quark couplings to fix the scale in our study of the phase diagram below. As our discussion of the one-channel approximation in Section 4.1.3 showed, we can translate the "strength" $\Delta\lambda_{(\sigma\text{-}\pi)}$ into a corresponding chiral symmetry breaking scale k_{cr} according to the relation (4.18). At this scale the scalar-pseudoscalar coupling diverges, indicating the onset of spontaneous symmetry breaking. With the help of this relation, we can now compute the value of the chiral symmetry breaking scale in the mean-field approximation. Using $\Delta\lambda_{(\sigma\text{-}\pi)} \approx 0.234$ extracted from the mean-field calculation above for $\bar{m}_{\mathrm{q}} \approx 0.300\,\mathrm{GeV}$ and $\Lambda/\bar{m}_{\mathrm{q}} \approx 10/3$, we obtain $k_0/\bar{m}_{\mathrm{q}} \equiv k_{\mathrm{cr}}/\bar{m}_{\mathrm{q}} \approx 1.613$, where k_0 serves as a reference scale in the following, i.e., we shall measure all physical observables in units of k_0.

In all our studies of the phase diagram presented below, we shall set all four-quark couplings to zero at the initial RG scale Λ except for the scalar-pseudoscalar coupling $\lambda_{(\sigma\text{-}\pi)}$. The latter is tuned at this scale such that, at $T = \mu = 0$, we obtain $k_{\mathrm{cr}} = k_0$, i.e., the value of the critical scale is always tuned to agree identically with its value in the mean-field approximation. This ensures comparability between the results of our studies from different approximations. Moreover, since k_0 is directly related to the constituent quark mass in the mean-field approximation, $k_0/\bar{m}_{\mathrm{q}} \approx 1.613$, this allows at least for a rough translation of our results for the phase transition temperatures obtained from, e.g., our *Fierz*-complete set of flow equations into physical units. Of course, such a translation is only approximative. We always have to keep in mind that the use of the same value for k_0 in different approximations may not necessarily translate into the same value for the low-energy observables, such as the constituent quark mass. In any case, considering the critical temperature at $\mu = 0$ as an example for an low-energy observable being sensitive to the vacuum constituent quark mass and also accessible within our framework, we find that this quantity does not depend strongly on our approximations associated with different numbers of four-quark channels. This observation may be traced back to the fact that we find the scalar-pseudoscalar channel to be most dominant at $\mu = 0$, therefore governing the low-energy dynamics in this regime, see our discussion below.

To close this section on the scale fixing procedure, let us briefly add that we can obtain the one-channel approximation from the set of flow equations for the *Fierz*-complete basis of four-quark interactions given in Appendix F.2 by setting all couplings but the scalar-pseudoscalar coupling to zero and also dropping their flow equations. In this way we recover Eq. (4.15) discussed in Section 4.1.3 with the non-*Gaußian* fixed point

$$\lambda^{*}_{(\sigma\text{-}\pi)} = \frac{2\pi^2}{N_{\mathrm{c}} + \frac{1}{2}}\,. \tag{4.71}$$

As noted below Eq. (4.15), the value of the non-*Gaußian* fixed point indeed agrees with the critical value of the scalar-pseudoscalar coupling in the mean-field approximation for $N_{\mathrm{c}} \gg 1$. The contribution $\sim 1/N_{\mathrm{c}}$ can be shown to be related to quantum corrections to the *Yukawa* coupling in a partially bosonized formulation of our model [333, 397]. On account of the *Fierz* ambiguity, however, note that the prefactor of the term quadratic in the four-quark coupling is not unique. Yet again, the actual value of the non-*Gaußian* fixed point is of no importance in regard to the formation of a non-trivial ground state as only the "strength" $\Delta\lambda_{(\sigma\text{-}\pi)}$ at the initial RG scale Λ matters, see Section 4.1.3 for a more detailed discussion.

4.3.2 Phase structure

Mean-field and one-channel approximation

Let us now study the phase diagram in the plane spanned by the temperature and quark chemical potential. To begin with, we consider once more an approximation in which we only take into account the scalar-pseudoscalar four-quark coupling. As described above, we obtain the RG flow equation from the full set of equations for the *Fierz*-complete basis of four-quark interactions by setting all couplings but the scalar-pseudoscalar coupling to zero and also neglecting their flow equations. In this way, we essentially recover Eq. (4.1.3), i.e.,

$$\partial_t \lambda_{(\sigma\text{-}\pi)} = 2\lambda_{(\sigma\text{-}\pi)} - 16 v_4 \left(2N_{\mathrm{c}} + 1\right) \lambda^2_{(\sigma\text{-}\pi)}\, \mathcal{L}(\tau, \tilde{\mu}_\tau)\,, \tag{4.72}$$

here with

$$\mathcal{L}(\tau, \tilde{\mu}_\tau) = 4\left(l^{(\mathrm{F})}_{\parallel +}(\tau, 0, -i\tilde{\mu}_\tau) + l^{(\mathrm{F})}_{\perp +}(\tau, 0, -i\tilde{\mu}_\tau)\right) \tag{4.73}$$

and the corresponding non-Gaussian fixed point (4.71) in the vacuum limit.[24] Note that the auxiliary function is again normalized in the limit of zero temperature and chemical potential, i.e., $\mathcal{L}(0,0) = 1$. The threshold functions appearing in Eq. (4.73) are associated with the loop integral depicted in the left panel of Fig. 4.1.

As outlined in Section 4.1.3, the flow equation (4.72) can be solved analytically, even at finite temperature and quark chemical potential. The solution can then be employed to compute the critical temperature $T_{\mathrm{cr}} = T_{\mathrm{cr}}(\mu)$ as a function of the quark chemical potential μ. The critical temperature is again defined as the temperature at which the scalar-pseudoscalar four-quark coupling diverges at $k \to 0$, i.e., it is defined as the highest temperature for which the four-quark coupling still diverges, see Eq. (4.22). The formal solution of the flow equation then allows the derivation of the implicit equation (4.24) for the critical temperature,

---

[24] As before in Section 4.2, we do not take into account the renormalization of the chemical potential, i.e., we set $Z_\mu = 1$.

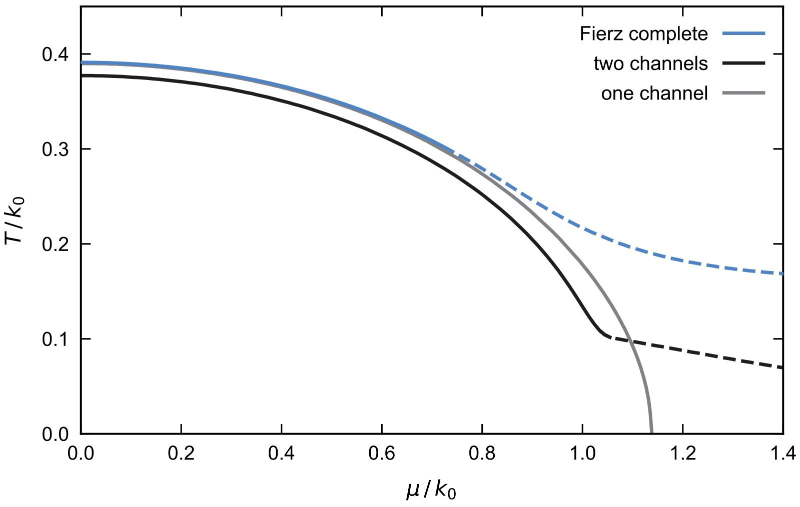

Figure 4.10: Phase boundary associated with the spontaneous breakdown of at least one of the fundamental symmetries of our NJL-type model as obtained from a one-channel, two-channel, and *Fierz*-complete study of the ansatz (4.3) with the *Fierz*-complete basis defined by Eqs. (4.59)-(4.68), see main text for details.

illustrating that the critical temperature depends on our choice for the UV scale Λ as well as the scale k_0 which we keep fixed. We generalize again this definition of the critical temperature to the case of more than one channel as described in Section 4.1.3.

In Fig. 4.10, we show the critical temperature as a function of the quark chemical potential for the one-channel approximation (gray line) as obtained from a solution of the corresponding implicit equation (4.24) derived from the flow equation (4.72). For $\mu = 0$, we obtain $T_{\mathrm{cr}}/k_0 \approx 0.390$ ($T_{\mathrm{cr}} \approx 0.190\,\mathrm{GeV}$). For increasing μ, the critical temperature then decreases monotonously and eventually vanishes at $\mu/k_0 = \mu_{\mathrm{cr}}/k_0 \approx 1.14$ ($\mu_{\mathrm{cr}} \approx 0.552\,\mathrm{GeV}$).

We emphasize again that our definition of the critical temperature is associated with a sign change of the chiral order-parameter potential at the origin. In our present approximation, our result for $T_{\mathrm{cr}}(\mu)$ therefore only describes the phase boundary in case of a second-order transition. Our criterion is not sensitive to a first-order transition. However, it allows us to detect the line of metastability separating a regime associated with a negative curvature of the order-parameter potential at the origin (e.g. at low temperature and small quark chemical potential) from a regime where the curvature changes its sign but the true ground state is still assumed for a finite expectation value of the order-parameter field. Such lines of metastability usually emerge in the vicinity of a first-order transition. In particular, for a given temperature, the chemical potential associated with the emergence of a metastable state at the origin of the potential is less or equal than the chemical potential of the associated first-order transition, see Ref. [118] for the first NJL model analysis of this aspect.

It is instructive to compare the results for the phase boundary from our RG study with those obtained from a solution of the mean-field gap equation (4.12).[25] To ensure comparability,

---

[25] The gap equation for finite T and μ is obtained from Eq. (4.12) with Eq. (4.9) by replacing $\int \mathrm{d}^4p/(2\pi)^4$ with $T\sum_n \int \mathrm{d}^3p/(2\pi)^3$. Moreover, we have to replace p^2 with $(\nu_n^2 - \mathrm{i}\mu)^2 + \vec{p}^{\,2}$, where $\nu_n = (2n+1)\pi T$, except in the argument of the regulator shape function due to our conventions.

we employ of course the same regularization scheme as in our RG study. We then find that the phase transition line from our RG study agrees identically with the second-order phase transition line of the mean-field study up to a first-order endpoint at $(\mu/k_0, T/k_0) \approx (0.951, 0.207)$. As expected, beyond this point, the phase transition line obtained from our RG study agrees identically with the line of metastability in the mean-field phase diagram. The comparatively large extent of the phase boundary in μ-direction can be traced back to the comparatively large σ-meson mass $\bar{m}_\sigma/\bar{m}_\mathrm{q} \approx 2.67$ ($\bar{m}_\sigma \approx 0.800\,\mathrm{GeV}$) found in the vacuum limit of our mean-field calculation for the employed set of parameters, i.e., $\Delta\lambda_{(\sigma\text{-}\pi)}$ and Λ.[26] In fact, it has already been found in previous mean-field calculations that the critical point separating a first-order phase transition line from a second-order phase transition line can be shifted continuously to larger values of the quark chemical potential by increasing the mass of the σ meson [419]. Even more, for suitably chosen sets of model parameters it can even be made disappear, leaving us with only a second-order transition line [117]. Note that this highlights the strong scheme dependence as the σ-meson mass can be tuned by suitable variations of the constituent quark mass and the UV cutoff Λ. Since the actual value of the latter should always be viewed against the background of the employed regularization scheme, the scheme unavoidably belongs to the definition of the model, at least in four *Euclidean* space-time dimensions. Of course, we could also use smaller values for Λ which would lead to a smaller mass of the σ-meson. However, this then leads to strong cutoff effects as both the temperatures as well as the quark chemical potentials considered in this work would then be of the order of the UV scale Λ. In order to at least suppress such unwanted effects, we have simply chosen $\Lambda/k_0 \approx 2.07$ as the primary focus is here on the effect of *Fierz* completeness. In our discussion of RG consistency in Section 3.3, we have presented a general approach based on the FRG perspective how cutoff artifacts and renormalization scheme dependences can be consistently removed in low-energy effective models which are subject to a validity bound. We shall apply this approach in Section 6.1.2 and analyze in detail the effect of such cutoff corrections as entailed by the RG consistency criterion.

Symmetry breaking patterns and *Fierz* completeness

Let us now analyze the phase diagram as obtained from an RG flow study of the *Fierz*-complete set of four-quark interactions, see Appendix F.2 for the RG flow equations. Such an analysis goes well beyond studies in the mean-field limit. Indeed, mean-field studies of NJL-type low-energy models have been found to exhibit a residual ambiguity related to the possibility to perform *Fierz* transformations, even if a *Fierz*-complete set of four-quark interactions is taken into account [336], see also our discussion in Section 4.1.1 and Ref. [211] for an introduction. Results from mean-field calculations therefore potentially depend on an unphysical parameter which reflects the actual choice of the mean field in the various channels.

As discussed above, we fix the scale in our *Fierz*-complete studies by setting all but the scalar-pseudoscalar coupling to zero at the initial RG scale Λ. The latter is tuned at $T = \mu = 0$ such that the critical scale k_0 associated with diverging four-quark couplings agrees identically with its counterpart in the mean-field calculation. For our calculations at finite temperature

---

[26] The computation of the σ-meson mass requires fixing the *Yukawa* coupling $\bar{h}$ since $m_q = \langle\sigma\rangle = \bar{h} f_\pi$. Here, we use $\bar{h} \approx 3.45$ corresponding to $f_\pi \approx 87.0\,\mathrm{MeV}$ for the pion decay constant.

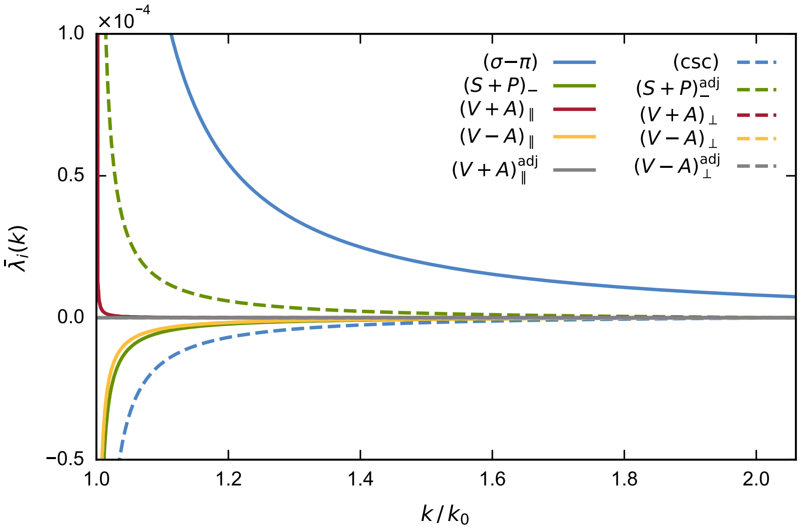

Figure 4.11: Renormalized (dimensionful) four-quark couplings as a function of the RG scale k at $T = 0$ and $\mu = 0$ as obtained from our *Fierz*-complete study. Note that the *Fierz*-complete basis is effectively composed of only six channels in the vacuum limit since $\mathcal{C}$ invariance is intact and the *Euclidean* time direction is not distinguished. In particular, we have $\bar{\lambda}_{(V+A)_\parallel^{\mathrm{adj}}} \equiv 0 \equiv \bar{\lambda}_{(V-A)_\perp^{\mathrm{adj}}}$ in this limit.

and/or quark chemical potential, we then use the same set of initial conditions as in the vacuum limit, i.e., at $T = \mu = 0$. The scale dependence of the (dimensionful) renormalized four-quark couplings at $T = \mu = 0$ is shown in Fig. 4.11. We observe that the dynamics of the theory in this case is clearly dominated by the scalar-pseudoscalar interaction channel; the modulus of all other couplings is at least one order of magnitude smaller than the modulus of the scalar-pseudoscalar coupling. The dominance of this channel may indicate that the ground state in the vacuum limit is governed by chiral symmetry breaking. However, we emphasize again that such an analysis based on the strength of four-quark interactions has to be taken with some care: It neither rules out the possible formation of other condensates associated with subdominant channels nor proves the formation of a condensate associated with the most dominant channel. Such an analysis can only yield indications for the actual structure of the ground state, see Section 4.1.3 for a detailed discussion and also Ref. [395].

In the vacuum limit, the observation of the dominance of the scalar-pseudoscalar channel may be considered trivial as it may be exclusively triggered by our choice for the initial conditions. Increasing now the temperature at vanishing quark chemical potential, we still observe a dominance of the scalar-pseudoscalar channel which persists even up to high temperatures beyond the critical temperature $T_{\mathrm{cr}}(\mu = 0)/k_0 \approx 0.391$. This is illustrated in the left panel of Fig. 4.12 where the scale dependence of the various four-quark couplings is shown for $T \simeq T_{\mathrm{cr}}(\mu = 0)$ at $\mu = 0$. At least in units of k_0, it also appears that the critical temperature at $\mu = 0$ in our *Fierz*-complete study agrees very well with the one from the one-channel approximation. However, we note that this could be misleading as choosing the same value for k_0 in our *Fierz*-complete study and in our one-channel approximation may not necessarily lead to the same values of low-energy observables (e.g. the constituent quark mass),

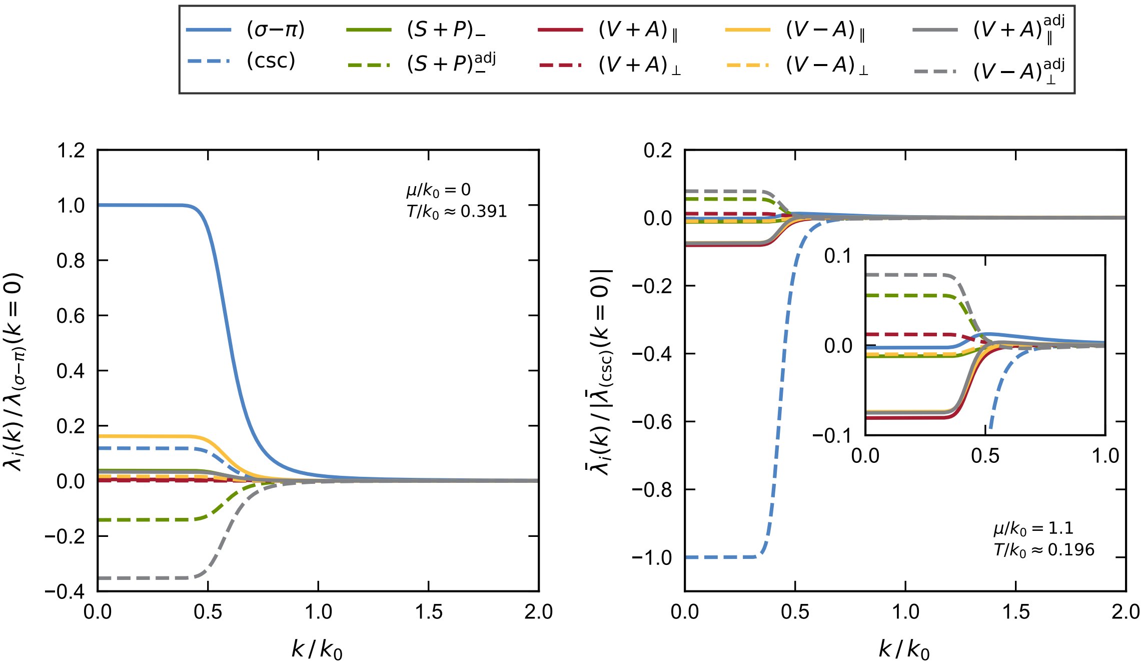

FIGURE 4.12: Scale dependence of the various renormalized (dimensionful) four-quark couplings at $\mu = 0$ and $T/k_0 \simeq T_{\mathrm{cr}}(\mu = 0)/k_0 \approx 0.391$ (left panel) as well as at $\mu/k_0 \approx 1.1$ and $T/k_0 \simeq T_{\mathrm{cr}}(\mu)/k_0 \approx 0.196$ (right panel).

although the flow in the vacuum limit is also strongly dominated by the scalar-pseudoscalar channel in the *Fierz*-complete analysis. Thus, direct quantitative comparisons of the results from our various different approximations should be taken with care. Still, we expect that qualitative comparisons are meaningful.

Following now the critical temperature T_{cr} as a function of μ starting from $\mu = 0$, we find that the scalar-pseudoscalar channel continues to dominate the dynamics up to $\mu/k_0 = \mu_\chi/k_0 \approx 0.734$, as depicted by the blue solid line in Fig. 4.10. In this regime, we also observe that the phase transition temperatures from our one-channel approximation agree almost identically with those from the *Fierz*-complete study, at least in units of the vacuum symmetry breaking scale k_0.[27] At first glance, this may come as a surprise. We shall therefore analyze this observation in detail in Section 4.3.4 below. Following the phase transition line beyond the point associated with the quark chemical potential μ_χ, we find that the dynamics is now clearly and exclusively dominated by the CSC (color superconducting) channel associated with the emergence of a diquark condensate Δ^l and a corresponding gap in the quark propagator, see blue dashed line in Fig. 4.10. Exemplary, this change in the "hierarchy" of the channels is illustrated in the right panel of Fig. 4.12 where the scale dependence of the various four-quark couplings is shown for $\mu/k_0 \approx 1.1$ and $T/k_0 \gtrsim T_{\mathrm{cr}}(\mu)/k_0 \approx 0.196$. We emphasize that this change in the "hierarchy" of the channels is non-trivial as it is fully triggered by the dynamics of the system when the quark chemical potential is increased. There is no fine-tuning of, e.g., the CSC coupling involved. Recall that we use identical initial conditions in the vacuum limit

---

[27] Note that $\mu_\chi/k_0 \approx 0.734$ roughly corresponds to $\mu_\chi/\bar{m}_{\mathrm{q}} \approx 1.18$ in our mean-field approximation, where $\bar{m}_{\mathrm{q}} \approx 0.3\,\mathrm{GeV}$.

as well as at finite temperature and/or quark chemical potential. From a phenomenological standpoint, it is interesting to speculate whether such a change in the "hierarchy" of the channels points to the existence of a nearby tricritical point in the phase diagram. However, as discussed above, this question cannot be unambiguously resolved here because of the approximations underlying our present study.

4.3.3 $U_{\mathrm{A}}(1)$ symmetry

Our choice for the initial conditions of the RG flow equations explicitly breaks the $U_{\mathrm{A}}(1)$ symmetry since we only choose the coupling $\lambda_{(\sigma\text{-}\pi)}$ to be finite and set all the other four-quark couplings to zero at the initial RG scale Λ. By using the sum rules (4.69) and (4.70), we can now study the fate of the (broken) $U_{\mathrm{A}}(1)$ symmetry at finite temperature and quark chemical potential when quantum fluctuations are taken into account. To be specific, in case of $U_{\mathrm{A}}(1)$-violating initial conditions, we consider the following two dimensionless quantities to "measure" the strength of the explicit $U_{\mathrm{A}}(1)$ symmetry breaking:

$$R_i = \mathcal{N}\left|\mathcal{S}^{(i)}_{U_{\mathrm{A}}(1)}\right| \,, \tag{4.74}$$

see Eqs. (4.69) and (4.70) for a definition of $\mathcal{S}^{(i)}_{U_{\mathrm{A}}(1)}$. The normalization $\mathcal{N}$ is chosen to be independent of the index i and is implicitly determined by

$$1 = (R_1 + R_2)\big|_{k=\Lambda} \,. \tag{4.75}$$

Thus, the auxiliary quantities defined in Eq. (4.74) essentially measure the strength of $U_{\mathrm{A}}(1)$ symmetry breaking relative to its strength at the initial RG scale Λ. In case of a $U_{\mathrm{A}}(1)$-symmetric theory defined by a suitable choice for the initial conditions, we find that the couplings fulfill the sum rules (4.69) and (4.70) at *all* scales k greater than the symmetry breaking scale, as it should be. Therefore, there is no need at all to consider the auxiliary quantities defined in Eq. (4.74) in such a scenario.

In Fig. 4.13, we show the scale dependence of R_1 and R_2 for two values of the quark chemical potential, $\mu = 0$ and $\mu/k_0 \approx 1.1$, and three values of the temperature for each of the two cases as obtained for our $U_{\mathrm{A}}(1)$-violating initial conditions. Let us first note that, for all values of μ considered in this work, we observe that $U_{\mathrm{A}}(1)$ breaking as "measured" by our sum rules in form of R_1 and R_2 is continuously softened when the temperature is increased. More specifically, at $\mu = 0$, for example, we already find that the strength of $U_{\mathrm{A}}(1)$ breaking remains on the level of its strength at the initial scale Λ for temperatures $T/T_{\mathrm{c}} \gtrsim 2$, i.e., its strength remains on the level as present in the classical action in this temperature regime. A qualitatively similar behavior can also be observed at finite chemical potential when the temperature is increased, see Fig. 4.13. These observations at high temperature are explained by the fact that the strength of $U_{\mathrm{A}}(1)$ symmetry breaking is controlled by the strength of the four-quark couplings. Quantum corrections to the latter are thermally suppressed at high temperature due to the presence of a thermal mass of the fermions, thus entailing the softening of $U_{\mathrm{A}}(1)$ breaking.

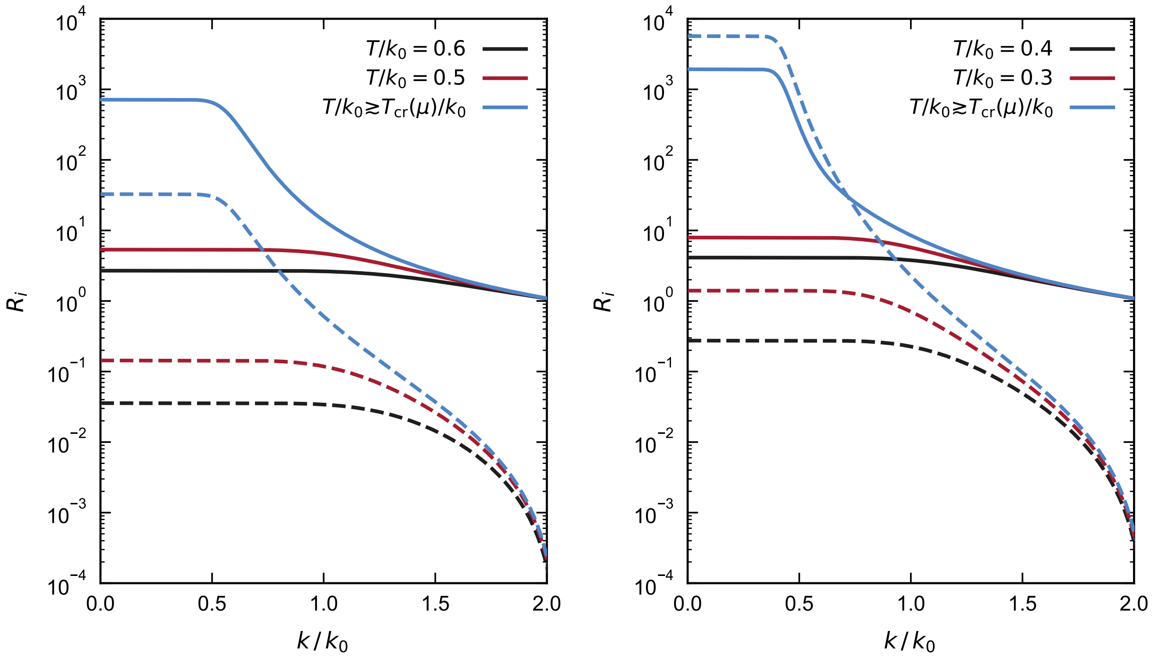

FIGURE 4.13: Scale dependence of the explicit $U_A(1)$ breaking as measured by the functions R_1 (dashed lines) and R_2 (solid lines) at $\mu = 0$ (left panel) and at $\mu/k_0 \approx 1.1$ (right panel) for three values of the temperature for each of the two cases.

Conversely, approaching the phase transition from above for a given value of the chemical potential μ, we find that the violation of the $U_A(1)$ symmetry becomes continuously stronger, in the sense that the functions R_1 and R_2 start to increase, eventually deviating significantly from their values at the initial RG scale. Thus, quantum corrections to the four-quark couplings appear to amplify $U_A(1)$ symmetry breaking when the phase governed by spontaneous symmetry breaking is approached from above, provided that $U_A(1)$ symmetry breaking is explicitly broken at the initial RG scale.

In accordance with our observation that the scalar-pseudoscalar channel is most dominant at small chemical potential (see, e.g., left panel of Fig. 4.12), we also note that $R_2 \gg R_1$ in this part of the phase diagram, see left panel of Fig. 4.13. For $\mu \gtrsim \mu_\chi$, the CSC channel then dominates the dynamics and thus R_1 and R_2 are of the same order of magnitude as both depend on the CSC coupling, see the right panels of Figs. 4.12 and 4.13. Thus, our results suggest that the dynamically generated violation of the $U_A(1)$ symmetry is driven by the dynamics of the pions at small chemical potential whereas it is driven by the dynamics of diquark degrees of freedom associated with the CSC channel at large chemical potential.

Let us finally compare the phase diagram obtained from our *Fierz*-complete study employing $U_A(1)$-symmetry violating initial conditions with the one obtained from a manifestly $U_A(1)$-symmetric *Fierz*-complete study. The latter has been calculated by tuning the couplings $\bar{\lambda}_{(\sigma\text{-}\pi)}$ and $\bar{\lambda}_{(S+P)_-}$ at the initial RG scale such that the sum rule (4.70) is fulfilled and the same value for the symmetry breaking scale k_0 as in the case with $U_A(1)$-symmetry violating initial conditions is obtained in the vacuum limit. If we choose the initial conditions in this way, i.e., such that they respect the $U_A(1)$ symmetry, then this symmetry remains intact in the

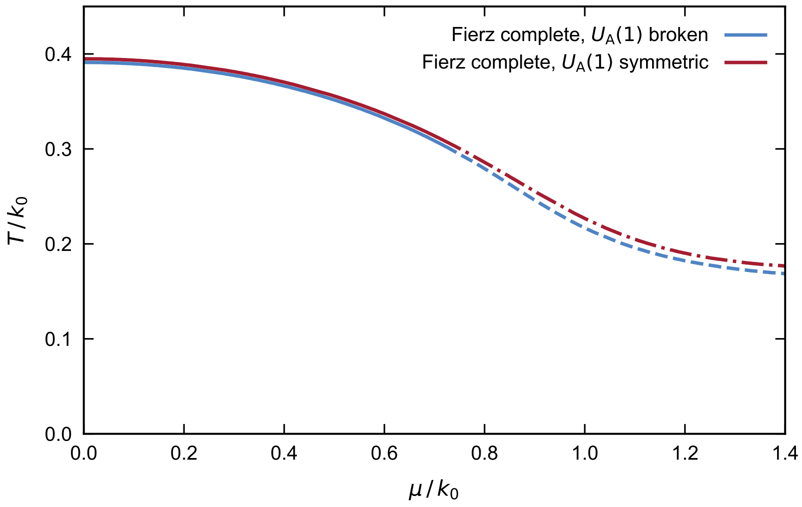

FIGURE 4.14: Phase boundary associated with the spontaneous breakdown of at least one of the fundamental symmetries of our NJL-type model as obtained from a manifestly $U_\mathrm{A}(1)$-symmetric *Fierz*-complete study of the ansatz (4.3) (red lines) and from a *Fierz*-complete study with broken $U_\mathrm{A}(1)$ symmetry (blue lines), see main text for details.

RG flow for all values of the RG scale, at least for those values of the temperature and the quark chemical potential for which the four-quark couplings remain finite on all scales $k \leq \Lambda$. For values of the temperature and the quark chemical potential at which the four-quark couplings diverge at a finite scale $k_\mathrm{cr}(T,\mu)$, the sum rules (4.69) and (4.70) are only fulfilled for $k > k_\mathrm{cr}(T,\mu)$. Below the symmetry breaking scale, the $U_\mathrm{A}(1)$ symmetry may potentially be broken spontaneously, e.g. alongside with the chiral symmetry. However, this cannot be resolved in our present study.

As already discussed above, a quantitative comparison of the results from our $U_\mathrm{A}(1)$-symmetric calculation with the ones from our explicitly $U_\mathrm{A}(1)$-violating calculation is generically difficult and has to be taken with some care. Leaving this concern aside for a moment, we observe that the phase transition lines from both studies agree almost identically on the scale of the plot. Only for larger values of the quark chemical potential, we find that the two phase transition lines start to deviate from each other. In particular, we observe that, along the phase transition line, a chemical potential μ_χ/k_0 associated with a change in the "hierarchy" of the four-quark couplings exists in both cases. Even the corresponding values of μ_χ/k_0 agree almost identically. Even more, for $\mu < \mu_\chi$, we find that the scalar-pseudoscalar channel dominates the dynamics of the theory in both cases, see solid lines in Fig. 4.14. For $\mu > \mu_\chi$, the dynamics is then dominated by the CSC channel in case of $U_\mathrm{A}(1)$-symmetry violating initial conditions, see blue dashed line in Fig. 4.14. In case of our $U_\mathrm{A}(1)$-symmetric study, however, we have a dominance of the $(V+A)_\parallel^\mathrm{adj}$-channel in this regime as depicted by the red dashed-dotted line in Fig. 4.14; see Eq. (4.63) for the definition of this channel. The condensate associated with this channel also breaks the color symmetry of our theory. In mean-field studies (see, e.g., Ref. [115] for a review), the appearance of a corresponding condensate has also been discussed. However, its generation has been found to be induced by a simultaneous formation of a color-symmetry breaking diquark condensate. In accordance with this, we observe that the four most dominant channels along the phase transition line for $\mu > \mu_\chi$ are the $(V+A)^{\mathrm{adj}}_{\parallel}$-, $(S+P)^{\mathrm{adj}}_{-}$-, CSC and $(V-A)^{\mathrm{adj}}_{\perp}$-channel in our present study. These channels are all associated with the formation of a color-symmetry breaking condensate. Apart from the $(V \pm A)_{\parallel}$-channels, color-singlet channels are found to be subdominant in this part of the phase diagram. The observed difference in the dominance pattern at large chemical potential in the $U_{\mathrm{A}}(1)$-symmetric and $U_{\mathrm{A}}(1)$-violating calculation may point to the importance of explicit $U_{\mathrm{A}}(1)$ breaking for the formation of the conventional CSC ground state at intermediate and large values of the chemical potential as discussed in early seminal works on color superconductivity, see, e.g., Refs. [98–100, 102–104, 109, 110, 420, 421].

By simply looking at the shape of the phase boundary, one may be tempted to conclude that $U_{\mathrm{A}}(1)$ breaking does not strongly affect the position of the phase transition line. However, this may be a too bold statement at this point as the same value of k_0 in the two studies potentially corresponds to different values of the low-energy observables and therefore renders a direct quantitative comparison difficult, see our discussion above. In any case, the apparent insensitivity of the phase transition line under a "transition" from $U_{\mathrm{A}}(1)$-symmetry violating initial conditions to $U_{\mathrm{A}}(1)$-symmetric initial conditions (while keeping the vacuum symmetry breaking scale fixed) is still an interesting observation. At least at small values of the chemical potential, the latter can in principle be understood from an analysis of the large-N_{c} limit which we shall consider next.

4.3.4 RG flow in the large-N_{c} limit

In order to better understand the phase structure at small chemical potential, we now analyze our RG flow equations in the large-N_{c} limit, i.e., we only take into account the leading order of the right-hand sides of our flow equations in an expansion in powers of N_{c}. For the scalar-pseudoscalar coupling, for example, we then obtain

$$\begin{aligned}
\partial_t \lambda_{(\sigma\text{-}\pi)} = {}& 2\lambda_{(\sigma\text{-}\pi)} + 32 N_{\mathrm{c}} v_4 \Big(-4\lambda^2_{(\sigma\text{-}\pi)} - 8\lambda_{(\sigma\text{-}\pi)}\lambda_{(S+P)_-} - 8\lambda^2_{(S+P)_-} \\
& - 2\lambda_{(\sigma\text{-}\pi)}\lambda_{(S+P)^{\mathrm{adj}}_-} - 4\lambda_{(S+P)_-}\lambda_{(S+P)^{\mathrm{adj}}_-} + \lambda_{(\sigma\text{-}\pi)}\lambda_{(V+A)^{\mathrm{adj}}_\parallel} \\
& + 2\lambda_{(\sigma\text{-}\pi)}\lambda_{\mathrm{csc}} + 4\lambda_{(S+P)_-}\lambda_{\mathrm{csc}} + 2\lambda_{(S+P)^{\mathrm{adj}}_-}\lambda_{\mathrm{csc}} \Big) l^{(\mathrm{F})}_{\parallel +}(\tau, 0, -i\tilde{\mu}_\tau) \\
& + 16 N_{\mathrm{c}} v_4 \Big(-8\lambda^2_{(\sigma\text{-}\pi)} - 16\lambda_{(\sigma\text{-}\pi)}\lambda_{(S+P)_-} - 16\lambda^2_{(S+P)_-} - 4\lambda_{(\sigma\text{-}\pi)}\lambda_{(S+P)^{\mathrm{adj}}_-} \\
& - 8\lambda_{(S+P)_-}\lambda_{(S+P)^{\mathrm{adj}}_-} - \frac{4}{3}\lambda^2_{(S+P)^{\mathrm{adj}}_-} + 2\lambda_{(\sigma\text{-}\pi)}\lambda_{(V+A)^{\mathrm{adj}}_\parallel} - \frac{1}{3}\lambda^2_{(V+A)^{\mathrm{adj}}_\parallel} \\
& + 4\lambda_{(\sigma\text{-}\pi)}\lambda_{\mathrm{csc}} + 8\lambda_{(S+P)_-}\lambda_{\mathrm{csc}} + \frac{4}{3}\lambda_{(S+P)^{\mathrm{adj}}_-}\lambda_{\mathrm{csc}} - \frac{4}{3}\lambda^2_{\mathrm{csc}} \Big) l^{(\mathrm{F})}_{\perp +}(\tau, 0, -i\tilde{\mu}_\tau)\,. \qquad (4.76)
\end{aligned}$$

For the remaining nine four-quark couplings, we find that the right-hand sides of their flow equations do not contain terms quadratic in the scalar-pseudoscalar coupling $\lambda_{(\sigma\text{-}\pi)}$ but at most terms linear in $\lambda_{(\sigma\text{-}\pi)}$ in the large-N_{c} limit. At first glance, this may not appear noteworthy. However, by setting all four-quark couplings but the scalar-pseudoscalar coupling to zero on the right-hand sides of the flow equations, we therefore observe that only the right-hand side of the flow equation of the scalar-pseudoscalar coupling remains finite. Indeed, from Eq. (4.76), we deduce that

$$\partial_t \lambda_{(\sigma\text{-}\pi)} = 2\lambda_{(\sigma\text{-}\pi)} - 128 N_{\mathrm{c}} v_4 \, \lambda_{(\sigma\text{-}\pi)}^2 \Big(l_{\parallel +}^{(\mathrm{F})}(\tau, 0, -i\tilde{\mu}_\tau) + l_{\perp +}^{(\mathrm{F})}(\tau, 0, -i\tilde{\mu}_\tau) \Big) \,. \tag{4.77}$$

Note that this flow equation is identical to Eq. (4.72) in the large-N_{c} limit.

The right-hand sides of the flow equations of the remaining nine couplings are identical to zero when we set all four-quark couplings but the scalar-pseudoscalar coupling to zero at the initial scale in the large-N_{c} limit. Thus, we have found a non-trivial fixed point of the RG flow at

$$\lambda_{(\sigma\text{-}\pi)}^* = \frac{2\pi^2}{N_{\mathrm{c}}} \quad \text{and} \quad \lambda_j^* = 0 \,, \tag{4.78}$$

which "sits" on the pure scalar-pseudoscalar axis of our ten-dimensional space spanned by the four-quark couplings. Here, we have $j \in \mathcal{B}$ but $j \neq (\sigma\text{-}\pi)$ and $\mathcal{B}$ denotes the set of indices associated with our *Fierz*-complete basis of four-quark interactions.

The fixed point (4.78) has only one IR repulsive direction, namely the one associated with the scalar-pseudoscalar axis. The remaining nine directions are all IR attractive. This observation already suggests that the scalar-pseudoscalar channel dominates the low-energy dynamics, provided that we initiate the RG flow sufficiently close to this fixed point.[28] We add that, the dynamics of our *Fierz*-complete system is governed by $2^{10} = 1024$ fixed points. Depending on the temperature and the quark chemical potential, some of these fixed points even appear in complex-conjugated pairs as we shall discuss in Section 4.3.5.

We emphasize that, for any finite value of N_{c}, we do not find an interacting fixed point on the pure scalar-pseudoscalar axis.[29] In fact, not only the flow equation of the scalar-pseudoscalar coupling contains terms proportional to the square of the scalar-pseudoscalar coupling but they also appear in the flow equations of other four-quark couplings. These terms now dynamically generate interactions in channels other than the scalar-pseudoscalar channel, pushing the fixed point (4.78) away from the scalar-pseudoscalar axis. We add that the very same behavior has also been observed in the vacuum limit of the $U_{\mathrm{A}}(1)$-symmetric NJL model in the large-N_{c} limit [333] and the three-dimensional *Thirring* model in the large-N_{f} limit [422].

The existence of the fixed point (4.78) and its properties provides us with an explanation of the phase structure at small quark chemical potential. First of all, from the standpoint of model studies, the existence of this fixed point in the large-N_{c} limit implies that the system always remains on the scalar-pseudoscalar axis, provided that we only choose a finite initial value for the scalar-pseudoscalar coupling and set all the other couplings to zero. Thus, the other channels do not contribute at all. Given the scale-fixing procedure underlying our calculations, it then follows that the phase boundary found in the scalar-pseudoscalar one-channel approximation agrees identically with the one from the *Fierz*-complete study in the large-N_{c} limit.[30]

---

[28] We do not aim at a precise determination of the size of the associated domain of attraction.

[29] The scalar-pseudoscalar axis may be viewed as the axis associated with conventional NJL model studies taking into account only this channel.

[30] Note that, strictly speaking, invariance under *Fierz* transformations is violated in the large-N_{c} limit.

Beyond the large-N_{c} limit, the fixed point (4.78) is pushed away from the scalar-pseudoscalar axis and now all four-quark interactions are generated dynamically even if only the scalar-pseudoscalar coupling is chosen to be finite at the initial RG scale, see, e.g., Fig. 4.11 and also our discussion in Section 4.3.5 below. However, the observed agreement of the results for the phase boundary from the one-channel and the *Fierz*-complete study suggests that this fixed point still controls the dynamics of the theory at small quark chemical potential, see Fig. 4.10. Even non-universal quantities such as the curvature of the phase boundary at $\mu = 0$ appear to be independent of the inclusion of the dynamics described by the channels other than the scalar-pseudoscalar channel. Only for large values of the quark chemical potential, $\mu > \mu_{\chi}$, the influence of the other channels becomes significant. Recall that, in the mean-field approximation, μ_{χ} is of the order of the vacuum constituent quark mass.

A word of caution needs to be added to this intriguing observation: If we choose initial conditions such that not only the scalar-pseudoscalar coupling is finite at the initial RG scale but also other four-quark couplings, then the RG flow may be potentially controlled by a different interacting fixed point, even at small chemical potential. As a consequence, the phase boundary in this regime may become more sensitive to the dynamics described by the full set of four-quark interactions. For example, one may choose a $U_{\mathrm{A}}(1)$-symmetric starting point of the RG flow by tuning the couplings $\bar{\lambda}_{(\sigma\text{-}\pi)}$ and $\bar{\lambda}_{(S+P)_-}$ such that the sum rule (4.70) is fulfilled. However, even in this case, we observe that, at small μ, the phase boundary obtained from a *Fierz*-complete $U_{\mathrm{A}}(1)$-symmetric study agrees very well with the one from our one-channel approximation as well as with the one from our *Fierz*-complete study taking $U_{\mathrm{A}}(1)$-symmetry breaking into account, see, e.g., Fig. 4.14.

4.3.5 Symmetry breaking mechanisms and fixed-point structure

Let us finally analyze the mechanisms underlying the phase structure at large chemical potential where corrections beyond the large-N_{c} approximation become important. Looking at the modulus of the four-quark couplings depicted in Fig. 4.12, we observe that the scalar-pseudoscalar coupling and the CSC coupling are the two most dominant couplings in the range of quark chemical potentials considered in this study, at least close to and above the phase transition line. For an analysis of the symmetry breaking mechanisms, it therefore appears reasonable to consider an approximation which only includes the scalar-pseudoscalar coupling and the CSC coupling. The remaining eight couplings and their flows are set to zero. The flow equations of such a two-channel approximation then read

$$\begin{aligned}\partial_t \lambda_{(\sigma\text{-}\pi)} = 2\lambda_{(\sigma\text{-}\pi)} &+ 64 v_4 \left(-(2N_{\mathrm{c}}+1)\lambda_{(\sigma\text{-}\pi)}^2 + (N_{\mathrm{c}}+1)\lambda_{(\sigma\text{-}\pi)}\lambda_{\mathrm{csc}} \right) l_{\parallel +}^{(\mathrm{F})}(\tau, 0, -i\mu_\tau) \\ &+ 64 v_4 \Big(-(2N_{\mathrm{c}}+1)\lambda_{(\sigma\text{-}\pi)}^2 + \frac{1}{3}(3N_{\mathrm{c}}-1)\lambda_{(\sigma\text{-}\pi)}\lambda_{\mathrm{csc}} \\ &\qquad - \frac{1}{3}(N_{\mathrm{c}}-2)\lambda_{\mathrm{csc}}^2 \Big) l_{\perp +}^{(\mathrm{F})}(\tau, 0, -i\mu_\tau) \,, \end{aligned} \tag{4.79}$$

$$\partial_t \lambda_{\mathrm{csc}} = 2\lambda_{\mathrm{csc}} + 64 v_4 \left(-\lambda_{(\sigma\text{-}\pi)}^2 + (N_{\mathrm{c}}-2)\lambda_{\mathrm{csc}}^2 \right) l_{\parallel +}^{(\mathrm{F})}(\tau, 0, -i\mu_\tau)$$

$$\begin{aligned} &+ 64 v_4 \left(-\lambda_{(\sigma\text{-}\pi)}^2 - 2\lambda_{(\sigma\text{-}\pi)}\lambda_{\mathrm{csc}} + 4\lambda_{\mathrm{csc}}^2 \right) l_{\parallel\pm}^{(\mathrm{F})}(\tau, 0, -i\mu_\tau) \\ &+ 64 v_4 \, \lambda_{(\sigma\text{-}\pi)}^2 \, l_{\perp+}^{(\mathrm{F})}(\tau, 0, -i\mu_\tau) \\ &+ 64 v_4 \left(\lambda_{(\sigma\text{-}\pi)}^2 - 2\lambda_{(\sigma\text{-}\pi)}\lambda_{\mathrm{csc}} + 4\lambda_{\mathrm{csc}}^2 \right) l_{\perp\pm}^{(\mathrm{F})}(\tau, 0, -i\mu_\tau) \, . \end{aligned} \tag{4.80}$$

The initial conditions are chosen as in our *Fierz*-complete study, i.e., we set the CSC coupling to zero at the initial RG scale and only tune the scalar-pseudoscalar coupling such that the value for the symmetry breaking scale in the vacuum limit is identical to its value in the *Fierz*-complete study, $k_0 = k_{\mathrm{cr}}(T = 0, \mu = 0)$, which, in turn, is identical to the value of the critical scale in our mean-field approximation. From the set of the two flow equations (4.79) and (4.80), we immediately deduce that the CSC coupling is dynamically generated in the RG flow although we set it to zero at the initial RG scale.

An asset of our two-channel approximation is that it allows for a comparatively simple but still detailed analysis of the RG flow of our system and its fixed-point structure. Of course, such an analysis is also possible for more than two couplings but it then clearly becomes more involved. In any case, in our two-channel approximation, we have four fixed points $\mathcal{F}_j = (\lambda^*_{(\sigma\text{-}\pi),j}, \lambda^*_{\mathrm{csc},j})$ in total. At $T = 0$, $\mu = 0$ and $N_{\mathrm{c}} = 3$, their coordinates are

$$\mathcal{F}_1\big|_{N_{\mathrm{c}}=3} = (0, 0) \, , \tag{4.81}$$

$$\mathcal{F}_2\big|_{N_{\mathrm{c}}=3} \approx (5.165, -1.088) \, , \tag{4.82}$$

$$\mathcal{F}_3\big|_{N_{\mathrm{c}}=3} \approx (1.262 - \mathrm{i}1.567, -8.728 - \mathrm{i}0.841) \, , \tag{4.83}$$

$$\mathcal{F}_4\big|_{N_{\mathrm{c}}=3} \approx (1.262 + \mathrm{i}1.567, -8.728 + \mathrm{i}0.841) \, , \tag{4.84}$$

where $\mathcal{F}_1$ is the N_{c}-independent *Gaußian* fixed point with two IR attractive directions. Apparently, $\mathcal{F}_3$ and $\mathcal{F}_4$ form a pair of complex conjugate fixed points. The coordinates of the non-*Gaußian* fixed points up to order $1/N_{\mathrm{c}}^2$ in a large N_{c}-expansion read

$$\begin{aligned} \mathcal{F}_2(N_{\mathrm{c}}) &= \left(\frac{2\pi^2}{N_{\mathrm{c}}} - \frac{3\pi^2}{2N_{\mathrm{c}}^2}, -\frac{\pi^2}{N_{\mathrm{c}}^2} \right) , \\ \mathcal{F}_3(N_{\mathrm{c}}) &= \left(-\frac{(3 + \mathrm{i}\sqrt{23})\pi^2}{N_{\mathrm{c}}} + \frac{(235\sqrt{10} + \mathrm{i}6\sqrt{11481})\pi^2}{4\sqrt{10}N_{\mathrm{c}}^2}, -\frac{16\pi^2}{N_{\mathrm{c}}} + \frac{(393 - \mathrm{i}13\sqrt{23})\pi^2}{2N_{\mathrm{c}}^2} \right) , \\ \mathcal{F}_4(N_{\mathrm{c}}) &= \left(-\frac{(3 - \mathrm{i}\sqrt{23})\pi^2}{N_{\mathrm{c}}} + \frac{(235\sqrt{10} + \mathrm{i}6\sqrt{11481})\pi^2}{4\sqrt{10}N_{\mathrm{c}}^2}, -\frac{16\pi^2}{N_{\mathrm{c}}} + \frac{(393 + \mathrm{i}13\sqrt{23})\pi^2}{2N_{\mathrm{c}}^2} \right) . \end{aligned}$$

These expansions have been extracted from the full analytic N_{c}-dependent expressions for the coordinates of the fixed points. We observe that the suitably N_{c}-rescaled fixed point $N_{\mathrm{c}} \cdot \mathcal{F}_2$ is shifted onto the scalar-pseudoscalar axis for $N_{\mathrm{c}} \to \infty$. Moreover, we find that this fixed point has one IR repulsive and one IR attractive direction. Thus, this fixed point corresponds to the fixed point (4.78) in the full *Fierz*-complete set of RG flow equations in the large-N_{c} limit.

In the following, we shall not consider the large-N_{c} limit any further. In order to have spontaneous symmetry breaking in the IR limit, we then choose the initial condition of the

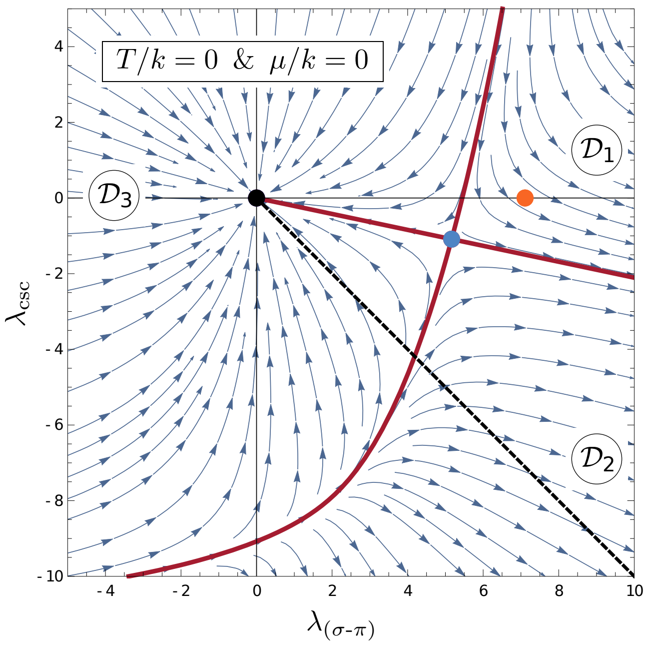

FIGURE 4.15: RG flow of the two-channel approximation at zero temperature and chemical potential in the plane spanned by the scalar-pseudoscalar coupling and the CSC coupling. The black dot represents the *Gaußian* fixed point whereas the blue dot represents the real-valued non-*Gaußian* fixed point, see Eq. (4.82). The orange dot depicts our choice for the initial condition. The RG trajectory starting at this point describes four-quark couplings diverging at a finite scale $k_0 = k_{\text{cr}}$, while approaching a separatrix (red solid line) as indicated by the arrows. The dominance of the scalar-pseudoscalar channel is illustrated by the slope of the corresponding separatrix relative to the bisectrix (dashed back line). The different domains separated by the separatrices (red solid lines) are labeled $\mathcal{D}_1$, $\mathcal{D}_2$, and $\mathcal{D}_3$.

scalar-pseudoscalar coupling to be greater than $\lambda^*_{(\sigma\text{-}\pi),2}$ but still set the initial value of the CSC coupling to zero, see our discussion above. As a consequence, we also find for this two-channel approximation that the low-energy dynamics is dominated by the scalar-pseudoscalar channel. The RG flow of this two-channel approximation is depicted in Fig. 4.15.

Next, let us discuss symmetry restoration at finite temperature and quark chemical potential with the aid of our two-channel approximation. We begin with the case of finite temperature and vanishing chemical potential. The fixed points now become pseudo fixed points due to the presence of a dimensionful external parameter, namely the temperature.[31] As a consequence, the positions of the non-*Gaußian* fixed points are shifted as a function of the dimensionless temperature T/k and therefore also the positions of the separatrices connecting the fixed points are shifted. This is illustrated in Fig. 4.16 for the RG flow in the plane spanned by the scalar-pseudoscalar and the CSC coupling at $T/k = 0.4$ and $\mu = 0$. While the fixed points $\mathcal{F}_3$ and $\mathcal{F}_4$ remain complex-valued when T/k is increased, the behavior of the real-valued (pseudo) non-*Gaußian* fixed point suggests that, for initial conditions chosen to be fixed in the domain $\mathcal{D}_1$ (see, e.g., orange dot in Fig. 4.16), a critical temperature T_{cr} exists above which the four-quark couplings do not diverge anymore at a finite RG scale k_{cr} but remain finite on all scales and approach zero in the IR limit, $k \to 0$. In other words, there is no (spontaneous)

---

[31] The same holds true in case of a finite chemical potential.

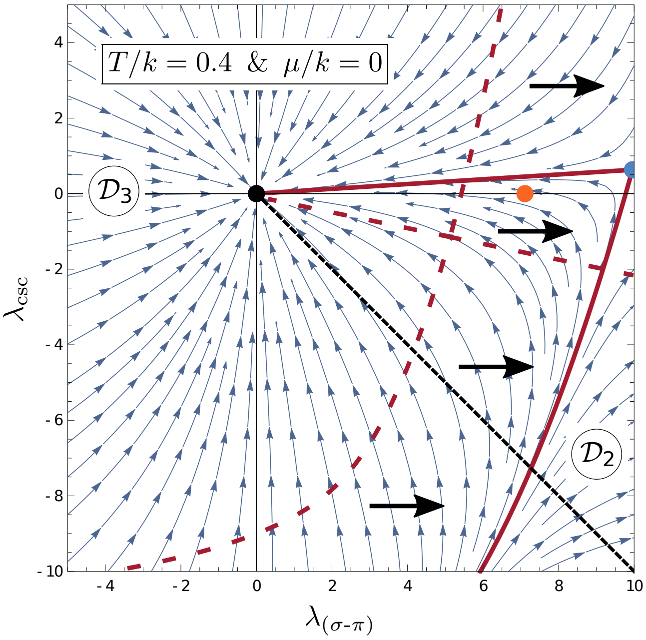

FIGURE 4.16: RG flow of the two-channel approximation at $T/k = 0.4$ and $\mu = 0$ in the plane spanned by the scalar-pseudoscalar coupling and the CSC coupling. The black dot represents the *Gaußian* fixed point. The blue dot represents the real-valued non-*Gaußian* fixed point. The orange dot depicts our choice for the initial condition. The dashed black line is the bisectrix of the bottom right quadrant. The different domains separated by the separatrices (red solid lines) are labeled $\mathcal{D}_2$, and $\mathcal{D}_3$, see also Fig. 4.15. $\mathcal{D}_1$ is not shown. The black arrows indicate the shift of the real-valued non-*Gaußian* fixed point together with the boundaries of the domains $\mathcal{D}_1$ and $\mathcal{D}_2$ when T/k is increased, see main text for details. The dashed red lines depict the position of the separatrices in the vacuum limit, see also Fig. 4.15.

symmetry breaking above the critical temperature. At least at high temperature, such a behavior is indeed expected since the quarks become effectively stiff degrees of freedom due to their thermal *Matsubara* mass $\sim T$. This mechanism has already been discussed in detail in Section 4.2.3, see also Ref. [333], and underlies symmetry restoration when the temperature is increased.

Before we continue with a discussion of the mechanisms underlying chiral symmetry restoration and an associated change to the dominance of the CSC coupling at zero temperature and finite quark chemical potential, we would like to comment on the curvature of the finite-temperature phase boundary at small μ. We observe that the curvature extracted from our two-channel approximation agrees almost identically with the curvatures found in the one-channel approximation as well as in the *Fierz*-complete study. The agreement of the latter two can be understood in terms of the fixed-point structure as discussed above. Of course, the agreement of the curvatures obtained from the two-channel approximation and the *Fierz*-complete study can also be understood from their fixed-point structure. However, we would like to recall that the flow equations of the two-channel approximation suffer from the *Fierz* ambiguity. Our two-channel approximation has been extracted from the *Fierz*-complete set of equations by only taking into account the scalar-pseudoscalar coupling and the CSC coupling. The remaining eight couplings and their flows have been set to zero. This is well justified for the purpose of analyzing the mechanisms underlying the structure of the phase diagram found in the *Fierz*-complete study. In practice, however, the flow equations for a two-channel approximation are usually not extracted from the full *Fierz*-complete set but rather by only taking into account the scalar-pseudoscalar channel and the CSC channel in our ansatz for the effective action (4.3). Owing to the freedom of performing *Fierz* transformations, the set of flow equations for these two couplings resulting from such a *Fierz*-incomplete ansatz will differ from the one used in our present analysis. For example, terms associated with a *Feynman* diagram of the type depicted in the right panel of Fig. 4.1 may be found to contribute to the flow of the scalar-pseudoscalar coupling. As we have seen in our discussion of the large-N_{c} limit, such contributions are parametrically suppressed by factors of $1/N_{\mathrm{c}}$ compared to those associated with *Feynman* diagrams of the type shown in the left panel of Fig. 4.1. Thus, these contributions drop out for $N_{\mathrm{c}} \to \infty$. For finite N_{c}, however, they may still alter the curvature significantly, see Section 4.2.

Let us now turn to the discussion of the dense regime of the phase diagram. At zero temperature, we do not observe symmetry restoration in our *Fierz*-complete study when the quark chemical potential is increased, see Fig. 4.10. As can also be seen in Fig. 4.10, the same behavior is found in our present two-channel approximation. Even though we do not observe symmetry restoration at zero temperature when the chemical potential μ is increased, we find that the “hierarchy” of the channels changes as a function of μ, i.e., the CSC channel becomes the most dominant channel for sufficiently large values of the chemical potential, $\mu \gtrsim \mu_{\chi}$. Note that a dominance of the CSC channel is associated with a divergence of the RG flow into the direction defined by the CSC coupling. Given our choice for the initial condition (see the orange dot in Figs. 4.15, 4.16 and 4.17), such a dominance is not immediately apparent. In fact, even if we chose the initial condition to be located in the domain $\mathcal{D}_2$, we would still observe a dominance of the scalar-pseudoscalar channel at low energies in the vacuum limit. Thus, a dominance of the CSC channel is prohibited by the vacuum fixed-point structure. This can be traced back to the fact that the fixed point $\mathcal{F}_2$ has one IR attractive and one IR repulsive direction.[32] Increasing the quark chemical potential starting from the vacuum limit, we find that the fixed-point structure together with the position of the separatrices remain unchanged up to a “critical value” $(\mu/k)_0$ of the dimensionless chemical potential.[33] At $\mu/k = (\mu/k)_0$, we then observe that two new real-valued fixed points emerge in the plane spanned by the scalar-pseudoscalar coupling and the CSC coupling, which “sit” on top of each other, see top right panel of Fig. 4.17. These two “new” fixed points are nothing but the fixed points $\mathcal{F}_3$ and $\mathcal{F}_4$ which become real-valued at $\mu/k = (\mu/k)_0$. As a consequence of this “creation” of two real-valued fixed points, new separatrices emerge in the plane spanned by the two four-quark couplings which divide the parameter space into five domains $\mathcal{D}_i$, see, e.g., top right panel of Fig. 4.17. Still, an RG trajectory associated with a dominance of the CSC coupling cannot be established for initial conditions located in the domain $\mathcal{D}_1$. Increasing μ/k further, the two new real-valued non-*Gaußian* (pseudo) fixed points are shifted in different directions as indicated by the blue arrows in the bottom left panel of Fig. 4.17. One of these two fixed

---

[32] Recall that the fixed point $\mathcal{F}_2$ corresponds to the fixed point (4.78) in the *Fierz*-complete study.

[33] We observe slight changes of the fixed-point structure and the associated positions of the separatrices for $\mu/k \lesssim (\mu/k)_0$ which arise due to a mild violation of the *Silver-Blaze* property by our covariant regularization scheme, see Section 4.2.4 for a detailed discussion of this aspect.

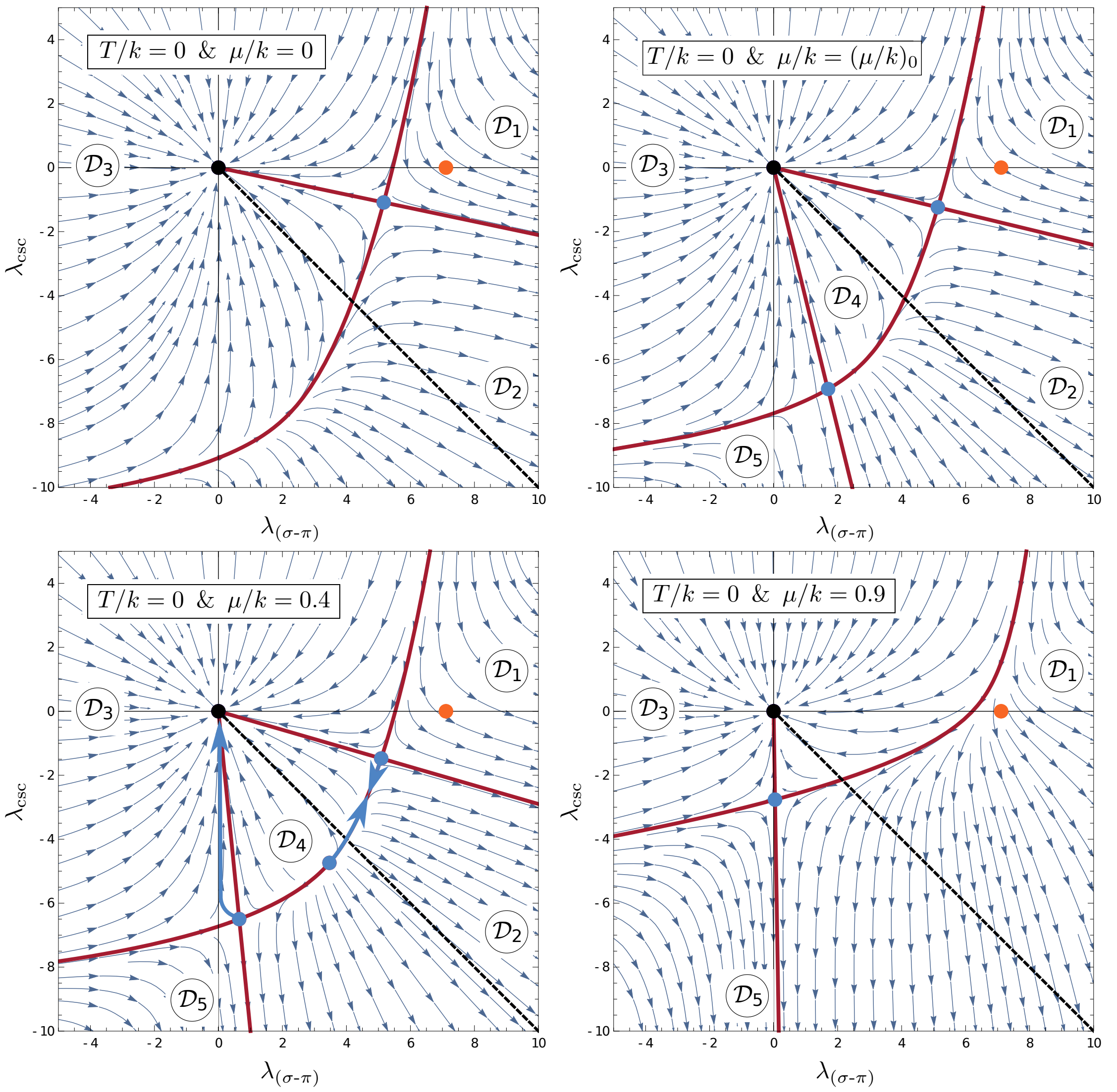

FIGURE 4.17: RG flow of the two-channel approximation at $T = 0$ for different values of μ/k: $\mu/k = 0$ (top left panel; same as Fig. 4.15), $\mu/k = (\mu/k)_0 \approx 0.298$ (top right panel), $\mu/k = 0.4$ (bottom left panel), and $\mu/k = 0.9$ (bottom right panel) in the plane spanned by the scalar-pseudoscalar coupling and the CSC coupling. The black dot represents the *Gaußian* fixed point. Blue dots represent real-valued non-*Gaußian* fixed points. The orange dot depicts our choice for the initial condition. The dashed black line is the bisectrix of the bottom right quadrant. Different domains $\mathcal{D}_i$ are separated by separatrices (red solid lines). The blue arrows in the bottom left panel indicate the shift of the real-valued non-*Gaußian* fixed points when μ/k is increased, see main text for details.

points has one attractive and one repulsive direction and is shifted toward the *Gaußian* fixed point. The other one is shifted toward the fixed point $\mathcal{F}_2$. At sufficiently large $\mu/k > (\mu/k)_0$, the latter two then annihilate each other in the sense that they become complex-valued fixed points. This annihilation also removes the separatrix separating the domains $\mathcal{D}_1$ and $\mathcal{D}_2$. As a consequence, any initial condition of the RG flow located in the domain $\mathcal{D}_1$ now yields an RG trajectory eventually pointing into the direction associated with the CSC coupling with the two couplings diverging at a finite critical scale k_{cr}. In other words, for sufficiently large μ/k, the low-energy physics is potentially dominated by the dynamics associated with the CSC channel.[34] The remaining real-valued fixed point at large μ/k is eventually shifted toward the *Gaußian* fixed point for $\mu/k \to \infty$. As discussed in Section 4.2.3, the merging of the latter two fixed points is associated with the *Cooper* instability. Indeed, this behavior leaves its imprint in the μ-dependence of the symmetry breaking scale, exhibiting the typical BCS-type exponential scaling behavior.

4.3.6 Conclusions

In this section, we have extended our analysis to a *Fierz*-complete NJL model with massless quarks coming in two flavors and N_c colors. We have analyzed the phase structure of this model based on the RG flow equations at leading order of the derivative expansion of the effective action. With this study, we aimed at an understanding on how *Fierz*-incomplete approximations affect the predictive power of this class of models which still underlies to a large extent our understanding of the dynamics of QCD at high density. The employed leading-order approximation of the effective action already includes corrections beyond the often considered mean-field approximation. Note that such corrections are ultimately required to preserve the invariance of the results under *Fierz* transformations [336].

Our results suggest that *Fierz* incompleteness strongly affects the phase structure. For example, the phase transition temperature at large chemical potential almost increases by a factor of two compared to a study which only includes the conventional scalar-pseudoscalar interaction channel together with a channel associated with the formation of a color superconducting ground state. Although we do not have direct access to the gap within the present study, the observed shift of the phase boundary may suggest that the use of *Fierz*-incomplete approximations also affects the magnitude of the gap in the high-density regime. This is in accord with mean-field studies of this regime (see, e.g., Refs. [115, 119–121, 386] for reviews). However, we rush to add that the strength of the effect is expected to depend on the specific choice of four-quark interaction channels taken into account in a *Fierz*-incomplete consideration and the actual choice for the initial conditions of the RG flow equations, i.e., the choice for the parameters appearing in the classical action.

Despite the fact that the study presented here relies on a *Fierz*-complete approximation, it is clear that our results are mostly qualitative. In fact, our study based on the analysis of RG flow equations of four-quark interactions at leading order of the derivative expansion is limited with respect to a determination of the properties of the actual ground state in the phase governed by spontaneous symmetry breaking. In order to gain at least some insight into the structure of the ground state, we have analyzed the “hierarchy” of the four-quark interactions (in terms of their strength) as a function of the temperature and the quark chemical potential. A dominance of a given channel may then be considered as an indication for the formation of a corresponding condensate. Of course, such an analysis has to be taken with some care as a dominance of a given channel may not necessarily entail condensation in this channel.

---

[34] Note that, as we solve the RG flow from $k = \Lambda$ to $k \to 0$, the dimensionless chemical potential μ/k changes from $\mu/\Lambda \gtrsim 0$ to $\mu/k \to \infty$. In terms of the RG “time” $t = \ln(k/\Lambda)$, however, the four-quark couplings may already diverge at a finite value of k before the RG flow fully changes its direction at a certain value of μ/k. Large values of μ/k may therefore not be reached in the RG flow and the scalar-pseudoscalar channel may still dominate the dynamics at sufficiently small values of μ.

Moreover, more than one condensate may be formed, e.g., at large chemical potential. Still, it allows us to gain some insight into the dynamics underlying the phase structure. Interestingly, in this *Fierz*-complete study, we observe that the dynamics close to the phase boundary at small quark chemical potential is clearly dominated by the scalar-pseudoscalar interaction channel whereas the channel associated with the formation of the most conventional color superconducting condensate dominates the dynamics at large chemical potential. In the latter regime, the scalar-pseudoscalar channel is found to be only subdominant. Even more, the channels associated with the formation of color-symmetry breaking condensates are most dominant in this regime.

In order to understand better the dynamics underlying the phase structure, we have analyzed our *Fierz*-complete study in several ways. For example, we have monitored the strength of $U_{\mathrm{A}}(1)$ symmetry breaking and even studied a $U_{\mathrm{A}}(1)$-symmetric variation of our model which indicated that the "hierarchy" of the channels changes at large chemical potential in this case. Moreover, we considered our flow equation in the large-N_{c} limit which revealed the existence of a fixed point which controls the dynamics at least for small values of the chemical potential, provided the initial conditions have been chosen to be located in a specific domain in the space spanned by our set of four-quark couplings. At large chemical potential, the leading order of the large-N_{c} expansion cannot be used to explain the phase structure since channels subleading in this expansion become important. With the aid of a suitably chosen two-channel approximation, however, we have found that the phase structure and the dominance of the color superconducting channel at large chemical potential is a consequence of an intriguing creation and annihilation of pairs of (pseudo) fixed points.

Finally, we emphasize again that, at the present order of the derivative expansion, our analysis is still qualitative regarding the determination of the actual properties of the ground state. In order to unambiguously determine the ground state properties, a calculation of the full at least ten-dimensional order-parameter potential would in principle be required, representing an ambitious continuation of, e.g., recent beyond-mean field calculations of the order-parameter potential with a scalar-pseudoscalar and a diquark channel [128, 139, 230, 329] as well as with a scalar-pseudoscalar and a vector channel [381]. Nevertheless, our present analysis already provides new insights into the phase structure and the ground-state properties of NJL-type models at finite temperature and density. In the context of QCD, with the four-quark self-interactions being dynamically generated by two-gluon exchange, our study shows that *Fierz* completeness is essential to fully capture the quark dynamics toward the low-energy regime, in particular at large quark chemical potential. The understanding of and control over the sector of four-quark interactions form the basis for our study including dynamical gauge degrees of freedom in Chapter 5.

5

GAUGE DYNAMICS AND FOUR-FERMION INTERACTIONS

In the previous chapter, we have studied the relevance of *Fierz* completeness of four-quark self-interactions in NJL-type models at finite temperature and quark chemical potential. The analysis of the “hierarchy” of the various interaction channels in terms of their relative strengths allowed us to gain some insight into the structure of the ground state. Particularly at large chemical potential, we found the aspect of *Fierz* completeness to be of great importance, leading to a significantly increased phase transition temperature as compared to conventional NJL model studies. This observation might have crucial implications for the properties of cold dense quark matter as the increased critical temperature is associated with a larger energy gap in the color superconducting phase of quark matter at zero temperature.

The four-quark couplings appearing in the ansatz of an NJL-type model are usually considered as fundamental parameters. In fact, owing to the non-renormalizability of NJL-type models in four space-time dimensions, both on the perturbative as well as on the non-perturbative level (see, e.g., Refs. [333, 334]), the UV cutoff scale Λ becomes a parameter of the model, too.[1] The initial values of the four-quark couplings are then chosen such that a given set of low-energy observables is reproduced in the vacuum limit. In Section 4.3, guided by the findings of RG studies of QCD [192, 195, 384] and in order to relate to conventional NJL model studies, all four-quark couplings were initially set to zero except for the scalar-pseudoscalar coupling. As the only remaining parameter, the scalar-pseudoscalar coupling was subsequently adjusted to connect to low-energy observables, cf. our discussion in Section 4.3.1.

However, this scale fixing procedure can be problematic. The distinct role of the scalar-pseudoscalar interaction channel at the initial UV cutoff scale can be questioned since a specific four-quark interaction channel is reducible by means of *Fierz* transformations. Yet adopting more complex initial conditions by also taking into account four-quark couplings other than the scalar-pseudoscalar interaction channel might face the difficulty that the parameters cannot be determined by a certain set of low-energy observables. The values of the low-energy observables may in general be reproduced by various different parameter sets or certain parameters might

---

[1] Against this background, the regularization scheme is also part of the definition of the model.

be even left undetermined at all. Moreover, boundary conditions which are defined in the vacuum limit are possibly inappropriate for computations at finite external control parameters such as temperature and/or quark chemical potential. With NJL-type models considered to be rooted in QCD, the RG evolution of gluon-induced four-quark interactions in fact suggests a dependence of these model parameters on external control parameters [335]. In particular at finite quark chemical potential, as observed in Sections 4.2 and 4.3 (see also, e.g., Refs. [97, 107, 115, 385] for reviews), effective degrees of freedom associated with four-quark interaction channels other than the scalar-pseudoscalar interaction channel are expected to become important or even dominant. The particular choice for the initial conditions with the distinct role of the scalar-pseudoscalar channel might then amount to an unjustified constraint which potentially biases the outcome in terms of dominances or might even affect other results such as for the critical temperature.

Thus far, we have not yet addressed the role of the UV cutoff scale itself apart from mentioning that it in fact belongs to the definition of the model. In the context of NJL-type models, we have to deal with the existence of a finite UV extent, i.e., the cutoff scale Λ is limited by a validity bound which in turn limits the model's range of applicability in terms of external parameters, see our discussion in Section 3.3. This validity bound is actually twofold: Firstly, NJL-type models eventually become unstable in the UV and develop a *Landau* pole at a certain scale. Secondly, giving rise to a phenomenological validity bound Λ_{phys}, the description of the physics becomes invalid as NJL-type models lack the fundamental microscopic degrees of freedom, i.e., gluodynamics, which become important at high momentum scales $\Lambda > \Lambda_{\mathrm{phys}}$. As a consequence, having to choose the UV cutoff scale within the validity bound either limits the applicable range of external parameters or, for external parameters outside of this range, implies that the initial effective action is already a complicated object itself. Considering NJL-type models to be embedded in QCD, a possibility to resolve this problem might be for instance the determination of the boundary conditions by employing RG studies of the fundamental theory, see, e.g., Refs. [335, 366, 383]. In recent theoretical works based on functional methods, the objective has focused more and more on a "top-down" approach (see, e.g., Refs. [192, 194–197, 341–343]), i.e., the only input is given by the fundamental parameters of QCD such as the current quark masses or the value of the strong coupling set at a large, perturbative momentum scale. These approaches do not rely on additional model parameters which would require further experimental values of, e.g., low-energy observables. Recently, studies of first-principles approaches to QCD with the FRG have achieved impressive results on a quantitative level, see, e.g., Refs. [192, 194–197]. The self-consistent approximations based on apparent convergence in the vertex expansion scheme thereby give access to systematic error estimates. The studies range from, e.g., a quantitative analysis of chiral symmetry breaking in quenched two-flavor QCD in the vacuum limit [192], a study of the dynamical creation of the gluon mass-gap at non-perturbative momenta as well as of the momentum-dependent ghost-gluon, three-gluon and four-gluon vertices [194], over to an analysis of quark-, gluon- and meson 1PI correlation functions in unquenched *Landau*-gauge QCD with two flavors in the vacuum [195], obtaining results, e.g., for the gluon propagator and the quark mass function, in very good agreement with lattice QCD studies. In Ref. [196], the 1PI correlation functions in *Landau*-gauge *Yang-Mills* theory are studied at finite temperature. The results of this study were found to compare very well to results as obtained from lattice QCD studies as well as from hard thermal loop perturbation theory. These works aiming at quantitative precision constitute essential advances to predictive first-principles investigations of the QCD phase diagram with functional methods.

In the study presented in this chapter, we take the first step toward a top-down first-principles approach to analyze the phase structure of QCD at high densities. With our analysis of the *Fierz*-complete NJL model in Sections 4.2 and 4.3 we have gained valuable insights into the quark dynamics. Building on these insights, we now proceed to incorporate gluodynamics by extending our *Fierz*-complete ansatz to include dynamical gauge degrees of freedom. Our approach bases on the earlier FRG studies [193, 392, 393, 397]. In full QCD, the values of the four-quark couplings are no longer considered fundamental parameters since these effective self-interactions are fluctuation-induced by the dynamic gauge fields. This aspect resolves the issues associated with the initial conditions discussed above such as ambiguities related to the possibility to *Fierz* transform given initial conditions and to the potential existence of more than one parameter set reproducing equally well the set of low-energy observables, or as the possibly problematic distinct role of the scalar-pseudoscalar interaction channel and the neglect of any dependencies of the initial conditions on external control parameters. Incorporating gauge dynamics and thus resolving the fundamental microscopic degrees of freedom allows the initiation of the RG flow at higher scales, which corresponds to starting in the vacuum as we have $T/\Lambda \ll 1$ and $\mu/\Lambda \ll 1$. In this way, the finite UV extent as implied by the validity bound of the NJL model is surmounted and the limit on the range of applicability in terms of external parameters is lifted. Working in the chiral limit, the strong coupling g_{s} of the quark-gluon vertex is the only parameter which is set at a large initial UV scale in the perturbative regime. In the approach taken here, the sector of the truncation describing the running of the gauge coupling is based on Refs. [392, 393]. By integrating out fluctuations, i.e., lowering the RG scale k, the quark-gluon vertex gives rise to 1PI box diagrams with two-gluon exchange which dynamically generate the four-quark interaction channels. Depending on the strength of the strong coupling and the external parameters, the quark sector can be subsequently driven to criticality, signaling the onset of spontaneous symmetry breaking. Following the same approach taken in Chapter 4, we employ the RG flow of the four-quark couplings in the pointlike limit to study the phase structure at finite temperature and quark chemical potential. We again analyze the “hierarchy” of the four-quark couplings in terms of their strength which proved very valuable in order to gain some insight into the structure of the ground state in the regime of spontaneously broken symmetry. Within our *Fierz*-complete framework including 10 four-quark channels, which takes into account the explicit breaking of *Poincaré* invariance due to non-zero temperature and chemical potential, we find that the inclusion of dynamic gauge fields leads to a significant increase of the critical temperature at larger quark chemical potentials. The dominance pattern among the various four-quark couplings is observed to be remarkably robust in particular against variations in the details of the scale dependence of the running gauge coupling. The clear dominances of the scalar-pseudoscalar interaction channel at low densities and of the CSC channel at higher densities is even amplified in the case of $U_{\mathrm{A}}(1)$-violating initial conditions.

This chapter is organized as follows: In Section 5.1, we discuss our ansatz for the effective average action with an emphasis on the incorporation of the gauge fields. We review some aspects of the running gauge coupling as derived in Refs. [392, 393] which enters our computation as external input. The general structure of the RG flow equations for the couplings of the four-quark interaction channels as obtained from the ansatz employing the *Wetterich* equation is subsequently discussed in Section 5.2. We briefly discuss how the gluodynamics affect the fixed-point structure of the β functions which provides a comprehensive picture of the underlying mechanisms related to the dynamical generation of the effective four-quark interactions and to driving the quark sector to criticality. In this section, we also introduce the scale fixing procedure. In all numerical studies we exclusively consider the case of quarks coming in $N_{\mathrm{c}} = 3$ colors and $N_{\mathrm{f}} = 2$ flavors. The phase structure and symmetry braking patterns at finite temperature and density is analyzed in Section 5.3. We also compare the results for the finite-temperature phase boundary to the phase boundary as obtained from the NJL-type model discussed in Section 4.3. In Section 5.3.1, we estimate the in-medium effects on the quark contribution to the gauge anomalous dimension and its impact on the phase structure. In Section 5.3.2, lastly, we analyze the effect of explicit $U_{\mathrm{A}}(1)$ symmetry breaking initial conditions at the UV cutoff scale in comparison to $U_{\mathrm{A}}(1)$-symmetric RG flows. There, we also comment on the curvature of the finite-temperature phase boundary at small chemical potential resulting from the various computations. Our conclusions can be found in Section 5.4.

5.1 ANSATZ FOR THE EFFECTIVE AVERAGE ACTION

The introduction of the dynamic gauge fields $A_\mu \equiv A_\mu^a T^a$ associated with the local $SU(N_{\mathrm{c}})$ symmetry does not affect the symmetry considerations presented in Section 4.3.1, which lead to the *Fierz*-complete basis of the four-quark interactions in the pointlike limit. In the following, we thus employ the same basis as before, parametrized by the interaction channels (4.59)-(4.68). The ansatz for the effective average action is given by[2]

$$\Gamma_k[\bar{\psi},\psi,A] = \int_0^\beta d\tau \int d^3x \Big\{ \bar{\psi}\left(Z_\psi^{\parallel} \mathrm{i}\gamma_0\partial_0 + Z_\psi^{\perp}\mathrm{i}\gamma_i\partial_i - Z_\mu \mathrm{i}\mu\gamma_0 \right)\psi + \frac{1}{2} A_\mu^a G_{\mu\nu}^{-1,ab} A_\nu^b + Z_g \bar{g}_{\mathrm{s}} \bar{\psi} \not{A} \psi + \frac{1}{2}\sum_{j\in\mathcal{B}} Z_j \bar{\lambda}_j \,\mathcal{L}_j \Big\}, \tag{5.1}$$

with the bare strong coupling $\bar{g}_{\mathrm{s}}$ of the quark-gluon vertex accompanied by the vertex renormlization Z_g and the gauge-fixed kinetic term $\frac{1}{2} A_\mu^a G_{\mu\nu}^{-1,ab} A_\nu^b$ for the gauge fields, see also our discussion of the *Faddeev-Popov Lagrangian* (2.17) in Section 2.1. At finite temperature and chemical potential, the transversal vacuum projection of the gluon propagator is divided into a magnetic and an electric component in order to distinguish the directions transversal and longitudinal to the heat bath, respectively. Accompanied by corresponding wavefunction

---

[2] The ansatz does not include ghost fields, cf. Eq. (2.16) with the *Faddeev-Popov Lagrangian* (2.17), as these are not relevant for the RG flow equations of the four-quark couplings.

renormalizations, the *Lorentz* structure of the inverse gluon propagator in momentum space is given by [216, 423]

$$\begin{aligned}\left[\Gamma^{(1,1)}_{AA}\right]^{ab}_{\mu\nu}(p,p') &= G^{-1,ab}_{\mu\nu}(p)\delta^{(4)}(p-p') \\ &= \delta^{ab}p^2\left(Z^{\mathrm{M}}_A P^{\perp}_{\mathrm{M},\mu\nu} + Z^{\mathrm{E}}_A P^{\perp}_{\mathrm{E},\mu\nu} + \frac{1}{\xi}P^{\parallel}_{\mu\nu}\right)\delta^{(4)}(p-p'),\end{aligned} \tag{5.2}$$

with the gauge fixing parameter ξ and the projection operators defined by

$$\begin{aligned} P^{\parallel}_{\mu\nu} &= \frac{p_\mu p_\nu}{p^2}\,, & P^{\perp}_{\mathrm{M},\mu\nu} &= (1-\delta_{\mu 0})(1-\delta_{\nu 0})\left(\delta_{\mu\nu} - \frac{p_\mu p_\nu}{\vec{p}^{\,2}}\right), \\ P^{\perp}_{\mu\nu} &= \left(\delta_{\mu\nu} - \frac{p_\mu p_\nu}{p^2}\right), & P^{\perp}_{\mathrm{E},\mu\nu} &= P^{\perp}_{\mu\nu} - P^{\perp}_{\mathrm{M},\mu\nu}\,. \end{aligned} \tag{5.3}$$

Here, we have introduced the longitudinal and transversal vacuum projection operators $P^{\parallel}$ and $P^{\perp}$, respectively, and the transversal magnetic and electric projection operators $P^{\perp}_{\mathrm{M}}$ and $P^{\perp}_{\mathrm{M}}$, respectively. Note that the projection operators $P^{\parallel}$, $P^{\perp}_{\mathrm{M}}$ and $P^{\perp}_{\mathrm{E}}$ are mutually orthogonal and fulfill the relation $P^{\parallel} + P^{\perp}_{\mathrm{M}} + P^{\perp}_{\mathrm{E}} = P^{\parallel} + P^{\perp} = \mathbb{1}$. The gauge propagator receives corrections from the gluon self-energy in the form

$$G^{-1,ab}_{\mu\nu} = G^{-1,ab}_{(0),\mu\nu} + \Pi^{ab}_{\mu\nu}\,, \tag{5.4}$$

where $G^{-1}_{(0)}$ denotes the inverse of the bare gluon propagator and $\Pi^{ab}_{\mu\nu}$ the polarization tensor [108, 216]. These corrections give rise to the wavefunction renormalizations Z^{M}_A and Z^{E}_A in Eq. (5.2) which are related to the *Meissner* mass m_{M} and *Debye* mass m_{D} in the limits

$$m^2_{\mathrm{M}} = \lim_{\vec{p}\to 0}\vec{p}^{\,2}(Z^{\mathrm{M}}_A(0,\vec{p}) - 1)\,, \qquad m^2_{\mathrm{D}} = \lim_{\vec{p}\to 0}\vec{p}^{\,2}(Z^{\mathrm{E}}_A(0,\vec{p}) - 1)\,, \tag{5.5}$$

respectively [107, 108, 216]. On the account of *Ward* identities, the longitudinal component of the gauge propagator does not receive any corrections in *Abelian* gauge theories as well as in the vacuum limit of non-*Abelian* gauge theories. In non-*Abelian* gauge theories at finite temperature and/or chemical potential, the structure of the gluon propagator becomes even more complicated because of non-transversal corrections, see, e.g., Refs. [312, 423] for reviews.[3] In the present study, however, we assume a simplified structure of the gluon propagator which does not take into account the splitting into magnetic and electric components, i.e., we set $Z^{\mathrm{E}}_A = Z^{\mathrm{M}}_A = Z_A$. In the *Feynman* gauge, i.e., $\xi = 1$, the regularized gluon propagator is then given by

$$\left[(\Gamma^{(1,1)} + R_k)^{-1}_{AA}\right]^{ab}_{\mu\nu}(p,p') = \frac{1}{Z_A}\frac{1}{p^2(1+r_A)}\delta^{ab}\delta_{\mu\nu}\delta^{(4)}(p-p')\,, \tag{5.6}$$

where we have employed the regulator function $R^A_k = Z_A p^2 r_A$ for the gauge fields with the exponential shape function r_A for bosonic fields introduced in Section 3.2, see Eq. (3.29), to be consistent with the *Fermi*-surface-adapted shape function (3.44) for the quark fields.

---

[3] In color superconducting quark matter the structure might be ever more complicated involving non-trivial color structures [423].

The gluon wavefunction renormalization Z_A does not appear explicitly in the flow equations of the dimensionless renormalized four-quark couplings since these factors can be absorbed into the strong coupling $\bar{g}_\mathrm{s}$ resulting in the renormalized gauge coupling $g_\mathrm{s} = Z_A^{-1/2}\bar{g}_\mathrm{s}$, see also below.[4] Apart from that, we drop the explicit dependence of the flow equations on the anomalous dimensions of the quark and the gluon fields since they have been found to be subleading in the symmetric regime [380, 391–393, 424].[5] As a result, the RG flow of the gauge sector enters the flow equations of the four-quark couplings only via the running of the strong coupling. Since we take into account the scale-dependence of the strong coupling but neglect the explicit dependence of the flow equations of the four-quark couplings on the gauge anomalous dimension, this approximation amounts to an RG-improved one-loop computation. Although the gluon propagator is assumed in the rather simple form (5.6), we consider the approximations concerning the gluonic sector as sufficient since we expect the important dynamics approaching the low-energy regime to occur within the matter sector.

In our present approach, we incorporate the RG running of the strong coupling g_s as an external input taken from Refs. [392, 393]. We briefly recapitulate in the following the main aspects of this study relevant for our considerations and refer to Ref. [393] for a detailed discussion. In this FRG study, the QCD running gauge coupling was calculated for all scales and temperatures in the background-field formalism, including the back-reaction of induced quark dynamics on the gluon sector. The employed non-perturbative definition of the running gauge coupling is based on a non-renormalization property of the product of the coupling and the background-field wavefunction renormalization which is implied by gauge invariance [359]. The corresponding $\beta_{g_\mathrm{s}^2}$ function of the renormalized strong coupling $g_\mathrm{s}^2 = Z_A^{-1}\bar{g}_\mathrm{s}^2$ is then given in terms of the anomalous dimension of the background field:

$$\beta_{g_\mathrm{s}^2} \equiv \partial_t g_\mathrm{s}^2 = \eta_A g_\mathrm{s}^2\,, \qquad \eta_A = -\frac{1}{Z_A}\partial_t Z_A\,. \tag{5.7}$$

In our approach, we determine the scale dependence of the strong coupling g_s^2 from this flow equation with the anomalous dimension η_A taken from the computation presented in Refs. [392, 393] as external input. Note that quark fluctuations directly contribute to the anomalous dimension η_A which account for the screening property of fermionic fluctuations. In fact, the fluctuation-field running coupling which is relevant for the induced four-quark self-interactions in the matter sector can also receive corrections from a vertex renormalization. These contributions have been derived in Ref. [424] which are constrained by gauge invariance in terms of modified *Ward-Takahashi* identities [350, 361], leading to a β function in the form

$$\partial_t g_\mathrm{s}^2 = \eta_A g_\mathrm{s}^2 - 2\chi\frac{g_\mathrm{s}^2}{1-\chi\sum c_i\lambda_i}\sum c_i\beta_{\lambda_i}\,, \tag{5.8}$$

---

[4] The running gauge coupling is defined in terms of the background-field wavefunction renormalization, i.e., through the kinetic term of the gauge fields, and shall be identified with the coupling of the quark-gluon vertex, see below.

[5] We again set the wavefunction renormalizations of the quark fields to one, which implies the anomalous dimension of the quark fields to vanish, and do not take into account the renormalization of the quark chemical potential, i.e., we also set $Z_\mu = 1$.

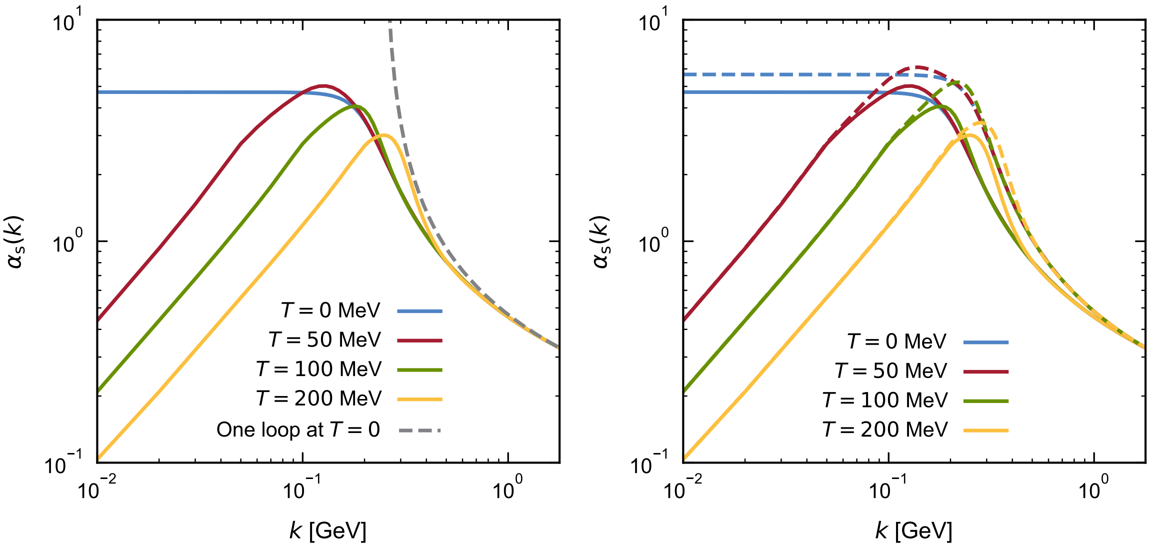

FIGURE 5.1: Left panel: Running $SU(N_c = 3)$ gauge coupling $\alpha_s = g_s^2/(4\pi)$ for $N_f = 2$ quark flavors as a function of the RG scale k for the temperatures $T = 0, 50, 100, 200$ MeV in comparison to the one-loop running at zero temperature. Right panel: Running $SU(N_c = 3)$ gauge coupling α_s as a function of k at $T = 0, 50, 100, 200$ MeV for $N_f = 2$ quark flavors (solid lines) and in pure *Yang-Mills* theory, i.e., $N_f = 0$. Results are taken from Refs. [392, 393], see main text for details.

where χ and the c_i's are numerical constants, the latter depending on the number of quark flavors. The crucial aspect is the proportionality of the vertex correction to the β functions of the four-quark couplings λ_i, implying that these contributions vanish as long as the RG flow of the couplings λ_i are located at or close to a fixed point [391, 424]. As the four-quark couplings follow the (shifted) IR attractive *Gaußian* fixed point in the symmetric regime, see our discussion of the fixed-point structure below, we can thus neglect these contributions in the following. The results for the running gauge coupling as obtained from Eq. (5.7) are shown in Fig. 5.1 for various temperatures. For the computation we have used the experimental value $\alpha_s(M_\tau) = 0.330$ at the τ mass scale $M_\tau = 1.78$ GeV [38] as initial condition. Toward the UV at high RG scales $k/T \gg 1$, the temperature effect becomes negligible and the different solutions converge to the zero temperature running and eventually to the perturbative one-loop running. In fact, the results also reproduce the perturbative two-loop solution at zero temperature very well.[6] The one-loop running of the strong coupling $g_s^2 = 4\pi\alpha_s$ given by

$$\alpha_s(k) = \frac{\alpha_s(\Lambda)}{1 + \frac{\alpha_s(\Lambda)}{4\pi}\left(\frac{22}{3}N_c - \frac{4}{3}N_f\right)\log(k/\Lambda)}, \tag{5.9}$$

with the initial coupling $\alpha_s(\Lambda)$ at the UV scale Λ, see also Eqs. (2.18) and (2.20) in Section 2.1, develops a *Landau* pole toward the IR. Employing the scale fixing described above, the pole is located at $k_{\text{pole}} = 0.248$ GeV. In contrast to that, the behavior of the running coupling at zero temperature as obtained from Eq. (5.7) is determined by a stable non-*Gaußian* IR fixed point:

---

[6] In pure $SU(N_c = 3)$ *Yang-Mills* theory, the two-loop coefficient as obtained from the results of this RG study [392, 393] at zero temperature agrees within 95% with the coefficient as determined from perturbative calculations.

Toward lower scales, the gauge coupling increases at first to finally assume a constant value as it approaches the fixed point. At finite temperature, the running gauge coupling develops a maximum near the scale $k \sim T$. With increasing temperature, the maximum is shifted to higher scales and its value decreases. This behavior is of phenomenological relevance as it determines whether the gauge coupling is strong enough to be able to drive the quark sector to criticality, see our discussion below, and is thus related to the restoration of spontaneously broken symmetries at high temperatures. Toward the IR, the typical wavelength of the fluctuations becomes larger than the extent of the compactified *Euclidean* time direction and the system is hence effectively described by a reduced three-dimensional theory. As shown in Refs. [392, 393], also in the theory of reduced dimensions there exists a non-*Gaußian* IR fixed point $g^2_{3\mathrm{d},*}$. This fixed point of the three-dimensional theory leaves its imprint on the IR behavior of the running gauge coupling in the four-dimensional theory and explains the observed power law toward lower scales in Fig. 5.1, which can be described by the relation $g^2_{\mathrm{s}}(k \ll T) \sim g^2_{3\mathrm{d},*} k/T$.

In the right panel of Fig. 5.1, we also show a comparison of the running gauge coupling for $N_{\mathrm{f}} = 2$ quark flavors, depicted by the solid lines, to the scale dependence of the strong coupling as obtained in pure *Yang-Mills* (YM) theory, i.e., $N_{\mathrm{f}} = 0$, depicted by the dashed lines, again for different temperatures. The running gauge coupling for two flavors evolves with a smaller slope toward the IR and develops a maximum at $k \sim T$ which is smaller and shifted to slightly lower scales as compared to the $N_{\mathrm{f}} = 0$ case. This tendency can be explained by the screening nature of fermionic fluctuations. Toward lower scales, the quarks decouple from the flow at finite temperature due to screening by their thermal mass, i.e., the non-existence of soft thermal modes in the fermionic spectrum, and the solution converges to the pure YM running controlled by the IR fixed point of the reduced three-dimensional theory. Note that the running gauge coupling discussed here does not incorporate the effect of quarks developing a mass gap in the spontaneously broken regime which is also of no relevance for our analysis below.

5.2 STRUCTURE OF THE RG FLOW EQUATIONS AND SCALE FIXING

With the ansatz (5.1) for the effective average action, we derive the RG flow equations for the couplings of the four-quark interaction channels from the *Wetterich* equation (3.23).[7] Owing to the size of this system of equations for the *Fierz*-complete set of four-quark interactions, we refrain from listing these equations explicitly. The general structure of the β functions for the dimensionless renormalized couplings $\lambda_i = Z_i k^2 \bar{\lambda}_i$ is given by

$$\partial_t \lambda_i = 2\lambda_i - \mathcal{A}^{(i)}_{mn}(\tau, \tilde{\mu}_\tau)\lambda_m\lambda_n - \mathcal{B}^{(i)}_{j}(\tau, \tilde{\mu}_\tau)\lambda_j g_{\mathrm{s}}^2 - \mathcal{C}^{(i)}(\tau, \tilde{\mu}_\tau) g_{\mathrm{s}}^4 \,, \tag{5.10}$$

with $\tau = T/k$ and $\tilde{\mu}_\tau = \mu/(2\pi T)$. The temperature- and chemical-potential-dependent coefficients $\mathcal{A}^{(i)}_{mn}$, $\mathcal{B}^{(i)}_{j}$ and $\mathcal{C}^{(i)}$ are auxiliary functions describing sums of threshold functions which are associated with the 1PI diagrams depicted in Fig. 5.2. All threshold functions

---

[7] We refer to Appendix F for further details about the derivation.

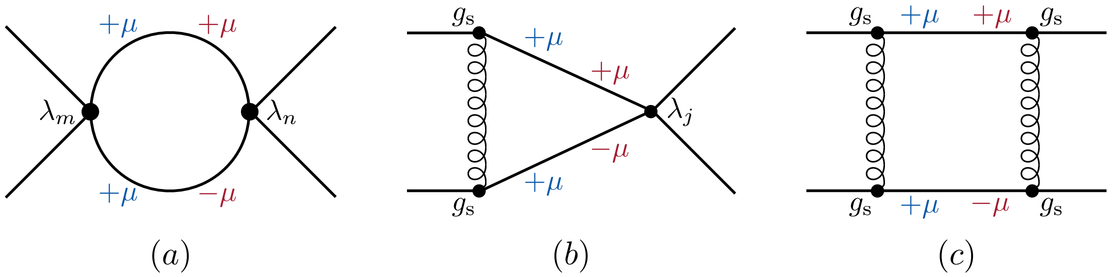

FIGURE 5.2: The 1PI diagrams contributing to the RG flow (5.10) of the couplings λ_i of the four-quark self-interactions. The purely fermionic diagram (a) involving only quark propagators (solid lines) was already introduced in Section 4.2 and gives rise to contributions which are quadratic in the four-quark couplings. The contributions generated by the triangle diagrams (b) with one-gluon exchange (wiggly lines) are proportional to $g_s^2\lambda_j$, while the contributions from the box diagrams (c) with two-gluon exchange are proportional to g_s^4. There are two classes of each diagram which distinguish the sign structure of the dependence of the two fermionic propagators on the quark chemical potential: one class represents the case of equal signs as depicted by the blue labels and the other the case of opposite signs as depicted by the red labels.

come again in the two variations, $l_{\|}$ and $l_{\perp}$, corresponding to contributions longitudinal and transversal to the heat bath, respectively. Furthermore, there are two classes of 1PI diagrams which distinguish the relative sign structure of the dependence of the fermionic propagators on the quark chemical potential. The terms bilinear in the four-quark couplings with the coefficients $\mathcal{A}_{mn}^{(i)}$ are associated with the purely fermionic diagrams (a) in Fig. 5.2 which we have already encountered in Chapter 4. The contributions proportional to $\lambda_j g_s^2$ with the coefficients $\mathcal{B}_j^{(i)}$ are generated by the triangle diagrams (b) and the contributions proportional to g_s^4 with the coefficient $\mathcal{C}^{(i)}$ by the box diagrams (c) in Fig. 5.2. In the limit $T/k \to \infty$, all threshold functions and thus all coefficients $\mathcal{A}_{mn}^{(i)}$, $\mathcal{B}_j^{(i)}$ and $\mathcal{C}^{(i)}$ in Eq. (5.10) become zero which describes the decoupling of the fermionic modes as the quarks acquire a thermal mass. The threshold functions also approach zero in the limit $\mu/k \to \infty$, only the purely fermionic threshold functions which belong to the type depicted by the red labeling in panel (a) in Fig. 5.2 increase as $l_{\pm}^{(\mathrm{F})} \sim (\mu/k)^2$ for $\mu/k \gg 1$ at zero temperature. As discussed in Section 4.2.3, this behavior plays an essential role in the formation of a *Cooper* pair condensate, i.e., a diquark condensate in the present context, and can be associated with the typical BCS-type exponential scaling behavior of the critical scale, see Eq. (4.51).

The mechanism of the dynamical generation of the four-quark couplings and the role of the running gauge coupling in spontaneous symmetry breaking can be understood in simple terms by analyzing the fixed-point structure of the RG flow equations for the four-quark couplings. Here, we follow the lines of Refs. [392, 393]. For a detailed discussion, we refer to, e.g., Ref. [333]. A sketch of the β function of a four-quark coupling λ at zero temperature and chemical potential is shown in Fig. 5.3 which illustrates the influence of the gauge coupling g_s. At vanishing gauge coupling the β function possesses a *Gaußian* fixed point and a non-*Gaußian* fixed point located at λ^*. The initial values of the four-quark couplings are not considered as fundamental parameters and are set to zero, i.e., the couplings are initially located at the IR attractive *Gaußian* fixed point at the UV scale Λ. In the course of the RG flow toward the IR, the value of the gauge coupling increases and shifts the parabola on the account of the

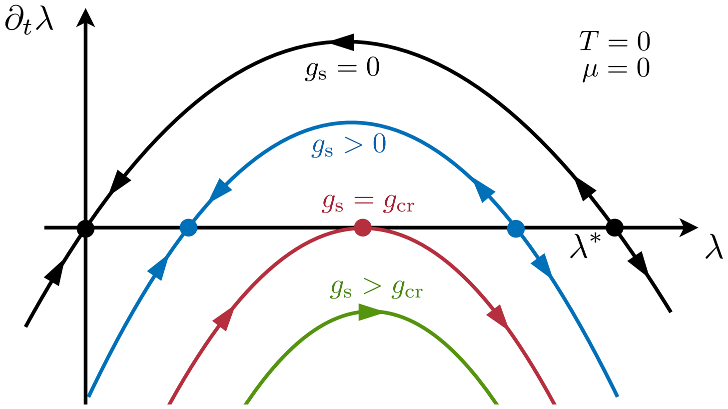

FIGURE 5.3: Sketch of the β function of a four-quark coupling λ at zero temperature and chemical potential with the arrows indicating the direction of the RG flow toward the IR. The sketch illustrates the influence of the gauge coupling g_s: At $g_s = 0$ the β function has a *Gaußian* fixed point and a non-*Gaußian* fixed point λ^*. As soon as the gauge coupling assumes a finite value, the term proportional to g_s^4 shifts the parabola down and turns the former *Gaußian* fixed point into an interacting fixed point. For increasing gauge coupling, the two fixed points approach each other until they annihilate each other at a critical value g_{cr}. See main text for details.

term proportional to g_s^4 in Eq. (5.10) which is generated by 1PI box diagrams with two-gluon exchange, see panel (c) in Fig. 5.2. The shift of the parabola turns the former *Gaußian* fixed point into an interacting non-*Gaußian* fixed point. Due to its IR attractive property, the four-quark couplings follow the fixed point and assume finite values. This mechanism underlies the dynamical generation of the four-quark couplings in the course of the RG flow. For increasing values of the gauge coupling, the parabola is shifted further downwards and the two non-*Gaußian* fixed points approach each other. At a critical value g_{cr} of the gauge coupling, the fixed points eventually merge and annihilate. This opens the way for a rapid increase of the four-quark couplings before they finally diverge at a finite critical scale k_{cr}, signaling the onset of spontaneous symmetry breaking. Note that if the system remains in the symmetric regime, the values of the four-quark couplings stay close to the former *Gaußian* fixed point which assumes non-zero values and becomes an interacting fixed point as the gauge coupling assumes finite values. The β functions of the four-quark couplings thus remain small at all RG scales k in this case. As a consequence, the additional contributions in Eq. (5.8) proportional to the β functions are negligibly small and the running gauge coupling is correctly described by Eq. (5.7) for a description of the RG flow in the symmetric regime.

In summary, the fixed-point structure explains the dynamic generation of four-quark couplings in a directly accessible manner as well as how the gauge dynamics can drive the quark sector to criticality. However, we emphasize that these mechanisms are to be understood against the background of the complex interplay among the various four-quark couplings themselves and of the influence of the external parameters temperature and chemical potential as discussed in Sections 4.2 and 4.3, see also our discussion of the behavior of the threshold functions as functions of the temperature and the quark chemical potential above. For instance, the temperature does not only influence the running of the gauge coupling but also the fermionic fluctuations themselves as in form of thermal screening and hence the critical value $g_{\rm cr}$ which is necessary to drive the quark sector to criticality. Indeed, such a critical value $g_{\rm cr}$ becomes even irrelevant for large values of the quark chemical potential and at sufficiently small temperatures, as the formation of a diquark condensate requires only an arbitrarily small positive coupling, see our discussion of the BCS-type exponential scaling behavior in Section 4.2.3. The dominance pattern of the four-quark couplings is still strongly influenced by the competing interplay within the quark sector itself. A great advantage of the dynamical generation of four-quark couplings by gluodynamics as compared to the approach presented in Section 4.3 is that a potential bias in regard to the RG flow and the observed dominance pattern given by the particular choice of the initial UV values of the four-quark couplings is avoided. In fact, the values of the four-quark couplings are rather predicted from the underlying quark-gluon dynamics.

Scale fixing

As already mentioned above, the initial values of the four-quark interaction channels are not considered as fundamental parameters in our present approach and are set to zero at the UV scale Λ. The only free parameter is the initial condition of the running gauge coupling $g_{\rm s}(\Lambda)$. This value is adjusted at the UV scale $\Lambda = 10\,\text{GeV}$ to obtain a critical temperature $T_{\rm cr}(\mu = 0) \equiv T_0 = 132\,\text{MeV}$ at zero quark chemical potential, cf. the scale fixing in Section 4.2. The large value of the initial UV scale ensures the conditions $T/\Lambda \ll 1$ and $\mu/\Lambda \ll 1$ for the range of external parameters we intend to study to avoid cutoff effects and regularization-scheme dependences, see our discussion of renormalization group consistency and ranges of validity in Section 3.3. The value $T_{\rm cr}(\mu = 0) = 132\,\text{MeV}$ of the critical temperature beyond which no spontaneous symmetry breaking occurs at zero chemical potential is chosen to agree with recent lattice QCD results [425].[8] In order to obtain this critical temperature, we tune the initial UV value of the running gauge coupling such that $\alpha_{\rm s}(\Lambda = 10\,\text{GeV}) = 0.2137$. Evolved to the Z-boson mass scale $M_Z = 91.19\,\text{GeV}$, the value of the gauge coupling fixed in this way is almost 6% greater than the experimental results [39]. The necessity of a slightly larger running gauge coupling in order to appropriately trigger criticality in the quark sector is a common aspect of functional methods on the approximation level at hand, see, e.g., Ref. [193].[9] Throughout this chapter, we shall employ this scale fixing procedure for all computations of the phase structure including dynamic gauge fields.

5.3 Phase diagram and symmetry breaking patterns

Let us now study the phase diagram in the plane spanned by the temperature and the quark chemical potential. The critical temperature $T_{\rm cr}(\mu)$ at a given value of the quark chemical potential beyond which no spontaneous symmetry breaking occurs is defined as the highest

---

[8] The lattice QCD study presented in Ref. [425] considering two degenerate massless quarks and a physical strange quark mass finds the chiral phase transition $T_{\rm cr} = 132^{+3}_{-6}\,\text{MeV}$ at zero quark chemical potential.

[9] Only most advanced truncations with a very accurate treatment of momentum structures do not require such an "IR-enhancement" anymore, see, e.g., Refs. [192, 195].

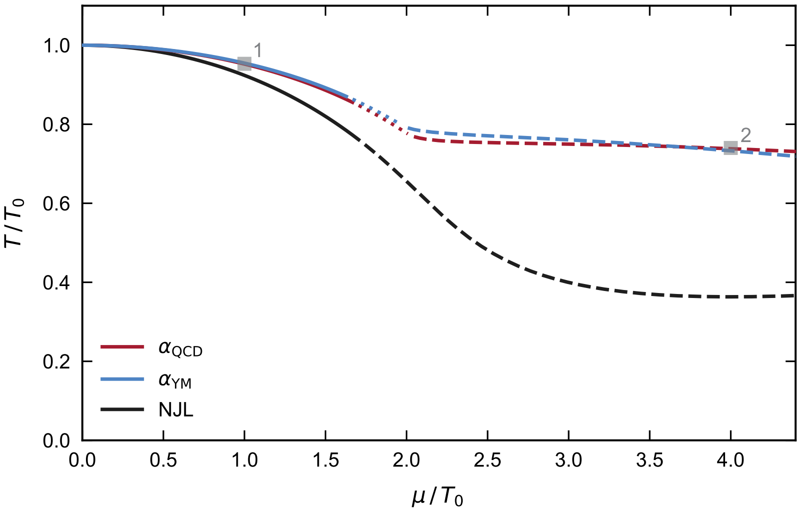

FIGURE 5.4: Phase boundary associated with the spontaneous breakdown of at least one of the fundamental symmetries as obtained from the *Fierz*-complete ansatz (5.1) including dynamic gauge fields in comparison to the phase boundary resulting from the *Fierz*-complete NJL model discussed in Section 4.3. The running gauge coupling enters as external input as derived from Eq. (5.7) with the gauge anomalous dimension η_A taken from Refs. [392, 393] for $N_{\mathrm{f}} = 2$ (red line, denoted by α_{QCD}) and in pure YM theory (blue line, denoted by α_{YM}). The gray boxes labeled “1” and “2” indicate the values for temperature and quark chemical potential used for the exemplary RG flows shown in Fig. 5.5, see also main text for details.

temperature for which the four-quark couplings still diverge at $k \to 0$, see our discussion in Section 4.1.3. Keep in mind that a singularity in the flow of one four-quark coupling at a critical scale $k_{\mathrm{cr}}(T, \mu)$ entails corresponding divergences in all other couplings as well. However, the four-quark couplings in general develop distinct relative strengths and a dominant four-quark channel can be identified, i.e., the modulus of the coupling of this channel is significantly greater than the absolute values of the other four-quark couplings. Such a dominance serves us as an indication of which associated *Hubbard-Stratonovich* transformed field begins to acquire a finite ground-state expectation value, i.e., which condensate is starting to form as the corresponding order parameter potential develops a non-trivial minimum. Note again, however, that this approach is only able to detect phase transitions of second order as the definition of the critical temperature is associated with a change from positive to negative curvature of the order parameter potential at the origin. In case of a first-order phase transition, a non-trivial minimum of the potential is formed but the curvature at the origin remains positive. Although our criterion is consequently not sensitive to transitions of first order, it still allows us to detect the line of metastability, see also Sections 4.1.3 and 4.3.2 for a more detailed discussion of this aspect.

We emphasize again that in our computation of the phase boundary no parameters are used as input other than the initial UV value of the gauge coupling $g_{\mathrm{s}}(\Lambda)$. All couplings associated with the *Fierz*-complete basis of four-quark interaction channels are initially set to zero and only dynamically generated by gluodynamics in the course of the RG flow. The initial gauge coupling at the UV scale $\Lambda = 10\,\mathrm{GeV}$ is tuned such that the critical temperature $T_0 = 132\,\mathrm{MeV}$ at zero quark chemical potential is obtained. This initial value is then kept for

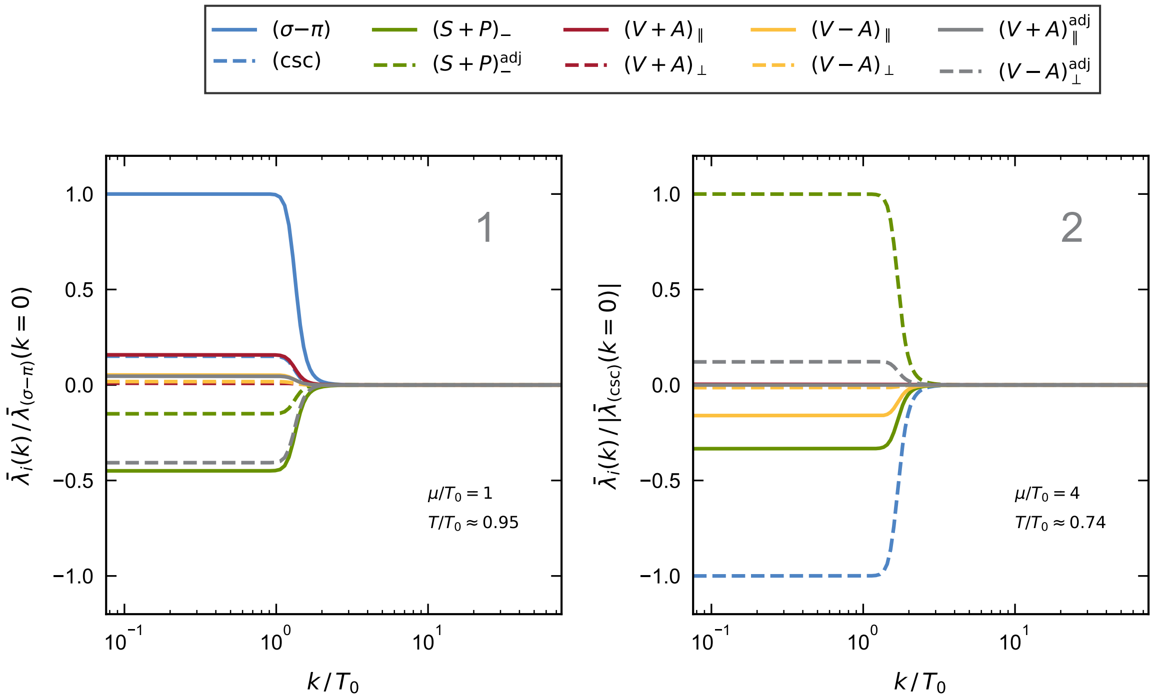

FIGURE 5.5: Scale dependence of the various renormalized (dimensionful) four-quark couplings at $\mu/T_0 = 1$ and $T/T_0 \approx 0.95$ (left panel) as well as at $\mu/T_0 = 4$ and $T/T_0 \approx 0.74$ (right panel) corresponding to the little gray boxes in the phase diagram shown in Fig. 5.4. Note that, in the right panel, the intact $U_{\mathrm{A}}(1)$ symmetry implies $\bar\lambda_{\mathrm{csc}} = -\bar\lambda_{(S+P)_-^{\mathrm{adj}}}$ according to the sum rules (4.69) and (4.70) introduced in Section 4.3, see main text for details.

our computations at finite quark chemical potential which is justified as long as $T/\Lambda \ll 1$ and $\mu/\Lambda \ll 1$. In the following, T_0 serves as a reference scale to "measure" physical observables.

As a first non-trivial result, we observe a dominance of the scalar-pseudoscalar coupling in the vacuum limit. The couplings diverge at a symmetry breaking scale $k_{\mathrm{cr}}(\mu=0)/T_0 \approx 2.62$. In this process, the modulus of the scalar-pseudoscalar coupling is at least two times greater than the modulus of all other couplings, indicating that the ground state is governed by chiral symmetry breaking in the vacuum limit. This case is very similar to the one discussed in Section 4.3.2. However, the crucial difference is given by the initial conditions for the four-quark couplings. In the present case, we can exclude that the dominance might be triggered by the choice for the initial conditions as all four-quark couplings are initially zero and only dynamically generated. The dominance of the scalar-pseudoscalar coupling indicating chiral symmetry breaking is hence solely determined by the dynamics of the gluons and quarks.

The dominance of the scalar-pseudoscalar interaction channel persists again even up to high temperatures beyond the critical temperature. The red line in Fig. 5.4 depicts the critical temperature as a function of the quark chemical potential which has been computed with the running gauge coupling as obtained from Eq. (5.7) for $N_{\mathrm{f}} = 2$, here denoted by α_{QCD}. Following the phase boundary from small to large chemical potential, we first observe that the dominance of the scalar-pseudoscalar interaction channel persists up to $\mu/T_0 \approx 1.7$ as indicated by the red solid line. To illustrate the relative strengths of the various four-quark couplings in this regime, we show in the left panel of Fig. 5.5 the scale dependence of the (dimensionful) renormalized couplings at $\mu/T_0 = 1$ for a temperature $T/T_0 \approx 0.95$ just above the critical temperature. This point is indicated in the phase diagram by the little gray box labeled "1". The various couplings are normalized by the value of the scalar-pseudoscalar coupling $\bar{\lambda}_{(\sigma\text{-}\pi)}$ at $k = 0$. The dynamics are clearly dominated by the scalar-pseudoscalar coupling which is at least two times greater than the modulus of all other couplings. This dominance indicates that in this regime the phase boundary continues to be governed by chiral symmetry breaking.

There exists a short transition region depicted by the red dotted line from approximately $\mu/T_0 \approx 1.7$ to $\mu/T_0 = \mu_\chi/T_0 \approx 2.0$ where we observe that the scalar-pseudoscalar channel, the CSC channel, as well as the $(S+P)_-^{\mathrm{adj}}$-, $(V+A)_\parallel^{\mathrm{adj}}$- and $(V-A)_\perp^{\mathrm{adj}}$-channel are of similar strength and equally dominant, in the sense that the channels are significantly greater in comparison to the remaining interaction channels. Such a region of "mixed" dominances might potentially indicate a metastable or mixed phase [395], while the selection of dominant channels primarily involving adjoint interaction channels points to a non-trivial color-structure of the ground state. However, this transition region of "mixed" dominances might also be a consequence of the $U_\mathrm{A}(1)$-preserving initial conditions as the resulting $U_\mathrm{A}(1)$-symmetric RG flow possibly constraints the development of dominances. The entanglement of several equally strong four-quark couplings might thus be resolved by taking into account $U_\mathrm{A}(1)$-violating fluctuations as well, see our discussion in Section 5.3.2.

From $\mu_\chi/T_0 \approx 2.0$ on, depicted by the red dashed line in Fig. 5.4, we then observe a clear and exclusive dominance of the CSC channel indicating the emergence of a diquark condensate Δ^l. This dominance is again illustrated by the scale dependence of the couplings in this region shown in the right panel of Fig. 5.5. The RG flow is shown at $\mu/T_0 = 4$ for a temperature $T/T_0 \approx 0.74$ again just right above the critical temperature, indicated by the little gray box labeled "2" in the phase diagram 5.5. In this panel, the couplings are now normalized by the modulus of the dominant CSC coupling $|\bar{\lambda}_\mathrm{csc}|$ at $k = 0$. The modulus of the remaining four-quark couplings are at most less than half the value of the CSC coupling. The figure also shows that the $(S+P)_-^{\mathrm{adj}}$ coupling assumes the same value in the IR as the CSC coupling, only with opposite sign. The reason for this behavior is that the boundary conditions with all four-quark couplings initially set to zero at the UV scale Λ leaves the axial $U_\mathrm{A}(1)$ intact, as already briefly mentioned above. The RG flow as derived from the *Wetterich* equation preserves the symmetries of the initial effective average action. As a consequence, the sum rules (4.69) and (4.70) introduced in Section 4.3.1 as a measure of axial $U_\mathrm{A}(1)$ breaking are exactly fulfilled at all scales k, with the first sum rule implying $\bar{\lambda}_\mathrm{csc} = -\bar{\lambda}_{(S+P)_-^{\mathrm{adj}}}$. In fact, the sum rules show that two of the 10 four-quark couplings of our *Fierz*-complete basis are not independent in a $U_\mathrm{A}(1)$-symmetric RG flow, i.e., a $U_\mathrm{A}(1)$-symmetric *Fierz*-complete basis is composed of only eight interaction channels, see also our discussion in Appendix B.3.2. In our computation of the critical temperature as a function of the quark chemical potential we have not included $U_\mathrm{A}(1)$-violating operators, as they are expected to be only relevant inside the IR regime governed by spontaneous symmetry breaking [393]. Nevertheless, in Section 5.3.2, we briefly discuss the influence of $U_\mathrm{A}(1)$-violating initial discussions.

Fig. 5.6 shows the dominance pattern among the four-quark couplings along the finite-temperature phase boundary presented in Fig. 5.4. The IR values of the (dimensionful)

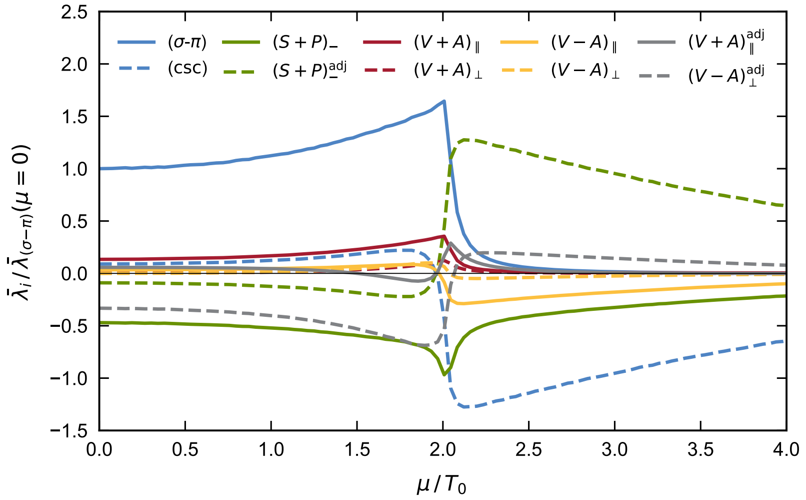

FIGURE 5.6: Values of the various (dimensionful) renormalized couplings at $k = 0$ as functions of the quark chemical potential for temperatures $(T - T_{\mathrm{cr}}(\mu))/T_0 \approx 0.004$, i.e., slightly above the respective critical temperature $T_{\mathrm{cr}}(\mu)$, illustrating the "hierarchy" of the four-quark couplings in terms of their relative strength along the phase boundary as obtained from a computation with the QCD running gauge coupling α_{QCD} (red line in Fig. 5.4). The values are normalized by the coupling $\bar{\lambda}_{(\sigma\text{-}\pi)}$ of the scalar-pseudoscalar interaction channel at $k = 0$ and zero quark chemical potential.

renormalized couplings are shown at $k = 0$ as functions of the quark chemical potential for temperatures just right above the critical temperature $T_{\mathrm{cr}}(\mu)$. The values are normalized by the scalar-pseudoscalar coupling $\bar{\lambda}_{(\sigma\text{-}\pi)}$ at $k = 0$ and at zero chemical potential. As already mentioned above, we first observe a clear dominance of the scalar-pseudoscalar interaction channel below $\mu_\chi/T_0 \approx 2.0$ followed by a change of the dominance pattern to a dominance of the CSC coupling. In the region of CSC dominance, the intact $U_{\mathrm{A}}(1)$ symmetry is again recognizable by the values of the CSC and the $(S + P)_-^{\mathrm{adj}}$-coupling being identical, only with opposite sign. The dominance of the CSC coupling beyond $\mu_\chi/T_0 \approx 2.0$ is similarly pronounced as the dominance of the scalar-pseudoscalar coupling below $\mu_\chi/T_0 \approx 2.0$. In fact, the modulus of the second largest, i.e., subdominant, coupling is even further reduced in this region. Note, however, that in this figure the values of the four-quark couplings are taken slightly above the critical temperature with a distance of about $(T - T_{\mathrm{cr}}(\mu))/T_0 \approx 0.004$. This distance ensures that the RG flow is located in the symmetric regime and the flow can be followed down to $k \to 0$. Owing to this small distance, the transition region in the interval $1.7 \lesssim \mu/T_0 \lesssim 2.0$ with the "mixed" dominances observed above is not fully resolved here.

Fig. 5.6 illustrates the distinct dominance and evident "hierarchy" among the four-quark self-interactions in the two main regions. We emphasize again that the change in the "hierarchy" from a dominance of the scalar-pseudoscalar coupling to a dominance of the CSC coupling at $\mu_\chi/T_0 \approx 2.0$ is a non-trivial outcome completely determined by the dynamics of the system itself. The four-quark couplings are initially set to zero at the UV scale Λ and are dynamically generated by gluodynamics in the course of the RG flow. Thus, the dynamics are not influenced by any kind of fine-tuning of the boundary conditions of the four-quark couplings which could potentially favor particular channels. As already mentioned in Section 4.3.2, this change in the "hierarchy" might point to the existence of a nearby tricritical point in the phase diagram. Yet, this aspect is speculative as the presently employed approximation does not allow a definite answer to this question.

At this point, let us once more bring to attention that the dominance of a four-quark coupling only indicates the onset of the formation of an associated condensate. It does neither guarantee the actual formation, as, e.g., fluctuations in the deep IR could restore the associated symmetries, nor does it strictly exclude the possible formation of other condensates related to subdominant couplings. The analysis based on the dominance pattern of the four-quark couplings must be considered in this context and therefore be taken with some care, see also our discussion in Section 4.1.3.

In Fig. 5.4, we also show the finite-temperature phase boundary resulting from the NJL model (black line) discussed in Section 4.3. In this computation, the initial scalar-pseudoscalar coupling at the UV scale $\Lambda/T_0 \approx 75.76$ has been tuned to obtain the critical temperature $T_{\mathrm{cr}}(\mu = 0) = 132\,\mathrm{MeV}$ at zero quark chemical potential. The remaining initial four-quark couplings are set to zero. The finite-temperature phase boundary agrees with the one obtained from the QCD running gauge coupling α_{QCD} for small quark chemical potential by construction. For values greater than $\mu/T_0 \approx 0.5$, however, the phase boundary as determined from the NJL model starts to deviate significantly and indicates much lower critical temperatures. At the largest quark chemical potential shown in Fig. 5.4, $\mu/T_0 = 4.4$, the critical temperature resulting from the NJL model computation is $T_{\mathrm{cr}}/T_0 \approx 0.366$. In contrast to that, the computation including dynamic gauge fields yields a much higher critical temperature $T_{\mathrm{cr}}(\mu/T_0 = 4.4)/T_0 \approx 0.731$ which is almost twice as large. This observation may have further phenomenological consequences. In standard BCS theory, the critical temperature can be related to the diquark gap at zero temperature, i.e., $T_{\mathrm{cr}} \sim |\Delta|$, see Section 2.2. Thus, the observed increase in the critical temperature in the computation including dynamical gauge degrees of freedom suggests a much greater diquark gap at zero temperature.

Let us recall that in these two computations different initial conditions for the four-quark couplings are assumed, as well as different underlying mechanisms are at play which drive the quark sector to criticality. In our NJL-type model, a finite initial scalar-pseudoscalar coupling ensures that the RG flow diverges at a finite symmetry breaking scale k_{cr} for sufficiently low temperatures, signaling the onset of spontaneous symmetry breaking. In the present approach, the four-quark couplings are dynamically generated and the quark sector is driven to criticality by a sufficiently large gauge coupling, see our discussion in Section 5.2. These differences affect the results for the critical temperature at large quark chemical potential. It might be argued that the initial conditions in case of the NJL model actually favor the scalar-pseudoscalar coupling and do not sufficiently support the dynamics associated with the formation of a diquark condensate which becomes important at high chemical potentials. The boundary conditions enforce that the dynamics are initially driven by the scalar-pseudoscalar self-interaction. Still, at large chemical potential, the CSC channel takes over by itself, although the actual position might be nonetheless biased by our choice for the initial condition. In contrast to that, the dynamic gauge fields are able to drive the quark sector to criticality not only through the scalar-pseudoscalar coupling but also by directly triggering the interaction channels with non-trivial color structure. However, we observe the intriguing outcome that in both computations the "hierarchy" of the various interaction channels starts to change at approximately the same quark chemical potential $\mu/T_0 \approx 1.7$, the dominance as obtained from the NJL model changes directly from the scalar-pseudoscalar coupling (black solid line) to the CSC coupling (black dashed line) whereas the system resulting from the computation including dynamic gauge fields first enters a short transition region of "mixed" dominances, before the region characterized by a clear dominance of the CSC coupling begins at $\mu_\chi/T_0 \approx 2.0$. This observation indicates that the "hierarchy" of the interaction channels in terms of their strength might be determined to a large extent by the interplay of the various four-quark couplings themselves.

In Fig. 5.4, depicted by the blue line labeled α_{YM}, we also included results for the finite-temperature phase boundary of a computation including dynamic gauge fields where we have used a running gauge coupling as obtained in pure YM theory, i.e., the scale dependence of the strong coupling was derived from Eq. (5.7) with $N_{\mathrm{f}} = 0$. The phase boundary as well as the dominances agree almost perfectly with the results of the computation using α_{QCD}. We observe a dominance of the scalar-pseudoscalar coupling at small quark chemical potentials, a transition region characterized by a "mixed" dominance pattern between $1.7 \lesssim \mu/T_0 \lesssim 2.0$, and finally a clear dominance of the CSC coupling at larger quark chemical potentials. This is noteworthy since the pure YM coupling α_{YM} as a function of the RG scale k is greater compared to the QCD coupling α_{QCD}, see the right panel of Fig. 5.1. The coupling starts to increase earlier in the RG flow and assumes a higher maximum for a given temperature. However, the effect of this difference in the scale dependence of the running gauge couplings is also to a certain extent compensated by the scale fixing procedure. The initial UV value of the pure YM gauge coupling is by approximately 13% smaller in comparison to the α_{QCD} coupling in order to obtain the same critical temperature $T_{\mathrm{cr}}(\mu = 0) = 132\,\mathrm{MeV}$ at zero quark chemical potential. Nonetheless, the YM gauge coupling α_{YM} amplifies the effect of the gauge dynamics on the quark sector. As argued above, a stronger influence of the gauge fields potentially favors the dominance of interaction channels with non-trivial color structure. Still, we observe that the dominances along the phase boundary are not changed. This serves as another indication that the "hierarchy" of the various couplings in terms of their relative strength is predominantly determined by the dynamics within the quark sector.[10]

As a closing remark, we note that the comparison of the different phase boundaries shown in Fig. 5.4 have to be taken with some care. Although all three computations (labeled α_{QCD}, α_{YM} and NJL in Fig. 5.4) yield approximately the same critical scale $k_{\mathrm{cr}}/T_0 \approx 2.6$ in the vacuum limit, the different approaches do not necessarily lead to the same values of low-energy observables.

---

[10] Using "deformed" initial conditions, i.e., a given finite UV value of the scalar-pseudoscalar interaction and the initial value of the running gauge coupling α_{QCD} adjusted to obtain the critical temperature $T_{\mathrm{cr}}(\mu = 0) = 132\,\mathrm{MeV}$, the critical temperature as a function of the quark chemical potential assumes values in between the phase boundary resulting from the NJL model and the original phase boundary determined with the QCD running coupling α_{QCD} (black and red line in Fig. 5.4, respectively). The dominances along the phase boundary, however, are very robust and remain largely unaffected. We still observe the two main regions with the dominance of the scalar-pseudoscalar interaction channel at small chemical potential and the dominance of the CSC channel at large chemical potential.

5.3.1 In-medium effects on the gauge anomalous dimension

In our study, the anomalous dimension η_A determines the scale dependence of the gauge coupling g_s, see Eq. (5.7) and our discussion in Section 5.1. It receives contributions from the gluonic sector as well as from quark fluctuations. For our computations presented in this chapter thus far, we have taken the anomalous dimension η_A as external input from Refs. [392, 393], where these contributions were calculated for all scales and temperatures. However, the quark fluctuations which contribute to the anomalous dimension are modified at finite density. We briefly discuss in the following some aspects of in-medium effects on the anomalous dimension η_A and the resulting implications for the finite-temperature phase boundary. In order to estimate the influence of such effects, we adopt the following form for the anomalous dimension:

$$\eta_A = \eta_A^{\mathrm{YM}} + \Delta\eta_A \,, \tag{5.11}$$

where the quark contribution $\Delta\eta_A$ is added to the anomalous dimension η_A^{YM} as obtained in pure YM theory. This approximation has been applied earlier in Refs. [186, 187, 193, 397], and has also been used in *Dyson-Schwinger* studies, see, e.g., Refs. [188, 426–428]. The pure YM anomalous dimension η_A^{YM} is again taken from Refs. [392, 393]. Following Refs. [193, 429, 430], the quark contribution to the gluon anomalous dimension is given by:

$$\Delta\eta_A = \frac{-Z_A^{-1}}{3(N_\mathrm{c}^2-1)\mathcal{V}}\,\frac{\partial}{\partial p^2}\bigg|_{p=0} \mathrm{tr}\left(\delta^{ab}P^{\perp}_{\mu\nu}\cdot\right. \tag{5.12}$$

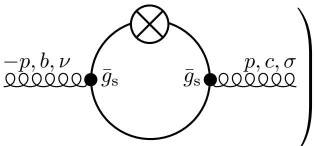

$$\left.\vphantom{\frac{1}{1}}\right)\,,$$

with the transversal projection operator $P^{\perp}_{\mu\nu}$ defined in Eq. (5.3) and the four-dimensional space-time volume $\mathcal{V}$. The diagram represents the expression

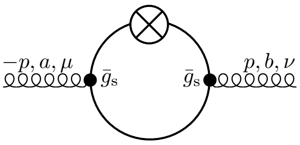

$$:= \left(\frac{\delta}{\delta A^a_\mu(-p)}\,\frac{\delta}{\delta A^b_\nu(p)}\,\frac{1}{2}\mathrm{STr}\left\{\frac{\partial_t R_k}{\Gamma_k^{(2)}+R_k}\right\}\right)\Bigg|_{\substack{A=0\\ \bar{\psi}=\psi=0}}\,, \tag{5.13}$$

where p is the external momentum and the crossed circle depicts the regulator insertion. As the quark propagators depend on the quark chemical potential, we can thus incorporate in-mediums effects on the gauge anomalous dimension η_A with this contribution. Only the class of diagrams associated with fermionic propagators of equal sign structure in their μ-dependence contributes in Eq. (5.12), corresponding to the blue labels in Fig. 5.2. For the computation of the quark contribution $\Delta\eta_A$, we employ the three-dimensional *Litim* regulator (3.31) introduced in Section 3.2 to regularize the fermion loop (5.13).[11] In the vacuum limit, the quark contribution (5.12) reduces to the perturbative one-loop result

---

[11] The application of covariant regularization schemes to computations beyond the leading order of the derivative expansion is possible but very difficult due to the non-analyticity at the *Fermi* surface in the zero-temperature limit and is not considered here.

$\Delta\eta_A = g_s^2/(6\pi^2)$. However, employing a different three-dimensional regularization scheme introduces deviating relations of scales as opposed to the covariant regularization scheme used otherwise. We therefore emphasize that we here only aim for a qualitative analysis of in-medium effects on the quark contribution $\Delta\eta_A$. Moreover, note that the applicability of the approximation (5.12) relies on a mild momentum dependence of the quark contribution, we refer to Ref. [193] for a detailed discussion. Such a mild momentum dependence is guaranteed as long as the quark propagator remains gapped as entailed by, e.g., a finite RG scale k, a thermal mass or non-zero quark masses.

At high temperatures, the quark contribution to the gauge anomalous dimension is suppressed as the quarks decouple because of their thermal mass. Consequently, the scale dependence of the gauge coupling is only very mildly modified by the quark chemical potential. At large RG scales k, the running gauge coupling remains unchanged and approaches the vacuum limit as $T/k \ll 1$ and $\mu/k \ll 1$. For increasing quark chemical potential, however, the quark contribution becomes significant in the regime where $\mu > T$. The gauge coupling starts to increase at larger scales and the location of the maximum of the gauge coupling, cf. Fig. 5.1, is more and more dominated by the scale of the chemical potential. For small temperatures and high quark chemical potential, the maximum is located near $k \sim \mu$, while its maximum value increases for greater chemical potentials. For the RG scale k approaching zero at finite temperature, the quarks decouple and the scale dependence of the gauge couplings remains unaffected by the quark chemical potential, i.e., the gauge couplings agree with the running as obtained in pure YM theory.

In Fig. 5.7, the finite-temperature phase boundary resulting from a computation based on the running gauge coupling with the quark contribution (5.11) and (5.12) is shown in comparison to the former results shown in Fig. 5.4, obtained with the strong coupling α_{QCD} determined from Eq. (5.7) with the anomalous dimension η_A for $N_{\mathrm{f}} = 2$ taken from Refs. [392, 393]. We first neglect the dependence on the quark chemical potential by setting $\mu = 0$ in the expression (5.12) in order to estimate the influence of the different three-dimensional scheme used to regularize this particular fermionic loop. The corresponding phase boundary is given by the yellow line in Fig. 5.7 labeled $\alpha_{\mathrm{QCD}}|_{\Delta\eta_A(\mu=0)}$. The phase boundary agrees quite well with the former results depicted by the red line. Only at large quark chemical potential a deviation of approximately 5% is observed. This may be traced back to the fact that the gauge coupling α_{QCD} from Refs. [392, 393] incorporates higher-order quark fluctuation effects as compared to Eq. (5.12), resulting in a decrease in the running gauge coupling owing to fermionic screening. As a consequence, the running gauge coupling determined from Eq. (5.11) with (5.12) is generally stronger. However, the scale fixing procedure anchoring our computation at the critical temperature $T_{\mathrm{cr}}(\mu = 0) = 132\,\mathrm{MeV}$ entails a smaller initial UV value for the $\alpha_{\mathrm{QCD}}|_{\Delta\eta_A(\mu=0)}$ coupling and thus partially counteracts the stronger running. As a result, the gauge coupling α_{QCD} still starts to increase at higher scales and is thus capable of driving the quark sector to criticality even at temperatures slightly above the critical temperature associated with the coupling $\alpha_{\mathrm{QCD}}|_{\Delta\eta_A(\mu=0)}$ at a given finite quark chemical potential. In summary, the influence of the three-dimensional regularization scheme appears to be rather mild which, however, might be a consequence of the applied scale fixing procedure.

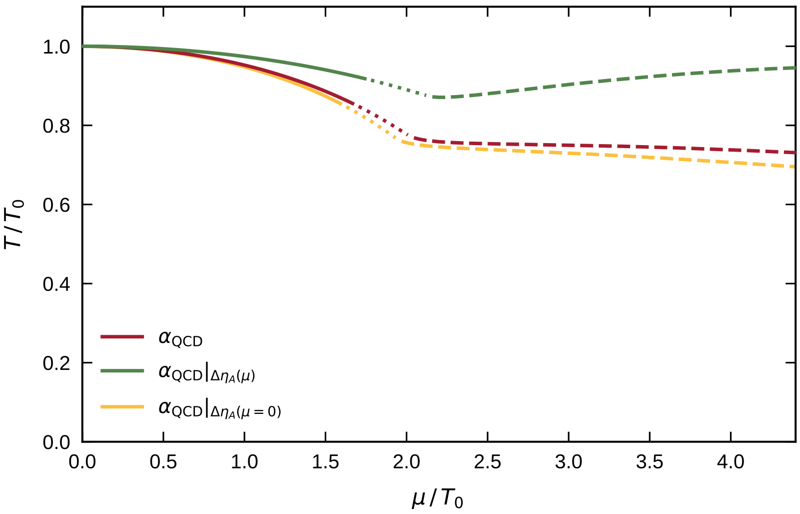

FIGURE 5.7: Phase boundary associated with the spontaneous breakdown of at least one of the fundamental symmetries as obtained from the *Fierz*-complete ansatz (5.1) including dynamic gauge fields. The scale dependence of the gauge coupling g_s is computed from Eq. (5.7) with the anomalous dimension η_A for $N_f = 2$ either taken from Refs. [392, 393] (red line denoted by α_{QCD}) or given by the approximation (5.11), with the quark contribution (5.12) evaluated at zero quark chemical potential (yellow line denoted by $\alpha_{\mathrm{QCD}}|_{\Delta\eta_A(\mu=0)}$) or at finite quark chemical (green line denoted by $\alpha_{\mathrm{QCD}}|_{\Delta\eta_A(\mu)}$), see main text for details.

The finite-temperature phase boundary as determined with a μ-dependent quark contribution to the gauge anomalous dimension is depicted by the green line in Fig. 5.7 labeled $\alpha_{\mathrm{QCD}}|_{\Delta\eta_A(\mu)}$. The in-medium effects on the running gauge coupling tend to further increase the critical temperature while the effect is stronger for larger chemical potentials. At $\mu/T_0 = 4.4$, the critical temperature is increased by almost 40% compared to the results computed with the coupling α_{QCD}. An intriguing result is that the dominances along each phase boundary in Fig. 5.7 remain completely unaffected. The solid lines indicate again a dominance of the scalar-pseudoscalar coupling, the dashed lines a CSC dominance and the dotted lines a transition region characterized by a “mixed” dominance pattern. As the differences between the underlying computations concern the gauge sector, this finding is another indicator that the dominance pattern is determined by the dynamics in the quark sector.

At this point, let us emphasize once more that the results of the computation with the quark contribution (5.12) has to be taken with care and that our analysis of such in-medium effects is only qualitative. Foremost, the three-dimensional regularization scheme used in the computation of the quark contribution implies a different relation of scales and therefore the comparability to the computation based on a covariant regularization scheme is limited. As discussed in Sections 3.2 and 4.2.4, three-dimensional regularization schemes lack locality in the temporal direction and potentially amplify effects which are associated with this temporal direction such as the influence of the temperature or the quark chemical potential, see also our discussion of the curvature of the finite-temperature phase boundary at zero quark chemical potential in Section 5.3.2. Thus, the increased critical temperature resulting from a computation with the coupling $\alpha_{\mathrm{QCD}}|_{\Delta\eta_A(\mu)}$ might be overestimated. Furthermore, the applied scale fixing procedure leads to a critical scale $k_{\mathrm{cr}}/T_0 \approx 3.5$ in the vacuum limit as compared to $k_{\text{cr}}/T_0 \approx 2.6$ obtained in a computation with the coupling α_{QCD}. The different approaches will therefore lead to different values for the low-energy observables, with the consequence that a direct quantitative comparison is limited. Nonetheless, qualitative comparisons are still considered meaningful.

5.3.2 $U_{\text{A}}(1)$ symmetry

The initial conditions of the RG flow chosen so far leave the axial $U_{\text{A}}(1)$ symmetry intact. All couplings of the four-quark self-interactions are set to zero at the UV scale Λ and are generated dynamically by gluodynamics in the course of the flow. In, e.g., Refs. [392, 393], the omission of $U_{\text{A}}(1)$-violating interaction channels is based on the assumption that these interactions become relevant only in the regime governed by spontaneous symmetry breaking. Our *Fierz*-complete basis $\mathcal{B}$ composed of the 10 four-quark interaction channels (4.59)-(4.68) is effectively reduced to eight interaction channels in case of the $U_{\text{A}}(1)$ symmetry being intact. Recall that the sum rules (4.69) and (4.70) imply that two of the couplings associated with the four $U_{\text{A}}(1)$-violating interaction channels of our basis $\mathcal{B}$ are not independent. The sum rules are exactly fulfilled at all scales in the symmetric phase and for all $k \gtrsim k_{\text{cr}}$ in the phase governed by spontaneous symmetry breaking. In the latter case, the $U_{\text{A}}(1)$ symmetry may potentially be broken spontaneously below the symmetry breaking scale k_{cr}, although this cannot be resolved in our present study.

In our analysis of the NJL model in Section 4.3.3, we have observed that $U_{\text{A}}(1)$ symmetry breaking influences the dominances of the four-quark couplings in terms of their relative strength along the finite-temperature phase boundary. In particular, we have found explicit $U_{\text{A}}(1)$ symmetry breaking to be important for the formation of the conventional CSC ground state at intermediate and large values of the chemical potential. In the present study, the four-quark couplings are dynamically generated by the gauge fields. Following the critical temperature $T_{\text{cr}}(\mu)$ as a function of the quark chemical potential, we observe different regions characterized by a distinct "hierarchy" of four-quark couplings which are remarkably robust against variations of the running gauge coupling, see Figs. 5.4 and 5.7. The scalar-pseudoscalar interaction channel dominates the dynamics at small quark chemical potential, signaling the formation of the chiral condensate, while at higher quark chemical potential the dominance of the conventional CSC coupling indicates the formation of a diquark condensate. The latter is observed in spite of the intact $U_{\text{A}}(1)$ symmetry in our considerations thus far. Only at chemical potentials between $1.7 \lesssim \mu/T_0 \lesssim 2.0$, we observe a transition region which is characterized by several equally strong interaction channels, see our discussion above. Moreover, the dominance of the CSC coupling is always accompanied by an equally strong $(S+P)_{-}^{\text{adj}}$-channel as a direct consequence of the intact $U_{\text{A}}(1)$ symmetry: The sum rule (4.69) ties the modulus of the CSC coupling to the modulus of the $(S+P)_{-}^{\text{adj}}$-coupling.

In order to probe the influence of explicit $U_{\text{A}}(1)$ symmetry breaking, we study in the following the RG flow for $U_{\text{A}}(1)$-violating boundary conditions for the four-quark couplings. The strength of $U_{\text{A}}(1)$ breaking is controlled by the initial value of the $(S+P)_{-}$-coupling. The associated four-quark interaction channel is related to the so-called *'t Hooft* determinant [223, 224], see Eq. (4.57) in Section 4.3.1 and also Refs. [119, 239, 416–418]. The values of the other

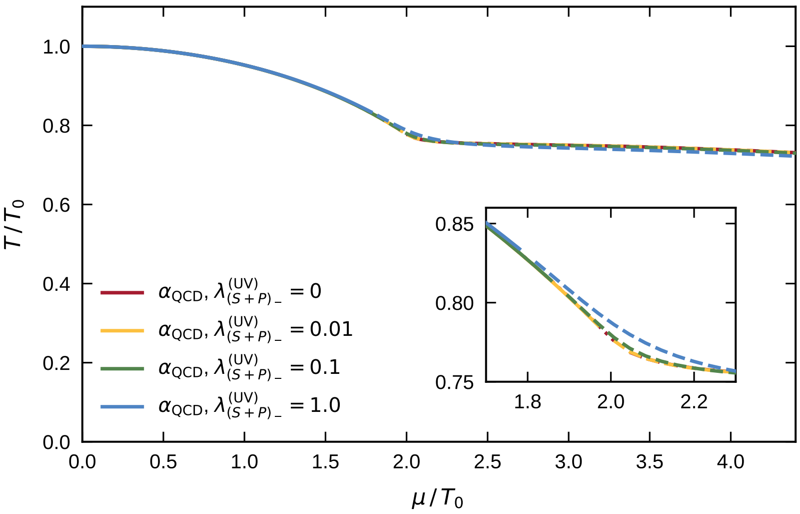

FIGURE 5.8: Phase boundary associated with the spontaneous breakdown of at least one of the fundamental symmetries as obtained from the *Fierz*-complete ansatz (5.1) under the influence of explicit $U_{\mathrm{A}}(1)$ symmetry breaking. The running gauge coupling α_{QCD} is derived from Eq. (5.7) with the anomalous dimension η_A for $N_{\mathrm{f}} = 2$ taken from Refs. [392, 393]. The strength of the initial explicit $U_{\mathrm{A}}(1)$ symmetry breaking is controlled by the value of the (dimensionless) renormalized coupling of the $(S+P)_-$-channel at the UV scale Λ, the values of all other four-quark couplings continue to be initially zero. The phase boundary is shown for $U_{\mathrm{A}}(1)$-symmetric boundary conditions and for the $U_{\mathrm{A}}(1)$-violating initial conditions $\lambda^{(\mathrm{UV})}_{(S+P)_-} = 0.01,\, 0.1,\, 1.0$. A dominance of the scalar-pseudoscalar interaction channel is depicted by a solid line and a dominance of the CSC channel by a dashed line (the case of "mixed" dominances occurring for $U_{\mathrm{A}}(1)$-symmetric boundary conditions is indicated by a dotted line although hardly visible in this depiction, see inset or Fig. 5.4). See main text for details.

four-quark couplings remain zero at the UV scale Λ, while for each choice of the initial $(S+P)_-$-coupling the UV value of the gauge coupling $g_{\mathrm{s}}(\Lambda)$ is adjusted to preserve the critical temperature $T_{\mathrm{cr}}(\mu = 0) = 132\,\mathrm{MeV}$ at zero chemical potential.

First, we can again analyze the fate of the $U_{\mathrm{A}}(1)$ symmetry breaking at finite temperature and quark chemical potential as measured by the sum rules (4.69) and (4.70). Adopting the normalization (4.74), we observe the exact same qualitative behavior as discussed in Section 4.3.3: At small quark chemical potential close to the critical temperature $T_{\mathrm{cr}}(\mu)$, the $U_{\mathrm{A}}(1)$ breaking is driven by the dynamics of pions and increases toward the IR as indicated by increasing ratios R_1 and R_2, with $R_2 \gg R_1$ owing to the dominance of the scalar-pseudoscalar interaction channel. At larger chemical potentials, the strength of $U_{\mathrm{A}}(1)$ symmetry breaking becomes also stronger as the phase boundary is approached from above, now driven by the dynamics of diquark degrees of freedom associated with the CSC channel. As a consequence, R_1 and R_2 are of the same order of magnitude since both depend on the CSC coupling. In either case, for increasing temperature, the $U_{\mathrm{A}}(1)$ breaking remains more and more on the initial level as defined by the $U_{\mathrm{A}}(1)$-violating boundary conditions in the UV since quark fluctuations become thermally suppressed. Note that the exact quantitative results certainly depend on the choice for the initial UV value of the $(S+P)_-$-coupling.

Let us now compare the phase diagram as obtained with the $U_{\mathrm{A}}(1)$-symmetric initial conditions employed before, i.e., all four-quark couplings are initially set to zero, to the phase diagrams resulting from $U_{\mathrm{A}}(1)$-violating initial conditions. The strength of the explicit $U_{\mathrm{A}}(1)$

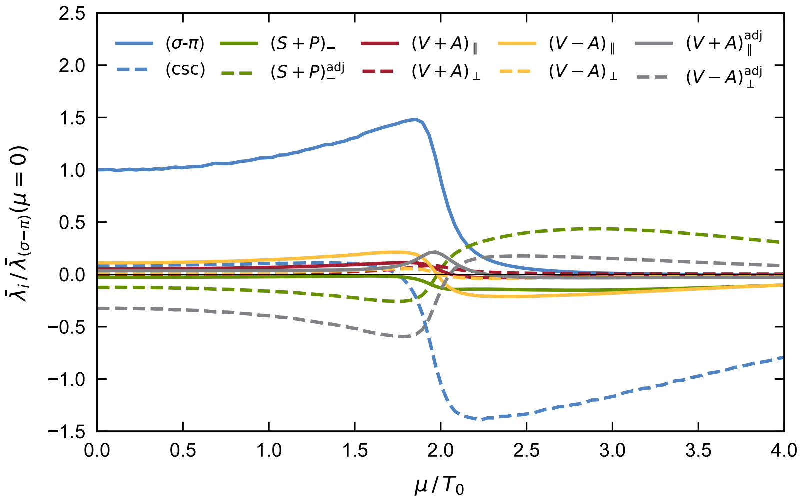

FIGURE 5.9: Values of the various (dimensionful) renormalized couplings at $k = 0$ as functions of the quark chemical potential for temperatures $(T - T_{\mathrm{cr}}(\mu))/T_0 \approx 0.002$ slightly above the respective critical temperature at given quark chemical potential, illustrating the "hierarchy" of the four-quark couplings in terms of their relative strength along the phase boundary (blue line in Fig. 5.8). The values of the couplings are shown for the $U_{\mathrm{A}}(1)$-violating initial conditions with $\lambda^{(\mathrm{UV})}_{(S+P)_-} = 1.0$, normalized by the coupling $\bar{\lambda}_{(\sigma\text{-}\pi)}$ of the scalar-pseudoscalar interaction channel at $k = 0$ and zero quark chemical potential.

breaking at the initial UV scale Λ is controlled by the value of the (dimensionless) renormalized coupling of the $(S{+}P)_-$-channel which we choose to assume the values $\lambda^{(\mathrm{UV})}_{(S+P)_-} = 0.01,\ 0.1,\ 1.0$. In all computations we use the running gauge coupling α_{QCD} determined from Eq. (5.12) with the gauge anomalous dimension η_A taken from Refs. [392, 393] for $N_{\mathrm{f}} = 2$. In Fig. 5.8, the various phase diagrams as obtained with the different boundary conditions are shown. It is remarkable how little the critical phase temperature as a function of the quark chemical potential is affected by the strength of the initial explicit breaking of the $U_{\mathrm{A}}(1)$ symmetry, although the strength in terms of the initial value of the $(S + P)_-$-coupling is varied over three orders of magnitude. Across the entire range of chemical potentials shown in this figure, the variation of the critical temperature is less than 1.3%.[12] In all cases, we observe a dominance of the scalar-pseudoscalar coupling at small quark chemical potentials, depicted by the solid lines in Fig. 5.8. The transition region of "mixed" dominances for chemical potentials between $1.7 \lesssim \mu/T_0 \lesssim 2.0$ present in case of $U_{\mathrm{A}}(1)$-symmetric initial conditions vanishes for all considered $U_{\mathrm{A}}(1)$-violating initial conditions. The dominance changes directly from the scalar-pseudoscalar channel to the CSC channel at $\mu_\chi/T_0 \approx 2.0\,(1.9,\ 1.8)$ for the initial coupling $\lambda^{(\mathrm{UV})}_{(S+P)_-} = 0.01\,(0.1,\ 1.0)$ of the $U_{\mathrm{A}}(1)$-violating $(S + P)_-$-channel as indicated by the dashed lines in Fig. 5.8.

The "hierarchy" of the various four-quark couplings in terms of their relative strength along the phase boundary is shown in Fig. 5.9 for the initial coupling $\lambda^{(\mathrm{UV})}_{(S+P)_-} = 1.0$. This

---

[12] For all initial conditions of the computations shown in Fig. 5.8, the symmetry breaking scale in the vacuum limit remains at approximately $k_{\mathrm{cr}}/T_0 \approx 2.6$. Still, the direct quantitative comparison of the phase boundaries has to be taken with some care as the different computations do not necessarily lead to the same values of low-energy observables.

figure shows again the IR values of the (dimensionful) renormalized couplings at $k = 0$ as functions of the quark chemical potential for temperatures $(T - T_{\mathrm{cr}}(\mu))/T_0 \approx 0.002$ just above the respective critical temperature at given chemical potential. The values are normalized by the scalar-pseudoscalar coupling $\bar{\lambda}_{(\sigma\text{-}\pi)}$ at zero chemical potential. We again observe a clear dominance first of the scalar-pseudoscalar interaction channel below $\mu_\chi/T_0 \approx 2.0$ and a clear dominance of the CSC interaction channel for larger values of the chemical potential. Compared to Fig. 5.6 with the values obtained from a computation with $U_{\mathrm{A}}(1)$-symmetric boundary conditions, the dominances appear even more pronounced in the present case. In particular, the CSC channel is not accompanied anymore by an equally strong $(S+P)_-^{\mathrm{adj}}$-coupling. The latter assumes considerably smaller values for $\mu_\chi/T_0 \gtrsim 2.0$ in comparison to the computation with intact $U_{\mathrm{A}}(1)$ symmetry, while the CSC coupling assumes even slightly larger values. We conclude from our findings that the breaking of the $U_A(1)$ symmetry plays an important role in shaping the "hierarchy" of four-quark couplings and thus in the formation of associated condensates as indicated by the dominances. This observation specifically confirms the importance of explicit $U_{\mathrm{A}}(1)$ breaking for the formation of the conventional CSC ground state at higher chemical potentials as already discussed in Section 4.3.3. In this respect, we again refer to early seminal works on color superconductivity, see, e.g., Refs. [98–100, 102–104, 109, 110, 420, 421]. Let us emphasize, however, that the change in the "hierarchy" from a dominance of the scalar-pseudoscalar coupling to a dominance of the CSC coupling at $\mu_\chi/T_0 \approx 2.0$ is remarkably insensitive to the initial strength of explicit $U_{\mathrm{A}}(1)$ symmetry breaking as controlled by the initial coupling $\lambda_{(S+P)_-}^{(\mathrm{UV})}$. This change in the "hierarchy" of four-quark couplings is a non-trivial outcome completely determined by the dynamics of the system itself.

To close this section, we briefly comment on the curvature of the finite-temperature phase boundary at small chemical potential, see Eq. (4.40) in Section 4.2.3 for the definition. The values of the curvature as obtained from the various computations presented in this section are summarized in Table 5.1. Compared to the phase boundary from the NJL model study, we find the curvature to be significantly decreased in our study including dynamical gauge degrees of freedom. The value is reduced by approximately 38%. At least as long as the gauge coupling does not receive any corrections from the presence of a finite chemical potential, the critical temperature at small chemical potentials as measured by the curvature appears to be insensitive to the different settings considered here. These different settings include computations using the running gauge couplings denoted by α_{QCD} and α_{YM} as well as computations with varied initial conditions to incorporate explicit $U_{\mathrm{A}}(1)$ symmetry breaking at the initial cutoff scale. Taking into account in-medium effects on the quark contribution to the gauge anomalous dimension, however, the curvature might be significantly changed. With our estimate of such effects as discussed in Section 5.3.1, we observe the curvature to be further reduced by about 43%. However, note that the adopted scale fixing procedure applied to the different computations of the finite-temperature phase boundary might lead to different values of low-energy observables in each setting which makes a direct quantitative comparison difficult. In particular the computation with the μ-dependent quark contribution to the gauge anomalous dimension is to be understood as only a qualitative assessment of the impact since the regularization of the associated loop diagram employs a different three-dimensional scheme.

setting	curvature κ
α_{QCD}	0.046
α_{YM}	0.044
NJL	0.074
$\alpha_{\mathrm{QCD}}\|_{\Delta\eta_A(\mu)}$	0.026
$\alpha_{\mathrm{QCD}}, \lambda^{(\mathrm{UV})}_{(S+P)_-} = 1.0$	0.046

Table 5.1: Curvature κ of the finite-temperature phase boundary at $\mu = 0$ as obtained from the various computations discussed in this section, see Figs. 5.4, 5.7, and 5.8.

Moreover, the symmetry breaking scale k_{cr} in the vacuum limit differs already significantly, see our discussion in Section 5.3.1. In fact, the comparison of our results for the curvature to lattice QCD studies [63, 431] suggests that the computation (5.12) of a μ-dependent quark contribution to the gauge anomalous dimension tend to overestimate the in-medium effects, thus leading to a probably too strong decrease of the value of the curvature. A summary of recent results for the curvature extracted from lattice computations indicate the range $\kappa \sim 0.045 \ldots 0.203$ [431]. However, a direct comparison to these results is only possible to a limited extent as they were typically obtained from computations close to the physical point including strange quark fluctuations. Indeed, the curvature determined in the chiral limit by assuming a second-order critical scaling rather tend to the lower bound of this range [431], approximately agreeing with the results from our computations neglecting in-medium effects on the gauge anomalous dimension.

5.4 Conclusions

In the studies presented in this chapter, we have analyzed the RG flow of the couplings of effective four-quark interactions in the pointlike limit which are dynamically generated by gluodynamics. Building on our *Fierz*-complete NJL model study with two quark flavors coming in $N_{\mathrm{c}} = 3$ colors, see Section 4.3, we have incorporated the gluodynamics by extending the ansatz (4.3) for the effective action with the basis of four-quark interaction channels parametrized by Eqs. (4.59)-(4.68) to include dynamic gauge fields, leading to the ansatz given by Eq. (5.1). For our computation in the *Feynman* gauge, the gauge propagator was assumed to be of the simplified form (5.6). With this study, we have taken a step toward a top-down first-principles approach to analyze the phase structure of QCD at finite temperature and quark chemical potential. Working in the chiral limit, the only parameter is given by the strong coupling g_{s} which we set at a large initial UV scale in the perturbative regime while the scale dependence was determined by the gluon anomalous dimension η_A. Incorporating the fundamental microscopic degrees of freedom allowed us to initiate the RG flow at much higher scales, thereby extending the range of applicability in terms of the external control parameters, namely temperature and quark chemical potential.

Our findings indicate that the incorporation of gluodynamics with fluctuation induced effective four-quark self-interactions leads to significantly increased critical temperatures at larger values of the quark chemical potential in comparison to the results as obtained from our NJL-type model discussed in Section 4.3. Assuming that the critical temperature can be related to the magnitude of the energy gap in a color superconducting phase of quark matter at vanishing temperature, the results of our computation including dynamic gauge fields suggest a larger energy gap associated with the diquark condensate at higher densities. The finite-temperature phase boundary appears to be very stable against variations in the specific scale dependence of the strong coupling, at least as long as in-medium effects on the quark contribution to the gauge anomalous dimension are not included. We have found the shape of the finite-temperature phase boundary to be significantly affected by the μ-dependent quark contribution (5.12) to the gauge anomalous dimensions. This finding suggests that in-medium effects on the matter back-coupling to the gauge sector might play a more important role at higher densities. We emphasize, however, that our analysis of such in-medium effects were only qualitative. The observed effect is possibly overestimated as the employed three-dimensional regularization scheme lacks locality in the direction of time-like momenta as opposed to covariant regularization schemes and might thus tend to amplify these effects.

In order to improve our results on a quantitative level, the truncation (5.1) which we have employed as an ansatz for the effective average action can be extended in the gluon sector as well as in the matter sector, see, e.g., Refs. [192, 195, 196] for recent FRG studies at vanishing quark chemical potential aiming at quantitative precision. Already at the present level, the quark propagator receives corrections in form of the wavefunction renormalizations $Z_{\psi}^{\parallel}$ and $Z_{\psi}^{\perp}$ which we have set to one in our computation thus far. Further improvements can be achieved by taking into account the explicit dependence of the RG flow equations of the four-quark couplings on the anomalous dimensions and, in particular in the presence of a heat bath and at finite quark chemical potential, the splitting of the gluon propagator into electric and magnetic components as shown in Eq. (5.2), see also Ref. [196].

Toward the IR, the treatment of the four-quark interactions in the pointlike limit does not allow us to access the phase governed by spontaneous symmetry breaking. The introduction of mesonic auxiliary fields by means of a *Hubbard-Stratonovich* transformation or applying the more advanced technique of dynamical hadronization [337, 380, 396, 398], see, e.g., Refs. [192, 193, 195, 397] for their application to QCD, would allow us to access the phase of spontaneously broken symmetry. The latter effectively implements continuous *Hubbard-Stratonovich* transformations of four-quark interactions in the RG flow. Following the approach of our NJL-type model studies in Chapter 4, in order to gain at least some insight into the structure of the ground state in the phase governed by spontaneous symmetry breaking, we have analyzed the “hierarchy” of the four-quark couplings in terms of their relative strength. At small quark chemical potential, a clear dominance of the scalar-pseudoscalar interaction channel associated with chiral symmetry breaking is observed. Interestingly, this dominance is not trigged by the specific choice for the initial conditions of the four-quark couplings as all couplings are initially set to zero and are only fluctuation-induced in the course of the RG flow. This means that it is solely determined by the dynamics of the gluons and quarks. Starting from approximately $\mu_{\chi}/T_0 \gtrsim 2.0$, we observe a change in the “hierarchy” to find the phase boundary to be clearly dominated by the CSC coupling which is related to the formation of the most conventional color superconducting condensate in two-flavor QCD. We emphasize that the dominances themselves as well as the location μ_χ of the transition to the CSC dominance were found to be remarkably robust against the various settings of our computations. The little influence of the different running gauge couplings which we have considered might point to the fact that the dominances are largely determined within the quark sector. Note again that the dynamics were not influenced by any kind of fine-tuning of the boundary conditions for the four-quark couplings which would in general favor particular channels. However, the analysis based on the "hierarchy" of the four-quark couplings must certainly be taken with some care. A dominance of a specific four-quark coupling does neither guarantee the formation of an associated condensate in the IR nor does it exclude the formation of other condensates.

In order to probe the underlying dynamics further, we have analyzed the influence of $U_\mathrm{A}(1)$-violating initial conditions on the critical temperature as a function of the quark chemical potential and on the dominances of the four-quark couplings along this finite-temperature phase boundary. Even at large chemical potential, the considered strengths of explicit $U_\mathrm{A}(1)$ symmetry breaking at the initial UV scale showed surprisingly little effect on the shape of the phase boundary. The $U_\mathrm{A}(1)$-violating initial conditions as opposed to the $U_\mathrm{A}(1)$-symmetric RG flow, however, do influence the "hierarchy" of the four-quark couplings along the phase boundary, visible in the vanishing of the "mixed" phase and the amplification of the dominance of the scalar-pseudoscalar interaction channel at small chemical potential as well as of the CSC-channel dominance at high chemical potential. The location μ_χ of the change of the dominances is again not affected. From this observation we conclude that the $U_\mathrm{A}(1)$ symmetry breaking plays indeed an important part in the formation of the condensates as associated with the dominances, in particular regarding the formation of the conventional CSC ground state at higher chemical potentials [98–100, 102–104, 109, 110, 420, 421].

Lastly, we would like to note again that our present truncation can be further improved on a quantitative level. Still, our analysis already provides important insights into the phase structure at finite temperature and quark chemical potential and consolidates the findings obtained earlier from our *Fierz*-complete NJL-type model study in Section 4.3. Moreover, incorporating the fundamental microscopic degrees of freedom of QCD, i.e., quarks and gluons, combined with the *Fierz*-complete set of four-quark interactions enables us to identify the relevant low-energy effective degrees of freedom in approaching the long-range physics and to determine, or at least to constrain from first principles the couplings of a suitable truncation in order to describe the low-energy dynamics, especially at finite temperature and/or quark chemical potential. In this way, the range of applicability of such an approach in terms of the external control parameters can be extended. This might prove very valuable, e.g., to study the thermodynamics of cold quark matter at higher densities.

6

LOW-ENERGY REGIME AND EQUATION OF STATE

In spite of substantial advances in the development of fully first-principles approaches to QCD in recent years, the regime of cold strong-interaction matter at higher densities remains notoriously difficult to access. This applies in particular to the EOS of cold QCD matter at baryon number densities $n_{\mathrm{B}} \sim (2-10)\, n_0$, in terms of the nuclear saturation density $n_0 \approx 0.16/\mathrm{fm}^3$, which are believed to be reached inside neutron stars, see, e.g., the reviews [56, 148]. The understanding of QCD matter at these densities is thus essential for studies of neutron stars, with the EOS being the key input. However, while lattice Monte Carlo techniques are being plagued by the sign problem [74], only the two limits of low and asymptotically large densities are currently considered accessible in a well-controlled manner: Nuclear matter at lower densities up to $n_{\mathrm{B}} \lesssim 2\, n_0$ can be very successfully described by employing chiral EFT, see, e.g., Refs. [283, 286], and asymptotic freedom allows the application of perturbation theory at very high densities beyond $n_{\mathrm{B}} \gtrsim 70\, n_0$ [302, 306], see also our discussion in Section 2.3. Still, toward intermediate densities both approaches develop large uncertainties and do not allow reliable theoretical calculations of the EOS in this regime.

Given the obstacles to perform calculations from first principles at intermediate densities, much of our knowledge about strong-interaction matter in this regime relies thus far on phenomenological low-energy effective models (LEMs) of QCD such as the NJL model and its relatives. However, model studies inevitably bear certain shortcomings. First of all, a specific LEM must define *a priori* the relevant degrees of freedom, commonly based on phenomenological reasoning. While quarks and gluons are expected to play an important role at higher densities, the overall conception of relevant effective degrees of freedom in terms of condensates, important interaction channels and essential driving fluctuations is still not definite. For instance, the transition from hadronic matter at low densities to quark matter at high densities is still far from being fully understood, see, e.g., Refs. [50, 51, 56] for reviews. In fact, the relevant fluctuations and degrees of freedom are in general dynamically changing across scales, and in particular across different density regimes. Moreover, every LEM depends on a set of model parameters which must be fixed. Typically, the parameters are chosen such that a certain set of low-energy observables is reproduced in the vacuum limit. Unfortunately, this procedure might not determine every model parameter unambiguously. In addition to that, the parameters fixed in this way are usually kept at their vacuum values also for an analysis of the physical system at finite values of external control parameters such as temperature and/or quark chemical potential, thereby neglecting the possible dependence of the model parameters on these external control parameters. Lastly, LEMs, such as the NJL model and the quark-meson model, trade in the fundamental microscopic degrees of freedom for effective low-energy ones, in this way achieving a more efficient description of the low-energy dynamics. This entails, however, that the LEM is subject to a finite UV extent as it is limited by a validity bound, see our discussion in Section 3.3. This also limits the range of applicability in terms of external parameters. Choosing then too large values for the external control parameters bears the risk to resolve unphysical details of the regularization scheme. As a results, although LEMs are still very valuable for our understanding of strong-interaction matter at higher densities, they are not capable of providing an overall description of QCD matter over a wider range of scales and densities, especially with regard to the necessity to account for changing relevant degrees of freedom which govern the dynamics.

Against this background, functional methods are very promising, as these approaches are able to incorporate the change from fundamental microscopic degrees of freedom at high momentum scales to effective ones associated with a low-energy description at small momentum scales, see, e.g., Refs. [193]. Thus, they might provide the ideal tools allowing the computation of cold strong-interaction matter at intermediate densities, i.e., in the regime between the limits of small and very large densities which are accessible by nuclear theory methods such as chiral EFT and by perturbative QCD, respectively. Recent FRG studies of QCD, see, e.g., Refs. [192, 194–197], mark important milestones in the progress toward quantitative studies of strong-interaction matter from first principles.

In our approach adopted so far, the EOS of cold dense QCD matter is not directly accessible as its computation requires to solve the RG flow down to the long-range limit $k \to 0$: With our ansatz (5.1) discussed in Section 5.1, the RG flow of the four-quark couplings in QCD is described by the corresponding β functions which are derived with the help of the *Wetterich* equation. Starting with gluodynamics at high energy scales from first principles, the four-quark self-interactions are dynamically generated and constitute the first effective interactions being essential for the dynamics of the matter sector toward the low-energy regime. There, the fermion self-interactions are treated in the pointlike limit, i.e., in the limit of vanishing external momenta, which allows us to make use of a *Fierz*-complete basis capturing all possible interactions of this type compatible with the underlying symmetries. The pointlike approximation breaks down when a condensate is generated, leading to the spontaneous breaking of related symmetries. The regime of cold dense QCD matter, however, is governed by spontaneous symmetry breaking. As a consequence, the RG flow in terms of four-quark couplings associated with the fermion self-interactions in the pointlike limit can only be evolved from the initial UV scale Λ down to the critical scale k_{cr}. At this scale, the four-quark couplings develop a singularity, signaling the onset of spontaneous symmetry breaking and the formation of a corresponding condensate. Still, in order to compute thermodynamic observables, the remaining low-energy fluctuations associated with the remaining RG flow down to $k = 0$ must be integrated out as well. This requires to go beyond the pointlike limit as the information on bound-state formation is encoded in the momentum structure dependencies of the associated vertices. In the study presented here, we thus connect the RG flow of the four-quark couplings to a new ansatz at a transition scale Λ_0, i.e., a new parametrization of the truncation in order to describe the dynamics at scales $k < \Lambda_0$ and to integrate out the remaining associated low-energy fluctuations. As this new ansatz for the low-energy regime defines in fact a low-energy effective model if it is considered by itself, we shall refer to this ansatz as *LEM ansatz* or *LEM truncation.* In order to find a suitable ansatz, we make use of the "hierarchy" of the four-quark couplings in terms of their relative strength to identify the dominant interactions among the *Fierz*-complete basis and hence the associated condensates which are expected to be formed in the IR. Guided by these dominances, the LEM ansatz is chosen to include corresponding auxiliary fields to account for the formation of these condensates. This amounts to a *Hubbard-Stratonovich* transformation of the dominant interaction channels at the given scale Λ_0, which introduces the auxiliary bosonic degrees of freedom.[1] Since we find the scalar-pseudoscalar channel to be most dominant at low densities and the diquark channel to be most dominant at intermediate and high densities, the *Hubbard-Stratonovich* transforms of these two couplings lead to a quark-meson-diquark-model truncation for the description of the dynamics in the low-energy regime. The formation of a condensate is then indicated by the system developing a ground state with a non-zero expectation value of the associated auxiliary field. We use the QCD flow of the four-quark couplings not only to determine the relevant auxiliary bosonic degrees of freedom in the low-energy regime but also to fix the couplings of the LEM truncation at the transition scale Λ_0. In this way, these free parameters can be unambiguously determined and also take into account modifications due to finite values of the external control parameters temperature and quark chemical potential. Moreover, we apply the concept of RG consistency discussed in Section 3.3 in order to remove potential cutoff and regularization scheme dependencies in the computation based on the LEM ansatz. By making use of "pre-initial" flows which provide an RG-consistent UV completion, together with the determination of the free parameters by employing the temperature- and chemical-potential-dependent QCD flow of the four-quark couplings, the range of applicability of the LEM truncation in terms of the external control parameters can be extended in comparison to conventional low-energy effective models as, e.g., defined by the LEM ansatz considered by itself. Eventually, the effective action as computed from the LEM truncation in the limit $k \to 0$ gives access to thermodynamic quantities. To be specific, with this approach we are able to compute the EOS of isospin-symmetric QCD matter at intermediate densities. Remarkably, our results for the pressure as a function of the baryonic number density are found to be consistent with computations based on chiral EFT interactions at lower densities as well as with perturbative QCD at asymptotically high densities.

This chapter is organized as follows: In Section 6.1.1, we identify the relevant low-energy effective degrees of freedom by analyzing the dominances of the four-quark couplings in

---

[1] In fact, the divergence of the four-quark couplings at a finite scale k_{cr} is an artifact of the pointlike approximation. The partial bosonization in terms of the *Hubbard-Stratonovich* then allows to resolve part of the momentum dependences and thus to access the deep IR.

the pointlike limit at zero temperature and finite quark chemical potential. Based on these considerations, in order to describe the dynamics in the low-energy regime, we introduce the LEM ansatz for the effective action as found from a *Hubbard-Stratonovich* transformation of the dominant four-quark interaction channels, leading to a quark-meson-diquark-model truncation. Applying the concept of RG consistency, potential cutoff and regularization scheme dependences are at least partially removed from our computation by implementing "pre-initial flows". The latter serve as an RG-consistent UV completion to the LEM truncation. The details of our procedure to integrate out the remaining low-energy fluctuations, i.e., to solve the RG flow down to the long-range limit $k \to 0$, are outlined in Section 6.1.2. There, we also illustrate the effect of an RG-consistent computation as opposed to conventional LEM computations by discussing different examples. In Section 6.1.3, we discuss how the free parameters of the LEM truncation are determined with the help of the RG flow of the four-quark couplings in QCD. We finally compute the EOS of cold dense isospin-symmetric QCD matter resulting from the effective action of the LEM truncation in Section 6.2. Along with the pressure as a function of the density, we also present our findings on the speed of sound which is an important quantity in astrophysical studies to characterize neutron star matter. We discuss our results in the context of the findings as obtained from chiral EFT studies at low densities and perturbative QCD approaches at high densities.

6.1 LOW-ENERGY DYNAMICS

6.1.1 Low-energy effective degrees of freedom

As strong-interaction matter in the zero-temperature limit is governed by spontaneous symmetry breaking associated with the formation of condensates, the four-quark couplings develop a singularity at a finite critical scale $k_{\mathrm{cr}}(\mu)$. In order to integrate out the remaining fluctuations in the low-energy regime, we employ an LEM ansatz to resolve the effective bosonic degrees of freedom and thus to account for the formation of the corresponding condensates. The relevant bosonic degrees of freedom are identified from first principles in QCD by making use of the *Fierz*-complete RG flow of the four-quark couplings as obtained from the ansatz (5.1) discussed in Section 5.1. In this approach, the aspect of *Fierz* completeness is essential in order to determine the low-energy effective degrees of freedom in an unconstrained and unbiased manner. The RG flow is initiated at the UV cutoff scale $\Lambda = 10\,\mathrm{GeV}$. This large value ensures that the condition $\mu/\Lambda \ll 1$ holds true for the considered range of values of the quark chemical potential to avoid any cutoff and regularization scheme dependences. The four-quark couplings are initially set to zero and are therefore dynamically generated by the gluodynamics as soon as the RG scale k is lowered and fluctuations are integrated out, see our discussion in Section 5.2. The scale dependence of the strong coupling is given by the one-loop running (5.9) which has the advantage of being universal and not depending on details of the gauge fixing process. Extracted from experimental measurements at the τ mass scale $M_\tau = 1.78\,\mathrm{GeV}$, the gauge coupling is found to assume the value $\alpha_{\mathrm{s}}(M_\tau) = 0.330 \pm 0.014$ [38]. Evolved to higher scales on the assumption of the one-loop running, this value corresponds to $\alpha_{\mathrm{s}}(\Lambda) \approx 0.176 \pm 0.004$

at $\Lambda = 10\,\text{GeV}$, which shall serve as the initial UV value of the strong coupling in our computations. The scale dependence of the gauge coupling as obtained from a computation at one-loop order is completely sufficient for our purpose in this study. Well before the *Landau* pole (LP) of the running gauge coupling at $k_{\text{LP}} \approx 248\,\text{MeV}$ shows any effect, the RG flow of the four-quark couplings shall be stopped at a transition scale $\Lambda_0 = 450 - 600\,\text{MeV}$ in order to continue with the LEM ansatz to integrate out the remaining low-energy dynamics. The transition scale might be considered as the defined upper boundary of the low-energy sector. The figure in the left panel of Fig. 5.1 in Section 5.1 shows that the running gauge coupling at one-loop order differs only marginally at the relevant scales $k \geq 450\,\text{MeV}$ in comparison to, e.g., α_{QCD} taken from Refs. [392, 393]. Only for scales $k \lesssim 800\,\text{MeV}$, the running gauge coupling in one-loop approximation assumes slightly larger values. In Section 5.3, we have tested the influence of using the scale-dependent strong coupling α_{YM} as obtained from Eq. (5.7) with η_A taken from Refs. [392, 393] for $N_{\text{f}} = 0$, i.e., in pure YM theory. This coupling is similarly increased at the scales $450\,\text{MeV} \leq k \lesssim 1\,\text{GeV}$, in fact even stronger than the gauge coupling at one-loop order, cf. the right panel of Fig. 5.1. Still, we have found very little influence on the dominance pattern of the four-quark couplings. Our findings suggest that the relative strengths of these couplings are predominantly determined by the dynamics within the quark sector. Moreover, see our discussion below in Section 6.1.3, the values of the four-quark couplings, which are extracted from the RG flow at the transition scale Λ_0 in order to determine the couplings of the LEM ansatz, are rescaled such that the constituent quark mass is obtained in the vacuum limit. This procedure fixes the scale of the low-energy dynamics and suppresses possible influences which might originate from details of the scale dependence of the strong coupling.

In Fig. 6.1, the "hierarchy" of the (dimensionless) renormalized four-quark couplings along the zero-temperature axis is shown as a function of the quark chemical potential. Note that the finite-density region in the zero-temperature limit is governed by spontaneous symmetry breaking, implying that the four-quark couplings always develop a singularity at a critical scale $k_{\text{cr}} = k_{\text{cr}}(\mu)$ which itself depends on the quark chemical potential. In order to determine the relative strengths, the couplings are evaluated at a scale slightly higher than the particular critical scale at a given value of the chemical potential. To be specific, the couplings are evaluated at $k/k_0 = k_{\text{cr}}(\mu)/k_0 + 0.0039$, with the critical scale $k_{\text{cr}}(\mu = 0) \equiv k_0 \approx 256\,\text{MeV}$ in the vacuum limit. Moreover, the values of the couplings are normalized to the coupling $\lambda_{(\sigma\text{-}\pi)}$ of the scalar-pseudoscalar interaction channel at zero quark chemical potential and at the corresponding scale $k/k_0 = k_{\text{cr}}(0)/k_0 + 0.0039$. The relative strengths show a clear dominance of the scalar-pseudoscalar coupling at smaller chemical potentials and of the CSC coupling at higher chemical potentials, indicating the formation of a chiral and a diquark condensate, respectively. Note that the magnitude of the CSC coupling is equal to the magnitude of the $(S+P)_{-}^{\text{adj}}$-coupling as a consequence of the $U_{\text{A}}(1)$-symmetric RG flow. Here, we do not take into account $U_{\text{A}}(1)$-violating boundary conditions at the UV cutoff scale Λ as the effect is found to be negligible at the scale Λ_0 at which the RG flow of the four-quark couplings is paused in order to continue with the LEM ansatz for the low-energy regime.[2] Entering the

---

[2] Comparing Figs. 5.6 and 5.9 in Chapter 5 suggests that explicit $U_{\text{A}}(1)$-breaking initial conditions even amplifies the dominances of the scalar-pseudoscalar coupling at small chemical potential and of the CSC coupling at high chemical potential by suppressing the remaining couplings, in particular the $(S+P)_{-}^{\text{adj}}$-coupling. The impact on the absolute values of the scalar-pseudoscalar and the CSC coupling is surprisingly small.

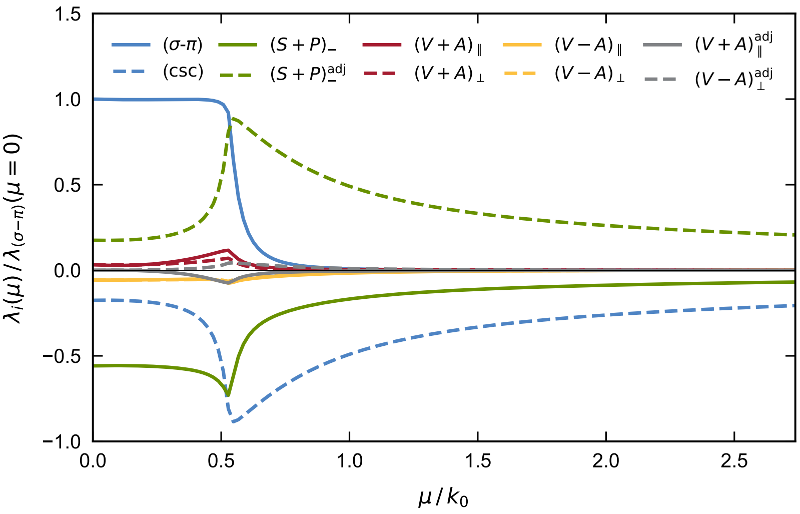

FIGURE 6.1: Values of the various (dimensionless) renormalized couplings at $k/k_0 = k_{\text{cr}}(\mu)/k_0 + 0.0039$ (with the critical scale $k_{\text{cr}}(\mu = 0) \equiv k_0 \approx 256\,\text{MeV}$ in the vacuum limit) as functions of the quark chemical potential at zero temperature, illustrating the "hierarchy" of the four-quark couplings in terms of their relative strength along the zero-temperature finite-density axis. The finite-density region at zero temperature is governed by spontaneous symmetry breaking, implying a μ-dependent critical scale $k_{\text{cr}}(\mu)$ at which the four-quark couplings develop a singularity. In order to evaluate the relative strengths of the four-quark couplings, the RG flow is stopped slightly above the particular critical scale at the given quark chemical potential. The values of the couplings are normalized to the coupling $\lambda_{(\sigma\text{-}\pi)}$ of the scalar-pseudoscalar interaction channel at zero quark chemical potential and $k/k_0 = k_{\text{cr}}(0)/k_0 + 0.0039$, see main text for further details.

regime governed by spontaneous symmetry breaking, however, the $U_{\text{A}}(1)$ symmetry is broken simultaneously. Therefore, it is legitimate to consider an ansatz for the low-energy sector which explicitly breaks $U_{\text{A}}(1)$ invariance.

At this point, a comment is in order to put the dominance pattern observed in Fig. 6.1 into context with the ones studied earlier, see, e.g., Fig. 5.6 in Section 5.3. Here, the dominances appear to change from the scalar-pseudoscalar to the CSC channel already at the rather small quark chemical potential $\mu_\chi/k_0 \approx 0.5$. Note, however, that in our present calculation the critical scale $k_0 \approx 256\,\text{MeV}$ in the vacuum limit is significantly smaller compared to the critical scales obtained in our previous studies. As the critical scale sets the scale for the low-energy observables, the small value of k_0 implies that, e.g., the corresponding constituent quark mass is smaller than the typically assumed value. For instance, the mean-field computation in the one-channel approximation discussed in Section 4.1.3, which was used to fix the scale in the *Fierz*-complete NJL model, relates the constituent quark mass $m_{\text{q}} = 0.3\,\text{GeV}$ to the value $k_0 \approx 484\,\text{MeV}$ of the critical scale in the vacuum limit (for the regularization scheme also presently applied), which is almost twice as large as the critical scale obtained here. On account of these deviating low-energy scales, a direct comparison of the four-quark couplings as a function of the quark chemical potential is not meaningful. This observation indicates, however, that the four-quark couplings as extracted from the RG flow in QCD in order to determine the couplings of the LEM truncation must be appropriately rescaled to adjust the ansatz to the low-energy scales as given by, e.g., the constituent quark mass, see our discussion below in Section 6.1.3. Alternatively, we may adapt the value of the strong coupling at the initial scale Λ to adapt the low-energy scales accordingly.[3]

As indicated by the "hierarchy" of the four-quark couplings in Fig. 6.1, toward the IR the dynamics of the quark sector is dominated by either the scalar-pseudoscalar interaction channel or the CSC interaction channel. Since the gluon sector is expected to decouple from the matter sector at lower momentum scales, see, e.g., Refs. [186, 192, 193, 195, 211, 380, 381, 432], and all the remaining four-quark interactions become insignificant in contrast to the dominant channels, we assume the effective action at the transition scale Λ_0 to be well described by the (purely fermionic (F)) form

$$\Gamma_{\Lambda_0}^{(\mathrm{QCD})} \equiv S_{\mathrm{LEM}}^{(\mathrm{F})} = \int_x \left\{ \bar{\psi}\left(\mathrm{i}\partial\!\!\!/ - \mathrm{i}\mu\gamma_0\right)\psi + \frac{1}{2}\bar{\lambda}_{(\sigma\text{-}\pi)}\mathcal{L}_{(\sigma\text{-}\pi)} + \frac{1}{2}\bar{\lambda}_{\mathrm{csc}}\mathcal{L}_{\mathrm{csc}} \right\}, \tag{6.1}$$

at leading order of the derivative expansion. The effective action $\Gamma_{\Lambda_0}^{(\mathrm{QCD})}$ at the transition scale $k = \Lambda_0$ as obtained from the RG flow in QCD at higher scales thus provides the initial form of the LEM truncation. We emphasize again that Λ_0 should not be confused with $k_{\mathrm{cr}}(\mu)$. In particular, Λ_0 is chosen to be μ-independent in order to simplify scale fixing. Note that in this spirit the renormalized four-quark couplings of $\Gamma_{\Lambda_0}^{(\mathrm{QCD})}$ become the initial bare couplings from the perspective of the LEM ansatz. However, the pointlike approximation of the four-quark interactions does not allow us to access the regime governed by spontaneous symmetry breaking as the formation of bound states requires to resolve the momentum dependence of the associated vertices. In order to resolve part of the momentum structure, we introduce auxiliary bosonic fields by means of a *Hubbard-Stratonovich* transformation of the purely fermionic action $S_{\mathrm{LEM}}^{(\mathrm{F})}$ given by Eq. (6.1). On the level of the path integral, as discussed in Section 4.1.3, this amounts to inserting the identity

$$\frac{1}{\mathcal{N}} \int \mathcal{D}\phi\mathcal{D}\Delta\mathcal{D}\Delta^* \, \mathrm{e}^{-\int_x \left\{ \frac{1}{2}\bar{m}_{(\sigma\text{-}\pi)}^2 \phi^2 + \bar{m}_{\mathrm{csc}}^2 \Delta_A \Delta_A^* \right\}} = 1\,, \tag{6.2}$$

with appropriate normalization $\mathcal{N}$. The auxiliary fields can be considered as composites of two quark fields. Phenomenologically, the scalar fields $\phi^{\mathrm{T}} = (\sigma, \vec{\pi}^{\,\mathrm{T}})$ carry the quantum numbers of the σ meson, $\sigma \sim (\bar{\psi}\psi)$, and the pions, $\vec{\pi} \sim (\bar{\psi}\vec{\tau}\gamma_5\,\psi)$, respectively. Here, the τ_i's are the *Pauli* matrices which couple the quark spinors ψ in flavor space. The sigma and the pion field do not carry an internal charge, e.g., color, flavor or baryon number. The complex-valued scalar fields Δ_A carry the quantum numbers of diquark states, $\Delta_A \sim (\bar{\psi}\gamma_5\tau_2 T^A \psi^C)$. As introduced in Section 2.2, the latter corresponds to a $J^P = 0^+$ state, with the color index A referring only to the antisymmetric color generators T^A in the fundamental representation. By shifting the auxiliary fields according to

$$\sigma \to \sigma + \mathrm{i}\frac{\bar{h}_{(\sigma\text{-}\pi)}}{\bar{m}_{(\sigma\text{-}\pi)}^2}\left(\bar{\psi}\psi\right), \qquad \Delta_A \to \Delta_A + \frac{\bar{h}_{\mathrm{csc}}}{\bar{m}_{\mathrm{csc}}^2}\left(\mathrm{i}\bar{\psi}\gamma_5\tau_2 T^A \psi^C\right), \tag{6.3}$$

---

[3] For QCD in the chiral limit, there is in principle only one parameter, e.g., Λ_{QCD}, and the values of all physical quantities are universal in units of this parameter.

$$\pi_i \to \pi_i - \frac{\bar{h}_{(\sigma\text{-}\pi)}}{\bar{m}^2_{(\sigma\text{-}\pi)}} \left(\bar{\psi}\gamma_5\tau_i\psi\right) , \qquad \Delta^*_A \to \Delta^*_A + \frac{\bar{h}_{\text{csc}}}{\bar{m}^2_{\text{csc}}} \left(\mathrm{i}\bar{\psi}^C\gamma_5\tau_2 T^A\psi\right) , \tag{6.4}$$

and choosing the parameters to fulfill the relations[4]

$$\bar{\lambda}_{(\sigma\text{-}\pi)} = \frac{\bar{h}^2_{(\sigma\text{-}\pi)}}{\bar{m}^2_{(\sigma\text{-}\pi)}} , \qquad 2(-\bar{\lambda}_{\text{csc}}) = \frac{\bar{h}^2_{\text{csc}}}{\bar{m}^2_{\text{csc}}} , \tag{6.5}$$

we obtain the partially bosonized action

$$\begin{aligned} S_{\text{LEM}} = \int_x \Big\{ & \bar{\psi}\left(\mathrm{i}\partial\!\!\!/ - \mathrm{i}\mu\gamma_0 + \mathrm{i}\bar{h}_{(\sigma\text{-}\pi)}\left(\sigma + \mathrm{i}\gamma_5\tau_i\pi_i\right)\right)\psi + \frac{1}{2}\bar{m}^2_{(\sigma\text{-}\pi)}\phi^2 + \bar{m}^2_{\text{csc}}\Delta^*_A\Delta_A \\ & + \mathrm{i}\bar{h}_{\text{csc}}\left(\bar{\psi}^C\gamma_5\tau_2\Delta_A T^A\psi + \bar{\psi}\gamma_5\tau_2\Delta^*_A T^A\psi^C\right)\Big\} . \end{aligned} \tag{6.6}$$

The four-quark interactions have been replaced by *Yukawa*-type interactions between the quark fields and the scalar fields ϕ and between the quark fields and the diquark fields Δ_A and Δ^*_A, associated with the *Yukawa* couplings $\bar{h}_{(\sigma\text{-}\pi)}$ and $\bar{h}_{\text{csc}}$, respectively. More precisely, the auxiliary bosonic fields mediate the four-quark interactions which effectively resolve part of the momentum dependence of these interactions. The access to the momentum structure now allows us to integrate out the remaining low-energy dynamics in the IR regime governed by spontaneous symmetry breaking and to explicitly study the formation of condensates.

In our approach presented here, we employ the partial bosonized version in its instant form and compute the effective action in a one-loop approximation where only the purely fermionic loops are taken into account. To be more specific, we neglect the RG running of the wavefunction renormalizations of the meson and diquark fields and set them to zero, i.e., we shall drop terms of the following form in our computation of the effective action:

$$\begin{aligned} \int_x \Big\{ & \frac{1}{2}Z^{(\phi)}_{\perp}\left(\vec{\nabla}\phi\right)^2 + \frac{1}{2}Z^{(\phi)}_{\parallel}\left(\partial_\tau\phi\right)^2 + Z^{(\Delta)}_{\perp}(|\Delta|^2)|\vec{\nabla}\Delta|^2 + Z^{(\Delta)}_{\parallel}(|\Delta|^2)|\partial_\tau\Delta|^2 \\ & + 2\mu Z^{(\Delta)}_{\mu}(|\Delta|^2)(\Delta\partial_\tau\Delta^* - \Delta^*\partial_\tau\Delta)\Big\} , \end{aligned} \tag{6.7}$$

where $\Delta^*\mathcal{O}\Delta \equiv \sum_A \Delta^*_A\mathcal{O}\Delta_A$ and $|\mathcal{O}\Delta|^2 \equiv \sum_A |\mathcal{O}\Delta_A|^2$ with $\mathcal{O}$ being some operator acting on the diquark fields. In general, such terms are dynamically generated due to quantum effects, even if only purely fermionic loops are taken into account. Note that the fields in Eq. (6.7) denote the corresponding classical fields associated with the quantum fields appearing in the classical action (6.6). As before, in line with the approximations introduced above, we neglect corrections to the wavefunction renormalization factors of the quark fields (as well as to the quark chemical potential) and also the RG runnings of the *Yukawa*-type couplings. The latter can thus be absorbed into the fields by appropriate redefinitions, leading to the mappings

$$\bar{h}_{(\sigma\text{-}\pi)}\phi \to \phi , \qquad \bar{h}_{\text{csc}}\Delta_A \to \Delta_A , \qquad \bar{h}_{\text{csc}}\Delta^*_A \to \Delta^*_A . \tag{6.8}$$

---

[4] Note that the four-quark coupling $\bar{\lambda}_{\text{csc}}$ always assumes negative values in the RG flow, see, e.g., Fig. 6.1, implying that the mass parameter $\bar{m}^2_{\text{csc}}$ is positive - if we assume the *Yukawa* coupling $\bar{h}_{\text{csc}}$ to be positive as well - as it should be for the identity (6.2) to be well-defined.

This allows us to recast the initial form of the LEM truncation into a formulation in terms of the four-quark couplings again which directly connects to the effective action $\Gamma_{\Lambda_0}^{(\mathrm{QCD})}$ as obtained from the QCD flow at the transition scale Λ_0:

$$\Gamma_{\Lambda_0}^{(\mathrm{LEM})} = \int_x \Big\{ \bar{\psi}\left(\mathrm{i}\partial\!\!\!/ - \mathrm{i}\mu\gamma_0 + \mathrm{i}\left(\sigma + \mathrm{i}\gamma_5\tau_i\pi_i\right)\right)\psi + \frac{1}{2}\frac{1}{\bar{\lambda}_{(\sigma\text{-}\pi)}}\phi^2 - \frac{1}{2}\frac{1}{\bar{\lambda}_{\mathrm{csc}}}\Delta_A^*\Delta_A \\ + \mathrm{i}\bar{\psi}^C\gamma_5\tau_2\Delta_A T^A\psi + \mathrm{i}\bar{\psi}\gamma_5\tau_2\Delta_A^* T^A\psi^C \Big\}. \tag{6.9}$$

With this ansatz we can eventually integrate out the remaining fluctuations in the low-energy regime. From the effective action determined in the one-loop approximation, we can then derive the *Ginzburg-Landau*-type effective potential for the bosonic fields which allows a straightforward analysis of the ground-state properties. The formation of a chiral or a diquark condensate corresponds to the chiral field ϕ or the diquark fields Δ_A acquiring a non-zero ground-state expectation value, respectively. The details of this computation are discussed in the next section before we proceed to combine the LEM truncation (6.9) with the RG flow in QCD at higher scales.

6.1.2 The quark-meson-diquark model and RG consistency

The ansatz (6.9) defines the low-energy effective degrees of freedom and, viewed as a low-energy effective model by itself, amounts to the so-called *quark-meson-diquark* (QMD) model. Here, we discuss some details of the QMD model and the computation of the effective action in a one-loop approximation. In doing so, we adopt a more general point of view and also include finite temperature in our considerations. In particular, we outline the implementation of "pre-initial" flows to ensure RG consistency as introduced in Section 3.3, aiming at a consistent removal of cutoff effects and at least parts of regularization scheme dependencies from the QMD-model computation in the presence of finite external control parameters. The discussion here sets the stage for the continuation of our QCD RG flow to access the IR regime governed by spontaneous symmetry breaking, and to integrate out the remaining low-energy dynamics based on the LEM/QMD-model truncation (6.9). Having obtained the RG-consistent effective action in the long-range limit $k \to 0$, we can eventually compute the EOS of isospin-symmetric strong-interaction matter at finite densities in the zero-temperature limit.

Our discussion of RG consistency in the context of the QMD model has actually broad implications and might prove very valuable for general studies of LEMs in QCD. Such models are in fact consistent quantum field theories by themselves and can be embedded in QCD, but typically have a physical ultraviolet cutoff which restricts their range of validity. The recipe discussed here to ensure RG consistency might thus generally be helpful to remove cutoff artifacts in studies of LEMs. It is worth noting that different LEM representations of low-energy QCD can be mapped into each other within self-consistent and systematic expansion schemes. Accordingly, the conceptional results obtained below in the context of the QMD model extends straightforwardly to a broader class of representations of low-energy QCD. The impact of truncation artifacts, however, might be limited to the specific model under investigation. For illustration, we analyze the impact of cutoff corrections enforced by the RG-consistency condition on the zero-temperature EOS as obtained in a computation taking into account only the quark-diquark sub-sector as well as the impact on the phase diagram of the full QMD model in the plane spanned by the temperature and the quark chemical potential. We demonstrate that violations of RG consistency significantly affect the predictive power of the corresponding model calculations. Lastly, we consider the influence of RG consistency on the zero-temperature EOS of the full QMD model which is the most important case for our computation of the EOS of cold dense strong-interaction matter based on the RG flow of the *Fierz*-complete set of four-quark couplings in QCD at higher scales.

The classical action S_{QMD} underlying the QMD model, which corresponds to the ansatz (6.9), is given by

$$\begin{aligned} S_{\mathrm{QMD}} = \int_x \Big\{ & \bar{\psi}\left(\mathrm{i}\not{\partial} - \mathrm{i}\mu\gamma_0 + \mathrm{i}\bar{h}\left(\sigma + \mathrm{i}\gamma_5\tau_i\pi_i\right)\right)\psi + \frac{1}{2}\bar{m}^2\phi^2 + \bar{\nu}^2\Delta_A^*\Delta_A \\ & + \mathrm{i}\bar{\psi}^C\gamma_5\tau_2\Delta_A T^A\psi + \mathrm{i}\bar{\psi}\gamma_5\tau_2\Delta_A^* T^A\psi^C \Big\}\,, \end{aligned} \tag{6.10}$$

where $\bar{h}$, $\bar{m}^2$ and $\bar{\nu}^2$ are parameters at our disposal. For the computation in a one-loop approximation, we employ the *Wetterich* equation in the form (3.24) and expand the meson and diquark fields about homogeneous backgrounds $\bar{\phi}$ and $\bar{\Delta}_A$, respectively. We then arrive at the following result for the RG-scale dependent effective action:

$$\frac{1}{\mathcal{V}}\Gamma_k[\bar{\phi},\{\bar{\Delta}_A\}] = \frac{1}{\mathcal{V}}\Gamma_{\Lambda_0}[\bar{\phi},\{\bar{\Delta}_A\}] - 4L_k^{(T)}(\Lambda_0,\bar{h}^2\bar{\phi}^2) - 8M_k^{(T)}(\Lambda_0,\bar{h}^2\bar{\phi}^2,|\bar{\Delta}|^2)\,, \tag{6.11}$$

where $\mathcal{V} = \beta V = V/T$ is the space-time volume and $|\bar{\Delta}|^2 = \sum_A |\bar{\Delta}_A|^2$. The scale Λ_0 denotes the initial cutoff scale at which we assume a simple form of the effective action $\Gamma_{\Lambda_0}[\bar{\phi},\{\bar{\Delta}_A\}]$, see Eq. (6.9). Note that we do not indicate the dependence of Γ_k on the classical quark fields corresponding to the quantum fields ψ in the action S_{QMD} here and in the following as they are set to zero.

The auxiliary functions $L_k^{(T)}$ and $M_k^{(T)}$ parametrize the loop integrals associated with the effective action (6.11) in the presence of a heat bath with temperature $T = 1/\beta$. To regularize the loop integrals, we employ the three-dimensional sharp regulator given by Eq. (3.30) with (3.28) (and the replacement $p \to \vec{p}$) in Section 3.2, which preserves chiral symmetry. Despite conceptional deficits,[5] the class of three-dimensional regularization schemes is frequently used in QCD model studies since it allows to perform analytically the *Matsubara* sums in at least some of the loop diagrams. The auxiliary functions then read

$$\begin{aligned} L_k^{(T)}(\Lambda,\chi) = \frac{1}{2}\int\frac{\mathrm{d}^3p}{(2\pi)^3}\sum_{\sigma=\pm 1}\Big\{ & \left(\omega_\phi^{(\sigma)} + 2T\ln\left(1+\mathrm{e}^{-\beta\omega_\phi^{(\sigma)}}\right)\right)\Big|_k \\ & - \left(\omega_\phi^{(\sigma)} + 2T\ln\left(1+\mathrm{e}^{-\beta\omega_\phi^{(\sigma)}}\right)\right)\Big|_\Lambda\Big\} \end{aligned} \tag{6.12}$$

---

[5] Three-dimensional regularization schemes break the *Poincaré* symmetry explicitly since, by construction, they do not regularize the time-like momentum modes and thus treat time-like and spatial momentum modes differently. The explicit breaking of *Poincaré* invariance, which is even present in the vacuum limit, potentially distorts the RG flow, see our discussions in Sections 3.2 and 4.2.4.

with

$$\omega_{\phi}^{(\sigma)} = \sqrt{\vec{p}^{\,2}(1+r_{\psi})^2+\chi}+\sigma\mu\,, \tag{6.13}$$

and

$$\begin{aligned} M_k^{(T)}(\Lambda,\chi,\xi) = \frac{1}{2}\int\frac{\mathrm{d}^3p}{(2\pi)^3}\sum_{\sigma=\pm1}\Bigg\{ &\left(\omega_{\Delta}^{(\sigma)}+2T\ln\left(1+\mathrm{e}^{-\beta\omega_{\Delta}^{(\sigma)}}\right)\right)\Big|_k \\ &-\left(\omega_{\Delta}^{(\sigma)}+2T\ln\left(1+\mathrm{e}^{-\beta\omega_{\Delta}^{(\sigma)}}\right)\right)\Big|_{\Lambda}\Bigg\} \end{aligned} \tag{6.14}$$

with

$$\omega_{\Delta}^{(\sigma)} = \sqrt{\left(\sqrt{\vec{p}^{\,2}(1+r_{\psi})^2+\chi}+\sigma\mu\right)^2+\xi}\,. \tag{6.15}$$

The auxiliary quantities $\omega_{\phi}^{(\sigma)}$ and $\omega_{\Delta}^{(\sigma)}$ may be viewed as (infrared) regularized quasiparticle energies. For $\xi=0$, we use $\omega_{\Delta}^{(\sigma)}=\omega_{\phi}^{(\sigma)}$ to preserve the *Silver-Blaze* property along the axis associated with $\bar{\Delta}=0$. Evidently, for $\xi=0$ and $\chi=0$, we then have $\omega_{\phi}^{(\sigma)}=\omega_{\Delta}^{(\sigma)}=|\vec{p}\,|(1+r_{\psi})+\sigma\mu$. For the sharp-cutoff shape function these functions simplify to

$$\begin{aligned} L_k^{(T)}(\Lambda,\chi) = \frac{1}{2}\int\frac{\mathrm{d}^3p}{(2\pi)^3}\,&\theta(\Lambda^2-\vec{p}^{\,2})\theta(\vec{p}^{\,2}-k^2)\times \\ &\times\sum_{\sigma=\pm1}\left(\omega_{\phi}^{(\sigma)}+2T\ln\left(1+\mathrm{e}^{-\beta\omega_{\phi}^{(\sigma)}}\right)\right)\Big|_{(1+r_{\psi})\to1} \end{aligned} \tag{6.16}$$

and

$$\begin{aligned} M_k^{(T)}(\Lambda,\chi,\xi) = \frac{1}{2}\int\frac{\mathrm{d}^3p}{(2\pi)^3}\,&\theta(\Lambda^2-\vec{p}^{\,2})\theta(\vec{p}^{\,2}-k^2)\times \\ &\times\sum_{\sigma=\pm1}\left(\omega_{\Delta}^{(\sigma)}+2T\ln\left(1+\mathrm{e}^{-\beta\omega_{\Delta}^{(\sigma)}}\right)\right)\Big|_{(1+r_{\psi})\to1}\,. \end{aligned} \tag{6.17}$$

As expected, this regulator function cuts off small as well as large momenta sharply. For $k\to0$, Eq. (6.11) together with the auxiliary functions $L_0^{(T)}$ and $M_0^{(T)}$ yields the standard result for the effective action $\Gamma[\bar{\phi},\{\bar{\Delta}_A\}]\equiv\Gamma_{k\to0}[\bar{\phi},\{\bar{\Delta}_A\}]$ in the mean-field approximation.

Before we discuss the initial condition given by $\Gamma_{\Lambda_0}[\bar{\phi},\{\bar{\Delta}_A\}]$ in Eq. (6.11) and how RG consistency can be ensured, we would like to address first a subtlety in our calculation: In contrast to a possible renormalization of the quark chemical potential driven by diagrams with internal bosonic and fermionic lines, the renormalization of the chemical potential of the diquarks associated with a term $\sim\mu^2|\Delta|^2$ is already included in our present analysis. Indeed, the field-dependent renormalization factor $Y\equiv Y_{k\to0}$ of the diquark chemical potential is given by

$$Y_k(\bar{\phi}^2,|\bar{\Delta}|^2) = -\frac{1}{4\mathcal{V}}\partial_{\mu}^2\Gamma_k[\bar{\phi},\{\bar{\Delta}_A\}]\Big|_{\mu=0}\,. \tag{6.18}$$

Using Eq. (6.11) for the effective action, we find $Y \sim |\Delta|^2 \ln \Lambda_0 + \dots$. Thus, Y exhibits the same dependence on the initial cutoff scale as expected for the renormalization factors of kinetic terms, such as the ones for the diquark fields in Eq. (6.7). This coincidence in the dependence on the initial scale of Y and, e.g., $Z_{\parallel}^{(\Delta)}$ is by no means accidental. It is rather related to the more abstract symmetry of our model in the zero-temperature limit which is associated with the *Silver-Blaze* property of quantum field theories [228–231] discussed in Section 2.1.2, see in particular Eq. (2.37) for the definition of the associated symmetry transformation. In general, this property is linked to the fact that the free energy should not exhibit a dependence on the baryon/quark chemical potential at *zero* temperature, provided that it is smaller than some critical value. Then, the corresponding symmetry is not violated. The critical value is set by the (mass) gaps in the propagators of the fields associated with a finite baryon number. Note that the gap is not necessarily given by the pole mass at a finite scale k. In our RG study, for example, the gap may also arise for $k > 0$ from the IR regularization of the propagator, see Ref. [230] for details.

In the presence of the symmetry associated with the *Silver-Blaze* property, a finite renormalization factor Y of the diquark chemical potential implies that the renormalization factors $Z_{\perp}^{(\Delta)}$, $Z_{\parallel}^{(\Delta)}$, and $Z_{\mu}^{(\Delta)}$ of the diquark fields are in principle finite as well. In mean-field calculations, these renormalization factors are usually set to zero. Therefore, the resulting effective action violates the *Silver-Blaze* property.[6] As already stated above, we shall not compute these renormalization factors in this work but set them to zero too. Since we shall fix the couplings/parameters of our model at a scale $k = \Lambda_0 > \mu$ in the zero-temperature limit, i.e., at a point where the model is expected to respect the symmetry associated with the *Silver-Blaze* property, we set the initial condition for the renormalization factor Y to zero as well. This ensures that this property is at least manifestly present at the scale Λ_0 at which we fix the parameters of the model. However, the choice $Y_{k=\Lambda_0} = 0$ does not imply that Y remains zero at scales $k \neq \Lambda_0$. Since we do not take into account the running of the renormalization factors $Z_{\perp}^{(\Delta)}$, $Z_{\parallel}^{(\Delta)}$, and $Z_{\mu}^{(\Delta)}$, the symmetry associated with the *Silver-Blaze* property is therefore in general violated away from the scale Λ_0. Still, the consideration of the renormalization factor Y is required to ensure RG consistency within our model study, see below.

We assume that the parameters of the model are fixed at the scale $k = \Lambda_0$ by means of an ansatz for Γ_{Λ_0} in Eq. (6.11). To be specific, we make the following ansatz for the effective action at the scale Λ_0 in the vacuum limit:

$$\lim_{T\to 0} \frac{1}{\mathcal{V}} \Gamma_{\Lambda_0}[\bar{\phi}, \{\bar{\Delta}_A\}] = \frac{1}{2} \bar{m}_{\Lambda_0}^2 \bar{\phi}^2 + \bar{\nu}_{\Lambda_0}^2 |\bar{\Delta}|^2 \,, \tag{6.19}$$

where $\bar{m}_{\Lambda_0}^2$ and $\bar{\nu}_{\Lambda_0}^2$ are at our disposal and correspond to the parameters $\bar{m}^2$ and $\bar{\nu}^2$ in the classical action (6.10). In conventional LEM studies of QCD, the model parameters are typically fixed such that the physical values of a given set of low-energy observables are recovered in the long-range limit from the effective action $\Gamma_{k\to 0}$. Here, we fix the parameters $\bar{h}$, $\bar{m}_{\Lambda_0}^2$ at $\Lambda_0/\bar{m}_{\mathrm{q}} = 2$ in the vacuum limit such that we obtain $\bar{m}_{\mathrm{q}} = \bar{h}|\bar{\phi}_0| \approx 0.300\,\mathrm{GeV}$ for the

---

[6] Irrespective of the regularization scheme, the *Silver-Blaze* property of the theory is already violated by the fact that the quasiparticle energies $\omega_{\Delta}^{(\sigma)}$ are only positive semi-definite in (standard) mean-field approximations, see Eq. (6.15).

constituent quark mass and $f_\pi = \bar{m}_{\mathrm{q}}/\bar{h} \approx 0.088\,\mathrm{GeV}$ for the pion decay constant.[7] As often done in QMD model studies [106, 107, 115, 116], the remaining parameter $\bar{\nu}^2_{\Lambda_0}$ is eventually fixed via $\bar{m}^2_{\Lambda_0}/(2\bar{h}^2) = (3/4)\bar{\nu}^2_{\Lambda_0}$.

It is worth mentioning that it is not only conventional to parametrize the effective action as a quadratic form as given in Eq. (6.19) at some scale $\Lambda_0 \sim 0.4\ldots1\,\mathrm{GeV}$. It rather mimics the form of the mesonic part of the effective action in QCD in this energy regime. Indeed, it has been found in FRG studies of fundamental QCD that mesonic self-interactions of higher orders are suppressed [186, 192, 193, 195, 211, 380, 381].

Although our ansatz Γ_{Λ_0} for the effective action at the scale Λ_0 mimics the situation in QCD, the effective action in the long-range limit $k \to 0$ as obtained from this ansatz does not yet obey the RG-consistency condition (3.45) introduced in Section 3.3, i.e., we have $\Lambda_0 \partial_{\Lambda_0} \Gamma \neq 0$. Therefore, we now apply our general line of arguments detailed in Section 3.3 to obtain an RG-consistent result for the effective action of our QMD model in the mean-field approximation. Along these lines, cf. particularly Eq. (3.52) in our general discussion, we can construct an RG-consistent effective action $\Gamma_{k\to0}$ from (6.11) by adapting the effective action at a scale $\Lambda > \Lambda_0$ such that the effective action at scales $k \leq \Lambda_0$ remains unchanged in the vacuum limit:

$$\frac{1}{\mathcal{V}}\Gamma_k[\bar{\phi}, \{\bar{\Delta}_A\}] = \frac{1}{\mathcal{V}}\Gamma_\Lambda[\bar{\phi}, \{\bar{\Delta}_A\}] - 4L_k^{(T)}(\Lambda, \bar{h}^2\bar{\phi}^2) - 8M_k^{(T)}(\Lambda, \bar{h}^2\bar{\phi}^2, |\bar{\Delta}|^2)\,, \tag{6.20}$$

with

$$\begin{aligned}\frac{1}{\mathcal{V}}\Gamma_\Lambda[\bar{\phi}, \{\bar{\Delta}_A\}] =& \frac{1}{\mathcal{V}}\Gamma_{\Lambda_0}[\bar{\phi}, \{\bar{\Delta}_A\}] + 4L_{\Lambda_0}^{(T)}(\Lambda, \bar{h}^2\bar{\phi}^2)\Big|_{T=\mu=0} + 8M_{\Lambda_0}^{(T)}(\Lambda, \bar{h}^2\bar{\phi}^2, |\bar{\Delta}|^2)\Big|_{T=\mu=0} \\ &+ 4\mu^2\left(\partial_\mu^2 M_{\Lambda_0}^{(T)}(\Lambda, \bar{h}^2\bar{\phi}^2, |\bar{\Delta}|^2)\Big|_{T=\mu=0}\right)\,.\end{aligned} \tag{6.21}$$

Here, the term $\sim \mu^2$ in Eq. (6.21) accounts for the renormalization of the chemical potential of the diquarks. From our general discussion, see Eq. (3.53), we immediately conclude that by construction the effective action $\Gamma \equiv \Gamma_{k\to0}$ in the vacuum limit does not depend on the actual scale Λ at which we fix Γ_Λ , i.e., $\Lambda\partial_\Lambda\Gamma|_{\mathrm{vac}} = 0$.

Note that $\Gamma_{\Lambda_0}[\bar{\phi}, \{\bar{\Delta}_A\}]$ and $\Gamma_\Lambda[\bar{\phi}, \{\bar{\Delta}_A\}]$ obey a different dependence on the fields $\bar{\phi}$ and $\bar{\Delta}_A$. This can readily be demonstrated for asymptotically large scales Λ. In this case, the initial effective action Γ_Λ receives Λ-dependent corrections only from terms up to fourth order in these fields as higher orders are suppressed by powers of Λ:

$$\begin{aligned}\Lambda\partial_\Lambda\Gamma_\Lambda[\bar{\phi}, \{\bar{\Delta}_A\}] =& \frac{6\mathcal{V}}{\pi^2}\Lambda^4 + \frac{\mathcal{V}}{\pi^2}\left(3\bar{h}^2\bar{\phi}^2 + 2|\bar{\Delta}|^2\right)\Lambda^2 + \frac{\mathcal{V}}{4\pi^2}\left(-3\bar{h}^4\bar{\phi}^4 - 4\bar{h}^2\bar{\phi}^2|\bar{\Delta}|^2\right. \\ &\left.+8\mu^2|\bar{\Delta}|^2 - 2|\bar{\Delta}|^4\right) + \mathcal{O}\left(\frac{1}{\Lambda^2}\right)\,.\end{aligned} \tag{6.22}$$

---

[7] In principle, the three parameters $\bar{h}_{(\sigma\text{-}\pi)}$, $\bar{m}^2_{\Lambda_0}$, and Λ_0 can be used to fix the constituent quark mass, the pion decay constant, and the mass of the σ meson. Our line of arguments with respect to the RG-consistency criterion can also be applied to this case. The appearance of three parameters is related to the fact that the *Yukawa* coupling is marginally relevant with its RG flow being governed only by a *Gaußian* fixed point [333, 334].

Here, we consider the derivative with respect to the scale Λ in order to remove any terms which do not depend on Λ. The terms in Eq. (6.22) are related to the standard counterterms in a perturbative computation corresponding to our present approximation. Note that constant terms in this expansion of $\Lambda\partial_\Lambda\Gamma_\Lambda$ about asymptotically large scales Λ gives rise to $\sim \log\Lambda$ terms in the associated expression for Γ_Λ. In any case, in the long-range limit $k \to 0$ at $T = \mu = 0$, the effective action (6.20) agrees identically with the one given in (6.11), as it should be.

For a study with finite external control parameters, i.e., finite temperature and/or quark chemical potential, the scale Λ must then be chosen sufficiently large such that cutoff artifacts are suppressed. The latter may appear if $\Lambda > \Lambda_0$ has initially been chosen too small for a specific range of the considered parameter set. A priori, it may indeed be difficult to choose a suitable value for Λ. However, our line of arguments given in Section 3.3 shows how this issue can be resolved. Even more, it allows us to investigate systematically cutoff effects in the presence of external parameters since the vacuum physics is left unchanged.[8] Now, using Eq. (6.20), we indeed find that the effective action Γ obeys the RG-consistency condition (3.45), i.e., $\Lambda\partial_\Lambda\Gamma[\bar{\phi},\{\bar{\Delta}_A\}] = 0$, in a strict sense in the limit $\Lambda \to \infty$ since

$$\Lambda\partial_\Lambda\Gamma[\bar{\phi},\{\bar{\Delta}_A\}] = -2\mathcal{V}|\bar{\Delta}|^2\mu^2\left(\frac{\mu}{\pi\Lambda}\right)^2 + \mathcal{O}(1/\Lambda^4)\,. \tag{6.23}$$

Moreover, we find from Eq. (6.20) that the renormalization of the diquark chemical potential still vanishes identically at the scale Λ_0, i.e.,

$$Y_{\Lambda_0}(\bar{\phi}^2, |\bar{\Delta}|^2) = 0\,, \tag{6.24}$$

as it should be. From Eqs. (6.20) and (6.21), however, we infer that Γ_{Λ_0} depends on the temperature as well as on the quark chemical potential and is no longer only quadratic in the fields for $T > 0$ and/or $\mu > 0$. This implies that RG consistency is in general violated in conventional QCD low-energy model studies with fixed $\Lambda_0 = \Lambda$ since these modifications of Γ_{Λ_0} in case of non-zero external control parameters are not taken into account and the quadratic form (6.19) is rather left unchanged for any value of the external parameters.

With our RG-consistent effective action at hand, i.e., Eq. (6.20) together with Eq. (6.21), we are now in a position to determine the ground state of the system and to derive thermodynamic quantities. Assuming a homogeneous ground state, the effective action is proportional to the *Ginzburg-Landau*-type effective potential, i.e., $\Gamma[\bar{\phi},\{\bar{\Delta}_A\}] = \mathcal{V}U[\bar{\phi},\{\bar{\Delta}_A\}]$, where the proportionality factor is given by the space-time volume $\mathcal{V}$ as the effective action is an extensive quantity. The global minimum of the effective potential in terms of the fields $\bar{\phi}$ and $\bar{\Delta}_A$ determines the stable quantum state of the theory. The formation of condensates associated with spontaneous symmetry breaking is then described by a qualitative change of the shape of the effective potential as corresponding fields acquire non-zero expectation values. Moreover, from the point of view of statistical physics, the effective action is related

---

[8] Of course, it is mandatory that the vacuum contributions to the effective action as well as those arising in the presence of finite external parameters are regularized consistently, i.e., in exactly the same way, as worked out in detail in Section 3.3, see also Ref. [433] for a discussion of this issue in terms of a *Polyakov*-loop extended NJL model.

to the *Gibbs* free energy and hence gives direct access to the EOS. More specifically, based on the thermodynamic relations (2.23) introduced in Section 2.1.1, the pressure P is directly obtained from the effective action in the form:

$$P = -\frac{1}{\mathcal{V}}\Gamma[\bar{\phi}_{\mathrm{gs}}, \{\bar{\Delta}_A\}_{\mathrm{gs}}] + \frac{1}{\mathcal{V}}\Gamma[\bar{\phi}_{\mathrm{gs}}, \{\bar{\Delta}_A\}_{\mathrm{gs}}]\Big|_{T=\mu=0} . \tag{6.25}$$

Here, the subscript 'gs' indicates that the effective action is evaluated on the global minimum, i.e., on the ground-state (gs) configuration of the fields $\bar{\phi}$ and $\{\bar{\Delta}_A\}$, which depends on the external control parameters. Note that we have normalized the pressure with respect to the pressure in the vacuum limit. The latter is given by the second term on the right-hand side of Eq. (6.25).

Before we shall demonstrate the implications of RG consistency, e.g., by an actual computation of the pressure, we stress that our line of arguments, which eventually led us to the RG-consistency criterion in Section 3.3, goes qualitatively beyond what is sometimes called extended mean-field theory in the literature. In fact, the vacuum fermion loop associated with extended mean-field calculations is naturally included in an RG treatment and should anyway not be discarded in any other approach, see, e.g., Refs. [333, 370, 434] for detailed discussions of mean-field theory in the RG context and Refs. [366, 435] for approximative treatments of RG consistency in LEMs of QCD. Moreover, it is clear from our line of arguments that the manifestation of RG consistency in general requires to include the fully field-dependent fermion loop and, beyond the mean-field approximation, it even requires to include the fully field-dependent contributions from *all* loop diagrams considered in a specific calculation of the quantum effective action. This also becomes apparent from the right-hand side of the differential equation (3.50) which includes contributions from all fields of a given theory, e.g., by means of the *Wetterich* equation.

RG consistency I: the EOS of a quark-diquark model

In order to illustrate the effect of cutoff corrections as enforced by the RG-consistency condition, we analyze in the following computations based on the developed RG-consistent effective action (6.20) in different scenarios. We begin with a quark-diquark model as a reduced version of the QMD model, i.e., we only keep the quark and diquark fields in the classical action (6.10), and compute the EOS in terms of the pressure as a function of the quark chemical potential in the zero-temperature limit. The corresponding RG-consistent effective action of such a quark-diquark model can be obtained from the effective action (6.20) by setting the scalar field to zero, i.e., $\bar{\phi} = 0$. In the limit $T \to 0$, we obtain:

$$\frac{1}{\mathcal{V}}\Gamma_k[\{\bar{\Delta}_A\}] = \frac{1}{\mathcal{V}}\Gamma_\Lambda[\{\bar{\Delta}_A\}] - \frac{\mu^4}{6\pi^2} - 8M_k^{(T\to 0)}(\Lambda, 0, |\bar{\Delta}|^2)\,, \tag{6.26}$$

with

$$\frac{1}{\mathcal{V}}\Gamma_\Lambda[\{\bar{\Delta}_A\}] = \bar{\nu}^2_{\Lambda_0}|\bar{\Delta}|^2 + 8M_{\Lambda_0}^{(T\to 0)}(\Lambda, 0, |\bar{\Delta}|^2)\Big|_{\mu=0} + 4\mu^2\Big(\partial_\mu^2 M_{\Lambda_0}^{(T\to 0)}(\Lambda, 0, |\bar{\Delta}|^2)\Big|_{\mu=0}\Big)\,, \tag{6.27}$$

where the last term on the right-hand side accounts again for the renormalization of the diquark chemical potential. The contribution $\sim \mu^4$ in Eq. (6.26) arises from quark degrees of freedom which do not couple to the diquark fields and therefore appear as non-interacting "spectators". The parameter $\bar{\nu}_{\Lambda_0}$ is at our disposal and can be used to determine the ground-state properties of the vacuum in this model. From a general fixed-point analysis, see our discussion in Section 4.1.3 and, e.g., Ref. [109] for a mean-field analysis, it follows immediately that two qualitatively distinct scenarios are possible. To be specific, we may choose $\bar{\nu}_{\Lambda_0}$ to be positive but small such that already the ground state in the vacuum limit is governed by the formation of a diquark condensate breaking the $U_{\mathrm{V}}(1)$ symmetry of our model. Alternatively, we may choose a sufficiently large value of $\bar{\nu}_{\Lambda_0}$ such that the $U_{\mathrm{V}}(1)$ symmetry is only broken at finite quark chemical potential due to the existence of a *Cooper* instability in the system but remains intact in the vacuum limit. We therefore conclude that a critical value $\bar{\nu}_*$ (associated with a non-*Gaußian* fixed point) exists which separates these two distinct scenarios from each other.

The auxiliary function $M_k^{(T)}$ in the limit $T \to 0$ appearing in Eq. (6.26) simplifies for $\chi = 0$ and $\xi = |\bar{\Delta}|^2 > 0$ to

$$M_k^{(T\to 0)}(\Lambda, 0, \xi = |\bar{\Delta}|^2) = \frac{1}{2}\int \frac{\mathrm{d}^3 p}{(2\pi)^3} \sum_{\sigma=\pm 1} \left(\omega_{\Delta}^{(\sigma)}\Big|_k - \omega_{\Delta}^{(\sigma)}\Big|_{\Lambda} \right) , \tag{6.28}$$

and for the three-dimensional sharp regulator function eventually to

$$\begin{aligned} M_k^{(T\to 0)}(\Lambda, 0, |\bar{\Delta}|^2) = \frac{1}{2}\int \frac{\mathrm{d}^3 p}{(2\pi)^3}\, &\theta(\Lambda^2 - \vec{p}^{\,2})\theta(\vec{p}^{\,2} - k^2)\times \\ &\times \left\{ \sqrt{(|\vec{p}| + \mu)^2 + |\bar{\Delta}|^2} + \sqrt{(|\vec{p}| - \mu)^2 + |\bar{\Delta}|^2} \right\} . \end{aligned} \tag{6.29}$$

As an explicit example, with the effective action (6.26) at hand, we compute the pressure of the pure diquark model according to Eq. (6.25) (with $\bar{\phi}_{\mathrm{gs}}$ set to zero). We set the free parameter of this model to $(\bar{\nu}_{\Lambda_0}/\bar{\nu}_*)^2 = 4/3$ where $\bar{\nu}_*^2 \approx 0.036$. Moreover, we set $\Lambda_0 = 0.6\,\mathrm{GeV}$ in the following. Phenomenologically speaking, our parameter choice implies that the $U_{\mathrm{V}}(1)$ symmetry is only broken at finite μ but remains intact in the vacuum limit, see our discussion above. Thus, the ground state in the vacuum limit is governed by ungapped quarks.

In the left panel of Fig. 6.2, we show our results for the pressure P/P_{SB} of our diquark model, where $P_{\mathrm{SB}} = \mu^4/(2\pi^2)$ denotes the *Stefan-Boltzmann* limit of the pressure, i.e., the pressure of a free quark gas at zero temperature. We observe that cutoff effects become continuously smaller when Λ/Λ_0 is increased. Recall that, in our RG-consistent calculations, an increase of Λ leaves the model in the vacuum limit unchanged. Moreover, we find that the corrections to the results from the conventional mean-field study are significant. Indeed, the pressure obtained from the conventional mean-field study underestimates the (effectively) cutoff-independent result for the pressure as obtained from our RG-consistent mean-field study (with $\Lambda/\Lambda_0 = 10$) by about 10% at $\mu/\Lambda_0 = 1/2$. Thus, "cutoff contaminations" are clearly visible even at values of the chemical potential which seem to be sufficiently small compared to the originally chosen scale Λ_0. At $\mu/\Lambda_0 = 1$, the results from the conventional mean-field study and our RG-consistent mean-field study (with $\Lambda/\Lambda_0 = 10$) then already

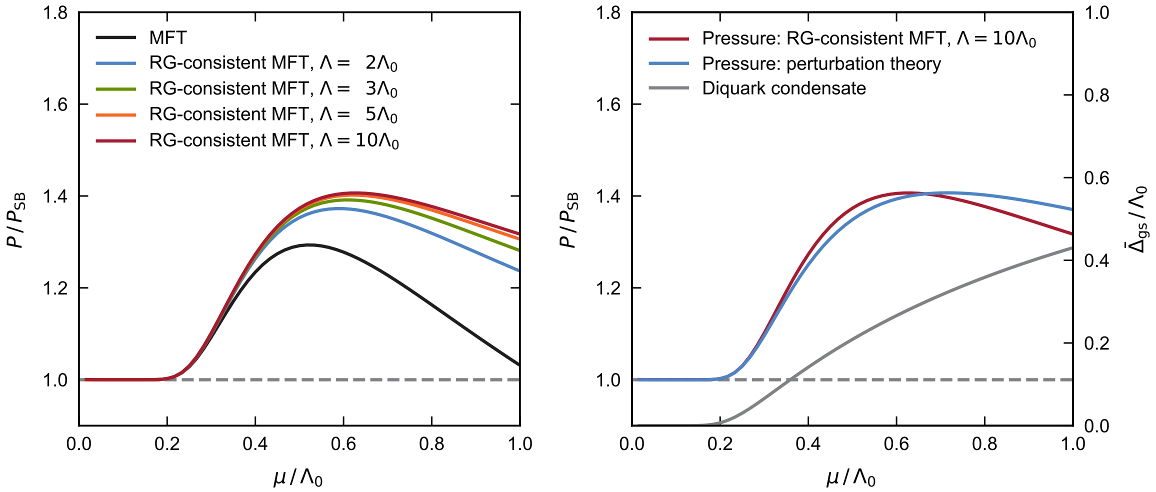

FIGURE 6.2: Left panel: Pressure $P/P_{\rm SB}$ of our diquark model as a function of the quark chemical potential μ/Λ_0 (with $\Lambda_0 = 0.6\,\mathrm{GeV}$) as obtained from conventional mean-field theory (MFT) with a UV cutoff $\Lambda = \Lambda_0$ (black line) as well as from RG-consistent MFT with $\Lambda/\Lambda_0 = 2, 3, 5, 10$. Right panel: Pressure $P/P_{\rm SB}$ of our diquark model as a function of the quark chemical potential μ/Λ_0 as obtained from RG-consistent MFT with $\Lambda/\Lambda_0 = 10$ together with the perturbative expression for the pressure at leading order in the weak-coupling expansion, see Eq. (6.30). Moreover, we also show the gap $\bar{\Delta}_{\rm gs}/\Lambda_0$ (gray line) as extracted from RG-consistent MFT with $\Lambda/\Lambda_0 = 10$.

deviate by about 30%. Increasing μ even further, we observe that the pressure approaches the *Stefan-Boltzmann* limit from above, provided Λ/Λ_0 has been chosen sufficiently large.

From Eq. (6.25), we can also derive the perturbative result for the pressure. At leading order of $|\bar{\Delta}_{\rm gs}|^2/\mu^2$ in the weak-coupling expansion, we indeed recover the well-known result [436, 437]:

$$\frac{P}{P_{\rm SB}} = 1 + \frac{2|\bar{\Delta}_{\rm gs}|^2}{\mu^2} + \dots\,, \tag{6.30}$$

where $\bar{\Delta}_{\rm gs}$ denotes the gap as obtained from a minimization of the effective action. In the right panel of Fig. 6.2, we compare this perturbative result for the pressure with the results from our RG-consistent mean-field calculation with $\Lambda/\Lambda_0 = 10$. Moreover, the gap as obtained from the same RG-consistent calculation is shown. Plugging this result for the gap into the perturbative expression (6.30) for $P/P_{\rm SB}$, we find very good agreement with the RG-consistent results for the pressure in the regime where $|\bar{\Delta}_{\rm gs}|/\mu \lesssim 0.5$. For larger values of the quark chemical potential, the results from the perturbative approximation of the pressure then exceed the results from the RG-consistent calculation. Still, the perturbative expression for the pressure appears to provide us with a reasonable estimate for the pressure over a wide range of the chemical potential, at least for our present choice for the model parameter $\bar{\nu}_{\Lambda_0}$.

RG consistency II: the phase diagram of the QMD model

We now return to the full QMD model with the RG-consistent effective action (6.20). To further illustrate the effect of cutoff corrections as enforced by the RG-consistency criterion, we compute the phase diagram in the plane spanned by the temperature and the quark chemical potential. Before we present the results of this computation, however, we first examine the

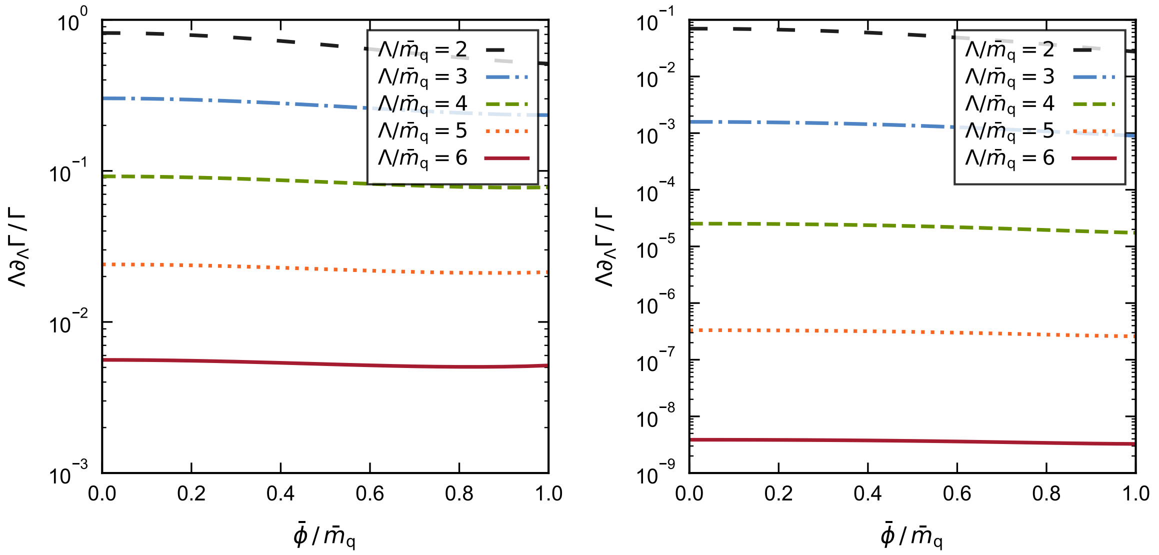

FIGURE 6.3: Change of the effective action at $\bar{\Delta} = 0$ under a variation of the UV scale Λ, i.e., $\Lambda\partial_\Lambda\Gamma$, relative to the effective action Γ itself as a function of $\bar{\phi}$ for $T/\bar{m}_q = 1/2$ and $\mu = 0$ (left panel) as well as for $T/\bar{m}_q = 1/5$ and $\mu/\bar{m}_q = 1$ (right panel) for various different values of $\Lambda/\bar{m}_q$, where $\bar{m}_q \approx 0.300\,\text{GeV}$ is the vacuum quark mass.

direct influence of the scale Λ on the effective action. In Fig. 6.3, we show $(\Lambda\partial_\Lambda\Gamma)/\Gamma$, i.e., the change of the effective action under variation of the scale $\Lambda > \Lambda_0$ relative to Γ itself, at $\bar{\Delta} = 0$ as a function of $\bar{\phi}$ for various different values of $\Lambda/\bar{m}_q$. We observe that Γ exhibits a strong dependence on our choice for Λ in the phenomenologically most relevant regime $\bar{\phi} \lesssim f_\pi$. In particular, this is true close to the critical temperature at $\mu = 0$, see left panel of Fig. 6.3, where cutoff artifacts are still clearly present in the effective action even for already seemingly large values of $\Lambda > \Lambda_0$.[9] At low temperature but large quark chemical potential $\mu \gtrsim \bar{m}_q$, see right panel of Fig. 6.3, cutoff contaminations of the effective action are also present but appear to be less strong compared to the case with $\mu = 0$. However, this is misleading as the minimum of the effective action is pushed away from the axis of the scalar field $\bar{\phi}$ with $\bar{\Delta} = 0$ in this regime. There, the dynamics is no longer governed by the pions and the σ meson but rather by the diquark degrees of freedom. Indeed, close to the physical minimum of the effective action in this regime, cutoff effects even appear to be stronger as in the case with $\mu = 0$. This can be inferred from the phase diagram in the (T, μ) plane as well as from the pressure at zero temperature. We emphasize that the value of Λ associated with effectively converged results depends on the temperature, the quark chemical potential, and the employed regularization scheme. Recall that, by construction, the effective actions associated with different values of $\Lambda > \Lambda_0$ agree identically in the vacuum limit, i.e., we have $\Lambda\partial_\Lambda\Gamma = 0$ in this limit.

In Fig. 6.4, we present the results for the (T, μ) phase diagram of our QMD model. Qualitatively, the structure of the phase diagram is determined by the emergence of three different phases: a phase governed by spontaneous chiral symmetry breaking at low temperature and small quark chemical potential, a phase governed by spontaneous $U_V(1)$ symmetry breaking as associated with diquark condensation at low temperature and large chemical potential,

---

[9] Note that the critical temperature is given by $T/\bar{m}_q \approx 0.55$ at $\mu = 0$.

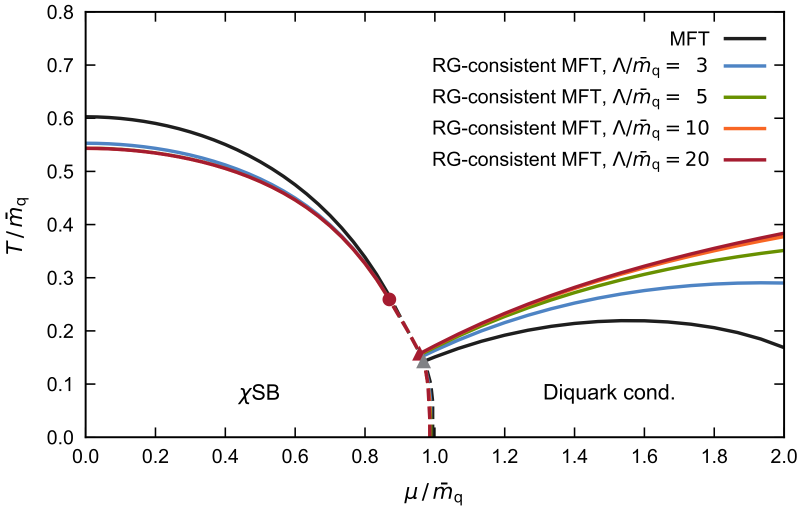

FIGURE 6.4: Phase diagram of the quark-meson-diquark model in the plane spanned by the dimensionless temperature $T/\bar{m}_{\mathrm{q}}$ and the dimensionless quark chemical potential $\mu/\bar{m}_{\mathrm{q}}$ for various different values of $\Lambda/\bar{m}_{\mathrm{q}}$ (with $\bar{m}_{\mathrm{q}} \approx 0.300\,\mathrm{GeV}$). Solid lines are associated with second-order phase transitions whereas dashed lines are associated with first-order phase transitions. Note that the effective actions obtained with different values of Λ agree identically in the vacuum limit, i.e., the RG-consistency condition (3.45) is strictly satisfied in this limit.

and a symmetric high-temperature phase. Moreover, for our parameter choice, we observe the existence of a critical endpoint (depicted by the dot in Fig. 6.4), at which the line of chiral second-order phase transitions meets a line of chiral first-order phase transitions, as well as a triple point (depicted by the triangle in Fig. 6.4), at which the phase governed by chiral symmetry breaking meets the diquark phase and the symmetric high-temperature phase. The general structure of the phase diagram suggests that a description of the dynamics in terms of only quarks, pions, and σ mesons is insufficient for $T/\mu \lesssim 0.2$ and $\mu/\bar{m}_{\mathrm{q}} \gtrsim 1$. Below this line, diquark degrees of freedom become relevant, as well-known from previous mean-field studies [106, 107, 115, 116]. Note that these general statements on the structure of the phase diagram are also in accordance with our findings in Chapters 4 and 5. Of course, in addition to the issue of an RG-consistent treatment of cutoff artifacts as discussed here, artifacts from specific truncations of the effective action may become relevant in the dense and/or low-temperature regime, see, e.g., Refs. [414, 438, 439].

The general structure of the phase diagram appears to be insensitive with respect to an increase of the cutoff scale Λ, at least for the values of the model parameters used in our numerical studies. However, the positions of the two second-order phase transition lines exhibit a strong dependence on Λ, meaning that they converge only slowly when Λ is increased, in particular at large chemical potential, see Fig. 6.4. To be more specific, the critical temperature at $\mu = 0$ is lowered by about 10% compared to the conventional mean-field study (associated with $\Lambda = \Lambda_0$) when we take into account cutoff corrections enforced by the RG-consistency condition (3.45). In the regime governed by diquark dynamics, we observe that the critical temperature is not decreased but rather significantly increased when cutoff corrections are taken into account. Compared to the conventional mean-field study, we indeed find a change of about 30% at $\mu/\bar{m}_\mathrm{q} \approx 4/3$ and about 100% at $\mu/\bar{m}_\mathrm{q} \approx 2$. This clearly shows that it is crucial to ensure RG consistency, in particular in the high-density regime.

RG consistency III: the EOS of the QMD model

In the following, we examine the influence of cutoff corrections enforced by the RG-consistency criterion on the zero-temperature EOS as derived from the QMD model. The EOS is again given in terms of the pressure as a function of the quark chemical potential. This analysis directly contributes to our study of the EOS as obtained by employing the RG flow of the *Fierz*-complete set of four-quark couplings in QCD, since the procedure to integrate out the remaining low-energy fluctuations relies on the LEM truncation (6.9) which directly corresponds to the QMD model. In particular, our findings in the context of the QMD model serve as a basis for an estimate of the scale Λ at which cutoff artifacts can be considered removed in regard to our subsequent computations.

From the RG-consistent effective action (6.20) in the limit $k \to 0$, we compute the pressure (6.25) as a function of the quark chemical potential. Here, see Fig. 6.5, the strength of cutoff artifacts in the high-density regime becomes apparent again. We find that the pressure now exceeds the *Stefan-Boltzmann* pressure P_SB of the free quark gas once cutoff artifacts have been removed. Increasing the quark chemical potential further, we eventually observe that the pressure approaches the pressure of the free gas from above, as also observed for the pure diquark model, see Fig. 6.2. Clearly, as compared to the pressure obtained from a conventional MFT computation (again associated with $\Lambda = \Lambda_0$), the EOS is significantly altered by imposing the RG-consistency criterion. As a consequence, it appears crucial to enforce RG consistency in the high-density regime in order to remove cutoff artifacts. We observe a convergence of our results for the pressure as a function of the scale Λ at approximately $\Lambda/\bar{m}_\mathrm{q} \approx 20$, as the change compared to the results as obtained with $\Lambda/m_\mathrm{q} = 10$ is negligible, cf. the yellow and red solid lines in Fig. 6.5 (see also Fig. 6.4 for the convergence at non-zero temperature). We thus consider cutoff artifacts and regularization scheme dependencies to be removed at this scale. Based on this estimation, we shall use the scale $\Lambda_\mathrm{RG}/\bar{m}_\mathrm{q} = 20$ to implement RG consistency in our LEM truncation to integrate out the remaining low-energy fluctuations.

In summary, the discussed exemplary computations clearly show the importance of RG consistency. The implementation of RG consistency appears to be crucial specifically in the high-density regime of the examined QCD models. For regularization schemes and values of the UV cutoff scale Λ as widely employed in mean-field studies of QCD models, our results already suggest that "cutoff contaminations" of physical observables can be significant. Especially with our analysis of the influence of cutoff corrections enforced by the RG-consistency criterion on the EOS in terms of the pressure as a function of the quark chemical potential and the observation that the EOS is significantly altered once cutoff artifacts are removed, our findings certainly show that it is of phenomenological relevance to ensure RG consistency in general model studies, even in the mean-field approximation.

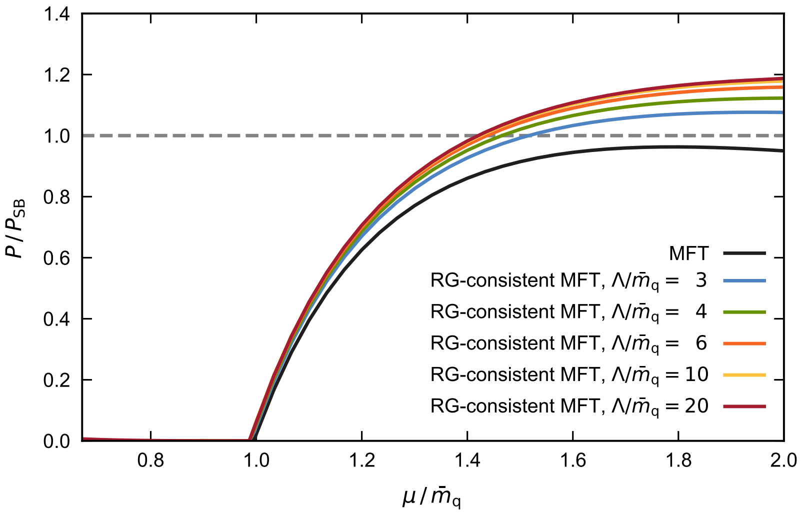

FIGURE 6.5: Pressure P/P_{SB} of our QMD model as a function of the chemical potential $\mu/\bar{m}_{\mathrm{q}}$ (with $\bar{m}_{\mathrm{q}} \approx 0.300\,\mathrm{GeV}$) as obtained from conventional MFT associated with $\Lambda/\bar{m}_{\mathrm{q}} \equiv \Lambda_0/\bar{m}_{\mathrm{q}} = 2$ (black line) as well as from RG-consistent MFT with $\Lambda/\bar{m}_{\mathrm{q}} = 3, 4, 6, 10, 20$.

6.1.3 LEM-truncation couplings from QCD

The details of the computation to integrate out the remaining fluctuations in the low-energy regime based on the LEM ansatz (6.9) have been outlined in our discussion of the QMD model. The free parameters of the QMD model are typically fixed in the vacuum limit to low-energy observables such as the constituent quark mass and the pion decay constant. The parameter $\bar{\nu}^2_{\Lambda_0}$ related to the diquark fields in Eq. (6.19) is often fixed via a certain ratio to the parameters associated with the chiral fields, see, e.g., Refs. [106, 107, 115, 116]. In our approach, however, the LEM truncation (6.9) follows from the RG flow in QCD at higher scales and constitutes the continuation of the RG flow in the low-energy regime governed by spontaneous symmetry breaking. The low-energy ansatz is based on the observed dominances among the four-quark interaction channels and the coefficients of the terms quadratic in the scalar and diquark fields follow from the RG flow of the four-quark couplings. At the transition scale Λ_0, we stop the RG flow in QCD in order to extract the values of the four-quark couplings. The extracted couplings are only rescaled to ensure that we obtain the constituent quark mass $\bar{m}_{\mathrm{q}} = 0.300\,\mathrm{GeV}$ in the vacuum limit but otherwise are left unchanged:[10] In the vacuum limit, we find that the diquark condensate vanishes and the system as described by the QMD-model truncation reduces to pure chiral dynamics in the present approximation. For a given scale Λ_0, the constituent quark mass then depends only on the initial scalar-pseudoscalar coupling $\bar{\lambda}^{(\mathrm{MFT})}_{(\sigma\text{-}\pi),\Lambda_0}$, see also our discussion of the mean-field gap equation in Section 4.1.3. The

---

[10] As mentioned in Section 6.1.1, the RG flow of the four-quark couplings in QCD leads to a significantly smaller value of the critical scale k_0 in the vacuum limit, which sets the scale for the low-energy observables, as compared to our previous computations. As also discussed there, instead of rescaling the couplings, we could have equivalently adjusted the value of the strong coupling at the UV scale Λ to adjust k_{cr} in the vacuum.

four-quark couplings $\bar{\lambda}_{(\sigma\text{-}\pi)}$ and $\bar{\lambda}_{\text{csc}}$ as obtained at the scale Λ_0 from the RG flow in QCD are therefore rescaled by the factor

$$r := \frac{\bar{\lambda}^{(\text{MFT})}_{(\sigma\text{-}\pi),\Lambda_0}}{\bar{\lambda}_{(\sigma\text{-}\pi)}\Big|_{\mu=0}}\,, \tag{6.31}$$

i.e., the values which enter the ansatz (6.9) for the low-energy regime are given by

$$\bar{\lambda}^{(\text{QCD})}_{(\sigma\text{-}\pi),\Lambda_0} = r\cdot\bar{\lambda}_{(\sigma\text{-}\pi)}(k=\Lambda_0)\,,\qquad \bar{\lambda}^{(\text{QCD})}_{\text{csc},\Lambda_0} = r\cdot\bar{\lambda}_{\text{csc}}(k=\Lambda_0)\,. \tag{6.32}$$

In Fig. 6.6, we illustrate the RG flow of the four-quark couplings in the vacuum limit (solid lines) and for $\mu/\bar{m}_{\text{q}} \approx 1.67$ at $T=0$ (dashed lines). The vertical line depicts a specific choice for the transition scale Λ_0 at which the values of the four-quark couplings are extracted in order to determine the couplings of the LEM truncation (6.9). As they follow from the RG flow at higher scales, the initial values now take into account modifications arising from the quark chemical potential as an external control parameter. To illustrate these modifications, the obtained values for the couplings $\bar{\lambda}^{(\text{QCD})}_{(\sigma\text{-}\pi),\Lambda_0}$ and $\bar{\lambda}^{(\text{QCD})}_{(\sigma\text{-}\pi),\Lambda_0}$ are shown in the right panel of Fig. 6.6 as a function of the quark chemical potential. The scalar-pseudoscalar coupling decreases with increasing quark chemical potential whereas the CSC coupling shows the opposite behavior. As the inverse values of the four-quark couplings appear as the coefficients of the terms quadratic in the scalar and the diquark fields, this behavior of the couplings indicates that the chiral condensate is more and more suppressed with increasing quark chemical potential whereas the formation of the diquark condensate is increasingly facilitated. Depicted by the gray lines, we have also included the remaining couplings of the *Fierz*-complete basis. Two of these couplings appear to have a similar strength compared to the scalar-pseudoscalar and the CSC coupling. Recall, however, that this is merely an artifact of the $U_{\text{A}}(1)$ symmetry being intact, see our discussion in Section 5.3.2.

At this point, let us bring to attention important differences between our present analysis and the dominance pattern discussed in Section 6.1.1. It appears that the behavior of the couplings as a function of the quark chemical potential observed in the right panel of Fig. 6.6 is not in agreement with the one in Fig. 6.1 considered in our discussion of the relevant low-energy effective degrees of freedom. In particular, the earlier observation of the CSC coupling to decrease for higher chemical potentials after reaching a maximum seems to be in contradiction to the present case of a monotonously increasing CSC coupling. However, keep in mind that Fig. 6.1 shows the values of the couplings as a function of the quark chemical potential at the scales $k/k_0 = k_{\text{cr}}/k_0 + 0.0039$. The critical scale $k_{\text{cr}} = k_{\text{cr}}(\mu)$ is a function of the chemical potential itself and increases for higher densities. Analyzing the four-quark couplings as close as possible to the symmetry breaking scale $k_{\text{cr}}(\mu)$ is advantageous for a definite identification of the dominant channels based on their relative strengths. While the comparison of the couplings to each other at a given quark chemical potential is meaningful, this analysis does not allow the comparison of values obtained at different quark chemical potentials since the couplings are evaluated at different RG scales. As a consequence, the actual behavior of the couplings as a function of the quark chemical potential is obscured

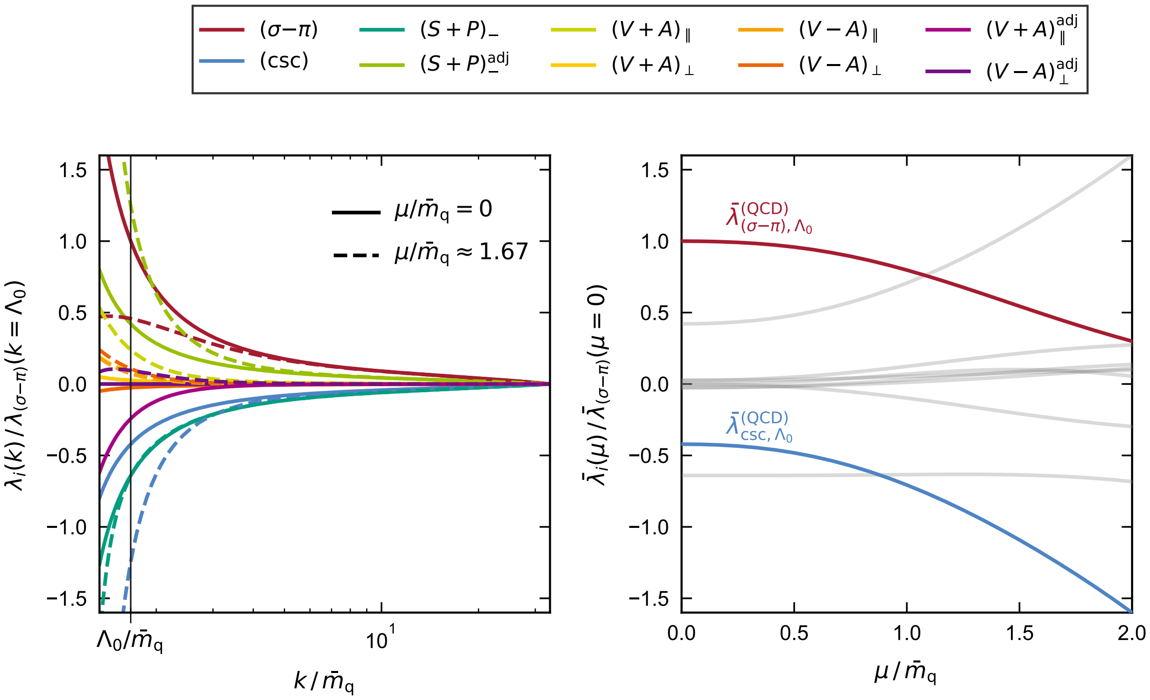

Figure 6.6: The determination of the couplings of the LEM truncation at the transition scale Λ_0 in terms of the couplings $\bar{\lambda}^{(\mathrm{QCD})}_{(\sigma\text{-}\pi),\Lambda_0}$ and $\bar{\lambda}^{(\mathrm{QCD})}_{(\sigma\text{-}\pi),\Lambda_0}$ from the RG flow in QCD is illustrated. Left panel: Scale dependence of the (dimensionless) renormalized four-quark couplings in the zero-temperature limit for zero quark chemical potential (solid lines) and for $\mu/\bar{m}_\mathrm{q} \approx 1.67$ (dashed lines), normalized to the scalar-pseudoscalar coupling $\lambda_{(\sigma\text{-}\pi)}(k=\Lambda_0)$ at the transition scale. The black vertical line depicts a specific choice for the location of the transition scale, here at $\Lambda_0/\bar{m}_\mathrm{q} \approx 1.67$, at which the four-quark couplings are evaluated to serve as initial couplings of the LEM ansatz. Right panel: Four-quark couplings extracted at the transition scale Λ_0 as functions of the quark chemical potential, normalized to the corresponding value of the scalar-pseudoscalar coupling in the vacuum limit, see main text for details.

and the behavior observed in Fig. 6.1 rather resolves the effect of the μ-dependence of the critical scale k_cr. In contrast to that, the four-quark couplings depicted in the right panel of Fig. 6.6 are obtained at a fixed RG transition scale Λ_0 and allow the comparison across different chemical potentials, thus revealing the actual dependence of the four-quark couplings on the quark chemical potential.

6.2 The equation of state of dense QCD matter

We now employ the QMD-model truncation (6.9), with the couplings determined by the RG flow of the four-quark couplings in QCD at higher scales, to compute the zero-temperature EOS of isospin-symmetric QCD matter in an RG-consistent way. The effective potential $U = \Gamma/\mathcal{V}$ in the long-range limit $k \to 0$ is given by[11]

$$U[\bar{\phi}, \{\bar{\Delta}_A\}]] = \frac{1}{\mathcal{V}}\Gamma_{\Lambda'}[\bar{\phi}, \{\bar{\Delta}_A\}] - 4L^{(T\to 0)}_{k\to 0}(\Lambda', \bar{\phi}^2) - 8M^{(T\to 0)}_{k\to 0}(\Lambda', \bar{\phi}^2, |\bar{\Delta}|^2)\,, \tag{6.33}$$

with

$$\begin{aligned}\frac{1}{\mathcal{V}}\Gamma_{\Lambda'}[\bar{\phi}, \{\bar{\Delta}_A\}] =& \frac{1}{\mathcal{V}}\Gamma_{\Lambda_0}[\bar{\phi}, \{\bar{\Delta}_A\}] + 4L^{(T\to 0)}_{\Lambda_0}(\Lambda', \bar{\phi}^2)\Big|_{\mu=0} + 8M^{(T\to 0)}_{\Lambda_0}(\Lambda', \bar{\phi}^2, |\bar{\Delta}|^2)\Big|_{\mu=0} \\ &+ 4\mu^2\left(\partial_\mu^2 M^{(T\to 0)}_{\Lambda_0}(\Lambda', \bar{\phi}^2, |\bar{\Delta}|^2)\Big|_{\mu=0}\right)\,,\end{aligned} \tag{6.34}$$

where the term $\sim \mu^2$ accounts for the renormalization of the diquark chemical potential again. Here, we have introduced the UV cutoff scale Λ' for the "pre-initial" flow in order to distinguish from the UV scale Λ of the RG flow in QCD. This "pre-initial" flow realizes the RG consistency of the low-energy dynamics as described by the QMD truncation. In our QMD-model study, see Section 6.1.2, the analysis of the Λ'-dependence of the zero-temperature EOS showed that the results for the pressure are converged for approximately $\Lambda'/\bar{m}_{\rm q} \approx 20$, in particular in the regime of higher chemical potentials. This convergence indicates that the scale Λ' is sufficiently large for the considered range of quark chemical potentials such that the condition $\mu/\Lambda' \ll 1$ holds. The latter implies that the condition (3.47) holds as well and the RG-consistency criterion is fulfilled. Cutoff artifacts and regularization scheme dependences can thus be considered removed at this scale. Here, based on theses finding, we shall set $\Lambda'/\bar{m}_{\rm q} = 20$ in our computation of the EOS.

The effective action Γ_{Λ_0} of our QMD-model truncation, which by itself amounts to the initial effective action at the scale Λ_0 in the vacuum limit, is given by

$$\frac{1}{\mathcal{V}}\Gamma_{\Lambda_0}[\bar{\phi}, \{\bar{\Delta}_A\}] = \frac{1}{2}\frac{1}{\bar{\lambda}^{(\rm QCD)}_{(\sigma\text{-}\pi),\Lambda_0}}\bar{\phi}^2 - \frac{1}{2}\frac{1}{\bar{\lambda}^{(\rm QCD)}_{{\rm csc},\Lambda_0}}|\bar{\Delta}|^2\,, \tag{6.35}$$

with the values $\bar{\lambda}^{(\rm QCD)}_{(\sigma\text{-}\pi),\Lambda_0}$ and $\bar{\lambda}^{(\rm QCD)}_{{\rm csc},\Lambda_0}$ determined by the RG flow of the four-quark couplings in QCD at higher scales as described in Section 6.1.3. Note that the effective action at the scale Λ_0 is given by the expression (6.35) alone only in the vacuum limit and receives otherwise additional contributions in form of cutoff corrections as entailed by the RG-consistency criterion.

With the effective potential U at hand, the ground state values of the fields $\bar{\phi}$ and $\bar{\Delta}_A$ are determined by the global minimum of the effective potential. The pressure P is then obtained from the latter as follows:

$$P = -U\left(\bar{\phi}_{\rm gs}, \{\bar{\Delta}_A\}_{\rm gs}\right) + U\left(\bar{\phi}_{\rm gs}, \{\bar{\Delta}_A\}_{\rm gs}\right)\Big|_{\mu=0}\,, \tag{6.36}$$

where we have normalized the pressure with respect to the pressure in the vacuum limit. In Fig. 6.7, we show our results (light-red band) for the zero-temperature EOS of isospin-

---

[11] Recall that the scalar field ϕ has been redefined to absorb the *Yukawa* coupling $\bar{h}_{(\sigma\text{-}\pi)}$.

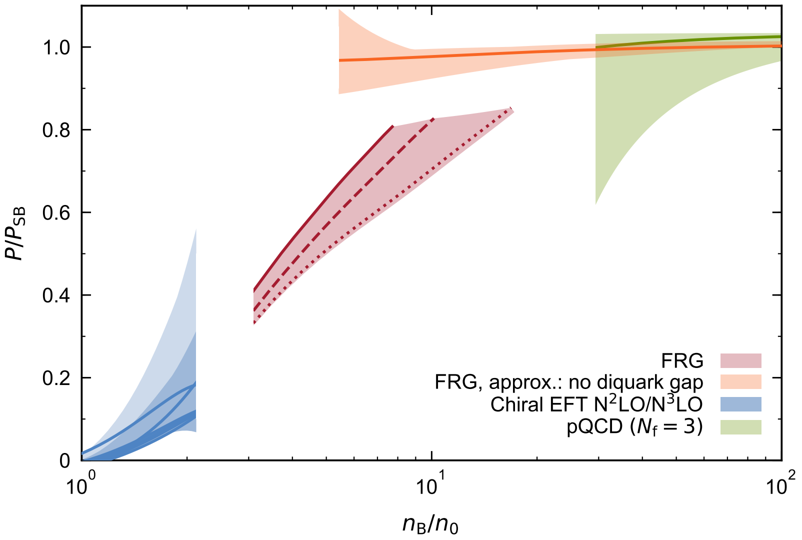

FIGURE 6.7: Pressure P of symmetric nuclear matter normalized by the *Stefan-Boltzmann* pressure of the free quark gas P_{SB} as a function of the baryon number density n_{B}/n_0 in units of the nuclear saturation density as obtained from chiral EFT, FRG, including results from an approximation without taking into account a diquark gap (FRG, approx.: no diquark gap), and perturbative QCD (pQCD), see main text for details.

symmetric QCD matter at intermediate densities. The EOS is given in terms of the pressure as a function of the baryon number density n_{B}, where the latter is readily obtained from the pressure according to

$$n_{\mathrm{B}} = \frac{1}{3}\frac{\partial P(\mu)}{\partial \mu}\,, \tag{6.37}$$

cf. the thermodynamic relations (2.23) introduced in Section 2.1.1. In Fig. 6.7, the density is given in units of the nuclear saturation density n_0 and the pressure is normalized by the *Stefan-Boltzmann* pressure P_{SB} of the free quark gas. To estimate the uncertainties arising from the presence of the scale Λ_0 describing the "transition" in the effective degrees of freedom, we vary this scale from $\Lambda_0 = 450\ldots600\,\mathrm{MeV}$. Together with the uncertainty in the RG flow of the four-quark couplings due to fixing of the strong coupling within the experimental error, i.e., the uncertainty related to the values of $\bar{\lambda}^{(\mathrm{QCD})}_{(\sigma\text{-}\pi),\Lambda_0}$ and $\bar{\lambda}^{(\mathrm{QCD})}_{\mathrm{csc},\Lambda_0}$, this gives rise to the light-red band. Within the band, we show three representative EOSs associated with $\Lambda_0 = 450, 500, 600\,\mathrm{MeV}$ depicted by the solid, dashed and dotted red line, respectively. The extent of the light-red band at high densities is set by the constraint $\mu \leq \Lambda_0$.

In Fig. 6.7, we have included results for the EOS in the low-density regime obtained from computations based on chiral EFT interactions. For this regime, chiral EFT represents a powerful framework to describe the nuclear dynamics and interactions within a systematic expansion based on nucleons and pions as the low-energy degrees of freedom [89, 90]. Substantial progress has been achieved in recent years in deriving new nuclear forces and computing the EOS microscopically based on nucleon-nucleon (NN), three-nucleon (3N) and four-nucleon (4N) interactions derived within chiral EFT [91–93, 281, 283, 440–444]. In particular, an efficient framework was presented in Ref. [93] to compute the energy of nuclear matter at zero temperature within many-body perturbation theory (MBPT) up to high orders in the many-body expansion and for general proton fractions. It allows to include all contributions from two- and many-body forces up to N^{3}LO and to explore the connection of properties of matter and nuclei [445]. Moreover, in Ref. [92], a set of NN and 3N interactions was fitted to few-body observables, where all derived interactions led to good saturation properties without adjustment of free parameters. In particular, one interaction of this set was found to also correctly predict the ground state energies of medium-mass nuclei up to ^{100}Sn [446, 447]. In Fig. 6.7, we show the results for the pressure of symmetric nuclear matter up to twice nuclear density based on the set of interactions of Ref. [92] (individual blue lines) as well as the interactions up to N^{3}LO fitted to the empirical saturation point of Ref. [93] (blue bands). The uncertainty bands at N^{2}LO (light-blue band) and N^{3}LO (dark-blue band) have been determined following the strategy of Ref. [448] and represent the combined uncertainties based on the results at the two cutoff scales $\Lambda = 450$ and $500\,\mathrm{MeV}$ (see also Ref. [93]). We observe that the results for the pressure as obtained from our FRG analysis at intermediate densities are remarkably consistent with those obtained from the many-body framework based on chiral EFT interactions at lower densities. However, our present approximation does not allow us to reliably compute the pressure at densities smaller than $n_{\mathrm{B}} \lesssim 3\,n_0$ and is not capable to resolve the exact position of any chiral transition or crossover, since we do not observe a clear dominance pattern in the spectrum of the four-quark couplings in this regime. Moreover, in order to resolve this regime more reliably, the incorporation of fermionic six-point functions associated with baryon dynamics is expected to be necessary.

In the regime of very high densities, the EOS can be calculated using perturbative methods [302–306] owing to the fact that the dynamics is dominated by modes with momenta $|p| \sim \mu$. This effectively renders the QCD coupling $g_{\mathrm{s}}^2/4\pi$ small. Although the ground state is expected to be governed by diquark condensation [98, 99, 102, 103, 110], calculations which do not include condensation effects are reliable, provided that the chemical potential is much larger than the scale set by the diquark gap. With respect to this high-density limit, we find that the results from our FRG approach at intermediate densities are also found to be consistent with those from perturbative QCD calculations (light-green band) [306]. We indicate, however, that these results have been obtained in a perturbative calculation at order $\mathcal{O}(g_{\mathrm{s}}^4)$ for isospin-symmetric nuclear matter including the strange quark. In this calculation with massless up and down quarks, the chemical potential of the strange quark has been set to zero. Still, the consideration of three flavors in contrast to our two-flavor computation may restrict a direct comparison.

In our RG study, the gluon-induced four-quark interactions serve as proxies for the various order parameters. The analysis of their RG flows indeed indicate that the ground state is governed by spontaneous symmetry breaking, even at high densities. This can be effectively described by a transition in the relevant degrees of freedom at a finite scale. In order to make contact with perturbative calculations, we drop the running of the four-quark interactions and consider an FRG computation restricted to the running of the quark and gluon wavefunction renormalization factors at leading order in the derivative expansion. From the latter, the dressed quark and gluon propagators are obtained which are then used to compute the pressure.[12] In

---

[12] Details of this computation are not part of this thesis and can be found in Ref. [449].

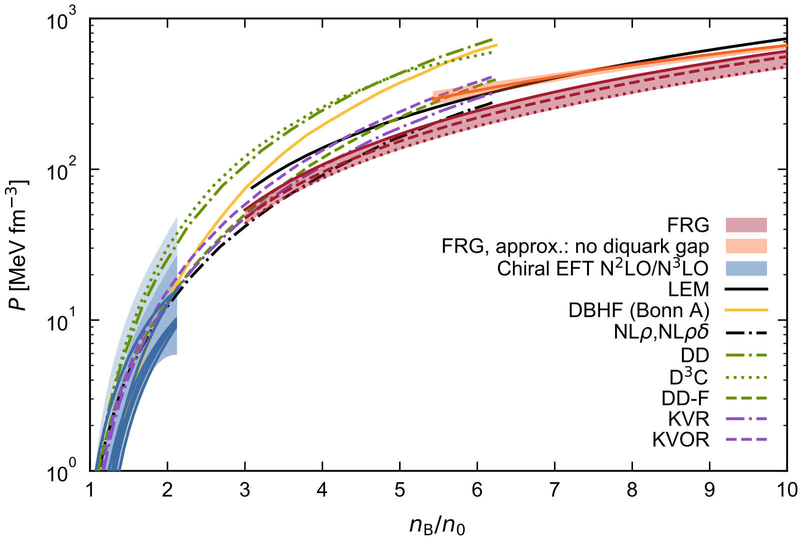

FIGURE 6.8: Pressure of symmetric nuclear matter as obtained from chiral EFT, FRG, and perturbative QCD (pQCD), as in Fig. 6.7, in comparison with different models (see main text and also Ref. [450]).

this case, the RG flow of the pressure can be followed from high-energy scales down to the deep IR limit without encountering any pairing instabilities as associated with spontaneous symmetry breaking. In Fig. 6.7, we show our results for the pressure from this calculation (orange band). We observe very good agreement with recent perturbative calculations [306]. The width of this band illustrates the uncertainty arising from a variation of the regularization scheme and a variation of the running gauge coupling within the experimental error bars at the τ mass scale [38]. Following the pressure toward smaller densities, we observe that our results for the intermediate-density and high-density regime are consistent in the sense that a naive extrapolation of our results at intermediate densities "flows" into the results for perturbative QCD at (very) high densities. However, our findings make apparent that toward the regime of intermediate densities condensation effects eventually become essential.

In Fig. 6.8, we compare our results with different models. These include relativistic mean-field calculations, such as NLρ and NL$\rho\delta$ [451], DD, D^{3}C and DD-F [452] as well as KVR and KVOR [453] (see also Ref. [450]). In addition, we show results of *Dirac-Brueckner Hartree-Fock* calculations (DBHF) [454] and from a 'conventional' LEM, see Ref. [115] and the third example in Section 6.1.2.[13] At densities up to around twice nuclear saturation density, the different models are compatible with the chiral EFT uncertainty bands at N^{2}LO (but not all at N^{3}LO). At higher densities, however, the pressure obtained from most models is found to be significantly higher than our FRG results. Considering the 'conventional' LEM calculation, the values are significantly increased as compared to our present results and tend to overestimate the pressure toward lower densities as well as toward higher densities. In particular, the pressure appears to be inconsistent with perturbative QCD computations at asymptotically high densities, which is also true for the results obtained from most of the other models shown in Fig. 6.8. This comes as no surprise as in conventional LEM studies the applicability in

---

[13] The 'conventional' LEM refers to the QMD model with UV cutoff $\Lambda = \Lambda_0 = 600\,\text{MeV}$, see Section 6.1.2 for details.

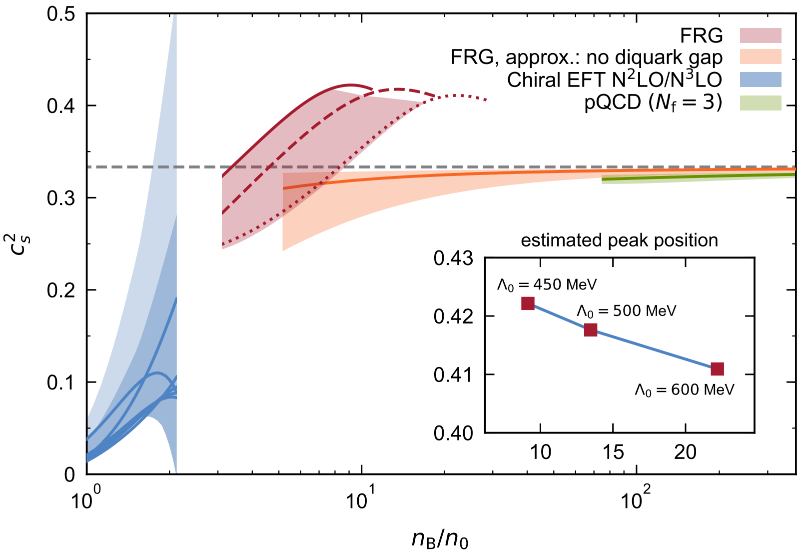

Figure 6.9: The speed of sound squared c_s^2 as a function of the baryon number density n_B/n_0 in units of the nuclear saturation density as derived from the pressure shown in Fig. 6.7. The inset shows the estimated position of the maximum of the speed of sound.

terms of the range of external parameters such as the quark chemical potential is typically limited. Toward higher densities, the condition $\mu/\Lambda \ll 1$ becomes violated and the model begins to resolve cutoff artifacts and regularization scheme dependencies.

Let us now turn to the speed of sound which is given by

$$c_s^2 = \frac{\partial P}{\partial \epsilon} = \frac{1}{\mu} \frac{\partial P/\partial \mu}{\partial^2 P/\partial \mu^2}\,, \tag{6.38}$$

where we have used the relation $\epsilon = 3\mu n_B - P$ for the energy density in the zero-temperature limit.[14] In Fig. 6.9, we present our results for the speed of sound squared c_s^2 as derived from the pressure shown in Fig. 6.7. The light-red band, corresponding to the one in Fig. 6.7, is associated with the results from our FRG approach taking diquark condensation into account. The band describes again the uncertainty estimate obtained from varying the "transition" scale Λ_0 and a variation of the running gauge coupling within the experimental error bars. Its extent at high densities is set by the constraint $\mu \leq \Lambda_0$ as before. Also, we show once more three representative computations associated with the transition scales $\Lambda_0 = 450$, $500\,, 600\,\mathrm{MeV}$ depicted by the solid, dashed and dotted red line, respectively. Toward lower densities, the obtained speed of sound is consistent with the N^{3}LO derived from chiral EFT interactions, while the N^{2}LO uncertainty increases rapidly at densities around twice nuclear saturation density and would constrain only very large values for the speed of sound. Our results for the speed of sound exceed the non-interacting limit $c_s^2 = 1/3$ (indicated by the dashed gray line in Fig. 6.9), which is expected to be approached from below at asymptotically high densities according to perturbative QCD studies [302–306]. Thus, our findings at intermediate densities suggest that the speed of sound assumes a maximum. In order to estimate the maximal value

---

[14] The pressure as a function of the quark chemical potential was interpolated with *Chebyshev* polynomials in order to numerically compute the second derivative with respect to the chemical potential.

and the location of the maximum, we show the results also for values of the quark chemical potential slightly above the respective "transition" scale Λ_0. The resulting estimate for the position and the height of the maximum is shown in the inset of Fig. 6.9. The maximal value of the speed of sound obtained from our calculations is approximately $\max(c_s^2) \approx 0.42$ and is found to be remarkably robust against the variation in the scale Λ_0. The location of the maximum, however, varies from approximately $n_B \approx 9\,n_0$ ($\Lambda_0 = 450\,\text{MeV}$) to $n_B \approx 22\,n_0$ ($\Lambda_0 = 600\,\text{MeV}$). In Fig. 6.9, we show again results from perturbative QCD calculations at high densities, i.e., $n_B > 75\,n_0$. Note that the computation of the speed of sound from the corresponding data for the pressure in this high-density branch becomes numerically unstable for $n_B \lesssim 75\,n_0$. We also included the results for the speed of sound as determined from our FRG computation which does not take into account condensation effects. These results show the expected behavior, i.e., they approach the non-interacting limit at asymptotically high densities and agree well with the speed of sound resulting from the perturbative QCD calculations at densities beyond $n_B > 75\,n_0$. Toward the regime of intermediate densities, however, the speed of sound as obtained from the FRG computation without condensation effects stays below the non-interacting limit $c_s^2 = 1/3$. For the appearance of a maximum in the speed of sound, we thus find that the inclusion of condensation effects in the regime $n_B \lesssim 30\,n_0$ is crucial.

6.3 CONCLUSIONS

In the study presented in this chapter, we have connected the RG flow of the four-quark couplings of a *Fierz*-complete basis in QCD to an LEM truncation in order to integrate out the remaining low-energy fluctuations and to access the regime governed by spontaneous symmetry breaking. With this approach, we aimed at a computation of the EOS of cold strong-interaction matter at intermediate densities. By analyzing the dominance pattern of the four-quark interactions in terms of their relative strength along the density axis in the zero-temperature limit, we have identified the chiral fields and the diquark fields as the essential low-energy effective degrees of freedom. As implied by these findings, we have employed a corresponding QMD-model truncation for the low-energy sector.

Based on our discussion of the concept of RG consistency in Section 3.3, we have implemented a "pre-initial" flow to ensure the RG-consistency criterion. In general, this criterion requires that the effective action Γ of a given theory does not depend on the cutoff scale, i.e., $\Lambda\partial_\Lambda\Gamma = 0$, also in the presence of external control parameters such as the quark chemical potential. We have illustrated the effect of cutoff corrections as enforced by the RG-consistency criterion in mean-field studies of a pure diquark model at finite density and of the QMD model at finite temperature and density. We note that we had to take into account the renormalization of the diquark chemical potential to ensure RG consistency. For regularization schemes and values of the cutoff scale as widely employed in mean-field studies of QCD models, our analysis already suggests that "cutoff contaminations" of physical observables can be significant. For example, the critical temperature of our quark-meson-diquark model at $\mu = 0$ is lowered by about 10% when we take into account cutoff corrections enforced by the RG-consistency condition as given in Eq. (3.45). In general, such corrections do not necessarily only lead to a decrease of the critical temperature. In fact, in the regime governed by diquark condensation, cutoff corrections rather tend to increase it. To be specific, the critical temperature is increased by about 30% at $\mu/\bar{m}_{\mathrm{q}} = 4/3$ (with $\bar{m}_{\mathrm{q}} \approx 0.300\,\mathrm{GeV}$) and already by more than 100% at $\mu/\bar{m}_{\mathrm{q}} = 2$ compared to the results from a conventional mean-field study. Thus, the implementation of RG consistency appears to be very relevant in the high-density regime of such LEMs of QCD. Crucially, the associated corrections may significantly affect the computation of the EOS of dense strong-interaction matter based on such LEMs. In particular, this might be the case for the most relevant regime of intermediate densities from the standpoint of astrophysical applications. Indeed, for the zero-temperature pressure of the QMD model, we found corrections of up to 30% in the considered range for the quark chemical potential. Based on the latter analysis, we could determine a sufficiently large cutoff Λ' for the "pre-inital" flow in order to ensure an RG-consistent QMD-model truncation for the low-energy sector, with cutoff artifacts and regularization scheme dependencies removed at least for the considered range of quark chemical potentials.

Employing the QMD-model truncation to describe the dynamics at scales $k < \Lambda_0$, with the couplings of the ansatz fixed by the RG flow of the four-quark couplings in QCD at higher scales, we were able to compute the EOS of isospin-symmetric cold strong-interaction matter in an RG-consistent way at intermediate densities. Even though the present approximations underlying our study are not reliable at densities smaller than $n_{\mathrm{B}} \lesssim 3\,n_0$, our results already show a remarkable consistency with computations based on chiral EFT forces at lower densities and indicate that they can be combined via simple extrapolations. It should be mentioned as well that our findings are also consistent with well-known results from perturbative QCD calculations at very high densities ($n_{\mathrm{B}} > 75\,n_0$). Ignoring the diquark gap, our FRG calculations are then found to be in good agreement with these perturbative calculations. However, we observe that condensation effects eventually become essential toward lower densities.

At intermediate densities, our study suggests that the ground state is governed by diquark dynamics which give rise to a maximum in the speed of sound. The speed of sound assumes the maximal value $\max(c_{\mathrm{s}}^2) \approx 0.42$ which exceeds the non-interacting limit $c_{\mathrm{s}}^2 = 1/3$. While the maximal value is surprisingly insensitive to a variation in the "transition" scale Λ_0 at which the effective action is recast in terms of the most relevant low-energy effective degrees of freedom, the position of the maximum varies from $n_{\mathrm{B}} \approx 9\,n_0$ to approximately $22\,n_0$. This finding might have implications for the EOS of cold and dense strong-interaction matter in the context of astrophysical applications such as the description of neutron stars. Recent studies based on approaches to interpolate the EOS between the limits of small and asymptotically high densities or to directly parametrize the speed of sound indeed indicate that the speed of sound is likely to exceed the non-interacting limit at densities relevant for the description of neutron stars [310, 455, 456]. In fact, our observation of the only mild overshooting of the non-interacting limit potentially supports the existence of sizable cores composed of deconfined quark matter in heavy neutron stars with masses of around twice the solar mass [310]. However, we rush to add that an application of our findings to neutron stars is certainly only qualitative at this stage as our study does not yet include an isospin chemical potential to directly describe neutron matter. Moreover, the strange quark might become relevant in the regime of intermediate densities. A generalization of the presented framework to general isospin asymmetries will eventually give us access to the EOS in the neutron-rich regime, which is most relevant for astrophysical applications. With respect to future applications, we would like to mention that our approach is already formulated for general temperatures which will allow us to also study the temperature dependence of the EOS of dense QCD matter from microscopic calculations.

In our present approach, we have employed different regularization schemes for the flow at high and low RG scales, i.e., the four-dimensional *Fermi*-surface-adapted regulator was used in the RG flow of the four-quark couplings at higher scales and the three-dimensional sharp regulator for the QMD-model truncation in the low-energy regime. As the transition to the QMD-model truncation at a given scale Λ_0 requires the equivalence of the RG scale in the high- and low-energy regime, the use of different regularization schemes is potentially problematic. Here, the implications of using different regularization schemes might be compensated to a certain extent by the corrections enforced by the RG-consistency condition. Also, the applied procedure to employ only the ratio of the four-quark couplings to determine the couplings of the QMD-model truncation, instead of using absolute values, might further contribute to mitigate possible implications. Lastly, the uncertainty has been tested by varying the transition scale Λ_0. However, we expect further improvements, e.g., in terms of reduced uncertainties, by employing the same regularization scheme at all RG scales. In particular, dynamical hadronization techniques would allow us to conveniently resolve the momentum dependencies of the corresponding vertices [337, 380, 396, 398], see, e.g., Refs. [192, 193, 195, 397, 399] for their application to QCD. With such techniques the computation does not rely on a separate ansatz for the low-energy dynamics in form of a *Hubbard-Stratonovich* transformation performed at a given scale Λ_0. In fact, dynamical hadronization techniques effectively implement continuous *Hubbard-Stratonovich* transformations of four-quark interactions in the RG flow. We expect that the application of these techniques allows us to connect our results for the EOS at intermediate densities with the results at high densities as obtained from our FRG analysis without taking into account condensation effects in a consistent manner. In this scenario, the EOS could be obtained over a wide density range from a single computation which directly connects to the perturbative QCD results at asymptotically high densities. The latter would be an advantageous aspect compared to model studies. Nevertheless, our present findings already provide us with important insights into the zero-temperature EOS of strong-interaction matter at intermediate densities, which we obtained directly from the fundamental quark-gluon dynamics.

7

CONCLUSIONS AND OUTLOOK

In this thesis, we have studied dense strong-interaction matter with two massless quark flavors at finite temperature as well as in the zero-temperature limit. The functional renormalization group has been our key method, representing an ideal non-perturbative approach for the analysis of QCD matter at finite chemical potential. In particular, it allows us to anchor our analysis directly in the fundamental quark-gluon dynamics.

We studied in detail the importance of four-quark self-interactions which are dynamically generated by two-gluon exchange. They play an essential role in the description of strongly correlated low-energy dynamics and are related to condensate formation in the long-range limit. We have constructed a *Fierz*-complete basis of four-quark interactions in the pointlike limit only constrained by the symmetries of the underlying theory, i.e., QCD, which are reduced due to the presence of a heat bath and the finite quark chemical potential. This basis allowed us to incorporate any dynamically generated four-quark interaction compatible with the remaining symmetries and thus to fully capture the related dynamics.

In order to analyze in depth the impact of *Fierz* completeness, we initially considered the gauge degrees of freedom to be integrated out and studied *Fierz*-complete versions of the NJL model. First, we temporarily reduced the number of fermion species to one, which greatly simplified the analysis and allowed us to study the mechanisms in an accessible and clear manner while still retaining essential characteristics of the low-energy dynamics in QCD. Based on the RG flow of the four-quark couplings at leading order of the derivative expansion, where the incorporation of beyond mean-field corrections was necessary to establish *Fierz* completeness, we analyzed the fixed-point and phase structure at finite temperature and chemical potential, focusing on an understanding of how *Fierz* incompleteness affects the predictive power of such model studies. We indeed found that *Fierz*-incomplete approximations strongly affect predictions, e.g., the position of the finite-temperature phase boundary, its curvature at vanishing quark chemical potential, or the critical quark chemical potential beyond which no spontaneous symmetry breaking occurs. The precise form of the influences arising from *Fierz*-incomplete considerations in general depends on the specific choice of interaction channels taken into account. We observed that *Fierz* completeness is particularly important at large chemical potentials. In order to obtain insights into the ground-state properties in the phase governed by spontaneous symmetry breaking, we analyzed the relative strength of the four-quark couplings as well as the scaling behavior of the loop diagrams contributing to the RG flow of the couplings.

In the next step, we extended our analysis of the *Fierz*-complete NJL-type model to the case of fermions coming in two flavors and $N_{\rm c}$ colors. We observed again that *Fierz* completeness strongly affects the phase structure, in particular at larger values of the quark chemical potential. The critical temperature was found to be significantly increased in a *Fierz*-complete consideration, with potentially important implications for the magnitude of the gap in the zero-temperature limit at high densities. In order to shed light on the formation of condensates close to the finite-temperature phase boundary, we analyzed again the dominances of the four-quark couplings in terms of their relative strength. The dominance of a specific four-quark coupling served us as an indication for the formation of a corresponding condensate. For smaller chemical potentials, we observed a clear dominance of the scalar-pseudoscalar interaction channel associated with the formation of the chiral condensate. At a specific critical value of the quark chemical potential, the “hierarchy” of the four-quark couplings was found to undergo a transition to yield a pronounced dominance of the CSC four-quark coupling related to the formation of the most conventional color superconducting condensate for higher chemical potentials. To obtain a better understanding of the underlying dynamics, we also studied the strength of the $U_{\rm A}(1)$ symmetry breaking, including a $U_{\rm A}(1)$-symmetric variation, the RG flow in the large-$N_{\rm c}$ limit and a two-channel approximation taking into account only the scalar-pseudoscalar interaction channel and the channel related to the conventional diquark condensate. Specifically, the analysis of the fixed-point structure in the two-channel approximation revealed an intriguing mechanism associated with the change of the “hierarchy” at higher chemical potentials to a dominance indicating the formation of a color-superconducting ground state.

Our examination of the *Fierz*-complete versions of the NJL model set the stage for our study including dynamical gauge fields, taking the first step toward a “top-down” first-principles approach at high densities. In the chiral limit, the only free parameter was given by the initial UV value of the strong coupling which was fixed at a perturbative momentum scale to the value as extracted from experiment. The four-quark couplings were initially set to zero and only dynamically generated in the course of the RG flow. The sector of the truncation describing the running of the gauge coupling is based on Refs. [392, 393]. We again analyzed the phase structure at finite temperature and finite quark chemical potential based on the RG flow of the four-quark couplings and their “hierarchy” in terms of their relative strength. The incorporation of gluodynamics was observed to further increase the critical temperature, in particular at larger values of the quark chemical potential. This observation might have again implications for the size of the corresponding energy gap in the zero-temperature limit. Variations in the specific scale dependence of the strong coupling showed remarkably little effect on the finite-temperature phase boundary. Only in-medium effects on the matter back-coupling to the gauge sector were found to potentially have an effect on the critical temperature at larger values of the quark chemical potential as inferred from an estimate based on a μ-dependent quark contribution to the gauge anomalous dimension. The analysis of the “hierarchy” of the four-quark couplings in terms of their strength showed again a clear dominance of the scalar-pseudoscalar coupling at lower quark chemical potentials and a clear dominance of the CSC coupling associated with the formation of a diquark condensate at large values of the chemical potential. This finding is remarkable as the observed dominances has not been triggered by a specific choice or even fine-tuning of the initial conditions of the four-quark couplings and must be therefore solely arise from the underlying quark-gluon dynamics. The dominances themselves as well as the location of the change from the dominance of the scalar-pseudoscalar coupling to the dominance of the CSC coupling were observed to be remarkably robust against details of the scale dependence of the strong coupling, suggesting that the dominances are to a large extent determined by the dynamics within the quark sector. We probed the underlying dynamics further by studying the influence of $U_{\mathrm{A}}(1)$-violating initial conditions on the phase structure. Astonishingly little effect was observed on the finite-temperature phase boundary even at large chemical potentials and over a wide range of the strength of explicit $U_{\mathrm{A}}(1)$ symmetry breaking. This strength was controlled by the initial value of the four-quark coupling associated with the so-called *'t Hooft* determinant. However, the explicit $U_{\mathrm{A}}(1)$ breaking did influence the "hierarchy" of the four-quark channels by accentuating even more the dominances of the scalar-pseudoscalar channel at smaller chemical potentials and of the CSC coupling at higher chemical potentials, pointing to the importance of $U_{\mathrm{A}}(1)$ symmetry breaking in regard to the formation of theses condensates.

In the final part of this thesis, we employed the developed FRG framework to compute the EOS of cold isospin-symmetric QCD matter at intermediate densities, i.e., the density regime not accessible anymore by computations based on chiral EFT interactions and not yet accessible by perturbative approaches. In order to suitably describe the low-energy regime governed by spontaneous symmetry breaking, we identified the relevant low-energy effective degrees of freedom based on the dominance pattern of the four-quark couplings as obtained from the RG flow in QCD at higher scales and performed a *Hubbard-Stratonovich* transformation of these dominant channels at a "transition" scale to account for the formation of the corresponding condensates. This led to the connection of the RG flow of the four-quark couplings at higher scales to a quark-meson-diquark-model truncation as a customized low-energy effective ansatz in order to integrate out the remaining fluctuations at lower scales. The presence of a corresponding transition scale required the implementation of a "pre-initial" flow to ensure RG consistency, i.e., the removal of cutoff effects and regularization scheme dependences. A discussion of exemplary mean-field computations demonstrated the importance of this criterion for low-energy effective theories, in particular in the presence of external control parameters such as temperature or chemical potentials. We found that the associated corrections were especially important at larger densities, thus being essential for the computation of the EOS of dense QCD matter. We also discussed the concept of RG consistency from a very general perspective which might prove valuable for a broad range of low-energy effective model studies. The continuation of the RG flow in QCD at higher scales into the low-energy regime employing the quark-meson-diquark-model truncation enabled us to compute the EOS at intermediated densities directly based on quark-gluon dynamics. Toward lower densities, our results were found to be remarkably consistent with computations based on chiral EFT forces, although the present approximation does not allow us to reliably describe the density regime around the chiral phase transition. Moreover, our results for the EOS were also found to be consistent with well-known results from perturbative QCD computations at high densities. We also presented an FRG computation of the EOS without taking into account condensation effects, which was found to be in good agreement with the aforementioned perturbative calculations. A continuation of the EOS as obtained from the latter FRG computation in the high-density regime toward lower densities made apparent that condensation effects eventually become essential. These condensation effects were then observed to give rise to a maximum in the speed of sound which exceeds the non-interacting limit at intermediate densities. While we found that the location of the maximum depends on the choice for the scale of the transition to low-energy effective degrees of freedom, the maximal value was observed to be remarkably robust.

For future studies, it will be very interesting to make use of dynamical hadronization techniques which allow us to efficiently resolve the momentum dependencies of associated vertices. In fact, these techniques implement continuous *Hubbard-Stratonovich* transformations in the RG flow, thus directly incorporating emerging degrees of freedom and eventually making the presence of the aforementioned explicit transition scale obsolete. Such an approach possibly enables us to predict the location of the maximum in the speed of sound more precisely. Also the analysis of the phase structure could be further improved as dynamical hadronization techniques would allow us to access the phase of spontaneously broken symmetries and to probe the ground state properties more directly. Our analysis based on the four-quark interaction in the pointlike limit could only provide indications on the formation of corresponding condensates, while it could neither guarantee the formation in the deep IR nor exclude the formation of other condensates. In combination with further refinements of the employed truncation - such as taking into account the wavefunction renormalizations of the quark propagator associated with the components parallel and transversal to the heat bath, analogously the splitting of the gluon propagator into electric and magnetic components, or the back-coupling of the matter fields to the gluonic sector, also including in-medium effects - we expect that an approach based on dynamical hadronization opens up the possibility to connect our results of the EOS at intermediate densities directly with the regime at high densities. This approach would thus establish a single framework capable of providing the EOS over a wide density range, from asymptotically high densities to intermediate densities. Finally, the generalization to isospin asymmetries will give access to the EOS of neutron-rich matter, the most relevant form of matter for a description of neutron stars.

To conclude, the work presented in this thesis provides valuable insights into the phase structure and the ground-state properties at finite temperature and density, in particular in regard to the essential role of *Fierz* completeness. Our findings also contribute to our understanding of the zero-temperature EOS of isospin-symmetric QCD matter at intermediate densities, which we obtained within an FRG framework directly based on the fundamental quark-gluon dynamics. Drawing from this, future investigations of dense QCD matter hold promise to gain further exciting insights to unravel this great unsolved mystery of modern science.

DANKSAGUNG

Mein besonderer und großer Dank gilt Jens Braun für die Betreuung meiner Dissertation. Ohne Deine Unterstützung wäre diese Arbeit so nicht möglich gewesen. Ich schätze sehr, dass Du stets die Zeit für unsere vielen, manchmal wohl längeren Diskussionen aufgebracht hast. Von Deinem Wissen und Erfahrungsschatz konnte ich sehr profitieren. Vielen Dank dafür, dass Du zu den Konferenzteilnahmen ermuntert und diese ermöglicht hast. Danke auch, dass Du jederzeit unermüdlich zur Stelle warst. Das gemeinsame Forschen und die Zusammenarbeit mit Dir haben mir immer viel Spaß und Freude bereitet!

Großen Dank an Achim Schwenk für seine Ratschläge und Ermutigungen sowie für die Erstellung eines Dissertationsgutachtens. Darüber hinaus möchte ich ihm für sein Engagement und Einsatz für die sehr erfolgreiche, schöne und wertvolle Gestaltung des wissenschaftlichen Betriebes, insbesondere im Rahmen des Sonderforschungsbereichs, vielmals danken.

Ich möchte mich bei Kai Hebeler als meinen Zweitbetreuer für die Unterstützung, Zusammenarbeit und für die wissenschaftlichen Diskussionen sowie für all jene über die Wissenschaft hinaus herzlich bedanken.

Meinen großen Dank möchte ich an Jan Pawlowski richten; für die wissenschaftlichen Ratschläge, für die Gastfreundschaft bei unseren Heidelberg-Besuchen und insbesondere für seine Unterstützung und für die Zusammenarbeit, die zu einer gemeinsamen Publikation geführt hat.

Meinen Dank an die *fQCD Kollaboration*: Vielen Dank an Fabian Rennecke, Mario Mitter, Anton Cyrol, und Nicolas Wink für die sehr hilfreichen Diskussionen und Unterstützung, ebenso an die anderen *fQCD*-Mitglieder. Insbesondere großen Dank für die Bereitstellung von FormTracer. An dieser Stelle auch meinen Dank an Markus Huber für seine schnellen Hilfen mit DoFun.

Meinen Dank an das Projekt *B05*: Vielen Dank an Christian Drischler für die sehr gute Zusammenarbeit sowie für die bereichernden Unterhaltungen über chiral EFT. In diesem Rahmen möchte ich mich auch bei Benedikt Schallmo bedanken, der mit seiner Masterarbeit zu unseren Ergebnissen beigetragen hat.

Große Teile des Weges bin ich zusammen mit Martin Pospiech gegangen; Dir gilt natürlich ein besonderer Dank. Unsere gemeinsamen Unternehmungen - sowohl in als auch außerhalb der Physik - haben immer viel Spaß gemacht. Vielen Dank dafür!

Ich möchte mich auch bei den anderen Gruppenmitglieder, das sind Daniel Rosenblüh, Sebastian Töpfel und Florian Ehmann, sowie bei den ehemaligen Gruppenmitgliedern, Sandra Kemler, Dietrich Roscher, und Stefan Rechenberger bedanken, für die schöne Arbeitsatmosphäre und unsere vielen physikbezogenen und nicht-physikbezogenen Diskussionen.

Großen Dank natürlich an meine Korrekturleser Marius Eichler, Rodric Seutin und Matthias Heinz. An dieser Stelle möchte ich noch einmal Jens vielmals für seine wertvollen Kommentare danken.

What goes? Einiges! Lukas und Marius - bessere Bürokollegen könnte ich mir nicht vorstellen. Mit Eurem feinen Sinn für Humor wurde der Alltag gewiss nie langweilig. Großen Dank an Euch beide in so vieler Hinsicht.

Vielen Dank an die „Coffee Crew“ Christian Appel, Thorsten Haase, Rodric Seutin sowie Philipp, Sabrina und Frieda Klos für die schöne Zeit zusammen.

Zu guter Letzt möchte ich mich bei meinen Eltern, meiner Schwester und meinem Großvater für die große Unterstützung während meiner gesamten Studienzeit und Promotion bedanken.

Kristina, ich bin sehr froh Dich an meiner Seite zu haben. Vielen Dank für Deine Unterstützung und Deinen Halt, besonders in dieser anstrengenden Zeit der vergangenen Wochen.

A

BASIC CONVENTIONS

A.1 UNITS

Throughout this work, we employ so-called natural units, i.e., we set $\hbar = c = k_{\mathrm{B}} = 1$. As a consequence, the dimension of all quantities can be related to the dimension of energy or mass to some power, e.g.,

$$[\text{length}]^{-1} = [\text{time}]^{-1} = [\text{momentum}] = [\text{temperature}] = [\text{mass}] = [\text{energy}] \, . \tag{A.1}$$

To be more specific, the relation $\hbar c \approx 200$ MeV fm for instance implies

$$1 \text{ fm} \approx \frac{1}{200} \, \text{MeV}^{-1} \, . \tag{A.2}$$

For the dimension of spinors and bosonic fields in a four-dimensional space-time it follows that

$$[\psi] = [\text{energy}]^{3/2} \, , \qquad [\varphi] = [\text{energy}] \, . \tag{A.3}$$

A.2 FROM MINKOWSKI TO EUCLIDEAN SPACE-TIME

This work is formulated in the imaginary time formalism, i.e., the time integration is rotated clockwise onto the purely imaginary axis. This so-called *Wick* rotation changes the signature of space-time from *Minkowski* to *Euclidean* space-time. Since we exclusively employ the *Euclidean* space-time we drop any labels distinguishing between these two signatures. Yet, in the following discussion of the transition from *Minkowski* to *Euclidean* space-time and the resulting relations, quantities in *Minkowski* space-time are labeled with the subscript M and quantities in *Euclidean* space-time with the subscript E for the sake of clarity. The components of the position-space variable x in the two space-time formulations can be related in the following way:

$$\tau \equiv x_{\mathrm{E}}^{0} = \mathrm{i}x_{\mathrm{M}}^{0} \equiv \mathrm{i}t\,, \qquad \vec{x}_{\mathrm{E}} = \vec{x}_{\mathrm{M}}\,. \tag{A.4}$$

The metric of the *Minkowski* space-time, which is given by $g_{\mathrm{M}}^{\mu\nu} = \mathrm{diag}(1,-1,-1,-1)$, translates into the *Euclidean* metric $g_{\mathrm{E}}^{\mu\nu} = \mathrm{diag}(1,1,1,1) = \delta^{\mu\nu}$ up to a global minus sign:

$$\begin{aligned} x_{\mathrm{M}}^{2} &= x_{\mathrm{M}}^{\mu} x_{\mathrm{M},\mu} = x_{\mathrm{M}}^{\mu} x_{\mathrm{M}}^{\nu} g_{\mathrm{M},\mu\nu} = \left(x_{\mathrm{M}}^{0}\right)^{2} - (\vec{x}_{\mathrm{M}})^{2} \\ &= -\left(\left(x_{\mathrm{E}}^{0}\right)^{2} + (\vec{x}_{\mathrm{E}})^{2}\right) = -g_{\mathrm{E},\mu\nu} x_{\mathrm{E}}^{\mu} x_{\mathrm{E}}^{\nu} = -x_{\mathrm{E}}^{\mu} x_{\mathrm{E},\mu} = -x_{\mathrm{E},\mu} x_{\mathrm{E},\mu} = -x_{\mathrm{E}}^{2}\,. \end{aligned} \tag{A.5}$$

The *Euclidean* momentum is defined as

$$p_{\mathrm{E}}^{0} = -\mathrm{i}p_{\mathrm{M}}^{0}\,, \quad \vec{p}_{\mathrm{E}} = \vec{p}_{\mathrm{M}}\,, \tag{A.6}$$

in order to preserve the direction of propagation of a plain wave, i.e., $\exp(-\mathrm{i}p_{\mathrm{M}}x_{\mathrm{M}}) = \exp(-\mathrm{i}p_{\mathrm{E}}x_{\mathrm{E}})$. The components of a vector field A_μ transform like the components of the gradient ∂_μ, i.e.,

$$A_{\mathrm{E}}^{0}(x_{\mathrm{E}}) = -\mathrm{i}A_{\mathrm{M}}^{0}(x_{\mathrm{M}})\,, \quad \vec{A}_{\mathrm{E}}(x_{\mathrm{E}}) = -\vec{A}_{\mathrm{M}}(x_{\mathrm{M}})\,, \tag{A.7}$$

such that the two summands of the covariant derivative $D_\mu = \partial_\mu - \mathrm{i}g_s A_\mu$ transform uniformly. To illustrate the transition to the *Euclidean* space-time, we briefly discuss the modifications to the functional integral of a fermionic theory. Therefore, we consider the following fermionic path integral in *Minkowski* space-time:

$$\int \mathcal{D}\bar{\psi}\mathcal{D}\psi \mathrm{e}^{\mathrm{i}S_{\mathrm{M}}[\bar{\psi},\psi]} = \int \mathcal{D}\bar{\psi}\mathcal{D}\psi \exp\left[\mathrm{i}\int \mathrm{d}^4 x_{\mathrm{M}}\, \bar{\psi}(\mathrm{i}\gamma_{\mathrm{M}}^{\mu}(D_{\mathrm{M}})_\mu - m)\psi\right]. \tag{A.8}$$

We apply the *Wick* rotation according to the relations (A.4)-(A.7) and redefine the field $\bar{\psi} \to \mathrm{i}\bar{\psi}$. This can be done as the field variables ψ and $\bar{\psi}$ are independent integration variables of the path integral [203]. The additional imaginary unit appears in the exponent but can be neglected in regard to the integration measure as such factors are canceled by the normalization. The *Dirac* matrices in *Euclidean* space-time are defined as follows:

$$\gamma_{\mathrm{E}}^{0} = \gamma_{\mathrm{M}}^{0}\,, \qquad \gamma_{\mathrm{E}}^{i} = -\mathrm{i}\gamma_{\mathrm{M}}^{i}\,. \tag{A.9}$$

With these relations we finally obtain

$$\int \mathcal{D}\bar{\psi}\mathcal{D}\psi \mathrm{e}^{\mathrm{i}S_{\mathrm{M}}[\bar{\psi},\psi]} = \int \mathcal{D}\bar{\psi}\mathcal{D}\psi \exp\left[\mathrm{i}(-\mathrm{i})\int \mathrm{d}^4 x_{\mathrm{E}}\, \mathrm{i}\bar{\psi}(\mathrm{i}^2\gamma_{\mathrm{E}}^{\mu}(D_{\mathrm{E}})_\mu - m)\psi\right] \tag{A.10}$$

$$\begin{aligned} &= \int \mathcal{D}\bar{\psi}\mathcal{D}\psi \exp\left[-\int \mathrm{d}^4 x_{\mathrm{E}}\, \bar{\psi}(\mathrm{i}\gamma_{\mathrm{E}}^{\mu}(D_{\mathrm{E}})_\mu + \mathrm{i}m)\psi\right] \\ &\equiv \int \mathcal{D}\bar{\psi}\mathcal{D}\psi \mathrm{e}^{-S_{\mathrm{E}}[\bar{\psi},\psi]}\,. \end{aligned} \tag{A.11}$$

A.3 POSITION SPACE AND MOMENTUM SPACE

We work in four-dimensional *Euclidean* space-time at finite temperature. The *Euclidean* time direction is compactified and the associated integration extends from zero to the inverse temperature $\beta = 1/T$, with periodic boundary conditions for bosonic fields, i.e., $\varphi(0,\vec{x}) = \varphi(\beta,\vec{x})$, and antiperiodic boundary conditions for fermionic fields, i.e., $\psi(0,\vec{x}) = -\psi(\beta,\vec{x})$. This compactification of the time direction leads to discrete *Matsubara* frequencies in momentum space. We define the field variable ϕ and the current-vector J as generalized vectors in field space, i.e.,

$$\phi(x) = \begin{pmatrix} \varphi(x) \\ \psi(x) \\ \bar{\psi}^{\mathrm{T}}(x) \\ \vdots \end{pmatrix}, \qquad J(x) = \begin{pmatrix} j(x) \\ \bar{\eta}^{\mathrm{T}}(x) \\ -\eta(x) \\ \vdots \end{pmatrix}, \tag{A.12}$$

and we employ the shorthand notation

$$\int \mathrm{d}^4x\ J^{\mathrm{T}}\phi \equiv \int \mathrm{d}^4x\ J^{\mathrm{T}} \cdot \phi = \int \mathrm{d}^4x\ \Big\{ j(x)\varphi(x) + \bar{\eta}(x)\psi(x) + \bar{\psi}(x)\bar{\eta}(x) + \dots \Big\}\,. \tag{A.13}$$

Note that a position-space variable x or momentum-space variable p without any specification of indices always denotes the set of all four components, i.e., x stands for $\{x_0, \dots, x_3\}$ and p for $\{p_0, \dots, p_3\}$. If we only want to refer to the spatial components of, e.g., the position-space variable x, we use the notation $\vec{x}$. In general, we use Latin indices for three-vectors and Greek indices for four-vectors.

In momentum space, the field variable and the current-vector are defined as

$$\phi(p) := \begin{pmatrix} \varphi(p) \\ \psi(p) \\ \bar{\psi}^{\mathrm{T}}(-p) \\ \vdots \end{pmatrix}, \qquad \phi^{T}(-p) := \Big(\varphi(-p), \psi^{\mathrm{T}}(-p), \bar{\psi}(p), \dots\Big)\,, \tag{A.14}$$

$$J(p) := \begin{pmatrix} j(p) \\ \bar{\eta}^{\mathrm{T}}(-p) \\ -\eta(p) \\ \vdots \end{pmatrix}, \qquad J^{T}(-p) := \Big(j(-p), \bar{\eta}(p), -\eta^{\mathrm{T}}(-p), \dots\Big)\,. \tag{A.15}$$

To make the transition from position space to momentum space, we adopt in case of vanishing temperature the following convention for *Fourier* transforms:

$$\varphi(x) = \int \frac{\mathrm{d}^D p}{(2\pi)^D}\ \mathrm{e}^{\mathrm{i}px}\varphi(p)\,, \tag{A.16}$$

$$\psi(x) = \int \frac{\mathrm{d}^D p}{(2\pi)^D}\ \mathrm{e}^{\mathrm{i}px}\psi(p)\,, \quad \bar{\psi}(x) = \int \frac{\mathrm{d}^D p}{(2\pi)^D}\ \mathrm{e}^{-\mathrm{i}px}\bar{\psi}(p)\,, \tag{A.17}$$

and in case of finite temperature:

$$\varphi(x) = \frac{1}{\beta}\sum_{n=-\infty}^{\infty}\int \frac{\mathrm{d}^d p}{(2\pi)^d}\ \mathrm{e}^{\mathrm{i}px}\varphi(p)\,, \qquad \text{with } p = (\omega_n, \vec{p})\,, \tag{A.18}$$

$$\psi(x) = \frac{1}{\beta}\sum_{n=-\infty}^{\infty}\int \frac{\mathrm{d}^d p}{(2\pi)^d}\ \mathrm{e}^{\mathrm{i}px}\psi(p)\,, \qquad \text{with } p = (\nu_n, \vec{p})\,, \tag{A.19}$$

$$\bar{\psi}(x) = \frac{1}{\beta}\sum_{n=-\infty}^{\infty}\int \frac{\mathrm{d}^d p}{(2\pi)^d}\ \mathrm{e}^{-\mathrm{i}px}\bar{\psi}(p)\,, \qquad \text{with } p = (\nu_n, \vec{p})\,, \tag{A.20}$$

where $\omega_n := 2\pi nT$ and $\nu_n := (2n+1)\pi T$ denote bosonic and fermionic *Matsubara* frequencies, respectively. In position and momentum space, we employ the shorthand notations

$$\int \mathrm{d}^4 x \ \equiv \int_x\,, \qquad \int \frac{\mathrm{d}^4 p}{(2\pi)^4} \ \equiv \int_p\,, \tag{A.21}$$

in case of zero temperature and

$$\int_0^\beta \mathrm{d}\tau \int \mathrm{d}^3 x \ \equiv \int_x\,, \qquad \frac{1}{\beta}\sum_{n=-\infty}^{\infty}\int \frac{\mathrm{d}^3 p}{(2\pi)^3} \ \equiv \sum\!\!\!\!\!\!\!\int_p\,, \tag{A.22}$$

in case of non-zero temperature. Moreover, we adopt the shorthand notations

$$\begin{aligned} \int_x \mathrm{e}^{\mathrm{i}(p'-p)x} &\overset{T=0}{=} \int_{-\infty}^{+\infty}\mathrm{d}\tau \int_{-\infty}^{+\infty}\mathrm{d}^3 x \mathrm{e}^{\mathrm{i}(p'-p)x} \\ &= (2\pi)^4\delta^{(4)}(p-p') \equiv \delta^{(4)}(p-p'), \end{aligned} \tag{A.23}$$

$$\begin{aligned} \int_x \mathrm{e}^{\mathrm{i}(p'-p)x} &\overset{T>0}{=} \int_0^{\beta}\mathrm{d}\tau \int_{-\infty}^{+\infty}\mathrm{d}^3 x\ \mathrm{e}^{\mathrm{i}(f_{n'}-f_n)\tau}\mathrm{e}^{-\mathrm{i}(\vec{p}\,'-\vec{p})x} \\ &= \beta\delta_{n,n'}(2\pi)^d\delta^{(d)}(\vec{p}-\vec{p}\,') \equiv \delta^{(4)}(p-p'), \end{aligned} \tag{A.24}$$

where $f_n = \omega_n$ in case of bosonic frequencies or $f_n = \nu_n$ in case of fermionic frequencies.

B

GROUPS AND ALGEBRAS

B.1 EUCLIDEAN DIRAC ALGEBRA

The *Euclidean Dirac* matrices are defined through their relations to the *Dirac* matrices in *Minkowski* space-time, see Eq. (A.9). The *Clifford* algebra is then given by

$$\{\gamma_\mu, \gamma_\nu\} = \gamma_\mu\gamma_\nu + \gamma_\nu\gamma_\mu = 2\delta_{\mu\nu}\mathbb{1}_{\mathrm{D}}\,, \tag{B.1}$$

with the subscript D denoting *Dirac* space, i.e., $\mathbb{1}_{\mathrm{D}} = \mathbb{1}_{4\times}$. We define further

$$\gamma_5 := \gamma_1\gamma_2\gamma_3\gamma_0\,, \qquad \sigma_{\mu\nu} := \frac{\mathrm{i}}{2}\left[\gamma_\mu\,, \gamma_\nu\right] = \frac{\mathrm{i}}{2}(\gamma_\mu\gamma_\nu - \gamma_\nu\gamma_\mu)\,. \tag{B.2}$$

In *Euclidean* space-time the gamma matrices are hermitian, i.e., $\gamma_\mu^\dagger = \gamma_\mu$. Some helpful properties are given by:

$$\begin{aligned} \gamma_\mu^{-1} &= \gamma_\mu\,, & \gamma_5^\dagger &= \gamma_5\,, \\ \gamma_\mu^2 &= \mathbb{1}_{\mathrm{D}}\,, & \gamma_5^2 &= \mathbb{1}_{\mathrm{D}}\,, \\ \mathrm{tr}\left[\gamma_\mu\right] &= 0\,, & \mathrm{tr}\left[\gamma_5\right] &= 0\,, \\ \gamma_\mu\gamma_\nu &= \delta_{\mu\nu}\mathbb{1}_{\mathrm{D}} - \mathrm{i}\sigma_{\mu\nu}\,, & \{\gamma_5\,, \gamma_\mu\} &= 0\,. \end{aligned} \tag{B.3}$$

The 16 elements $\Gamma_{\mathrm{D}}^{(A)}$ given by

$$\Gamma_{\mathrm{D}}^{(A)} \in \{\mathbb{1}_{\mathrm{D}}, \gamma_\mu, \sigma_{\mu\nu}, \mathrm{i}\gamma_\mu\gamma_5, \gamma_5\}\,, \tag{B.4}$$

with $\mu < \nu$ regarding $\sigma_{\mu\nu}$, form a basis of the space of complex 4×4 matrices. The orthogonality relation (OR) and completeness relation (CR) read, respectively,

$$\mathrm{tr}\left[\Gamma_{\mathrm{D}}^{(A)}\Gamma_{\mathrm{D}}^{(B)}\right] = 4\delta_{AB}\,, \qquad \text{(OR)} \tag{B.5}$$

$$\sum_A \Gamma_{\mathrm{D},ij}^{(A)}\Gamma_{\mathrm{D},kl}^{(A)} = 4\delta_{ik}\delta_{lj}\,. \qquad \text{(CR)} \tag{B.6}$$

Consequently, a complex 4×4 matrix M can be expanded in terms of these basis elements according to

$$M = \frac{1}{4} \sum_{A} \mathrm{tr}\left[M \Gamma_{\mathrm{D}}^{(A)} \right] \Gamma_{\mathrm{D}}^{(A)} . \tag{B.7}$$

B.2 SU(N) Lie algebra

In the following, we summarize our conventions for the generators of an *SU*(N) *Lie* group and list some useful relations and properties. The *SU*(N) group can be defined as the group of unitary $N \times N$ matrices U with determinant $+1$. In terms of the $N^2 - 1$ generators T^a the elements of the group are given by

$$U = \exp\left(\mathrm{i} \theta^a T^a \right) , \tag{B.8}$$

with the real parameters θ^a specifying the element of the group. The generators T^a, which are hermitian and traceless, form the corresponding *Lie* algebra with the commutator as the *Lie* bracket. They fulfill the commutator relation

$$\left[T^a , T^b \right] = \mathrm{i} f^{abc} T^c , \tag{B.9}$$

where the so-called structure constants f^{abc} are totally antisymmetric. In the fundamental representation F, i.e., the group elements are given by $N \times N$ matrices and here explicitly indicated by a subscript for the sake of clarity, e.g., tr_{F}, the generators are normalized to obey the relation

$$\mathrm{tr}_{\mathrm{F}} \left[T^a T^b \right] = \frac{1}{2} \delta^{ab} . \tag{B.10}$$

Furthermore, we find an invariant by contracting two generators which reads

$$T^a T^a = \frac{N^2 - 1}{2N} \cdot \mathbb{1} , \tag{B.11}$$

with $\mathbb{1} \equiv \mathbb{1}_{N \times N}$ being the unit matrix. In the fundamental representation, due to the mentioned properties and relations, the $N^2 - 1$ generators together with the unit matrix $\mathbb{1}$ provide an orthogonal and complete basis of the vector space of all $N \times N$ complex matrices. Including appropriate normalizations, the orthonormal basis elements $\Gamma_{\mathrm{L}}^{(A)}$ are given by

$$\Gamma_{\mathrm{L}}^{(A)} \in \left\{ \frac{1}{\sqrt{N}} \mathbb{1} \, , \, \sqrt{2} \, T^a \right\} , \tag{B.12}$$

where the subscript L indicates the space the *Lie* group is associated with. The orthogonality relation (OR) and completeness relation (CR) read, respectively,

$$\mathrm{tr}_{\mathrm{F}} \left[\Gamma_{\mathrm{L}}^{(A)} \Gamma_{\mathrm{L}}^{(B)} \right] = \delta_{AB} , \qquad \text{(OR)} \tag{B.13}$$

$$\sum_A \Gamma^{(A)}_{\mathrm{L},ij}\Gamma^{(A)}_{\mathrm{L},kl} = \mathbb{1}_{ik}\mathbb{1}_{lj} \,. \qquad \text{(CR)} \tag{B.14}$$

The expansion of a complex 4×4 matrix M in terms of these basis elements is given by

$$M = \sum_A \mathrm{tr}_{\mathrm{F}}\left[M\Gamma^{(A)}_{\mathrm{L}}\right]\Gamma^{(A)}_{\mathrm{L}} \,. \tag{B.15}$$

In the case of $N = 2$, the generators in the fundamental representation are given by the *Pauli* matrices $T^a = \tau^a/2$ $(a = 1, 2, 3)$ and the structure constants f^{abc} are given by the *Levi-Civita* symbol ϵ^{abc}. The generators of the $SU(3)$ group in the fundamental representation are given by the *Gell-Mann* matrices $T^a = \lambda^a/2$ $(a = 1, 2, \dots, 8)$.

B.3 FIERZ IDENTITIES

Fierz transformations refer to a rearrangement of the fermionic fields in a product of two *Dirac* bilinears and lead to linear relations among four-fermion interactions channels, the so-called *Fierz* identities. *Fierz* identities are basically matrix identities that can be derived by exploiting corresponding completeness relations such as Eqs. (B.6) and (B.14). For example, in the fundamental representation of the $SU(N)$ *Lie* group with the completeness relation (B.14) we find for any complex $N \times N$ matrices M and $\tilde{M}$ the relation

$$\begin{aligned} M_{ij}\tilde{M}_{kl} &= M_{nr}\tilde{M}_{sm}\left(\sum_A \Gamma^{(A)}_{\mathrm{L},mn}\Gamma^{(A)}_{\mathrm{L},il}\right)\left(\sum_B \Gamma^{(B)}_{\mathrm{L},rs}\Gamma^{(B)}_{\mathrm{L},kj}\right) \\ &= \sum_{A,B} \mathrm{tr}_{\mathrm{F}}\left[\Gamma^{(A)}_{\mathrm{L}} M \Gamma^{(B)}_{\mathrm{L}} \tilde{M}\right]\Gamma^{(A)}_{\mathrm{L},il}\Gamma^{(B)}_{\mathrm{L},kj} \,. \end{aligned} \tag{B.16}$$

Note the changed ordering of the indices from $(ij), (kl)$ on the left-hand side to $(il), (kj)$ on the right-hand side, which corresponds to the above mentioned rearrangement of the fermionic fields. From this general relation we derive the following two important relations for the generators of the $SU(N)$ *Lie* group

$$(\mathbb{1}_{N\times N})_{ij}(\mathbb{1}_{N\times N})_{kl} = \frac{1}{N}(\mathbb{1}_{N\times N})_{il}(\mathbb{1}_{N\times N})_{kj} + 2(T^a)_{il}(T^a)_{kj} \,, \tag{B.17}$$

$$(T^a)_{ij}(T^a)_{kl} = \frac{N^2-1}{2N^2}(\mathbb{1}_{N\times N})_{il}(\mathbb{1}_{N\times N})_{kj} - \frac{1}{N}(T^a)_{il}(T^a)_{kj} \,. \tag{B.18}$$

Applied to four-fermion interaction channels, the *Fierz* transformations are then performed in the vector space of matrices defined by the direct product of the *Dirac* D, flavor f and color space c. The basis elements $\Gamma^{(A)}$ are build from the basis elements of the subspaces in the form of $\Gamma^{(A')}_{\mathrm{D}} \otimes \Gamma^{(A'')}_{\mathrm{f}} \otimes \Gamma^{(A''')}_{\mathrm{c}}$. In the following, the index (A) indicates the specific basis element. The general *Fierz* relation is then given by

$$\left(\bar{\psi}\Gamma^{(A)}\psi\right)\left(\bar{\psi}\Gamma^{(B)}\psi\right) = -\frac{1}{16}\sum_{C,D} \mathrm{tr}\left[\Gamma^{(C)}\Gamma^{(A)}\Gamma^{(D)}\Gamma^{(B)}\right]\left(\bar{\psi}\Gamma^{(C)}\psi\right)\left(\bar{\psi}\Gamma^{(D)}\psi\right) \,, \tag{B.19}$$

where the factor 1/16 arises from our convention for the normalization of the basis elements in *Dirac* space, see Eqs. (B.5) and (B.6), and the minus sign comes from the fermionic field variables being *Grassmann*-valued.

On the level of pointlike four-quark interaction channels, the introduction of diquark structures are again nothing else but rearrangements of the field variables, this time of the conceptual form $(\bar{\psi}\mathcal{O}\psi)(\bar{\psi}\mathcal{O}\psi) \to (\bar{\psi}\mathcal{O}\bar{\psi}^{\mathrm{T}})(\psi^{\mathrm{T}}\mathcal{O}\psi)$. Consequently, any diquark-type four-quark interaction channel can be mapped onto conventional four-quark interaction channels and vice versa. The *Dirac* structures of diquark-type interaction channels in the form $(\bar{\psi}\mathcal{O}\bar{\psi}^{\mathrm{T}})(\psi^{\mathrm{T}}\mathcal{O}\psi)$ additionally receive the charge operator $\mathcal{C} = \mathrm{i}\gamma_2\gamma_0$ in order to ensure *Lorentz* invariance. These operators can be absorbed by the field variables by introducing the charge-conjugated fields $\psi^{\mathcal{C}} = \mathcal{C}\bar{\psi}^{\mathrm{T}}$ and $\bar{\psi}^{\mathcal{C}} = \psi^{\mathrm{T}}\mathcal{C}$. An orthogonal basis of the *Dirac* space adapted to such diquark structures, i.e., involving the charge operator $\mathcal{C}$, is given by

$$\begin{aligned}\Gamma^{(A)}_{\mathrm{Di}} \in \{\, &\mathcal{C}\,,\ \gamma_5\mathcal{C}\,,\ \mathrm{i}\gamma_0\mathcal{C}\,,\ \gamma_1\mathcal{C}\,,\ \mathrm{i}\gamma_2\mathcal{C}\,,\ \gamma_3\mathcal{C}\,,\ \gamma_0\gamma_5\mathcal{C}\,,\ \mathrm{i}\gamma_1\gamma_5\mathcal{C}\,,\ \gamma_2\gamma_5\mathcal{C}\,,\ \mathrm{i}\gamma_3\gamma_5\mathcal{C}\,,\\ &\mathrm{i}\sigma_{01}\mathcal{C}\,,\ \sigma_{02}\mathcal{C}\,,\ \mathrm{i}\sigma_{03}\mathcal{C}\,,\ \mathrm{i}\sigma_{12}\mathcal{C}\,,\ \sigma_{13}\mathcal{C}\,,\ \mathrm{i}\sigma_{23}\mathcal{C}\,\}\,,\end{aligned} \tag{B.20}$$

with the convention $\mathrm{tr}\Big[\Gamma^{(A)}_{\mathrm{Di}}\Gamma^{(B)}_{\mathrm{Di}}\Big] = 4\delta_{AB}$. The orthogonality of these elements follows immediately from the orthogonality of the basis (B.4) and from the property $\mathcal{C}^2 = 1$ of the charge operator. In the following, we denote the associated basis elements including color and flavor space by $\Delta^{(A)}$. In order to project a quark-antiquark interaction channel onto the quark-quark basis, we employ the relation

$$\left(\bar{\psi}\Gamma^{(A)}_{\mathrm{D}}\psi\right)\left(\bar{\psi}\Gamma^{(B)}_{\mathrm{D}}\psi\right) = \frac{1}{16}\sum_{C,D}\mathrm{tr}\left[\Delta^{(C)}\Gamma^{(A)}_{\mathrm{D}}\Delta^{(D)}\Gamma^{(B),\mathrm{T}}_{\mathrm{D}}\right]\left(\bar{\psi}\Delta^{(C)}\bar{\psi}^{\mathrm{T}}\right)\left(\psi^{\mathrm{T}}\Delta^{(D)}\psi\right). \tag{B.21}$$

Note that the additional minus sign does *not* appear owing to the different ordering of the fermionic field variables as compared to the relation (B.19). For the projection of diquark structures onto the quark-antiquark basis we use

$$\left(\bar{\psi}\Delta^{(A)}\bar{\psi}^{\mathrm{T}}\right)\left(\psi^{\mathrm{T}}\Delta^{(B)}\psi\right) = -\frac{1}{16}\sum_{C,D}\mathrm{tr}\left[\Gamma^{(C)}_{\mathrm{D}}\Delta^{(A)}\Gamma^{(D),\mathrm{T}}_{\mathrm{D}}\Delta^{(B),\mathrm{T}}\right]\left(\bar{\psi}\Gamma^{(C)}_{\mathrm{D}}\psi\right)\left(\bar{\psi}\Gamma^{(D)}_{\mathrm{D}}\psi\right). \tag{B.22}$$

B.3.1 Single fermion species

In the *Fierz*-complete study of an NJL model with a single fermion species in Section 4.2, we have used the following *Fierz* identites to derive Eq. (4.33) from Eq. (4.28):

$$(\mathrm{A}_{\parallel}) = \frac{1}{2}(\mathrm{S}-\mathrm{P}) - \frac{1}{2}\left(\mathrm{V}_{\parallel}\right) + \frac{1}{2}\left(\mathrm{V}_{\perp}\right), \tag{B.23}$$

$$(\mathrm{A}_{\perp}) = \frac{3}{2}(\mathrm{S}-\mathrm{P}) + \frac{3}{2}\left(\mathrm{V}_{\parallel}\right) + \frac{1}{2}\left(\mathrm{V}_{\perp}\right), \tag{B.24}$$

$$\left(\mathrm{T}_{\parallel}\right) = 3\left(\mathrm{V}_{\parallel}\right) - \left(\mathrm{V}_{\perp}\right). \tag{B.25}$$

The *Fierz* transformations from the fermion-antifermion channels to the difermion-type channels are given by

$$(\mathrm{S}\mathcal{C}-\mathrm{P}\mathcal{C}) = -(\mathrm{S}-\mathrm{P}) - \left(\mathrm{V}_{\parallel}\right) - (\mathrm{V}_{\perp}) \,, \tag{B.26}$$

$$\left(\mathrm{A}_{\parallel}\mathcal{C}\right) = -\frac{1}{2}(\mathrm{S}-\mathrm{P}) - \frac{3}{2}\left(\mathrm{V}_{\parallel}\right) + \frac{1}{2}(\mathrm{V}_{\perp}) \,, \tag{B.27}$$

$$(\mathrm{A}_{\perp}\mathcal{C}) = -\frac{3}{2}(\mathrm{S}-\mathrm{P}) + \frac{3}{2}\left(\mathrm{V}_{\parallel}\right) - \frac{1}{2}(\mathrm{V}_{\perp}) \,, \tag{B.28}$$

where

$$(\mathrm{S}\mathcal{C}-\mathrm{P}\mathcal{C}) = (\bar{\psi}\mathcal{C}\bar{\psi}^T)(\psi^T\mathcal{C}\psi) - (\bar{\psi}\gamma_5\mathcal{C}\bar{\psi}^T)(\psi^T\mathcal{C}\gamma_5\psi)\,, \tag{B.29}$$

$$\left(\mathrm{A}_{\parallel}\mathcal{C}\right) = (\bar{\psi}\gamma_0\gamma_5\mathcal{C}\bar{\psi}^T)(\psi^T\mathcal{C}\gamma_0\gamma_5\psi)\,, \tag{B.30}$$

$$(\mathrm{A}_{\perp}\mathcal{C}) = (\bar{\psi}\gamma_i\gamma_5\mathcal{C}\bar{\psi}^T)(\psi^T\mathcal{C}\gamma_i\gamma_5\psi)\,. \tag{B.31}$$

B.3.2 Quarks with two flavors and N_c colors

In the study of an NJL model with quarks coming in two flavors and N_c colors presented in Section 4.3, a *Fierz*-complete basis of pointlike four-quark interaction channels is given by

$$\mathcal{L}_{(V+A)_\parallel} = (\bar{\psi}\gamma_0\psi)^2 + (\bar{\psi}\mathrm{i}\gamma_0\gamma_5\psi)^2\,, \tag{B.32}$$

$$\mathcal{L}_{(V+A)_\perp} = (\bar{\psi}\gamma_i\psi)^2 + (\bar{\psi}\mathrm{i}\gamma_i\gamma_5\psi)^2\,, \tag{B.33}$$

$$\mathcal{L}_{(V-A)_\parallel} = (\bar{\psi}\gamma_0\psi)^2 - (\bar{\psi}\mathrm{i}\gamma_0\gamma_5\psi)^2\,, \tag{B.34}$$

$$\mathcal{L}_{(V-A)_\perp} = (\bar{\psi}\gamma_i\psi)^2 - (\bar{\psi}\mathrm{i}\gamma_i\gamma_5\psi)^2\,, \tag{B.35}$$

$$\mathcal{L}_{(V+A)^{\mathrm{adj}}_\parallel} = (\bar{\psi}\gamma_0T^a\psi)^2 + (\bar{\psi}\mathrm{i}\gamma_0\gamma_5T^a\psi)^2\,, \tag{B.36}$$

$$\mathcal{L}_{(V+A)^{\mathrm{adj}}_\perp} = (\bar{\psi}\gamma_iT^a\psi)^2 + (\bar{\psi}\mathrm{i}\gamma_i\gamma_5T^a\psi)^2\,, \tag{B.37}$$

$$\mathcal{L}_{(V-A)^{\mathrm{adj}}_\parallel} = (\bar{\psi}\gamma_0T^a\psi)^2 - (\bar{\psi}\mathrm{i}\gamma_0\gamma_5T^a\psi)^2\,, \tag{B.38}$$

$$\mathcal{L}_{(V-A)^{\mathrm{adj}}_\perp} = (\bar{\psi}\gamma_iT^a\psi)^2 - (\bar{\psi}\mathrm{i}\gamma_i\gamma_5T^a\psi)^2\,, \tag{B.39}$$

$$\mathcal{L}_{(S+P)_-} = (\bar{\psi}\psi)^2 - (\bar{\psi}\gamma_5\tau_i\psi)^2 + (\bar{\psi}\gamma_5\psi)^2 - (\bar{\psi}\tau_i\psi)^2\,, \tag{B.40}$$

$$\mathcal{L}_{(S+P)^{\mathrm{adj}}_-} = (\bar{\psi}T^a\psi)^2 - (\bar{\psi}\gamma_5\tau_iT^a\psi)^2 + (\bar{\psi}\gamma_5T^a\psi)^2 - (\bar{\psi}\tau_iT^a\psi)^2\,. \tag{B.41}$$

The construction of this basis was guided by the paradigm to employ simple and mostly similar structures in order to achieve a concise formulation. The basis, however, does not include the phenomenologically important channels

$$\mathcal{L}_{(\sigma\text{-}\pi)} = (\bar{\psi}\psi)^2 - (\bar{\psi}\gamma_5\tau_i\psi)^2\,, \tag{B.42}$$

$$\mathcal{L}_{\text{csc}} = (\mathrm{i}\bar{\psi}^C\gamma_5\epsilon_{(f)}\varepsilon^l_{(c)}\psi)(\mathrm{i}\bar{\psi}\gamma_5\epsilon_{(f)}\varepsilon^l_{(c)}\psi^C) = 4\left(\mathrm{i}\bar{\psi}\gamma_5\tau_2 T^A\psi^C\right)\left(\mathrm{i}\bar{\psi}^C\gamma_5\tau_2 T^A\psi\right), \tag{B.43}$$

which are associated with the formation of chiral condensate and a diquark condensate, respectively. The diquark interaction channel has been constructed according to the condensate (2.47) in the scalar $J^P = 0^+$ state, see Section 2.2, and subsequently rewritten in terms of antisymmetric generators in flavor and color space. With the help of *Fierz* transformations, these phenomenologically important interaction channels can be introduced to a *Fierz*-complete basis as they can be written in terms of the above listed set of *Fierz*-complete interaction channels:

$$\begin{aligned}\mathcal{L}_{(\sigma\text{-}\pi)} &= -\mathcal{L}_{(V+A)^{\text{adj}}_{\parallel}} - \mathcal{L}_{(V+A)^{\text{adj}}_{\perp}} - \frac{1}{2N_{\text{c}}}\mathcal{L}_{(V+A)_{\parallel}} - \frac{1}{2N_{\text{c}}}\mathcal{L}_{(V+A)_{\perp}} + \frac{1}{2}\mathcal{L}_{(S+P)_-}\\ &= -\mathcal{L}_{(V+A)^{\text{adj}}} - \frac{1}{2N_{\text{c}}}\mathcal{L}_{(V+A)} + \frac{1}{2}\mathcal{L}_{(S+P)_-}\,,\end{aligned} \tag{B.44}$$

$$\begin{aligned}\mathcal{L}_{\text{csc}} =& \mathcal{L}_{(S+P)^{\text{adj}}_-} + \mathcal{L}_{(V-A)^{\text{adj}}_{\parallel}} + \mathcal{L}_{(V-A)^{\text{adj}}_{\perp}}\\ &- \frac{N_{\text{c}}-1}{2N_{\text{c}}}\left(\mathcal{L}_{(S+P)_-} + \mathcal{L}_{(V-A)_{\parallel}} + \mathcal{L}_{(V-A)_{\perp}}\right)\\ =& \mathcal{L}_{(S+P)^{\text{adj}}_-} + \mathcal{L}_{(V-A)^{\text{adj}}} - \frac{N_{\text{c}}-1}{2N_{\text{c}}}\left(\mathcal{L}_{(S+P)_-} + \mathcal{L}_{(V-A)}\right)\,,\end{aligned} \tag{B.45}$$

where we have combined the contributions parallel and transversal to the heat bath to *Poincaré*-invariant structures, exploiting the fact that the channels $\mathcal{L}_{(\sigma\text{-}\pi)}$ and $\mathcal{L}_{\text{csc}}$ are *Lorentz* scalars. Note that in this way the scalar-pseudoscalar channel can be rewritten in terms of $(V{+}A)$ structures whereas the diquark channel in terms of $(V{-}A)$ structures. Thus, as we also want to keep $\mathcal{L}_{(S+P)_-}$ and $\mathcal{L}_{(S+P)^{\text{adj}}_-}$ (the former is associated with the presence of topological non-trivial gauge configurations and plays an important role in the breaking of the $U_{\text{A}}(1)$ symmetry), our *Fierz*-complete basis of 10 interaction channels (4.59)-(4.68) including the scalar-pseudoscalar and the diquark interaction channel must necessarily break the pairs of channels parallel and transversal to the heat bath if these phenomenological channels are traded for vector-like adjoint interaction channels.

The interaction channels $\mathcal{L}_{(\sigma\text{-}\pi)}$, $\mathcal{L}_{\text{csc}}$, $\mathcal{L}_{(S+P)_-}$ and $\mathcal{L}_{(S+P)^{\text{adj}}_-}$ are not invariant under axial $U_{\text{A}}(1)$ transformations, whereas the vector-like channels $\mathcal{L}_{(V\pm A)}$ and $\mathcal{L}_{(V\pm A)^{\text{adj}}}$ are $U_{\text{A}}(1)$-symmetric. From Eqs. (B.44) and (B.45) we infer that the combinations

$$\mathcal{L}_{(\sigma\text{-}\pi)} - \frac{1}{2}\mathcal{L}_{(S+P)_-} \tag{B.46}$$

$$\mathcal{L}_{\text{csc}} - \mathcal{L}_{(S+P)^{\text{adj}}_-} + \frac{N_{\text{c}}-1}{2N_{\text{c}}}\mathcal{L}_{(S+P)_-} \tag{B.47}$$

are invariant under $U_{\text{A}}(1)$ transformations as well. In Section 4.3, we have parametrized the *Fierz*-complete basis $\mathcal{B}$ with six $U_{\text{A}}(1)$-symmetric interaction channels, Eqs. (4.59)-(4.63), and four interaction channels (4.65)-(4.68) that are not invariant. In fact, the *Fierz*-complete basis could have been parametrized by eight invariant and two breaking interaction channels as well, see Eqs. (B.32)-(B.41). A *Fierz*-complete basis invariant under $SU(N_{\text{c}}) \otimes SU_{\text{L}}(2) \otimes SU_{\text{R}}(2) \otimes$

$U_{\mathrm{V}}(1) \otimes U_{\mathrm{A}}(1)$ would be composed of eight interaction channels in total. Consequently, the couplings of the two $U_{\mathrm{A}}(1)$-breaking interaction channels must be identical to zero in a $U_{\mathrm{A}}(1)$-symmetric RG flow. Regarding the basis $\mathcal{B}$ with four $U_{\mathrm{A}}(1)$-breaking interaction channels, we can now use the relations (B.46) and (B.47) to identify the remaining $U_{\mathrm{A}}(1)$-symmetric subspace. For the $U_{\mathrm{A}}(1)$-breaking sector of four-quark interaction channels we find:

$$\begin{aligned}
&\frac{1}{2}\bar{\lambda}_{(\sigma\text{-}\pi)}\mathcal{L}_{(\sigma\text{-}\pi)} + \frac{1}{2}\bar{\lambda}_{\mathrm{csc}}\mathcal{L}_{\mathrm{csc}} + \frac{1}{2}\bar{\lambda}_{(S+P)_-}\mathcal{L}_{(S+P)_-} + \frac{1}{2}\bar{\lambda}_{(S+P)_-^{\mathrm{adj}}}\mathcal{L}_{(S+P)_-^{\mathrm{adj}}} \\
= \;& \frac{1}{2}\bar{\lambda}_{(\sigma\text{-}\pi)}\left(\mathcal{L}_{(\sigma\text{-}\pi)} - \frac{1}{2}\mathcal{L}_{(S+P)_-}\right) + \frac{1}{2}\bar{\lambda}_{\mathrm{csc}}\left(\mathcal{L}_{\mathrm{csc}} - \mathcal{L}_{(S+P)_-^{\mathrm{adj}}} + \frac{N_{\mathrm{c}}-1}{2N_{\mathrm{c}}}\mathcal{L}_{(S+P)_-}\right) \\
&+ \frac{1}{2}\mathcal{L}_{(S+P)_-}\left(\bar{\lambda}_{(S+P)_-} - \frac{N_{\mathrm{c}}-1}{2N_{\mathrm{c}}}\bar{\lambda}_{\mathrm{csc}} + \frac{1}{2}\bar{\lambda}_{(\sigma\text{-}\pi)}\right) \\
&+ \frac{1}{2}\mathcal{L}_{(S+P)_-^{\mathrm{adj}}}\left(\bar{\lambda}_{(S+P)_-^{\mathrm{adj}}} + \bar{\lambda}_{\mathrm{csc}}\right), \qquad \text{(B.48)}
\end{aligned}$$

where we have complemented the first two summands such that the second line consists of the combinations (B.46) and (B.47), thus being $U_{\mathrm{A}}(1)$-invariant. Rewritten in this way, the only $U_{\mathrm{A}}(1)$-breaking contributions are given by the last two lines in Eq. (B.48) which must consequently vanish in a $U_{\mathrm{A}}(1)$-symmetric RG flow. For these contributions to vanish, the couplings appearing in the parentheses must add to zero. As a result, we obtain the sum rules

$$\mathcal{S}^{(1)}_{U_{\mathrm{A}}(1)} = \bar{\lambda}_{\mathrm{csc}} + \bar{\lambda}_{(S+P)_-^{\mathrm{adj}}} = 0\,, \qquad \text{(B.49)}$$

$$\mathcal{S}^{(2)}_{U_{\mathrm{A}}(1)} = \bar{\lambda}_{(S+P)_-} - \frac{N_{\mathrm{c}}-1}{2N_{\mathrm{c}}}\,\bar{\lambda}_{\mathrm{csc}} + \frac{1}{2}\bar{\lambda}_{(\sigma\text{-}\pi)} = 0\,. \qquad \text{(B.50)}$$

which must hold in case of a $U_{\mathrm{A}}(1)$-invariant RG flow, i.e., only two of the four couplings are independent.

C

REVIEW OF SPONTANEOUS SYMMETRY BREAKING

In the following, we briefly recapitulate *spontaneous symmetry breaking* (SSB) which is a crucial mechanism in quantum field theories. Our discussion bases on Refs. [202, 203, 207, 457]. The spontaneous breakdown of a symmetry basically means that the theory itself, i.e., the action, is invariant under a certain symmetry transformation, whereas the realized ground state is not invariant. The mechanism of SSB has several important implications. First, it explains why a symmetry of an assumed *Lagrangian* or *Hamiltonian* is possibly not manifest, i.e., hidden, in nature. An example is given by chiral symmetry breaking in the theory of the strong interaction, cf. Section 2.1.2. Moreover, SSB provides an elegant mechanism for the dynamical generation of mass. An important consequence of SSB is formulated in *Goldstone*'s theorem [48, 49]: The spontaneous breakdown of a continuous symmetry gives rise to the appearance of massless so-called *Goldstone* bosons in the channel of each broken symmetry, i.e., the bosons possess, loosely speaking, the quantum numbers of the associated generators of the broken symmetries. In the following, we illustrate these aspects by considering the linear sigma model in classical field theory. The *Lagrangian* of this model reads

$$\begin{aligned}\mathcal{L} &= \frac{1}{2}\partial_\mu\varphi_i\partial^\mu\varphi_i + \frac{1}{2}m^2\varphi_i\varphi_i + \frac{1}{4}\lambda\left(\varphi_i\varphi_i\right)^2 \\ &\equiv \frac{1}{2}\partial_\mu\varphi_i\partial^\mu\varphi_i + V(\varphi^i\varphi^i)\,, \end{aligned} \tag{C.1}$$

with a quartic self-interaction term accompanied by the coupling constant λ. The set of N elementary scalar fields φ_i are assumed to be real valued. The *Lagrangian* is invariant under global $O(N)$ transformations which transform the fields according to

$$\varphi_i(x) \mapsto D_{ij}\varphi_j(x)\,, \tag{C.2}$$

with D_{ij} being an orthogonal $N\times N$ matrix, i.e., $D^{\mathrm{T}}D = \mathbb{1}_{N\times N}$. The classical ground-state field configuration, which corresponds to the vacuum expectation value in a quantized theory in lowest order tree approximation [203], is given by a constant field $\vec{\varphi}_0$ which minimizes the potential in Eq. (C.1). The parameter λ of the potential has to be positive in order to ensure a stable vacuum, i.e., the energy is bounded from below. Regarding the parameter m^2 we can distinguish two cases. If m^2 is positive, the field configuration minimizing the energy is given by $\vec{\varphi}_0 = \vec{0}$. In this case, the ground state is invariant under $O(N)$ transformations as well and the symmetry is realized in the so-called *Wigner-Weyl* phase. For an illustration of this configuration for $N = 2$ fields see the left panel in Fig. C.1. In contrast to that, if m^2 is negative, the field configuration minimizing the potential has to satisfy the condition

$$|\vec{\varphi}_0|^2 = -\frac{m^2}{\lambda}. \tag{C.3}$$

There are uncountably many degenerate states satisfying this condition which are connected to each other by $O(N)$ transformations. The specific realization of the ground state is arbitrarily or "spontaneously" chosen. By a rotation of the internal coordinate system we can choose without loss of generality the ground state to be

$$\vec{\varphi}_0 = (0, 0, \ldots, 0, v)^{\mathrm{T}}, \tag{C.4}$$

with $v = \sqrt{-m^2/\lambda}$. The ground state is not invariant under $O(N)$ transformations anymore and the symmetry is spontaneously broken, i.e., the symmetry is now realized in the so-called *Nambu-Goldstone* phase, see the right panel of Fig. C.1. We define the shifted fields

$$\vec{\varphi}(x) = \Big(\pi^i(x), v + \sigma(x)\Big)^{\mathrm{T}}, \quad i = 1, \ldots, N-1, \tag{C.5}$$

in order to ensure the orthogonality of the vacuum and the one-particle states [203].[1] In terms of the dynamical fields $\sigma(x)$ and $\pi^i(x)$ the *Lagrangian* reads

$$\begin{aligned}\mathcal{L} =& \frac{1}{2}\partial_\mu \pi^i \partial^\mu \pi^i + \frac{1}{2}\partial_\mu \sigma \partial^\mu \sigma + \frac{1}{2}(-2m^2)\sigma^2 + \sqrt{-m^2\lambda}\sigma^3 \\ &+ \sqrt{-m^2\lambda}(\pi^i\pi^i)\sigma + \frac{\lambda}{4}\sigma^4 + \frac{\lambda}{2}(\pi^i\pi^i)\sigma^2 + \frac{\lambda}{4}(\pi^i\pi^i)^2 .\end{aligned} \tag{C.6}$$

The *Lagrangian* written in this form reveals several implications of SSB: The original $O(N)$ symmetry is not manifest anymore, i.e., hidden. We are left with the intact subgroup $O(N-1)$ which rotates only the π^i fields into each other. Moreover, the σ field is now massive which is due to the restoring forces in the radial direction giving rise to the mass term of the σ field, cf. the right panel in Fig. C.1. In contrast to that, there are no such restoring forces in the tangential direction. Terms involving the π^i fields are at least cubic in the fields and there is no corresponding mass term for the π^i fields, i.e., the excitations of the π^i fields are massless. What is more, the *Lagrangian* (C.6) shows a greater variety of different interaction terms. Nevertheless, the couplings of these interaction terms are composed of the original parameters m^2 and λ, i.e., the hidden symmetry entails relations among the couplings of the interactions between the σ and π^i fields. In other words, the mechanism of SSB results in

---

[1] In the case of SSB the generating functionals yield the various types of n-point *Green*'s functions in terms of the shifted fields. The vacuum expectation values of these fields vanish, see Ref. [203].

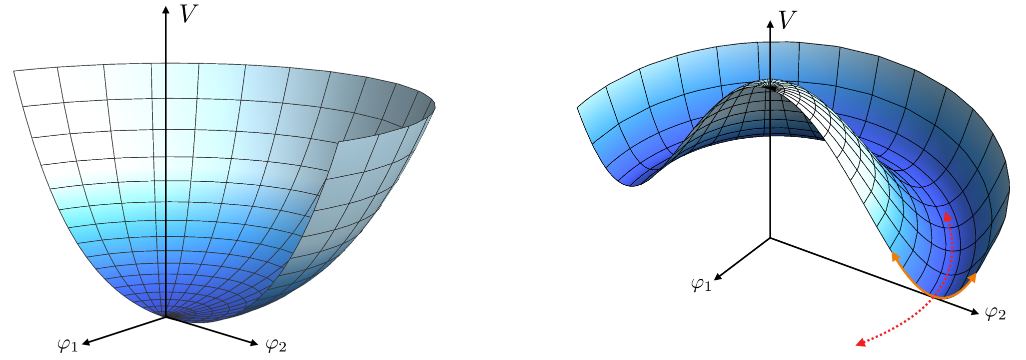

FIGURE C.1: Left panel: $V = m^2|\vec{\varphi}|^2 + \lambda|\vec{\varphi}|^4$, with $m^2, \lambda > 0$. The minimum of the potential is located at $|\vec{\varphi}_0| = 0$, i.e., the ground state is invariant under the continuous symmetry transformation, which is the so-called *Wigner-Weyl* realization of the symmetry. Right panel: $V = m^2|\vec{\varphi}|^2 + \lambda|\vec{\varphi}|^4$, with $m^2 < 0$ and $\lambda > 0$. The minimum of the potential becomes non-trivial. In fact, we find infinitely many degenerate minima located along the "valley" of this "Mexican hat" shaped potential. The ground state is not invariant anymore under the symmetry transformation, which is the so-called *Nambu-Goldstone* realization of the symmetry. The arrows indicate the direction of the radial massive mode and the tangential massless mode, colored orange and red respectively.

various new mass parameters and couplings but these depend only on the parameters of the original symmetric *Lagrangian*.

Goldstone's theorem can be established in a more general manner. For this reason, let us consider a *Lagrangian* of a multiplet of real fields φ^i with the general potential $V(\varphi)$. The *Lagrangian* and thus the potential is assumed to be invariant under a continuous symmetry (*Lie*) group G that transforms the fields in a given representation according to

$$\varphi_i(x) \mapsto \varphi'_i(x) = \left(\exp(-\mathrm{i}\epsilon^a T^a)\right)_{ij} \varphi_j(x) \approx \varphi_i(x) - \mathrm{i}\epsilon^a T^a_{ij}\varphi_j(x)\,, \tag{C.7}$$

with the n_G generators T^a. Moreover, the ground state of the theory is assumed to be invariant under a subgroup H of the symmetry group G, with a total of n_H generators. The ground state $\vec{\varphi}_0$ minimizes the potential, i.e., first order derivatives vanish, and we find for the potential expanded about its minimum

$$V(\varphi^i) = V(\varphi^i_0) + \frac{1}{2}\left(\frac{\partial^2}{\partial\varphi^i\partial\varphi^j}V\right)\Bigg|_{\vec{\varphi}_0} (\varphi - \varphi_0)^i\,(\varphi - \varphi_0)^j + \mathcal{O}\left((\varphi - \varphi_0)^3\right)\,. \tag{C.8}$$

The coefficients of the quadratic terms can be interpreted as the mass matrix, which is symmetric and positive semidefinite. Because of the invariance of the potential under the group transformations we find

$$V(\varphi_i) = V(\varphi_i - \mathrm{i}\epsilon^a T^a_{ij}\varphi_j) \quad\Longrightarrow\quad \frac{\partial V}{\partial\varphi^i}T^a_{ij}\varphi_j = 0\,. \tag{C.9}$$

Taking the derivative of the expression in Eq. (C.9), evaluated at the minimum $\vec{\varphi}_0$, the first order derivative of the potential vanishes again and we find

$$\left(\frac{\partial^2}{\partial\varphi^i\partial\varphi^j}V\right)\bigg|_{\vec{\varphi}_0} T^a_{ij}\varphi^j_0 = 0\,. \tag{C.10}$$

We can now distinguish two cases. The first case is that a symmetry transformation generated by the generator T^a belongs to the subgroup H and therefore leaves the ground state invariant, i.e., the generator annihilates the ground state:

$$T^a_{ij}\varphi^j_0 = 0\,. \tag{C.11}$$

As a consequence, the equation (C.10) provides no information about the eigenvalues of the mass matrix. On the other hand, if the ground state is not invariant under a transformation generated by T^a, i.e.,

$$T^a_{ij}\varphi^j_0 \neq 0\,, \tag{C.12}$$

the change of the ground state $T^a_{ij}\varphi^j_0$ describes an eigenvector of the mass matrix with the eigenvalue zero according to Eq. (C.10). Hence, for each generator of the original symmetry group of the *Lagrangian* which does not leave the ground state invariant (or said differently, for each generator whose corresponding symmetry transformation is broken by the ground state) a field excitation of zero mass appears, i.e., in total $n_G - n_H$ *Goldstone* bosons. The fields of the *Goldstone* bosons are given by

$$\Pi^k = \mathrm{i}(T^k\vec{\varphi}_0)_i\varphi_i, \tag{C.13}$$

with T^a being a generator of a broken symmetry [203].

So far, we have illustrated the implications of SSB in a classical description. We now comment on SSB in the context of a quantized theory. The generators of a symmetry transformation are given by the Noether charges Q^a. Thus, a general state $|\chi\rangle$ transforms according to $|\chi\rangle \longrightarrow |\chi\rangle + \mathrm{i}\epsilon^a Q^a|\chi\rangle$. The realization of a symmetry in the *Nambu-Goldstone* phase is indicated by a vacuum state $|0\rangle$ which does not respect a symmetry of the *Lagrangian*, i.e., we find for the corresponding charge

$$Q^a|0\rangle \neq 0\,. \tag{C.14}$$

In contrast to that, if a certain continuous symmetry of the *Lagrangian* is not broken by the vacuum state, the generator of this transformation annihilates the vacuum state, i.e., we have $Q^a|0\rangle = 0$. Relation (C.14) actually means that the integral in $Q^a = \int \mathrm{d}^3x\; j^a_0(x)$ is divergent and therefore does not exist [458]. In order to obtain a well-defined indicator for SSB in a quantized theory, we consider instead of Eq. (C.14) the vacuum expectation value of the following commutator:

$$\langle 0|\,[\mathrm{i}Q^a,\Phi(y)]\,|0\rangle = \langle 0|\int \mathrm{d}^3x\;\mathrm{i}\,[j^a_0(x),\Phi(y)]\,|0\rangle := \langle 0|\delta^a\Phi(y)|0\rangle \equiv \langle\delta^a\Phi(y)\rangle, \tag{C.15}$$

where Φ can in principal be an elementary field or a polynomial of fields. As the commutator is only non-vanishing in the vicinity of the space-time point y, this object is well-defined. As a result, we have found an order parameter for SSB in the following sense: A non-vanishing expectation value $\langle \delta^a \Phi(y) \rangle$ is a sufficient criterion for $Q^a|0\rangle \neq 0$ and thus for the spontaneous breakdown of the related symmetry. If we take Φ to be an elementary field φ_i of our previous discussion, see Eqs. (C.7)-(C.13), we find

$$\langle [\mathrm{i}Q^a, \varphi_i(x)] \rangle = \langle 0|(-\mathrm{i})T^a_{ij}\varphi^j(x)|0\rangle = -\mathrm{i}T^a_{ij}\langle \varphi^j(x) \rangle = -\mathrm{i}T^a_{ij}\varphi^j_0 \,. \tag{C.16}$$

The latter relation, cf. Eqs. (C.11) and (C.12), brings us back to our previous considerations. The proof of *Goldstone*'s theorem in a quantized theory can be easily achieved by employing the effective action formalism introduced in Section 2.1. The same arguments given above in order to prove *Goldstone*'s theorem in classical field theory directly apply to a quantum theory if the classical potential is replaced by the effective potential U. The effective potential already includes quantum corrections to all orders and possesses the same symmetries as the original *Lagrangian*. The minimum of the effective potential yields the vacuum expectation value of the fields and therefore indicates if a symmetry is spontaneously broken by the ground state. By simply repeating the arguments given above, we find for each broken generator an eigenvector of the matrix of second-order derivatives of the effective potential U with the eigenvalue zero. On the other hand, the second functional derivative of the effective action is the inverse of the full propagator. Thus, it contains the mass spectrum of the theory: In momentum space, a particle of mass m is related to an eigenvector with zero eigenvalue of the matrix

$$\frac{\delta^2 \Gamma}{\delta \Phi^i(p) \delta \Phi^j(-p)} \tag{C.17}$$

for $p^2 = m^2$. For a massless particle, the matrix has to be evaluated at $p = 0$. In position space, this corresponds to homogeneous, i.e., constant fields. Therefore, the search for a zero eigenvalue of the matrix of second functional derivatives of the effective action reduces to the search for a zero eigenvalue of the matrix of second derivatives of the effective potential:

$$\frac{\delta^2 \Gamma}{\delta \Phi^i(p) \delta \Phi^j(-p)} \xrightarrow{p=0} \frac{\partial^2 U}{\partial \Phi^i \partial \Phi^j} \,. \tag{C.18}$$

This finally proves *Goldstone*'s theorem in a quantum field theory.

D

CUTOFF SCALE DEPENDENCE OF THE INITIAL EFFECTIVE ACTION

We formally discuss the dependence of the initial bare action Γ_Λ on the UV cutoff scale Λ for asymptotically free theories such as QCD. From this general consideration, we can derive a procedure for constructing the initial effective action in a well-defined and practically applicable way.

The flow equation in its generic form

$$k\partial_k \Gamma_k[\Phi] = \mathcal{F}_k[\Phi] \tag{D.1}$$

can formally be integrated from the initial UV scale Λ to $k < \Lambda$ to yield the average effective action

$$\Gamma_k[\Phi] = \Gamma_\Lambda[\Phi] + \int_\Lambda^k \frac{dk'}{k'} \mathcal{F}_{k'}[\Phi] \,, \tag{D.2}$$

which provides the full quantum effective action Γ in the limit $k \to 0$. The condition of RG consistency introduced in Section 3.3 requires the independence of the effective action from the cutoff scale Λ. We find

$$\Lambda\partial_\Lambda \Gamma[\Phi] = \Lambda\partial_\Lambda \Gamma_\Lambda[\Phi] - \mathcal{F}_\Lambda[\Phi] = 0 \,. \tag{D.3}$$

Assuming an asymptotically large cutoff, i.e., $s_i/\Lambda \ll 1$ with $s = \{m_{\text{phys}}, m_{\text{ext}}\}$, the Λ-dependence of the initial effective action Γ_Λ can be extracted from the relations (D.2)-(D.3) and an expansion in powers of Λ leads to

$$\Gamma_\Lambda[\Phi] = \sum_{n \le N_{\max}} \tilde{\gamma}_n[\Phi]\, \Lambda^n + \tilde{\gamma}_{\log}[\Phi]\, \ln \frac{\Lambda}{s_0} \,, \tag{D.4a}$$

where the term with $n = 0$ carries the physics part of the initial condition at the scale Λ. Here, we have normalized the logarithmic term with some physical scale $s_0 \in s$, e.g., the physical mass gap of the theory at hand. Choosing a different reference scale shifts terms from $\tilde{\gamma}_0$ to $\tilde{\gamma}_{\log}$. Note that the $\tilde{\gamma}_n$'s can be a collection of different field-dependent terms with the same Λ-behavior. The right-hand side of the flow equation can also be expanded in powers of Λ, and the expansion coefficients only depend on the shape function $r(x)$ and $\tilde{\gamma} = \{\tilde{\gamma}_{N_{\max}}, \tilde{\gamma}_{N_{\max}-1}, ..., \tilde{\gamma}_{\log}, \tilde{\gamma}_0, \tilde{\gamma}_{-1}, \dots\}$,

$$\mathcal{F}_\Lambda[\Phi] = \sum_{n\leq N_{\max}} f_n[\Phi; \tilde{\gamma}, r]\, \Lambda^n \,. \tag{D.4b}$$

Inserting Eqs. (D.4a) and (D.4b) into the flow equation (D.1) leads to

$$\tilde{\gamma}_{n\neq 0} = \frac{1}{n} f_n[\Phi, \tilde{\gamma}, r]\,, \qquad \tilde{\gamma}_{\log} = f_0[\Phi, \tilde{\gamma}, r]\,, \tag{D.4c}$$

where we have used $\Lambda\partial_\Lambda \Lambda^n = n\Lambda^n$, $\Lambda\partial_\Lambda \ln\Lambda = 1$. Note that there is no relation for $\tilde{\gamma}_0$ as it contains the physics input. Nonetheless, $\tilde{\gamma}_0$ appears on the right-hand side of the relations for the $\tilde{\gamma}_{n\neq 0}$ and $\tilde{\gamma}_{\log}$.

The set of relations (D.4c) can be solved recursively and provides the initial effective action in a well-defined and practically applicable way. Note that only a finite number of terms matter due to the Λ-suppression of the rest. The relations (D.4a)-(D.4c) also make apparent that, for asymptotically large values of Λ, the initial effective action is nothing but the bare action for the given FRG scheme. As such, it depends explicitly on the cutoff Λ, see, e.g., Refs. [337, 459].

E

THRESHOLD FUNCTIONS

Here, we define the threshold functions which appear in the RG flow equations in Chapter 4. The threshold functions essentially represent 1PI diagrams and depend on the employed regularization scheme. In order to define these functions, we make use of various auxiliary dimensionless quantities, namely the dimensionless temperature $\tau = T/k$, the dimensionless (renormalized) chemical potential $\tilde{\mu}_\tau = Z_\mu \mu/(2\pi T)$, and the dimensionless fermionic and bosonic *Matsubara* frequencies $\tilde{\nu}_n = (2n+1)\pi\tau$ and $\tilde{\omega}_n = 2\pi n\tau$, respectively.

E.1 Covariant Regulator

For the four-dimensional regularization scheme, see Eq. (3.40) in Section 3.2, it is convenient to define the dimensionless (regularized) propagator for the fermions:

$$\tilde{G}_\psi(y_0, y, \omega) = \frac{1}{(y_0 + y)(1 + r_\psi)^2 + \omega} \,. \tag{E.1}$$

The following purely fermionic threshold functions appear in the RG flow equations in Chapter 4:

$$\begin{aligned} l_{\parallel +}^{(\mathrm{F})}(\tau, \omega, \tilde{\mu}_\tau) = -\frac{\tau}{2} \sum_{n=-\infty}^{+\infty} \int_0^\infty \mathrm{d}y\, y^{\frac{1}{2}} \tilde{\partial}_t \Big[& (\tilde{\nu}_n + 2\pi\tau\tilde{\mu}_\tau)^2 \, (1 + r_\psi)^2 \\ & \times \Big(\tilde{G}_\psi((\tilde{\nu}_n + 2\pi\tau\tilde{\mu}_\tau)^2, y, \omega) \Big)^2 \Big] \,, \end{aligned} \tag{E.2}$$

$$\begin{aligned} l_{\perp +}^{(\mathrm{F})}(\tau, \omega, \tilde{\mu}_\tau) = -\frac{\tau}{2} \sum_{n=-\infty}^{+\infty} \int_0^\infty \mathrm{d}y\, y^{\frac{1}{2}} \tilde{\partial}_t \Big[& \Big(y(1 + r_\psi)^2 + \omega \Big) \\ & \times \Big(\tilde{G}_\psi((\tilde{\nu}_n + 2\pi\tau\tilde{\mu}_\tau)^2, y, \omega) \Big)^2 \Big] \,, \end{aligned} \tag{E.3}$$

$$l^{(\mathrm{F})}_{\parallel\pm}(\tau,\omega,\tilde{\mu}_\tau) = -\frac{\tau}{2}\sum_{n=-\infty}^{+\infty}\int_0^\infty \mathrm{d}y\, y^{\frac{1}{2}}\tilde{\partial}_t\Big[(\tilde{\nu}_n + 2\pi\tau\tilde{\mu}_\tau)(\tilde{\nu}_n - 2\pi\tau\tilde{\mu}_\tau)(1+r_\psi)^2 \\ \times\, \tilde{G}_\psi((\tilde{\nu}_n + 2\pi\tau\tilde{\mu}_\tau)^2, y,\omega)\tilde{G}_\psi((\tilde{\nu}_n - 2\pi\tau\tilde{\mu}_\tau)^2, y,\omega)\Big]\,, \quad \text{(E.4)}$$

$$l^{(\mathrm{F})}_{\perp\pm}(\tau,\omega,\tilde{\mu}_\tau) = -\frac{\tau}{2}\sum_{n=-\infty}^{+\infty}\int_0^\infty \mathrm{d}y\, y^{\frac{1}{2}}\tilde{\partial}_t\Big[\Big(y(1+r_\psi)^2 + \omega\Big) \\ \times\, \tilde{G}_\psi((\tilde{\nu}_n + 2\pi\tau\tilde{\mu}_\tau)^2, y,\omega)\tilde{G}_\psi((\tilde{\nu}_n - 2\pi\tau\tilde{\mu}_\tau)^2, y,\omega)\Big]\,, \quad \text{(E.5)}$$

where $y = \vec{p}^{\,2}/k^2$ and the formal derivative $\tilde{\partial}_t$ is defined as $\tilde{\partial}_t = (\partial_t r_\psi)\frac{\partial}{\partial r_\psi}$. Here, we have already used that $\partial_t Z^{\parallel} = \partial_t Z^{\perp} = \partial_t Z_\mu = 0$ in our present study. For the regulator function (3.44), the latter assumes the following form:

$$\tilde{\partial}_t = \frac{(y_0+y)\mathrm{e}^{-(y_0+y)}}{(1-\mathrm{e}^{-(y_0+y)})^{\frac{3}{2}}}\frac{\partial}{\partial r_\psi}\,. \quad \text{(E.6)}$$

In the limit $\tilde{\mu}_\tau = 0$, the above set of four distinct threshold functions collapses to a set of merely two threshold functions:

$$l^{(\mathrm{F})}_{\parallel +}(\tau,\omega,0) = l^{(\mathrm{F})}_{\parallel\pm}(\tau,\omega,0) \equiv l^{(\mathrm{F})}_{\parallel}(\tau,\omega,0)\,,$$
$$l^{(\mathrm{F})}_{\perp +}(\tau,\omega,0) = l^{(\mathrm{F})}_{\perp\pm}(\tau,\omega,0) \equiv l^{(\mathrm{F})}_{\perp}(\tau,\omega,0)\,.$$

Furthermore, we find

$$l^{(\mathrm{F})}_{\parallel}(\tau,\omega,0) + l^{(\mathrm{F})}_{\perp}(\tau,\omega,0) = \tau\sum_{n=-\infty}^{+\infty}\int_0^\infty \mathrm{d}y\, y^{\frac{1}{2}}\frac{(\partial_t r_\psi)(1+r_\psi)(\tilde{\nu}_n^2+y)}{[(\tilde{\nu}_n^2+y)\,(1+r_\psi)^2+\omega]^2}\,. \quad \text{(E.7)}$$

For the regulator function (3.44) and $T=\mu=\omega=0$, we then obtain $l^{(\mathrm{F})}_{\parallel}(0,0,0)+l^{(\mathrm{F})}_{\perp}(0,0,0) = \frac{1}{4}$. In the limit $T=\mu=\omega=0$, the threshold functions indeed only enter the RG flow equations in this particular combination.

E.2 SPATIAL REGULATOR

Also in case of spatial regulator functions, see Eq. (3.30) in Section 3.2, it is convenient to define a dimensionless propagator:

$$\tilde{G}^{\mathrm{spatial}}_{\psi}(y_0,y,\omega) = \frac{1}{y_0 + y(1+r_\psi)^2+\omega}\,. \quad \text{(E.8)}$$

The threshold functions then read

$$l^{(\mathrm{F})}_{\|+,\mathrm{spatial}}(\tau,\omega,\tilde{\mu}_\tau) = -\frac{1}{2}\tau \sum_{n=-\infty}^{+\infty} \int_0^\infty \mathrm{d}y\, y^{\frac{1}{2}}\tilde{\partial}_t \Big[(\tilde{\nu}_n + 2\pi\tau\tilde{\mu}_\tau)^2 \\ \times \left(\tilde{G}^{\mathrm{spatial}}_\psi((\tilde{\nu}_n + 2\pi\tau\tilde{\mu}_\tau)^2, y, \omega)\right)^2 \Big], \tag{E.9}$$

$$l^{(\mathrm{F})}_{\perp+,\mathrm{spatial}}(\tau,\omega,\tilde{\mu}_\tau) = -\frac{1}{2}\tau \sum_{n=-\infty}^{+\infty} \int_0^\infty \mathrm{d}y\, y^{\frac{1}{2}}\tilde{\partial}_t \Big[\left(y(1+r_\psi)^2 + \omega\right) \\ \times \left(\tilde{G}^{\mathrm{spatial}}_\psi((\tilde{\nu}_n + 2\pi\tau\tilde{\mu}_\tau)^2, y, \omega)\right)^2 \Big], \tag{E.10}$$

$$l^{(\mathrm{F})}_{\|\pm,\mathrm{spatial}}(\tau,\omega,\tilde{\mu}_\tau) = -\frac{1}{2}\tau \sum_{n=-\infty}^{+\infty} \int_0^\infty \mathrm{d}y\, y^{\frac{1}{2}}\tilde{\partial}_t \Big[(\tilde{\nu}_n + 2\pi\tau\tilde{\mu}_\tau)(\tilde{\nu}_n - 2\pi\tau\tilde{\mu}_\tau)\times \\ \times\, \tilde{G}^{\mathrm{spatial}}_\psi((\tilde{\nu}_n + 2\pi\tau\tilde{\mu}_\tau)^2, y, \omega)\tilde{G}^{\mathrm{spatial}}_\psi((\tilde{\nu}_n - 2\pi\tau\tilde{\mu}_\tau)^2, y, \omega) \Big], \tag{E.11}$$

$$l^{(\mathrm{F})}_{\perp\pm,\mathrm{spatial}}(\tau,\omega,\tilde{\mu}_\tau) = -\frac{1}{2}\tau \sum_{n=-\infty}^{+\infty} \int_0^\infty \mathrm{d}y\, y^{\frac{1}{2}}\tilde{\partial}_t \Big[\left(y(1+r_\psi)^2 + \omega\right) \times \\ \times\, \tilde{G}^{\mathrm{spatial}}_\psi((\tilde{\nu}_n + 2\pi\tau\tilde{\mu}_\tau)^2, y, \omega)\tilde{G}^{\mathrm{spatial}}_\psi((\tilde{\nu}_n - 2\pi\tau\tilde{\mu}_\tau)^2, y, \omega) \Big], \tag{E.12}$$

where $y = \vec{p}^{\,2}/k^2$ and

$$\tilde{\partial}_t = \frac{1}{y^{\frac{1}{2}}}\theta(1-y)\frac{\partial}{\partial r_\psi} \tag{E.13}$$

for $\partial_t Z^{\|} = \partial_t Z^{\perp} = \partial_t Z_\mu = 0$. For the shape function (3.31), i.e., the *Litim* or linear regulator, the threshold functions can be computed analytically. For example, we find

$$l^{(\mathrm{F})}_{\|+,\mathrm{spatial}}(\tau,\omega,-\mathrm{i}\tilde{\mu}_\tau) + l^{(\mathrm{F})}_{\perp+,\mathrm{spatial}}(\tau,\omega,-\mathrm{i}\tilde{\mu}_\tau) \\ = \frac{1}{6}\frac{\partial}{\partial\omega}\left\{ \frac{1}{\sqrt{1+\omega}} \left[\tanh\left(\frac{2\pi\tau\tilde{\mu}_\tau - \sqrt{1+\omega}}{2\tau}\right) - \tanh\left(\frac{2\pi\tau\tilde{\mu}_\tau + \sqrt{1+\omega}}{2\tau}\right) \right] \right\}, \tag{E.14}$$

$$l^{(\mathrm{F})}_{\|\pm,\mathrm{spatial}}(\tau,\omega,-\mathrm{i}\tilde{\mu}_\tau) + l^{(\mathrm{F})}_{\perp\pm,\mathrm{spatial}}(\tau,\omega,-\mathrm{i}\tilde{\mu}_\tau) \\ = -\frac{1}{6}\frac{\partial}{\partial\omega}\Big\{ \frac{1}{|\sqrt{1+\omega} - 2\pi\tau\tilde{\mu}|} \tanh\left(\frac{|\sqrt{1+\omega} - 2\pi\tau\tilde{\mu}|}{2\tau}\right) \\ + \frac{1}{|\sqrt{1+\omega} + 2\pi\tau\tilde{\mu}|} \tanh\left(\frac{|\sqrt{1+\omega} + 2\pi\tau\tilde{\mu}|}{2\tau}\right) \Big\}. \tag{E.15}$$

Note that not only the sum of the two threshold functions in Eq. (E.15) has a second-order pole at $\sqrt{k^2+\omega}=\mu$ at $T=0$ but also the individual functions. Moreover, in the limit $\tau \to 0$, $\omega \to 0$, and $\tilde{\mu}_\tau \to 0$, we find

$$l^{(\mathrm{F})}_{\parallel +,\mathrm{spatial}}(0,0,0) = l^{(\mathrm{F})}_{\perp +,\mathrm{spatial}}(0,0,0) = l^{(\mathrm{F})}_{\parallel \pm,\mathrm{spatial}}(0,0,0) = l^{(\mathrm{F})}_{\perp \pm,\mathrm{spatial}}(0,0,0) = \frac{1}{12}\,. \tag{E.16}$$

F

RG FLOW EQUATIONS

For the derivation of the RG flow equations in Chapters 4 and 5, we have made use of existing software packages [460, 461]. The size of the considered truncations and the resulting complexity of the algebraic expressions make such software solutions indispensable. Here, we briefly outline the essential parts in order to derive the RG flow equations for the couplings of the *Fierz*-complete system of four-quark interactions:[1]

The *Mathematica* package *DoFun (2.0.4)* [460] allows an automatic derivation of FRG equations for n-point functions from a symbolic representation of the effective action. The definition of this symbolic effective action includes the *Fierz*-complete four-quark interaction channels. With this effective action as input, the fermionic four-point correlation function is derived by *DoFun* in symbolic form. By employing the *DoAE* package, which is included in *DoFun*, the symbolic form is subsequently transformed into an actual algebraic expression. This transformation requires the definition of *Feynman* rules, i.e., the definitions of the explicit algebraic expressions for all propagators and vertices. The FRG equation for the four-point correlation function at this stage is a tensorial object. In order to obtain the particular scalar flow equations of the four-quark couplings, this equation must be projected on appropriate tensor structures. Such tensor structures are for example given by the operator structures of the four-quark interaction channels. They provide a linearly independent basis of projection operators which, however, are not orthogonal. Consequently, the projections must be linearly recombined in order to yield the flow equations of specific couplings: The left-hand side (regarding the *Wetterich* equation) of the tensorial FRG equation for the four-point correlation function is obtained by using the *getFR* command to derive the fermionic four-point vertex.[2] The projections of this expression onto the basis of tensor structures leads to a system of linear equations in terms of the four-quark couplings. The solution to this system then provides the required recombinations of the projections of the right-hand side of the *Wetterich* equation in order to eventually obtain the particular scalar flow equations of the four-quark couplings. In

---

[1] For an introduction to the derivation of RG flow equations of four-fermion interactions, we refer the reader to Ref. [333].

[2] This operation essentially amounts to taking the appropriate number of functional derivatives of the effective action with respect to the fermionic fields.

this process, we have used the *Mathematica* package *FormTracer (1.7.5)* [461], which is based on *FORM* [462, 463], to compute the various projections, i.e., to perform the traces in *Dirac*, flavor and color space. In order to facilitate the numerical solution of the RG flow equations, we have identified the various threshold functions appearing in the flow equations and solved the momentum integration of the corresponding loop integrals separately.[3] The threshold functions then entered the flow equations as interpolated functions of the dimensionless temperature and the dimensionless chemical potential only.

The RG flow equations appearing in the *Fierz*-complete NJL model study with a single fermion species in Section 4.2 are listed below in Appendix F.1, and the RG flow equations underlying the *Fierz*-complete NJL model study in Section 4.3 for general N_{c} and $N_{\mathrm{f}} = 2$ are listed in Appendix F.2. We do not explicitly list the RG flow equations of the model (5.1) underlying our study with dynamical gauge degrees of freedom in Chapter 5 due to the excessive size of the expressions.

F.1 NJL MODEL WITH A SINGLE FERMION SPECIES

We list here the RG flow equations underlying our *Fierz*-complete NJL model study with a single fermion species presented in Section 4.2. For the covariant regulator function, we find the following set of flow equations for the dimensionless four-fermion couplings λ_σ, $\lambda_{\mathrm{V}}^{\parallel}$ and $\lambda_{\mathrm{V}}^{\perp}$ of the model defined in Eq. (4.33):

$$\begin{aligned}\partial_t \lambda_\sigma \equiv \beta_{\lambda_\sigma} = 2\lambda_\sigma &- 16 v_4 \left(-\lambda_\sigma^2 + 2\lambda_{\mathrm{V}}^{\parallel}\lambda_{\mathrm{V}}^{\perp} + (\lambda_{\mathrm{V}}^{\perp})^2 - 2\lambda_\sigma\lambda_{\mathrm{V}}^{\perp}\right) l_{\perp\pm}^{(\mathrm{F})}(\tau, 0, -\mathrm{i}\tilde{\mu}_\tau)\\ &- 16 v_4 \left(3\lambda_\sigma^2 + 2\lambda_{\mathrm{V}}^{\parallel}(\lambda_\sigma + \lambda_{\mathrm{V}}^{\perp}) + (\lambda_{\mathrm{V}}^{\perp})^2 + 8\lambda_\sigma\lambda_{\mathrm{V}}^{\perp}\right) l_{\perp+}^{(\mathrm{F})}(\tau, 0, -\mathrm{i}\tilde{\mu}_\tau)\\ &- 16 v_4 \left(-\lambda_\sigma^2 - 2\lambda_\sigma\lambda_{\mathrm{V}}^{\parallel} + 3(\lambda_{\mathrm{V}}^{\perp})^2\right) l_{\parallel\pm}^{(\mathrm{F})}(\tau, 0, -\mathrm{i}\tilde{\mu}_\tau)\\ &- 16 v_4 \left(3\lambda_\sigma^2 + 4\lambda_\sigma\lambda_{\mathrm{V}}^{\parallel} + 3(\lambda_{\mathrm{V}}^{\perp})^2 + 6\lambda_\sigma\lambda_{\mathrm{V}}^{\perp}\right) l_{\parallel+}^{(\mathrm{F})}(\tau, 0, -\mathrm{i}\tilde{\mu}_\tau)\,,\end{aligned} \tag{F.1}$$

$$\begin{aligned}\partial_t \lambda_{\mathrm{V}}^{\parallel} \equiv \beta_{\lambda_{\mathrm{V}}^{\parallel}} = 2\lambda_{\mathrm{V}}^{\parallel} &+ 16 v_4 \Big(- \lambda_\sigma^2 + 2\lambda_\sigma\lambda_{\mathrm{V}}^{\parallel} + 4\lambda_{\mathrm{V}}^{\parallel}\lambda_{\mathrm{V}}^{\perp} - (\lambda_{\mathrm{V}}^{\perp})^2 - 4\lambda_\sigma\lambda_{\mathrm{V}}^{\perp}\Big) l_{\perp\pm}^{(\mathrm{F})}(\tau, 0, -\mathrm{i}\tilde{\mu}_\tau)\\ &+ 16 v_4 \Big(- \lambda_\sigma^2 - 2(\lambda_{\mathrm{V}}^{\parallel})^2 - 2\lambda_\sigma\lambda_{\mathrm{V}}^{\parallel} - 6\lambda_{\mathrm{V}}^{\parallel}\lambda_{\mathrm{V}}^{\perp} - (\lambda_{\mathrm{V}}^{\perp})^2\\ &\qquad - 4\lambda_\sigma\lambda_{\mathrm{V}}^{\perp}\Big) l_{\perp+}^{(\mathrm{F})}(\tau, 0, -\mathrm{i}\tilde{\mu}_\tau)\\ &+ 16 v_4 \left(3\lambda_\sigma^2 + (\lambda_{\mathrm{V}}^{\parallel})^2 + 6(\lambda_{\mathrm{V}}^{\perp})^2 + 6\lambda_\sigma\lambda_{\mathrm{V}}^{\perp}\right) l_{\parallel\pm}^{(\mathrm{F})}(\tau, 0, -\mathrm{i}\tilde{\mu}_\tau)\\ &+ 16 v_4 \left(-\lambda_\sigma^2 + (\lambda_{\mathrm{V}}^{\parallel})^2 + 4\lambda_\sigma\lambda_{\mathrm{V}}^{\parallel} + 6\lambda_{\mathrm{V}}^{\parallel}\lambda_{\mathrm{V}}^{\perp} + 6\lambda_\sigma\lambda_{\mathrm{V}}^{\perp}\right) l_{\parallel+}^{(\mathrm{F})}(\tau, 0, -\mathrm{i}\tilde{\mu}_\tau)\,,\end{aligned} \tag{F.2}$$

---

[3] The identification and symbolic replacement of threshold functions is simplified by making use of the *tDerivative→False* option in the symbolic derivation of the flow equations with *DoFun*. This option suppresses the derivative $\tilde{\partial}_t$ [460], which makes the algebraic structure of the threshold functions simpler.

$$\begin{aligned}\partial_t \lambda_{\mathrm{V}}^{\perp} \equiv \beta_{\lambda_{\mathrm{V}}^{\perp}} = 2\lambda_{\mathrm{V}}^{\perp} - \frac{16}{3} v_4 \Big(&- \lambda_\sigma^2 - (\lambda_{\mathrm{V}}^{\parallel})^2 - 2\lambda_{\mathrm{V}}^{\parallel}(\lambda_{\mathrm{V}}^{\perp} - \lambda_\sigma) - 10(\lambda_{\mathrm{V}}^{\perp})^2 \\ &- 4\lambda_\sigma \lambda_{\mathrm{V}}^{\perp}\Big) l_{\perp\pm}^{(\mathrm{F})}(\tau, 0, -\mathrm{i}\tilde{\mu}_\tau) \\ &- \frac{16}{3} v_4 \Big(3\lambda_\sigma^2 + (\lambda_{\mathrm{V}}^{\parallel})^2 + 2\lambda_\sigma \lambda_{\mathrm{V}}^{\parallel} + 10(\lambda_{\mathrm{V}}^{\perp})^2\Big) l_{\perp +}^{(\mathrm{F})}(\tau, 0, -\mathrm{i}\tilde{\mu}_\tau) \\ &- 16 v_4 \left(\lambda_\sigma^2 - 2\lambda_{\mathrm{V}}^{\parallel}\lambda_{\mathrm{V}}^{\perp} - (\lambda_{\mathrm{V}}^{\perp})^2 + 2\lambda_\sigma \lambda_{\mathrm{V}}^{\perp}\right) l_{\parallel\pm}^{(\mathrm{F})}(\tau, 0, -\mathrm{i}\tilde{\mu}_\tau) \\ &- 16 v_4 \left(\lambda_\sigma^2 + 4\lambda_{\mathrm{V}}^{\parallel}\lambda_{\mathrm{V}}^{\perp} + 5(\lambda_{\mathrm{V}}^{\perp})^2 + 6\lambda_\sigma \lambda_{\mathrm{V}}^{\perp}\right) l_{\parallel +}^{(\mathrm{F})}(\tau, 0, -\mathrm{i}\tilde{\mu}_\tau) \,. \end{aligned} \tag{F.3}$$

In the limit of vanishing temperature and chemical potential, these RG flow equations simplify to

$$\beta_{\lambda_\sigma} = 2\lambda_\sigma - 4v_4 \left(2\lambda_\sigma^2 + 2\lambda_\sigma(\lambda_{\mathrm{V}}^{\parallel} + 3\lambda_{\mathrm{V}}^{\perp}) + 3(\lambda_{\mathrm{V}}^{\perp})^2 + 3\lambda_{\mathrm{V}}^{\parallel}\lambda_{\mathrm{V}}^{\perp}\right), \tag{F.4}$$

$$\beta_{\lambda_{\mathrm{V}}^{\parallel}} = 2\lambda_{\mathrm{V}}^{\parallel} - 4v_4 \left(\lambda_\sigma^2 + (\lambda_{\mathrm{V}}^{\parallel})^2 + \lambda_\sigma(-\lambda_{\mathrm{V}}^{\parallel} + 3\lambda_{\mathrm{V}}^{\perp})\right), \tag{F.5}$$

$$\beta_{\lambda_{\mathrm{V}}^{\perp}} = 2\lambda_{\mathrm{V}}^{\perp} - 4v_4 \left(\lambda_\sigma^2 + (\lambda_{\mathrm{V}}^{\perp})^2 + \lambda_\sigma(\lambda_{\mathrm{V}}^{\parallel} + \lambda_{\mathrm{V}}^{\perp})\right). \tag{F.6}$$

Choosing *Poincaré*-invariant initial conditions, i.e., choosing $\lambda_{\mathrm{V}}^{\parallel} = \lambda_{\mathrm{V}}^{\perp} = \lambda_{\mathrm{V}}$ at the initial RG scale, we deduce from Eqs. (F.1)-(F.3) that *Poincaré* invariance remains intact in the RG flow:

$$\beta_{\lambda_{\mathrm{V}}} = \beta_{\lambda_{\mathrm{V}}^{\parallel}}\Big|_{\lambda_{\mathrm{V}}^{\parallel}=\lambda_{\mathrm{V}}^{\perp}=\lambda_{\mathrm{V}}} = \beta_{\lambda_{\mathrm{V}}^{\perp}}\Big|_{\lambda_{\mathrm{V}}^{\parallel}=\lambda_{\mathrm{V}}^{\perp}=\lambda_{\mathrm{V}}} \tag{F.7}$$

with

$$\beta_{\lambda_{\mathrm{V}}} = 2\lambda_{\mathrm{V}} - 4v_4(\lambda_\sigma + \lambda_{\mathrm{V}})^2 \,. \tag{F.8}$$

The flow equations in case of the spatial regulator function (3.30) are obtained from the flow equations (F.1)-(F.3) by simply replacing the threshold functions with their counterparts for the spatial regulator defined in Section E.2. However, note that Eqs. (F.4)-(F.8) are altered for the spatial regulator as the actual values of the threshold functions for a given set of values of τ, ω, and $\tilde{\mu}_\tau$ depend in general on the details of the regularization scheme. For example, we find that the values of the threshold functions associated with the covariant regulator, see Eqs. (3.40) and (3.44), and the spatial regulator, see Eqs. (3.30) and (3.31), differ in the limit $\tau \to 0$, $\omega \to 0$, and $\tilde{\mu}_\tau \to 0$. In any case, we stress that Eq. (F.7) no longer holds for the spatial regulator function as the latter breaks explicitly *Poincaré* invariance, even at $T = \mu = 0$.

F.2 NJL MODEL WITH TWO FLAVORS AND N_{C} COLORS

In the following, we list the set of RG flow equations of the $SU(N_{\mathrm{c}})\otimes SU_{\mathrm{L}}(2)\otimes SU_{\mathrm{R}}(2)\otimes U_{\mathrm{V}}(1)$ symmetric model (4.3) with the four-quark interactions channels (4.59)- (4.68) underlying our *Fierz*-complete study in Section 4.3 for general N_{c} and $N_{\mathrm{f}}=2$:

$$
\begin{aligned}
&\partial_t\lambda_{(\sigma\text{-}\pi)} = \\
&2\lambda_{(\sigma\text{-}\pi)} + 64v_4\Big(- \lambda_{(\sigma\text{-}\pi)}^2 - 4\lambda_{(\sigma\text{-}\pi)}\lambda_{(S+P)_-} - 4\lambda_{(S+P)_-}^2 + \lambda_{(\sigma\text{-}\pi)}\lambda_{(V+A)_\parallel} + \lambda_{(\sigma\text{-}\pi)}\lambda_{(V-A)_\parallel} \\
&+ 3\lambda_{(\sigma\text{-}\pi)}\lambda_{(V+A)_\perp} - \lambda_{(V+A)_\parallel^{\mathrm{adj}}}\lambda_{(V+A)_\perp} + \lambda_{(\sigma\text{-}\pi)}\lambda_{(V-A)_\perp} + 2\lambda_{(\sigma\text{-}\pi)}\lambda_{(V-A)_\perp^{\mathrm{adj}}} - \frac{1}{N_{\mathrm{c}}^2}\lambda_{(S+P)_-^{\mathrm{adj}}}^2 \\
&+ \frac{2}{N_{\mathrm{c}}}\lambda_{(\sigma\text{-}\pi)}\lambda_{(S+P)_-^{\mathrm{adj}}} + \frac{4}{N_{\mathrm{c}}}\lambda_{(S+P)_-}\lambda_{(S+P)_-^{\mathrm{adj}}} + \frac{1}{N_{\mathrm{c}}}\lambda_{(S+P)_-^{\mathrm{adj}}}^2 - \frac{1}{2N_{\mathrm{c}}}\lambda_{(\sigma\text{-}\pi)}\lambda_{(V+A)_\parallel^{\mathrm{adj}}} \\
&- \frac{1}{2N_{\mathrm{c}}}\lambda_{(\sigma\text{-}\pi)}\lambda_{(V-A)_\perp^{\mathrm{adj}}} - 2N_{\mathrm{c}}\lambda_{(\sigma\text{-}\pi)}^2 - 4N_{\mathrm{c}}\lambda_{(\sigma\text{-}\pi)}\lambda_{(S+P)_-} - 4N_{\mathrm{c}}\lambda_{(S+P)_-}^2 - N_{\mathrm{c}}\lambda_{(\sigma\text{-}\pi)}\lambda_{(S+P)_-^{\mathrm{adj}}} \\
&- 2N_{\mathrm{c}}\lambda_{(S+P)_-}\lambda_{(S+P)_-^{\mathrm{adj}}} + \frac{N_{\mathrm{c}}}{2}\lambda_{(\sigma\text{-}\pi)}\lambda_{(V+A)_\parallel^{\mathrm{adj}}} + \lambda_{(\sigma\text{-}\pi)}\lambda_{\mathrm{csc}} - \lambda_{(S+P)_-^{\mathrm{adj}}}\lambda_{\mathrm{csc}} + N_{\mathrm{c}}\lambda_{(\sigma\text{-}\pi)}\lambda_{\mathrm{csc}} \\
&+ 2N_{\mathrm{c}}\lambda_{(S+P)_-}\lambda_{\mathrm{csc}} + N_{\mathrm{c}}\lambda_{(S+P)_-^{\mathrm{adj}}}\lambda_{\mathrm{csc}}\Big) l_{\parallel+}^{(\mathrm{F})}\left(\tau,0,-i\tilde{\mu}_\tau\right) \\
&+ 64v_4\Big(- \lambda_{(\sigma\text{-}\pi)}\lambda_{(V+A)_\parallel} + \lambda_{(\sigma\text{-}\pi)}\lambda_{(V+A)_\perp} + \lambda_{(V+A)_\parallel^{\mathrm{adj}}}\lambda_{(V+A)_\perp} \\
&+ \frac{1}{2N_{\mathrm{c}}}\lambda_{(\sigma\text{-}\pi)}\lambda_{(V+A)_\parallel^{\mathrm{adj}}}\Big) l_{\parallel\pm}^{(\mathrm{F})}\left(\tau,0,-i\tilde{\mu}_\tau\right) \\
&+ 64v_4\Big(- \lambda_{(\sigma\text{-}\pi)}^2 - 4\lambda_{(\sigma\text{-}\pi)}\lambda_{(S+P)_-} - 4\lambda_{(S+P)_-}^2 - \frac{2}{3}\lambda_{(\sigma\text{-}\pi)}\lambda_{(S+P)_-^{\mathrm{adj}}} - \frac{4}{3}\lambda_{(S+P)_-}\lambda_{(S+P)_-^{\mathrm{adj}}} \\
&+ \lambda_{(\sigma\text{-}\pi)}\lambda_{(V+A)_\parallel} + \frac{1}{3}\lambda_{(\sigma\text{-}\pi)}\lambda_{(V-A)_\parallel} - \frac{1}{3}\lambda_{(V+A)_\parallel}\lambda_{(V+A)_\parallel^{\mathrm{adj}}} + 3\lambda_{(\sigma\text{-}\pi)}\lambda_{(V+A)_\perp} \\
&+ \frac{1}{3}\lambda_{(\sigma\text{-}\pi)}\lambda_{(V-A)_\perp} + \frac{2}{3}\lambda_{(\sigma\text{-}\pi)}\lambda_{(V-A)_\perp^{\mathrm{adj}}} - \frac{1}{N_{\mathrm{c}}^2}\lambda_{(S+P)_-^{\mathrm{adj}}}^2 + \frac{2}{N_{\mathrm{c}}}\lambda_{(\sigma\text{-}\pi)}\lambda_{(S+P)_-^{\mathrm{adj}}} \\
&+ \frac{5}{3N_{\mathrm{c}}}\lambda_{(S+P)_-^{\mathrm{adj}}}^2 - \frac{1}{2N_{\mathrm{c}}}\lambda_{(\sigma\text{-}\pi)}\lambda_{(V+A)_\parallel^{\mathrm{adj}}} + \frac{1}{6N_{\mathrm{c}}}\lambda_{(V+A)_\parallel^{\mathrm{adj}}}^2 - \frac{1}{6N_{\mathrm{c}}}\lambda_{(\sigma\text{-}\pi)}\lambda_{(V-A)_\perp^{\mathrm{adj}}} - 2N_{\mathrm{c}}\lambda_{(\sigma\text{-}\pi)}^2 \\
&- 4N_{\mathrm{c}}\lambda_{(\sigma\text{-}\pi)}\lambda_{(S+P)_-} - 4N_{\mathrm{c}}\lambda_{(S+P)_-}^2 - N_{\mathrm{c}}\lambda_{(\sigma\text{-}\pi)}\lambda_{(S+P)_-^{\mathrm{adj}}} - 2N_{\mathrm{c}}\lambda_{(S+P)_-}\lambda_{(S+P)_-^{\mathrm{adj}}} - \frac{N_{\mathrm{c}}}{3}\lambda_{(S+P)_-^{\mathrm{adj}}}^2 \\
&+ \frac{N_{\mathrm{c}}}{2}\lambda_{(\sigma\text{-}\pi)}\lambda_{(V+A)_\parallel^{\mathrm{adj}}} - \frac{N_{\mathrm{c}}}{12}\lambda_{(V+A)_\parallel^{\mathrm{adj}}}^2 - \frac{1}{3}\lambda_{(\sigma\text{-}\pi)}\lambda_{\mathrm{csc}} - \frac{4}{3}\lambda_{(S+P)_-}\lambda_{\mathrm{csc}} - \frac{1}{3}\lambda_{(S+P)_-^{\mathrm{adj}}}\lambda_{\mathrm{csc}} \\
&+ \frac{2}{3N_{\mathrm{c}}}\lambda_{(S+P)_-^{\mathrm{adj}}}\lambda_{\mathrm{csc}} + N_{\mathrm{c}}\lambda_{(\sigma\text{-}\pi)}\lambda_{\mathrm{csc}} + 2N_{\mathrm{c}}\lambda_{(S+P)_-}\lambda_{\mathrm{csc}} + \frac{N_{\mathrm{c}}}{3}\lambda_{(S+P)_-^{\mathrm{adj}}}\lambda_{\mathrm{csc}} + \frac{2}{3}\lambda_{\mathrm{csc}}^2 \\
&- \frac{2}{3}\lambda_{(V+A)_\parallel^{\mathrm{adj}}}\lambda_{(V+A)_\perp} + \frac{4}{N_{\mathrm{c}}}\lambda_{(S+P)_-}\lambda_{(S+P)_-^{\mathrm{adj}}} - \frac{N_{\mathrm{c}}}{3}\lambda_{\mathrm{csc}}^2\Big) l_{\perp+}^{(\mathrm{F})}\left(\tau,0,-i\tilde{\mu}_\tau\right) \\
&+ 64v_4\Big(\frac{1}{3}\lambda_{(\sigma\text{-}\pi)}\lambda_{(V+A)_\parallel} + \frac{1}{3}\lambda_{(V+A)_\parallel}\lambda_{(V+A)_\parallel^{\mathrm{adj}}} - \frac{5}{3}\lambda_{(\sigma\text{-}\pi)}\lambda_{(V+A)_\perp} - \frac{2}{3}\lambda_{(V+A)_\parallel^{\mathrm{adj}}}\lambda_{(V+A)_\perp} \\
&- \frac{1}{6N_{\mathrm{c}}}\lambda_{(\sigma\text{-}\pi)}\lambda_{(V+A)_\parallel^{\mathrm{adj}}} - \frac{1}{6N_{\mathrm{c}}}\lambda_{(V+A)_\parallel^{\mathrm{adj}}}^2\Big) l_{\perp\pm}^{(\mathrm{F})}\left(\tau,0,-i\tilde{\mu}_\tau\right)\ ,
\end{aligned}
$$

$$
\begin{aligned}
&\partial_t \lambda_{\text{csc}} = \\
&2\lambda_{\text{csc}} + 64 v_4 \Big(- \lambda^2_{(\sigma\text{-}\pi)} + 2\lambda_{(\sigma\text{-}\pi)}\lambda_{(V+A)^{\text{adj}}_{\parallel}} - \lambda^2_{(V+A)^{\text{adj}}_{\parallel}} + 3\lambda_{(V-A)_{\perp}}\lambda_{(V-A)^{\text{adj}}_{\perp}} - \frac{3}{2N_{\text{c}}}\lambda^2_{(V-A)^{\text{adj}}_{\perp}} \\
&+ \frac{3N_{\text{c}}}{4}\lambda^2_{(V-A)^{\text{adj}}_{\perp}} + 2\lambda_{(V-A)_{\parallel}}\lambda_{\text{csc}} - \frac{3}{2}\lambda_{(V-A)^{\text{adj}}_{\perp}}\lambda_{\text{csc}} + \frac{3N_{\text{c}}}{2}\lambda_{(V-A)^{\text{adj}}_{\perp}}\lambda_{\text{csc}} - 2\lambda^2_{\text{csc}} \\
&+ N_{\text{c}}\lambda^2_{\text{csc}}\Big) l^{(\text{F})}_{\parallel +}\left(\tau, 0, -i\tilde{\mu}_\tau\right) \\
&+ 64 v_4 \Big(- \lambda^2_{(\sigma\text{-}\pi)} - 4\lambda_{(\sigma\text{-}\pi)}\lambda_{(S+P)_-} - 4\lambda^2_{(S+P)_-} - 4\lambda_{(\sigma\text{-}\pi)}\lambda_{(S+P)^{\text{adj}}_{-}} - 8\lambda_{(S+P)_-}\lambda_{(S+P)^{\text{adj}}_{-}} \\
&- 3\lambda_{(V-A)_{\perp}}\lambda_{(V-A)^{\text{adj}}_{\perp}} - \frac{1}{N_{\text{c}}^2}\lambda^2_{(S+P)^{\text{adj}}_{-}} + \frac{2}{N_{\text{c}}}\lambda_{(\sigma\text{-}\pi)}\lambda_{(S+P)^{\text{adj}}_{-}} + \frac{4}{N_{\text{c}}}\lambda_{(S+P)_-}\lambda_{(S+P)^{\text{adj}}_{-}} \\
&+ \frac{3}{2N_{\text{c}}}\lambda^2_{(V-A)^{\text{adj}}_{\perp}} - 2\lambda_{(\sigma\text{-}\pi)}\lambda_{\text{csc}} - 4\lambda_{(S+P)_-}\lambda_{\text{csc}} + 2\lambda_{(S+P)^{\text{adj}}_{-}}\lambda_{\text{csc}} - \lambda_{(V-A)_{\parallel}}\lambda_{\text{csc}} - 3\lambda_{(V-A)_{\perp}}\lambda_{\text{csc}} \\
&+ \frac{3}{2}\lambda_{(V-A)^{\text{adj}}_{\perp}}\lambda_{\text{csc}} + \frac{2}{N_{\text{c}}}\lambda_{(S+P)^{\text{adj}}_{-}}\lambda_{\text{csc}} + \frac{3}{2N_{\text{c}}}\lambda_{(V-A)^{\text{adj}}_{\perp}}\lambda_{\text{csc}} \\
&- \lambda^2_{(S+P)^{\text{adj}}_{-}} + \frac{4}{N_{\text{c}}}\lambda^2_{(S+P)^{\text{adj}}_{-}} + 4\lambda^2_{\text{csc}}\Big) l^{(\text{F})}_{\parallel \pm}\left(\tau, 0, -i\tilde{\mu}_\tau\right) \\
&+ 64 v_4 \Big(\lambda^2_{(\sigma\text{-}\pi)} - 2\lambda_{(\sigma\text{-}\pi)}\lambda_{(V+A)^{\text{adj}}_{\parallel}} + \lambda^2_{(V+A)^{\text{adj}}_{\parallel}} + \lambda_{(V-A)_{\parallel}}\lambda_{(V-A)^{\text{adj}}_{\perp}} - 2\lambda_{(V-A)_{\perp}}\lambda_{(V-A)^{\text{adj}}_{\perp}} \\
&- \frac{N_{\text{c}}}{2}\lambda^2_{(V-A)^{\text{adj}}_{\perp}} + 2\lambda_{(V-A)_{\perp}}\lambda_{\text{csc}} + \frac{1}{2}\lambda_{(V-A)^{\text{adj}}_{\perp}}\lambda_{\text{csc}} - \frac{1}{N_{\text{c}}}\lambda_{(V-A)^{\text{adj}}_{\perp}}\lambda_{\text{csc}} \\
&+ \frac{1}{N_{\text{c}}}\lambda^2_{(V-A)^{\text{adj}}_{\perp}} - \frac{N_{\text{c}}}{2}\lambda_{(V-A)^{\text{adj}}_{\perp}}\lambda_{\text{csc}}\Big) l^{(\text{F})}_{\perp +}\left(\tau, 0, -i\tilde{\mu}_\tau\right) \\
&+ 64 v_4 \Big(\lambda^2_{(\sigma\text{-}\pi)} + 4\lambda_{(\sigma\text{-}\pi)}\lambda_{(S+P)_-} + 4\lambda^2_{(S+P)_-} + \lambda^2_{(S+P)^{\text{adj}}_{-}} - \lambda_{(V-A)_{\parallel}}\lambda_{(V-A)^{\text{adj}}_{\perp}} \\
&+ \frac{1}{N_{\text{c}}^2}\lambda^2_{(S+P)^{\text{adj}}_{-}} - \frac{2}{N_{\text{c}}}\lambda_{(\sigma\text{-}\pi)}\lambda_{(S+P)^{\text{adj}}_{-}} - \frac{4}{N_{\text{c}}}\lambda_{(S+P)_-}\lambda_{(S+P)^{\text{adj}}_{-}} + \frac{1}{N_{\text{c}}}\lambda^2_{(V-A)^{\text{adj}}_{\perp}} - 2\lambda_{(\sigma\text{-}\pi)}\lambda_{\text{csc}} \\
&- 4\lambda_{(S+P)_-}\lambda_{\text{csc}} + 2\lambda_{(S+P)^{\text{adj}}_{-}}\lambda_{\text{csc}} - \lambda_{(V-A)_{\parallel}}\lambda_{\text{csc}} - 3\lambda_{(V-A)_{\perp}}\lambda_{\text{csc}} + \frac{3}{2}\lambda_{(V-A)^{\text{adj}}_{\perp}}\lambda_{\text{csc}} \\
&+ \frac{2}{N_{\text{c}}}\lambda_{(S+P)^{\text{adj}}_{-}}\lambda_{\text{csc}} + \frac{3}{2N_{\text{c}}}\lambda_{(V-A)^{\text{adj}}_{\perp}}\lambda_{\text{csc}} + 4\lambda^2_{\text{csc}} - 2\lambda_{(V-A)_{\perp}}\lambda_{(V-A)^{\text{adj}}_{\perp}}\Big) l^{(\text{F})}_{\perp \pm}\left(\tau, 0, -i\tilde{\mu}_\tau\right) \,,
\end{aligned}
$$

$$
\begin{aligned}
&\partial_t \lambda_{(S+P)^{\text{adj}}_{-}} = \\
&2\lambda_{(S+P)^{\text{adj}}_{-}} + 64 v_4 \Big(\lambda^2_{(\sigma\text{-}\pi)} + 2\lambda_{(S+P)^{\text{adj}}_{-}}\lambda_{(V+A)_{\parallel}} - \frac{3}{2}\lambda_{(\sigma\text{-}\pi)}\lambda_{(V+A)^{\text{adj}}_{\parallel}} + \lambda_{(S+P)_-}\lambda_{(V+A)^{\text{adj}}_{\parallel}} \\
&+ \lambda^2_{(V+A)^{\text{adj}}_{\parallel}} + 2\lambda_{(\sigma\text{-}\pi)}\lambda_{(V+A)_{\perp}} + 4\lambda_{(S+P)_-}\lambda_{(V+A)_{\perp}} + 2\lambda_{(S+P)^{\text{adj}}_{-}}\lambda_{(V+A)_{\perp}} - 3\lambda_{(V-A)_{\perp}}\lambda_{(V-A)^{\text{adj}}_{\perp}} \\
&- \frac{3}{2N_{\text{c}}}\lambda_{(S+P)^{\text{adj}}_{-}}\lambda_{(V+A)^{\text{adj}}_{\parallel}} - \frac{2}{N_{\text{c}}}\lambda_{(S+P)^{\text{adj}}_{-}}\lambda_{(V+A)_{\perp}} + \frac{3}{2N_{\text{c}}}\lambda^2_{(V-A)^{\text{adj}}_{\perp}} + \frac{N_{\text{c}}}{2}\lambda_{(S+P)^{\text{adj}}_{-}}\lambda_{(V+A)^{\text{adj}}_{\parallel}} \\
&- \frac{3N_{\text{c}}}{4}\lambda^2_{(V-A)^{\text{adj}}_{\perp}} + 2\lambda_{(V+A)_{\parallel}}\lambda_{\text{csc}} - 2\lambda_{(V-A)_{\parallel}}\lambda_{\text{csc}} - \frac{1}{2}\lambda_{(V+A)^{\text{adj}}_{\parallel}}\lambda_{\text{csc}} + \frac{3}{2}\lambda_{(V-A)^{\text{adj}}_{\perp}}\lambda_{\text{csc}} \\
&- \frac{1}{N_{\text{c}}}\lambda_{(V+A)^{\text{adj}}_{\parallel}}\lambda_{\text{csc}} + \frac{N_{\text{c}}}{2}\lambda_{(V+A)^{\text{adj}}_{\parallel}}\lambda_{\text{csc}} - \frac{3N_{\text{c}}}{2}\lambda_{(V-A)^{\text{adj}}_{\perp}}\lambda_{\text{csc}} + 2\lambda^2_{\text{csc}} - N_{\text{c}}\lambda^2_{\text{csc}}\Big) l^{(\text{F})}_{\parallel +}\left(\tau, 0, -i\tilde{\mu}_\tau\right) \\
&+ 64 v_4 \Big(\lambda^2_{(\sigma\text{-}\pi)} + 4\lambda_{(\sigma\text{-}\pi)}\lambda_{(S+P)_-} + 4\lambda^2_{(S+P)_-} + 4\lambda_{(\sigma\text{-}\pi)}\lambda_{(S+P)^{\text{adj}}_{-}} + 8\lambda_{(S+P)_-}\lambda_{(S+P)^{\text{adj}}_{-}}
\end{aligned}
$$

$$
\begin{aligned}
&+\lambda^2_{(S+P)_-^{\mathrm{adj}}}-\lambda_{(S+P)_-^{\mathrm{adj}}}\lambda_{(V-A)_\parallel}+2\lambda_{(\sigma\text{-}\pi)}\lambda_{(V-A)_\perp}+4\lambda_{(S+P)_-}\lambda_{(V-A)_\perp}-\lambda_{(S+P)_-^{\mathrm{adj}}}\lambda_{(V-A)_\perp}\\
&-\frac{1}{2}\lambda_{(\sigma\text{-}\pi)}\lambda_{(V-A)_\perp^{\mathrm{adj}}}-\lambda_{(S+P)_-}\lambda_{(V-A)_\perp^{\mathrm{adj}}}+\lambda_{(S+P)_-^{\mathrm{adj}}}\lambda_{(V-A)_\perp^{\mathrm{adj}}}+3\lambda_{(V-A)_\perp}\lambda_{(V-A)_\perp^{\mathrm{adj}}}\\
&+\frac{1}{N_{\mathrm{c}}^2}\lambda_{(S+P)_-^{\mathrm{adj}}}\lambda_{(V-A)_\perp^{\mathrm{adj}}}-\frac{2}{N_{\mathrm{c}}}\lambda_{(\sigma\text{-}\pi)}\lambda_{(S+P)_-^{\mathrm{adj}}}-\frac{4}{N_{\mathrm{c}}}\lambda_{(S+P)_-}\lambda_{(S+P)_-^{\mathrm{adj}}}-\frac{4}{N_{\mathrm{c}}}\lambda^2_{(S+P)_-^{\mathrm{adj}}}\\
&-\frac{2}{N_{\mathrm{c}}}\lambda_{(S+P)_-^{\mathrm{adj}}}\lambda_{(V-A)_\perp}-\frac{1}{N_{\mathrm{c}}}\lambda_{(\sigma\text{-}\pi)}\lambda_{(V-A)_\perp^{\mathrm{adj}}}-\frac{2}{N_{\mathrm{c}}}\lambda_{(S+P)_-}\lambda_{(V-A)_\perp^{\mathrm{adj}}}+\frac{1}{N_{\mathrm{c}}}\lambda_{(S+P)_-^{\mathrm{adj}}}\lambda_{(V-A)_\perp^{\mathrm{adj}}}\\
&+\frac{1}{N_{\mathrm{c}}^2}\lambda^2_{(S+P)_-^{\mathrm{adj}}}-\frac{3}{2N_{\mathrm{c}}}\lambda^2_{(V-A)_\perp^{\mathrm{adj}}}\Big)\,l^{(\mathrm{F})}_{\parallel\pm}(\tau,0,-i\tilde{\mu}_\tau)\\
&+64v_4\Big(-\lambda^2_{(\sigma\text{-}\pi)}+\frac{2}{3}\lambda_{(\sigma\text{-}\pi)}\lambda_{(V+A)_\parallel}+\frac{4}{3}\lambda_{(S+P)_-}\lambda_{(V+A)_\parallel}+\frac{2}{3}\lambda_{(S+P)_-^{\mathrm{adj}}}\lambda_{(V+A)_\parallel}+\frac{11}{6}\lambda_{(\sigma\text{-}\pi)}\lambda_{(V+A)_\parallel^{\mathrm{adj}}}\\
&-\frac{1}{3}\lambda_{(S+P)_-}\lambda_{(V+A)_\parallel^{\mathrm{adj}}}-\lambda^2_{(V+A)_\parallel^{\mathrm{adj}}}+\frac{4}{3}\lambda_{(\sigma\text{-}\pi)}\lambda_{(V+A)_\perp}+\frac{8}{3}\lambda_{(S+P)_-}\lambda_{(V+A)_\perp}+\frac{10}{3}\lambda_{(S+P)_-^{\mathrm{adj}}}\lambda_{(V+A)_\perp}\\
&-\lambda_{(V-A)_\parallel}\lambda_{(V-A)_\perp^{\mathrm{adj}}}+2\lambda_{(V-A)_\perp}\lambda_{(V-A)_\perp^{\mathrm{adj}}}+\frac{1}{3N_{\mathrm{c}}^2}\lambda_{(S+P)_-^{\mathrm{adj}}}\lambda_{(V+A)_\parallel^{\mathrm{adj}}}-\frac{2}{3N_{\mathrm{c}}}\lambda_{(S+P)_-^{\mathrm{adj}}}\lambda_{(V+A)_\parallel}\\
&-\frac{1}{3N_{\mathrm{c}}}\lambda_{(\sigma\text{-}\pi)}\lambda_{(V+A)_\parallel^{\mathrm{adj}}}-\frac{2}{3N_{\mathrm{c}}}\lambda_{(S+P)_-}\lambda_{(V+A)_\parallel^{\mathrm{adj}}}-\frac{1}{6N_{\mathrm{c}}}\lambda_{(S+P)_-^{\mathrm{adj}}}\lambda_{(V+A)_\parallel^{\mathrm{adj}}}-\frac{4}{3N_{\mathrm{c}}}\lambda_{(S+P)_-^{\mathrm{adj}}}\lambda_{(V+A)_\perp}\\
&-\frac{1}{N_{\mathrm{c}}}\lambda^2_{(V-A)_\perp^{\mathrm{adj}}}-\frac{N_{\mathrm{c}}}{6}\lambda_{(S+P)_-^{\mathrm{adj}}}\lambda_{(V+A)_\parallel^{\mathrm{adj}}}+\frac{N_{\mathrm{c}}}{2}\lambda^2_{(V-A)_\perp^{\mathrm{adj}}}+\frac{1}{6}\lambda_{(V+A)_\parallel^{\mathrm{adj}}}\lambda_{\mathrm{csc}}+2\lambda_{(V+A)_\perp}\lambda_{\mathrm{csc}}\\
&-2\lambda_{(V-A)_\perp}\lambda_{\mathrm{csc}}-\frac{1}{2}\lambda_{(V-A)_\perp^{\mathrm{adj}}}\lambda_{\mathrm{csc}}+\frac{1}{N_{\mathrm{c}}}\lambda_{(V-A)_\perp^{\mathrm{adj}}}\lambda_{\mathrm{csc}}-\frac{N_{\mathrm{c}}}{6}\lambda_{(V+A)_\parallel^{\mathrm{adj}}}\lambda_{\mathrm{csc}}\\
&+\frac{N_{\mathrm{c}}}{2}\lambda_{(V-A)_\perp^{\mathrm{adj}}}\lambda_{\mathrm{csc}}\Big)\,l^{(\mathrm{F})}_{\perp+}(\tau,0,-i\tilde{\mu}_\tau)\\
&+64v_4\Big(-\lambda^2_{(\sigma\text{-}\pi)}-4\lambda_{(\sigma\text{-}\pi)}\lambda_{(S+P)_-}-4\lambda^2_{(S+P)_-}-\lambda^2_{(S+P)_-^{\mathrm{adj}}}+\frac{2}{3}\lambda_{(\sigma\text{-}\pi)}\lambda_{(V-A)_\parallel}+\frac{4}{3}\lambda_{(S+P)_-}\lambda_{(V-A)_\parallel}\\
&-\frac{1}{3}\lambda_{(S+P)_-^{\mathrm{adj}}}\lambda_{(V-A)_\parallel}+\frac{4}{3}\lambda_{(\sigma\text{-}\pi)}\lambda_{(V-A)_\perp}+\frac{8}{3}\lambda_{(S+P)_-}\lambda_{(V-A)_\perp}-\frac{5}{3}\lambda_{(S+P)_-^{\mathrm{adj}}}\lambda_{(V-A)_\perp}\\
&-\frac{5}{6}\lambda_{(\sigma\text{-}\pi)}\lambda_{(V-A)_\perp^{\mathrm{adj}}}-\frac{5}{3}\lambda_{(S+P)_-}\lambda_{(V-A)_\perp^{\mathrm{adj}}}+\frac{2}{3}\lambda_{(S+P)_-^{\mathrm{adj}}}\lambda_{(V-A)_\perp^{\mathrm{adj}}}+\lambda_{(V-A)_\parallel}\lambda_{(V-A)_\perp^{\mathrm{adj}}}\\
&+2\lambda_{(V-A)_\perp}\lambda_{(V-A)_\perp^{\mathrm{adj}}}-\frac{1}{N_{\mathrm{c}}^2}\lambda^2_{(S+P)_-^{\mathrm{adj}}}+\frac{2}{3N_{\mathrm{c}}^2}\lambda_{(S+P)_-^{\mathrm{adj}}}\lambda_{(V-A)_\perp^{\mathrm{adj}}}+\frac{2}{N_{\mathrm{c}}}\lambda_{(\sigma\text{-}\pi)}\lambda_{(S+P)_-^{\mathrm{adj}}}\\
&+\frac{4}{N_{\mathrm{c}}}\lambda_{(S+P)_-}\lambda_{(S+P)_-^{\mathrm{adj}}}-\frac{2}{3N_{\mathrm{c}}}\lambda_{(S+P)_-^{\mathrm{adj}}}\lambda_{(V-A)_\parallel}-\frac{4}{3N_{\mathrm{c}}}\lambda_{(S+P)_-^{\mathrm{adj}}}\lambda_{(V-A)_\perp}-\frac{2}{3N_{\mathrm{c}}}\lambda_{(\sigma\text{-}\pi)}\lambda_{(V-A)_\perp^{\mathrm{adj}}}\\
&-\frac{4}{3N_{\mathrm{c}}}\lambda_{(S+P)_-}\lambda_{(V-A)_\perp^{\mathrm{adj}}}+\frac{5}{3N_{\mathrm{c}}}\lambda_{(S+P)_-^{\mathrm{adj}}}\lambda_{(V-A)_\perp^{\mathrm{adj}}}-\frac{1}{N_{\mathrm{c}}}\lambda^2_{(V-A)_\perp^{\mathrm{adj}}}\Big)\,l^{(\mathrm{F})}_{\perp\pm}(\tau,0,-i\tilde{\mu}_\tau)\ ,
\end{aligned}
$$

$$
\begin{aligned}
&\partial_t\lambda_{(S+P)_-}=\\
&2\lambda_{(S+P)_-}+64v_4\Big(-\frac{1}{2}\lambda^2_{(\sigma\text{-}\pi)}+\lambda_{(\sigma\text{-}\pi)}\lambda_{(S+P)_-}+2\lambda^2_{(S+P)_-}+\frac{1}{2}\lambda_{(\sigma\text{-}\pi)}\lambda_{(V+A)_\parallel}+2\lambda_{(S+P)_-}\lambda_{(V+A)_\parallel}\\
&-\frac{1}{2}\lambda_{(\sigma\text{-}\pi)}\lambda_{(V-A)_\parallel}+\lambda_{(\sigma\text{-}\pi)}\lambda_{(V+A)_\parallel^{\mathrm{adj}}}+\frac{1}{4}\lambda_{(S+P)_-^{\mathrm{adj}}}\lambda_{(V+A)_\parallel^{\mathrm{adj}}}-\frac{1}{2}\lambda^2_{(V+A)_\parallel^{\mathrm{adj}}}-\frac{1}{2}\lambda_{(\sigma\text{-}\pi)}\lambda_{(V+A)_\perp}\\
&+2\lambda_{(S+P)_-}\lambda_{(V+A)_\perp}+\lambda_{(S+P)_-^{\mathrm{adj}}}\lambda_{(V+A)_\perp}+\frac{1}{2}\lambda_{(V+A)_\parallel^{\mathrm{adj}}}\lambda_{(V+A)_\perp}-\frac{1}{2}\lambda_{(\sigma\text{-}\pi)}\lambda_{(V-A)_\perp}\\
&-\lambda_{(\sigma\text{-}\pi)}\lambda_{(V-A)_\perp^{\mathrm{adj}}}+\frac{3}{2}\lambda_{(V-A)_\perp}\lambda_{(V-A)_\perp^{\mathrm{adj}}}-\frac{3}{8}\lambda^2_{(V-A)_\perp^{\mathrm{adj}}}+\frac{1}{2N_{\mathrm{c}}^2}\lambda^2_{(S+P)_-^{\mathrm{adj}}}-\frac{1}{4N_{\mathrm{c}}^2}\lambda_{(S+P)_-^{\mathrm{adj}}}\lambda_{(V+A)_\parallel^{\mathrm{adj}}}\\
&-\frac{1}{N_{\mathrm{c}}^2}\lambda_{(S+P)_-^{\mathrm{adj}}}\lambda_{(V+A)_\perp}+\frac{3}{4N_{\mathrm{c}}^2}\lambda^2_{(V-A)_\perp^{\mathrm{adj}}}+\frac{1}{2N_{\mathrm{c}}}\lambda^2_{(\sigma\text{-}\pi)}-\frac{1}{2N_{\mathrm{c}}}\lambda_{(\sigma\text{-}\pi)}\lambda_{(S+P)_-^{\mathrm{adj}}}-\frac{2}{N_{\mathrm{c}}}\lambda_{(S+P)_-}\lambda_{(S+P)_-^{\mathrm{adj}}}
\end{aligned}
$$

$$
\begin{aligned}
&- \frac{1}{2N_{\mathrm{c}}}\lambda^{2}_{(S+P)_{-}^{\mathrm{adj}}} - \frac{1}{N_{\mathrm{c}}}\lambda_{(\sigma\text{-}\pi)}\lambda_{(V+A)_{\parallel}^{\mathrm{adj}}} - \frac{1}{2N_{\mathrm{c}}}\lambda_{(S+P)_{-}}\lambda_{(V+A)_{\parallel}^{\mathrm{adj}}} + \frac{1}{2N_{\mathrm{c}}}\lambda^{2}_{(V+A)_{\parallel}^{\mathrm{adj}}} \\
&+ \frac{1}{N_{\mathrm{c}}}\lambda_{(\sigma\text{-}\pi)}\lambda_{(V+A)_{\perp}} + \frac{2}{N_{\mathrm{c}}}\lambda_{(S+P)_{-}}\lambda_{(V+A)_{\perp}} + \frac{1}{4N_{\mathrm{c}}}\lambda_{(\sigma\text{-}\pi)}\lambda_{(V-A)_{\perp}^{\mathrm{adj}}} - \frac{3}{2N_{\mathrm{c}}}\lambda_{(V-A)_{\perp}}\lambda_{(V-A)_{\perp}^{\mathrm{adj}}} \\
&- \frac{3}{4N_{\mathrm{c}}}\lambda^{2}_{(V-A)_{\perp}^{\mathrm{adj}}} + 2N_{\mathrm{c}}\lambda^{2}_{(S+P)_{-}} + N_{\mathrm{c}}\lambda_{(S+P)_{-}}\lambda_{(S+P)_{-}^{\mathrm{adj}}} + \frac{N_{\mathrm{c}}}{2}\lambda_{(S+P)_{-}}\lambda_{(V+A)_{\parallel}^{\mathrm{adj}}} + \frac{3N_{\mathrm{c}}}{8}\lambda^{2}_{(V-A)_{\perp}^{\mathrm{adj}}} \\
&- \lambda_{(\sigma\text{-}\pi)}\lambda_{\mathrm{csc}} + \frac{1}{2}\lambda_{(S+P)_{-}^{\mathrm{adj}}}\lambda_{\mathrm{csc}} - \lambda_{(V+A)_{\parallel}}\lambda_{\mathrm{csc}} + \lambda_{(V-A)_{\parallel}}\lambda_{\mathrm{csc}} + \frac{1}{2}\lambda_{(V+A)_{\parallel}^{\mathrm{adj}}}\lambda_{\mathrm{csc}} - \frac{3}{2}\lambda_{(V-A)_{\perp}^{\mathrm{adj}}}\lambda_{\mathrm{csc}} \\
&- \frac{1}{2N_{\mathrm{c}}^{2}}\lambda_{(V+A)_{\parallel}^{\mathrm{adj}}}\lambda_{\mathrm{csc}} + \frac{1}{N_{\mathrm{c}}}\lambda_{(V+A)_{\parallel}}\lambda_{\mathrm{csc}} - \frac{1}{N_{\mathrm{c}}}\lambda_{(V-A)_{\parallel}}\lambda_{\mathrm{csc}} + \frac{1}{4N_{\mathrm{c}}}\lambda_{(V+A)_{\parallel}^{\mathrm{adj}}}\lambda_{\mathrm{csc}} \\
&- N_{\mathrm{c}}\lambda_{(S+P)_{-}}\lambda_{\mathrm{csc}} - \frac{N_{\mathrm{c}}}{2}\lambda_{(S+P)_{-}^{\mathrm{adj}}}\lambda_{\mathrm{csc}} - \frac{N_{\mathrm{c}}}{4}\lambda_{(V+A)_{\parallel}^{\mathrm{adj}}}\lambda_{\mathrm{csc}} + \frac{3N_{\mathrm{c}}}{4}\lambda_{(V-A)_{\perp}^{\mathrm{adj}}}\lambda_{\mathrm{csc}} - \frac{3}{2}\lambda^{2}_{\mathrm{csc}} + \frac{1}{N_{\mathrm{c}}}\lambda^{2}_{\mathrm{csc}} \\
&+ \frac{3}{4N_{\mathrm{c}}}\lambda_{(V-A)_{\perp}^{\mathrm{adj}}}\lambda_{\mathrm{csc}} + \frac{N_{\mathrm{c}}}{2}\lambda^{2}_{\mathrm{csc}}\Big)l^{(\mathrm{F})}_{\parallel+}\left(\tau,0,-i\tilde{\mu}_{\tau}\right) \\
&+ 64v_{4}\Big(- \frac{1}{2}\lambda^{2}_{(\sigma\text{-}\pi)} - 2\lambda_{(\sigma\text{-}\pi)}\lambda_{(S+P)_{-}} - 2\lambda^{2}_{(S+P)_{-}} - 2\lambda_{(\sigma\text{-}\pi)}\lambda_{(S+P)_{-}^{\mathrm{adj}}} - 4\lambda_{(S+P)_{-}}\lambda_{(S+P)_{-}^{\mathrm{adj}}} \\
&- \frac{1}{2}\lambda^{2}_{(S+P)_{-}^{\mathrm{adj}}} + \frac{1}{2}\lambda_{(\sigma\text{-}\pi)}\lambda_{(V+A)_{\parallel}} - \frac{1}{2}\lambda_{(\sigma\text{-}\pi)}\lambda_{(V-A)_{\parallel}} - \lambda_{(S+P)_{-}}\lambda_{(V-A)_{\parallel}} - \frac{1}{2}\lambda_{(\sigma\text{-}\pi)}\lambda_{(V+A)_{\perp}} \\
&- \frac{1}{2}\lambda_{(V+A)_{\parallel}^{\mathrm{adj}}}\lambda_{(V+A)_{\perp}} - \frac{1}{2}\lambda_{(\sigma\text{-}\pi)}\lambda_{(V-A)_{\perp}} - \lambda_{(S+P)_{-}}\lambda_{(V-A)_{\perp}} + \lambda_{(S+P)_{-}^{\mathrm{adj}}}\lambda_{(V-A)_{\perp}} \\
&+ \frac{1}{2}\lambda_{(\sigma\text{-}\pi)}\lambda_{(V-A)_{\perp}^{\mathrm{adj}}} + \lambda_{(S+P)_{-}}\lambda_{(V-A)_{\perp}^{\mathrm{adj}}} - \frac{1}{4}\lambda_{(S+P)_{-}^{\mathrm{adj}}}\lambda_{(V-A)_{\perp}^{\mathrm{adj}}} - \frac{3}{2}\lambda_{(V-A)_{\perp}}\lambda_{(V-A)_{\perp}^{\mathrm{adj}}} \\
&+ \frac{1}{2N_{\mathrm{c}}^{3}}\lambda^{2}_{(S+P)_{-}^{\mathrm{adj}}} + \frac{1}{2N_{\mathrm{c}}^{3}}\lambda_{(S+P)_{-}^{\mathrm{adj}}}\lambda_{(V-A)_{\perp}^{\mathrm{adj}}} - \frac{1}{N_{\mathrm{c}}^{2}}\lambda_{(\sigma\text{-}\pi)}\lambda_{(S+P)_{-}^{\mathrm{adj}}} - \frac{2}{N_{\mathrm{c}}^{2}}\lambda_{(S+P)_{-}}\lambda_{(S+P)_{-}^{\mathrm{adj}}} \\
&- \frac{5}{2N_{\mathrm{c}}^{2}}\lambda^{2}_{(S+P)_{-}^{\mathrm{adj}}} - \frac{1}{N_{\mathrm{c}}^{2}}\lambda_{(S+P)_{-}^{\mathrm{adj}}}\lambda_{(V-A)_{\perp}} - \frac{1}{2N_{\mathrm{c}}^{2}}\lambda_{(\sigma\text{-}\pi)}\lambda_{(V-A)_{\perp}^{\mathrm{adj}}} - \frac{1}{N_{\mathrm{c}}^{2}}\lambda_{(S+P)_{-}}\lambda_{(V-A)_{\perp}^{\mathrm{adj}}} \\
&+ \frac{1}{4N_{\mathrm{c}}^{2}}\lambda_{(S+P)_{-}^{\mathrm{adj}}}\lambda_{(V-A)_{\perp}^{\mathrm{adj}}} - \frac{3}{4N_{\mathrm{c}}^{2}}\lambda^{2}_{(V-A)_{\perp}^{\mathrm{adj}}} + \frac{1}{2N_{\mathrm{c}}}\lambda^{2}_{(\sigma\text{-}\pi)} + \frac{2}{N_{\mathrm{c}}}\lambda_{(\sigma\text{-}\pi)}\lambda_{(S+P)_{-}} + \frac{2}{N_{\mathrm{c}}}\lambda^{2}_{(S+P)_{-}} \\
&+ \frac{3}{N_{\mathrm{c}}}\lambda_{(\sigma\text{-}\pi)}\lambda_{(S+P)_{-}^{\mathrm{adj}}} + \frac{6}{N_{\mathrm{c}}}\lambda_{(S+P)_{-}}\lambda_{(S+P)_{-}^{\mathrm{adj}}} + \frac{5}{2N_{\mathrm{c}}}\lambda^{2}_{(S+P)_{-}^{\mathrm{adj}}} - \frac{1}{4N_{\mathrm{c}}}\lambda_{(\sigma\text{-}\pi)}\lambda_{(V+A)_{\parallel}^{\mathrm{adj}}} \\
&+ \frac{1}{N_{\mathrm{c}}}\lambda_{(\sigma\text{-}\pi)}\lambda_{(V-A)_{\perp}} + \frac{2}{N_{\mathrm{c}}}\lambda_{(S+P)_{-}}\lambda_{(V-A)_{\perp}} - \frac{1}{2N_{\mathrm{c}}}\lambda_{(S+P)_{-}^{\mathrm{adj}}}\lambda_{(V-A)_{\perp}^{\mathrm{adj}}} + \frac{3}{2N_{\mathrm{c}}}\lambda_{(V-A)_{\perp}}\lambda_{(V-A)_{\perp}^{\mathrm{adj}}} \\
&+ \frac{3}{4N_{\mathrm{c}}}\lambda^{2}_{(V-A)_{\perp}^{\mathrm{adj}}}\Big)l^{(\mathrm{F})}_{\parallel\pm}\left(\tau,0,-i\tilde{\mu}_{\tau}\right) \\
&+ 64v_{4}\Big(\frac{1}{2}\lambda^{2}_{(\sigma\text{-}\pi)} + \lambda_{(\sigma\text{-}\pi)}\lambda_{(S+P)_{-}} + 2\lambda^{2}_{(S+P)_{-}} + \frac{1}{3}\lambda_{(\sigma\text{-}\pi)}\lambda_{(S+P)_{-}^{\mathrm{adj}}} + \frac{2}{3}\lambda_{(S+P)_{-}}\lambda_{(S+P)_{-}^{\mathrm{adj}}} \\
&- \frac{1}{6}\lambda_{(\sigma\text{-}\pi)}\lambda_{(V+A)_{\parallel}} + \frac{2}{3}\lambda_{(S+P)_{-}}\lambda_{(V+A)_{\parallel}} + \frac{1}{3}\lambda_{(S+P)_{-}^{\mathrm{adj}}}\lambda_{(V+A)_{\parallel}} - \frac{1}{6}\lambda_{(\sigma\text{-}\pi)}\lambda_{(V-A)_{\parallel}} - \frac{5}{6}\lambda_{(\sigma\text{-}\pi)}\lambda_{(V+A)_{\parallel}^{\mathrm{adj}}} \\
&+ \frac{1}{3}\lambda_{(S+P)_{-}}\lambda_{(V+A)_{\parallel}^{\mathrm{adj}}} - \frac{1}{12}\lambda_{(S+P)_{-}^{\mathrm{adj}}}\lambda_{(V+A)_{\parallel}^{\mathrm{adj}}} + \frac{1}{6}\lambda_{(V+A)_{\parallel}}\lambda_{(V+A)_{\parallel}^{\mathrm{adj}}} + \frac{1}{2}\lambda^{2}_{(V+A)_{\parallel}^{\mathrm{adj}}} \\
&+ \frac{1}{6}\lambda_{(\sigma\text{-}\pi)}\lambda_{(V+A)_{\perp}} + \frac{10}{3}\lambda_{(S+P)_{-}}\lambda_{(V+A)_{\perp}} + \frac{2}{3}\lambda_{(S+P)_{-}^{\mathrm{adj}}}\lambda_{(V+A)_{\perp}} + \frac{1}{3}\lambda_{(V+A)_{\parallel}^{\mathrm{adj}}}\lambda_{(V+A)_{\perp}} \\
&- \frac{1}{6}\lambda_{(\sigma\text{-}\pi)}\lambda_{(V-A)_{\perp}} - \frac{1}{3}\lambda_{(\sigma\text{-}\pi)}\lambda_{(V-A)_{\perp}^{\mathrm{adj}}} + \frac{1}{2}\lambda_{(V-A)_{\parallel}}\lambda_{(V-A)_{\perp}^{\mathrm{adj}}} - \lambda_{(V-A)_{\perp}}\lambda_{(V-A)_{\perp}^{\mathrm{adj}}} + \frac{1}{4}\lambda^{2}_{(V-A)_{\perp}^{\mathrm{adj}}} \\
&+ \frac{1}{6N_{\mathrm{c}}^{3}}\lambda_{(S+P)_{-}^{\mathrm{adj}}}\lambda_{(V+A)_{\parallel}^{\mathrm{adj}}} + \frac{1}{2N_{\mathrm{c}}^{2}}\lambda^{2}_{(S+P)_{-}^{\mathrm{adj}}} - \frac{1}{3N_{\mathrm{c}}^{2}}\lambda_{(S+P)_{-}^{\mathrm{adj}}}\lambda_{(V+A)_{\parallel}} - \frac{1}{6N_{\mathrm{c}}^{2}}\lambda_{(\sigma\text{-}\pi)}\lambda_{(V+A)_{\parallel}^{\mathrm{adj}}} \\
&- \frac{1}{3N_{\mathrm{c}}^{2}}\lambda_{(S+P)_{-}}\lambda_{(V+A)_{\parallel}^{\mathrm{adj}}} + \frac{1}{12N_{\mathrm{c}}^{2}}\lambda_{(S+P)_{-}^{\mathrm{adj}}}\lambda_{(V+A)_{\parallel}^{\mathrm{adj}}} - \frac{2}{3N_{\mathrm{c}}^{2}}\lambda_{(S+P)_{-}^{\mathrm{adj}}}\lambda_{(V+A)_{\perp}} - \frac{1}{2N_{\mathrm{c}}^{2}}\lambda^{2}_{(V-A)_{\perp}^{\mathrm{adj}}}
\end{aligned}
$$

$$\begin{aligned}
&- \frac{1}{2N_{\mathrm{c}}}\lambda^2_{(\sigma\text{-}\pi)} - \frac{1}{2N_{\mathrm{c}}}\lambda_{(\sigma\text{-}\pi)}\lambda_{(S+P)^{\mathrm{adj}}_{-}} - \frac{2}{N_{\mathrm{c}}}\lambda_{(S+P)_-}\lambda_{(S+P)^{\mathrm{adj}}_{-}} - \frac{5}{6N_{\mathrm{c}}}\lambda^2_{(S+P)^{\mathrm{adj}}_{-}} + \frac{1}{3N_{\mathrm{c}}}\lambda_{(\sigma\text{-}\pi)}\lambda_{(V+A)_{\parallel}} \\
&+ \frac{2}{3N_{\mathrm{c}}}\lambda_{(S+P)_-}\lambda_{(V+A)_{\parallel}} + \frac{1}{N_{\mathrm{c}}}\lambda_{(\sigma\text{-}\pi)}\lambda_{(V+A)^{\mathrm{adj}}_{\parallel}} - \frac{1}{2N_{\mathrm{c}}}\lambda_{(S+P)_-}\lambda_{(V+A)^{\mathrm{adj}}_{\parallel}} - \frac{1}{3N_{\mathrm{c}}}\lambda_{(S+P)^{\mathrm{adj}}_{-}}\lambda_{(V+A)^{\mathrm{adj}}_{\parallel}} \\
&- \frac{7}{12N_{\mathrm{c}}}\lambda^2_{(V+A)^{\mathrm{adj}}_{\parallel}} + \frac{2}{3N_{\mathrm{c}}}\lambda_{(\sigma\text{-}\pi)}\lambda_{(V+A)_{\perp}} + \frac{4}{3N_{\mathrm{c}}}\lambda_{(S+P)_-}\lambda_{(V+A)_{\perp}} + \frac{1}{12N_{\mathrm{c}}}\lambda_{(\sigma\text{-}\pi)}\lambda_{(V-A)^{\mathrm{adj}}_{\perp}} \\
&- \frac{1}{2N_{\mathrm{c}}}\lambda_{(V-A)_{\parallel}}\lambda_{(V-A)^{\mathrm{adj}}_{\perp}} + \frac{1}{N_{\mathrm{c}}}\lambda_{(V-A)_{\perp}}\lambda_{(V-A)^{\mathrm{adj}}_{\perp}} + \frac{1}{2N_{\mathrm{c}}}\lambda^2_{(V-A)^{\mathrm{adj}}_{\perp}} + 2N_{\mathrm{c}}\lambda^2_{(S+P)_-} \\
&+ N_{\mathrm{c}}\lambda_{(S+P)_-}\lambda_{(S+P)^{\mathrm{adj}}_{-}} + \frac{N_{\mathrm{c}}}{6}\lambda^2_{(S+P)^{\mathrm{adj}}_{-}} + \frac{N_{\mathrm{c}}}{2}\lambda_{(S+P)_-}\lambda_{(V+A)^{\mathrm{adj}}_{\parallel}} + \frac{N_{\mathrm{c}}}{6}\lambda_{(S+P)^{\mathrm{adj}}_{-}}\lambda_{(V+A)^{\mathrm{adj}}_{\parallel}} \\
&+ \frac{N_{\mathrm{c}}}{24}\lambda^2_{(V+A)^{\mathrm{adj}}_{\parallel}} - \frac{N_{\mathrm{c}}}{4}\lambda^2_{(V-A)^{\mathrm{adj}}_{\perp}} - \frac{1}{3}\lambda_{(\sigma\text{-}\pi)}\lambda_{\mathrm{csc}} + \frac{2}{3}\lambda_{(S+P)_-}\lambda_{\mathrm{csc}} + \frac{1}{6}\lambda_{(S+P)^{\mathrm{adj}}_{-}}\lambda_{\mathrm{csc}} - \lambda_{(V+A)_{\perp}}\lambda_{\mathrm{csc}} \\
&+ \lambda_{(V-A)_{\perp}}\lambda_{\mathrm{csc}} + \frac{1}{2}\lambda_{(V-A)^{\mathrm{adj}}_{\perp}}\lambda_{\mathrm{csc}} + \frac{1}{2N_{\mathrm{c}}^2}\lambda_{(V-A)^{\mathrm{adj}}_{\perp}}\lambda_{\mathrm{csc}} - \frac{1}{3N_{\mathrm{c}}}\lambda_{(S+P)^{\mathrm{adj}}_{-}}\lambda_{\mathrm{csc}} + \frac{1}{12N_{\mathrm{c}}}\lambda_{(V+A)^{\mathrm{adj}}_{\parallel}}\lambda_{\mathrm{csc}} \\
&+ \frac{1}{N_{\mathrm{c}}}\lambda_{(V+A)_{\perp}}\lambda_{\mathrm{csc}} - \frac{1}{N_{\mathrm{c}}}\lambda_{(V-A)_{\perp}}\lambda_{\mathrm{csc}} - \frac{3}{4N_{\mathrm{c}}}\lambda_{(V-A)^{\mathrm{adj}}_{\perp}}\lambda_{\mathrm{csc}} - N_{\mathrm{c}}\lambda_{(S+P)_-}\lambda_{\mathrm{csc}} - \frac{N_{\mathrm{c}}}{6}\lambda_{(S+P)^{\mathrm{adj}}_{-}}\lambda_{\mathrm{csc}} \\
&- \frac{N_{\mathrm{c}}}{12}\lambda_{(V+A)^{\mathrm{adj}}_{\parallel}}\lambda_{\mathrm{csc}} - \frac{N_{\mathrm{c}}}{4}\lambda_{(V-A)^{\mathrm{adj}}_{\perp}}\lambda_{\mathrm{csc}} - \frac{1}{3}\lambda^2_{\mathrm{csc}} + \frac{N_{\mathrm{c}}}{6}\lambda^2_{\mathrm{csc}}\Big) l^{(\mathrm{F})}_{\perp +}(\tau, 0, -i\tilde{\mu}_\tau) \\
&+ 64 v_4 \Big(\frac{1}{2}\lambda^2_{(\sigma\text{-}\pi)} + 2\lambda_{(\sigma\text{-}\pi)}\lambda_{(S+P)_-} + 2\lambda^2_{(S+P)_-} + \frac{1}{2}\lambda^2_{(S+P)^{\mathrm{adj}}_{-}} - \frac{1}{6}\lambda_{(\sigma\text{-}\pi)}\lambda_{(V+A)_{\parallel}} - \frac{1}{6}\lambda_{(\sigma\text{-}\pi)}\lambda_{(V-A)_{\parallel}} \\
&- \frac{1}{3}\lambda_{(S+P)_-}\lambda_{(V-A)_{\parallel}} + \frac{1}{3}\lambda_{(S+P)^{\mathrm{adj}}_{-}}\lambda_{(V-A)_{\parallel}} - \frac{1}{6}\lambda_{(V+A)_{\parallel}}\lambda_{(V+A)^{\mathrm{adj}}_{\parallel}} + \frac{5}{6}\lambda_{(\sigma\text{-}\pi)}\lambda_{(V+A)_{\perp}} \\
&+ \frac{1}{3}\lambda_{(V+A)^{\mathrm{adj}}_{\parallel}}\lambda_{(V+A)_{\perp}} - \frac{5}{6}\lambda_{(\sigma\text{-}\pi)}\lambda_{(V-A)_{\perp}} - \frac{5}{3}\lambda_{(S+P)_-}\lambda_{(V-A)_{\perp}} + \frac{2}{3}\lambda_{(S+P)^{\mathrm{adj}}_{-}}\lambda_{(V-A)_{\perp}} \\
&+ \frac{1}{3}\lambda_{(\sigma\text{-}\pi)}\lambda_{(V-A)^{\mathrm{adj}}_{\perp}} + \frac{2}{3}\lambda_{(S+P)_-}\lambda_{(V-A)^{\mathrm{adj}}_{\perp}} - \frac{5}{12}\lambda_{(S+P)^{\mathrm{adj}}_{-}}\lambda_{(V-A)^{\mathrm{adj}}_{\perp}} - \frac{1}{2}\lambda_{(V-A)_{\parallel}}\lambda_{(V-A)^{\mathrm{adj}}_{\perp}} \\
&- \lambda_{(V-A)_{\perp}}\lambda_{(V-A)^{\mathrm{adj}}_{\perp}} - \frac{1}{2N_{\mathrm{c}}^3}\lambda^2_{(S+P)^{\mathrm{adj}}_{-}} + \frac{1}{3N_{\mathrm{c}}^3}\lambda_{(S+P)^{\mathrm{adj}}_{-}}\lambda_{(V-A)^{\mathrm{adj}}_{\perp}} + \frac{1}{N_{\mathrm{c}}^2}\lambda_{(\sigma\text{-}\pi)}\lambda_{(S+P)^{\mathrm{adj}}_{-}} \\
&+ \frac{2}{N_{\mathrm{c}}^2}\lambda_{(S+P)_-}\lambda_{(S+P)^{\mathrm{adj}}_{-}} + \frac{1}{2N_{\mathrm{c}}^2}\lambda^2_{(S+P)^{\mathrm{adj}}_{-}} - \frac{1}{3N_{\mathrm{c}}^2}\lambda_{(S+P)^{\mathrm{adj}}_{-}}\lambda_{(V-A)_{\parallel}} - \frac{2}{3N_{\mathrm{c}}^2}\lambda_{(S+P)^{\mathrm{adj}}_{-}}\lambda_{(V-A)_{\perp}} \\
&- \frac{1}{3N_{\mathrm{c}}^2}\lambda_{(\sigma\text{-}\pi)}\lambda_{(V-A)^{\mathrm{adj}}_{\perp}} - \frac{2}{3N_{\mathrm{c}}^2}\lambda_{(S+P)_-}\lambda_{(V-A)^{\mathrm{adj}}_{\perp}} + \frac{5}{12N_{\mathrm{c}}^2}\lambda_{(S+P)^{\mathrm{adj}}_{-}}\lambda_{(V-A)^{\mathrm{adj}}_{\perp}} - \frac{1}{2N_{\mathrm{c}}^2}\lambda^2_{(V-A)^{\mathrm{adj}}_{\perp}} \\
&- \frac{1}{2N_{\mathrm{c}}}\lambda^2_{(\sigma\text{-}\pi)} - \frac{2}{N_{\mathrm{c}}}\lambda_{(\sigma\text{-}\pi)}\lambda_{(S+P)_-} - \frac{2}{N_{\mathrm{c}}}\lambda^2_{(S+P)_-} - \frac{1}{N_{\mathrm{c}}}\lambda_{(\sigma\text{-}\pi)}\lambda_{(S+P)^{\mathrm{adj}}_{-}} - \frac{2}{N_{\mathrm{c}}}\lambda_{(S+P)_-}\lambda_{(S+P)^{\mathrm{adj}}_{-}} \\
&- \frac{1}{2N_{\mathrm{c}}}\lambda^2_{(S+P)^{\mathrm{adj}}_{-}} + \frac{1}{3N_{\mathrm{c}}}\lambda_{(\sigma\text{-}\pi)}\lambda_{(V-A)_{\parallel}} + \frac{2}{3N_{\mathrm{c}}}\lambda_{(S+P)_-}\lambda_{(V-A)_{\parallel}} + \frac{1}{12N_{\mathrm{c}}}\lambda_{(\sigma\text{-}\pi)}\lambda_{(V+A)^{\mathrm{adj}}_{\parallel}} \\
&+ \frac{1}{12N_{\mathrm{c}}}\lambda^2_{(V+A)^{\mathrm{adj}}_{\parallel}} + \frac{2}{3N_{\mathrm{c}}}\lambda_{(\sigma\text{-}\pi)}\lambda_{(V-A)_{\perp}} + \frac{4}{3N_{\mathrm{c}}}\lambda_{(S+P)_-}\lambda_{(V-A)_{\perp}} - \frac{1}{3N_{\mathrm{c}}}\lambda_{(S+P)^{\mathrm{adj}}_{-}}\lambda_{(V-A)^{\mathrm{adj}}_{\perp}} \\
&+ \frac{1}{2N_{\mathrm{c}}}\lambda_{(V-A)_{\parallel}}\lambda_{(V-A)^{\mathrm{adj}}_{\perp}} + \frac{1}{N_{\mathrm{c}}}\lambda_{(V-A)_{\perp}}\lambda_{(V-A)^{\mathrm{adj}}_{\perp}} + \frac{1}{2N_{\mathrm{c}}}\lambda^2_{(V-A)^{\mathrm{adj}}_{\perp}}\Big) l^{(\mathrm{F})}_{\perp \pm}(\tau, 0, -i\tilde{\mu}_\tau) \ ,
\end{aligned}$$

$$\begin{aligned}
&\partial_t \lambda_{(V+A)_{\parallel}} = \\
&2\lambda_{(V+A)_{\parallel}} + 64 v_4 \Big(\frac{1}{2}\lambda^2_{(\sigma\text{-}\pi)} + 2\lambda_{(\sigma\text{-}\pi)}\lambda_{(S+P)_-} + 2\lambda^2_{(S+P)_-} + \frac{1}{2}\lambda_{(\sigma\text{-}\pi)}\lambda_{(S+P)^{\mathrm{adj}}_{-}} + \lambda_{(S+P)_-}\lambda_{(S+P)^{\mathrm{adj}}_{-}} \\
&+ \lambda^2_{(S+P)^{\mathrm{adj}}_{-}} + \frac{1}{2}\lambda^2_{(V+A)_{\parallel}} + 2\lambda_{(\sigma\text{-}\pi)}\lambda_{(V-A)_{\parallel}} + \lambda_{(V+A)_{\parallel}}\lambda_{(V-A)_{\parallel}} + \frac{1}{8}\lambda^2_{(V+A)^{\mathrm{adj}}_{\parallel}} + \frac{3}{2}\lambda^2_{(V+A)_{\perp}}
\end{aligned}$$

$$- 3\lambda_{(V+A)_\parallel}\lambda_{(V-A)_\perp} + \frac{3}{4}\lambda_{(\sigma\text{-}\pi)}\lambda_{(V-A)_\perp^{\mathrm{adj}}} - \frac{1}{2N_{\mathrm{c}}^2}\lambda^2_{(S+P)_-^{\mathrm{adj}}} - \frac{1}{8N_{\mathrm{c}}^2}\lambda^2_{(V+A)_\parallel^{\mathrm{adj}}} - \frac{1}{N_{\mathrm{c}}^2}\lambda_{(\sigma\text{-}\pi)}\lambda_{(V-A)_\perp^{\mathrm{adj}}}$$

$$- \frac{1}{2N_{\mathrm{c}}}\lambda^2_{(S+P)_-^{\mathrm{adj}}} - \frac{1}{2N_{\mathrm{c}}}\lambda_{(V+A)_\parallel^{\mathrm{adj}}}\lambda_{(V+A)_\perp} + \frac{2}{N_{\mathrm{c}}}\lambda_{(\sigma\text{-}\pi)}\lambda_{(V-A)_\perp} + \frac{1}{N_{\mathrm{c}}}\lambda_{(\sigma\text{-}\pi)}\lambda_{(V-A)_\perp^{\mathrm{adj}}}$$

$$+ \frac{3}{2N_{\mathrm{c}}}\lambda_{(V+A)_\parallel}\lambda_{(V-A)_\perp^{\mathrm{adj}}} - 4N_{\mathrm{c}}\lambda_{(V+A)_\parallel}\lambda_{(V-A)_\parallel} - \frac{3N_{\mathrm{c}}}{2}\lambda_{(V+A)_\parallel}\lambda_{(V-A)_\perp^{\mathrm{adj}}} - \lambda_{(\sigma\text{-}\pi)}\lambda_{\mathrm{csc}}$$

$$+ \frac{3}{2}\lambda_{(S+P)_-^{\mathrm{adj}}}\lambda_{\mathrm{csc}} - \lambda_{(V+A)_\parallel}\lambda_{\mathrm{csc}} - \frac{1}{N_{\mathrm{c}}^2}\lambda_{(S+P)_-^{\mathrm{adj}}}\lambda_{\mathrm{csc}} + \frac{2}{N_{\mathrm{c}}}\lambda_{(\sigma\text{-}\pi)}\lambda_{\mathrm{csc}} + \frac{2}{N_{\mathrm{c}}}\lambda_{(S+P)_-}\lambda_{\mathrm{csc}}$$

$$- \lambda_{(S+P)_-}\lambda_{\mathrm{csc}} - \frac{1}{2N_{\mathrm{c}}}\lambda_{(S+P)_-^{\mathrm{adj}}}\lambda_{\mathrm{csc}} + N_{\mathrm{c}}\lambda_{(V+A)_\parallel}\lambda_{\mathrm{csc}} + \lambda^2_{\mathrm{csc}} - \frac{1}{N_{\mathrm{c}}}\lambda^2_{\mathrm{csc}}\Big) l^{(\mathrm{F})}_{\parallel +}\left(\tau, 0, -i\tilde{\mu}_\tau\right)$$

$$+ 64 v_4 \Big(- \frac{1}{2}\lambda^2_{(\sigma\text{-}\pi)} - \frac{1}{2}\lambda^2_{(V+A)_\parallel} + \frac{1}{4}\lambda_{(\sigma\text{-}\pi)}\lambda_{(V+A)_\parallel^{\mathrm{adj}}} - \frac{1}{8}\lambda^2_{(V+A)_\parallel^{\mathrm{adj}}} - \frac{3}{2}\lambda^2_{(V+A)_\perp}$$

$$+ \frac{1}{8N_{\mathrm{c}}^2}\lambda^2_{(V+A)_\parallel^{\mathrm{adj}}} + \frac{2}{N_{\mathrm{c}}}\lambda_{(\sigma\text{-}\pi)}\lambda_{(V+A)_\perp} + \frac{1}{2N_{\mathrm{c}}}\lambda_{(V+A)_\parallel^{\mathrm{adj}}}\lambda_{(V+A)_\perp}\Big) l^{(\mathrm{F})}_{\parallel \pm}\left(\tau, 0, -i\tilde{\mu}_\tau\right)$$

$$+ 64 v_4 \Big(\frac{1}{2}\lambda_{(\sigma\text{-}\pi)}\lambda_{(S+P)_-^{\mathrm{adj}}} + \lambda_{(S+P)_-}\lambda_{(S+P)_-^{\mathrm{adj}}} + \frac{1}{3}\lambda^2_{(S+P)_-^{\mathrm{adj}}} - 2\lambda_{(\sigma\text{-}\pi)}\lambda_{(V-A)_\parallel} - \lambda_{(V+A)_\parallel}\lambda_{(V-A)_\parallel}$$

$$- \frac{1}{24}\lambda^2_{(V+A)_\parallel^{\mathrm{adj}}} + \lambda_{(V+A)_\parallel}\lambda_{(V+A)_\perp} + \lambda^2_{(V+A)_\perp} + 3\lambda_{(V+A)_\parallel}\lambda_{(V-A)_\perp} - \frac{3}{4}\lambda_{(\sigma\text{-}\pi)}\lambda_{(V-A)_\perp^{\mathrm{adj}}}$$

$$+ \frac{1}{3N_{\mathrm{c}}^2}\lambda^2_{(S+P)_-^{\mathrm{adj}}} + \frac{1}{12N_{\mathrm{c}}^2}\lambda^2_{(V+A)_\parallel^{\mathrm{adj}}} + \frac{2}{3N_{\mathrm{c}}^2}\lambda_{(\sigma\text{-}\pi)}\lambda_{(V-A)_\perp^{\mathrm{adj}}} - \frac{1}{3N_{\mathrm{c}}}\lambda_{(\sigma\text{-}\pi)}\lambda_{(S+P)_-^{\mathrm{adj}}}$$

$$- \frac{2}{3N_{\mathrm{c}}}\lambda_{(S+P)_-}\lambda_{(S+P)_-^{\mathrm{adj}}} - \frac{1}{2N_{\mathrm{c}}}\lambda^2_{(S+P)_-^{\mathrm{adj}}} + \frac{2}{3N_{\mathrm{c}}}\lambda_{(\sigma\text{-}\pi)}\lambda_{(V-A)_\parallel} - \frac{1}{6N_{\mathrm{c}}}\lambda_{(V+A)_\parallel}\lambda_{(V+A)_\parallel^{\mathrm{adj}}}$$

$$- \frac{1}{3N_{\mathrm{c}}}\lambda_{(V+A)_\parallel^{\mathrm{adj}}}\lambda_{(V+A)_\perp} - \frac{4}{3N_{\mathrm{c}}}\lambda_{(\sigma\text{-}\pi)}\lambda_{(V-A)_\perp} + \frac{1}{3N_{\mathrm{c}}}\lambda_{(\sigma\text{-}\pi)}\lambda_{(V-A)_\perp^{\mathrm{adj}}} - \frac{3}{2N_{\mathrm{c}}}\lambda_{(V+A)_\parallel}\lambda_{(V-A)_\perp^{\mathrm{adj}}}$$

$$+ 4N_{\mathrm{c}}\lambda_{(V+A)_\parallel}\lambda_{(V-A)_\parallel} + \frac{3N_{\mathrm{c}}}{2}\lambda_{(V+A)_\parallel}\lambda_{(V-A)_\perp^{\mathrm{adj}}} + \lambda_{(\sigma\text{-}\pi)}\lambda_{\mathrm{csc}} + \lambda_{(S+P)_-}\lambda_{\mathrm{csc}} + \frac{1}{6}\lambda_{(S+P)_-^{\mathrm{adj}}}\lambda_{\mathrm{csc}}$$

$$+ \lambda_{(V+A)_\parallel}\lambda_{\mathrm{csc}} + \frac{1}{3N_{\mathrm{c}}^2}\lambda_{(S+P)_-^{\mathrm{adj}}}\lambda_{\mathrm{csc}} - \frac{2}{3N_{\mathrm{c}}}\lambda_{(\sigma\text{-}\pi)}\lambda_{\mathrm{csc}} - \frac{2}{3N_{\mathrm{c}}}\lambda_{(S+P)_-}\lambda_{\mathrm{csc}} - \frac{1}{6N_{\mathrm{c}}}\lambda_{(S+P)_-^{\mathrm{adj}}}\lambda_{\mathrm{csc}}$$

$$- N_{\mathrm{c}}\lambda_{(V+A)_\parallel}\lambda_{\mathrm{csc}} - \frac{1}{6}\lambda^2_{\mathrm{csc}} + \frac{1}{3N_{\mathrm{c}}}\lambda^2_{\mathrm{csc}}\Big) l^{(\mathrm{F})}_{\perp +}\left(\tau, 0, -i\tilde{\mu}_\tau\right)$$

$$+ 64 v_4 \Big(\frac{1}{4}\lambda_{(\sigma\text{-}\pi)}\lambda_{(V+A)_\parallel^{\mathrm{adj}}} - \lambda_{(V+A)_\parallel}\lambda_{(V+A)_\perp} + \lambda^2_{(V+A)_\perp} - \frac{1}{3N_{\mathrm{c}}^2}\lambda_{(\sigma\text{-}\pi)}\lambda_{(V+A)_\parallel^{\mathrm{adj}}}$$

$$+ \frac{2}{3N_{\mathrm{c}}}\lambda_{(\sigma\text{-}\pi)}\lambda_{(V+A)_\parallel} + \frac{1}{6N_{\mathrm{c}}}\lambda_{(V+A)_\parallel}\lambda_{(V+A)_\parallel^{\mathrm{adj}}} - \frac{4}{3N_{\mathrm{c}}}\lambda_{(\sigma\text{-}\pi)}\lambda_{(V+A)_\perp}$$

$$- \frac{1}{12N_{\mathrm{c}}^2}\lambda^2_{(V+A)_\parallel^{\mathrm{adj}}} - \frac{1}{3N_{\mathrm{c}}}\lambda_{(V+A)_\parallel^{\mathrm{adj}}}\lambda_{(V+A)_\perp}\Big) l^{(\mathrm{F})}_{\perp \pm}\left(\tau, 0, -i\tilde{\mu}_\tau\right) \ ,$$

$$\partial_t \lambda_{(V+A)_\perp} =$$

$$2\lambda_{(V+A)_\perp} + 64 v_4 \Big(- \frac{1}{2N_{\mathrm{c}}}\lambda^2_{(S+P)_-^{\mathrm{adj}}} + \frac{1}{2}\lambda^2_{(S+P)_-^{\mathrm{adj}}} + \frac{1}{2}\lambda_{\mathrm{csc}}\lambda_{(S+P)_-^{\mathrm{adj}}} + \frac{1}{2}\lambda_{(\sigma\text{-}\pi)}\lambda_{(S+P)_-^{\mathrm{adj}}}$$

$$+ \lambda_{(S+P)_-}\lambda_{(S+P)_-^{\mathrm{adj}}} - \frac{1}{2N_{\mathrm{c}}}\lambda_{\mathrm{csc}}\lambda_{(S+P)_-^{\mathrm{adj}}} + \lambda^2_{(V+A)_\perp} + \lambda_{\mathrm{csc}}\lambda_{(\sigma\text{-}\pi)} + \lambda_{\mathrm{csc}}\lambda_{(S+P)_-}$$

$$- 2\lambda_{(\sigma\text{-}\pi)}\lambda_{(V-A)_\perp} - \frac{1}{4}\lambda_{(\sigma\text{-}\pi)}\lambda_{(V-A)_\perp^{\mathrm{adj}}} + \lambda_{\mathrm{csc}}\lambda_{(V+A)_\perp} + \lambda_{(V-A)_\parallel}\lambda_{(V+A)_\perp} + \lambda_{(V-A)_\perp}\lambda_{(V+A)_\perp}$$

$$+ \lambda_{(V+A)_\parallel}\lambda_{(V+A)_\perp} - N_{\mathrm{c}}\lambda_{\mathrm{csc}}\lambda_{(V+A)_\perp} + 4N_{\mathrm{c}}\lambda_{(V-A)_\perp}\lambda_{(V+A)_\perp} + \frac{N_{\mathrm{c}}}{2}\lambda_{(V-A)_\perp^{\mathrm{adj}}}\lambda_{(V+A)_\perp}$$

$$
\begin{aligned}
&+\frac{1}{N_{\mathrm{c}}}\lambda_{(\sigma\text{-}\pi)}\lambda_{(V-A)_\perp^{\mathrm{adj}}}-\frac{1}{2N_{\mathrm{c}}}\lambda_{(V-A)_\perp^{\mathrm{adj}}}\lambda_{(V+A)_\perp}-\frac{1}{2N_{\mathrm{c}}}\lambda_{(V+A)_\parallel^{\mathrm{adj}}}\lambda_{(V+A)_\perp}\Big)l^{(\mathrm{F})}_{\parallel +}(\tau,0,-\mathrm{i}\tilde{\mu}_\tau)\\
&+64v_4\Big(\lambda^2_{(V+A)_\perp}-\lambda_{(V+A)_\parallel}\lambda_{(V+A)_\perp}+\frac{1}{2N_{\mathrm{c}}}\lambda_{(V+A)_\parallel^{\mathrm{adj}}}\lambda_{(V+A)_\perp}+\frac{1}{4}\lambda_{(\sigma\text{-}\pi)}\lambda_{(V+A)_\parallel^{\mathrm{adj}}}\Big)l^{(\mathrm{F})}_{\parallel \pm}(\tau,0,-\mathrm{i}\tilde{\mu}_\tau)\\
&+64v_4\Big(\frac{1}{6}\lambda^2_{\mathrm{csc}}+\frac{1}{3}\lambda_{(\sigma\text{-}\pi)}\lambda_{\mathrm{csc}}+\frac{1}{3}\lambda_{(S+P)_-}\lambda_{\mathrm{csc}}+\frac{1}{2}\lambda_{(S+P)_-^{\mathrm{adj}}}\lambda_{\mathrm{csc}}+\frac{1}{3}\lambda_{(V+A)_\perp}\lambda_{\mathrm{csc}}\\
&-\frac{N_{\mathrm{c}}}{3}\lambda_{(V+A)_\perp}\lambda_{\mathrm{csc}}-\frac{1}{6N_{\mathrm{c}}}\lambda_{(S+P)_-^{\mathrm{adj}}}\lambda_{\mathrm{csc}}+\frac{1}{6}\lambda^2_{(\sigma\text{-}\pi)}+\frac{2}{3}\lambda^2_{(S+P)_-}+\frac{1}{2}\lambda^2_{(S+P)_-^{\mathrm{adj}}}+\frac{1}{6}\lambda^2_{(V+A)_\parallel}\\
&+\frac{7}{6}\lambda^2_{(V+A)_\perp}+\frac{2}{3}\lambda_{(\sigma\text{-}\pi)}\lambda_{(S+P)_-}+\frac{1}{2}\lambda_{(\sigma\text{-}\pi)}\lambda_{(S+P)_-^{\mathrm{adj}}}+\lambda_{(S+P)_-}\lambda_{(S+P)_-^{\mathrm{adj}}}-\frac{2}{3}\lambda_{(\sigma\text{-}\pi)}\lambda_{(V-A)_\perp}\\
&-\frac{1}{12}\lambda_{(\sigma\text{-}\pi)}\lambda_{(V-A)_\perp^{\mathrm{adj}}}+\frac{1}{3}\lambda_{(V-A)_\parallel}\lambda_{(V+A)_\perp}+\frac{1}{3}\lambda_{(V-A)_\perp}\lambda_{(V+A)_\perp}+\frac{2}{3}\lambda_{(V+A)_\parallel}\lambda_{(V+A)_\perp}\\
&+\frac{4}{3}N_{\mathrm{c}}\lambda_{(V-A)_\perp}\lambda_{(V+A)_\perp}+\frac{N_{\mathrm{c}}}{6}\lambda_{(V-A)_\perp^{\mathrm{adj}}}\lambda_{(V+A)_\perp}-\frac{1}{2N_{\mathrm{c}}}\lambda^2_{(S+P)_-^{\mathrm{adj}}}-\frac{1}{3N_{\mathrm{c}}}\lambda_{(\sigma\text{-}\pi)}\lambda_{(S+P)_-^{\mathrm{adj}}}\\
&-\frac{2}{3N_{\mathrm{c}}}\lambda_{(S+P)_-}\lambda_{(S+P)_-^{\mathrm{adj}}}+\frac{1}{3N_{\mathrm{c}}}\lambda_{(\sigma\text{-}\pi)}\lambda_{(V-A)_\perp^{\mathrm{adj}}}-\frac{1}{6N_{\mathrm{c}}}\lambda_{(V+A)_\parallel}\lambda_{(V+A)_\parallel^{\mathrm{adj}}}-\frac{1}{6N_{\mathrm{c}}}\lambda_{(V-A)_\perp^{\mathrm{adj}}}\lambda_{(V+A)_\perp}\\
&-\frac{1}{3N_{\mathrm{c}}}\lambda_{(V+A)_\parallel^{\mathrm{adj}}}\lambda_{(V+A)_\perp}+\frac{1}{6N_{\mathrm{c}}^2}\lambda^2_{(S+P)_-^{\mathrm{adj}}}+\frac{1}{24N_{\mathrm{c}}^2}\lambda^2_{(V+A)_\parallel^{\mathrm{adj}}}\Big)l^{(\mathrm{F})}_{\perp +}(\tau,0,-\mathrm{i}\tilde{\mu}_\tau)\\
&+64v_4\Big(-\frac{1}{6}\lambda^2_{(\sigma\text{-}\pi)}-\frac{1}{12}\lambda_{(V+A)_\parallel^{\mathrm{adj}}}\lambda_{(\sigma\text{-}\pi)}-\frac{1}{6}\lambda^2_{(V+A)_\parallel}-\frac{1}{24}\lambda^2_{(V+A)_\parallel^{\mathrm{adj}}}-\frac{7}{6}\lambda^2_{(V+A)_\perp}\\
&+\frac{1}{6N_{\mathrm{c}}}\lambda_{(V+A)_\parallel}\lambda_{(V+A)_\parallel^{\mathrm{adj}}}-\frac{1}{3N_{\mathrm{c}}}\lambda_{(V+A)_\parallel^{\mathrm{adj}}}\lambda_{(V+A)_\perp}\\
&+\frac{2}{3}\lambda_{(V+A)_\parallel}\lambda_{(V+A)_\perp}-\frac{1}{24N_{\mathrm{c}}^2}\lambda^2_{(V+A)_\parallel^{\mathrm{adj}}}\Big)l^{(\mathrm{F})}_{\perp \pm}(\tau,0,-\mathrm{i}\tilde{\mu}_\tau)\,,
\end{aligned}
$$

$$
\begin{aligned}
&\partial_t\lambda_{(V-A)_\parallel}=\\
&2\lambda_{(V-A)_\parallel}+64v_4\Big(\frac{1}{2}N_{\mathrm{c}}\lambda^2_{\mathrm{csc}}-\frac{1}{2}\lambda^2_{\mathrm{csc}}-\lambda_{(V-A)_\parallel}\lambda_{\mathrm{csc}}-\frac{3}{2}\lambda_{(V-A)_\perp^{\mathrm{adj}}}\lambda_{\mathrm{csc}}+N_{\mathrm{c}}\lambda_{(V-A)_\parallel}\lambda_{\mathrm{csc}}\\
&+\frac{3}{2}N_{\mathrm{c}}\lambda_{(V-A)_\perp^{\mathrm{adj}}}\lambda_{\mathrm{csc}}-\frac{1}{2}\lambda^2_{(\sigma\text{-}\pi)}+\frac{3}{2}\lambda^2_{(V-A)_\parallel}+\frac{3}{2}\lambda^2_{(V-A)_\perp}-\frac{1}{2}\lambda^2_{(V+A)_\parallel^{\mathrm{adj}}}-3\lambda_{(V-A)_\parallel}\lambda_{(V-A)_\perp}\\
&+\frac{3}{2}\lambda_{(V-A)_\perp}\lambda_{(V-A)_\perp^{\mathrm{adj}}}+2\lambda_{(\sigma\text{-}\pi)}\lambda_{(V+A)_\parallel}+\lambda_{(\sigma\text{-}\pi)}\lambda_{(V+A)_\parallel^{\mathrm{adj}}}-2N_{\mathrm{c}}\lambda^2_{(V-A)_\parallel}+\frac{3}{8}N_{\mathrm{c}}\lambda^2_{(V-A)_\perp^{\mathrm{adj}}}\\
&-2N_{\mathrm{c}}\lambda^2_{(V+A)_\parallel}-\frac{3}{2}N_{\mathrm{c}}\lambda_{(V-A)_\parallel}\lambda_{(V-A)_\perp^{\mathrm{adj}}}-\frac{3}{4N_{\mathrm{c}}}\lambda^2_{(V-A)_\perp^{\mathrm{adj}}}+\frac{1}{2N_{\mathrm{c}}}\lambda^2_{(V+A)_\parallel^{\mathrm{adj}}}\\
&+\frac{3}{2N_{\mathrm{c}}}\lambda_{(V-A)_\parallel}\lambda_{(V-A)_\perp^{\mathrm{adj}}}-\frac{3}{2N_{\mathrm{c}}}\lambda_{(V-A)_\perp}\lambda_{(V-A)_\perp^{\mathrm{adj}}}-\frac{1}{N_{\mathrm{c}}}\lambda_{(\sigma\text{-}\pi)}\lambda_{(V+A)_\parallel^{\mathrm{adj}}}\\
&+\frac{3}{8N_{\mathrm{c}}^2}\lambda^2_{(V-A)_\perp^{\mathrm{adj}}}\Big)l^{(\mathrm{F})}_{\parallel +}(\tau,0,-\mathrm{i}\tilde{\mu}_\tau)\\
&+64v_4\Big(-\frac{3}{2}\lambda^2_{(\sigma\text{-}\pi)}-6\lambda_{(S+P)_-}\lambda_{(\sigma\text{-}\pi)}-3\lambda_{(S+P)_-^{\mathrm{adj}}}\lambda_{(\sigma\text{-}\pi)}+\frac{3}{N_{\mathrm{c}}}\lambda_{(S+P)_-^{\mathrm{adj}}}\lambda_{(\sigma\text{-}\pi)}-6\lambda^2_{(S+P)_-}\\
&-\frac{3}{2}\lambda^2_{(S+P)_-^{\mathrm{adj}}}-\frac{1}{2}\lambda^2_{(V-A)_\parallel}-\frac{3}{2}\lambda^2_{(V-A)_\perp}-\frac{3}{8}\lambda^2_{(V-A)_\perp^{\mathrm{adj}}}-6\lambda_{(S+P)_-}\lambda_{(S+P)_-^{\mathrm{adj}}}\\
&-\frac{3}{2}\lambda_{(V-A)_\perp}\lambda_{(V-A)_\perp^{\mathrm{adj}}}+\frac{3}{N_{\mathrm{c}}}\lambda^2_{(S+P)_-^{\mathrm{adj}}}+\frac{3}{4N_{\mathrm{c}}}\lambda^2_{(V-A)_\perp^{\mathrm{adj}}}+\frac{6}{N_{\mathrm{c}}}\lambda_{(S+P)_-}\lambda_{(S+P)_-^{\mathrm{adj}}}\\
&+\frac{3}{2N_{\mathrm{c}}}\lambda_{(V-A)_\perp}\lambda_{(V-A)_\perp^{\mathrm{adj}}}-\frac{3}{2N_{\mathrm{c}}^2}\lambda^2_{(S+P)_-^{\mathrm{adj}}}-\frac{3}{8N_{\mathrm{c}}^2}\lambda^2_{(V-A)_\perp^{\mathrm{adj}}}\Big)l^{(\mathrm{F})}_{\parallel \pm}(\tau,0,-\mathrm{i}\tilde{\mu}_\tau)
\end{aligned}
$$

$$
\begin{aligned}
&+64v_4\Big(\frac{1}{2}\lambda^2_{(\sigma\text{-}\pi)} - 2\lambda_{(V+A)_\parallel}\lambda_{(\sigma\text{-}\pi)} - \lambda_{(V+A)^{\mathrm{adj}}_{\parallel}}\lambda_{(\sigma\text{-}\pi)} + \frac{1}{N_{\mathrm{c}}}\lambda_{(V+A)^{\mathrm{adj}}_{\parallel}}\lambda_{(\sigma\text{-}\pi)} - \lambda^2_{(V-A)_\parallel} - \lambda^2_{(V-A)_\perp}\\
&+\frac{1}{2}\lambda^2_{(V+A)^{\mathrm{adj}}_{\parallel}} + \lambda_{\mathrm{csc}}\lambda_{(V-A)_\parallel} + 4\lambda_{(V-A)_\parallel}\lambda_{(V-A)_\perp} + \lambda_{\mathrm{csc}}\lambda_{(V-A)^{\mathrm{adj}}_{\perp}} + \frac{1}{2}\lambda_{(V-A)_\parallel}\lambda_{(V-A)^{\mathrm{adj}}_{\perp}}\\
&-\lambda_{(V-A)_\perp}\lambda_{(V-A)^{\mathrm{adj}}_{\perp}} + 2N_{\mathrm{c}}\lambda^2_{(V-A)_\parallel} - \frac{N_{\mathrm{c}}}{4}\lambda^2_{(V-A)^{\mathrm{adj}}_{\perp}} + 2N_{\mathrm{c}}\lambda^2_{(V+A)_\parallel} - N_{\mathrm{c}}\lambda_{\mathrm{csc}}\lambda_{(V-A)_\parallel}\\
&-N_{\mathrm{c}}\lambda_{\mathrm{csc}}\lambda_{(V-A)^{\mathrm{adj}}_{\perp}} + \frac{3}{2}N_{\mathrm{c}}\lambda_{(V-A)_\parallel}\lambda_{(V-A)^{\mathrm{adj}}_{\perp}} + \frac{1}{2N_{\mathrm{c}}}\lambda^2_{(V-A)^{\mathrm{adj}}_{\perp}} - \frac{1}{2N_{\mathrm{c}}}\lambda^2_{(V+A)^{\mathrm{adj}}_{\parallel}}\\
&-\frac{2}{N_{\mathrm{c}}}\lambda_{(V-A)_\parallel}\lambda_{(V-A)^{\mathrm{adj}}_{\perp}} + \frac{1}{N_{\mathrm{c}}}\lambda_{(V-A)_\perp}\lambda_{(V-A)^{\mathrm{adj}}_{\perp}} - \frac{1}{4N_{\mathrm{c}}^2}\lambda^2_{(V-A)^{\mathrm{adj}}_{\perp}}\Big)\, l^{(\mathrm{F})}_{\perp+}(\tau,0,-\mathrm{i}\tilde{\mu}_\tau)\\
&+64v_4\Big(\frac{1}{2}\lambda^2_{(\sigma\text{-}\pi)} + 2\lambda_{(S+P)_-}\lambda_{(\sigma\text{-}\pi)} + \lambda_{(S+P)^{\mathrm{adj}}_{-}}\lambda_{(\sigma\text{-}\pi)} - \frac{1}{N_{\mathrm{c}}}\lambda_{(S+P)^{\mathrm{adj}}_{-}}\lambda_{(\sigma\text{-}\pi)} + 2\lambda^2_{(S+P)_-}\\
&-\lambda^2_{(V-A)_\perp} - \frac{1}{4}\lambda^2_{(V-A)^{\mathrm{adj}}_{\perp}} + 2\lambda_{(S+P)_-}\lambda_{(S+P)^{\mathrm{adj}}_{-}} - \lambda_{(V-A)_\parallel}\lambda_{(V-A)_\perp} - \frac{1}{2}\lambda_{(V-A)_\parallel}\lambda_{(V-A)^{\mathrm{adj}}_{\perp}}\\
&-\lambda_{(V-A)_\perp}\lambda_{(V-A)^{\mathrm{adj}}_{\perp}} - \frac{1}{N_{\mathrm{c}}}\lambda^2_{(S+P)^{\mathrm{adj}}_{-}} + \frac{1}{2N_{\mathrm{c}}}\lambda^2_{(V-A)^{\mathrm{adj}}_{\perp}} - \frac{2}{N_{\mathrm{c}}}\lambda_{(S+P)_-}\lambda_{(S+P)^{\mathrm{adj}}_{-}}\\
&+\frac{1}{2N_{\mathrm{c}}}\lambda_{(V-A)_\parallel}\lambda_{(V-A)^{\mathrm{adj}}_{\perp}} + \frac{1}{N_{\mathrm{c}}}\lambda_{(V-A)_\perp}\lambda_{(V-A)^{\mathrm{adj}}_{\perp}} + \frac{1}{2N_{\mathrm{c}}^2}\lambda^2_{(S+P)^{\mathrm{adj}}_{-}} - \frac{1}{4N_{\mathrm{c}}^2}\lambda^2_{(V-A)^{\mathrm{adj}}_{\perp}}\\
&+\frac{1}{2}\lambda^2_{(S+P)^{\mathrm{adj}}_{-}}\Big)\, l^{(\mathrm{F})}_{\perp\pm}(\tau,0,-\mathrm{i}\tilde{\mu}_\tau)\,,
\end{aligned}
$$

$$
\begin{aligned}
&\partial_t\lambda_{(V-A)_\perp} =\\
&2\lambda_{(V-A)_\perp} + 64v_4\Big(\frac{N_{\mathrm{c}}}{2}\lambda^2_{\mathrm{csc}} + \frac{1}{N_{\mathrm{c}}}\lambda^2_{\mathrm{csc}} - \frac{3}{2}\lambda^2_{\mathrm{csc}} + \lambda_{(V-A)_\perp}\lambda_{\mathrm{csc}} - \frac{3}{2}\lambda_{(V-A)^{\mathrm{adj}}_{\perp}}\lambda_{\mathrm{csc}} - N_{\mathrm{c}}\lambda_{(V-A)_\perp}\lambda_{\mathrm{csc}}\\
&+\frac{N_{\mathrm{c}}}{2}\lambda_{(V-A)^{\mathrm{adj}}_{\perp}}\lambda_{\mathrm{csc}} + \frac{1}{N_{\mathrm{c}}}\lambda_{(V-A)^{\mathrm{adj}}_{\perp}}\lambda_{\mathrm{csc}} - \frac{1}{2}\lambda^2_{(\sigma\text{-}\pi)} - \frac{5}{8}\lambda^2_{(V-A)^{\mathrm{adj}}_{\perp}} - \frac{1}{2}\lambda^2_{(V+A)^{\mathrm{adj}}_{\parallel}} + 2\lambda_{(V-A)_\parallel}\lambda_{(V-A)_\perp}\\
&+\frac{3}{2}\lambda_{(V-A)_\perp}\lambda_{(V-A)^{\mathrm{adj}}_{\perp}} + \lambda_{(\sigma\text{-}\pi)}\lambda_{(V+A)^{\mathrm{adj}}_{\parallel}} - 2\lambda_{(\sigma\text{-}\pi)}\lambda_{(V+A)_\perp} + 2N_{\mathrm{c}}\lambda^2_{(V-A)_\perp} + \frac{3}{8}N_{\mathrm{c}}\lambda^2_{(V-A)^{\mathrm{adj}}_{\perp}}\\
&+2N_{\mathrm{c}}\lambda^2_{(V+A)_\perp} + \frac{N_{\mathrm{c}}}{2}\lambda_{(V-A)_\perp}\lambda_{(V-A)^{\mathrm{adj}}_{\perp}} + \frac{1}{N_{\mathrm{c}}}\lambda^2_{(\sigma\text{-}\pi)} - \frac{3}{4N_{\mathrm{c}}}\lambda^2_{(V-A)^{\mathrm{adj}}_{\perp}} + \frac{1}{2N_{\mathrm{c}}}\lambda^2_{(V+A)^{\mathrm{adj}}_{\parallel}}\\
&-\frac{2}{N_{\mathrm{c}}}\lambda_{(V-A)_\perp}\lambda_{(V-A)^{\mathrm{adj}}_{\perp}} - \frac{1}{N_{\mathrm{c}}}\lambda_{(\sigma\text{-}\pi)}\lambda_{(V+A)^{\mathrm{adj}}_{\parallel}} + \frac{1}{N_{\mathrm{c}}^2}\lambda^2_{(V-A)^{\mathrm{adj}}_{\perp}}\Big)\, l^{(\mathrm{F})}_{\parallel+}(\tau,0,-\mathrm{i}\tilde{\mu}_\tau)\\
&+64v_4\Big(\frac{1}{N_{\mathrm{c}}}\lambda^2_{(\sigma\text{-}\pi)} - \frac{1}{2}\lambda^2_{(\sigma\text{-}\pi)} - 2\lambda_{(S+P)_-}\lambda_{(\sigma\text{-}\pi)} - \lambda_{(S+P)^{\mathrm{adj}}_{-}}\lambda_{(\sigma\text{-}\pi)} + \frac{4}{N_{\mathrm{c}}}\lambda_{(S+P)_-}\lambda_{(\sigma\text{-}\pi)}\\
&+\frac{3}{N_{\mathrm{c}}}\lambda_{(S+P)^{\mathrm{adj}}_{-}}\lambda_{(\sigma\text{-}\pi)} - \frac{2}{N_{\mathrm{c}}^2}\lambda_{(S+P)^{\mathrm{adj}}_{-}}\lambda_{(\sigma\text{-}\pi)} - 2\lambda^2_{(S+P)_-} - \frac{1}{2}\lambda^2_{(S+P)^{\mathrm{adj}}_{-}} - \lambda^2_{(V-A)_\perp} - \frac{1}{4}\lambda^2_{(V-A)^{\mathrm{adj}}_{\perp}}\\
&-2\lambda_{(S+P)_-}\lambda_{(S+P)^{\mathrm{adj}}_{-}} - \lambda_{(V-A)_\parallel}\lambda_{(V-A)_\perp} - \frac{3}{2}\lambda_{(V-A)_\perp}\lambda_{(V-A)^{\mathrm{adj}}_{\perp}} + \frac{4}{N_{\mathrm{c}}}\lambda^2_{(S+P)_-} + \frac{2}{N_{\mathrm{c}}}\lambda^2_{(S+P)^{\mathrm{adj}}_{-}}\\
&+\frac{3}{4N_{\mathrm{c}}}\lambda^2_{(V-A)^{\mathrm{adj}}_{\perp}} + \frac{6}{N_{\mathrm{c}}}\lambda_{(S+P)_-}\lambda_{(S+P)^{\mathrm{adj}}_{-}} + \frac{3}{2N_{\mathrm{c}}}\lambda_{(V-A)_\perp}\lambda_{(V-A)^{\mathrm{adj}}_{\perp}} - \frac{5}{2N_{\mathrm{c}}^2}\lambda^2_{(S+P)^{\mathrm{adj}}_{-}}\\
&-\frac{1}{2N_{\mathrm{c}}^2}\lambda^2_{(V-A)^{\mathrm{adj}}_{\perp}} - \frac{4}{N_{\mathrm{c}}^2}\lambda_{(S+P)_-}\lambda_{(S+P)^{\mathrm{adj}}_{-}} + \frac{1}{N_{\mathrm{c}}^3}\lambda^2_{(S+P)^{\mathrm{adj}}_{-}}\Big)\, l^{(\mathrm{F})}_{\parallel\pm}(\tau,0,-\mathrm{i}\tilde{\mu}_\tau)\\
&+64v_4\Big(-\frac{1}{3N_{\mathrm{c}}}\lambda^2_{\mathrm{csc}} + \frac{1}{3}\lambda^2_{\mathrm{csc}} + \frac{1}{3}\lambda_{(V-A)_\perp}\lambda_{\mathrm{csc}} + \lambda_{(V-A)^{\mathrm{adj}}_{\perp}}\lambda_{\mathrm{csc}} - \frac{N_{\mathrm{c}}}{3}\lambda_{(V-A)_\perp}\lambda_{\mathrm{csc}}\\
&-\frac{N_{\mathrm{c}}}{3}\lambda_{(V-A)^{\mathrm{adj}}_{\perp}}\lambda_{\mathrm{csc}} - \frac{2}{3N_{\mathrm{c}}}\lambda_{(V-A)^{\mathrm{adj}}_{\perp}}\lambda_{\mathrm{csc}} + \frac{1}{2}\lambda^2_{(\sigma\text{-}\pi)} + \frac{1}{6}\lambda^2_{(V-A)_\parallel} + \frac{3}{2}\lambda^2_{(V-A)_\perp} + \frac{13}{24}\lambda^2_{(V-A)^{\mathrm{adj}}_{\perp}}
\end{aligned}
$$

$$
\begin{aligned}
&+\frac{1}{2}\lambda^2_{(V+A)_\parallel^{\mathrm{adj}}}-\frac{1}{3}\lambda_{(V-A)_\parallel}\lambda_{(V-A)_\perp}+\frac{1}{2}\lambda_{(V-A)_\parallel}\lambda_{(V-A)_\perp^{\mathrm{adj}}}-\lambda_{(V-A)_\perp}\lambda_{(V-A)_\perp^{\mathrm{adj}}}-\lambda_{(\sigma\text{-}\pi)}\lambda_{(V+A)_\parallel^{\mathrm{adj}}}\\
&-\frac{2}{3}\lambda_{(\sigma\text{-}\pi)}\lambda_{(V+A)_\perp}+\frac{2}{3}N_{\mathrm{c}}\lambda^2_{(V-A)_\perp}-\frac{N_{\mathrm{c}}}{4}\lambda^2_{(V-A)_\perp^{\mathrm{adj}}}+\frac{2}{3}N_{\mathrm{c}}\lambda^2_{(V+A)_\perp}+\frac{N_{\mathrm{c}}}{6}\lambda_{(V-A)_\perp}\lambda_{(V-A)_\perp^{\mathrm{adj}}}\\
&-\frac{1}{3N_{\mathrm{c}}}\lambda^2_{(\sigma\text{-}\pi)}+\frac{1}{2N_{\mathrm{c}}}\lambda^2_{(V-A)_\perp^{\mathrm{adj}}}-\frac{1}{2N_{\mathrm{c}}}\lambda^2_{(V+A)_\parallel^{\mathrm{adj}}}-\frac{1}{2N_{\mathrm{c}}}\lambda_{(V-A)_\parallel}\lambda_{(V-A)_\perp^{\mathrm{adj}}}\\
&+\frac{5}{6N_{\mathrm{c}}}\lambda_{(V-A)_\perp}\lambda_{(V-A)_\perp^{\mathrm{adj}}}+\frac{1}{N_{\mathrm{c}}}\lambda_{(\sigma\text{-}\pi)}\lambda_{(V+A)_\parallel^{\mathrm{adj}}}-\frac{19}{24N_{\mathrm{c}}^2}\lambda^2_{(V-A)_\perp^{\mathrm{adj}}}\Big)l^{(\mathrm{F})}_{\perp+}(\tau,0,-\mathrm{i}\tilde{\mu}_\tau)\\
&+64v_4\Big(-\frac{1}{3N_{\mathrm{c}}}\lambda^2_{(\sigma\text{-}\pi)}+\frac{1}{6}\lambda^2_{(\sigma\text{-}\pi)}+\frac{2}{3}\lambda_{(S+P)_-}\lambda_{(\sigma\text{-}\pi)}+\frac{1}{3}\lambda_{(S+P)_-^{\mathrm{adj}}}\lambda_{(\sigma\text{-}\pi)}-\frac{4}{3N_{\mathrm{c}}}\lambda_{(S+P)_-}\lambda_{(\sigma\text{-}\pi)}\\
&-\frac{1}{N_{\mathrm{c}}}\lambda_{(S+P)_-^{\mathrm{adj}}}\lambda_{(\sigma\text{-}\pi)}+\frac{2}{3N_{\mathrm{c}}^2}\lambda_{(S+P)_-^{\mathrm{adj}}}\lambda_{(\sigma\text{-}\pi)}+\frac{2}{3}\lambda^2_{(S+P)_-}+\frac{1}{6}\lambda^2_{(S+P)_-^{\mathrm{adj}}}-\frac{1}{6}\lambda^2_{(V-A)_\parallel}-\frac{7}{6}\lambda^2_{(V-A)_\perp}\\
&-\frac{7}{24}\lambda^2_{(V-A)_\perp^{\mathrm{adj}}}+\frac{2}{3}\lambda_{(S+P)_-}\lambda_{(S+P)_-^{\mathrm{adj}}}-\frac{2}{3}\lambda_{(V-A)_\parallel}\lambda_{(V-A)_\perp}-\frac{1}{2}\lambda_{(V-A)_\parallel}\lambda_{(V-A)_\perp^{\mathrm{adj}}}\\
&-\lambda_{(V-A)_\perp}\lambda_{(V-A)_\perp^{\mathrm{adj}}}-\frac{4}{3N_{\mathrm{c}}}\lambda^2_{(S+P)_-}-\frac{2}{3N_{\mathrm{c}}}\lambda^2_{(S+P)_-^{\mathrm{adj}}}+\frac{1}{2N_{\mathrm{c}}}\lambda^2_{(V-A)_\perp^{\mathrm{adj}}}-\frac{2}{N_{\mathrm{c}}}\lambda_{(S+P)_-}\lambda_{(S+P)_-^{\mathrm{adj}}}\\
&+\frac{1}{2N_{\mathrm{c}}}\lambda_{(V-A)_\parallel}\lambda_{(V-A)_\perp^{\mathrm{adj}}}+\frac{1}{N_{\mathrm{c}}}\lambda_{(V-A)_\perp}\lambda_{(V-A)_\perp^{\mathrm{adj}}}+\frac{5}{6N_{\mathrm{c}}^2}\lambda^2_{(S+P)_-^{\mathrm{adj}}}-\frac{5}{24N_{\mathrm{c}}^2}\lambda^2_{(V-A)_\perp^{\mathrm{adj}}}\\
&+\frac{4}{3N_{\mathrm{c}}^2}\lambda_{(S+P)_-}\lambda_{(S+P)_-^{\mathrm{adj}}}-\frac{1}{3N_{\mathrm{c}}^3}\lambda^2_{(S+P)_-^{\mathrm{adj}}}\Big)l^{(\mathrm{F})}_{\perp\pm}(\tau,0,-\mathrm{i}\tilde{\mu}_\tau)\,,
\end{aligned}
$$

$$
\begin{aligned}
&\partial_t\lambda_{(V+A)_\parallel^{\mathrm{adj}}}=\\
&2\lambda_{(V+A)_\parallel^{\mathrm{adj}}}+64v_4\Big(2N_{\mathrm{c}}\lambda_{\mathrm{csc}}\lambda_{(S+P)_-^{\mathrm{adj}}}-\frac{2}{N_{\mathrm{c}}}\lambda_{\mathrm{csc}}\lambda_{(S+P)_-^{\mathrm{adj}}}+N_{\mathrm{c}}\lambda^2_{\mathrm{csc}}-\frac{2}{N_{\mathrm{c}}}\lambda_{(\sigma\text{-}\pi)}\lambda_{(V-A)_\perp^{\mathrm{adj}}}\\
&+N_{\mathrm{c}}\lambda^2_{(S+P)_-^{\mathrm{adj}}}-\frac{2}{N_{\mathrm{c}}}\lambda^2_{(S+P)_-^{\mathrm{adj}}}+\frac{3}{2N_{\mathrm{c}}}\lambda_{(V-A)_\perp^{\mathrm{adj}}}\lambda_{(V+A)_\parallel^{\mathrm{adj}}}+\frac{N_{\mathrm{c}}}{4}\lambda^2_{(V+A)_\parallel^{\mathrm{adj}}}-\frac{1}{2N_{\mathrm{c}}}\lambda^2_{(V+A)_\parallel^{\mathrm{adj}}}\\
&+4\lambda_{\mathrm{csc}}\lambda_{(\sigma\text{-}\pi)}+4\lambda_{\mathrm{csc}}\lambda_{(S+P)_-}-2\lambda_{\mathrm{csc}}\lambda_{(S+P)_-^{\mathrm{adj}}}-\lambda_{\mathrm{csc}}\lambda_{(V+A)_\parallel^{\mathrm{adj}}}-2\lambda^2_{\mathrm{csc}}+2\lambda_{(\sigma\text{-}\pi)}\lambda_{(S+P)_-^{\mathrm{adj}}}\\
&+4\lambda_{(\sigma\text{-}\pi)}\lambda_{(V-A)_\perp}+2\lambda_{(\sigma\text{-}\pi)}\lambda_{(V-A)_\perp^{\mathrm{adj}}}+4\lambda_{(S+P)_-}\lambda_{(S+P)_-^{\mathrm{adj}}}+\lambda_{(V-A)_\parallel}\lambda_{(V+A)_\parallel^{\mathrm{adj}}}\\
&-3\lambda_{(V-A)_\perp}\lambda_{(V+A)_\parallel^{\mathrm{adj}}}+\lambda_{(V+A)_\parallel}\lambda_{(V+A)_\parallel^{\mathrm{adj}}}-\lambda_{(V+A)_\parallel^{\mathrm{adj}}}\lambda_{(V+A)_\perp}\Big)l^{(\mathrm{F})}_{\parallel+}(\tau,0,-\mathrm{i}\tilde{\mu}_\tau)\\
&+64v_4\Big(\frac{1}{2N_{\mathrm{c}}}\lambda^2_{(V+A)_\parallel^{\mathrm{adj}}}+4\lambda_{(\sigma\text{-}\pi)}\lambda_{(V+A)_\perp}-\lambda_{(V+A)_\parallel}\lambda_{(V+A)_\parallel^{\mathrm{adj}}}+\lambda_{(V+A)_\parallel^{\mathrm{adj}}}\lambda_{(V+A)_\perp}\Big)l^{(\mathrm{F})}_{\parallel\pm}(\tau,0,-\mathrm{i}\tilde{\mu}_\tau)\\
&+64v_4\Big(-\frac{2}{3}N_{\mathrm{c}}\lambda_{\mathrm{csc}}\lambda_{(S+P)_-^{\mathrm{adj}}}+\frac{2}{3N_{\mathrm{c}}}\lambda_{\mathrm{csc}}\lambda_{(S+P)_-^{\mathrm{adj}}}-\frac{N_{\mathrm{c}}}{3}\lambda^2_{\mathrm{csc}}+\frac{4}{3N_{\mathrm{c}}}\lambda_{(\sigma\text{-}\pi)}\lambda_{(V-A)_\perp^{\mathrm{adj}}}\\
&-\frac{N_{\mathrm{c}}}{3}\lambda^2_{(S+P)_-^{\mathrm{adj}}}+\frac{2}{3N_{\mathrm{c}}}\lambda^2_{(S+P)_-^{\mathrm{adj}}}-\frac{3}{2N_{\mathrm{c}}}\lambda_{(V-A)_\perp^{\mathrm{adj}}}\lambda_{(V+A)_\parallel^{\mathrm{adj}}}-\frac{N_{\mathrm{c}}}{12}\lambda^2_{(V+A)_\parallel^{\mathrm{adj}}}+\frac{1}{6N_{\mathrm{c}}}\lambda^2_{(V+A)_\parallel^{\mathrm{adj}}}\\
&-\frac{4}{3}\lambda_{\mathrm{csc}}\lambda_{(\sigma\text{-}\pi)}-\frac{4}{3}\lambda_{\mathrm{csc}}\lambda_{(S+P)_-}+\frac{2}{3}\lambda_{\mathrm{csc}}\lambda_{(S+P)_-^{\mathrm{adj}}}+\lambda_{\mathrm{csc}}\lambda_{(V+A)_\parallel^{\mathrm{adj}}}+\frac{2}{3}\lambda^2_{\mathrm{csc}}-\frac{2}{3}\lambda_{(\sigma\text{-}\pi)}\lambda_{(S+P)_-^{\mathrm{adj}}}\\
&+\frac{4}{3}\lambda_{(\sigma\text{-}\pi)}\lambda_{(V-A)_\parallel}-\frac{8}{3}\lambda_{(\sigma\text{-}\pi)}\lambda_{(V-A)_\perp}+\frac{2}{3}\lambda_{(\sigma\text{-}\pi)}\lambda_{(V-A)_\perp^{\mathrm{adj}}}-\frac{4}{3}\lambda_{(S+P)_-}\lambda_{(S+P)_-^{\mathrm{adj}}}-\lambda_{(V-A)_\parallel}\lambda_{(V+A)_\parallel^{\mathrm{adj}}}\\
&+3\lambda_{(V-A)_\perp}\lambda_{(V+A)_\parallel^{\mathrm{adj}}}-\frac{1}{3}\lambda_{(V+A)_\parallel}\lambda_{(V+A)_\parallel^{\mathrm{adj}}}+\frac{1}{3}\lambda_{(V+A)_\parallel^{\mathrm{adj}}}\lambda_{(V+A)_\perp}\Big)l^{(\mathrm{F})}_{\perp+}(\tau,0,-\mathrm{i}\tilde{\mu}_\tau)\\
&+64v_4\Big(-\frac{2}{3N_{\mathrm{c}}}\lambda_{(\sigma\text{-}\pi)}\lambda_{(V+A)_\parallel^{\mathrm{adj}}}-\frac{1}{6N_{\mathrm{c}}}\lambda^2_{(V+A)_\parallel^{\mathrm{adj}}}+\frac{4}{3}\lambda_{(\sigma\text{-}\pi)}\lambda_{(V+A)_\parallel}-\frac{8}{3}\lambda_{(\sigma\text{-}\pi)}\lambda_{(V+A)_\perp}\\
&+\frac{1}{3}\lambda_{(V+A)_\parallel}\lambda_{(V+A)_\parallel^{\mathrm{adj}}}-\frac{5}{3}\lambda_{(V+A)_\parallel^{\mathrm{adj}}}\lambda_{(V+A)_\perp}\Big)l^{(\mathrm{F})}_{\perp\pm}(\tau,0,-\mathrm{i}\tilde{\mu}_\tau)\,,
\end{aligned}
$$

$$
\begin{aligned}
&\partial_t \lambda_{(V-A)^{\mathrm{adj}}_{\perp}} = \\
&2\lambda_{(V-A)^{\mathrm{adj}}_{\perp}} + 64 v_4 \Big(-2N_{\mathrm{c}} \lambda_{\mathrm{csc}} \lambda_{(V-A)^{\mathrm{adj}}_{\perp}} - N_{\mathrm{c}} \lambda^2_{\mathrm{csc}} - \frac{5}{4} N_{\mathrm{c}} \lambda^2_{(V-A)^{\mathrm{adj}}_{\perp}} + \frac{2}{N_{\mathrm{c}}} \lambda^2_{(V-A)^{\mathrm{adj}}_{\perp}} \\
&+ 3\lambda_{\mathrm{csc}} \lambda_{(V-A)^{\mathrm{adj}}_{\perp}} + 2\lambda^2_{\mathrm{csc}} - 2\lambda_{(\sigma\text{-}\pi)} \lambda_{(V+A)^{\mathrm{adj}}_{\parallel}} + 2\lambda^2_{(\sigma\text{-}\pi)} + 2\lambda_{(V-A)_{\parallel}} \lambda_{(V-A)^{\mathrm{adj}}_{\perp}} \\
&- 4\lambda_{(V-A)_{\perp}} \lambda_{(V-A)^{\mathrm{adj}}_{\perp}} + \lambda^2_{(V-A)^{\mathrm{adj}}_{\perp}} + \lambda^2_{(V+A)^{\mathrm{adj}}_{\parallel}} \Big) l^{(\mathrm{F})}_{\parallel +}(\tau, 0, -\mathrm{i}\tilde{\mu}_\tau) \\
&+ 64 v_4 \Big(-\frac{4}{N_{\mathrm{c}}} \lambda_{(\sigma\text{-}\pi)} \lambda_{(S+P)^{\mathrm{adj}}_{-}} - \frac{8}{N_{\mathrm{c}}} \lambda_{(S+P)_{-}} \lambda_{(S+P)^{\mathrm{adj}}_{-}} - \frac{4}{N_{\mathrm{c}}} \lambda^2_{(S+P)^{\mathrm{adj}}_{-}} + \frac{2}{N^2_{\mathrm{c}}} \lambda^2_{(S+P)^{\mathrm{adj}}_{-}} \\
&- \frac{1}{2N_{\mathrm{c}}} \lambda^2_{(V-A)^{\mathrm{adj}}_{\perp}} + 8\lambda_{(\sigma\text{-}\pi)} \lambda_{(S+P)_{-}} + 4\lambda_{(\sigma\text{-}\pi)} \lambda_{(S+P)^{\mathrm{adj}}_{-}} + 2\lambda^2_{(\sigma\text{-}\pi)} + 8\lambda_{(S+P)_{-}} \lambda_{(S+P)^{\mathrm{adj}}_{-}} \\
&+ 8\lambda^2_{(S+P)_{-}} + 2\lambda^2_{(S+P)^{\mathrm{adj}}_{-}} - \lambda_{(V-A)_{\parallel}} \lambda_{(V-A)^{\mathrm{adj}}_{\perp}} + \lambda_{(V-A)_{\perp}} \lambda_{(V-A)^{\mathrm{adj}}_{\perp}} \Big) l^{(\mathrm{F})}_{\parallel \pm}(\tau, 0, -\mathrm{i}\tilde{\mu}_\tau) \\
&+ 64 v_4 \Big(\frac{4}{3} N_{\mathrm{c}} \lambda_{\mathrm{csc}} \lambda_{(V-A)^{\mathrm{adj}}_{\perp}} + \frac{N_{\mathrm{c}}}{3} \lambda^2_{\mathrm{csc}} + \frac{13}{12} N_{\mathrm{c}} \lambda^2_{(V-A)^{\mathrm{adj}}_{\perp}} - \frac{7}{3N_{\mathrm{c}}} \lambda^2_{(V-A)^{\mathrm{adj}}_{\perp}} - \lambda_{\mathrm{csc}} \lambda_{(V-A)^{\mathrm{adj}}_{\perp}} \\
&- \frac{2}{3} \lambda^2_{\mathrm{csc}} + 2\lambda_{(\sigma\text{-}\pi)} \lambda_{(V+A)^{\mathrm{adj}}_{\parallel}} - \frac{2}{3} \lambda^2_{(\sigma\text{-}\pi)} - \frac{4}{3} \lambda_{(V-A)_{\parallel}} \lambda_{(V-A)^{\mathrm{adj}}_{\perp}} + \frac{14}{3} \lambda_{(V-A)_{\perp}} \lambda_{(V-A)^{\mathrm{adj}}_{\perp}} \\
&+ \frac{1}{3} \lambda^2_{(V-A)^{\mathrm{adj}}_{\perp}} - \lambda^2_{(V+A)^{\mathrm{adj}}_{\parallel}} \Big) l^{(\mathrm{F})}_{\perp +}(\tau, 0, -\mathrm{i}\tilde{\mu}_\tau) \\
&+ 64 v_4 \Big(\frac{4}{3N_{\mathrm{c}}} \lambda_{(\sigma\text{-}\pi)} \lambda_{(S+P)^{\mathrm{adj}}_{-}} + \frac{8}{3N_{\mathrm{c}}} \lambda_{(S+P)_{-}} \lambda_{(S+P)^{\mathrm{adj}}_{-}} + \frac{4}{3N_{\mathrm{c}}} \lambda^2_{(S+P)^{\mathrm{adj}}_{-}} - \frac{2}{3N^2_{\mathrm{c}}} \lambda^2_{(S+P)^{\mathrm{adj}}_{-}} \\
&+ \frac{1}{6N_{\mathrm{c}}} \lambda^2_{(V-A)^{\mathrm{adj}}_{\perp}} - \frac{8}{3} \lambda_{(\sigma\text{-}\pi)} \lambda_{(S+P)_{-}} - \frac{4}{3} \lambda_{(\sigma\text{-}\pi)} \lambda_{(S+P)^{\mathrm{adj}}_{-}} - \frac{2}{3} \lambda^2_{(\sigma\text{-}\pi)} - \frac{8}{3} \lambda_{(S+P)_{-}} \lambda_{(S+P)^{\mathrm{adj}}_{-}} \\
&- \frac{8}{3} \lambda^2_{(S+P)_{-}} - \frac{2}{3} \lambda^2_{(S+P)^{\mathrm{adj}}_{-}} + \frac{1}{3} \lambda_{(V-A)_{\parallel}} \lambda_{(V-A)^{\mathrm{adj}}_{\perp}} - \frac{1}{3} \lambda_{(V-A)_{\perp}} \lambda_{(V-A)^{\mathrm{adj}}_{\perp}} \Big) l^{(\mathrm{F})}_{\perp \pm}(\tau, 0, -\mathrm{i}\tilde{\mu}_\tau)\,.
\end{aligned}
$$

BIBLIOGRAPHY

[1] F. Englert and R. Brout, “Broken Symmetry and the Mass of Gauge Vector Mesons,” *Phys. Rev. Lett.* **13** (1964) 321–323.

[2] P. W. Higgs, “Broken symmetries, massless particles and gauge fields,” *Phys. Lett.* **12** (1964) 132–133.

[3] P. W. Higgs, “Broken Symmetries and the Masses of Gauge Bosons,” *Phys. Rev. Lett.* **13** (1964) 508–509.

[4] G. S. Guralnik, C. R. Hagen, and T. W. B. Kibble, “Global Conservation Laws and Massless Particles,” *Phys. Rev. Lett.* **13** (1964) 585–587.

[5] C. P. Burgess and G. D. Moore, *The Standard Model: A Primer*. Cambridge University Press, 2006.

[6] K. Garrett and G. Duda, “Dark Matter: A Primer,” *Adv. Astron.* **2011** (2011) 968283.

[7] **ATLAS** Collaboration, G. Aad *et al.*, “Observation of a new particle in the search for the Standard Model Higgs boson with the ATLAS detector at the LHC,” *Phys. Lett. B* **716** (2012) 1–29.

[8] **CMS** Collaboration, S. Chatrchyan *et al.*, “Observation of a new boson at a mass of 125 GeV with the CMS experiment at the LHC,” *Phys. Lett. B* **716** (2012) 30–61.

[9] M. Gell-Mann, “A Schematic Model of Baryons and Mesons,” *Phys. Lett.* **8** (1964) 214–215.

[10] G. Zweig, “An SU(3) model for strong interaction symmetry and its breaking. Version 1,” *CERN-TH-401* (1964) .

[11] G. Zweig, “An SU(3) model for strong interaction symmetry and its breaking. Version 2,” *CERN-TH-412* (1964) .

[12] W. E. Lamb and P. Kusch, “Physics 1955,” in *Physics 1942–1962*, pp. 281 – 312. Elsevier, 2013.

[13] M. Gell-Mann, “The Eightfold Way: A Theory of strong interaction symmetry,” *CTSL-20, TID-12608* (1961) .

[14] Y. Ne’eman, “Derivation of strong interactions from a gauge invariance,” *Nuclear Physics* **26** (1961) 222–229.

[15] M. Breidenbach *et al.*, “Observed Behavior of Highly Inelastic Electron-Proton Scattering,” *Phys. Rev. Lett.* **23** (1969) 935–939.

[16] E. D. Bloom *et al.*, “High-Energy Inelastic $e - p$ Scattering at 6° and 10°,” *Phys. Rev. Lett.* **23** (1969) 930–934.

[17] R. E. Taylor, “Deep inelastic scattering: The Early years,” *Rev. Mod. Phys.* **63** (1991) 573–595.

[18] H. W. Kendall, “Deep inelastic scattering: Experiments on the proton and the observation,” *Rev. Mod. Phys.* **63** (1991) 597–614.

[19] J. I. Friedman, “Deep inelastic scattering: Comparisons with the quark model,” *Rev. Mod. Phys.* **63** (1991) 615–629.

[20] J. J. Aubert *et al.*, “Experimental Observation of a Heavy Particle J,” *Phys. Rev. Lett.* **33** (1974) 1404–1406.

[21] J. E. Augustin *et al.*, "Discovery of a narrow resonance in e^+e^- annihilation," *Phys. Rev. Lett.* **33** (1974) 1406–1408.

[22] J. D. Bjorken and S. L. Glashow, "Elementary Particles and SU(4)," *Phys. Lett.* **11** (1964) 255–257.

[23] D. Griffiths, *Introduction to Elementary Particles.* Wiley-VCH, 2 ed., 2008.

[24] S. W. Herb *et al.*, "Observation of a Dimuon Resonance at 9.5 GeV in 400-GeV Proton-Nucleus Collisions," *Phys. Rev. Lett.* **39** (1977) 252–255.

[25] **CDF** Collaboration, F. Abe *et al.*, "Observation of top quark production in $\bar{p}p$ collisions," *Phys. Rev. Lett.* **74** (1995) 2626–2631.

[26] **D0** Collaboration, S. Abachi *et al.*, "Observation of the top quark," *Phys. Rev. Lett.* **74** (1995) 2632–2637.

[27] O. W. Greenberg, "Spin and Unitary Spin Independence in a Paraquark Model of Baryons and Mesons," *Phys. Rev. Lett.* **13** (1964) 598–602.

[28] C.-N. Yang and R. L. Mills, "Conservation of Isotopic Spin and Isotopic Gauge Invariance," *Phys. Rev.* **96** (1954) 191–195.

[29] R. Mills, "Gauge fields," *Am. J. Phys.* **57** (1989) 493–507.

[30] J. R. Ellis, M. K. Gaillard, and G. G. Ross, "Search for Gluons in e^+e^- Annihilation," *Nucl. Phys. B* **111** (1976) 253. [Erratum: Nucl. Phys. B 130 (1977) 516].

[31] **TASSO** Collaboration, R. Brandelik *et al.*, "Evidence for Planar Events in e^+e^- Annihilation at High-Energies," *Phys. Lett. B* **86** (1979) 243–249.

[32] **PLUTO** Collaboration, C. Berger *et al.*, "Evidence for Gluon Bremsstrahlung in e^+e^- Annihilations at High-Energies," *Phys. Lett. B* **86** (1979) 418–425.

[33] **JADE** Collaboration, W. Bartel *et al.*, "Observation of Planar Three Jet Events in e^+e^- Annihilation and Evidence for Gluon Bremsstrahlung," *Phys. Lett. B* **91** (1980) 142–147.

[34] D. P. Barber *et al.*, "Discovery of Three Jet Events and a Test of Quantum Chromodynamics at PETRA Energies," *Phys. Rev. Lett.* **43** (1979) 830.

[35] D. J. Gross and F. Wilczek, "Ultraviolet Behavior of Nonabelian Gauge Theories," *Phys. Rev. Lett.* **30** (1973) 1343–1346.

[36] H. D. Politzer, "Reliable Perturbative Results for Strong Interactions?," *Phys. Rev. Lett.* **30** (1973) 1346–1349.

[37] S. Coleman and D. Gross, "Price of asymptotic freedom," *Phys. Rev. Lett.* **31** (1973) 851–854.

[38] S. Bethke, "The 2009 Wolrd Average of $\alpha_s(M_Z)$," *Eur. Phys. J. C* **64** (2009) 689–703.

[39] **Particle Data Group** Collaboration, M. Tanabashi *et al.*, "Review of Particle Physics," *Phys. Rev. D* **98** (2018) 030001.

[40] J. Greensite, "An introduction to the confinement problem," *Lect. Notes Phys.* **821** (2011) 1–211.

[41] N. Brambilla *et al.*, "QCD and Strongly Coupled Gauge Theories: Challenges and Perspectives," *Eur. Phys. J. C* **74** (2014) 2981.

[42] G. S. Bali, "QCD forces and heavy quark bound states," *Phys. Rept.* **343** (2001) 1–136.

[43] J. Greensite, "The Confinement problem in lattice gauge theory," *Prog. Part. Nucl. Phys.* **51** (2003) 1.

[44] R. Alkofer and J. Greensite, "Quark Confinement: The Hard Problem of Hadron Physics," *J. Phys. G* **34** (2007) .

[45] Y. Nambu and G. Jona-Lasinio, "Dynamical model of elementary particles based on an analogy with superconductivity. I," *Phys. Rev.* **122** (1961) 345–358.

[46] Y. Nambu and G. Jona-Lasinio, "Dynamical model of elementary particles based on an analogy with superconductivity. II," *Phys. Rev.* **124** (1961) 246–254.

[47] S. Coleman, “The invariance of the vacuum is the invariance of the world,” *J. Math. Phys.* **7** (1966) 787–787.

[48] J. Goldstone, “Field Theories with Superconductor Solutions,” *Nuovo Cim.* **19** (1961) 154–164.

[49] J. Goldstone, A. Salam, and S. Weinberg, “Broken Symmetries,” *Phys. Rev.* **127** (1962) 965–970.

[50] P. Braun-Munzinger and J. Wambach, “The Phase Diagram of Strongly-Interacting Matter,” *Rev. Mod. Phys.* **81** (2009) 1031–1050.

[51] K. Fukushima and T. Hatsuda, “The phase diagram of dense QCD,” *Rept. Prog. Phys.* **74** (2011) 014001.

[52] D. J. Schwarz, “Evolution of gravitational waves through cosmological transitions,” *Mod. Phys. Lett. A* **13** (1998) 2771–2778.

[53] A. Riotto and M. Trodden, “Recent progress in baryogenesis,” *Ann. Rev. Nucl. Part. Sci.* **49** (1999) 35–75.

[54] D. Boyanovsky, H. J. de Vega, and D. J. Schwarz, “Phase transitions in the early and the present universe,” *Ann. Rev. Nucl. Part. Sci.* **56** (2006) 441–500.

[55] M. Hindmarsh and O. Philipsen, “WIMP dark matter and the QCD equation of state,” *Phys. Rev. D* **71** (2005) 087302.

[56] G. Baym, T. Hatsuda, T. Kojo, P. D. Powell, Y. Song, and T. Takatsuka, “From hadrons to quarks in neutron stars: a review,” *Rept. Prog. Phys.* **81** (2018) 056902.

[57] L. Evans and P. Bryant, “LHC Machine,” *JINST* **3** (2008) S08001.

[58] P. Jacobs and X.-N. Wang, “Matter in extremis: Ultrarelativistic nuclear collisions at RHIC,” *Prog. Part. Nucl. Phys.* **54** (2005) 443–534.

[59] B. Müller and J. L. Nagle, “Results from the relativistic heavy ion collider,” *Ann. Rev. Nucl. Part. Sci.* **56** (2006) 93–135.

[60] B. Müller, J. Schukraft, and B. Wyslouch, “First Results from Pb+Pb collisions at the LHC,” *Ann. Rev. Nucl. Part. Sci.* **62** (2012) 361–386.

[61] B. Müller, “Investigation of Hot QCD Matter: Theoretical Aspects,” *Phys. Scripta* **T158** (2013) 014004.

[62] C. Ratti, “Lattice QCD and heavy ion collisions: a review of recent progress,” *Rept. Prog. Phys.* **81** (2018) 084301.

[63] S. Sharma, “Recent Progress on the QCD Phase Diagram,” *PoS* **LATTICE2018** (2019) 009.

[64] Y. Aoki, G. Endrodi, Z. Fodor, S. D. Katz, and K. K. Szabo, “The order of the quantum chromodynamics transition predicted by the standard model of particle physics,” *Nature* **443** (2006) 675–678.

[65] A. Bazavov *et al.*, “The chiral and deconfinement aspects of the QCD transition,” *Phys. Rev. D* **85** (2012) 054503.

[66] S. Borsanyi, Z. Fodor, C. Hoelbling, S. D. Katz, S. Krieg, and K. K. Szabo, “Full result for the QCD equation of state with 2+1 flavors,” *Phys. Lett. B* **730** (2014) 99–104.

[67] **HotQCD** Collaboration, A. Bazavov *et al.*, “Equation of state in (2+1)-flavor QCD,” *Phys. Rev. D* **90** (2014) 094503.

[68] Y. Aoki, Z. Fodor, S. D. Katz, and K. K. Szabo, “The QCD transition temperature: results with physical masses in the continuum limit,” *Phys. Lett. B* **643** (2006) 46–54.

[69] Y. Aoki, S. Borsanyi, S. Durr, Z. Fodor, S. D. Katz, S. Krieg, and K. K. Szabo, “The QCD transition temperature: results with physical masses in the continuum limit II.,” *JHEP* **06** (2009) 088.

[70] S. Borsanyi, G. Endrodi, Z. Fodor, A. Jakovac, S. D. Katz, S. Krieg, C. Ratti, and K. K. Szabo, “The QCD equation of state with dynamical quarks,” *JHEP* **11** (2010) 077.

[71] **Wuppertal-Budapest** Collaboration, S. Borsanyi *et al.*, “Is there still any T_c mystery in lattice QCD? Results with physical masses in the continuum limit III,” *JHEP* **09** (2010) 073.

[72] **HotQCD** Collaboration, A. Bazavov *et al.*, “Chiral crossover in QCD at zero and non-zero chemical potentials,” *Phys. Lett. B* **795** (2019) 15–21.

[73] S. Borsanyi, G. Endrodi, Z. Fodor, S. D. Katz, and K. K. Szabo, “Precision SU(3) lattice thermodynamics for a large temperature range,” *JHEP* **07** (2012) 056.

[74] P. de Forcrand, “Simulating QCD at finite density,” *PoS* **LAT2009** (2009) 010.

[75] O. Philipsen, “Status of the QCD Phase Diagram from Lattice Calculations,” *Acta Phys. Polon. Supp.* **5** (2012) 825–835.

[76] G. Aarts, “Developments in lattice quantum chromodynamics for matter at high temperature and density,” *Pramana* **84** (2015) 787–799.

[77] M. A. Stephanov, K. Rajagopal, and E. V. Shuryak, “Signatures of the tricritical point in QCD,” *Phys. Rev. Lett.* **81** (1998) 4816–4819.

[78] M. A. Stephanov, K. Rajagopal, and E. V. Shuryak, “Event-by-event fluctuations in heavy ion collisions and the QCD critical point,” *Phys. Rev. D* **60** (1999) 114028.

[79] M. A. Stephanov, “Non-Gaussian fluctuations near the QCD critical point,” *Phys. Rev. Lett.* **102** (2009) 032301.

[80] M. A. Stephanov, “On the sign of kurtosis near the QCD critical point,” *Phys. Rev. Lett.* **107** (2011) 052301.

[81] S. Ejiri *et al.*, “Study of QCD thermodynamics at finite density by Taylor expansion,” *Prog. Theor. Phys. Suppl.* **153** (2004) 118–126.

[82] R. V. Gavai and S. Gupta, “QCD at finite chemical potential with six time slices,” *Phys. Rev. D* **78** (2008) 114503.

[83] S. Datta, R. V. Gavai, and S. Gupta, “The QCD Critical Point : marching towards continuum,” *Nucl. Phys. A* **904-905** (2013) 883c–886c.

[84] P. de Forcrand and O. Philipsen, “The Chiral critical line of N(f) = 2+1 QCD at zero and non-zero baryon density,” *JHEP* **01** (2007) 077.

[85] P. de Forcrand and O. Philipsen, “The Chiral critical point of N(f) = 3 QCD at finite density to the order $(\mu/T)^4$,” *JHEP* **11** (2008) 012.

[86] G. Endrodi, Z. Fodor, S. D. Katz, and K. K. Szabo, “The QCD phase diagram at nonzero quark density,” *JHEP* **04** (2011) 001.

[87] A. Bazavov *et al.*, “The QCD Equation of State to $\mathcal{O}(\mu_B^6)$ from Lattice QCD,” *Phys. Rev. D* **95** (2017) 054504.

[88] F. Karsch, “Critical behavior and net-charge fluctuations from lattice QCD,” *PoS* **CORFU2018** (2019) 163.

[89] E. Epelbaum, H.-W. Hammer, and U.-G. Meißner, “Modern Theory of Nuclear Forces,” *Rev. Mod. Phys.* **81** (2009) 1773–1825.

[90] R. Machleidt and D. R. Entem, “Chiral effective field theory and nuclear forces,” *Phys. Rept.* **503** (2011) 1–75.

[91] K. Hebeler and A. Schwenk, “Chiral three-nucleon forces and neutron matter,” *Phys. Rev. C* **82** (2010) 014314.

[92] K. Hebeler, S. K. Bogner, R. J. Furnstahl, A. Nogga, and A. Schwenk, “Improved nuclear matter calculations from chiral low-momentum interactions,” *Phys. Rev. C* **83** (2011) 031301.

[93] C. Drischler, K. Hebeler, and A. Schwenk, “Chiral interactions up to next-to-next-to-next-to-leading order and nuclear saturation,” *Phys. Rev. Lett.* **122** (2019) 042501.

[94] P. Chomaz, “The nuclear liquid gas phase transition and phase coexistence,” *AIP Conf. Proc.* **610** (2002) 167.

[95] J. C. Collins and M. J. Perry, “Superdense Matter: Neutrons Or Asymptotically Free Quarks?,” *Phys. Rev. Lett.* **34** (1975) 1353.

[96] B. C. Barrois, “Superconducting Quark Matter,” *Nucl. Phys. B* **129** (1977) 390–396.

[97] D. Bailin and A. Love, “Superfluidity and Superconductivity in Relativistic Fermion Systems,” *Phys. Rept.* **107** (1984) 325.

[98] D. T. Son, “Superconductivity by long range color magnetic interaction in high density quark matter,” *Phys. Rev. D* **59** (1999) 094019.

[99] T. Schäfer and F. Wilczek, “Superconductivity from perturbative one gluon exchange in high density quark matter,” *Phys. Rev. D* **60** (1999) 114033.

[100] D. K. Hong, V. A. Miransky, I. A. Shovkovy, and L. C. R. Wijewardhana, “Schwinger-Dyson approach to color superconductivity in dense QCD,” *Phys. Rev. D* **61** (2000) 056001. [Erratum: Phys. Rev. D 62 (2000) 059903].

[101] S. D. H. Hsu and M. Schwetz, “Magnetic interactions, the renormalization group and color superconductivity in high density QCD,” *Nucl. Phys. B* **572** (2000) 211–226.

[102] R. D. Pisarski and D. H. Rischke, “Color superconductivity in weak coupling,” *Phys. Rev. D* **61** (2000) 074017.

[103] R. D. Pisarski and D. H. Rischke, “Gaps and critical temperature for color superconductivity,” *Phys. Rev. D* **61** (2000) 051501.

[104] W. E. Brown, J. T. Liu, and H.-c. Ren, “On the perturbative nature of color superconductivity,” *Phys. Rev. D* **61** (2000) 114012.

[105] Q. Wang and D. H. Rischke, “How the quark selfenergy affects the color superconducting gap,” *Phys. Rev. D* **65** (2002) 054005.

[106] K. Rajagopal and F. Wilczek, “The Condensed matter physics of QCD,” in *At the frontier of particle physics. Handbook of QCD. Vol. 1-3*, M. Shifman and B. Ioffe, eds., pp. 2061–2151. 2000.

[107] M. G. Alford, A. Schmitt, K. Rajagopal, and T. Schäfer, “Color superconductivity in dense quark matter,” *Rev. Mod. Phys.* **80** (2008) 1455–1515.

[108] A. Schmitt, “Introduction to Superfluidity,” *Lect. Notes Phys.* **888** (2015) 1–155.

[109] M. G. Alford, K. Rajagopal, and F. Wilczek, “QCD at finite baryon density: Nucleon droplets and color superconductivity,” *Phys. Lett. B* **422** (1998) 247–256.

[110] R. Rapp, T. Schäfer, E. V. Shuryak, and M. Velkovsky, “Diquark Bose condensates in high density matter and instantons,” *Phys. Rev. Lett.* **81** (1998) 53–56.

[111] J. Bardeen, L. N. Cooper, and J. R. Schrieffer, “Microscopic theory of superconductivity,” *Phys. Rev.* **106** (1957) 162.

[112] J. Bardeen, L. N. Cooper, and J. R. Schrieffer, “Theory of superconductivity,” *Phys. Rev.* **108** (1957) 1175–1204.

[113] L. N. Cooper, “Bound electron pairs in a degenerate Fermi gas,” *Phys. Rev.* **104** (1956) 1189–1190.

[114] M. G. Alford, “Color superconducting quark matter,” *Ann. Rev. Nucl. Part. Sci.* **51** (2001) 131–160.

[115] M. Buballa, “NJL model analysis of quark matter at large density,” *Phys. Rept.* **407** (2005) 205–376.

[116] I. A. Shovkovy, “Two lectures on color superconductivity,” *Found. Phys.* **35** (2005) 1309–1358.

[117] T. Hatsuda and T. Kunihiro, “Fluctuation Effects in Hot Quark Matter: Precursors of Chiral Transition at Finite Temperature,” *Phys. Rev. Lett.* **55** (1985) 158–161.

[118] M. Asakawa and K. Yazaki, “Chiral Restoration at Finite Density and Temperature,” *Nucl. Phys. A* **504** (1989) 668–684.

[119] S. P. Klevansky, “The Nambu-Jona-Lasinio model of quantum chromodynamics,” *Rev. Mod. Phys.* **64** (1992) 649–708.

[120] K. Fukushima, "QCD matter in extreme environments," *J. Phys. G* **39** (2012) 013101.

[121] J. O. Andersen, W. R. Naylor, and A. Tranberg, "Phase diagram of QCD in a magnetic field: A review," *Rev. Mod. Phys.* **88** (2016) 025001.

[122] D. U. Jungnickel and C. Wetterich, "Effective action for the chiral quark-meson model," *Phys. Rev. D* **53** (1996) 5142–5175.

[123] J. Berges, D. U. Jungnickel, and C. Wetterich, "Two flavor chiral phase transition from nonperturbative flow equations," *Phys. Rev. D* **59** (1999) 034010.

[124] J. Berges, N. Tetradis, and C. Wetterich, "Nonperturbative renormalization flow in quantum field theory and statistical physics," *Phys. Rept.* **363** (2002) 223–386.

[125] B.-J. Schäfer and J. Wambach, "Renormalization group approach towards the QCD phase diagram," *Phys. Part. Nucl.* **39** (2008) 1025–1032.

[126] J. Braun and B. Klein, "Scaling functions for the O(4)-model in d=3 dimensions," *Phys. Rev. D* **77** (2008) 096008.

[127] H. Abuki, G. Baym, T. Hatsuda, and N. Yamamoto, "The NJL model of dense three-flavor matter with axial anomaly: the low temperature critical point and BEC-BCS diquark crossover," *Phys. Rev. D* **81** (2010) 125010.

[128] K. Kamikado, N. Strodthoff, L. von Smekal, and J. Wambach, "Fluctuations in the quark-meson model for QCD with isospin chemical potential," *Phys. Lett. B* **718** (2013) 1044–1053.

[129] M. Mitter and B.-J. Schäfer, "Fluctuations and the axial anomaly with three quark flavors," *Phys. Rev. D* **89** (2014) 054027.

[130] J. M. Pawlowski and F. Rennecke, "Higher order quark-mesonic scattering processes and the phase structure of QCD," *Phys. Rev. D* **90** (2014) 076002.

[131] J. Eser, M. Grahl, and D. H. Rischke, "Functional Renormalization Group Study of the Chiral Phase Transition Including Vector and Axial-vector Mesons," *Phys. Rev. D* **92** (2015) 096008.

[132] C. Jung, F. Rennecke, R.-A. Tripolt, L. von Smekal, and J. Wambach, "In-Medium Spectral Functions of Vector- and Axial-Vector Mesons from the Functional Renormalization Group," *Phys. Rev. D* **95** (2017) 036020.

[133] F. Rennecke and B.-J. Schäfer, "Fluctuation-induced modifications of the phase structure in (2+1)-flavor QCD," *Phys. Rev. D* **96** (2017) 016009.

[134] B. Klein, "Modeling Finite-Volume Effects and Chiral Symmetry Breaking in Two-Flavor QCD Thermodynamics," *Phys. Rept.* **707-708** (2017) 1–51.

[135] T. Yokota, T. Kunihiro, and K. Morita, "Tachyonic instability of the scalar mode prior to the QCD critical point based on the functional renormalization-group method in the two-flavor case," *Phys. Rev. D* **96** (2017) 074028.

[136] H. Zhang, D. Hou, T. Kojo, and B. Qin, "Functional renormalization group study of the quark-meson model with ω meson," *Phys. Rev. D* **96** (2017) 114029.

[137] S. Resch, F. Rennecke, and B.-J. Schäfer, "Mass sensitivity of the three-flavor chiral phase transition," *Phys. Rev. D* **99** (2019) 076005.

[138] J. Eser, F. Divotgey, M. Mitter, and D. H. Rischke, "Low-energy limit of the $O(4)$ quark-meson model from the functional renormalization group approach," *Phys. Rev. D* **98** (2018) 014024.

[139] N. Strodthoff, B.-J. Schäfer, and L. von Smekal, "Quark-meson-diquark model for two-color QCD," *Phys. Rev. D* **85** (2012) 074007.

[140] L. von Smekal, "Universal Aspects of QCD-like Theories," *Nucl. Phys. Proc. Suppl.* **228** (2012) 179–220.

[141] P. Haensel, A. Y. Potekhin, and D. G. Yakovlev, "Neutron stars 1: Equation of state and structure," *Astrophys. Space Sci. Libr.* **326** (2007) 1–619.

[142] T. Schäfer and F. Wilczek, "Continuity of quark and hadron matter," *Phys. Rev. Lett.* **82** (1999) 3956–3959.

[143] N. Yamamoto, M. Tachibana, T. Hatsuda, and G. Baym, "Phase structure, collective modes, and the axial anomaly in dense QCD," *Phys. Rev. D* **76** (2007) 074001.

[144] A. Schmitt, "Dense matter in compact stars: A pedagogical introduction," *Lect. Notes Phys.* **811** (2010) 1–111.

[145] R. Kippenhahn, A. Weigert, and A. Weiss, *Stellar Structure and Evolution.* Springer-Verlag Berlin Heidelberg, 2. ed., 2012.

[146] A. W. Alsabti and P. Murdin, eds., *Handbook of Supernovae.* Springer International Publishing, 1st ed., 2017.

[147] D. G. Yakovlev and C. J. Pethick, "Neutron star cooling," *Ann. Rev. Astron. Astrophys.* **42** (2004) 169–210.

[148] A. L. Watts *et al.*, "Colloquium: Measuring the neutron star equation of state using x-ray timing," *Rev. Mod. Phys.* **88** (2016) 021001.

[149] J. M. Lattimer and M. Prakash, "The physics of neutron stars," *Science* **304** (2004) 536–542.

[150] R. C. Tolman, "Static solutions of Einstein's field equations for spheres of fluid," *Phys. Rev.* **55** (1939) 364–373.

[151] J. R. Oppenheimer and G. M. Volkoff, "On Massive neutron cores," *Phys. Rev.* **55** (1939) 374–381.

[152] B. D. Metzger *et al.*, "Electromagnetic Counterparts of Compact Object Mergers Powered by the Radioactive Decay of R-process Nuclei," *Mon. Not. Roy. Astron. Soc.* **406** (2010) 2650.

[153] K. Hotokezaka, K. Kyutoku, H. Okawa, M. Shibata, and K. Kiuchi, "Binary Neutron Star Mergers: Dependence on the Nuclear Equation of State," *Phys. Rev. D* **83** (2011) 124008.

[154] B. D. Lackey, K. Kyutoku, M. Shibata, P. R. Brady, and J. L. Friedman, "Extracting equation of state parameters from black hole-neutron star mergers. I. Nonspinning black holes," *Phys. Rev. D* **85** (2012) 044061.

[155] A. Bauswein, H. T. Janka, and R. Oechslin, "Testing Approximations of Thermal Effects in Neutron Star Merger Simulations," *Phys. Rev. D* **82** (2010) 084043.

[156] H.-T. Janka, K. Langanke, A. Marek, G. Martinez-Pinedo, and B. Müller, "Theory of Core-Collapse Supernovae," *Phys. Rept.* **442** (2007) 38–74.

[157] A. L. Watts, "Constraining the neutron star equation of state using Pulse Profile Modeling," *AIP Conf. Proc.* **2127** (2019) 020008.

[158] P. Danielewicz, R. Lacey, and W. G. Lynch, "Determination of the equation of state of dense matter," *Science* **298** (2002) 1592–1596.

[159] P. Demorest, T. Pennucci, S. Ransom, M. Roberts, and J. Hessels, "Shapiro Delay Measurement of A Two Solar Mass Neutron Star," *Nature* **467** (2010) 1081–1083.

[160] J. Antoniadis *et al.*, "A Massive Pulsar in a Compact Relativistic Binary," *Science* **340** (2013) 6131.

[161] E. Fonseca *et al.*, "The NANOGrav Nine-year Data Set: Mass and Geometric Measurements of Binary Millisecond Pulsars," *Astrophys. J.* **832** (2016) 167.

[162] H. T. Cromartie *et al.*, "Relativistic Shapiro delay measurements of an extremely massive millisecond pulsar," arXiv:1904.06759.

[163] K. Hebeler, J. M. Lattimer, C. J. Pethick, and A. Schwenk, "Equation of state and neutron star properties constrained by nuclear physics and observation," *Astrophys. J.* **773** (2013) 11.

[164] E. Annala, T. Gorda, A. Kurkela, J. Nättilä, and A. Vuorinen, "Constraining the properties of neutron-star matter with observations," in *12th INTEGRAL conference*

and 1st AHEAD Gamma-ray workshop (INTEGRAL 2019): INTEGRAL looks AHEAD to Multi-Messenger Astrophysics Geneva, Switzerland, February 11-15, 2019. arXiv:1904.01354.

[165] F. Özel and P. Freire, "Masses, Radii, and the Equation of State of Neutron Stars," *Ann. Rev. Astron. Astrophys.* **54** (2016) 401–440.

[166] A. W. Steiner, J. M. Lattimer, and E. F. Brown, "The Neutron Star Mass-Radius Relation and the Equation of State of Dense Matter," *Astrophys. J.* **765** (2013) L5.

[167] J. M. Lattimer and A. W. Steiner, "Neutron Star Masses and Radii from Quiescent Low-Mass X-ray Binaries," *Astrophys. J.* **784** (2014) 123.

[168] A. W. Steiner, J. M. Lattimer, and E. F. Brown, "The Equation of State from Observed Masses and Radii of Neutron Stars," *Astrophys. J.* **722** (2010) 33–54.

[169] Z. Arzoumanian *et al.*, "The neutron star interior composition explorer (NICER): mission definition," in *Space Telescopes and Instrumentation 2014: Ultraviolet to Gamma Ray*, vol. 9144 of *Proc. SPIE*, p. 914420. 2014.

[170] K. C. Gendreau *et al.*, "The Neutron star Interior Composition Explorer (NICER): design and development," in *Space Telescopes and Instrumentation 2016: Ultraviolet to Gamma Ray*, vol. 9905 of *Proc. SPIE*, p. 99051H. 2016.

[171] S. Bogdanov *et al.*, "Determining the Equation of State of Cold, Dense Matter with X-ray Observations of Neutron Stars," arXiv:1903.04648.

[172] **LIGO Scientific, Virgo** Collaboration, B. P. Abbott *et al.*, "Observation of Gravitational Waves from a Binary Black Hole Merger," *Phys. Rev. Lett.* **116** (2016) 061102.

[173] **LIGO Scientific, Virgo** Collaboration, B. P. Abbott *et al.*, "GW151226: Observation of Gravitational Waves from a 22-Solar-Mass Binary Black Hole Coalescence," *Phys. Rev. Lett.* **116** (2016) 241103.

[174] **LIGO Scientific, Virgo** Collaboration, B. P. Abbott *et al.*, "GW170104: Observation of a 50-Solar-Mass Binary Black Hole Coalescence at Redshift 0.2," *Phys. Rev. Lett.* **118** (2017) 221101. [Erratum: Phys. Rev. Lett. 121 (2018) 129901].

[175] **LIGO Scientific, Virgo** Collaboration, B. P. Abbott *et al.*, "GW170608: Observation of a 19-solar-mass Binary Black Hole Coalescence," *Astrophys. J.* **851** (2017) L35.

[176] **LIGO Scientific, Virgo** Collaboration, B. P. Abbott *et al.*, "GW170814: A Three-Detector Observation of Gravitational Waves from a Binary Black Hole Coalescence," *Phys. Rev. Lett.* **119** (2017) 141101.

[177] **LIGO Scientific, Virgo** Collaboration, B. P. Abbott *et al.*, "GW170817: Observation of Gravitational Waves from a Binary Neutron Star Inspiral," *Phys. Rev. Lett.* **119** (2017) 161101.

[178] **LIGO Scientific, Virgo** Collaboration, B. P. Abbott *et al.*, "Properties of the binary neutron star merger GW170817," *Phys. Rev. X* **9** (2019) 011001.

[179] K. Takami, L. Rezzolla, and L. Baiotti, "Constraining the Equation of State of Neutron Stars from Binary Mergers," *Phys. Rev. Lett.* **113** (2014) 091104.

[180] A. Bauswein and H. T. Janka, "Measuring neutron-star properties via gravitational waves from binary mergers," *Phys. Rev. Lett.* **108** (2012) 011101.

[181] A. Bauswein, H. T. Janka, K. Hebeler, and A. Schwenk, "Equation-of-state dependence of the gravitational-wave signal from the ring-down phase of neutron-star mergers," *Phys. Rev. D* **86** (2012) 063001.

[182] E. Annala, T. Gorda, A. Kurkela, and A. Vuorinen, "Gravitational-wave constraints on the neutron-star-matter Equation of State," *Phys. Rev. Lett.* **120** (2018) 172703.

[183] C. Wetterich, "Exact evolution equation for the effective potential," *Phys. Lett. B* **301** (1993) 90–94.

[184] J. S. Schwinger, "On the Green's functions of quantized fields. 1.," *Proc. Nat. Acad. Sci.* **37** (1951) 452–455.

[185] F. J. Dyson, "The S matrix in quantum electrodynamics," *Phys. Rev.* **75** (1949) 1736–1755.

[186] J. Braun, L. M. Haas, F. Marhauser, and J. M. Pawlowski, "Phase Structure of Two-Flavor QCD at Finite Chemical Potential," *Phys. Rev. Lett.* **106** (2011) 022002.

[187] J. M. Pawlowski, "The QCD phase diagram: Results and challenges," *AIP Conf. Proc.* **1343** (2011) 75–80.

[188] C. S. Fischer, J. Luecker, and J. A. Mueller, "Chiral and deconfinement phase transitions of two-flavour QCD at finite temperature and chemical potential," *Phys. Lett. B* **702** (2011) 438–441.

[189] K. G. Wilson, "Renormalization group and critical phenomena. 1. Renormalization group and the Kadanoff scaling picture," *Phys. Rev. B* **4** (1971) 3174–3183.

[190] K. G. Wilson, "Renormalization group and critical phenomena. 2. Phase space cell analysis of critical behavior," *Phys. Rev. B* **4** (1971) 3184–3205.

[191] K. G. Wilson and J. B. Kogut, "The Renormalization group and the epsilon expansion," *Phys. Rept.* **12** (1974) 75–199.

[192] M. Mitter, J. M. Pawlowski, and N. Strodthoff, "Chiral symmetry breaking in continuum QCD," *Phys. Rev. D* **91** (2015) 054035.

[193] J. Braun, L. Fister, J. M. Pawlowski, and F. Rennecke, "From Quarks and Gluons to Hadrons: Chiral Symmetry Breaking in Dynamical QCD," *Phys. Rev. D* **94** (2016) 034016.

[194] A. K. Cyrol, L. Fister, M. Mitter, J. M. Pawlowski, and N. Strodthoff, "Landau gauge Yang-Mills correlation functions," *Phys. Rev. D* **94** (2016) 054005.

[195] A. K. Cyrol, M. Mitter, J. M. Pawlowski, and N. Strodthoff, "Non-perturbative quark, gluon and meson correlators of unquenched QCD," *Phys. Rev. D* **97** (2018) 054006.

[196] A. K. Cyrol, M. Mitter, J. M. Pawlowski, and N. Strodthoff, "Nonperturbative finite-temperature Yang-Mills theory," *Phys. Rev. D* **97** (2018) 054015.

[197] L. Corell, A. K. Cyrol, M. Mitter, J. M. Pawlowski, and N. Strodthoff, "Correlation functions of three-dimensional Yang-Mills theory from the FRG," *SciPost Phys.* **5** (2018) 066.

[198] J. Braun, M. Leonhardt, and M. Pospiech, "Fierz-complete NJL model study: Fixed points and phase structure at finite temperature and density," *Phys. Rev. D* **96** (2017) 076003.

[199] J. Braun, M. Leonhardt, and M. Pospiech, "Fierz-complete NJL model study. II. Toward the fixed-point and phase structure of hot and dense two-flavor QCD," *Phys. Rev. D* **97** (2018) 076010.

[200] J. Braun, M. Leonhardt, and J. M. Pawlowski, "Renormalization group consistency and low-energy effective theories," *SciPost Phys.* **6** (2019) 056.

[201] M. Leonhardt, M. Pospiech, B. Schallmo, J. Braun, C. Drischler, K. Hebeler, and A. Schwenk, "Symmetric nuclear matter from the strong interaction," arXiv:1907.05814.

[202] M. E. Peskin and D. V. Schroeder, *An Introduction to quantum field theory*. Addison-Wesley, Reading, USA, 1995.

[203] S. Pokorski, *Gauge Field Theories*. Cambridge Monographs on Mathematical Physics. Cambridge University Press, 2 ed., 2000.

[204] M. D. Schwartz, *Quantum Field Theory and the Standard Model*. Cambridge University Press, 2014.

[205] L. H. Ryder, *Quantum Field Theory*. Cambridge University Press, 2 ed., 1996.

[206] K. Ottnad, B. Kubis, U.-G. Meißner, and F. K. Guo, "New insights into the neutron electric dipole moment," *Phys. Lett. B* **687** (2010) 42–47.

[207] S. Scherer and M. R. Schindler, *A Primer for Chiral Perturbation Theory*. Springer, Berlin, Heidelberg, 2012.

[208] J. I. Kapusta and C. Gale, *Finite-Temperature Field Theory: Principles and Applications*. Cambridge Monographs on Mathematical Physics. Cambridge University Press, 2 ed., 2006.

[209] C. Gattringer and C. B. Lang, *Quantum Chromodynamics on the Lattice - An Introductory Presentation*. Springer, Berlin, Heidelberg, 2010.

[210] H. Lehmann, K. Symanzik, and W. Zimmermann, "Zur Formulierung quantisierter Feldtheorien," *Il Nuovo Cimento* **1** (1955) 205–225.

[211] H. Gies, "Introduction to the functional RG and applications to gauge theories," *Lect. Notes Phys.* **852** (2012) 287–348.

[212] L. D. Faddeev and V. N. Popov, "Feynman Diagrams for the Yang-Mills Field," *Phys. Lett. B* **25** (1967) 29–30.

[213] V. N. Gribov, "Quantization of Nonabelian Gauge Theories," *Nucl. Phys. B* **139** (1978) 1.

[214] W. A. Bardeen, A. J. Buras, D. W. Duke, and T. Muta, "Deep Inelastic Scattering Beyond the Leading Order in Asymptotically Free Gauge Theories," *Phys. Rev. D* **18** (1978) 3998.

[215] A. Zee, *Quantum field theory in a nutshell*. Princeton University Press, 2010.

[216] M. Le Bellac, *Thermal Field Theory*. Cambridge University Press, Cambridge, 2008.

[217] E. Noether, "Invariante Variationsprobleme.," *Nachr. Ges. Wiss. Göttingen, Math.-Phys. Kl.* **1918** (1918) 235–257.

[218] E. Noether, "Invarianten beliebiger Differentialausdrücke.," *Nachr. Ges. Wiss. Göttingen, Math.-Phys. Kl.* **1918** (1918) 37–44.

[219] C. Vafa and E. Witten, "Restrictions on Symmetry Breaking in Vector-Like Gauge Theories," *Nucl. Phys. B* **234** (1984) 173–188.

[220] S. L. Adler and W. A. Bardeen, "Absence of higher order corrections in the anomalous axial vector divergence equation," *Phys. Rev.* **182** (1969) 1517–1536.

[221] S. L. Adler, "Axial vector vertex in spinor electrodynamics," *Phys. Rev.* **177** (1969) 2426–2438.

[222] J. S. Bell and R. Jackiw, "A PCAC puzzle: $\pi^0 \to \gamma\gamma$ in the σ model," *Nuovo Cim. A* **60** (1969) 47–61.

[223] G. 't Hooft, "Symmetry Breaking Through Bell-Jackiw Anomalies," *Phys. Rev. Lett.* **37** (1976) 8–11.

[224] G. 't Hooft, "Computation of the Quantum Effects Due to a Four-Dimensional Pseudoparticle," *Phys. Rev. D* **14** (1976) 3432–3450. [Erratum: Phys. Rev. D 18 (1978) 2199].

[225] M. Kobayashi and T. Maskawa, "Chiral symmetry and η-X mixing," *Prog. Theor. Phys.* **44** (1970) 1422–1424.

[226] M. Kobayashi, H. Kondo, and T. Maskawa, "Symmetry breaking of the chiral $U(3) \otimes U(3)$ and the quark model," *Prog. Theor. Phys.* **45** (1971) 1955–1959.

[227] T. P. Cheng and L. F. Li, *Gauge theory of elementary particle physics*. Oxford Science Publications, 1984.

[228] T. D. Cohen, "Functional integrals for QCD at nonzero chemical potential and zero density," *Phys. Rev. Lett.* **91** (2003) 222001.

[229] G. Markó, U. Reinosa, and Z. Szep, "Bose-Einstein condensation and Silver Blaze property from the two-loop Φ-derivable approximation," *Phys. Rev. D* **90** (2014) 125021.

[230] N. Khan, J. M. Pawlowski, F. Rennecke, and M. M. Scherer, "The Phase Diagram of QC2D from Functional Methods," arXiv:1512.03673.

[231] W.-j. Fu and J. M. Pawlowski, "Relevance of matter and glue dynamics for baryon number fluctuations," *Phys. Rev. D* **92** (2015) 116006.

[232] D. H. Rischke, "The Quark gluon plasma in equilibrium," *Prog. Part. Nucl. Phys.* **52** (2004) 197–296.

[233] N. Iwamoto, "Quark Beta Decay and the Cooling of Neutron Stars," *Phys. Rev. Lett.* **44** (1980) 1637–1640.

[234] W. Meissner and R. Ochsenfeld, "Ein neuer Effekt bei Eintritt der Supraleitfähigkeit," *Naturwissenschaften* **21** (1933) 787–788.

[235] P. W. Anderson, "Plasmons, Gauge Invariance, and Mass," *Phys. Rev.* **130** (1963) 439–442.

[236] W. E. Brown, J. T. Liu, and H.-c. Ren, "The Transition temperature to the superconducting phase of QCD at high baryon density," *Phys. Rev. D* **62** (2000) 054016.

[237] A. Schmitt, Q. Wang, and D. H. Rischke, "When the transition temperature in color superconductors is not like in BCS theory," *Phys. Rev. D* **66** (2002) 114010.

[238] A. Schmitt, "The Ground state in a spin-one color superconductor," *Phys. Rev. D* **71** (2005) 054016.

[239] T. Schäfer and E. V. Shuryak, "Instantons in QCD," *Rev. Mod. Phys.* **70** (1998) 323–426.

[240] D. H. Rischke, D. T. Son, and M. A. Stephanov, "Asymptotic deconfinement in high density QCD," *Phys. Rev. Lett.* **87** (2001) 062001.

[241] D. H. Rischke, "Debye screening and Meissner effect in a three flavor color superconductor," *Phys. Rev. D* **62** (2000) 054017.

[242] D. H. Rischke, "Debye screening and Meissner effect in a two flavor color superconductor," *Phys. Rev. D* **62** (2000) 034007.

[243] A. Schmitt, Q. Wang, and D. H. Rischke, "Mixing and screening of photons and gluons in a color superconductor," *Phys. Rev. D* **69** (2004) 094017.

[244] M. Alford and Q.-h. Wang, "Photons in gapless color-flavor-locked quark matter," *J. Phys. G* **31** (2005) 719–738.

[245] S. Elitzur, "Impossibility of Spontaneously Breaking Local Symmetries," *Phys. Rev. D* **12** (1975) 3978–3982.

[246] R. D. Pisarski and D. H. Rischke, "Gauge invariance of the color superconducting gap on the mass shell," *Nucl. Phys. A* **702** (2002) 177–184.

[247] A. Gerhold and A. Rebhan, "Gauge dependence identities for color superconducting QCD," *Phys. Rev. D* **68** (2003) 011502.

[248] D.-f. Hou, Q. Wang, and D. H. Rischke, "Generalized Ward identity and gauge invariance of the color superconducting gap," *Phys. Rev. D* **69** (2004) 071501.

[249] O. Philipsen, "The QCD equation of state from the lattice," *Prog. Part. Nucl. Phys.* **70** (2013) 55–107.

[250] E. Epelbaum, "Nuclear Forces from Chiral Effective Field Theory: A Primer," 2010. arXiv:1001.3229.

[251] D. B. Kaplan, "Five lectures on effective field theory," 2005. arXiv:nucl-th/0510023.

[252] K. G. Wilson, "Confinement of Quarks," *Phys. Rev. D* **10** (1974) 2445–2459.

[253] K. G. Wilson, "The Origins of lattice gauge theory," *Nucl. Phys. Proc. Suppl.* **140** (2005) 3–19.

[254] I. Montvay and G. Munster, *Quantum fields on a lattice*. Cambridge Monographs on Mathematical Physics. Cambridge University Press, 1997.

[255] S. Durr *et al.*, "Ab-Initio Determination of Light Hadron Masses," *Science* **322** (2008) 1224–1227.

[256] G. Aarts, "Introductory lectures on lattice QCD at nonzero baryon number," *J. Phys. Conf. Ser.* **706** (2016) 022004.

[257] Z. Fodor and S. D. Katz, "Critical point of QCD at finite T and μ, lattice results for physical quark masses," *JHEP* **04** (2004) 050.

[258] C. R. Allton *et al.*, "Thermodynamics of two flavor QCD to sixth order in quark chemical potential," *Phys. Rev. D* **71** (2005) 054508.

[259] P. de Forcrand and O. Philipsen, "The QCD phase diagram for small densities from imaginary chemical potential," *Nucl. Phys. B* **642** (2002) 290–306.

[260] M. D'Elia and F. Sanfilippo, "Thermodynamics of two flavor QCD from imaginary chemical potentials," *Phys. Rev. D* **80** (2009) 014502.

[261] J. N. Guenther *et al.*, "The QCD equation of state at finite density from analytical continuation," *Nucl. Phys. A* **967** (2017) 720–723.

[262] J. Goswami, F. Karsch, A. Lahiri, M. Neumann, and C. Schmidt, "Critical end points in (2+1)-flavor QCD with imaginary chemical potential," *PoS* **CORFU2018** (2019) 162.

[263] A. Hasenfratz and D. Toussaint, "Canonical ensembles and nonzero density quantum chromodynamics," *Nucl. Phys. B* **371** (1992) 539–549.

[264] A. Li, A. Alexandru, K.-F. Liu, and X. Meng, "Finite density phase transition of QCD with $N_f = 4$ and $N_f = 2$ using canonical ensemble method," *Phys. Rev. D* **82** (2010) 054502.

[265] P. de Forcrand and S. Kratochvila, "Finite density QCD with a canonical approach," *Nucl. Phys. Proc. Suppl.* **153** (2006) 62–67.

[266] Z. Fodor, S. D. Katz, and C. Schmidt, "The Density of states method at non-zero chemical potential," *JHEP* **03** (2007) 121.

[267] G. Endrodi, Z. Fodor, S. D. Katz, D. Sexty, K. K. Szabo, and C. Torok, "Applying constrained simulations for low temperature lattice QCD at finite baryon chemical potential," *Phys. Rev. D* **98** (2018) 074508.

[268] G. Aarts, E. Seiler, and I.-O. Stamatescu, "The Complex Langevin method: When can it be trusted?," *Phys. Rev. D* **81** (2010) 054508.

[269] G. Aarts, "Complex Langevin dynamics and other approaches at finite chemical potential," *PoS* **LATTICE2012** (2012) 017.

[270] G. Aarts, E. Seiler, D. Sexty, and I.-O. Stamatescu, "Complex Langevin dynamics and zeroes of the fermion determinant," *JHEP* **05** (2017) 044. [Erratum: JHEP 01 (2018) 128].

[271] D. Sexty, "Simulating full QCD at nonzero density using the complex Langevin equation," *Phys. Lett. B* **729** (2014) 108–111.

[272] Z. Fodor, S. D. Katz, D. Sexty, and C. Török, "Complex Langevin dynamics for dynamical QCD at nonzero chemical potential: A comparison with multiparameter reweighting," *Phys. Rev. D* **92** (2015) 094516.

[273] S. Weinberg, "Nuclear forces from chiral Lagrangians," *Phys. Lett. B* **251** (1990) 288–292.

[274] S. Weinberg, "Effective chiral Lagrangians for nucleon - pion interactions and nuclear forces," *Nucl. Phys. B* **363** (1991) 3–18.

[275] S. Weinberg, "Three body interactions among nucleons and pions," *Phys. Lett. B* **295** (1992) 114–121.

[276] **LENPIC** Collaboration, S. Binder *et al.*, "Few-nucleon systems with state-of-the-art chiral nucleon-nucleon forces," *Phys. Rev. C* **93** (2016) 044002.

[277] A. Gezerlis, I. Tews, E. Epelbaum, M. Freunek, S. Gandolfi, K. Hebeler, A. Nogga, and A. Schwenk, "Local chiral effective field theory interactions and quantum Monte Carlo applications," *Phys. Rev. C* **90** (2014) 054323.

[278] E. Epelbaum, H. Krebs, T. A. Lähde, D. Lee, U.-G. Meißner, and G. Rupak, "Ab Initio Calculation of the Spectrum and Structure of ^{16}O," *Phys. Rev. Lett.* **112** (2014) 102501.

[279] A. Gezerlis, I. Tews, E. Epelbaum, S. Gandolfi, K. Hebeler, A. Nogga, and A. Schwenk, "Quantum Monte Carlo Calculations with Chiral Effective Field Theory Interactions," *Phys. Rev. Lett.* **111** (2013) 032501.

[280] D. Lonardoni, J. Carlson, S. Gandolfi, J. E. Lynn, K. E. Schmidt, A. Schwenk, and X. Wang, "Properties of nuclei up to $A = 16$ using local chiral interactions," *Phys. Rev. Lett.* **120** (2018) 122502.

[281] J. E. Lynn, I. Tews, J. Carlson, S. Gandolfi, A. Gezerlis, K. E. Schmidt, and A. Schwenk, "Chiral Three-Nucleon Interactions in Light Nuclei, Neutron-α Scattering, and Neutron Matter," *Phys. Rev. Lett.* **116** (2016) 062501.

[282] R. Roth, S. Binder, K. Vobig, A. Calci, J. Langhammer, and P. Navratil, "Ab Initio Calculations of Medium-Mass Nuclei with Normal-Ordered Chiral NN+3N Interactions," *Phys. Rev. Lett.* **109** (2012) 052501.

[283] I. Tews, T. Krüger, K. Hebeler, and A. Schwenk, "Neutron matter at next-to-next-to-next-to-leading order in chiral effective field theory," *Phys. Rev. Lett.* **110** (2013) 032504.

[284] K. Hebeler, J. D. Holt, J. Menendez, and A. Schwenk, "Nuclear forces and their impact on neutron-rich nuclei and neutron-rich matter," *Ann. Rev. Nucl. Part. Sci.* **65** (2015) 457–484.

[285] J. E. Lynn, I. Tews, S. Gandolfi, and A. Lovato, "Quantum Monte Carlo Methods in Nuclear Physics: Recent Advances," arXiv:1901.04868.

[286] C. Drischler, A. Carbone, K. Hebeler, and A. Schwenk, "Neutron matter from chiral two- and three-nucleon calculations up to N^{3}LO," *Phys. Rev. C* **94** (2016) 054307.

[287] C. Drischler, T. Krüger, K. Hebeler, and A. Schwenk, "Pairing in neutron matter: New uncertainty estimates and three-body forces," *Phys. Rev. C* **95** (2017) 024302.

[288] J. Hu, Y. Zhang, E. Epelbaum, U.-G. Meißner, and J. Meng, "Nuclear matter properties with nucleon-nucleon forces up to fifth order in the chiral expansion," *Phys. Rev. C* **96** (2017) 034307.

[289] P. H. Ginsparg, "First Order and Second Order Phase Transitions in Gauge Theories at Finite Temperature," *Nucl. Phys. B* **170** (1980) 388–408.

[290] T. Appelquist and R. D. Pisarski, "High-Temperature Yang-Mills Theories and Three-Dimensional Quantum Chromodynamics," *Phys. Rev. D* **23** (1981) 2305.

[291] S. Nadkarni, "Dimensional Reduction in Hot QCD," *Phys. Rev. D* **27** (1983) 917.

[292] S. Nadkarni, "Dimensional Reduction in Finite Temperature Quantum Chromodynamics. 2.," *Phys. Rev. D* **38** (1988) 3287.

[293] E. Braaten and R. D. Pisarski, "Soft Amplitudes in Hot Gauge Theories: A General Analysis," *Nucl. Phys. B* **337** (1990) 569–634.

[294] J. C. Taylor and S. M. H. Wong, "The Effective Action of Hard Thermal Loops in QCD," *Nucl. Phys. B* **346** (1990) 115–128.

[295] J. Frenkel and J. C. Taylor, "High Temperature Limit of Thermal QCD," *Nucl. Phys. B* **334** (1990) 199–216.

[296] J.-P. Blaizot and J.-Y. Ollitrault, "Collective fermionic excitations in systems with a large chemical potential," *Phys. Rev. D* **48** (1993) 1390–1408.

[297] C. Manuel, "Hard dense loops in a cold non-Abelian plasma," *Phys. Rev. D* **53** (1996) 5866–5873.

[298] J.-P. Blaizot and E. Iancu, "The Quark gluon plasma: Collective dynamics and hard thermal loops," *Phys. Rept.* **359** (2002) 355–528.

[299] K. Kajantie, M. Laine, K. Rummukainen, and Y. Schroder, "The Pressure of hot QCD up to $g^6 \ln(1/g)$," *Phys. Rev. D* **67** (2003) 105008.

[300] A. Vuorinen, "The Pressure of QCD at finite temperatures and chemical potentials," *Phys. Rev. D* **68** (2003) 054017.

[301] J. O. Andersen, L. E. Leganger, M. Strickland, and N. Su, "Three-loop HTL QCD thermodynamics," *JHEP* **08** (2011) 053.

[302] A. Kurkela, P. Romatschke, and A. Vuorinen, "Cold Quark Matter," *Phys. Rev. D* **81** (2010) 105021.

[303] B. A. Freedman and L. D. McLerran, "Fermions and Gauge Vector Mesons at Finite Temperature and Density. 1. Formal Techniques," *Phys. Rev. D* **16** (1977) 1130.

[304] B. A. Freedman and L. D. McLerran, "Fermions and Gauge Vector Mesons at Finite Temperature and Density. 3. The Ground State Energy of a Relativistic Quark Gas," *Phys. Rev. D* **16** (1977) 1169.

[305] V. Baluni, "Nonabelian Gauge Theories of Fermi Systems: Chromotheory of Highly Condensed Matter," *Phys. Rev. D* **17** (1978) 2092.

[306] T. Gorda, A. Kurkela, P. Romatschke, M. Säppi, and A. Vuorinen, "Next-to-Next-to-Next-to-Leading Order Pressure of Cold Quark Matter: Leading Logarithm," *Phys. Rev. Lett.* **121** (2018) 202701.

[307] A. Kurkela and A. Vuorinen, "Cool quark matter," *Phys. Rev. Lett.* **117** (2016) 042501.

[308] A. Ipp, K. Kajantie, A. Rebhan, and A. Vuorinen, "The Pressure of deconfined QCD for all temperatures and quark chemical potentials," *Phys. Rev. D* **74** (2006) 045016.

[309] A. Kurkela, E. S. Fraga, J. Schaffner-Bielich, and A. Vuorinen, "Constraining neutron star matter with Quantum Chromodynamics," *Astrophys. J.* **789** (2014) 127.

[310] E. Annala, T. Gorda, A. Kurkela, J. Nättilä, and A. Vuorinen, "Quark-matter cores in neutron stars," arXiv:1903.09121.

[311] M. Laine and A. Vuorinen, "Basics of Thermal Field Theory," *Lect. Notes Phys.* **925** (2016) 1–281.

[312] A. Rebhan, "Hard thermal loops and QCD thermodynamics," in *QCD perspectives on hot and dense matter. Proceedings, NATO Advanced Study Institute, Summer School, Cargese, France, August 6-18, 2001*, pp. 327–351. arXiv:hep-ph/0111341.

[313] U. Kraemmer and A. Rebhan, "Advances in perturbative thermal field theory," *Rept. Prog. Phys.* **67** (2004) 351.

[314] S. Floerchinger and C. Wetterich, "Chemical freeze-out in heavy ion collisions at large baryon densities," *Nucl. Phys. A* **890-891** (2012) 11–24.

[315] M. Drews and W. Weise, "Functional renormalization group approach to neutron matter," *Phys. Lett. B* **738** (2014) 187–190.

[316] M. Drews and W. Weise, "From asymmetric nuclear matter to neutron stars: a functional renormalization group study," *Phys. Rev. C* **91** (2015) 035802.

[317] J. Weyrich, N. Strodthoff, and L. von Smekal, "Chiral mirror-baryon-meson model and nuclear matter beyond mean-field approximation," *Phys. Rev. C* **92** (2015) 015214.

[318] P. N. Meisinger and M. C. Ogilvie, "Finite temperature quark confinement," *Phys. Lett. B* **407** (1997) 297–302.

[319] R. D. Pisarski, "Quark gluon plasma as a condensate of SU(3) Wilson lines," *Phys. Rev. D* **62** (2000) 111501.

[320] C. Ratti, M. A. Thaler, and W. Weise, "Phases of QCD: Lattice thermodynamics and a field theoretical model," *Phys. Rev. D* **73** (2006) 014019.

[321] K. Fukushima, "Chiral effective model with the Polyakov loop," *Phys. Lett. B* **591** (2004) 277–284.

[322] S. Roessner, C. Ratti, and W. Weise, "Polyakov loop, diquarks and the two-flavour phase diagram," *Phys. Rev. D* **75** (2007) 034007.

[323] B.-J. Schäfer, J. M. Pawlowski, and J. Wambach, "The Phase Structure of the Polyakov–Quark-Meson Model," *Phys. Rev. D* **76** (2007) 074023.

[324] V. Skokov, B. Stokic, B. Friman, and K. Redlich, “Meson fluctuations and thermodynamics of the Polyakov loop extended quark-meson model,” *Phys. Rev. C* **82** (2010) 015206.

[325] V. Skokov, B. Friman, and K. Redlich, “Quark number fluctuations in the Polyakov loop-extended quark-meson model at finite baryon density,” *Phys. Rev. C* **83** (2011) 054904.

[326] T. K. Herbst, J. M. Pawlowski, and B.-J. Schäfer, “The phase structure of the Polyakov–quark–meson model beyond mean field,” *Phys. Lett. B* **696** (2011) 58–67.

[327] P. D. Powell and G. Baym, “Axial anomaly and the three-flavor Nambu–Jona-Lasinio model with confinement: Constructing the QCD phase diagram,” *Phys. Rev. D* **85** (2012) 074003.

[328] P. D. Powell and G. Baym, “Asymmetric pairing of realistic mass quarks and color neutrality in the Polyakov-Nambu-Jona-Lasinio model of QCD,” *Phys. Rev. D* **88** (2013) 014012.

[329] N. Strodthoff and L. von Smekal, “Polyakov-Quark-Meson-Diquark Model for two-color QCD,” *Phys. Lett. B* **731** (2014) 350–357.

[330] L. M. Haas, R. Stiele, J. Braun, J. M. Pawlowski, and J. Schaffner-Bielich, “Improved Polyakov-loop potential for effective models from functional calculations,” *Phys. Rev. D* **87** (2013) 076004.

[331] R. D. Pisarski and V. V. Skokov, “Chiral matrix model of the semi-QGP in QCD,” *Phys. Rev. D* **94** (2016) 034015.

[332] K. Fukushima and V. Skokov, “Polyakov loop modeling for hot QCD,” *Prog. Part. Nucl. Phys.* **96** (2017) 154–199.

[333] J. Braun, “Fermion Interactions and Universal Behavior in Strongly Interacting Theories,” *J. Phys. G* **39** (2012) 033001.

[334] J. Braun and T. K. Herbst, “On the Relation of the Deconfinement and the Chiral Phase Transition in Gauge Theories with Fundamental and Adjoint Matter,” arXiv:1205.0779.

[335] P. Springer, J. Braun, S. Rechenberger, and F. Rennecke *EPJ Web Conf.* **137** (2017) 03022.

[336] J. Jaeckel and C. Wetterich, “Flow equations without mean field ambiguity,” *Phys. Rev. D* **68** (2003) 025020.

[337] J. M. Pawlowski, “Aspects of the functional renormalisation group,” *Ann. Phys.* **322** (2007) 2831–2915.

[338] R. Alkofer and L. von Smekal, “The Infrared behavior of QCD Green’s functions: Confinement dynamical symmetry breaking, and hadrons as relativistic bound states,” *Phys. Rept.* **353** (2001) 281.

[339] P. Maris and C. D. Roberts, “Dyson-Schwinger equations: A Tool for hadron physics,” *Int. J. Mod. Phys. E* **12** (2003) 297–365.

[340] C. S. Fischer, “Infrared properties of QCD from Dyson-Schwinger equations,” *J. Phys. G* **32** (2006) R253–R291.

[341] D. Binosi, L. Chang, J. Papavassiliou, and C. D. Roberts, “Bridging a gap between continuum-QCD and ab initio predictions of hadron observables,” *Phys. Lett. B* **742** (2015) 183–188.

[342] M. Q. Huber, “Correlation functions of three-dimensional Yang-Mills theory from Dyson-Schwinger equations,” *Phys. Rev. D* **93** (2016) 085033.

[343] R. Williams, C. S. Fischer, and W. Heupel, “Light mesons in QCD and unquenching effects from the 3PI effective action,” *Phys. Rev. D* **93** (2016) 034026.

[344] J. Berges, “N-particle irreducible effective action techniques for gauge theories,” *Phys. Rev. D* **70** (2004) 105010.

[345] J. Berges, S. Borsanyi, U. Reinosa, and J. Serreau, "Nonperturbative renormalization for 2PI effective action techniques," *Ann. Phys.* **320** (2005) 344–398.

[346] D. F. Litim, "Optimization of the exact renormalization group," *Phys. Lett. B* **486** (2000) 92–99.

[347] D. F. Litim, "Mind the gap," *Int. J. Mod. Phys. A* **16** (2001) 2081–2088.

[348] D. F. Litim, "Optimized renormalization group flows," *Phys. Rev. D* **64** (2001) 105007.

[349] M. Bonini, M. D'Attanasio, and G. Marchesini, "BRS symmetry for Yang-Mills theory with exact renormalization group," *Nucl. Phys. B* **437** (1995) 163–186.

[350] U. Ellwanger, "Flow equations and BRS invariance for Yang-Mills theories," *Phys. Lett. B* **335** (1994) 364–370.

[351] U. Ellwanger, M. Hirsch, and A. Weber, "Flow equations for the relevant part of the pure Yang-Mills action," *Z. Phys. C* **69** (1996) 687–698.

[352] M. Reuter, "Effective average actions and nonperturbative evolution equations," in *5th Hellenic School and Workshops on Elementary Particle Physics (CORFU 1995) Corfu, Greece, September 3-24, 1995*. arXiv:hep-th/9602012.

[353] M. Reuter and C. Wetterich, "Gluon condensation in nonperturbative flow equations," *Phys. Rev. D* **56** (1997) 7893–7916.

[354] F. Freire, D. F. Litim, and J. M. Pawlowski, "Gauge invariance and background field formalism in the exact renormalization group," *Phys. Lett. B* **495** (2000) 256–262.

[355] T. R. Morris, "A Gauge invariant exact renormalization group II," *JHEP* **12** (2000) 012.

[356] O. J. Rosten, "A Manifestly gauge invariant and universal calculus for SU(N) Yang-Mills," *Int. J. Mod. Phys. A* **21** (2006) 4627–4762.

[357] S. Arnone, T. R. Morris, and O. J. Rosten, "A Generalised manifestly gauge invariant exact renormalisation group for SU(N) Yang-Mills," *Eur. Phys. J. C* **50** (2007) 467–504.

[358] J. M. Pawlowski, "Geometrical effective action and Wilsonian flows," arXiv:hep-th/0310018.

[359] L. F. Abbott, "The Background Field Method Beyond One Loop," *Nucl. Phys. B* **185** (1981) 189–203.

[360] L. F. Abbott, "Introduction to the Background Field Method," *Acta Phys. Polon. B* **13** (1982) 33.

[361] M. Reuter and C. Wetterich, "Effective average action for gauge theories and exact evolution equations," *Nucl. Phys. B* **417** (1994) 181–214.

[362] J. M. Pawlowski, "On Wilsonian flows in gauge theories," *Int. J. Mod. Phys. A* **16** (2001) 2105–2110.

[363] D. F. Litim and J. M. Pawlowski, "Wilsonian flows and background fields," *Phys. Lett. B* **546** (2002) 279–286.

[364] H. Gies, "Running coupling in Yang-Mills theory: A flow equation study," *Phys. Rev. D* **66** (2002) 025006.

[365] J. M. Pawlowski, M. M. Scherer, R. Schmidt, and S. J. Wetzel, "Physics and the choice of regulators in functional renormalisation group flows," *Ann. Phys.* **384** (2017) 165–197.

[366] J. Braun, K. Schwenzer, and H.-J. Pirner, "Linking the quark meson model with QCD at high temperature," *Phys. Rev. D* **70** (2004) 085016.

[367] B.-J. Schäfer and J. Wambach, "The Phase diagram of the quark meson model," *Nucl. Phys. A* **757** (2005) 479–492.

[368] J.-P. Blaizot, A. Ipp, R. Mendez-Galain, and N. Wschebor, "Perturbation theory and non-perturbative renormalization flow in scalar field theory at finite temperature," *Nucl. Phys. A* **784** (2007) 376–406.

[369] D. F. Litim and J. M. Pawlowski, "Non-perturbative thermal flows and resummations," *JHEP* **11** (2006) 026.

[370] J. Braun, “Thermodynamics of QCD low-energy models and the derivative expansion of the effective action,” *Phys. Rev. D* **81** (2010) 016008.

[371] A. J. Helmboldt, J. M. Pawlowski, and N. Strodthoff, “Towards quantitative precision in the chiral crossover: masses and fluctuation scales,” *Phys. Rev. D* **91** (2015) 054010.

[372] J. M. Pawlowski and N. Strodthoff, “Real time correlation functions and the functional renormalization group,” *Phys. Rev. D* **92** (2015) 094009.

[373] J. M. Pawlowski, N. Strodthoff, and N. Wink, “Finite temperature spectral functions in the O(N)-model,” *Phys. Rev. D* **98** (2018) 074008.

[374] S. Diehl, H. Gies, J. M. Pawlowski, and C. Wetterich, “Flow Equations for the BCS-BEC Crossover,” *Phys. Rev.* **A76** (2007) 021602.

[375] I. Boettcher, J. Braun, T. K. Herbst, J. M. Pawlowski, D. Roscher, and C. Wetterich, “Phase structure of spin-imbalanced unitary Fermi gases,” *Phys. Rev. A* **91** (2015) 013610.

[376] D. Roscher, J. Braun, and J. E. Drut, “Phase structure of mass- and spin-imbalanced unitary Fermi gases,” *Phys. Rev. A* **91** (2015) 053611.

[377] D. U. Jungnickel and C. Wetterich, “The Linear meson model and chiral perturbation theory,” *Eur. Phys. J. C* **2** (1998) 557–567.

[378] S. Floerchinger, “Analytic Continuation of Functional Renormalization Group Equations,” *JHEP* **05** (2012) 021.

[379] R.-A. Tripolt, N. Strodthoff, L. von Smekal, and J. Wambach, “Spectral Functions for the Quark-Meson Model Phase Diagram from the Functional Renormalization Group,” *Phys. Rev. D* **89** (2014) 034010.

[380] H. Gies and C. Wetterich, “Universality of spontaneous chiral symmetry breaking in gauge theories,” *Phys. Rev. D* **69** (2004) 025001.

[381] F. Rennecke, “Vacuum structure of vector mesons in QCD,” *Phys. Rev. D* **92** (2015) 076012.

[382] J. M. Pawlowski, “Equation of state and phase diagram of strongly interacting matter,” *Nucl. Phys. A* **931** (2014) 113–124.

[383] T. K. Herbst, M. Mitter, J. M. Pawlowski, B.-J. Schäfer, and R. Stiele, “Thermodynamics of QCD at vanishing density,” *Phys. Lett. B* **731** (2014) 248–256.

[384] J. Braun, *Functional renormalization group methods in quantum chromodynamics*. PhD thesis, Heidelberg U., 2006.

[385] R. Anglani, R. Casalbuoni, M. Ciminale, N. Ippolito, R. Gatto, M. Mannarelli, and M. Ruggieri, “Crystalline color superconductors,” *Rev. Mod. Phys.* **86** (2014) 509–561.

[386] T. Hatsuda and T. Kunihiro, “QCD phenomenology based on a chiral effective Lagrangian,” *Phys. Rept.* **247** (1994) 221–367.

[387] J. Braun, H. Gies, and D. D. Scherer, “Asymptotic safety: a simple example,” *Phys. Rev. D* **83** (2011) 085012.

[388] J. J. Rusnak and R. J. Furnstahl, “Two point fermion correlation functions at finite density,” *Z. Phys. A* **352** (1995) 345–350.

[389] J. Hubbard, “Calculation of partition functions,” *Phys. Rev. Lett.* **3** (1959) 77–80.

[390] R. Stratonovich *Dokl. Akad. Nauk.* **115** (1957) 1097.

[391] H. Gies and J. Jaeckel, “Chiral phase structure of QCD with many flavors,” *Eur. Phys. J. C* **46** (2006) 433–438.

[392] J. Braun and H. Gies, “Running coupling at finite temperature and chiral symmetry restoration in QCD,” *Phys. Lett. B* **645** (2007) 53–58.

[393] J. Braun and H. Gies, “Chiral phase boundary of QCD at finite temperature,” *JHEP* **06** (2006) 024.

[394] J. Braun, H. Gies, L. Janssen, and D. Roscher, “Phase structure of many-flavor QED$_3$,” *Phys. Rev. D* **90** (2014) 036002.

[395] D. Roscher, N. Gneist, M. M. Scherer, S. Trebst, and S. Diehl, "Cluster functional renormalization group and absence of a bilinear spin liquid in the J_1-J_2-Heisenberg model," *Phys. Rev. B* **100** (2019) 125130.

[396] H. Gies and C. Wetterich, "Renormalization flow of bound states," *Phys. Rev. D* **65** (2002) 065001.

[397] J. Braun, "The QCD Phase Boundary from Quark-Gluon Dynamics," *Eur. Phys. J. C* **64** (2009) 459–482.

[398] S. Floerchinger and C. Wetterich, "Exact flow equation for composite operators," *Phys. Lett. B* **680** (2009) 371–376.

[399] S. Floerchinger, "Exact Flow Equation for Bound States," *Eur. Phys. J. C* **69** (2010) 119–132.

[400] K.-I. Aoki and M. Yamada, "The RG flow of Nambu-Jona-Lasinio model at finite temperature and density," *Int. J. Mod. Phys. A* **30** (2015) 1550180.

[401] F. Gehring, H. Gies, and L. Janssen, "Fixed-point structure of low-dimensional relativistic fermion field theories: Universality classes and emergent symmetry," *Phys. Rev. D* **92** (2015) 085046.

[402] V. L. Berezinskii *Sov. Phys. JETP* **32** (1971) 493.

[403] V. L. Berezinskii *Sov. Phys. JETP* **34** (1972) 610.

[404] J. M. Kosterlitz and D. J. Thouless, "Ordering, metastability and phase transitions in two-dimensional systems," *J. Phys. C* **6** (1973) 1181–1203.

[405] V. A. Miransky, "Dynamics of Spontaneous Chiral Symmetry Breaking and Continuum Limit in Quantum Electrodynamics," *Nuovo Cim. A* **90** (1985) 149–170.

[406] V. A. Miransky and K. Yamawaki, "On Gauge Theories with Additional Four Fermion Interaction," *Mod. Phys. Lett. A* **4** (1989) 129–135.

[407] V. A. Miransky and K. Yamawaki, "Conformal phase transition in gauge theories," *Phys. Rev. D* **55** (1997) 5051–5066. [Erratum: Phys. Rev. D 56 (1997) 3768].

[408] J. Braun, C. S. Fischer, and H. Gies, "Beyond Miransky Scaling," *Phys. Rev. D* **84** (2011) 034045.

[409] J. D. Bjorken, "A Dynamical origin for the electromagnetic field," *Ann. Phys.* **24** (1963) 174–187.

[410] I. Bialynicki-Birula, "Quantum Electrodynamics without Electromagnetic Field," *Phys. Rev.* **130** (1963) 465–468.

[411] G. Guralnik, "Photon as a Symmetry-Breaking Solution to Field Theory. I," *Phys. Rev.* **136** (1964) B1404–B1416.

[412] T. Banks and A. Zaks, "Composite Gauge Bosons in Four Fermi Theories (Or Honey and Condensed Vectors)," *Nucl. Phys. B* **184** (1981) 303.

[413] P. Kraus and E. Tomboulis, "Photons and gravitons as Goldstone bosons, and the cosmological constant," *Phys. Rev. D* **66** (2002) 045015.

[414] W.-j. Fu, J. M. Pawlowski, F. Rennecke, and B.-J. Schäfer, "Baryon number fluctuations at finite temperature and density," *Phys. Rev. D* **94** (2016) 116020.

[415] N. Strodthoff, "Self-consistent spectral functions in the O(N) model from the functional renormalization group," *Phys. Rev. D* **95** (2017) 076002.

[416] M. A. Shifman, A. I. Vainshtein, and V. I. Zakharov, "Instanton Density in a Theory with Massless Quarks," *Nucl. Phys. B* **163** (1980) 46–56.

[417] E. V. Shuryak, "The Role of Instantons in Quantum Chromodynamics. 1. Physical Vacuum," *Nucl. Phys. B* **203** (1982) 93.

[418] J. M. Pawlowski, "Exact flow equations and the U(1) problem," *Phys. Rev. D* **58** (1998) 045011.

[419] B.-J. Schäfer and M. Wagner, "The Three-flavor chiral phase structure in hot and dense QCD matter," *Phys. Rev. D* **79** (2009) 014018.

[420] J. Berges and K. Rajagopal, "Color superconductivity and chiral symmetry restoration at nonzero baryon density and temperature," *Nucl. Phys. B* **538** (1999) 215–232.

[421] N. J. Evans, J. Hormuzdiar, S. D. H. Hsu, and M. Schwetz, "On the QCD ground state at high density," *Nucl. Phys. B* **581** (2000) 391–408.

[422] H. Gies and L. Janssen, "UV fixed-point structure of the three-dimensional Thirring model," *Phys. Rev. D* **82** (2010) 085018.

[423] A. Rebhan, "Thermal gauge field theories," *Lect. Notes Phys.* **583** (2002) 161–208.

[424] H. Gies, J. Jaeckel, and C. Wetterich, "Towards a renormalizable standard model without fundamental Higgs scalar," *Phys. Rev. D* **69** (2004) 105008.

[425] H. T. Ding *et al.*, "Chiral Phase Transition Temperature in (2+1)-Flavor QCD," *Phys. Rev. Lett.* **123** (2019) 062002.

[426] C. S. Fischer and J. Luecker, "Propagators and phase structure of $N_f = 2$ and $N_f = 2 + 1$ QCD," *Phys. Lett. B* **718** (2013) 1036–1043.

[427] C. S. Fischer, L. Fister, J. Luecker, and J. M. Pawlowski, "Polyakov loop potential at finite density," *Phys. Lett. B* **732** (2014) 273–277.

[428] C. S. Fischer, J. Luecker, and J. M. Pawlowski, "Phase structure of QCD for heavy quarks," *Phys. Rev. D* **91** (2015) 014024.

[429] F. Rennecke, *The Chiral Phase Transition of QCD.* PhD thesis, Heidelberg U., 2015.

[430] P. Springer, *Constraining low-energy models of QCD from fundamental interactions.* PhD thesis, Technische Universität München, 2016.

[431] M. D'Elia, "High-Temperature QCD: theory overview," *Nucl. Phys. A* **982** (2019) 99–105.

[432] R. Alkofer, A. Maas, W. A. Mian, M. Mitter, J. París-López, J. M. Pawlowski, and N. Wink, "Bound state properties from the functional renormalization group," *Phys. Rev. D* **99** (2019) 054029.

[433] J. Braun, F. Karbstein, S. Rechenberger, and D. Roscher, "Crystalline ground states in Polyakov-loop extended Nambu–Jona-Lasinio models," *Phys. Rev. D* **93** (2016) 014032.

[434] J. Meyer, K. Schwenzer, H.-J. Pirner, and A. Deandrea, "Renormalization group flow in large N_c," *Phys. Lett. B* **526** (2002) 79–89.

[435] V. Skokov, B. Friman, E. Nakano, K. Redlich, and B.-J. Schäfer, "Vacuum fluctuations and the thermodynamics of chiral models," *Phys. Rev. D* **82** (2010) 034029.

[436] K. Rajagopal and F. Wilczek, "Enforced electrical neutrality of the color flavor locked phase," *Phys. Rev. Lett.* **86** (2001) 3492–3495.

[437] I. A. Shovkovy and P. J. Ellis, "Thermal conductivity of dense quark matter and cooling of stars," *Phys. Rev. C* **66** (2002) 015802.

[438] T. K. Herbst, J. M. Pawlowski, and B.-J. Schäfer, "Phase structure and thermodynamics of QCD," *Phys. Rev. D* **88** (2013) 014007.

[439] R.-A. Tripolt, B.-J. Schäfer, L. von Smekal, and J. Wambach, "Low-temperature behavior of the quark-meson model," *Phys. Rev. D* **97** (2018) 034022.

[440] G. Hagen, T. Papenbrock, A. Ekström, K. A. Wendt, G. Baardsen, S. Gandolfi, M. Hjorth-Jensen, and C. J. Horowitz, "Coupled-cluster calculations of nucleonic matter," *Phys. Rev. C* **89** (2014) 014319.

[441] A. Carbone, A. Rios, and A. Polls, "Symmetric nuclear matter with chiral three-nucleon forces in the self-consistent Green's functions approach," *Phys. Rev. C* **88** (2013) 044302.

[442] L. Coraggio, J. W. Holt, N. Itaco, R. Machleidt, L. E. Marcucci, and F. Sammarruca, "Nuclear-matter equation of state with consistent two- and three-body perturbative chiral interactions," *Phys. Rev. C* **89** (2014) 044321.

[443] C. Wellenhofer, J. W. Holt, and N. Kaiser, "Thermodynamics of isospin-asymmetric nuclear matter from chiral effective field theory," *Phys. Rev. C* **92** (2015) 015801.

[444] C. Drischler, K. Hebeler, and A. Schwenk, "Asymmetric nuclear matter based on chiral two- and three-nucleon interactions," *Phys. Rev. C* **93** (2016) 054314.

[445] J. Hoppe, C. Drischler, K. Hebeler, A. Schwenk, and J. Simonis, "Probing chiral interactions up to next-to-next-to-next-to-leading order in medium-mass nuclei," *Phys. Rev. C* **100** (2019) 024318.

[446] J. Simonis, S. R. Stroberg, K. Hebeler, J. D. Holt, and A. Schwenk, "Saturation with chiral interactions and consequences for finite nuclei," *Phys. Rev. C* **96** (2017) 014303.

[447] T. D. Morris, J. Simonis, S. R. Stroberg, C. Stumpf, G. Hagen, J. D. Holt, G. R. Jansen, T. Papenbrock, R. Roth, and A. Schwenk, "Structure of the lightest tin isotopes," *Phys. Rev. Lett.* **120** (2018) 152503.

[448] E. Epelbaum, H. Krebs, and U. G. Meißner, "Improved chiral nucleon-nucleon potential up to next-to-next-to-next-to-leading order," *Eur. Phys. J. A* **51** (2015) 53.

[449] B. Schallmo. Master's thesis, Technische Universität Darmstadt (in preparation).

[450] T. Klähn *et al.*, "Constraints on the high-density nuclear equation of state from the phenomenology of compact stars and heavy-ion collisions," *Phys. Rev. C* **74** (2006) 035802.

[451] B. Liu, V. Greco, V. Baran, M. Colonna, and M. Di Toro, "Asymmetric nuclear matter: The Role of the isovector scalar channel," *Phys. Rev. C* **65** (2002) 045201.

[452] S. Typel, "Relativistic model for nuclear matter and atomic nuclei with momentum-dependent self-energies," *Phys. Rev. C* **71** (2005) 064301.

[453] E. E. Kolomeitsev and D. N. Voskresensky, "Relativistic mean-field models with effective hadron masses and coupling constants, and ρ^- condensation," *Nucl. Phys. A* **759** (2005) 373–413.

[454] E. N. E. van Dalen, C. Fuchs, and A. Faessler, "Momentum, density, and isospin dependence of the symmetric and asymmetric nuclear matter properties," *Phys. Rev. C* **72** (2005) 065803.

[455] P. Bedaque and A. W. Steiner, "Sound velocity bound and neutron stars," *Phys. Rev. Lett.* **114** (2015) 031103.

[456] S. K. Greif, G. Raaijmakers, K. Hebeler, A. Schwenk, and A. L. Watts, "Equation of state sensitivities when inferring neutron star and dense matter properties," *Mon. Not. Roy. Astron. Soc.* **485** (2019) 5363–5376.

[457] V. Koch, "Introduction to chiral symmetry," in *3rd TAPS Workshop on Electromagnetic and Mesonic Probes of Nuclear Matter Bosen, Germany*. 1995. arXiv:nucl-th/9512029.

[458] T. Kugo, *Eichtheorie*. Springer-Verlag Berlin Heidelberg (1997).

[459] O. J. Rosten, "Fundamentals of the Exact Renormalization Group," *Phys. Rept.* **511** (2012) 177–272.

[460] M. Q. Huber and J. Braun, "Algorithmic derivation of functional renormalization group equations and Dyson-Schwinger equations," *Comput. Phys. Commun.* **183** (2012) 1290–1320.

[461] A. K. Cyrol, M. Mitter, and N. Strodthoff, "FormTracer - A Mathematica Tracing Package Using FORM," *Comput. Phys. Commun.* **219** (2017) 346–352.

[462] J. A. M. Vermaseren, "New features of FORM," arXiv:math-ph/0010025.

[463] J. Kuipers, T. Ueda, J. A. M. Vermaseren, and J. Vollinga, "FORM version 4.0," *Comput. Phys. Commun.* **184** (2013) 1453–1467.

CURRICULUM VITAE

Zur Person

Name	Marc Leonhardt
Geburtsdatum	29.04.1988
Geburtsort	Offenbach a. M.
Nationalität	deutsch

Akademische Ausbildung

01/2016 – 10/2019	Promotion in Physik, im Rahmen des DFG-Sonderforschungsbereichs 1245, Institut für Kernphysik, Technische Universität Darmstadt
01/2015 – 12/2015	Wissenschaftlicher Mitarbeiter, Max-Planck-Institut für Hirnforschung, Frankfurt a. M.
10/2012 – 12/2014	Master of Science in Physik, Technische Universität Darmstadt, Thesis: *On Confinement Effects on Chiral Dynamics*, Betreuer: Professor Dr. Jens Braun
09/2011 – 04/2012	Auslandsstudium, University of Saskatchewan, Kanada *Integrated Studies Abroad Program* (DAAD)
04/2009 – 11/2012	Bachelor of Science in Physik, Technische Universität Darmstadt, Thesis: *Analyse von Spektren quantenmechanischer Systeme mittels der funktionalen Renormierungsgruppe*, Betreuer: Professor Dr. Jens Braun

Preise und Auszeichnungen

04/2018	Best Poster Prize der Wilhelm und Else Heraeus-Stiftung im Rahmen des 666. WE-Heraeus-Seminars
03/2018	Travel Prize des DFG-Sonderforschungsbereichs 1245
01/2015 – 12/2015	Stipendium der Max-Planck-Gesellschaft zur Förderung der Wissenschaften e.V.
03/2010 – 12/2014	Stipendium der Studienstiftung des deutschen Volkes
09/2011 – 04/2012	Stipendium des Deutschen Akademischen Austauschdienstes
04/2011	Auslandsstarthilfe der Gerhard Herzberg Gesellschaft

ERKLÄRUNG ZUR DISSERTATION

Gemäß §9 Promotionsordnung:

Hiermit versichere ich, dass ich die vorliegende Dissertation selbstständig angefertigt und keine anderen als die angegebenen Quellen und Hilfsmittel verwendet habe. Alle wörtlichen und paraphrasierten Zitate wurden angemessen kenntlich gemacht. Die Arbeit hat bisher noch nicht zu Prüfungszwecken gedient.

Darmstadt, den 16. Juli 2019

Marc Leonhardt